

Structural Engineering Report No. ST-07-1

**RELIABILITY-BASED PERFORMANCE-BASED
DESIGN OF RECTANGULAR
CONCRETE-FILLED STEEL TUBE (RCFT)
MEMBERS and FRAMES**

Cenk Tort and Jerome F. Hajjar

August 2007

**Department of Civil Engineering
Institute of Technology
University of Minnesota
Minneapolis, Minnesota 55455**

Acknowledgements

This work was supported by the National Science Foundation under Grant No. CMS-0084848 and by the University of Minnesota. Supercomputing resources were provided by the Minnesota Supercomputing Institute. The authors would like to thank Ms. Susan LaFore, Mr. Steven Gartner, Mr. Ryan Hopeman, Ms. Jennifer Collins, and Mr. Matthew Parkolap for their assistance with this research, Drs. Douglas Goode, Roberto Leon, Amit Varma, Shosuke Morino, and Jun Kawaguchi for providing experimental data, Drs. Donald White and Bulent Nedim Alemdar for providing the details of their computational studies, and Dr. Frank McKenna for his assistance with OpenSEES software development. Any opinions, findings, and conclusions or recommendations expressed in this work are those of the authors and do not necessarily reflect the views of the National Science Foundation.

Abstract

A computational study was conducted to develop a reliability-based performance-based design methodology for three-dimensional composite frames consisting of steel girders and braces framing into RCFT beam-columns. A new mixed finite element formulation was developed to simulate the geometrically and materially nonlinear response of both RCFT beam-columns and steel members. The RCFT beam-column element was derived with 18 degrees-of-freedom to account for the differential slip displacement between the steel tube and the concrete core. The interface of the steel tube and concrete core comprised a layer of nonlinear springs allowing shedding of force between the two media. Comprehensive constitutive relations were derived to model the material inelasticity of the steel tube, concrete core, and the steel and concrete interface under random cyclic loadings. A corresponding formulation was developed for hot-rolled wide-flange members to enable modeling of braced and unbraced composite frame structures. The constitutive relations were calibrated and verified with respect to experimental tests in the literature to account for key nonlinear phenomena such as bond breakage at the interface, cracking and confinement of concrete core, residual stress distributions, hardening, and local buckling of cold-formed steel tubes and hot-rolled steel members. The accuracy of the mixed finite element formulation along with the material constitutive relations were tested through analyzing a series RCFT and hot-rolled steel specimens from the literature and comparing the computational and experimental response parameters. The verification results confirm that the mixed finite element formulation has the capability of producing realistic simulations for RCFT beam-columns, hot-rolled steel girders, and RCFT frames subjected to three-dimensional static or transient dynamic loading. The mixed finite element formulation was then utilized to perform demand assessment and capacity assessment studies of RCFT frames. For this purpose, a series of RCFT frames were designed according to the up-to-date design specifications. Utilizing nonlinear time history analysis, the demand and capacity of these structures were quantified, documenting the key response parameters critical for composite structures. The dispersions in the analysis results due to randomness and uncertainties

were then evaluated to derive the demand and capacity factors to implement performance-based design of RCFT frames within a reliability framework.

Table of Contents

1. Introduction.....	1
1.1. Steel and Concrete Composite Columns.....	1
1.2. Performance-Based Design Methodology.....	4
1.3. Objectives.....	8
1.4. Research Scope.....	9
1.5. Overview of the Report.....	10
2. Finite Element Formulation of Rectangular Concrete-Filled Tube (RCFT) Beams, Columns and Beam-Columns.....	11
2.1. Introduction.....	11
2.2. Three-Dimensional Distributed Plasticity RCFT Beam-Column Element.....	16
2.2.1. Choice of Reference Axes.....	19
2.2.2. Kinematic Equations.....	20
2.2.3. Finite Element Discretization.....	22
2.2.4. The Equation of Equilibrium.....	25
2.2.5. The Virtual work Equation of Equilibrium.....	32
2.2.6. Updated-Lagrangian Formulation.....	37
2.2.7. Compatibility Equation.....	41
2.2.8. The Hellinger-Reissner Principle.....	42
2.2.9. Consistent Linearization of Cross-Section Equilibrium Equation.....	45
2.2.10. Consistent Linearization of Compatibility Equation.....	48
2.2.11. Consistent Linearization of Equilibrium Equation.....	52
2.2.12. Mapping of Element Forces, Displacements, and Stiffness between Natural and Global Coordinate Systems.....	65
2.2.13. Slip and Shear Constraints.....	76
2.2.14. Element Force Recovery.....	81
2.2.15. Element Stiffness Calculation.....	90
2.3. Three-Dimensional Distributed Plasticity STL Beam-Column Element.....	91
3. Uniaxial Cyclic Concrete Constitutive Model for RCFT Members.....	93
3.1. Introduction.....	93
3.2. Monotonic Compressive Response.....	95
3.3. Monotonic Tensile Response.....	101
3.4. Cyclic Response of Concrete.....	105
3.4.1. State Determination Algorithm of the Concrete Fibers.....	109
3.5. Numerical Simulation Examples for Cyclic Concrete Model.....	127
4. Uniaxial Cyclic Steel Constitutive Model for RCFT Members and Steel Girders.....	131
4.1. Introduction.....	131
4.2. Monotonic Response.....	133
4.3. Cyclic Response.....	148
4.3.1. Verification of the Cyclic Response.....	155
4.4. Steel Model for Hot-Rolled Steel Girders.....	159
4.4.1. Monotonic Response.....	160
4.4.2. Cyclic Response.....	167
5. Verification of the Mixed Finite Element Formulation.....	170

5.1. Introduction.....	170
5.2. Geometrically Nonlinear Elastic Problems.....	171
5.2.1. Euler Buckling of a Simply Supported RCFT Column	171
5.2.2. Elastic Stability of a Cantilever Column	172
5.2.3. RCFT Cantilever Under Pure Bending	173
5.2.4. RCFT Cantilever Under Transverse Tip Loading	175
5.2.5. Harrison’s Portal Frame.....	175
5.2.6. Right-Angled Simply Supported Frame	177
5.3. Geometrically and Materially Nonlinear Problems	181
5.3.1. Slip Critical Materially and Geometrically Nonlinear Problems.....	181
5.4. Materially and Geometrically Nonlinear RCFT Column Tests.....	194
5.5. Materially and Geometrically Nonlinear RCFT Beam Tests	217
5.6. Materially and Geometrically Nonlinear Proportionally-Loaded RCFT Beam- Column Tests	233
5.7. Materially and Geometrically Nonlinear Non-Proportionally-Loaded RCFT Beam- Column Tests	247
5.8. Materially and Geometrically Nonlinear Cyclically-Loaded RCFT Beam-Column Tests	261
5.9. Materially Linear and Geometrically Nonlinear Dynamically-Loaded RCFT Beam-Column Tests.....	284
5.10. Materially Linear and Geometrically Nonlinear Dynamically-Loaded RCFT Beam-Column Tests.....	286
5.11. Materially and Geometrically Nonlinear Monotonically-Loaded Steel Girders	292
5.12. Materially and Geometrically Nonlinear Cyclically-Loaded Steel Girders	296
6. Seismic Demand Evaluation of RCFT Frames	298
6.1. Introduction.....	298
6.2. Selection of Ground Motion Records	299
6.2.1. Time-History Analysis Results	304
7. Reliability Framework	335
7.1. Introduction.....	335
7.2. Treatment of Uncertainty and Randomness.....	339
7.2.1. Uncertainty of Capacity at the Local Level	340
7.2.2. Randomness of Capacity at the Local Level.....	346
7.2.3. Uncertainty of Capacity at the Global Level	347
7.2.4. Randomness of Capacity at the Global Level.....	347
7.2.5. Uncertainty and Randomness of Demand.....	347
7.3. Capacity Factors.....	348
7.4. Demand Factors	349
7.5. Confidence Level	350
7.6. Intended Performance Based-Design Methodology	350
8. Conclusion	354
8.1. Future Research Recommendations.....	363
APPENDIX A.....	365
A.1. RCFT Mixed Finite Element Formulation.....	365

A.1.1. Finite Element Discretization.....	365
A.1.2. Hellinger-Reissner Principle	366
A.1.3. Consistent Linearization of Compatibility Equation	371
A.1.4. Consistent Linearization of Equilibrium Equation	374
A.1.5. Derivation of Cross-Section Stiffness.....	380
A.2. Mapping of Element Forces, Displacements, and Stiffness between Natural and Global Coordinate Systems.....	382
A.2.1. Transformation of Element Forces	382
A.2.2. Derivation of External Stiffness Matrix.....	383
Bibliography	387

List of Tables

Table 3-1 Summary of Concrete Lateral Confinement Models (SI units).....	96
Table 3-2 Summary of Specimens for Concrete Stress-Strain Data.....	101
Table 4-1 Variation of Steel Material Properties Due to Cold Forming Process	137
Table 4-2 Specimens Selected for Calibration of the Compressive Steel Model.....	143
Table 4-3 Specimens Selected for Verification of the Compressive Steel and Concrete Model	147
Table 4-4 Steel Model Material Parameters	152
Table 4-5 Geometric and Material Properties of Representative Specimens of Low and High Slenderness Values	164
Table 5-1 Analysis Results for Cantilever RCFT Column with Axial Load.....	173
Table 5-2 Analysis Results for Harrison’s Portal Frame	178
Table 5-3 Error Analysis of Strain Distribution of the Steel Tube at 600 kN (Specimen E6, Shakir-Khalil, 1994).....	187
Table 5-4 Error Analysis of Strain Distribution of the Steel Tube at 800 kN	188
Table 5-5 Error Analysis of Strain Distribution of the Steel Tube at 600 kN (Specimen E8, Shakir-Khalil, 1994).....	190
Table 5-6 Error Analysis of Slip Value (Dunberry, 1987, Specimen D1).....	192
Table 5-7 Error Analysis of Axial Load (Dunberry, 1987, Specimen D1).....	193
Table 5-8 Concentrically Loaded RCFT Column Tests	200
Table 5-9 Comparison of Experimental and Computational Results for Concentrically-Loaded Short Column Tests.....	214
Table 5-10 Pure Bending Tests of RCFT Beams.....	223
Table 5-11 Comparison of Computational and Experimental Results for an RCFT Beam under Pure Bending.....	232
Table 5-12 Proportionally-Loaded RCFT Beam-Column Tests.....	238
Table 5-13 Comparison of Computational and Experimental Results for an Eccentrically-Loaded RCFT Beam-Column Tests.....	248
Table 5-14 Proportionally-Loaded RCFT Beam-Column Tests.....	252
Table 5-15 Comparison of Computational and Experimental Results for Non-Proportionally-Loaded RCFT Beam-Column Tests	262
Table 5-16 Geometric and Material Properties of Specimens to Verify the Steel Model	292
Table 6-1 Summary of Geometric and Material Properties of RCFT Columns	302
Table 6-2 Earthquake Records Selected For Frame IIIa Scaled to 2%/50	305
Table 6-3 The Maximum and Minimum Roof Displacement Values (Δ_r) of IIIa for 2%/50 Earthquake Records	307
Table 6-4 Maximum and Minimum Story Shear and Interstory Drift Ratios.....	308
Table 6-5 Damage Function Parameters of RCFT Columns of Frame IIIa for 2%/50 Hazard Level.....	312
Table 6-6 Earthquake Records Selected for Frame IIIa Scaled to 10%/50 Hazard Level	314

Table 6-7 The Maximum and Minimum Roof Displacement Values (Δ_r) of IIIa for 10%/50 Earthquake Records.....	316
Table 6-8 Maximum and Minimum Story Shear and Interstory Drift Ratios (Frame IIIa, 10%/50).....	317
Table 6-9 Damage Function Parameters of RCFT Columns for 10%/50 Hazard Level	319
Table 6-10 Earthquake Records Selected for Frame IIIId Scaled to 2%/50 Hazard Level.....	321
Table 6-11 The Maximum and Minimum Roof Displacement Values (Δ_r) of IIIId for 2%/50 Earthquake Records.....	323
Table 6-12 Maximum and Minimum Story Shear and Interstory Drift Ratios.....	324
Table 6-13 Damage Function Parameters of RCFT Columns of Frame IIIId for 2%/50 Hazard Level.....	328
Table 6-14 Earthquake Records Selected for Frame IIIId Scaled to 10%/50 Hazard Level.....	329
Table 6-15 The Maximum and Minimum Roof Displacement Values (Δ_r) of IIIId for 10%/50 Earthquake Records.....	330
Table 6-16 Maximum and Minimum Story Shear and Interstory Drift Ratios (Frame IIIId, 10%/50).....	332
Table 7-1 Summary of δ_{sc} for the Limit States of RCFT Beam-Columns	345
Table 7-2 Summary of β_{sc} for the Limit States of RCFT Beam-Columns	346
Table 7-3 Summary of β_{UC} for the Limit States of RCFT Beam-Columns	346
Table 7-4 Summary of β_{RD} for 3-story RCFT Frame Structures.....	348
Table 7-5 Summary of Capacity Factors for RCFT Members	349
Table 7-6 Summary of γ values for 3-story RCFT Frame Structures.....	350
Table 8-1 Ranges of Material and Geometric Properties of RCFT Specimens Studied in Verification Study.....	361

List of Figures

Figure 1.1 Typical Composite Column Types.....	2
Figure 2.1 Typical Loading and Bounding Surfaces for CFTs.....	13
Figure 2.2 Distributed Plasticity Finite Element Formulation.....	15
Figure 2.3 Nonlinear Slip Model.....	22
Figure 2.4 Element Deformations in the Corotational Frame.....	24
Figure 2.5 Internal Element Loading in the x - y plane.....	29
Figure 2.6 Internal Element Loading in the x - z plane.....	30
Figure 2.7 Incremental Element Displacements in Local and Global Coordinates.....	66
Figure 2.8 Incremental Element Forces in Natural Coordinates.....	67
Figure 2.9 Incremental Element Forces in Local Coordinates.....	69
Figure 2.10 RCFT Beam-Column in Three-Dimensional Space.....	69
Figure 2.11 Incremental Element Displacements in Natural and Local Coordinates.....	71
Figure 2.12 Element End Forces at C1 Configuration.....	76
Figure 2.13 (a) Resulting forces ${}^2\mathbf{F}$ at C2 with respect to (wrt.) C2 (b) Resulting forces ${}^2\mathbf{F}$ at C2 wrt. C1 (c) Initial forces ${}^1\mathbf{F}$ at C2 wrt. C1 (d) Forces generated by \mathbf{K}_e	78
Figure 2.14 (a) Resulting forces ${}^2\mathbf{F}$ at C2 with respect to (wrt.) C2 (b) Resulting forces ${}^2\mathbf{F}$ at C2 wrt. C1 (c) Initial forces ${}^1\mathbf{F}$ at C2 wrt. C1 (d) Forces generated by \mathbf{K}_e	79
Figure 2.15 Global Constraint Directions for an RCFT joint.....	80
Figure 2.16 Flow Chart of Curvature and Strain Calculations at the Integration Points..	83
Figure 2.17 Flow Chart of Calculating Nodal Forces.....	84
Figure 2.18 Flow Chart of Calculating Cross-Section Deformations.....	86
Figure 2.19 Flow Chart of Updating Constitutive Relations and Integrating over the RCFT Cross-Section for Stiffness and Force Calculations.....	89
Figure 2.20 Flow Chart of Calculating Element Internal Force.....	89
Figure 2.21 Flow Chart of Calculating Element Internal Force (cont'd).....	90
Figure 2.22 Flow Chart of Calculating Element Stiffness.....	92
Figure 3.1 Concrete Stress-Strain Curve under Compression.....	99
Figure 3.2 Correlation of K_c to R	102
Figure 3.3 Correlation of K_c / f'_c to R	104
Figure 3.4 Correlation of f_{rc} to R / f'_c	104
Figure 3.5 Calibration of r with Respect to the Experiments.....	105
Figure 3.6 Envelope Curves of the Concrete Model.....	108
Figure 3.7 Connecting and Transition Curves of the Concrete Model.....	110
Figure 3.8 Loading, Reloading, and Unloading Curves of the Concrete Model.....	112
Figure 3.9 Determination of Rule 1 in the Concrete Model.....	112
Figure 3.10 Determination of Rule 2 in the Concrete Model.....	113
Figure 3.11 Determination of Rule 3 in the Concrete Model.....	115
Figure 3.12 Definition of Offset Strain ${}^1\varepsilon_o$	116
Figure 3.13 Calculation of ${}^1\varepsilon_{unld}^+$ and ${}^1\sigma_{new}^+$	116
Figure 3.14 Determination of Rule 9 in the Concrete Model.....	117

Figure 3.15 Determination of Rule 4 in the Concrete Model	118
Figure 3.16 Determination of Rule 7 in the Concrete Model	119
Figure 3.17 Determination of Rule 8 in the Concrete Model	121
Figure 3.18 Determination of Rule 5 in the Concrete Model	122
Figure 3.19 Determination of Rule 5* in the Concrete Model.....	123
Figure 3.20 Determination of Rule 6 in the Concrete Model	123
Figure 3.21 Determination of Rule 6* in the Concrete Model.....	124
Figure 3.22 Determination of Rule 10 in the Concrete Model	125
Figure 3.23 Determination of Rule 13 in the Concrete Model	126
Figure 3.24 Determination of Rule 11 in the Concrete Model	127
Figure 3.25 Determination of Rule 12 in the Concrete Model	128
Figure 3.26 Comparison of Experimental and Analytical Results for Unconfined Concrete (Karsan and Jirsa, 1969).....	128
Figure 3.27 Comparison of Experimental and Analytical Results for Unconfined Concrete (Sinha et al. 1964).....	129
Figure 3.28 Comparison of Experimental and Analytical Results for UnConfined Concrete (Sinha et al. 1964).....	129
Figure 3.29 Comparison of Experimental and Analytical Results for Confined Concrete (Mander et al., 1984).....	130
Figure 3.30 Comparison of Experimental and Analytical Results for Confined Concrete (Mander et al., 1984).....	130
Figure 4.1 Envelope Curves of the Steel Model	134
Figure 4.2 Comparison of Experimental and Computational Coupon Test Results.....	136
Figure 4.3 Comparison of Experimental and Computational Coupon Test Results (cont'd)	137
Figure 4.4 Correlation of $\varepsilon_{lf} / \varepsilon_y$ with respect to $D/t\sqrt{f_y / E_s}$	142
Figure 4.5 Calibration of K_s with Respect to Axially Loaded Column Tests	144
Figure 4.6 Calibration of K_s with Respect to Axially Loaded Column Tests (cont'd) ..	145
Figure 4.7 Comparison of Experimental and Computational Results for K_s	145
Figure 4.8 Comparison of Experimental and Computational Results for f_{rs}	146
Figure 4.9 Verification of Steel and Concrete Models	147
Figure 4.10 Verification of Steel and Concrete Models (cont'd)	148
Figure 4.11 Reduction of Radius of the Loading Surface	149
Figure 4.12 Bounding Surface Model of Steel Model.....	151
Figure 4.13 Memory and Virtual Bounding Surfaces of Steel Model.....	153
Figure 4.14 Calibration of γ_{cc} with respect to CIVS3-2 (Tube: 100x100x4.21, $f_y = 295$ MPa, $f'_c = 24$ MPa, $L/D = 6.0$, $D/t = 24$)	154
Figure 4.15 Calibration of γ_{cc} with respect to SR4A4C (Tube: 210x210x5.80 mm, $f_y =$ 323 MPa, $f'_c = 39.2$ MPa, $L/D = 6.0$, $D/t = 36$)	155
Figure 4.16 Steel Model Subjected to Symmetric Constant Strain Cycles.....	156
Figure 4.17 Steel Model Subjected to Symmetric Increasing Strain Cycles	157
Figure 4.18 Steel Model Subjected to Symmetric Increasing Strain Cycles	157

Figure 4.19 Steel Model Subjected to Cyclic Ratcheting	158
Figure 4.20 Comparison of Experimental and Computational Results of Steel Coupon Specimen SM58E ($f_y = 524$ MPa)	158
Figure 4.21 Comparison of Experimental and Computational Results of Steel Coupon Specimen SM58F ($f_y = 524$ MPa)	159
Figure 4.22 Monotonic Stress-Strain Response of Hot-Rolled Steel	161
Figure 4.23 Monotonic Stress-Strain Response of Hot-Rolled Steel with Local Buckling	162
Figure 4.24 Computational Modeling of Specimens by Lukey and Adams (1969)	163
Figure 4.25 Determination of Local Buckling Strain Level for Specimens by Lukey and Adams (1969)	164
Figure 4.26 Calibration of K_{sg} for Specimen B2 (Lukey and Adams, 1969)	165
Figure 4.27 Calibration of K_{sg} for Specimen B5 (Lukey and Adams, 1969)	166
Figure 4.28 Comparison of $f_{rsg} = 0.5 \times f_y$ with the results from Huang (2005)	166
Figure 4.29 Cyclic Response of Structural Steel (Krawinkler et al., 1983)	168
Figure 4.30 Evolution of Bounding Surface Radius as a Function of Accumulated Plastic Work	168
Figure 4.31 Test Setup for EERC-RN2 (Bertero et al., 1995)	169
Figure 4.32 Calibration of γ with respect to EERC-RN2 (Bertero et al., 1995)	169
Figure 5.1 Buckling of a Simply Supported RCFT Column	171
Figure 5.2 Buckling of a Simply Supported RCFT Column	172
Figure 5.3 Buckling of Cantilever RCFT Column	173
Figure 5.4 Cantilever RCFT Column under Pure Bending	173
Figure 5.5 Analysis Results for RCFT Cantilever under Pure Bending	174
Figure 5.6 Displaced Shape of RCFT Cantilever under Pure Bending	174
Figure 5.7 RCFT Cantilever under Transverse Tip Loading	175
Figure 5.8 Load-Deflection Response of RCFT Cantilever under Transverse Tip Loading	176
Figure 5.9 Displaced Shape of RCFT Cantilever under Transverse Tip Loading	176
Figure 5.10 Harrison's Portal Frame	178
Figure 5.11 Load-Deflection Response of Harrison's Portal Frame	178
Figure 5.12 Right-Angled Simply Supported Frame	179
Figure 5.13 Load-Deflection Response of Hinged Right-Angle Frame	179
Figure 5.14 Displaced Shape of Right Angled Simply Supported Frame	180
Figure 5.15 Axially Loaded RCFT Cantilever	180
Figure 5.16 Load Deformation Response of Axially Loaded RCFT Cantilever	181
Figure 5.17 Constitutive Rule of Steel and Concrete Interface	183
Figure 5.18 Experimental Setup of Push-out Tests	183
Figure 5.19 Variation of Bond Strength wrt. Compressive Strength of Concrete	184
Figure 5.20 Variation of Bond Strength wrt. Compressive Strength of Concrete	186
Figure 5.21 Simple Connection Tests Setup by Shakir-Khalil (1994)	186
Figure 5.22 Axial Strain Distribution of the Steel Tube at 600 kN (Specimen E6, Shakir-Khalil, 1994)	187

Figure 5.23 Axial Strain Distribution of the Steel Tube at 800 kN (Specimen E6, Shakir-Khalil, 1994)	188
Figure 5.24 Axial Strain Distribution of the Steel Tube at 600 kN (Specimen E8, Shakir-Khalil, 1994)	189
Figure 5.25 Simple Connection Tests Setup (Dunberry et al., 1987, Specimen D1)	191
Figure 5.26 Slip Distribution (Dunberry et al., 1987, Specimen D1)	191
Figure 5.27 Axial Force Distribution (Dunberry et al., 1987, Specimen D1)	192
Figure 5.28 Simple Connection Tests Setup (Dunberry et al., 1987, Specimen C1).....	194
Figure 5.29 Simple Connection Tests Setup (Dunberry et al., 1987, Specimen C1).....	195
Figure 5.30 Short RCFT Columns under Concentric Axial Loading	195
Figure 5.31 Comparison of Computational and Experimental Results for an RCFT Stub Column Test (Nahakara et al., 1998, Specimen CR4-D-2, $f_y = 262$ MPa, $f'_c = 41.1$ MPa, $D/t = 73.7$, $L/D = 3$)	197
Figure 5.32 Comparison of Computational and Experimental Results for an RCFT Stub Column Test (Varma, 2000, Specimen SC48-46, $f_y = 471$ MPa, $f'_c = 110$ MPa, $D/t = 52.6$, $L/D = 4$).....	199
Figure 5.33 Comparison of Computational and Experimental Results for an RCFT Stub Column Test (Tomii and Sakino, 1979, Specimen IVA, $f_y = 284$ MPa, $f'_c = 19.81$ MPa, $D/t = 24$, $L/D = 3$)	199
Figure 5.34 Comparison of Computational and Experimental Results for an Axially-Loaded RCFT Short Column (Grauers, 1993, Specimen 3).....	201
Figure 5.35 Comparison of Computational and Experimental Results for an Axially-Loaded RCFT Short Column (Grauers, 1993, Specimen 4).....	201
Figure 5.36 Comparison of Computational and Experimental Results for an Axially-Loaded RCFT Short Column (Grauers, 1993, Specimen 8).....	202
Figure 5.37 Comparison of Computational and Experimental Results for an Axially-Loaded RCFT Short Column (Grauers, 1993, Specimen 27).....	202
Figure 5.38 Comparison of Computational and Experimental Results for an Axially-Loaded RCFT Short Column (Varma, 2000, SC32-46)	203
Figure 5.39 Comparison of Computational and Experimental Results for an Axially-Loaded RCFT Short Column (Varma, 2000, SC32-80)	203
Figure 5.40 Comparison of Computational and Experimental Results for an Axially-Loaded RCFT Short Column (Tomii and Sakino, 1979, IA)	204
Figure 5.41 Comparison of Computational and Experimental Results for an Axially-Loaded RCFT Short Column (Tomii and Sakino, 1979, IIA)	204
Figure 5.42 Comparison of Computational and Experimental Results for an Axially-Loaded RCFT Short Column (Tomii and Sakino, 1979, IIIA).....	205
Figure 5.43 Comparison of Computational and Experimental Results for an Axially-Loaded RCFT Short Column (Schneider, 1998, S1)	205
Figure 5.44 Comparison of Computational and Experimental Results for an Axially-Loaded RCFT Short Column (Schneider, 1998, R1).....	206
Figure 5.45 Comparison of Computational and Experimental Results for an Axially-Loaded RCFT Short Column (Nakahara et al., 1998, CR4-D-8)	206

Figure 5.46 Comparison of Computational and Experimental Results for an Axially-Loaded RCFT Short Column (Nakahara et al., 1998, CR4-C-4-1)	207
Figure 5.47 Comparison of Computational and Experimental Results for an Axially-Loaded RCFT Short Column (Nakahara et al., 1998, CR8-C-8).....	207
Figure 5.48 Comparison of Computational and Experimental Results for an Axially-Loaded RCFT Short Column (Grauers, 1993, Specimen 1).....	208
Figure 5.49 Comparison of Computational and Experimental Results for an Axially-Loaded RCFT Short Column (Grauers, 1993, Specimen 2).....	208
Figure 5.50 Comparison of Computational and Experimental Results for an Axially-Loaded RCFT Short Column (Schneider, 1998, S2)	209
Figure 5.51 Comparison of Computational and Experimental Results for an Axially-Loaded RCFT Short Column (Schneider, 1998, S3)	209
Figure 5.52 Comparison of Computational and Experimental Results for an Axially-Loaded RCFT Short Column (Schneider, 1998, S4)	210
Figure 5.53 Comparison of Computational and Experimental Results for an Axially-Loaded RCFT Short Column (Schneider, 1998, S5)	210
Figure 5.54 Comparison of Computational and Experimental Results for an Axially-Loaded RCFT Short Column (Schneider, 1998, R2).....	211
Figure 5.55 Comparison of Computational and Experimental Results for an Axially-Loaded RCFT Short Column (Schneider, 1998, R3).....	211
Figure 5.56 Comparison of Computational and Experimental Results for an Axially-Loaded RCFT Short Column (Schneider, 1998, R4).....	212
Figure 5.57 Comparison of Computational and Experimental Results for an Axially-Loaded RCFT Short Column (Schneider, 1998, R5).....	212
Figure 5.58 Comparison of Computational and Experimental Results for an Axially-Loaded RCFT Short Column (Schneider, 1998, R6).....	213
Figure 5.59 Variation of error for E_i with respect to $(D/t) \times \sqrt{f_y / E_s}$ and f'_c	215
Figure 5.60 Variation of error for P_o with respect to $(D/t) \times \sqrt{f_y / E_s}$ and f'_c	216
Figure 5.61 Variation of error for d_o with respect to $(D/t) \times \sqrt{f_y / E_s}$ and f'_c	216
Figure 5.62 Variation of error for d_o with respect to $(D/t) \times \sqrt{f_y / E_s}$ and f'_c	217
Figure 5.63 Pure Bending of RCFT Beams	217
Figure 5.64 Mesh-Convergence of Pure Bending of RCFT Beams	219
Figure 5.65 Comparison of Computational and Experimental Results for an RCFT Beam Pure Bending Test (Lu and Kennedy, 1994, Specimen CB12)	219
Figure 5.66 Comparison of Computational and Experimental Results for an RCFT Beam Pure Bending Test (Gho and Liu, 2004, Specimen B04)	220
Figure 5.67 Comparison of Computational and Experimental Results for an RCFT Beam Pure Bending Test (Tomii and Sakino, 2004, Specimen IV0)	221
Figure 5.68 Centrally Loaded Short RCFT Column Computational Model.....	222
Figure 5.69 Comparison of Computational and Experimental Results for an RCFT Beam under Four Point Bending (Lu and Kennedy, 1994, Specimen CB13)	223

Figure 5.70 Comparison of Computational and Experimental Results for an RCFT Beam under Four Point Bending (Lu and Kennedy, 1994, Specimen CB15)	224
Figure 5.71 Comparison of Computational and Experimental Results for an RCFT Beam under Four Point Bending (Lu and Kennedy, 1994, Specimen CB22)	224
Figure 5.72 Comparison of Computational and Experimental Results for an RCFT Beam under Four Point Bending (Lu and Kennedy, 1994, Specimen CB31)	225
Figure 5.73 Comparison of Computational and Experimental Results for an RCFT Beam under Four Point Bending (Lu and Kennedy, 1994, Specimen CB35)	225
Figure 5.74 Comparison of Computational and Experimental Results for an RCFT Beam under Four Point Bending (Lu and Kennedy, 1994, Specimen CB41)	226
Figure 5.75 Comparison of Computational and Experimental Results for an RCFT Beam under Four Point Bending (Lu and Kennedy, 1994, Specimen CB45)	226
Figure 5.76 Comparison of Computational and Experimental Results for an RCFT Beam under Four Point Bending (Lu and Kennedy, 1994, Specimen CB52)	227
Figure 5.77 Comparison of Computational and Experimental Results for an RCFT Beam under Four Point Bending (Lu and Kennedy, 1994, Specimen CB53)	227
Figure 5.78 Comparison of Computational and Experimental Results for an RCFT Beam under Four Point Bending (Lu and Kennedy, 1994, Specimen CB55)	228
Figure 5.79 Comparison of Computational and Experimental Results for an RCFT Beam under Four Point Bending (Assi et al., 2003, Specimen B1CSN)	228
Figure 5.80 Comparison of Computational and Experimental Results for an RCFT Beam under Four Point Bending (Assi et al., 2003, Specimen B1DRN)	229
Figure 5.81 Comparison of Computational and Experimental Results for an RCFT Beam under Four Point Bending (Assi et al., 2003, Specimen B02)	229
Figure 5.82 Comparison of Computational and Experimental Results for an RCFT Beam under Four Point Bending (Tomii and Sakino, 1979 Specimen II0)	230
Figure 5.83 Comparison of Computational and Experimental Results for an RCFT Beam under Four Point Bending (Tomii and Sakino, 1979, Specimen III0)	230
Figure 5.84 Variation of error for E_i with respect to $(D/t) \times \sqrt{f_y / E_s}$ and f'_c	231
Figure 5.85 Variation of error for M_o with respect to $(D/t) \times \sqrt{f_y / E_s}$ and f'_c	233
Figure 5.86 RCFT Columns under Eccentric Axial Loading	233
Figure 5.87 Mesh-Convergence of Eccentrically-Loaded RCFT Columns	235
Figure 5.88 Comparison of Computational and Experimental Results for an Eccentrically Loaded RCFT Column Test (Grauers, 1992, Specimen 13)	236
Figure 5.89 Comparison of Computational and Experimental Results for an Eccentrically Loaded RCFT Column Test (Shakir-Khalil and Zeghiche 1989, Specimen 6)	236
Figure 5.90 Proportionally-Loaded RCFT Column Computational Model	237
Figure 5.91 Comparison of Computational and Experimental Results for an Eccentrically-Loaded RCFT Column (Grauers 1992, Specimen 1)	239
Figure 5.92 Comparison of Computational and Experimental Results for an Eccentrically-Loaded RCFT Column (Grauers 1992, Specimen 2)	239
Figure 5.93 Comparison of Computational and Experimental Results for an Eccentrically-Loaded RCFT Column (Grauers 1992, Specimen 6)	239

Figure 5.94 Comparison of Computational and Experimental Results for an Eccentrically-Loaded RCFT Column (Grauers 1992, Specimen 7)	240
Figure 5.95 Comparison of Computational and Experimental Results for an Eccentrically-Loaded RCFT Column (Grauers 1992, Specimen 9)	240
Figure 5.96 Comparison of Computational and Experimental Results for an Eccentrically-Loaded RCFT Column (Grauers 1992, Specimen 10)	241
Figure 5.97 Comparison of Computational and Experimental Results for an Eccentrically-Loaded RCFT Column (Bridge 1976, SHC-1).....	241
Figure 5.98 Comparison of Computational and Experimental Results for an Eccentrically-Loaded RCFT Column (Bridge 1976, SHC-3).....	242
Figure 5.99 Comparison of Computational and Experimental Results for an Eccentrically-Loaded RCFT Column (Bridge 1976, SHC-4).....	242
Figure 5.100 Comparison of Computational and Experimental Results for an Eccentrically-Loaded RCFT Column (Bridge 1976, SHC-5).....	243
Figure 5.101 Comparison of Computational and Experimental Results for an Eccentrically-Loaded RCFT Column (Bridge 1976, SHC-6).....	243
Figure 5.102 Comparison of Computational and Experimental Results for an Eccentrically-Loaded RCFT Column (Bridge 1976, SHC-7).....	244
Figure 5.103 Comparison of Computational and Experimental Results for an Eccentrically-Loaded RCFT Column (Bridge 1976, SHC-8).....	244
Figure 5.104 Comparison of Computational and Experimental Results for an Eccentrically-Loaded RCFT Column (Shakir-Khalil and Zeghiche 1989, Specimen 2)	245
Figure 5.105 Comparison of Computational and Experimental Results for an Eccentrically-Loaded RCFT Column (Shakir-Khalil and Zeghiche 1989, Specimen 3)	245
Figure 5.106 Comparison of Computational and Experimental Results for an Eccentrically-Loaded RCFT Column (Shakir-Khalil and Zeghiche 1989, Specimen 5)	246
Figure 5.107 Comparison of Computational and Experimental Results for an Eccentrically-Loaded RCFT Column (Shakir-Khalil and Zeghiche 1989, Specimen 7)	246
Figure 5.108 RCFT Beam-Column under Non-Proportional Loading	249
Figure 5.109 Mesh-Convergence of Non-Proportionally-Loaded RCFT Columns	250
Figure 5.110 Comparison of Computational and Experimental Results for a Non-Proportionally-Loaded RCFT Beam-Column (Tomii and Sakino, 1979, Specimen III-3)	251
Figure 5.111 Comparison of Computational and Experimental Results for a Non-Proportionally-Loaded RCFT Beam-Column (Nakahara and Sakino, 1998, Specimen BR4-6-10-02).....	252
Figure 5.112 Comparison of Computational and Experimental Results for a Non-Proportionally-Loaded RCFT Beam-Column (Tomii and Sakino, 1979, Specimen III-1)	253
Figure 5.113 Comparison of Computational and Experimental Results for a Non-Proportionally-Loaded RCFT Beam-Column (Tomii and Sakino, 1979, Specimen III-2)	253

Figure 5.114 Comparison of Computational and Experimental Results for a Non-Proportionally-Loaded RCFT Beam-Column (Tomii and Sakino, 1979, Specimen III-4)	254
Figure 5.115 Comparison of Computational and Experimental Results for a Non-Proportionally-Loaded RCFT Beam-Column (Tomii and Sakino, 1979, Specimen III-5)	254
Figure 5.116 Comparison of Computational and Experimental Results for a Non-Proportionally-Loaded RCFT Beam-Column (Tomii and Sakino, 1979, Specimen III-6)	255
Figure 5.117 Comparison of Computational and Experimental Results for a Non-Proportionally-Loaded RCFT Beam-Column (Nakahara and Sakino, 1998, Specimen BR4-6-10-04)	255
Figure 5.118 Comparison of Computational and Experimental Results for a Non-Proportionally-Loaded RCFT Beam-Column (Nakahara and Sakino, 1998, Specimen BR8-6-10-02)	256
Figure 5.119 Comparison of Computational and Experimental Results for a Non-Proportionally-Loaded RCFT Beam-Column (Varma, 2000, Specimen BC32-80-20)	256
Figure 5.120 Comparison of Computational and Experimental Results for a Non-Proportionally-Loaded RCFT Beam-Column (Varma, 200, Specimen BC32-80-20)	257
Figure 5.121 Comparison of Computational and Experimental Results for a Non-Proportionally-Loaded RCFT Beam-Column (Varma, 2000, Specimen BC32-80-40)	257
Figure 5.122 Comparison of Computational and Experimental Results for a Non-Proportionally-Loaded RCFT Beam-Column (Varma, 2000, Specimen BC32-80-40)	258
Figure 5.123 Comparison of Computational and Experimental Results for a Non-Proportionally-Loaded RCFT Beam-Column (Varma, 2000, Specimen BC32-46-20)	258
Figure 5.124 Comparison of Computational and Experimental Results for a Non-Proportionally-Loaded RCFT Beam-Column (Varma, 2000, Specimen BC32-46-20)	259
Figure 5.125 Comparison of Computational and Experimental Results for a Non-Proportionally-Loaded RCFT Beam-Column (Varma, 2000, Specimen BC32-46-40)	259
Figure 5.126 Comparison of Computational and Experimental Results for a Non-Proportionally-Loaded RCFT Beam-Column (Varma, 2000, Specimen BC48-46-20)	260
Figure 5.127 Comparison of Computational and Experimental Results for a Non-Proportionally-Loaded RCFT Beam-Column (Varma, 2000, Specimen BC48-46-20)	260
Figure 5.128 Computational Modelling of Cyclically-Loaded RCFT Beam-Column Tests	263
Figure 5.129 Fiber Discretization of RCFT Cross-Section	263
Figure 5.130 Comparison of Computational and Experimental Results for a Cyclically-Loaded RCFT Beam-Column (Sakino and Tomii, 1981, Specimen CIIS3-3)	264
Figure 5.131 Stress-Strain Response of Steel and Concrete Fibers (Sakino and Tomii, 1981)	264
Figure 5.132 Comparison of Computational and Experimental Results for a Cyclically-Loaded RCFT Beam-Column (Inai et al., 2004, Specimen SR6A4C)	265
Figure 5.133 Stress-Strain Response of Steel and Concrete Fibers (Inai et al., 2004)	266

Figure 5.134 Cyclically-Loaded RCFT Cruciform Frame (Kawaguchi and Morino, 2001)	267
Figure 5.135 Computational Modeling of Cyclically-Loaded RCFT Cruciform Frame	267
Figure 5.136 Fiber Discretization of RCFT and Steel Cross-Sections	268
Figure 5.137 Comparison of Computational and Experimental Results for a Cyclically-Loaded RCFT Cruciform Frame (Kawaguchi and Morino, 2001)	268
Figure 5.138 Stress-Strain Response of Concrete Fibers (Kawaguchi and Morino, 2001)	269
Figure 5.139 Stress-Strain Response of Concrete Fibers (Kawaguchi and Morino, 2001)	270
Figure 5.140 Stress-Strain Response of Concrete Fibers (Kawaguchi and Morino, 2001)	271
Figure 5.141 Stress-Strain Response of Steel Fibers (Kawaguchi and Morino, 2001)	272
Figure 5.142 Stress-Strain Response of Steel Fibers (Kawaguchi and Morino, 2001)	273
Figure 5.143 Stress-Strain Response of Steel Fibers (Kawaguchi and Morino, 2001)	274
Figure 5.144 Stress-Strain Response of Steel Fibers (Kawaguchi and Morino, 2001)	275
Figure 5.145 Stress-Strain Response of Steel Fibers (Kawaguchi and Morino, 2001)	275
Figure 5.146 Computational Modeling of Cyclically-Loaded RCFT Portal Frame	276
Figure 5.147 Comparison of Computational and Experimental Results for a Cyclically-Loaded RCFT Cruciform Frame (Kawaguchi and Morino, 2001)	277
Figure 5.148 Stress-Strain Response of Concrete Fibers (Kawaguchi, 2000)	278
Figure 5.149 Stress-Strain Response of Concrete Fibers (Kawaguchi, 2000)	278
Figure 5.150 Stress-Strain Response of Concrete Fibers (Kawaguchi, 2000)	279
Figure 5.151 Stress-Strain Response of Concrete Fibers (Kawaguchi, 2000)	279
Figure 5.152 Stress-Strain Response of Concrete Fibers (Kawaguchi, 2000)	280
Figure 5.153 Stress-Strain Response of Steel Fibers (Kawaguchi, 2000)	280
Figure 5.154 Stress-Strain Response of Steel Fibers (Kawaguchi, 2000)	281
Figure 5.155 Stress-Strain Response of Steel Fibers (Kawaguchi, 2000)	281
Figure 5.156 Stress-Strain Response of Steel Fibers (Kawaguchi, 2000)	282
Figure 5.157 Stress-Strain Response of Steel Fibers (Kawaguchi, 2000)	282
Figure 5.158 Stress-Strain Response of Steel Fibers (Kawaguchi, 2000)	283
Figure 5.159 Stress-Strain Response of Steel Fibers (Kawaguchi, 2000)	283
Figure 5.160 Clamped Beam Subjected to Step Loading	284
Figure 5.161 Dynamic Response of Clamped Beam Subjected to Step Loading	285
Figure 5.162 Cantilever Beam Subjected to End Loading	286
Figure 5.163 Dynamic Response of Cantilever Beam Subjected to End Loading	286
Figure 5.164 RCFT Test Structure by Herrera (2005)	287
Figure 5.165 Roof Drift Time History Results for Design Basis Earthquake Loading	289
Figure 5.166 Roof Drift Time History Results for Maximum Considered Earthquake Loading	290
Figure 5.167 Story Shear vs, Intersory Drift Response at the 1 st Story for the Design Basis Earthquake Level	290
Figure 5.168 Story Shear vs, Intersory Drift Response at the 2 nd Story for the Design Basis Earthquake Level	291

Figure 5.169 Story Shear vs, Intersory Drift Response at the 1 st Story for the Maximum Considered Earthquake Level.....	291
Figure 5.170 Story Shear vs, Intersory Drift Response at the 2 nd Story for the Maximum Considered Earthquake Level.....	292
Figure 5.171 Computational Modeling of Specimens by Lukey and Adams (1969).....	293
Figure 5.172 Comparison Experimental and Computational Results for Specimen B1 by Lukey and Adams (1969).....	293
Figure 5.173 Comparison Experimental and Computational Results for Specimen B3 by Lukey and Adams (1969).....	294
Figure 5.174 Comparison Experimental and Computational Results for Specimen B4 by Lukey and Adams (1969).....	294
Figure 5.175 Comparison Experimental and Computational Results for Specimen C3 by Lukey and Adams (1969).....	295
Figure 5.176 Comparison Experimental and Computational Results for Specimen C5 by Lukey and Adams (1969).....	295
Figure 5.177 Test Setup for RC03 (Kim et al., 2002).....	296
Figure 5.178 Comparison Experimental and Computational Results for Specimen RC03 by Kim et al. (2002).....	297
Figure 6.1 Selection of Earthquake Records.....	301
Figure 6.2 Spectrum of Acceleration at Various Hazard Levels	303
Figure 6.3 Description of Frame IIIa (LaFore and Hajjar, 2005)	305
Figure 6.4 Scaled Earthquake Records of Frame IIIa to 2%/50	306
Figure 6.5 Roof Displacement Time History for Frame IIIa (2%/50).....	307
Figure 6.6 Interstory Drift Ratio and Shear Force Demand at 1 st , 2 nd and 3 rd stories (Frame IIIa, 2%/50)	308
Figure 6.7 Axial Force and Bending Moment Interaction Demands for Edge Columns at 1 st , 2 nd and 3 rd Stories (Frame IIIa, 2%/50).....	309
Figure 6.8 Push-Over Response of Frame IIIa	311
Figure 6.9 Push-Over vs. Time History Response of 1 st Story Interior Column (IIIa, 2%/50).....	311
Figure 6.10 Distribution of Mean Damage Function Values for the RCFT Columns....	312
Figure 6.11 Damage Distribution of RCFT Cross-Section at the Support under IV79 Ground Motion (Frame IIIa, 2%/50)	313
Figure 6.12 Scaled Earthquake Records of Frame IIIa to 10%/50	314
Figure 6.13 Roof Displacement Time History for Frame IIIa (10%/50).....	315
Figure 6.14 Interstory Drift Ratio and Shear Force Demand at 1 st , 2 nd and 3 rd stories (Frame IIIa, 10%/50)	316
Figure 6.15 Axial Force and Bending Moment Interaction Demands for the Exterior Columns at 1 st , 2 nd and 3 rd Stories (Frame IIIa, 10%/50).....	317
Figure 6.16 Distribution of Mean Damage Function Values for the RCFT Columns (Frame IIIa, 10%/50)	318
Figure 6.17 Damage Distribution of RCFT Cross-Section at the Support under IV79 Ground Motion (Frame IIIa, 10%/50)	319
Figure 6.18 Description of Frame IIIId.....	320

Figure 6.19 Scaled Earthquake Records of Frame IIIId to 2%/50	322
Figure 6.20 Roof Displacement Time History for Frame IIIId (2%/50).....	322
Figure 6.21 Interstory Drift Ratio and Shear Force Demand at the 1 st , 2 nd and 3 rd stories (Frame IIIId, 2%/50)	324
Figure 6.22 Axial Force and Bending Moment Interaction Demands for the Exterior Columns at 1 st , 2 nd and 3 rd Stories (Frame IIIId, 2%/50)	325
Figure 6.23 Static Push-Over Response of Frame IIIId	326
Figure 6.24 Push-Over vs. Time History Response of 1 st Story Exterior Column (Frame IIIId, 2%/50).....	327
Figure 6.25 Distribution of Mean Damage Function Values for the RCFT Columns....	327
Figure 6.26 Damage Distribution of RCFT Cross-Section at the Support under IV79 Ground Motion.....	328
Figure 6.27 Scaled Earthquake Records of Frame IIIId to 10%/50	329
Figure 6.28 Roof Displacement Time History for Frame IIIId (10%/50).....	330
Figure 6.29 Interstory Drift Ratio and Shear Force Demand at the 1 st , 2 nd and 3 rd stories (Frame IIIId, 10%/50)	331
Figure 6.30 Axial Force and Bending Moment Interaction Demands for the Exterior Columns at 1 st , 2 nd and 3 rd Stories (Frame IIIId, 10%/50)	332
Figure 6.31 Distribution of Mean Damage Function Values for the RCFT Columns (Frame IIIId, 10%/50)	333
Figure 7.1 Graphical Representation of Relation Between Hazard Curve, Seismic Demand and Capacity Adopted From Luco and Cornell (1998).....	339
Figure 7.2 Variation of Compressive Strength of Concrete	341
Figure 7.3 Variation of Yield Strength of the Steel Tube.....	342
Figure 7.4 Variation of \hat{D}_{cy} due to Scatter in the Experimental Data	343
Figure 7.5 Variation of \hat{D}_{ty} due to Scatter in the Experimental Data.....	344
Figure 7.6 Variation of \hat{D}_{lbf} due to Scatter in the Experimental Data	344
Figure 7.7 Variation of \hat{D}_{lbw} due to Scatter in the Experimental Data.....	345
Figure 7.8 Load Deformation Response of the RCFT Column to Calculate Damage Function Values	351
Figure 7.9 Calculation of Damage Function Values Imposed on a RCFT Column Based on Nonlinear Time History Analysis	353
Figure A 1 Discretization Scheme for RCFT Cross-Section.....	381
Figure A 2 Rigid Body Rotation of the RCFT Beam-Column in Local Coordinates.....	384

Chapter 1

1. Introduction

1.1. Steel and Concrete Composite Columns

Composite construction, which integrates steel and concrete materials in individual structural members, has been shown to produce efficient design solutions in building applications. This concept blends the most favorable characteristics of steel and concrete materials such that structural members may be designed with high strength, stiffness, and ductility.

Composite construction in the U.S. initiated in the 1960's with the use of composite steel girders in high-rise buildings. In late 1970's, composite columns started to become popular in the construction industry (Hooper et al., 1999). However, the limitations and uncertainties in the available design provisions prevented their wide spread and acceptance in the structural engineering communities. The recent computational and experimental studies on composite beam-columns and connections helped to improve understanding of their key inelastic characteristics such as slip, cracking, confinement, yielding and local buckling (Shakir-Khalil and Zeghiche, 1989; Shakir-Khalil and Mouli, 1990; Shakir-Khalil, 1993a, 1993b; Hajjar and Gourley, 1997, Hajjar et al., 1997; Schneider and Alostaz, 1997; Hajjar et al. 1998a, 1998b; Koester, 2000; Peng, 2001; El-Tawil and Deierlein, 2001; Mehanny and Deierlein, 2001; Varma et al., 2002a, b; Morino et al., 1993; Kawaguchi, 2000; Nishiyama et al., 2002; Tort and Hajjar, 2003; Lin et al., 2004; Herrera, 2005). The wealth of information gained from the research studies on composite beam-columns culminated in the development Chapter I of AISC (2005) design specification. Compared to its predecessors, in AISC 2005, the composite interaction is taken into account more accurately through improved quantification of the concrete contribution to the flexural response. This approach helps to reduce the over-conservatism introduced by neglecting the contribution of concrete

(Choi et al., 2006). Despite the improvement in design specifications for non-seismic applications, guidance on earthquake resistance design of composite columns still remains limited.

Three main types of composite beam-columns are commonly used in the construction industry as illustrated in Figure 1.1. Steel-Encased Concrete (SRC) columns are made up of a wide-flange steel cross-section placed inside a traditional reinforced concrete column. Concrete-filled steel tube columns are constructed by pouring concrete inside rectangular or circular steel tubes, which are designated as rectangular concrete filled steel tube (RCFT) and circular concrete-filled steel tube (CCFT), respectively. The manufacturing of the steel tubes is typically performed through cold-formed processes. The cold-forming processes to obtain circular or rectangular shape steel tubes are applied to a cooled steel plate of desired thickness and the final closed form is obtained with a continuous seam weld (Sherman, 1992). In Japan, China, and Australia, it is also common that the steel tube of RCFTs can be formed by welding of four plates at their edges or by welding of two channel sections. The manufacturing technique of the steel tubes might significantly affect the structural response since the type and distribution of residual stresses depend on the fabrication processes. However, this feature of the composite columns is not addressed in the current design specifications.

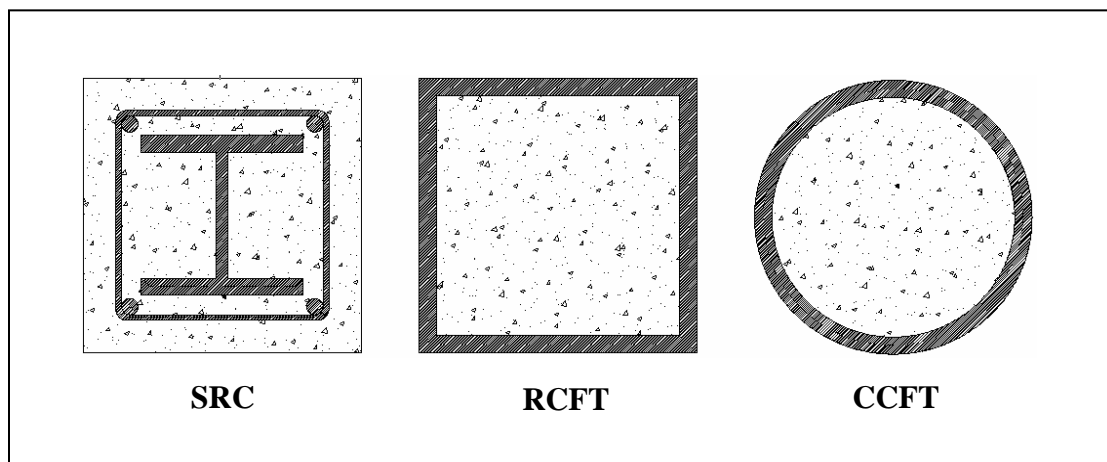


Figure 1.1 Typical Composite Column Types

Composite columns offer significant advantages over traditional steel and reinforced concrete structures. The steel media contributes to the speed of construction, light weight, strength, and ductility while concrete media provides damping, reduced cost, and stiffness (Muhummud, 2003). The increased ductility and strength of the concrete is attributed to the confinement pressure generated as a result of the composite interaction. The concrete core of RCFT and CCFT columns force local buckling to occur in an outward direction. Composite columns also maintain a significant proportion of their load carrying capacity following the limit states of concrete crushing and steel yielding. Concrete filling adds to the stiffness and strength of the steel columns and it allows designing slender members with reduced cross-section sizes. This increases the available floor area and reduces the painting costs to achieve an aesthetic appearance or rust free surfaces where needed. Concrete in composite columns acts as a heat sink causing a higher resistance against fire loadings. Under sustained loads, the performance of composite columns is often very satisfactory. The deformation of concrete due to creep and shrinkage causes load redistribution and increases the stresses in the steel section. Therefore, a reduction in the capacity of the composite column may take place. Despite the creep and shrinkage phenomena observed in composite columns, their effect on the load carrying capacity is less pronounced compared to reinforced concrete columns. The long term effects on composite column manifest themselves more significantly in the case of slender columns and columns with large concrete area (Grauers, 1993). For RCFT and CCFT columns, the concrete is well protected from shrinkage since it is placed inside the concrete core. The use of composite columns also provides benefits in the construction process. The separation of jobs at the construction site can be achieved by erecting the steel frame ahead of the concrete casting operations. In the case of RCFT and CCFT columns, no special formwork is required for concrete casting, which helps easing the construction operations.

The common applications of CCFTs in the U.S can be found in braced frames of high-rise buildings. CCFT columns with diameters ranging from 1 m to 3 m having D/t ratios of about 100 are often used (Roeder et al., 1999). The two Union Square building in Seattle is a typical example of buildings with large diameter and high strength

concrete CCFT columns. The application of RCFT columns in the U.S. is very rare. This research study is conducted to understand the behavioral aspect of buildings with RCFT columns and augment the existing design provision to promote their use around the nation.

1.2. Performance-Based Design Methodology

Performance-based design (PBD) methodologies in the U.S. have been developed for earthquake resistant design of buildings following significant losses in the Loma Prieta (1989) and Northridge (1994) earthquakes. The main motivation has been to provide guidelines for designing structures having predictable response at multiple loading levels with quantifiable confidence (Krawinkler, 1998). This approach is expected to lead to more economical and safer building population in earthquake prone regions.

PBD allows targeting multiple performance levels describing the damaged state of buildings following earthquakes. The performance levels range from minor damage (e.g., Immediate Occupancy) without any appreciable structural failure to significant damage that puts the building on the verge of global collapse (e.g., Collapse Prevention). Associating the structural performance levels with the expected ground motion hazard levels defines the performance objectives. The performance objectives are selected to meet the diverse needs of the stakeholders and they often have the same designation with the structural performance levels. For example, Immediate Occupancy performance objective often represents satisfying the Immediate Occupancy performance level under earthquake loading with 50 % probability of exceedence in 50 years (50%/50years). PBD guidelines provide the engineering procedures and parameters to design structures satisfying the selected performance objectives.

The extensive computational and experimental work in developing PBD guidelines for earthquake resistant design culminated in several documents that have addressed the implementation of the PBD concepts in the U.S., including VISION 2000 (1995), ATC (1996), and FEMA (1997a, 2000a, 2000b). VISION 2000 (1995), ATC-58 (2007) is the pioneering document introducing a general methodology of PBD and

describing its main concepts such as performance objectives and seismic evaluation techniques. In VISION 2000 (1995), several design and analysis approaches are proposed and their applicability to different structure types and performance levels is presented. FEMA (1997a) and FEMA (2000b) were prepared as the guidelines for seismic rehabilitation of all building structures. The provisions in these two documents discuss the improvement of seismic resistance of the overall structural system and its components including both structural and nonstructural types. Therefore, the building performance levels are also defined as a combination of individual structural and non-structural performance levels. The evaluation of the structural performance levels is conducted for each structural component considering their contribution to the global system response as primary or secondary. The structural components are further classified with respect to their behavioral pattern as deformation-controlled or force-controlled. Based on these classifications, the acceptance criteria of the structural components for the targeted performance levels are provided such that they will be checked whether the expected damage will exceed the threshold values. The performance evaluation of the structural components is conducted based on either force or displacement measures depending on the analysis method adopted in determining the force and displacements imposed by the earthquake loading. The structural performance at the global system level is mainly described using qualitative expressions of damage without any quantifiable acceptance criteria. FEMA (1997a) and FEMA (2000b) note the uncertainty in the proposed performance evaluations. However, no methodology to calculate the corresponding confidence levels is given. ATC (1996) provides guidelines for seismic retrofit and evaluation of concrete structures. The structural and non-structural performance levels are evaluated independently and together they define the building performance. To decide whether a building satisfies a structural performance level, design checks are conducted both at the global system level and at the structural component level. The gravity and lateral load resistance of the structure, as well as, the lateral deformations are compared to limiting values. In the case of structural components, similar to FEMA (1997a) and FEMA (2000b), classifications are made according to their behavioral nature (e.g., deformation-controlled and primary, force-

controlled and secondary etc.) and the performance is assessed based on force or deformation limits. ATC (1996) introduces a powerful analysis method designated as the Capacity Spectrum Method. This method utilizes the static nonlinear lateral load-deformation response of the structure with the elastic response spectrum to determine the maximum displacement expected under the given earthquake loading. No confidence level calculation method is provided for the performance assessments proposed in ATC (1996). FEMA (2000a) constitutes design recommendations of new steel moment-frames. The new connection details developed after the Northridge (1994) earthquake are introduced and their design methods are provided. FEMA (2000a) establishes a reliability-based performance evaluation technique applicable to regular welded steel moment frames, where uncertainties are taken into account through probabilistic confidence statements associated with the targeted performance level. The performance objectives are defined as Immediate Occupancy and Collapse Prevention. The performance evaluation can be made both at the global system level and at the structural component level. The recommended design parameters were selected as interstory drift value and axial force on individual columns.

The first generation of PBD guidelines served well in fulfilling its objectives. However, over the last decade, knowledge on structural response to earthquakes, as well as information on ground motions, have significantly improved allowing more advanced procedures to be used in PBD guidelines. The ATC-58 (2001) project, a ten-year long research program funded by FEMA, was initiated to develop a new generation of PBD guidelines for both seismic rehabilitation and new design of building structures. The new generation of PBD guidelines will have performance criteria in terms of direct economic losses, casualties, or down-time so that stakeholders can make more informed decisions about earthquake resistant design or upgrade of their buildings. The performance evaluation of the buildings will be done considering the interaction between the performance of structural components and the global structural system. Detailed guidance about the use of advanced analysis methods such as nonlinear time history analysis will also be provided. The current PBD guidelines offer limited direction regarding preliminary design of buildings to satisfy a targeted performance objective.

This leads to an expensive trial-error type procedure for design of buildings. ATC-58 aims to provide prescriptive guidelines while making decisions about the load-resisting system, stiffness, and strength of the structure to meet the desired performance objectives.

Despite the intensive research efforts following the 1994 Northridge Earthquake, the proposed PBD guidelines have remained limited primarily to steel, reinforced-concrete, and timber structures. The provisions related to composite construction were often prepared as an extension to those related to steel and concrete structures. There exist very few studies towards developing PBD methodologies of composite structures. The main focus of this research is to develop a reliability-based PBD methodology for structural systems having RCFT columns and steel girders.

One of the earliest attempts to develop PBD guidelines of composite structures was the work by Mehanny and Deierlein (2000), where a computational study was conducted to assess the seismic performance of composite frames made up of reinforced concrete columns and steel girders. It was aimed to evaluate the performance both at the component (local) and system (global) level. Damage functions were derived for the structural components including reinforced-concrete columns, steel girders, and connections. Based on the evolution of the damage of the structural members, the available local damage states were mapped on to the performance levels. A new method to evaluate the system performance was proposed utilizing the quantified damage assessments. The stiffness properties of the structural components are updated following the time history analysis results for a representative earthquake record. Then, a nonlinear static analysis is conducted under gravity loads until failure state is attained. The ratio of the vertical gravity load capacity to the unfactored gravity loads was defined as a stability index identifying the global performance of the structure. Muhummud (2003) investigated the performances of three 6-story RCFT building structures having variations with respect to the support conditions. The buildings were analyzed under a suite of far-field earthquake records. Two hazard levels were considered including 2% probability of exceedence in 50 years (maximum considered earthquake) and 10% probability of exceedence in 50 years (design basis earthquake). Static push-over and

nonlinear time history analysis were utilized to quantify the demand. Global response of the buildings was examined through global damage parameters e.g., roof drift, residual roof drift, base-shear and a stability index (Mehanny and Deierlein, 2000). The performance of the structural members was also studied and the common damage parameters investigated were interstory-drift, plastic rotation, and level of axial load. The structures were found to satisfy both Life Safety and Collapse Prevention performance objectives defined in FEMA (1997b) and FEMA (2000a).

1.3. Objectives

The primary objective of this research is to develop a performance-based design methodology of structures having RCFT columns and steel girders, with an emphasis on composite structural response, including development of a new mixed finite element formulation for detailed behavioral assessment of the three-dimensional cyclic dynamic response of composite RCFT frames. Within the framework of developing a performance-based methodology, the following issues will also be targeted:

1. To identify the failure and local damage characteristics of RCFT beam-columns, and frames;
2. To investigate the capacity of RCFT structures under seismic loadings;
3. To assess the seismic demand of RCFT structures and determine the effects of composite interaction; and other characteristics of RCFT structures on the seismic demand;
4. To quantify the randomness and uncertainty on the demand and capacity evaluation of RCFT structures; and
5. To develop a new reliability-based PBD methodology of RCFT buildings through enhancing the existing non-seismic and seismic design provisions.
6. To utilize mixed finite element methods for the analysis of RCFT frame structures under static and dynamic loadings so that their seismic performance can be quantified accurately exploiting the superior features of the mixed finite element formulation

including the ability to model slip, satisfactory coarse mesh accuracy, and simulation of both geometric and material nonlinearities.

1.4. Research Scope

The objective of this research study requires that the behavioral characteristics of RCFT members be explored in detail. For this purpose, in an initial phase of this work reported in Tort and Hajjar (2003, 2004), the experimental studies available in the literature were examined and their results were documented in a database. Only well reported studies were considered and the specimens were limited to the ones with steel tubes manufactured using cold forming techniques. The data values stored for the specimens provided information about the types of limit states and progression of damage seen in RCFT members, connections, and frames. Utilizing the available data values, a damage assessment study was conducted and the effects of local damage levels to the structural response were investigated. This helped to associate those local damage levels with the performance objectives. In addition, the capacity of the RCFT members were quantified in terms of deformation and energy-based damage function values.

A three-dimensional distributed plasticity beam-column finite element formulation was developed to evaluate the seismic demand and capacity of RCFT frames. Mixed finite element principles were utilized to develop the computational models of RCFT beam-columns and steel girders as components of a moment frame. Both geometric and material nonlinearities were accounted for, as was interlayer slip between the steel and concrete along the length. Comprehensive constitutive relations simulating the salient features of RCFT members and steel girders were developed. This was achieved based on the calibration and verification studies that are conducted using the information recorded in the experimental database. Nonlinear connection response was not modeled directly in this formulation.

Multiple RCFT frame structures were designed following up-to-date design provisions. The building configurations were varied to investigate the governing variables affecting their seismic demand and capacity. The designed structures were subjected to a set of ground motion records representing various hazard levels. Studying

the analysis results, the demand imposed on the structural members was quantified as the mean values of the appropriate engineering demand parameters. The capacity of the RCFT frames under seismic loads was determined utilizing parametric nonlinear time history analysis techniques and the resulting median values of capacity were recorded.

A demand and capacity factor approach was then adopted to account for the randomness and uncertainty in demand and capacity calculations. The dispersion in the analysis results was processed to obtain confidence levels for performance evaluations of RCFT frames, and the resulting reliability-based, performance-based design methodology for composite frame structures is presented.

1.5. Overview of the Report

Chapter 2 describes the theory of the distributed plasticity fiber-based geometrically and materially nonlinear mixed finite element formulation. Chapter 3 and Chapter 4 document the development of the concrete and steel constitutive relations to be used with the mixed finite element method to analyze RCFT frames, respectively. Chapter 5 contains the verification studies performed to assess the accuracy of the mixed finite element formulation and the concrete and steel constitutive relations. Chapter 6 has the demand evaluation studies of multistory RCFT frames using nonlinear time history analysis. Chapter 7 describes the methodology to quantify the aleatoric and epistemic uncertainties associated with demand and capacity evaluations and also introduces the proposed performance-based design methodology. In Chapter 8, the conclusions of the research study and the recommended future work are presented. Appendix A was generated to document the supplemental equations required for the mixed finite element theory developed in Chapter 2.

Chapter 2

2. Finite Element Formulation of Rectangular Concrete-Filled Tube (RCFT) Beams, Columns and Beam-Columns

2.1. Introduction

Accurate prediction of nonlinear response of structural members using finite element methods is an important consideration in quantifying seismic demand and capacity of frames with RCFT columns and steel girders. Different from traditional prescriptive design specifications, performance-based design guidelines often requires multiple performance levels (e.g., immediate occupancy, collapse prevention) to be considered while evaluating or designing seismically resistance structures. These performance levels can be defined based on limit states involving force, deformation, and energy quantities. Therefore, realistic estimations of the limit states can only be obtained if the complete load vs. deformation response of structural members is captured reliably. This requires addressing sources of nonlinearities adequately in the analysis model.

The nonlinearity exhibited in structures under high levels of seismic loading is often attributed to material inelasticity (material nonlinearity) and change in the geometry of the structure (geometric nonlinearity). In RCFTs, material nonlinearities due to both steel and concrete need attention in the analysis model. The steel tube is often subjected to residual strains and stresses due to cold forming process and welding. This causes an early softening in the modulus of steel before the yielding stress is attained. Following the yielding of the steel tube, strength degradation may be observed due to bi-directional stress state of the steel tube and also due to local buckling of the steel tube wall. Experiments also show cyclic response that includes cyclic hardening, a decrease in the elastic zone of the steel material during cycling, and the Bauschinger effect (Sakino and Tomii, 1981; Gourley and Hajjar, 1994). Concrete cracking, in turn, takes place when

the tensile strength of concrete is breached. At that instant, a steep stress drop occurs and the modulus of concrete approaches to zero asymptotically. In compression, the modulus of concrete starts decreasing when the stress level is approximately 30% of the compressive strength of concrete. Once the compressive strength is breached, a strength degradation region initiates due to crushing of concrete. The severity of stress drop in this region is determined based on the amount of confinement provided by the steel tube and based on the damage accumulation during cyclic response. A typical characteristic feature of RCFT members is that load transfer between the steel tube and the concrete core is achieved through the interface connecting these two media. The load transfer mechanism also exhibits a nonlinear response depending on the bond strength and the amount of slip. RCFT columns and beam-columns in frame structures also exhibit two types of geometric nonlinearities, including effects due to chord-rotation ($P-\Delta$) and member curvature ($P-\delta$).

Computational models available in the literature for composite steel/concrete structures evolved predominantly from prior work on steel and reinforced-concrete members. Following the recent advances in experimental testing (Lin et al., 2004) and computational modeling (OpenSees, 2001), it is now possible to account for typical characteristics of composite members in the analysis model comprehensively. In the order of increasing complexity, four groups of analysis methods for composite members can be distinguished:

- Strain compatibility method
- Concentrated plasticity models
- Distributed plasticity models
- Continuum models

In the strain compatibility method, plasticity is assumed to occur over a finite length and a plastic hinge length is determined, which is often taken as approximately equal to the depth of the steel tube (e.g., Varma, 2000). The moment of the critical cross-section located at the middle of the plastic hinge region is calculated based on a given curvature by integration of the steel and concrete stresses over the composite cross-section. The steel and concrete stresses are calculated from the appropriate constitutive

relations. These relations can be cyclic or monotonic depending on the given curvature history. Once the moment vs. curvature pair of the plastic hinge is obtained, the corresponding lateral load vs. displacement pair of the composite member can be attained by equilibrium and integration of the curvature along the element length. This method of analysis is often used for cantilever beam-columns (Kawaguchi, 2000). It is an efficient tool and produces accurate simulations. However, it is crude in accounting for geometric nonlinearities and also adopting this method for analysis of frame type structures is complicated.

In concentrated plasticity formulations, material inelasticity is assumed to be limited to plastic hinges (usually of zero length) at the element ends. Initiation and evolution of material inelasticity are often traced by means of multiple surfaces and flow rules defined in the stress resultant space. The element remains elastic if the force point stays inside the loading surface. Plastic deformation starts when the loading surface is breached. The extent of plastic deformation is decided based on the distance between the loading surface and the bounding surface. The bounding surface defines the force state at which a limiting stiffness is attained by the structural member. It has often the same shape as the loading surface but it is larger in size as can be seen in Figure 2.1.

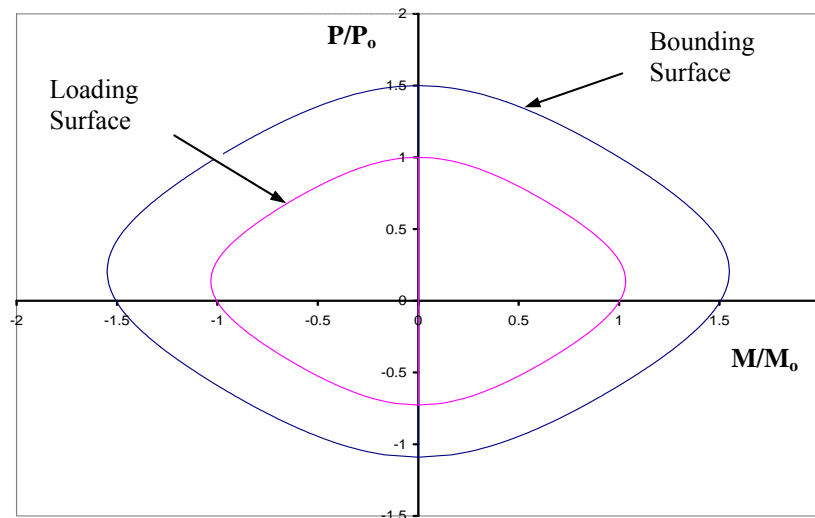


Figure 2.1 Typical Loading and Bounding Surfaces for CFTs

The loading and bounding surfaces harden isotropically and kinematically to simulate the load-deformation characteristics of RCFT members observed in the experimental tests. In the concentrated plasticity models, an element plastic reduction matrix is derived and included in the formulation of the total element tangent stiffness matrix. The plastic reduction matrix becomes effective if the force point contacts the loading surface at either end of the structural element. Throughout the analysis, the plastic reduction matrix is updated based on the degree of material inelasticity. The concentrated plasticity models become less accurate for members with high axial loads or for members under uniform bending, as in these situations stresses causing inelastic action are distributed along the member length rather than concentrated at the member ends. Therefore, they are often used for the analysis of unbraced structures, where elements deform in double curvature with maximum moments occurring at the element ends, or otherwise multiple elements are used along the member length. Concentrated plasticity models are computationally efficient and they can be easily adopted for frame analysis (Hajjar and Gourley, 1997; Hajjar et al., 1997; El-Tawil and Deierlein, 2001a, 2001b).

Distributed plasticity models account for the spread of plasticity through numerical integration over the volume of the element. Material inelasticity is monitored at the integration points located along the element length. At each integration point, the cross-section is divided into individual material fibers as shown in Figure 2.2. Physically, each fiber represents a two-dimensional (2D) media defined by its area, located with respect to the centroid of the cross-section, and a constitutive relation.

In distributed plasticity formulations, an assumption of plane sections remaining plane is often exploited to derive the strain at the centroid of each fiber from cross-sectional deformations. For the given strain, the stress and modulus of each fiber is calculated from the associated constitutive rule. Performing numerical integration over the cross-section, cross-sectional force and stiffness values may be obtained. Internal element forces and element tangent stiffness are calculated by integration of cross-section forces and stiffnesses along the element length, respectively. Compared to the concentrated plasticity models, the distributed plasticity approach is numerically more elaborate. However, it produces more accurate results since material inelasticity is traced

at multiple points through the cross section and along the element length rather than only at the element ends. The distributed plasticity models are also appealing for analysis of RCFT members. It is possible to account either explicitly or implicitly for the salient features of RCFTs (e.g., concrete cracking, confinement, local buckling etc.) using comprehensive constitutive relations for the steel and concrete fibers (Schiller and Hajjar, 1998; Hajjar et al., 1998a, 1998b; Domenech et al., 2002). As will be seen, accounting explicitly for slip between the constituent materials is also possible with distributed plasticity formulations.

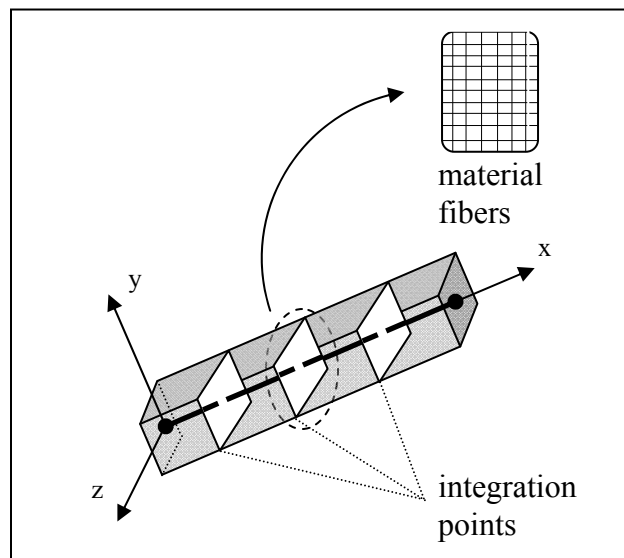


Figure 2.2 Distributed Plasticity Finite Element Formulation

Three-dimensional (3D) continuum analysis allows detailed simulation of RCFT members and provides significant information about their nonlinear response. The steel tube and concrete core are modeled by means of 3D finite elements. It is common to use brick elements for the concrete core and shell elements for the steel tube (Schneider, 1998; Varma 2000; Johansson and Gylltoft, 2002; Shakir-Khalil and Al-Rawdan, 1995). The composite interaction between the steel tube and concrete core can be modeled both in the transverse and longitudinal directions. Gap elements simulate the load-transfer in the transverse direction. In the longitudinal direction, the load transfer can be modeled using spring elements (Varma, 2000) or friction models (Schneider, 1998; Johansson and

Gylltoft, 2002). Since multi-dimensional constitutive models are employed to account for material inelasticity, softening response of the steel tube due to bidirectional stresses and confinement of concrete can be captured more reliably. In addition, local buckling of the steel tube can be treated as a geometric nonlinear phenomena rather than simulating it as a material nonlinear phenomena by degrading the steel tube strength, as may be done with concentrated or distributed plasticity formulations. Despite the improved accuracy and rationality of the 3D continuum analysis, it is computationally expensive for analyzing complete frame structures.

This chapter presents a distributed plasticity model for static and transient analysis of composite frames comprised of RCFT columns and steel girders (and braces, where included). The finite element formulation developed for RCFT and steel beam-columns are described.

2.2. Three-Dimensional Distributed Plasticity RCFT Beam-Column Element

Finite element formulations available in the literature often adopt different approaches based on the type of governing variables in the derivation of element internal forces and tangent stiffness matrices. As its name implies, in displacement (stiffness)-based formulations, nodal displacements are considered as the primary unknowns. Therefore, element deformations are obtained from displacement interpolations. It is common to adopt cubic Hermitian interpolation (shape) functions for transverse deformation fields. This assumption produces a linear distribution of curvature along the element length. However, inaccurate results are obtained in the case of nonlinear curvature fields unless the number of finite elements per member is increased. Element equilibrium is satisfied only in the variational sense (Zienkiewicz and Taylor, 2005). Therefore, the element internal forces calculated from the assumed displacement field often do not satisfy equilibrium. This also requires decreasing the mesh size by using more finite elements per member. The displacement-based formulations have been studied by many researchers in the literature for steel, reinforced concrete, and composite members (e.g., Zeris and Mahin, 1988; Izzuddin and Elnashai, 1993; Morales, 1994; Teh

and Clarke, 1998; Salari et al., 1998; Limkatanyu and Spacone, 2001; Alemdar, 2001). Despite the low accuracy of coarse meshes, the displacement-based formulations are often considered as easy to implement and expedient methods for analysis of structural members. In the case of composite members, the differential axial movement between the steel and concrete media can be derived directly from the deformation fields defined in the axial direction. Therefore, the bond force can be calculated with a direct calculation once the constitutive relation is defined for the interface.

In flexibility (force, equilibrium)-based finite element formulations, element internal forces are considered to be the primary unknowns. The stress resultants along the element length are obtained from interpolation functions. Therefore, element equilibrium is strictly satisfied. The compatibilities of nodal displacements and cross-section deformations are ensured in a variational sense. Since internal force distributions can be accurately estimated, the flexibility-based formulations provide better coarse mesh accuracy under nonlinear curvature fields (e.g., Backlund, 1976; Carol and Murcia, 1989; Salari et al., 1998; Neuenhofer and Filippou, 1998; Souza, 2000; Alemdar, 2001). For example, in the case of geometrically linear problems without any distributed span loading, a linear distribution of bending moments is always exact independent of the irregularity of the curvature field. The flexibility-based finite element formulations often have a computationally expensive and elaborate stiffness calculation and force recovery procedure compared to the displacement-based formulations. For example, calculation of the element stiffness matrix requires inversion of the element flexibility. In addition, the cross-section flexibility needs to be calculated by taking the inverse of the cross-sectional stiffness matrix when obtaining the cross-section deformations. In the case of 3D frame elements, these inversion operations increase the computation time. The satisfaction of the element compatibility involves iterative operations during the state determination process, which also increases the computation time. With respect to including a slip, when modeling composite elements using a flexibility-based formulation, the nonlinear distribution of bond forces along the element length is expressed using interpolation functions similar to those employed for axial forces and bending moments. . This results in lengthier expressions for internal force and stiffness derivations as compared to mixed

and displacement-based formulations because bond forces need to be calculated independent of other element forces.

Mixed (hybrid) finite element formulations offer an alternative method for calculation of element internal forces and tangent stiffness matrices by considering both displacements and forces as the primary unknowns. Independent interpolation functions are used to estimate element deformation and force fields. Selecting linear distributions of element forces, it is possible to satisfy element equilibrium exactly in the absence of geometric nonlinearity or distributed span loading. In addition, in the mixed finite element formulation, the element deformations from an interpolated displacement field and the element deformations from an interpolated force field are both assessed and enforced to be compatible to each other in a variational sense (Taucer et al., 1991; Nukala and White 2004; Alemdar and White 2005). Therefore, selecting accurate force interpolation functions also improves the accuracy of the nonlinear curvature fields. The mixed finite element formulations also have a more complicated force recovery procedure than the displacement-based and flexibility-based formulations. This is due to the fact that in mixed-formulations element stiffness and internal force calculations are performed based on two primary variables (Alemdar, 2001). Compared to the flexibility-based formulations, selecting independent shape functions for the displacements and element forces helps in the solution of problems with significant interaction between internal forces and nodal displacements (e.g., geometric nonlinearity) because in the flexibility-based formulation it becomes difficult to select the appropriate force interpolation functions (Ayoub and Filippou, 2000). On the other hand, incorporation of geometric nonlinearity is the least cumbersome in the displacement-based formulations: employing comprehensive strain measures and high-degree interpolation functions, it is possible to simulate problems with significant nonlinearity. Nevertheless, it is the mixed formulations that provide the best balance between accurate assessment of nonlinear curvatures along the length, particularly due to material inelasticity, coupled with comprehensive capability to include geometric nonlinearity directly and cohesively in the formulation. In addition, when employing a mixed formulation for modeling of

composite members, similar to the displacement-based formulation, the slip response can be captured with simplified expressions of internal forces and element stiffness.

In this section, a 3D geometrically and materially nonlinear mixed finite element formulation for RCFT beam-columns is presented. Slip between the steel tube and concrete core is accounted for following the prior work by Hajjar et al. (1998a, 1998b). The governing differential equations of element equilibrium, compatibility, and cross-section equilibrium are adapted from Alemdar and White (2005).

2.2.1. Choice of Reference Axes

The deformation of an element can be divided into two components: the deformational displacements straining the element and the rigid body displacements causing rigid body rotations and translations. The deformational displacements are then defined with respect to a reference frame that is attached to the chord of the element and rotates with it (Crisfield, 1991). Elements developed in this corotational frame are often referred to as corotational elements.

In a corotational formulation, the deformational displacements are obtained by initially excluding (i.e., prior to accounting for) rigid body effects from the global element displacements. This type of decomposition allows representation of the element displacements with a reduced number of degrees-of-freedom (DOF). For example, in the case of 3D beam-column elements without torsional effects, two rotational deformations at each end and an axial elongation at a single end are sufficient to represent the element displacements completely. Therefore, the lengthy expressions in developing stiffness matrices and element internal forces are simplified. Despite the computational effort needed for transformations between corotational and global coordinates, the corotational formulation also reduces the number of operations in calculating stiffness matrices and element internal forces (Alemdar, 2001). The DOFs in the corotational frame are often designated as element natural DOFs. The element forces corresponding to natural displacements and the element stiffness matrix formulated in the corotational frame are referred as natural element forces and natural element stiffness matrix,

respectively. In this study, a corotational approach is employed in formulating the RCFT beam-column element.

2.2.2. Kinematic Equations

The cross-sectional deformations of a conventional 3D beam-column element without torsional effects can be represented by an axial strain (ε) and two curvatures (κ) about two orthogonal axes. These deformations are defined for the centroidal axes of the element volume and if it is required to obtain similar deformations at an arbitrary point on the cross-section, certain transformation rules should be applied as it is described while deriving the virtual work equation of equilibrium.

While defining the cross-sectional strains for an RCFT beam-column element, the steel and concrete volumes need to be considered independently. A total of six deformations are introduced including an axial strain and two curvatures defined for the concrete core and steel tube, separately, including ε^c , κ_z^c , κ_y^c , ε^s , κ_z^s , and κ_y^s . All shear deformation components of the cross-section, including both torsion and beam shear about both axes, are neglected. The curvatures of the steel tube and concrete core will later be constrained to be the same due the rotational compatibility between the two media. Similarly, the corresponding cross-sectional forces are represented by an axial force (P) and two moments (M) defined for the concrete core and steel tube, separately, which yields six force components as P^c , M_z^c , M_y^c , P^s , M_z^s , and M_y^s . The vectorial forms of the cross-sectional strains (\hat{d}) and forces (D) and their variations are given in Equations 2.1 and 2.2, respectively. In Equations 2.1 and 2.2 and also for the rest of the equations in this report, the variables associated with the steel tube or concrete core alone are designated by right superscripts where “s” stand for the steel tube and “c” stands for the concrete core. In addition, the δ operator denotes the variation of the adjacent variable. The symbols in bold represent either vector or matrix quantities while the non-bold symbols designate scalar quantities.

$$\hat{\mathbf{d}} = \left[\varepsilon^c \ \kappa_z^c \ \kappa_y^c \ \varepsilon^s \ \kappa_z^s \ \kappa_y^s \right]^T \quad [2.1a]$$

$$\delta \hat{\mathbf{d}} = \left[\delta \varepsilon^c \quad \delta \kappa_z^c \quad \delta \kappa_y^c \quad \delta \varepsilon^s \quad \delta \kappa_z^s \quad \delta \kappa_y^s \right]^T \quad [2.1b]$$

$$\mathbf{D} = \left[P^c \quad M_z^c \quad M_y^c \quad P^s \quad M_z^s \quad M_y^s \right]^T \quad [2.2a]$$

$$\delta \mathbf{D} = \left[\delta P^c \quad \delta M_z^c \quad \delta M_y^c \quad \delta P^s \quad \delta M_z^s \quad \delta M_y^s \right]^T \quad [2.2b]$$

In the current formulation large rotations and translations take place with respect to the global coordinates due to rigid body motion. However, by eliminating rigid body effects, small curvatures and axial strains are assumed in the corotational frame. The Green-Lagrange strain measure is selected to define the elongation of the element chord. The Green-Lagrange strain is presented in Equations 2.3 and 2.4 in terms of the deformation fields of u , v , and w in the x , y , and z directions, respectively.

$$\varepsilon^c = u_{,x}^c + \frac{1}{2}(u_{,x}^c)^2 + \frac{1}{2}(v_{,x}^c)^2 + \frac{1}{2}(w_{,x}^c)^2 \quad [2.3]$$

$$\varepsilon^s = u_{,x}^s + \frac{1}{2}(u_{,x}^s)^2 + \frac{1}{2}(v_{,x}^s)^2 + \frac{1}{2}(w_{,x}^s)^2 \quad [2.4]$$

The first variation of the axial strains can be obtained as given below in Equations 2.5 and 2.6.

$$\delta \varepsilon^c = \delta(u^c)_{,x} + (u^c)_{,x} \times \delta(u^c)_{,x} + (v^c)_{,x} \times \delta(v^c)_{,x} + (w^c)_{,x} \times \delta(w^c)_{,x} \quad [2.5]$$

$$\delta \varepsilon^s = \delta(u^s)_{,x} + (u^s)_{,x} \times \delta(u^s)_{,x} + (v^s)_{,x} \times \delta(v^s)_{,x} + (w^s)_{,x} \times \delta(w^s)_{,x} \quad [2.6]$$

Curvatures can be expressed as the second derivatives of the translational deformation fields as given in Equation 2.7. The first variations of the curvatures are presented in Equation 2.8. Due to the compatibility of rotations, the curvatures of the steel tube and the concrete are imposed to be equal to each other.

$$\kappa_z^c = v_{,xx}^c \quad \kappa_y^c = w_{,xx}^c \quad \kappa_z^s = v_{,xx}^s \quad \kappa_y^s = w_{,xx}^s \quad [2.7]$$

$$\delta \kappa_z^c = \delta v_{,xx}^c \quad \delta \kappa_y^c = \delta w_{,xx}^c \quad \delta \kappa_z^s = \delta v_{,xx}^s \quad \delta \kappa_y^s = \delta w_{,xx}^s \quad [2.8]$$

In this study, the interaction between the steel tube and concrete core is considered to be provided by friction and interlocking effects between the two media, or via shear connectors. Therefore, a distributed bond along the element length is assumed to ensure the composite action. In the proposed model, the steel tube and concrete core are

separated by a layer of nonlinear springs located at each integration point along the element length as shown in Figure 2.3. In this work, the constitutive calibration of the slip springs assumes no shear connectors are present within the tube, but other constitutive calibrations of the slip springs may be used. The slip between the steel tube and concrete core is only allowed in the axial direction. The same transverse displacements are assumed via the use of penalty functions (see Section 2.2.13). The slip layer deformation field (\hat{d}_{sc}) and its variation ($\delta\hat{d}_{sc}$) can be expressed in terms of axial deformations of the steel tube and concrete core as follows in Equations 9 and 10, respectively.

$$\hat{d}_{sc} = u^s - u^c \quad [2.9]$$

$$\delta\hat{d}_{sc} = \delta u^s - \delta u^c \quad [2.10]$$

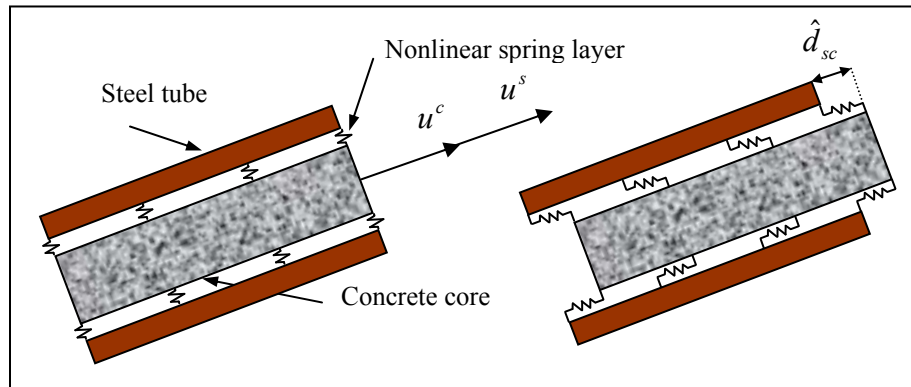


Figure 2.3 Nonlinear Slip Model

2.2.3. Finite Element Discretization

The element deformations with respect to the corotational frame are selected such that when they are transformed into the global coordinates, the steel tube and concrete core will have independent translational DOFs. This approach is adopted to allow the slip formation at the interface between the steel tube and concrete core for an arbitrarily oriented element.

In the corotational frame, the element deformations (\mathbf{q}) are comprised of axial deformations, rotations at both ends of the member with respect to local y and z axes, and deformation of the slip layer. An additional node with a single DOF is defined at the middle of the member chord. With the introduction of this extra mid-node, it is possible to have a quadratic interpolation function for the axial deformations. Defining the axial deformation fields in this fashion allows accurate representation of axial strains in the presence of nonlinear material response that is different at the two ends of the element, particularly in the presence of differential slip along the element length. In addition, utilizing a high degree of interpolation function for the axial deformation fields reduces the membrane locking effects (White, 1986; Alemdar, 2001). Two axial deformation DOFs are defined for both the steel tube and concrete core corresponding to the first and mid-node of the element. For the RCFT beam-column element, external loads are assumed to be applied only at the element ends. Therefore, the DOFs corresponding to the extra mid-node should be condensed out during transformations of the natural forces and natural stiffness from the corotational frame to the global coordinates. Despite the fact that the concrete and steel rotations for an RCFT member are assumed to be the same, independent rotational DOFs are defined. This approach allows quantifying the shear force carried by the steel tube and concrete core individually when the natural element forces are transformed into the global coordinates. A DOF for the deformation of the slip layer is also introduced in natural coordinates. A summary of the corotational DOFs for the RCFT beam-column element can be seen in Figure 2.4 and in Equation 2.11. The notation designating the element deformations in the corotational frame is described below:

e_m^c is the axial deformation of concrete between i-end of the member and the midpoint node

e^c is the axial deformation of concrete between i-end and j-end of the member

θ_{yi}^c is the rotation of the concrete at the i-end node about y axis

θ_{yj}^c is the rotation of the concrete at the j-end node about y axis

θ_{zi}^c is the rotation of the concrete at the i-end node about z axis

θ_{zj}^c is the rotation of the concrete at the j-end node about z axis

The corotational deformations corresponding to the steel tube can be described similarly

e^{sc} is the deformation of the slip layer

$$\mathbf{q} = \left[e^{sc} \ e^c \ \theta_{zi}^c \ \theta_{yi}^c \ \theta_{zj}^c \ \theta_{yj}^c \ e^s \ \theta_{zi}^s \ \theta_{yi}^s \ \theta_{zj}^s \ \theta_{yj}^s \ e_m^c \ e_m^s \right]^T \quad [2.11]$$

As was discussed previously, quadratic interpolation functions are employed to represent the axial deformation fields (u^s, u^c) along the element length. The transverse deformation fields (v^s, v^c, w^s, w^c) are defined using cubic Hermitian shape functions (McGuire et al., 2000). It is possible to express the deformation, velocity ($\dot{u}^s, \dot{u}^c, \dot{v}^s, \dot{v}^c, \dot{w}^s, \dot{w}^c$), and acceleration ($\ddot{u}^s, \ddot{u}^c, \ddot{v}^s, \ddot{v}^c, \ddot{w}^s, \ddot{w}^c$) fields in terms of element deformations as given in Equation 2.12.

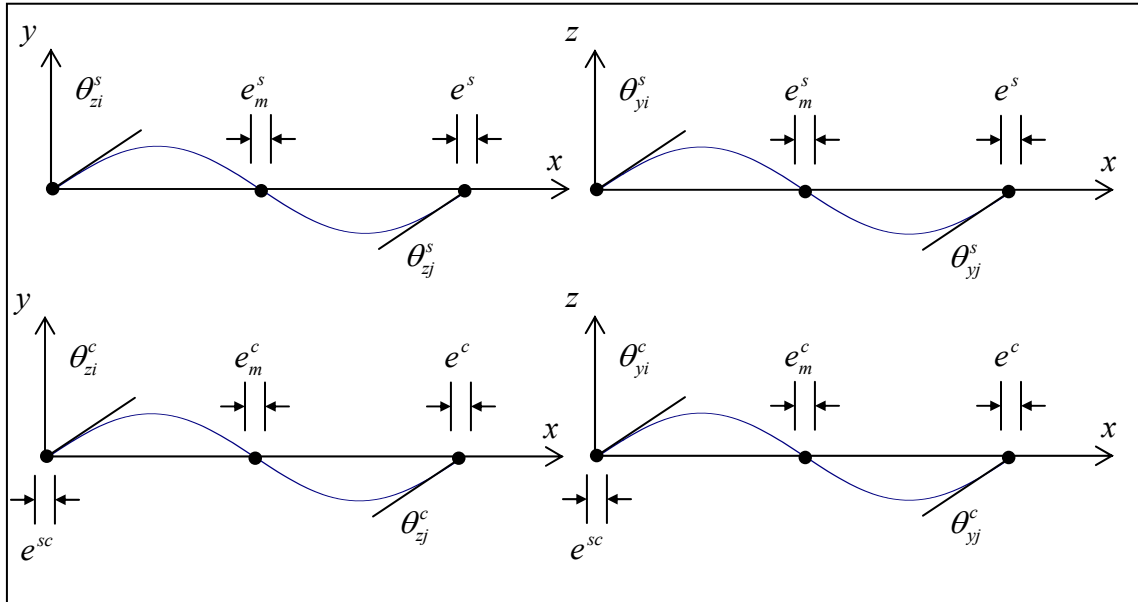


Figure 2.4 Element Deformations in the Corotational Frame

$$\mathbf{u} = \mathbf{N}_u \times \mathbf{q} \quad [2.12a]$$

$$\mathbf{u}^c = \mathbf{N}_u^c \times \mathbf{q}, \quad \mathbf{u}^s = \mathbf{N}_u^s \times \mathbf{q} \quad [2.12b]$$

$$\dot{\mathbf{u}}^c = \mathbf{N}_u^c \times \dot{\mathbf{q}}, \quad \dot{\mathbf{u}}^s = \mathbf{N}_u^s \times \dot{\mathbf{q}} \quad [2.12c]$$

$$\ddot{\mathbf{u}}^c = \mathbf{N}_u^c \times \ddot{\mathbf{q}}, \quad \ddot{\mathbf{u}}^s = \mathbf{N}_u^s \times \ddot{\mathbf{q}} \quad [2.12d]$$

where: $\mathbf{u} = [u^c \ v^c \ w^c \ u^s \ v^s \ w^s]^T$

$$\mathbf{u}^c = [u^c \ v^c \ w^c]^T, \quad \mathbf{u}^s = [u^s \ v^s \ w^s]^T$$

$$\dot{\mathbf{u}}^c = [\dot{u}^c \ \dot{v}^c \ \dot{w}^c]^T, \quad \dot{\mathbf{u}}^s = [\dot{u}^s \ \dot{v}^s \ \dot{w}^s]^T$$

$$\ddot{\mathbf{u}}^c = [\ddot{u}^c \ \ddot{v}^c \ \ddot{w}^c]^T, \quad \ddot{\mathbf{u}}^s = [\ddot{u}^s \ \ddot{v}^s \ \ddot{w}^s]^T$$

\mathbf{N}_u is the displacement interpolation functions in matrix form (see Appendix A)

\mathbf{N}_u^c is the concrete core displacement interpolation functions in matrix form (see Appendix A)

\mathbf{N}_u^s is the steel tube displacement interpolation functions in matrix form (see Appendix A)

The natural element end forces (\mathbf{Q}) are selected to be axial forces and bending moments about local y and z axis. They are also defined independently for the steel tube and concrete core. Equation 2.13 shows the element end forces in the corotational frame. Linear interpolation functions are adopted for expressing the force resultants given in Equation 2.14. However, second order moments due to $P - \delta$ effects are included in the interpolation functions for the moment field (see Appendix A).

Therefore, the linear variation of moment field is not valid due to geometric nonlinearity.

$$\mathbf{Q} = [P_i^c \ P_j^c \ M_{zi}^c \ M_{yi}^c \ M_{zj}^c \ M_{yj}^c \ P_i^s \ P_j^s \ M_{zi}^s \ M_{yi}^s \ M_{zj}^s \ M_{yj}^s]^T \quad [2.13]$$

$$\mathbf{D} = \mathbf{N}_{D1} \times \mathbf{Q} \quad [2.14]$$

where: \mathbf{N}_{D1} is the force interpolations in matrix form (see Appendix A)

2.2.4. The Equation of Equilibrium

The statement of equilibrium in differential form can be obtained considering an infinitesimal length (dx) and infinitesimal interface area (dI) of the proposed RCFT beam-column element. Figure 2.5 and Figure 2.6 illustrate the internal element loading for the infinitesimal length with respect to the natural coordinate system. From Figure 2.5 and 2.6, the corresponding equilibrium equations of axial forces, shear forces, and

bending moments can be obtained as given in Equation 2.15. It was assumed that RCFT members exhibit a linear torsional response. Therefore, torsional moment is excluded in the equilibrium equations and it will be incorporated into the formulation later in Section 2.2.12.

The nomenclature described in Yang and Kuo (1994) is used in this report in order to identify the configurations of the variables that they were defined and referenced. Both superscripts and subscripts located to left of a symbol refer to two configurations of interest. C1 represents the last converged state and C2 stands for the current state of the element body. A left superscript designates the configuration in which the quantity is measured. If a left superscript is omitted, the quantity is considered as an increment between C1 and C2 or between the current and the next C2 configuration (e.g., during an iteration process). A left subscript identifies the reference configuration of the quantity. It is a common practice not to use a left subscript if a quantity is defined in the same configuration in which it is measured.

$$-\frac{d({}^2P^s)}{d({}^2x)} + \frac{{}^2D_{sc} \times d({}^2I)}{d({}^2x)} = 0, \quad -\frac{d({}^2P^c)}{d({}^2x)} - \frac{{}^2D_{sc} \times d({}^2I)}{d({}^2x)} = 0 \quad [2.15a]$$

$$\frac{d({}^2V_y^c)}{d({}^2x)} = 0, \quad \frac{d({}^2V_y^s)}{d({}^2x)} = 0, \quad \frac{d({}^2V_z^c)}{d({}^2x)} = 0, \quad \frac{d({}^2V_z^s)}{d({}^2x)} = 0 \quad [2.15b]$$

$${}^2P^c \times \frac{d({}_2v^c)}{d({}^2x)} - \frac{d({}^2M_z^c)}{d({}^2x)} + {}^2V_y^c = 0, \quad {}^2P^s \times \frac{d({}_2v^s)}{d({}^2x)} - \frac{d({}^2M_z^s)}{d({}^2x)} + {}^2V_y^s = 0 \quad [2.15c]$$

$${}^2P^c \times \frac{d({}_2w^c)}{d({}^2x)} - \frac{d({}^2M_y^c)}{d({}^2x)} + {}^2V_z^c = 0, \quad {}^2P^s \times \frac{d({}_2w^s)}{d({}^2x)} - \frac{d({}^2M_y^s)}{d({}^2x)} + {}^2V_z^s = 0 \quad [2.15d]$$

where: ${}^2P^c$ is the axial force of steel tube in configuration C2

${}^2V_y^c$ is the shear force of concrete core in y direction in configuration C2

${}^2V_z^c$ is the shear force of concrete core in z direction in configuration C2

${}^2M_y^c$ is the bending moment of concrete core in y direction in configuration C2

${}^2M_z^c$ is the bending moment of concrete core in z direction in configuration C2
 ${}^2P^s$ is the axial force of steel tube in configuration C2
 ${}^2V_y^s$ is the shear force of concrete core in y direction in configuration C2
 ${}^2V_z^s$ is the shear force of concrete core in z direction in configuration C2
 ${}^2M_y^s$ is the bending moment of concrete core in y direction in configuration C2
 ${}^2M_z^s$ is the bending moment of concrete core in z direction in configuration C2
 ${}^2D_{sc}$ is the force transferred between steel tube and concrete core per unit area in configuration C2 (units of force/length²)
 ${}_2u^c$ is the incremental displacement field of concrete core in x direction with respect to configuration C2
 ${}_2v^c$ is the incremental displacement field of concrete core in y direction with respect to configuration C2
 ${}_2w^c$ is the incremental displacement field of concrete core in z direction with respect to configuration C2
 ${}_2u^s$ is the incremental displacement field of steel tube in x direction with respect to configuration C2
 ${}_2v^s$ is the incremental displacement field of steel tube in y direction with respect to configuration C2
 ${}_2w^s$ is the incremental displacement field of steel tube in z direction with respect to configuration C2
 2I is the interface area in configuration C2

Differentiating Equations 2.15c and 2.15d with respect to x , and then substituting Equation 2.15b, Equations 2.15c and 15d become as follows:

$$-{}^2P^c \times \frac{d^2({}_2v_y^c)}{d({}^2x)^2} + \frac{d^2({}^2M_z^c)}{d({}^2x)^2} = 0, \quad -{}^2P^s \times \frac{d^2({}_2v_y^s)}{d({}^2x)^2} + \frac{d^2({}^2M_z^s)}{d({}^2x)^2} = 0 \quad [2.16a]$$

$$-{}^2P^c \times \frac{d^2({}_2v_z^c)}{d({}^2x)^2} + \frac{d^2({}^2M_y^c)}{d({}^2x)^2} = 0, \quad -{}^2P^s \times \frac{d^2({}_2v_z^s)}{d({}^2x)^2} + \frac{d^2({}^2M_y^s)}{d({}^2x)^2} = 0 \quad [2.16b]$$

The weak form of the equilibrium equations stated above can be obtained if Equations 2.15a, 2.16a, 2.16b are multiplied by weight functions and integrated along the element length (L).

$$\begin{aligned} & \int_0^{2L} \delta_2 u^s \times \left(-\frac{d({}^2P^s)}{d({}^2x)} + \frac{{}^2D_{sc} \times d^2I}{d^2x} \right) \times d^2x + \\ & \int_0^{2L} \delta_2 u^c \times \left(-\frac{d({}^2P^c)}{d({}^2x)} - \frac{{}^2D_{sc} \times d^2I}{d^2x} \right) \times d^2x + \\ & \int_0^{2L} \delta_2 v^c \times \left(-{}^2P^c \times \frac{d^2({}_2v_y^c)}{d({}^2x)^2} + \frac{d^2({}^2M_z^c)}{d({}^2x)^2} \right) \times d^2x + \int_0^{2L} \delta_2 v^s \times \left(-{}^2P^s \times \frac{d^2({}_2v_y^s)}{d({}^2x)^2} + \frac{d^2({}^2M_z^s)}{d({}^2x)^2} \right) \times d^2x + \\ & \int_0^{2L} \delta_2 w^c \times \left(-{}^2P^c \times \frac{d^2({}_2v_z^c)}{d({}^2x)^2} + \frac{d^2({}^2M_y^c)}{d({}^2x)^2} \right) \times d^2x + \int_0^{2L} \delta_2 w^s \times \left(-{}^2P^s \times \frac{d^2({}_2v_z^s)}{d({}^2x)^2} + \frac{d^2({}^2M_y^s)}{d({}^2x)^2} \right) \times d^2x = 0 \end{aligned} \quad [2.17]$$

In order to reduce the order of differentiation of the dependent variables (e.g., ${}^2P^c$, ${}^2M_y^c$, ${}^2M_z^c$, ${}^2P^s$, ${}^2M_y^s$, ${}^2M_z^s$, ${}^2D_{sc}$) and distribute differentiation to the weighting functions (e.g., $\delta_2 u^s$, $\delta_2 v_y^c$, $\delta_2 w_y^c$, $\delta_2 u^s$, $\delta_2 v_y^c$, $\delta_2 w_y^c$), the integral terms in Equation 2.17 are reformatted through integration by parts as in Equations 2.18 through 2.23 (Reddy, 1993). It should be noted that the integration by parts is applied to the second through fifth terms two times until the second derivative of the dependent variables are transferred to the weight functions. Throughout the rest of the discussions and equations, the operators “ $,x$ ” and “ $,xx$ ” are used as right subscripts representing first and second derivatives with respect to the x direction, respectively.

$$-\int_0^{2L} \delta_2 u^c \times {}^2P^c_{,x} \times d^2x - \int_0^{2L} \delta_2 u^c \times {}^2D_{sc} \times d^2I = -\delta_2 u^c \times {}^2P^c \Big|_0^{2L} + \int_0^{2L} {}^2P^c \times (\delta_2 u^c)_{,x} \times d^2x - \int_0^{2L} \delta_2 u^c \times {}^2D_{sc} \times d^2I \quad [2.18]$$

$$-\int_0^{2L} \delta_2 u^s \times {}^2P^s_{,x} \times d^2x + \int_0^{2L} \delta_2 u^s \times {}^2D_{sc} \times d^2I = -\delta_2 u^s \times {}^2P^s \Big|_0^{2L} + \int_0^{2L} {}^2P^s \times (\delta_2 u^s)_{,x} \times d^2x + \int_0^{2L} \delta_2 u^s \times {}^2D_{sc} \times d^2I \quad [2.19]$$

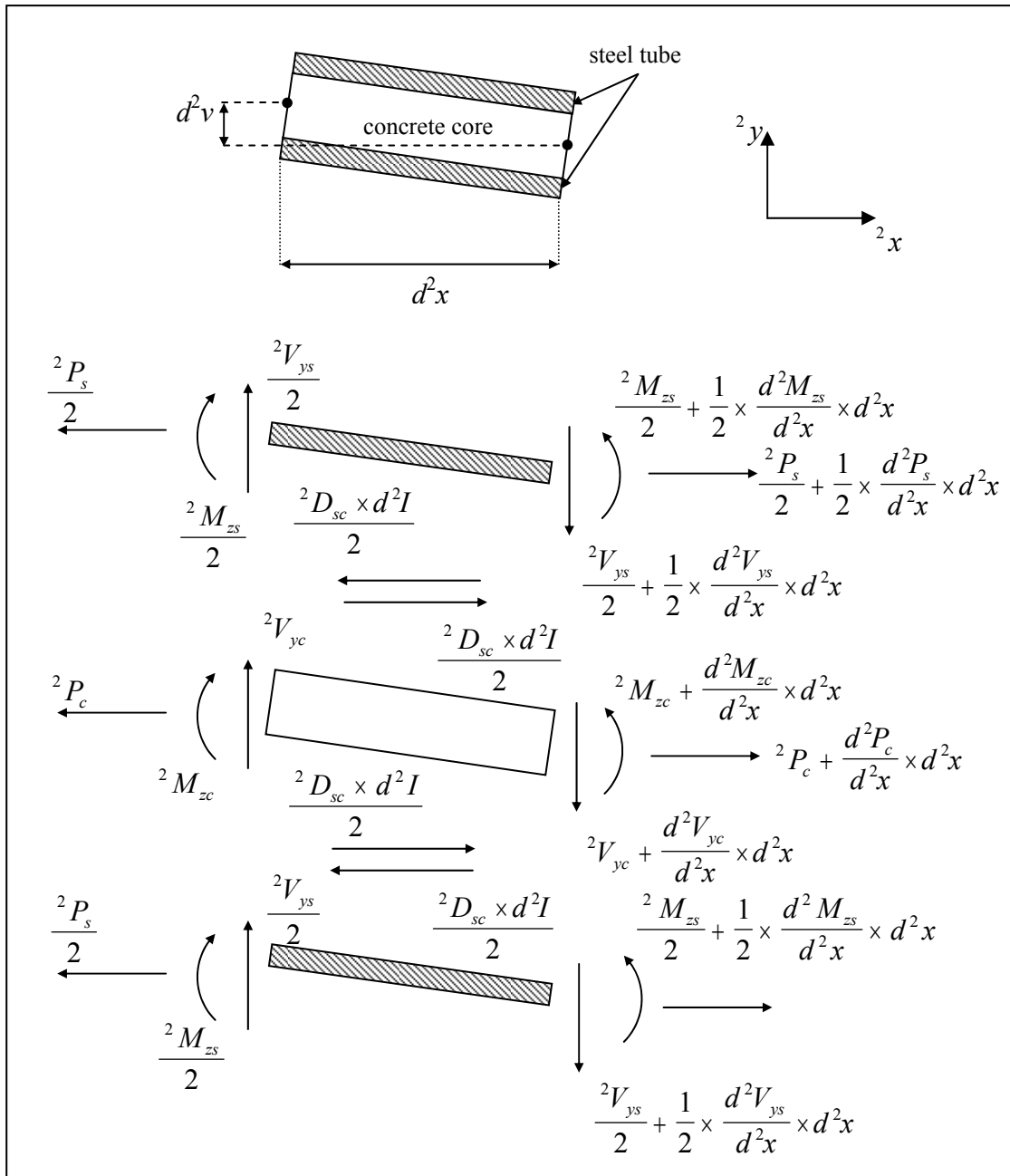


Figure 2.5 Internal Element Loading in the x - y plane

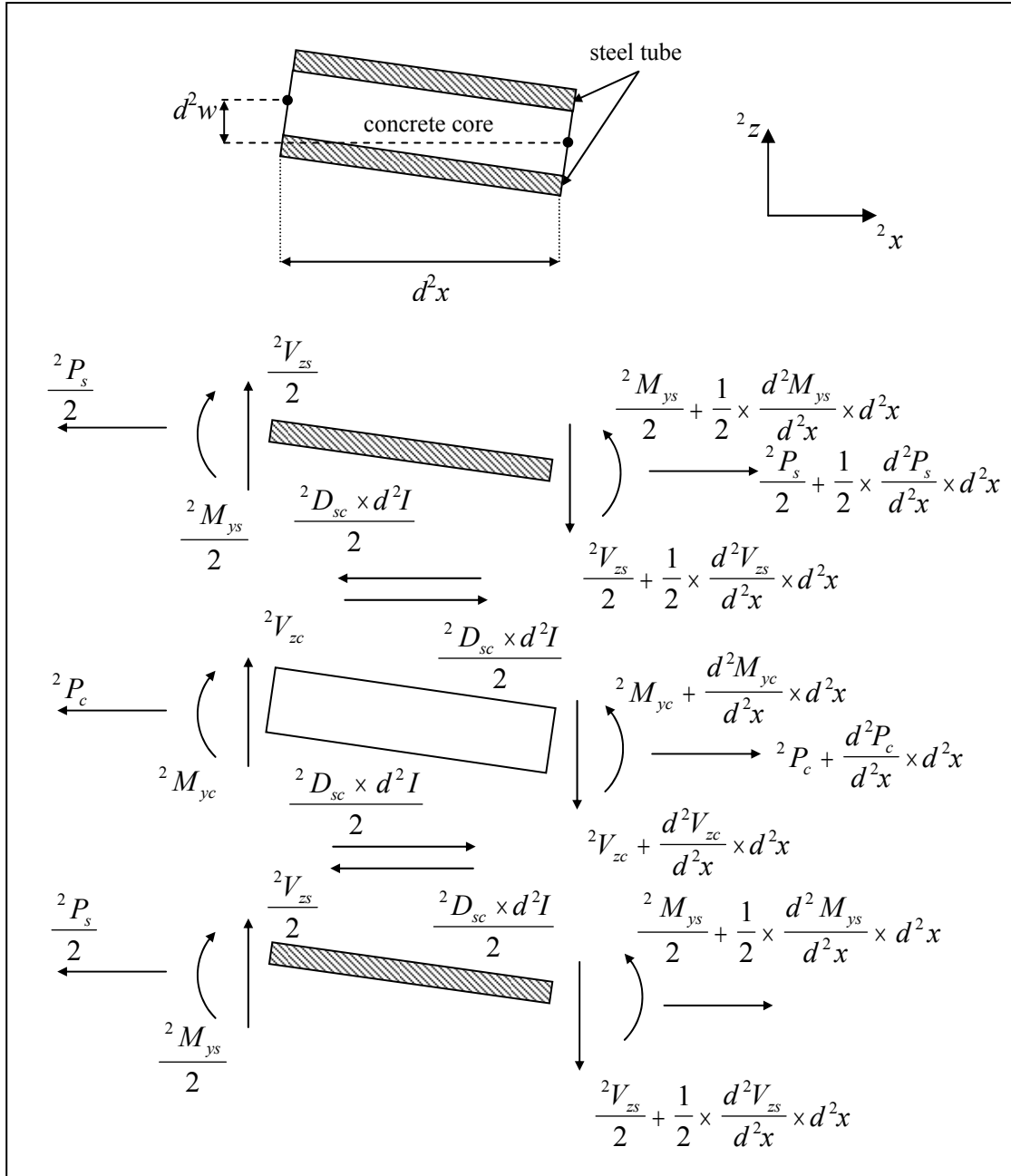


Figure 2.6 Internal Element Loading in the x - z plane

$$\int_0^{2L} \delta_2 v^c \times \left(-2P^c \times (2v^c)_{,xx} + (2M_z^c)_{,xx} \right) \times d^2x =$$

$$\left(\delta_2 v^c \times (2M_z^c)_{,xx} - (\delta_2 v^c)_{,x} \times 2M_z^c - \delta_2 v^c \times 2P^c \times (2v^c)_{,x} \right) \Big|_0^{2L} + \int_0^{2L} \left(2M_z^c \times (\delta_2 v^c)_{,xx} + 2P^c \times (2v^c)_{,x} \times (\delta_2 v^c)_{,x} \right) \times d^2x$$

[2.20]

$$\begin{aligned}
& \int_0^{2L} \delta_2 v^s \times \left(-{}^2P^s \times ({}_2v^s)_{,xx} + ({}^2M_z^s)_{,xx} \right) \times d^2x = \\
& \left(\delta_2 v^s \times ({}^2M_z^s)_{,xx} - (\delta_2 v^s)_{,x} \times {}^2M_z^s - \delta_2 v^s \times {}^2P^s \times ({}_2v^s)_{,x} \right) \Big|_0^{2L} + \int_0^{2L} \left({}^2M_z^s \times (\delta_2 v^s)_{,xx} + {}^2P^s \times ({}_2v^s)_{,x} \times (\delta_2 v^s)_{,x} \right) \times d^2x
\end{aligned} \tag{2.21}$$

$$\begin{aligned}
& \int_0^{2L} \delta_2 w^c \times \left(-{}^2P^c \times ({}_2w^c)_{,xx} + ({}^2M_y^c)_{,xx} \right) \times d^2x = \\
& \left(\delta_2 w^c \times ({}^2M_y^c)_{,xx} - (\delta_2 w^c)_{,x} \times {}^2M_y^c - \delta_2 w^c \times {}^2P^c \times ({}_2w^c)_{,x} \right) \Big|_0^{2L} + \int_0^{2L} \left({}^2M_y^c \times (\delta_2 w^c)_{,xx} + {}^2P^c \times ({}_2w^c)_{,x} \times (\delta_2 w^c)_{,x} \right) \times d^2x
\end{aligned} \tag{2.22}$$

$$\begin{aligned}
& \int_0^{2L} \delta_2 w^s \times \left(-{}^2P^s \times ({}_2w^s)_{,xx} + ({}^2M_y^s)_{,xx} \right) \times d^2x = \\
& \left(\delta_2 w^s \times ({}^2M_y^s)_{,xx} - (\delta_2 w^s)_{,x} \times {}^2M_y^s - \delta_2 w^s \times {}^2P^s \times ({}_2w^s)_{,x} \right) \Big|_0^{2L} + \int_0^{2L} \left({}^2M_y^s \times (\delta_2 w^s)_{,xx} + {}^2P^s \times ({}_2w^s)_{,x} \times (\delta_2 w^s)_{,x} \right) \times d^2x
\end{aligned} \tag{2.23}$$

Substituting Equation 2.18 through 2.23 into Equation 2.17, the weak form of equilibrium equation becomes as follows:

$$\begin{aligned}
& \int_0^{2L} \begin{bmatrix} (\delta_2 u^c)_{,x} + ({}_2v^c)_{,x} \times (\delta_2 v^c)_{,x} + ({}_2w^c)_{,x} \times (\delta_2 w^c)_{,x} \\ (\delta_2 v^c)_{,xx} \\ (\delta_2 w^c)_{,xx} \\ (\delta_2 u^s)_{,x} + ({}_2v^s)_{,x} \times (\delta_2 v^s)_{,x} + ({}_2w^s)_{,x} \times (\delta_2 w^s)_{,x} \\ (\delta_2 v^s)_{,xx} \\ (\delta_2 w^s)_{,xx} \end{bmatrix}^T \times \begin{bmatrix} {}^2P^c \\ {}^2M_z^c \\ {}^2M_y^c \\ {}^2P^s \\ {}^2M_z^s \\ {}^2M_y^s \end{bmatrix} \times d^2x \tag{2.24} \\
& + \int_0^{2L} (\delta_2 u^s - \delta_2 u^c) \times {}^2D_{sc} \times d^2I + \left(-\delta_2 u^s \times {}^2P^s - \delta_2 u^c \times {}^2P^c \right) \Big|_0^{2L} \\
& \left(\delta_2 v^c \times ({}^2M_z^c)_{,x} - (\delta_2 v^c)_{,x} \times {}^2M_z^c - \delta_2 v^c \times {}^2P^c \times ({}_2v^c)_{,x} \right) \Big|_0^{2L} \\
& \left(\delta_2 v^s \times ({}^2M_z^s)_{,x} - (\delta_2 v^s)_{,x} \times {}^2M_z^s - \delta_2 v^s \times {}^2P^s \times ({}_2v^s)_{,x} \right) \Big|_0^{2L} \\
& \left(\delta_2 w^c \times ({}^2M_y^c)_{,x} - (\delta_2 w^c)_{,x} \times {}^2M_y^c - \delta_2 w^c \times {}^2P^c \times ({}_2w^c)_{,x} \right) \Big|_0^{2L} \\
& \left(\delta_2 w^s \times ({}^2M_y^s)_{,x} - (\delta_2 w^s)_{,x} \times {}^2M_y^s - \delta_2 w^s \times {}^2P^s \times ({}_2w^s)_{,x} \right) \Big|_0^{2L} = 0
\end{aligned}$$

2.2.5. The Virtual work Equation of Equilibrium

The principle of virtual work can be derived substituting the kinematic relations stated in Equations 2.1 through 2.10 into Equation 2.24 as given below:

$$\begin{aligned}
& \int_0^{2L} \delta_2 \hat{\mathbf{d}} \times {}^2\mathbf{D} \times d^2x + \int_0^{2L} \delta_2 d_{sc} \times {}^2D_{sc} \times d^2I + \\
& \left(-\delta_2 u^s \times {}^2P^s - \delta_2 u^c \times {}^2P^c \right) \Big|_0^{2L} + \\
& \left(\delta_2 v^c \times \left({}^2M_z^c \right)_{,x} - \left(\delta_2 v^c \right)_{,x} \times {}^2M_z^c - \delta_2 v^c \times {}^2P^c \times \left({}^2v^c \right)_{,x} \right) \Big|_0^{2L} + \\
& \left(\delta_2 v^s \times \left({}^2M_z^s \right)_{,x} - \left(\delta_2 v^s \right)_{,x} \times {}^2M_z^s - \delta_2 v^s \times {}^2P^s \times \left({}^2v^s \right)_{,x} \right) \Big|_0^{2L} + \\
& \left(\delta_2 w^c \times \left({}^2M_y^c \right)_{,x} - \left(\delta_2 w^c \right)_{,x} \times {}^2M_y^c - \delta_2 w^c \times {}^2P^c \times \left({}^2w^c \right)_{,x} \right) \Big|_0^{2L} + \\
& \left(\delta_2 w^s \times \left({}^2M_y^s \right)_{,x} - \left(\delta_2 w^s \right)_{,x} \times {}^2M_y^s - \delta_2 w^s \times {}^2P^s \times \left({}^2w^s \right)_{,x} \right) \Big|_0^{2L} = 0
\end{aligned}$$

[2.25]

where: ${}^2\mathbf{D}$ is the cross-sectional forces in C2

${}^2\hat{\mathbf{d}}$ is the incremental cross-sectional strains with respect to C2

It should be noted the variation of axial strains defined in Equation 2.24

$(\delta \mathcal{E}^c = (\delta_2 u^c)_{,x} + ({}^2v^c)_{,x} \times (\delta_2 v^c)_{,x} + ({}^2w^c)_{,x} \times (\delta_2 w^c)_{,x})$ and

$\delta \mathcal{E}^s = (\delta_2 u^s)_{,x} + ({}^2v^s)_{,x} \times (\delta_2 v^s)_{,x} + ({}^2w^s)_{,x} \times (\delta_2 w^s)_{,x})$ does not have the terms of

$({}^2u^c)_{,x} \times (\delta_2 u^c)_{,x}$ and $({}^2u^s)_{,x} \times (\delta_2 u^s)_{,x}$ as given in Equations 2.5 and 2.6. However,

these terms represent high order effects that become significant under large axial strains, which are not commonly observed for structural members. Therefore, Equation 2.25 still can be considered an accurate representation of equilibrium.

In Equation 2.25, the third through seventh terms on the left hand side represent the boundary conditions of the RCFT beam-column element. Introducing the interpolation functions of the force and displacement variables given in Equations 2.11

through 2.14, the aforementioned expressions can be derived as ${}^2\mathbf{q}^T \times {}^2\mathbf{Q}_{ext}$. Therefore, the virtual work equation of equilibrium can further be simplified as follows:

$$\int_0^{2L} \delta_2 \hat{\mathbf{d}}^T \times {}^2\mathbf{D} \times d^2x + \int_0^{2L} \delta_2 \hat{\mathbf{d}}_{sc}^T \times {}^2D_{sc} \times d^2I - \delta_2 \mathbf{q}^T \times {}^2\mathbf{Q}_{ext} = 0 \quad [2.26]$$

where: ${}^2\mathbf{q}$ is the incremental nodal displacements with respect to configuration C2

${}^2\mathbf{Q}_{ext}$ is the external load in configuration C2

The virtual work equation of equilibrium in Equation 2.26 is expressed at the cross-section level with the corresponding deformation and force variables. The derivation initiated by writing the partial differential equations obtained through static equilibrium of an infinitesimal beam-element. The final format was attained when the weak form of the partial differential equations is derived by performing integration by parts. On the other hand, Hajjar et al. (1998a, 1998b) derived the virtual work equation of equilibrium at the material fiber level allowing separate volumes for the steel tube and concrete core to be introduced. The derivation was solely based on the statement that the work done by external forces and internal stresses are equal to each other. The contributions of the steel tube and concrete core to the equilibrium equation were decomposed by defining independent strain and stress resultant terms for the two media. It was also assumed that a spring layer exists between these two media for the load transfer and an additional term was introduced into the virtual work equation of equilibrium to account for the strain energy resulting from the deformation of the layer of springs as given in Equation 2.27. In Equation 2.27, on the left hand side, the first two terms represent the work done by internal stresses and the third term designates the energy due to slip. The terms on the right hand side accounts for the work done by external loads.

$$\int_{{}^2V^c} {}^2\boldsymbol{\tau}_{ij}^c \times \delta_2 \mathbf{e}_{ij}^c \times d^2V^c + \int_{{}^2V^s} {}^2\boldsymbol{\tau}_{ij}^s \times \delta_2 \mathbf{e}_{ij}^s \times d^2V^s + \int_{{}^2I} \delta_2 \hat{\mathbf{d}}_{sc} \times {}^2D_{sc} \times d^2I = \int_{{}^2S^c} {}^2\mathbf{t}_i^c \times \delta_2 \mathbf{u}^c \times d^2S^c + \int_{{}^2S^s} {}^2\mathbf{t}_i^s \times \delta_2 \mathbf{u}^s \times d^2S^s \quad [2.27]$$

where: ${}^2\boldsymbol{\tau}_{ij}^c$ is the Cauchy stress tensor of the concrete core in configuration C2

${}^2\mathbf{e}_{ij}^c$ is the incremental engineering strain tensor of the concrete core with respect to configuration C2

${}^2\boldsymbol{\tau}_{ij}^s$ is the Cauchy stress tensor of the concrete core in configuration C2

${}^2\mathbf{e}_{ij}^s$ is the incremental engineering strain tensor of the concrete core with respect to configuration C2

${}^2\mathbf{t}_i^c$ is the surface tractions acting on the concrete core in configuration C2

${}^2\mathbf{t}_i^s$ is the surface tractions acting on the steel tube in configuration C2

${}^2S^c$ is the surface area of the concrete core in configuration C2

${}^2S^s$ is the surface area of the steel tube in configuration C2

${}^2V^c$ is the volume of the concrete core in configuration C2

${}^2V^s$ is the volume of the steel tube in configuration C2

Since shear strains of RCFT members are neglected, the tensorial quantities of Cauchy stress (${}^2\boldsymbol{\tau}_{ij}^c, {}^2\boldsymbol{\tau}_{ij}^s$) and engineering strain (${}^2\mathbf{e}_{ij}^c, {}^2\mathbf{e}_{ij}^s$) become axial stress (${}^2\sigma^c, {}^2\sigma^s$) and axial strain (${}_2e^c, {}_2e^s$), respectively as scalar variables. Exploiting the plane sections remain plain assumption, the axial strain values of the material fibers at an arbitrary location over the RCFT cross-section can be expressed in terms of deformations of the centroidal axes (e.g., $\boldsymbol{\varepsilon}^c, \boldsymbol{\kappa}_z^c, \boldsymbol{\kappa}_y^c, \boldsymbol{\varepsilon}^s, \boldsymbol{\kappa}_z^s, \boldsymbol{\kappa}_y^s$) as given in Equations 2.28 and 2.29.

$${}_2e^c = \mathbf{y}^T \times {}_2\hat{\mathbf{d}}^c \quad [2.28]$$

$${}_2e^s = \mathbf{y}^T \times {}_2\hat{\mathbf{d}}^s \quad [2.29]$$

where: $\mathbf{y} = [1 \quad -\tilde{y} \quad -\tilde{z}]^T$

$${}_2\hat{\mathbf{d}}^c = [{}_2\boldsymbol{\varepsilon}^c \quad {}_2\boldsymbol{\kappa}_z^c \quad {}_2\boldsymbol{\kappa}_y^c]^T$$

$${}_2\hat{\mathbf{d}}^s = [{}_2\boldsymbol{\varepsilon}^s \quad {}_2\boldsymbol{\kappa}_z^s \quad {}_2\boldsymbol{\kappa}_y^s]^T$$

\tilde{y} is the y coordinate of the material fiber on the RCFT cross-section

\tilde{z} is the z coordinate of the material fiber on the RCFT cross-section

Substituting Equations 2.28 and 2.29 into Equation 2.27, the virtual work equation of equilibrium by Hajjar et al. (1998a, 1998b) becomes as follows:

$$\int_{^2V^c} {}^2\boldsymbol{\sigma}^c \times \mathbf{y}^T \times \delta_2 \hat{\mathbf{d}}^c \times d^2V^c + \int_{^2V^s} {}^2\boldsymbol{\sigma}^s \times \mathbf{y}^T \times \delta_2 \hat{\mathbf{d}}^s \times d^2V^s + \int_{^2I} \delta_2 \hat{\mathbf{d}}_{sc} \times {}^2D_{sc} \times d^2I = \int_{^2S^c} {}^2\mathbf{t}_i^c \times \delta_2 \mathbf{u}^c \times d^2S^c + \int_{^2S^s} {}^2\mathbf{t}_i^s \times \delta_2 \mathbf{u}^s \times d^2S^s \quad [2.30]$$

Separating the volume integrals in Equation 2.30 into area and length integrals:

$$\int_0^{^2L} \left(\int_{^2S^c} {}^2\boldsymbol{\sigma}^c \times \mathbf{y}^T \times d^2A^c \right) \times \delta_2 \hat{\mathbf{d}}^c \times d^2x + \int_0^{^2L} \left(\int_{^2S^s} {}^2\boldsymbol{\sigma}^s \times \mathbf{y}^T \times d^2A^s \right) \times \delta_2 \hat{\mathbf{d}}^s \times d^2x + \int_{^2I} \delta_2 \hat{\mathbf{d}}_{sc} \times {}^2D_{sc} \times d^2I = \int_{^2S^c} {}^2\mathbf{t}_i^c \times \delta_2 \mathbf{u}^c \times d^2S^c + \int_{^2S^s} {}^2\mathbf{t}_i^s \times \delta_2 \mathbf{u}^s \times d^2S^s \quad [2.31]$$

where: ${}^1A^c$ is the cross-sectional area of the concrete core in configuration C1

${}^1A^s$ is the cross-sectional area of the steel tube in configuration C2

Evaluating the area integrals in Equation 2.31:

$$\int_0^{^2L} {}^2\mathbf{D}^c \times \delta_2 \hat{\mathbf{d}}^c \times d^2x + \int_0^{^2L} {}^2\mathbf{D}^s \times \delta_2 \hat{\mathbf{d}}^s \times d^2x + \int_{^2I} \delta_2 \hat{\mathbf{d}}_{sc} \times {}^2D_{sc} \times d^2I = \delta_2 \mathbf{q}^T \times {}^2\mathbf{Q}_{ext}^c + \delta_2 \mathbf{q}^T \times {}^2\mathbf{Q}_{ext}^s \quad [2.32]$$

$$\text{where: } {}^2\mathbf{D}^c = \begin{bmatrix} {}^2P^c & {}^2M_z^c & {}^2M_y^c \end{bmatrix}^T, \quad {}^2\mathbf{D}^s = \begin{bmatrix} {}^2P^s & {}^2M_z^s & {}^2M_y^s \end{bmatrix}^T$$

$${}^2\hat{\mathbf{d}}^c = \begin{bmatrix} {}^2\varepsilon^c & {}^2\kappa_z^c & {}^2\kappa_y^c \end{bmatrix}^T, \quad {}^2\hat{\mathbf{d}}^s = \begin{bmatrix} {}^2\varepsilon^s & {}^2\kappa_z^s & {}^2\kappa_y^s \end{bmatrix}^T$$

${}^2\mathbf{Q}_{ext}^c$ is the external load vector acting on the concrete core degree-of-freedom freedoms

${}^2\mathbf{Q}_{ext}^s$ is the external load vector acting on the steel tube degree-of-freedom freedoms

Equation 2.31 can further be simplified as given below:

$$\int_0^{2L} \left[{}^2\mathbf{D}^c \quad {}^2\mathbf{D}^s \right] \times \left[\delta_2 \hat{\mathbf{d}}_c \quad \delta_2 \hat{\mathbf{d}}_s \right]^T \times d^2x + \int_{{}^2I} \delta_2 \hat{\mathbf{d}}_{sc} \times {}^2D_{sc} \times d^2I = \delta_2 \mathbf{q}^T \times \left(\mathbf{Q}_{ext}^c + \mathbf{Q}_{ext}^s \right) \quad [2.33]$$

Based on the kinematic relations of Equation 2.1 and 2.2, the virtual work equation of equilibrium becomes:

$$\int_0^{2L} \delta_2 \hat{\mathbf{d}}^T \times {}^2\mathbf{D} \times d^2x + \int_{{}^2I} \delta_2 \hat{\mathbf{d}}_{sc} \times {}^2D_{sc} \times d^2I - \delta_2 \mathbf{q}^T \times \mathbf{Q}_{ext} = 0 \quad [2.34]$$

Comparing Equations 2.26 and 2.34, it can be seen that the virtual work equation of equilibrium written at the material fiber level is identical to that of at the cross-section level once the volume integrals are reduced to length integrals.

In the case of dynamic analysis, the externally applied loads include inertia and damping forces (Zienkiewicz et al., 2005). Therefore, the virtual work equation of equilibrium is modified to account for the work done by the inertia and damping forces as given in Equation 2.35.

$$\begin{aligned} & \int_0^{2L} \delta_2 \hat{\mathbf{d}}^T \times {}^2\mathbf{D} \times d^2x + \int_0^{2L} \delta_2 \hat{\mathbf{d}}_{sc}^T \times {}^2D_{sc} \times d^2I + \\ & \int_{{}^2V^c} {}^2\rho^c \times {}^2\ddot{\mathbf{u}}^c \times \delta_2 \mathbf{u}^c \times d^2V^c + \int_{{}^2V^c} {}^2\mu^c \times {}^2\dot{\mathbf{u}}^c \times \delta_2 \mathbf{u}^c \times d^2V^c + \\ & \int_{{}^2V^s} {}^2\rho^s \times {}^2\ddot{\mathbf{u}}^s \times \delta_2 \mathbf{u}^s \times d^2V^s + \int_{{}^2V^s} {}^2\mu^s \times {}^2\dot{\mathbf{u}}^s \times \delta_2 \mathbf{u}^s \times d^2V^s - \delta_2 \mathbf{q}^T \times {}^2\mathbf{Q}_{ext} = 0 \end{aligned} \quad [2.35]$$

where: ${}^2\rho^c$ is the unit weight of the concrete core in configuration C2

${}^2\rho^s$ is the unit weight of the steel tube in configuration C2

${}^2\mu^c$ is the viscosity parameter of the concrete core in configuration C2

${}^2\mu^s$ is the viscosity parameter of the steel tube in configuration C2

${}^2\mathbf{u}^c$ is the incremental displacement field of the concrete core with respect to configuration C2

${}^2\mathbf{u}^s$ is the incremental displacement field of the steel tube with respect to configuration C2

${}^2\dot{\mathbf{u}}^c$ is the incremental velocity field of the concrete core in configuration C2

${}^2\dot{\mathbf{u}}^s$ is the incremental velocity field of the steel tube in configuration C2

${}^2\ddot{\mathbf{u}}^c$ is the incremental acceleration field of the concrete core in configuration C2

${}^2\ddot{\mathbf{u}}^s$ is the incremental acceleration field of the steel tube in configuration C2

2.2.6. Updated-Lagrangian Formulation

Eulerian (spatial) and Lagrangian (referential) approaches are commonly employed for describing the motion of a continuum. In the Eulerian description, the motion is monitored at a fixed spatial location (Bathe, 1994). On the other hand, in the Lagrangian description, the motion of a fixed set of material particles is traced regardless of its location in space (Reddy, 1993). The Eulerian description of motion often works well for fluid mechanics applications while the Lagrangian description is widely used in the mechanics of solid bodies. In this study, the governing equations will be developed using the Lagrangian description.

In incremental nonlinear finite element formulations, two different versions of the Lagrangian description are followed based on the selection of the reference location while defining the state variables (e.g., strain, stress). In the Updated-Lagrangian formulation, all static and kinematic variables are referred to the last converged state (C1). In the Total-Lagrangian formulation, all static and kinematic variables are referred to the initial undeformed state (C0). Bathe and Bolourchi (1979) found that the Updated-Lagrangian and the Total-Lagrangian formulations produce the same numerical results. However, it was shown for many types of formulations that the Updated-Lagrangian approach is computationally more efficient.

The Updated-Lagrangian formulation is adopted in this study and the virtual work equation of equilibrium is modified by defining the state variables with respect to the C1 configuration as given in Equation 2.36.

$$\begin{aligned}
& \int_0^L \delta_1^2 \hat{\mathbf{d}}^T \times {}_1^2 \mathbf{D} \times d^1 x + \int_0^L \delta_1^2 \hat{\mathbf{d}}_{sc}^T \times {}_1^2 D_{sc} \times d^1 I + \\
& \int_{V^c} {}^1 \rho^c \times {}_1^2 \ddot{\mathbf{u}}^c \times \delta_1^2 \mathbf{u}^c \times d^1 V^c + \int_{V^s} {}^1 \rho^s \times {}_1^2 \ddot{\mathbf{u}}^s \times \delta_1^2 \mathbf{u}^s \times d^1 V^s + \\
& \int_{V^c} {}^1 \mu^c \times {}_1^2 \dot{\mathbf{u}}^c \times \delta_1^2 \mathbf{u}^c \times d^1 V^c + \int_{V^s} {}^1 \mu^s \times {}_1^2 \dot{\mathbf{u}}^s \times \delta_1^2 \mathbf{u}^s \times d^1 V^s - \delta_1^2 \mathbf{q}^T \times {}_1^2 \mathbf{Q}_{ext} = 0
\end{aligned} \tag{2.36}$$

where: ${}_1^2 \hat{\mathbf{d}}$ is the cross-sectional strains in configuration C2 with respect to configuration C1

${}_1^2 \mathbf{D}$ is the cross-sectional forces in configuration C2 with respect to configuration C1

${}_1^2 \hat{\mathbf{d}}_{sc}$ is the slip layer deformation in configuration C2 with respect to configuration C1

${}_1^2 D_{sc}$ is the force transferred between steel tube and concrete core per unit area in configuration C2 with respect to configuration C1 (units of force/length²)

${}_1^2 \mathbf{u}^c$ is the displacement field of the concrete core in configuration C2 with respect to configuration C1

${}_1^2 \mathbf{u}^s$ is the displacement field of the steel tube in configuration C2 with respect to configuration C1

${}_1^2 \dot{\mathbf{u}}^c$ is the velocity field of the concrete core in configuration C2 with respect to configuration C1

${}_1^2 \dot{\mathbf{u}}^s$ is the velocity field of the steel tube in configuration C2 with respect to configuration C1

${}_1^2 \ddot{\mathbf{u}}^c$ is the acceleration field of the concrete core in configuration C2 with respect to configuration C1

${}_1^2 \ddot{\mathbf{u}}^s$ is the acceleration field of the steel tube in configuration C2 with respect to configuration C1

${}_1^2 \mathbf{q}$ is the nodal displacements in configuration C2 with respect to configuration C1

${}^2_1\mathbf{Q}_{ext}$ is the nodal forces in configuration C2 with respect configuration C1

${}^1\rho^c$ is the unit weight of the concrete core in configuration C1

${}^1\rho^s$ is the unit weight of the steel tube in configuration C1

${}^1\mu^c$ is the viscosity parameter of the concrete core in configuration C1

${}^1\mu^s$ is the viscosity parameter of the steel tube in configuration C1

${}^1V^c$ is the volume of the concrete core in configuration C1

${}^1V^s$ is the volume of the steel tube in configuration C1

1I is the interface area in configuration C1

The strain vectors and force generated at the interface of the steel tube and concrete core can be decomposed into the incremental form as in Equation 2.37.

$${}^2_1\hat{\mathbf{d}} = {}^1\hat{\mathbf{d}} + {}_1\hat{\mathbf{d}} \quad [2.37a]$$

$${}^2_1\hat{\mathbf{d}}_{sc} = {}^1\hat{\mathbf{d}}_{sc} + {}_1\hat{\mathbf{d}}_{sc} \quad [2.37b]$$

$${}^2_1\mathbf{D}_{sc} = {}^1\mathbf{D}_{sc} + {}_1\mathbf{D}_{sc} = {}^1\mathbf{D}_{sc} + {}^1\bar{k}_{sc} \times {}_1\hat{\mathbf{d}}_{sc} \quad [2.37c]$$

$${}^2_1\mathbf{q} = {}^1\mathbf{q} + {}_1\mathbf{q} \quad [2.37d]$$

$${}^2_1\mathbf{u}^c = {}^1\mathbf{u}^c + {}_1\mathbf{u}^c \quad [2.37e]$$

$${}^2_1\dot{\mathbf{u}}^c = {}^1\dot{\mathbf{u}}^c + {}_1\dot{\mathbf{u}}^c \quad [2.37f]$$

$${}^2_1\ddot{\mathbf{u}}^c = {}^1\ddot{\mathbf{u}}^c + {}_1\ddot{\mathbf{u}}^c \quad [2.37g]$$

$${}^2_1\mathbf{u}^s = {}^1\mathbf{u}^s + {}_1\mathbf{u}^s \quad [2.37h]$$

$${}^2_1\dot{\mathbf{u}}^s = {}^1\dot{\mathbf{u}}^s + {}_1\dot{\mathbf{u}}^s \quad [2.37i]$$

$${}^2_1\ddot{\mathbf{u}}^s = {}^1\ddot{\mathbf{u}}^s + {}_1\ddot{\mathbf{u}}^s \quad [2.37j]$$

where: ${}_1\hat{\mathbf{d}}$ is the incremental cross-sectional strains with respect to configuration C1

${}_1\hat{\mathbf{d}}_{sc}$ is the incremental slip layer deformation with respect to configuration C1

${}_1\mathbf{q}$ is the incremental nodal displacements with respect to configuration C1

${}_1\mathbf{u}^c$ is the incremental displacement field of the concrete core in with respect to configuration C1

${}^1\dot{\mathbf{u}}^c$ is the incremental displacement field of the steel tube in with respect to configuration C1

${}^1\ddot{\mathbf{u}}^c$ is the incremental velocity field of the concrete core in with respect to configuration C1

${}^1\mathbf{u}^s$ is the incremental displacement field of the steel tube in with respect to configuration C1

${}^1\dot{\mathbf{u}}^s$ is the incremental velocity field of the steel tube in with respect to configuration C1

${}^1\ddot{\mathbf{u}}^s$ is the incremental velocity field of the steel tube in with respect to configuration C1

In the Updated-Lagrangian formulation, strain, deformation, and stress resultant terms in the C1 configuration are assumed to be known (e.g., ${}^1\hat{\mathbf{d}}$, ${}^1\mathbf{D}$, ${}^1\hat{\mathbf{d}}_{sc}$, ${}^1D_{sc}$, ${}^1\mathbf{Q}$, ${}^1\mathbf{q}$, ${}^1\mathbf{u}$, ${}^1\dot{\mathbf{u}}$, and ${}^1\ddot{\mathbf{u}}$). The variation symbol in Equation 2.3 corresponds to a differential operator (Reddy, 1993). Therefore, the variation of the known strain and deformation terms at C1 (e.g., $\delta^1\hat{\mathbf{d}}$, $\delta^1\hat{\mathbf{d}}_{sc}$, $\delta^1\mathbf{q}$, $\delta^1\mathbf{u}$, $\delta^1\dot{\mathbf{u}}$, and $\delta^1\ddot{\mathbf{u}}$) are considered to be zero, as given in Equation 2.5 (see, for example, Bathe and Bolourchi, 1979).

$$\delta^2\hat{\mathbf{d}} = \delta^1\hat{\mathbf{d}} + \delta_1\hat{\mathbf{d}} = 0 + \delta_1\hat{\mathbf{d}} = \delta_1\hat{\mathbf{d}} \quad [2.38a]$$

$$\delta^2\hat{\mathbf{d}}_{sc} = \delta^1\hat{\mathbf{d}}_{sc} + \delta_1\hat{\mathbf{d}}_{sc} = 0 + \delta_1\hat{\mathbf{d}}_{sc} = \delta_1\hat{\mathbf{d}}_{sc} \quad [2.38b]$$

$$\delta^2\mathbf{q} = \delta^1\mathbf{q} + \delta_1\mathbf{q} = 0 + \delta_1\mathbf{q} = \delta_1\mathbf{q} \quad [2.38c]$$

$$\delta^2\mathbf{u} = \delta^1\mathbf{u} + \delta_1\mathbf{u} = 0 + \delta_1\mathbf{u} = \delta_1\mathbf{u} \quad [2.38d]$$

$$\delta^2\dot{\mathbf{u}} = \delta^1\dot{\mathbf{u}} + \delta_1\dot{\mathbf{u}} = 0 + \delta_1\dot{\mathbf{u}} = \delta_1\dot{\mathbf{u}} \quad [2.38e]$$

$$\delta^2\ddot{\mathbf{u}} = \delta^1\ddot{\mathbf{u}} + \delta_1\ddot{\mathbf{u}} = 0 + \delta_1\ddot{\mathbf{u}} = \delta_1\ddot{\mathbf{u}} \quad [2.38f]$$

Substituting Equation 2.37 and Equation 2.38 into Equation 2.36, the virtual work equation of equilibrium becomes as follows:

$$\begin{aligned}
& \int_0^{1L} \delta_1 \hat{\mathbf{d}}^T \times {}_1^2 \mathbf{D} \times d^1 x + \int_0^{1L} \delta_1 \hat{\mathbf{d}}_{sc}^T \times {}^1 D_{sc} \times d^1 I + \int_0^{1L} \delta_1 \hat{\mathbf{d}}_{sc}^T \times {}_1^2 \bar{k}_{sc} \times {}_1 \hat{\mathbf{d}}_{sc} \times d^1 I \\
& \int_{1V^c} {}^1 \rho^c \times {}_1^2 \ddot{\mathbf{u}}^c \times \delta_1 \mathbf{u}^c \times d^1 V^c + \int_{1V^s} {}^1 \rho^s \times {}_1^2 \ddot{\mathbf{u}}^s \times \delta_1 \mathbf{u}^s \times d^1 V^s + \\
& \int_{1V^c} {}^1 \mu^c \times {}_1^2 \dot{\mathbf{u}}^c \times \delta_1 \mathbf{u}^c \times d^1 V^c + \int_{1V^s} {}^1 \mu^s \times {}_1^2 \dot{\mathbf{u}}^s \times \delta_1 \mathbf{u}^s \times d^1 V^s - \delta_1 \mathbf{q}^T \times {}_1^2 \mathbf{Q}_{ext} = 0
\end{aligned} \tag{2.39}$$

2.2.7. Compatibility Equation

The mixed finite element formulation requires satisfaction of compatibility and equilibrium equations simultaneously based on the selected variational principle (e.g., Hellinger-Reissner, as discussed in Section 2.2.8). The compatibility equation of the RCFT beam-column element will be presented in this section.

It is possible to obtain the cross-sectional strains defined at each integration point from the element displacements. The deformation fields are approximated by interpolation functions. The kinematic equations introduced in Section 2.2.2 are used to calculate the curvatures and elongations of the cross-sections ($\hat{\mathbf{d}}$). Since in the mixed finite element formulation, the internal element force fields are also treated as the primary variables, the cross-sectional forces can be obtained from force interpolations. Then, multiplying the cross-sectional force vector with cross-sectional flexibility (see Appendix A), the curvatures and elongations at the integration point of interest (\mathbf{d}) are calculated.

$$\mathbf{d} = \left[\varepsilon^c \quad \kappa_z^c \quad \kappa_y^c \quad \varepsilon^s \quad \kappa_z^s \quad \kappa_y^s \right]^T \tag{2.40}$$

The compatibility condition ensures that the cross-sectional strains from the element displacements are equal to the ones from the interpolated cross-section forces in a variational sense. The integral form of the compatibility equation can be expressed as:

$$\int_0^{1L} \delta_1^2 \mathbf{D}^T \times ({}_1 \hat{\mathbf{d}} - {}_1 \mathbf{d}) \times d^1 x = 0 \tag{2.41}$$

where: ${}_1 \mathbf{d}$ is the incremental cross-section strains calculated from cross-sectional forces and defined with respect to C1 configuration

$${}_1 \mathbf{d} = \left[{}_1 \varepsilon^c \quad {}_1 \kappa_z^c \quad {}_1 \kappa_y^c \quad {}_1 \varepsilon^s \quad {}_1 \kappa_z^s \quad {}_1 \kappa_y^s \right]^T$$

As presented in Section 2.2.5, the force generated at the interface between the steel tube and concrete core is directly calculated from the deformation of the slip layer (\hat{d}_{sc}). This implies that the slip deformation calculated from the shape functions (\hat{d}_{sc}) and the slip deformation obtained from the force at the interface become equal to each other, and that compatibility of the slip layer deformation is satisfied implicitly at each integration point along the element length. Therefore, Equation 2.41 does not contain any strain terms for the deformation of the slip layer.

2.2.8. The Hellinger-Reissner Principle

In the mixed finite element method, the stress-resultants are introduced as one of the primary variables. Using the Lagrange multiplier method, the compatibility equation is imposed as a constraint in the total potential energy equation. The Hellinger-Reissner variational principle is stated by taking the first variation of the modified total potential energy equation and equating it to zero. This corresponds to combining Equations 2.39 and 2.41 as given in Equation 2.42

The deformation fields approximated using interpolation functions are substituted into the kinematic equations of axial strains and curvatures for deriving the cross-sectional strains in Equations 2.1a, 2.3, 2.4, and 2.7. Equation 2.43 represents the cross-sectional strains in terms of the incremental element deformations. Equation 2.44 shows the first variation of cross-sectional strains in terms of element deformations. Similarly, the deformations of the slip layer can be obtained as given in Equation 2.45 after substitution of axial deformation fields of Equation 2.12b into Equation 2.9.

$$\begin{aligned}
& \int_0^{1L} \delta_1 \hat{\mathbf{d}}^T \times {}_1^2 \mathbf{D} \times d^1 x + \int_0^{1L} \delta_1 \hat{\mathbf{d}}_{sc}^T \times {}_1 \bar{k}_{sc} \times {}_1 \hat{\mathbf{d}}_{sc} \times d^1 I + \int_0^{1L} \delta_1 \hat{\mathbf{d}}_{sc}^T \times {}_1 \mathbf{D}_{sc} \times d^1 I + \\
& \int_{1V^c} {}_1 \rho^c \times {}_1^2 \ddot{\mathbf{u}}^c \times \delta_1 \mathbf{u}^c \times d^1 V^c + \int_{1V^s} {}_1 \rho^s \times {}_1^2 \ddot{\mathbf{u}}^s \times \delta_1 \mathbf{u}^s \times d^1 V^s + \\
& \int_{1V^c} {}_1 \mu^c \times {}_1^2 \ddot{\mathbf{u}}^c \times \delta_1 \mathbf{u}^c \times d^1 V^c + \int_{1V^s} {}_1 \mu^s \times {}_1^2 \ddot{\mathbf{u}}^s \times \delta_1 \mathbf{u}^s \times d^1 V^s + \\
& - \delta_1 \mathbf{q}^T \times {}_1^2 \mathbf{Q}_{ext} + \int_0^{1L} \delta_1^2 \mathbf{D}^T \times ({}_1 \hat{\mathbf{d}} - {}_1 \mathbf{d}) \times d^1 x = 0
\end{aligned} \tag{2.42}$$

where: ${}_1 \bar{k}_{sc}$ is the tangent stiffness of the interface between steel tube and concrete (in

units of force/length³) in C1 configuration with respect to C2 configuration

$${}^1\hat{\mathbf{d}} = {}^1\mathbf{N}_{\hat{d}} \times {}_1\mathbf{q} \quad [2.43]$$

where: ${}^1\mathbf{N}_{\hat{d}}$ is the matrix derived from kinematic relations of the strains and curvatures in configuration C1 (see Equation A.10 in Appendix A)

$$\delta {}^1\hat{\mathbf{d}} = {}^1\mathbf{N}_{\delta\hat{d}} \times \delta {}_1\mathbf{q} \quad [2.44]$$

where: ${}^1\mathbf{N}_{\delta\hat{d}}$ is the matrix resulting from the first variation of cross-section strains in C1 configuration (see Equation A.11 in Appendix A)

$${}^1\hat{\mathbf{d}}_{sc} = {}^1\mathbf{N}_{\hat{d}_{sc}} \times {}_1\mathbf{q} \quad [2.45]$$

where: ${}^1\mathbf{N}_{\hat{d}_{sc}}$ is the matrix derived from the kinematic relation of the deformation of the slip layer in C1 configuration (see Equation A.12 in Appendix A)

In Equation 2.46, first variation of the slip layer deformation is introduced as follows:

$${}^1\delta\hat{\mathbf{d}}_{sc} = {}^1\mathbf{N}_{\delta\hat{d}_{sc}} \times \delta {}_1\mathbf{q} \quad [2.46]$$

where: ${}^1\mathbf{N}_{\delta\hat{d}_{sc}}$ is the matrix resulting from the first variation of the deformation of slip layer in C1 configuration (see Equation A.13 in Appendix A)

The first variation of the stress resultant force field (${}^2\mathbf{D}$) is presented in Equation 2.47. The first term on the right hand side of Equation 2.47 can reformatted as given in Equation 2.48, by subtracting out the terms of $\delta {}_1\mathbf{q}$ (see Equation A.15 in Appendix A).

$$\delta {}^2\mathbf{D} = \delta {}^2_1\mathbf{N}_{D1} \times {}^2_1\mathbf{Q} + {}^2_1\mathbf{N}_{D1} \times \delta {}^2_1\mathbf{Q} \quad [2.47]$$

$$\delta {}^2\mathbf{D} = {}^2_1\mathbf{N}_{D2} \times \delta {}_1\mathbf{q} + {}^2_1\mathbf{N}_{D1} \times \delta {}^2_1\mathbf{Q} \quad [2.48]$$

where: ${}^2_1\mathbf{N}_{D2}$ is the matrix obtained by multiplying the first variation of ${}^2_1\mathbf{N}_{D1}$ with (${}^2_1\mathbf{Q}$) and then subtracting out the terms of $\delta {}_1\mathbf{q}$ (see Equation A.15 in Appendix A)

Substituting Equations 2.12, 2.43, 2.44, 2.45, 2.46, and 2.48 into 2.42, the Hellinger-Reissner variational principle can restated as in Equation 2.49.

$$\begin{aligned}
& \left[\begin{aligned}
& \int_0^{1L} {}^1\mathbf{N}_{\hat{d}}^T \times {}^2\mathbf{D} \times d^1x + \int_I {}^1\mathbf{N}_{\hat{d}_{sc}}^T \times {}^1\bar{k}_{sc} \times {}^1\mathbf{N}_{\hat{d}_{sc}} \times {}^1\mathbf{q} \times d^1I + \int_I {}^1\mathbf{N}_{\hat{d}_{sc}}^T \times {}^1D_{sc} \times d^1I \\
& - {}^2\mathbf{Q}_{ext} + \int_0^{1L} {}^2\mathbf{N}_{D2}^T \times ({}^1\hat{\mathbf{d}} - {}^1\mathbf{d}) \times d^1x + \\
& \left(\int_{V^c} {}^1\rho^c \times {}^1\mathbf{N}_u^{cT} \times {}^1\mathbf{N}_u^c \times d^1V^c + \int_{V^s} {}^1\rho^s \times {}^1\mathbf{N}_u^{sT} \times {}^1\mathbf{N}_u^s \times d^1V^s \right) \times {}^2\ddot{\mathbf{q}} + \\
& \left(\int_{V^c} {}^1\mu^c \times {}^1\mathbf{N}_u^{cT} \times {}^1\mathbf{N}_u^c \times d^1V^c + \int_{V^s} {}^1\mu^s \times {}^1\mathbf{N}_u^{sT} \times {}^1\mathbf{N}_u^s \times d^1V^s \right) \times {}^2\dot{\mathbf{q}}
\end{aligned} \right] + \\
& \delta_1^2\mathbf{Q}^T \times \left[\int_0^{1L} {}^2\mathbf{N}_{D1}^T \times ({}^1\hat{\mathbf{d}} - {}^1\mathbf{d}) \times d^1x \right] = 0
\end{aligned} \tag{2.49}$$

The terms $\delta_1\mathbf{q}^T$ and $\delta_1^2\mathbf{Q}^T$ are nonzero variables representing the variations of the element displacements and forces. Therefore, Equation 2.49 yields two sets of equations given below, with the first representing element equilibrium, and the second representing section compatibility:

$$\begin{aligned}
& \left[\begin{aligned}
& \int_0^{1L} {}^1\mathbf{N}_{\hat{d}}^T \times {}^2\mathbf{D} \times d^1x + \int_I {}^1\mathbf{N}_{\hat{d}_{sc}}^T \times {}^1\bar{k}_{sc} \times {}^1\mathbf{N}_{\hat{d}_{sc}} \times {}^1\mathbf{q} \times d^1I + \int_I {}^1\mathbf{N}_{\hat{d}_{sc}}^T \times {}^1D_{sc} \times d^1I \\
& - {}^2\mathbf{Q}_{ext} + \int_0^{1L} {}^2\mathbf{N}_{D2}^T \times ({}^1\hat{\mathbf{d}} - {}^1\mathbf{d}) \times d^1x + \\
& \left(\int_{V^c} {}^1\rho^c \times {}^1\mathbf{N}_u^{cT} \times {}^1\mathbf{N}_u^c \times d^1V^c + \int_{V^s} {}^1\rho^s \times {}^1\mathbf{N}_u^{sT} \times {}^1\mathbf{N}_u^s \times d^1V^s \right) \times {}^2\ddot{\mathbf{q}} + \\
& \left(\int_{V^c} {}^1\mu^c \times {}^1\mathbf{N}_u^{cT} \times {}^1\mathbf{N}_u^c \times d^1V^c + \int_{V^s} {}^1\mu^s \times {}^1\mathbf{N}_u^{sT} \times {}^1\mathbf{N}_u^s \times d^1V^s \right) \times {}^2\dot{\mathbf{q}}
\end{aligned} \right]
\end{aligned} \tag{2.50}$$

$$V = \int_0^{1L} {}^2\mathbf{N}_{D1}^T \times ({}^1\hat{\mathbf{d}} - {}^1\mathbf{d}) \times d^1x = 0 \tag{2.51}$$

In the mixed finite element formulation, the stress resultants from force interpolation functions and the stress resultants from material constitutive relations through numerical integration are ensured to be equal to each other. This condition is stated by a third equation representing the cross-section equilibrium as follows:

$$\mathbf{U} = {}^2\mathbf{D}_\Sigma - {}^2\mathbf{D} = 0 \tag{2.52}$$

where: ${}^2\mathbf{D}_\Sigma$ is the cross-sectional forces from integration over the cross-section in

C2 configuration with respect to C1 configuration and “ Σ ” used as right subscript represents the numerical integration

The analysis of the RCFT members using the mixed finite element formulation presented above requires the solution of Equations 2.50, 2.51, and 2.52 under a given set of external loads for nodal displacements (\mathbf{q}) and internal element forces (\mathbf{Q}). However, all the aforementioned equations are nonlinear for both \mathbf{q} and \mathbf{Q} . Therefore, these equations must be linearized first and then solved in an iterative and incremental manner. This process is discussed in the following sections.

2.2.9. Consistent Linearization of Cross-Section Equilibrium Equation

The cross-section equilibrium expression given in Equation 2.52 is a nonlinear function of the state variables ${}_1\mathbf{d}$ and ${}_1^2\mathbf{D}$. During nonlinear analysis, for a given ${}_1^2\mathbf{D}$, Equation 2.52 is solved yielding the value of ${}_1\mathbf{d}$ value to satisfy equilibrium. Linearization of Equation 2.52 is performed through expanding it about the current state. In this process ${}_1^2\mathbf{D}$ is kept as constant due to the fact that the cross-section equilibrium equation is used to obtain the cross-section strains for a given set of cross-section forces, which are obtained through compatibility relations (see Section 2.2.10).

$$\mathbf{U}^{j+1} = \mathbf{U}^j + \frac{d}{d\alpha} \Big|_{\alpha=0} \mathbf{U}({}_1\mathbf{d} + \alpha\Delta\mathbf{d}) \quad [2.53]$$

where the right superscripts j and $j + 1$ designate the previous and current iteration numbers, respectively and α is the Taylor Series expansion parameter. ${}_1^2\mathbf{D}_\Sigma$ is represented in the form of numerical integration of uniaxial stresses (σ) over the area of the RCFT cross-section as shown in Equation 2.54. In Equation 2.54, the components of ${}_1^2\mathbf{D}_\Sigma$ (e.g., ${}_1^2\mathbf{P}_\Sigma^c$, ${}_1^2\mathbf{M}_{\Sigma z}^c$, ${}_1^2\mathbf{M}_{\Sigma y}^c$, ${}_1^2\mathbf{P}_\Sigma^s$, ${}_1^2\mathbf{M}_{\Sigma z}^s$, ${}_1^2\mathbf{M}_{\Sigma y}^s$ where “ Σ ” used as right subscript represents the numerical integration) are obtained through multiplying the uniaxial stresses of the material fibers with the compatibility matrix and integrating all the terms over the RCFT cross-section.

$${}^2_1\mathbf{D}_\Sigma = \int_0^1 \mathbf{Y}^T \times {}^2_1\boldsymbol{\sigma} \times d^1A \quad [2.54]$$

where: $\mathbf{Y} = \begin{bmatrix} 1 & -\check{y}_c & -\check{z}_c & 0 & 0 & 0 \\ 0 & 0 & 0 & 1 & -\check{y}_s & -\check{z}_s \end{bmatrix}$ is the compatibility matrix (see Equation

A.26 in Appendix A)

\check{y}_c is the y coordinate of the concrete material fiber on the RCFT cross-section

\check{z}_c is the z coordinate of the concrete material fiber on the RCFT cross-section

\check{y}_s is the y coordinate of the steel material fiber on the RCFT cross-section

\check{z}_s is the z coordinate of the steel material fiber on the RCFT cross-section

${}^2_1\boldsymbol{\sigma} = \begin{bmatrix} {}^2_1\sigma^c & {}^2_1\sigma^s \end{bmatrix}^T$ is the uniaxial stress in the concrete (${}^2_1\sigma^c$) and steel material fibers (${}^2_1\sigma^s$) in C1 configuration with respect to C2 configuration

1A is the cross-sectional area

The derivative with respect to α evaluated at $\alpha = 0$ is performed using chain rule since $\boldsymbol{\sigma}$ is a function of uniaxial strain of material fibers (\mathbf{e}) and \mathbf{e} is related to \mathbf{d} through the assumption of plane sections remain plane as shown below:

$${}^2_1\mathbf{e} = \mathbf{Y} \times {}^2_1\mathbf{d} \quad [2.55]$$

where: ${}^2_1\mathbf{e} = \begin{bmatrix} {}^2_1e^c & {}^2_1e^s \end{bmatrix}^T$ is the uniaxial strain in the concrete (${}^2_1e^c$) and steel fibers (${}^2_1e^s$) in configuration C1 with respect to configuration C2 (see Appendix A1.5)

Substituting Equation 2.54 and 2.55, the second term on the right hand side of Equation 2.53 becomes:

$$\begin{aligned} \frac{d}{d\alpha} \Big|_{\alpha=0} \mathbf{U}({}_1\mathbf{d} + \alpha\Delta\mathbf{d}) &= \int_{{}_1A} \mathbf{Y}^T \times \frac{d}{d\alpha} \Big|_{\alpha=0} {}^2_1\boldsymbol{\sigma}({}_1\mathbf{d} + \alpha\Delta\mathbf{d}) \times d^1A \\ &= \int_{{}_1A} \mathbf{Y}^T \times \frac{d^2_1\boldsymbol{\sigma}}{de} \times \frac{d}{d\alpha} \Big|_{\alpha=0} {}^2_1\mathbf{e}({}_1\mathbf{d} + \alpha\Delta\mathbf{d}) \times d^1A \end{aligned} \quad [2.56]$$

Utilizing Equation 2.55 and representing ${}^2_1\mathbf{e}$ as ${}^2_1\mathbf{e} = {}^1\mathbf{e} + {}_1\mathbf{e}$, Equation 2.56 becomes as given in Equation 2.57.

$$\begin{aligned}
\frac{d}{d\alpha} \Big|_{\alpha=0} \mathbf{U}({}_1\mathbf{d} + \alpha\Delta\mathbf{d}) &= \int_{^1A} \mathbf{Y}^T \times \frac{d_1^2\boldsymbol{\sigma}}{de} \times \frac{d}{d\alpha} \Big|_{\alpha=0} ({}^1e({}_1\mathbf{d}) + {}_1e({}_1\mathbf{d} + \alpha\Delta\mathbf{d})) \times d^1A \\
&= \int_{^1A} \mathbf{Y}^T \times \frac{d_1^2\boldsymbol{\sigma}}{de} \times \frac{d}{d\alpha} \Big|_{\alpha=0} (\mathbf{Y} \times {}^1\mathbf{d} + \mathbf{Y} \times {}_1\mathbf{d} + \mathbf{Y} \times \alpha\Delta\mathbf{d}) \times d^1A
\end{aligned} \tag{2.57}$$

Performing the differentiation with respect to α in Equation 2.57:

$$\frac{d}{d\alpha} \Big|_{\alpha=0} (\mathbf{Y} \times {}^1\mathbf{d} + \mathbf{Y} \times {}_1\mathbf{d} + \mathbf{Y} \times \alpha\Delta\mathbf{d}) = \mathbf{Y} \times \Delta\mathbf{d} \tag{2.58}$$

Substituting Equation 2.58 into Equation 2.57:

$$\begin{aligned}
\frac{d}{d\alpha} \Big|_{\alpha=0} \mathbf{U}({}_1\mathbf{d} + \alpha\Delta\mathbf{d}) &= \int_{^1A} \mathbf{Y}^T \times \frac{d_1^2\boldsymbol{\sigma}}{d_1^2e} \times \frac{d}{d\alpha} \Big|_{\alpha=0} ({}^1e({}_1\mathbf{d}) + {}_1e({}_1\mathbf{d} + \alpha\Delta\mathbf{d})) \times d^1A \\
&= \int_{^1A} \mathbf{Y}^T \times \frac{d_1^2\boldsymbol{\sigma}}{d_1^2e} \times \mathbf{Y} \times \Delta\mathbf{d} \times d^1A
\end{aligned} \tag{2.59}$$

In Equation 2.59, the term $\frac{d_1^2\boldsymbol{\sigma}}{d_1^2e}$ represent rate of change axial stress with respect to axial strain. Therefore, $\frac{d_1^2\boldsymbol{\sigma}}{d_1^2e}$ is equivalent to the tangent modulus (${}^2_1\mathbf{E}_t$) of concrete (${}^2_1E_t^c$) and steel (${}^2_1E_t^s$) fibers as shown in Equation 2.60.

$$\frac{d}{d\alpha} \Big|_{\alpha=0} \mathbf{U}({}_1\mathbf{d} + \alpha\Delta\mathbf{d}) = \int_{^1A} \mathbf{Y}^T \times {}^2_1\mathbf{E}_t \times \mathbf{Y} \times \Delta\mathbf{d} \times d^1A \tag{2.60a}$$

where: ${}^2_1\mathbf{E}_t = \begin{bmatrix} {}^2_1E_t^c & 0 \\ 0 & {}^2_1E_t^s \end{bmatrix}$ is the tangent modulus matrix at C2 configuration with

respect to C1 configuration

Performing the area integration in Equation 2.60 yields the cross-sectional stiffness matrix as illustrated in Equation 2.61.

$$\left(\int_{^1A} \mathbf{Y}^T \times {}^2_1\mathbf{E}_t \times \mathbf{Y} \times d^1A \right) \times \Delta\mathbf{d} = {}^2_1\mathbf{k} \times \Delta\mathbf{d} \tag{2.60b}$$

${}^2_1\mathbf{k}$ is the cross-section stiffness in configuration C1 with respect to configuration C2 (see Appendix A)

The linearized form of cross-section equilibrium can be thus obtained as given in Equation 2.62 through substituting Equation 2.61 and 2.56 into Equation 2.52.

$${}^2_1\mathbf{k} \times \Delta \mathbf{d} = {}^2_1\mathbf{D}^j - {}^2_1\mathbf{D}^j_{\Sigma} \quad [2.61]$$

As it will be described later in Section 2.2.14, Equation 2.61 is used in the forces recovery stage of the nonlinear analysis solution algorithm to obtain cross-sectional deformations corresponding to the given cross-sectional forces.

2.2.10. Consistent Linearization of Compatibility Equation

The element compatibility stated in Equation 2.51 is nonlinear with respect to the state variables of ${}^1_1\mathbf{q}$ and ${}^2_1\mathbf{Q}$ since ${}^1_1\mathbf{d}$ and ${}^1_1\hat{\mathbf{d}}$ are functions of ${}^2_1\mathbf{Q}$ and ${}^1_1\mathbf{q}$, respectively (see Appendix A). The incremental form of the compatibility equation needed to derive the consistent tangent stiffness equations can be obtained by consistent linearization. The Taylor series expansion of Equation 2.51 about the current state can be stated as in Equation 2.62. The second and third terms on the right hand side of Equation 2.33 are expanded using the rules of differentiation following the substitution of the terms $({}^1_1\mathbf{q} + \alpha\Delta\mathbf{q})$ and $({}^2_1\mathbf{Q} + \gamma\Delta\mathbf{Q})$. The third term on the right hand side of Equation 2.62 is simplified into a single term since ${}^2_1\mathbf{N}_{D1}$ and ${}^1_1\hat{\mathbf{d}}$ are not functions of ${}^2_1\mathbf{Q}$ and therefore their derivative with respect to γ vanishes.

$$\mathbf{V}^{j+1} = \mathbf{V}^j + \frac{d}{d\alpha} \Big|_{\alpha,\gamma=0} \mathbf{V}({}^1_1\mathbf{q} + \alpha\Delta\mathbf{q}) + \frac{d}{d\gamma} \Big|_{\alpha,\gamma=0} \mathbf{V}({}^2_1\mathbf{Q} + \gamma\Delta\mathbf{Q}) \quad [2.62]$$

where:

$$\frac{d}{d\alpha} \Big|_{\alpha,\gamma=0} \mathbf{V}({}^1_1\mathbf{q} + \alpha\Delta\mathbf{q}, {}^2_1\mathbf{Q} + \gamma\Delta\mathbf{Q}) = \int_0^L \frac{d}{d\alpha} \Big|_{\alpha,\gamma=0} ({}^2_1\mathbf{N}_{D1}^T) \times ({}^1_1\hat{\mathbf{d}} - {}^1_1\mathbf{d}) \times d^1x +$$

$$\int_0^L {}^2_1\mathbf{N}_{D1}^T \times \frac{d}{d\alpha} \Big|_{\alpha,\gamma=0} ({}^1_1\hat{\mathbf{d}} - {}^1_1\mathbf{d}) \times d^1x$$

$$\frac{d}{d\gamma} \Big|_{\alpha,\gamma=0} \mathbf{V}({}^1_1\mathbf{q} + \alpha\Delta\mathbf{q}, {}^2_1\mathbf{Q} + \gamma\Delta\mathbf{Q}) = - \int_0^L {}^2_1\mathbf{N}_{D1}^T \times \frac{d}{d\gamma} \Big|_{\alpha,\gamma=0} ({}^1_1\mathbf{d}) \times d^1x$$

γ, α are the Taylor Series expansion parameters

Through expanding the expression in Equation 2.62, the second term on the right hand side can be expressed as given below:

$$\begin{aligned} \frac{d}{d\alpha} \Big|_{\alpha, \gamma=0} \mathbf{V}({}_1\mathbf{q} + \alpha\Delta\mathbf{q}, {}_1\mathbf{Q} + \gamma\Delta\mathbf{Q}) &= \left(\int_0^{1L} \frac{d}{d\alpha} \Big|_{\alpha, \gamma=0} ({}^2\mathbf{N}_{D1}^T) \times d^1x \right) \times ({}_1\hat{\mathbf{d}} - {}_1\mathbf{d}) + \int_0^{1L} {}^2\mathbf{N}_{D1}^T \times \frac{d}{d\alpha} \Big|_{\alpha, \gamma=0} {}_1\hat{\mathbf{d}} \times d^1x - \\ &\int_0^{1L} {}^2\mathbf{N}_{D1}^T \times \frac{d}{d\alpha} \Big|_{\alpha, \gamma=0} {}_1\mathbf{d} \times d^1x \end{aligned} \quad [2.63]$$

Despite the fact that the term ${}^2\mathbf{N}_{D1}$ represents force interpolation functions, it is still a function ${}^2\mathbf{q}$ to account for second order moments (e.g., $P - \delta$). In the first integral term on the right hand side of Equation 2.63, substituting the variables of ${}^2\boldsymbol{\theta}_{zi}^c + \alpha\Delta\boldsymbol{\theta}_{zi}^c$, ${}^2\boldsymbol{\theta}_{zj}^c + \alpha\Delta\boldsymbol{\theta}_{zj}^c$, ${}^2\boldsymbol{\theta}_{zi}^s + \alpha\Delta\boldsymbol{\theta}_{zi}^s$, ${}^2\boldsymbol{\theta}_{zj}^s + \alpha\Delta\boldsymbol{\theta}_{zj}^s$, ${}^2\boldsymbol{\theta}_{zi}^c + \alpha\Delta\boldsymbol{\theta}_{zi}^c$, ${}^2\boldsymbol{\theta}_{zj}^c + \alpha\Delta\boldsymbol{\theta}_{zj}^c$, ${}^2\boldsymbol{\theta}_{zi}^s + \alpha\Delta\boldsymbol{\theta}_{zi}^s$, ${}^2\boldsymbol{\theta}_{zj}^s + \alpha\Delta\boldsymbol{\theta}_{zj}^s$ into ${}^2\mathbf{N}_{D1}$, performing differentiation of the terms of the ${}^2\mathbf{N}_{D1}$ with respect to α , evaluating the integration along the element length at $\alpha = 0$, multiplying the result of the integration with ${}_1\hat{\mathbf{d}} - {}_1\mathbf{d}$, and finally factoring out the terms of $\Delta\mathbf{q}$, Equation 2.64 is obtained as given below:

$$\left(\int_0^{1L} \frac{d}{d\alpha} \Big|_{\alpha, \gamma=0} ({}^2\mathbf{N}_{D1}^T) \times d^1x \right) \times ({}_1\hat{\mathbf{d}} - {}_1\mathbf{d}) = \mathbf{M}_d \times \Delta\mathbf{q} \quad [2.64]$$

In the second term on the right hand side of Equation 2.63, ${}_1\hat{\mathbf{d}}$ is stated in terms of nodal displacements through replacing it with the expression ${}^1\mathbf{N}_{\hat{d}} \times {}_1\mathbf{q}$ as given in Equation 2.65 (see Equation 2.43).

$$\int_0^{1L} {}^2\mathbf{N}_{D1}^T \times \frac{d}{d\alpha} \Big|_{\alpha, \gamma=0} ({}_1\hat{\mathbf{d}}) \times d^1x = \int_0^{1L} {}^2\mathbf{N}_{D1}^T \times \frac{d}{d\alpha} \Big|_{\alpha, \gamma=0} ({}^1\mathbf{N}_{\hat{d}} \times {}_1\mathbf{q}) \times d^1x \quad [2.65]$$

In Equation 2.65, ${}_1\mathbf{q}$ is replaced by ${}_1\mathbf{q} + \alpha\Delta\mathbf{q}$ and differentiation with respect to α at $\alpha = 0$ is performed as shown in Equation 2.66.

$$\int_0^L {}^2\mathbf{N}_{D1}^T \times \frac{d}{d\alpha} \Big|_{\alpha,\gamma=0} \left({}^1\mathbf{N}_{\hat{d}} \times {}^1\mathbf{q} \right) \times d^1x = \int_0^L {}^2\mathbf{N}_{D1}^T \times \frac{d}{d\alpha} \Big|_{\alpha,\gamma=0} \left({}^1\mathbf{N}_{\hat{d}} \times ({}^1\mathbf{q} + \alpha \times \Delta\mathbf{q}) \right) \times d^1x \quad [2.66]$$

$$= \int_0^L {}^2\mathbf{N}_{D1}^T \times {}^1\mathbf{N}_{\hat{d}} \times \Delta\mathbf{q} \times d^1x$$

Performing the integration in Equation 2.66 along the element length and factoring out $\Delta\mathbf{q}$:

$$\int_0^L {}^2\mathbf{N}_{D1}^T \times {}^1\mathbf{N}_{\hat{d}} \times \Delta\mathbf{q} \times d^1x = {}^2\mathbf{G}_1 \times \Delta\mathbf{q} \quad [2.67]$$

While expanding the third term on the right hand side of Equation 2.63, chain rule of differentiation is utilized since the variable ${}^1\mathbf{d}$ can not be expressed in terms of ${}^1\mathbf{q}$ explicitly. ${}^1\mathbf{d}$ is related to ${}^2\mathbf{D}_\Sigma$ through cross-section constitutive relation (e.g., ${}^1\mathbf{d} = {}^1\mathbf{k}^{-1} \times {}^1\mathbf{D}_\Sigma = {}^1\mathbf{k}^{-1} \times ({}^2\mathbf{D}_\Sigma - {}^1\mathbf{D}_\Sigma)$). ${}^1\mathbf{D}_\Sigma$ is a function of ${}^1\mathbf{D}$ as it is presented in cross-section equilibrium equation (see Equation 2.52). ${}^1\mathbf{D}$ can be stated in terms of ${}^1\mathbf{q}$ since the \mathbf{N}_{D1} matrix having force interpolation functions contains nodal displacement terms. Therefore, the third term on the right hand side of Equation 2.63 is obtained as given below:

$$\int_0^L {}^2\mathbf{N}_{D1}^T \times \frac{d}{d\alpha} \Big|_{\alpha,\gamma=0} ({}^1\mathbf{d}) \times d^1x = \left(\int_0^L {}^2\mathbf{N}_{D1}^T \times \frac{\partial {}^1\mathbf{d}}{\partial {}^2\mathbf{D}_\Sigma} \times \frac{\partial {}^2\mathbf{D}_\Sigma}{\partial {}^2\mathbf{D}} \times \frac{\partial}{\partial \alpha} \Big|_{\alpha,\gamma=0} ({}^2\mathbf{D}) \times d^1x \right) \quad [2.68]$$

$$= \left(\int_0^L {}^2\mathbf{N}_{D1}^T \times {}^1\mathbf{k}^{-1} \times 1 \times \frac{\partial}{\partial \alpha} \Big|_{\alpha,\gamma=0} ({}^2\mathbf{N}_{D1} \times {}^2\mathbf{Q}) \times d^1x \right)$$

where: $\frac{\partial {}^1\mathbf{d}}{\partial {}^2\mathbf{D}_\Sigma} = {}^1\mathbf{k}^{-1}$, $\frac{\partial {}^2\mathbf{D}_\Sigma}{\partial {}^2\mathbf{D}} = 1$, ${}^2\mathbf{D} = {}^2\mathbf{N}_{D1} \times {}^2\mathbf{Q}$

${}^2\mathbf{D}_\Sigma$ is the cross-sectional forces in C2 configuration from integration over the cross-section defined with respect to C1 configuration

${}^2\mathbf{Q}$ is the incremental natural end forces defined with respect to C1 configuration

In Equation 2.68, the ${}^1\mathbf{q}$ terms of ${}^2\mathbf{N}_{D1}$ (e.g., ${}^2\mathbf{N}_{D1}$ is a function of ${}^2\mathbf{q} = {}^1\mathbf{q} + {}^1\mathbf{q}$)

) is replaced by ${}^1\mathbf{q} + \alpha\Delta\mathbf{q}$ terms (e.g., ${}^1\boldsymbol{\theta}_{zi}^c + \alpha\Delta\boldsymbol{\theta}_{zi}^c$, ${}^1\boldsymbol{\theta}_{zj}^c + \alpha\Delta\boldsymbol{\theta}_{zj}^c$, ${}^1\boldsymbol{\theta}_{zi}^s + \alpha\Delta\boldsymbol{\theta}_{zi}^s$,

${}^1\boldsymbol{\theta}_{zj}^s + \alpha\Delta\boldsymbol{\theta}_{zj}^s$, ${}^1\boldsymbol{\theta}_{zi}^s + \alpha\Delta\boldsymbol{\theta}_{zi}^s$, ${}^1\boldsymbol{\theta}_{zj}^s + \alpha\Delta\boldsymbol{\theta}_{zj}^s$) and differentiation

with respect to α at $\alpha = 0$ is evaluated. The resulting expression is multiplied with ${}^1\mathbf{Q}$ yielding N_{D2} as given below:

$$\frac{\partial}{\partial \alpha} \Big|_{\alpha, \gamma=0} \left({}^2\mathbf{N}_{D1} \times {}^2\mathbf{Q} \right) = {}^2\mathbf{N}_{D2} \quad (\text{see Equation A.15 in Appendix A}) \quad [2.69]$$

Substituting Equation 2.69, Equation 2.68 becomes:

$$\int_0^L {}^2\mathbf{N}_{D1}^T \times \frac{d}{d\alpha} \Big|_{\alpha, \gamma=0} ({}^1\mathbf{d}) \times d^1x = \int_0^L {}^2\mathbf{N}_{D1}^T \times {}^1\mathbf{k}^{-1} \times {}^2\mathbf{N}_{D2} \times d^1x = {}^2\mathbf{H}_{12} \quad [2.70]$$

While expanding the third term in Equation 2.63, differentiation of ${}^1\mathbf{d}$ with respect to the Taylor series expansion term of γ is performed using the chain rule of differentiation.

Since ${}^1\mathbf{d}$ can not be directly related to ${}^2\mathbf{Q}$, first ${}^1\mathbf{d}$ is related to ${}^2\mathbf{D}_\Sigma$ through cross-section constitutive relation of ${}^1\mathbf{d} = {}^1\mathbf{k}^{-1} \times {}^1\mathbf{D}_\Sigma = {}^1\mathbf{k}^{-1} \times ({}^2\mathbf{D}_\Sigma - {}^1\mathbf{D}_\Sigma)$. Then, ${}^2\mathbf{D}_\Sigma$ is expressed in terms of ${}^2\mathbf{D}$ based on the cross-section equilibrium. Finally, ${}^2\mathbf{D}$ is related to ${}^2\mathbf{Q}$ using force interpolation functions (e.g., ${}^2\mathbf{D} = {}^2\mathbf{N}_{D1} \times {}^2\mathbf{Q}$). Therefore, the third term of Equation 2.63 can be obtained as given below:

$$\begin{aligned} \int_0^L {}^2\mathbf{N}_{D1}^T \times \frac{d}{d\gamma} \Big|_{\alpha, \gamma=0} ({}^1\mathbf{d}) \times d^1x &= \int_0^L {}^2\mathbf{N}_{D1}^T \times \frac{\partial {}^1\mathbf{d}}{\partial {}^2\mathbf{D}_\Sigma} \times \frac{\partial {}^2\mathbf{D}_\Sigma}{\partial {}^2\mathbf{D}} \times \frac{d}{d\gamma} \Big|_{\alpha, \gamma=0} ({}^2\mathbf{D}) \times d^1x \\ &= \int_0^L {}^2\mathbf{N}_{D1}^T \times \frac{\partial {}^1\mathbf{d}}{\partial {}^2\mathbf{D}_\Sigma} \times \frac{\partial {}^2\mathbf{D}_\Sigma}{\partial {}^2\mathbf{D}} \times \frac{d}{d\gamma} \Big|_{\alpha, \gamma=0} \left({}^2\mathbf{N}_{D1} \times ({}^2\mathbf{Q} + \gamma \times \Delta\mathbf{Q}) \right) \times d^1x \end{aligned} \quad [2.71]$$

Evaluating the differentiation with respect to γ at $\gamma = 0$ and integrating the resulting expression along the element length, Equation 2.71 becomes:

$$\int_0^L {}^2\mathbf{N}_{D1}^T \times \frac{d}{d\gamma} \Big|_{\alpha, \gamma=0} ({}^1\mathbf{d}) \times d^1x = \left(\int_0^L {}^2\mathbf{N}_{D1}^T \times {}^1\mathbf{k}^{-1} \times {}^2\mathbf{N}_{D1} \times d^1x \right) \times \Delta\mathbf{Q} = {}^2\mathbf{H}_{11} \times \Delta\mathbf{Q} \quad [2.72]$$

Substituting Equation 2.72, 2.70, 2.67, 2.64 into Equation 2.63, the linearized form of compatibility can be derived as given below in Equation 2.73.

$$\mathbf{V}^{j+1} = \mathbf{V}^j + ({}^2\mathbf{G}_1^j + \mathbf{M}_d^j - {}^2\mathbf{H}_{12}^j) \times \Delta\mathbf{q} - \mathbf{H}_{11}^j \times \Delta\mathbf{Q} \quad [2.73]$$

where: ${}^2\mathbf{G}_1 = \int_0^L {}^2\mathbf{N}_{D1}^T \times {}^1\mathbf{N}_{\hat{\alpha}} \times d^1x$

$${}^2_1\mathbf{H}_{11} = \int_0^{1L} {}^2_1\mathbf{N}_{D1}^T \times {}^1\mathbf{k}^{-1} \times {}^2_1\mathbf{N}_{D1} \times d^1x$$

$${}^2_1\mathbf{H}_{12} = \int_0^{1L} {}^2_1\mathbf{N}_{D1}^T \times {}^1\mathbf{k}^{-1} \times {}^2_1\mathbf{N}_{D2} \times d^1x$$

${}^1\mathbf{k}^{-1}$ is the cross-section flexibility matrix in C1 configuration or inverse of cross-section stiffness in C1 configuration (see Section A1.5 in Appendix A)

\mathbf{M}_d is a matrix defining the results from the expansion process, as defined in Equation A.19 in Appendix A and in Equation 2.64.

From Equation 2.73, $\Delta\mathbf{Q}$ can be solved as given below:

$$\Delta\mathbf{Q} = \left({}^2_1\mathbf{H}_{11}^{-1}\right)^j \times \mathbf{V}^j + \left({}^2_1\mathbf{H}_{11}^{-1}\right)^j \times \left({}^2_1\mathbf{G}_1^j + \mathbf{M}_d^j - {}^2_1\mathbf{H}_{12}^j\right) \times \Delta\mathbf{q} \quad [2.74]$$

Equation 2.74 is used in deriving the element stiffness matrix as it will be described in Section 2.2.11 and Section 2.2.15.

The element compatibility equation also needs to be expanded when ${}^1\hat{\mathbf{d}}$ is kept constant. The resulting expression is used during the state determination stage of the nonlinear analysis to calculate the incremental element end forces (see more details in Section 2.2.14). Adopting the same processes of differentiation as in Equation 2.62:

$$\mathbf{V}^{j+1} = \mathbf{V}^j + \frac{d}{d\gamma} \Big|_{\alpha, \gamma=0} \mathbf{V}({}^2_1\mathbf{Q} + \alpha\Delta\mathbf{Q}) \quad [2.75]$$

$$\text{where: } \frac{d}{d\gamma} \Big|_{\gamma=0} \mathbf{V}({}^2_1\mathbf{Q} + \gamma\Delta\mathbf{Q}) = - \int_0^{1L} {}^2_1\mathbf{N}_{D1}^T \times \frac{d}{d\gamma} \Big|_{\gamma=0} ({}^1\mathbf{d}) \times d^1x$$

Expanding the second term on the right hand side of Equation 2.75 as described while deriving Equation 2.72, \mathbf{V}^{j+1} can be expressed as given below:

$$\mathbf{V}^{j+1} = \mathbf{V}^j - {}^2_1\mathbf{H}_{11}^j \times \Delta\mathbf{Q} \quad [2.76]$$

From Equation 2.76, $\Delta\mathbf{Q}$ can be solved as given in Equation 2.77.

$$\Delta\mathbf{Q} = \left({}^2_1\mathbf{H}_{11}^{-1}\right)^j \times \mathbf{V}^j \quad [2.77]$$

2.2.11. Consistent Linearization of Equilibrium Equation

Linearization of the equilibrium equation yields expressions to derive the element tangent stiffness. Examining Equation 2.50, it can be seen that the equilibrium equation is expressed in terms of the states variables including ${}_1\mathbf{q}$, ${}_1^2\mathbf{Q}$, ${}_1^2\mathbf{Q}_{ext}$, ${}_1^2\dot{\mathbf{q}}$, and ${}_1^2\ddot{\mathbf{q}}$. The Taylor series expansion of the equilibrium equation about the current state can be expressed as follows:

$$\begin{aligned}
\mathbf{g}^{j+1} = & \mathbf{g}^j + \frac{d}{d\alpha} \Big|_{\alpha,\lambda,\beta,\theta,\eta=0} \mathbf{g}({}_1\mathbf{q} + \alpha\Delta\mathbf{q}, {}_1^2\mathbf{Q} + \gamma\Delta\mathbf{Q}, {}_1^2\mathbf{Q}_{ext} + \beta\Delta\mathbf{Q}_{ext}, {}_1^2\dot{\mathbf{q}} + \theta\Delta\dot{\mathbf{q}}, {}_1^2\ddot{\mathbf{q}} + \eta\Delta\ddot{\mathbf{q}}) \\
& + \frac{d}{d\gamma} \Big|_{\alpha,\lambda,\beta,\theta,\eta=0} \mathbf{g}({}_1\mathbf{q} + \alpha\Delta\mathbf{q}, {}_1^2\mathbf{Q} + \gamma\Delta\mathbf{Q}, {}_1^2\mathbf{Q}_{ext} + \beta\Delta\mathbf{Q}_{ext}, {}_1^2\dot{\mathbf{q}} + \theta\Delta\dot{\mathbf{q}}, {}_1^2\ddot{\mathbf{q}} + \eta\Delta\ddot{\mathbf{q}}) \\
& + \frac{d}{d\beta} \Big|_{\alpha,\lambda,\beta,\theta,\eta=0} \mathbf{g}({}_1\mathbf{q} + \alpha\Delta\mathbf{q}, {}_1^2\mathbf{Q} + \gamma\Delta\mathbf{Q}, {}_1^2\mathbf{Q}_{ext} + \beta\Delta\mathbf{Q}_{ext}, {}_1^2\dot{\mathbf{q}} + \theta\Delta\dot{\mathbf{q}}, {}_1^2\ddot{\mathbf{q}} + \eta\Delta\ddot{\mathbf{q}}) \\
& + \frac{d}{d\theta} \Big|_{\alpha,\lambda,\beta,\theta,\eta=0} \mathbf{g}({}_1\mathbf{q} + \alpha\Delta\mathbf{q}, {}_1^2\mathbf{Q} + \gamma\Delta\mathbf{Q}, {}_1^2\mathbf{Q}_{ext} + \beta\Delta\mathbf{Q}_{ext}, {}_1^2\dot{\mathbf{q}} + \theta\Delta\dot{\mathbf{q}}, {}_1^2\ddot{\mathbf{q}} + \eta\Delta\ddot{\mathbf{q}}) \\
& + \frac{d}{d\eta} \Big|_{\alpha,\lambda,\beta,\theta,\eta=0} \mathbf{g}({}_1\mathbf{q} + \alpha\Delta\mathbf{q}, {}_1^2\mathbf{Q} + \gamma\Delta\mathbf{Q}, {}_1^2\mathbf{Q}_{ext} + \beta\Delta\mathbf{Q}_{ext}, {}_1^2\dot{\mathbf{q}} + \theta\Delta\dot{\mathbf{q}}, {}_1^2\ddot{\mathbf{q}} + \eta\Delta\ddot{\mathbf{q}})
\end{aligned} \tag{2.78}$$

The expanded forms of the terms on the right hand side of Equation 2.78 are obtained following the substitution of the variables ${}_1\mathbf{q} + \alpha\Delta\mathbf{q}$, ${}_1^2\mathbf{Q} + \gamma\Delta\mathbf{Q}$, ${}_1^2\mathbf{Q}_{ext} + \beta\Delta\mathbf{Q}_{ext}$, ${}_1^2\dot{\mathbf{q}} + \theta\Delta\dot{\mathbf{q}}$, ${}_1^2\ddot{\mathbf{q}} + \eta\Delta\ddot{\mathbf{q}}$, performing the differentiation with respect to the Taylor Series expansion parameters of $\alpha, \gamma, \beta, \theta, \eta$ and evaluating the derivatives when $\alpha = 0, \gamma = 0, \beta = 0, \theta = 0$, and $\eta = 0$. The details of the expansion process for the terms on the right hand side of Equation 2.78 are presented in Equation 2.79.

In Equation 2.79, the first term on the right hand side is expanded through substituting ${}_1\mathbf{q} + \alpha\Delta\mathbf{q}$ into ${}^1N_{\delta\hat{d}}$ and expressing ${}_1^2\mathbf{D}$ in terms of force interpolation functions (${}_1^2\mathbf{D} = {}^2N_{D1} \times {}_1^2\mathbf{Q}$). Following the differentiation with respect to α at $\alpha = 0$, $\Delta\mathbf{q}$ is factored out from the resulting expression to derive the geometric stiffness matrix (${}_1^2\mathbf{K}_g$) as given in Equation 2.80.

In the second term on the right hand side of Equation 2.79, ${}_1^2\mathbf{D}$ is expressed in terms of force interpolation functions as ${}_1^2\mathbf{D} = {}^2N_{D1} \times {}_1^2\mathbf{Q}$. The nodal displacement values

in ${}^2N_{D1}$ are replaced by ${}_1\mathbf{q} + \alpha\Delta\mathbf{q}$. Next, differentiation with respect to α at $\alpha = 0$ is performed and $\Delta\mathbf{q}$ is factored out from the resulting expression. Carrying out the integration along the element length, Equation 2.81 is obtained.

$$\begin{aligned} \frac{d}{d\alpha} \Big|_{\alpha,\gamma,\beta,\theta,\eta=0} g({}_1\mathbf{q} + \alpha\Delta\mathbf{q}, {}^2\mathbf{Q} + \gamma\Delta\mathbf{Q}, {}^2\mathbf{Q}_{ext} + \beta\Delta\mathbf{Q}_{ext}, {}^2\dot{\mathbf{q}} + \theta\Delta\dot{\mathbf{q}}, {}^2\ddot{\mathbf{q}} + \eta\Delta\ddot{\mathbf{q}}) = & \left[\int_0^{1L} \frac{d}{d\alpha} \Big|_{\alpha,\gamma,\beta,\theta,\eta=0} ({}^1N_{\delta\hat{d}}) \times {}^2\mathbf{D} \times d^1x \right] + \left[\int_0^{1L} {}^1N_{\delta\hat{d}}^T \times \frac{d}{d\alpha} \Big|_{\alpha,\gamma,\beta,\theta,\eta=0} ({}^2\mathbf{D}) \times d^1x \right] + \\ & \left[\int_0^{1L} \frac{d}{d\alpha} \Big|_{\alpha,\gamma,\beta,\theta,\eta=0} ({}^1N_{\delta\hat{d}_{sc}}^T) \times {}^1\bar{k}_{sc} \times {}^1N_{\delta\hat{d}_{sc}} \times ({}_1\mathbf{q} + \alpha\Delta\mathbf{q}) \times d^1x \right] + \left[\int_0^{1L} {}^1N_{\delta\hat{d}_{sc}}^T \times \frac{d}{d\alpha} \Big|_{\alpha,\gamma,\beta,\theta,\eta=0} ({}^1\bar{k}_{sc} \times {}^1N_{\delta\hat{d}_{sc}} \times ({}_1\mathbf{q} + \alpha\Delta\mathbf{q})) \times d^1x \right] + \\ & \left[\int_0^{1L} \frac{d}{d\alpha} \Big|_{\alpha,\gamma,\beta,\theta,\eta=0} ({}^1N_{\delta\hat{d}_{sc}}^T) \times {}^1\mathbf{D}_{sc} \times d^1l \right] + \left[\int_0^{1L} {}^1N_{\delta\hat{d}_{sc}}^T \times \frac{d}{d\alpha} \Big|_{\alpha,\gamma,\beta,\theta,\eta=0} ({}^1\mathbf{D}_{sc}) \times d^1l \right] + \\ & \left[\int_0^{1L} \frac{d}{d\alpha} \Big|_{\alpha,\gamma,\beta,\theta,\eta=0} ({}^2N_{D2}^T) \times ({}^1\hat{\mathbf{d}} - {}^1\mathbf{d}) \times d^1x \right] + \left[\int_0^{1L} {}^2N_{D2}^T \times \frac{d}{d\alpha} \Big|_{\alpha,\gamma,\beta,\theta,\eta=0} ({}^1\hat{\mathbf{d}} - {}^1\mathbf{d}) \times d^1x \right] - \\ & \left[\frac{d}{d\alpha} \Big|_{\alpha,\gamma,\beta,\theta,\eta=0} ({}^2\mathbf{Q}_{ext} + \beta\Delta\mathbf{Q}_{ext}) \right] + \\ & \left[\int_{1V^c} \frac{d}{d\alpha} \Big|_{\alpha,\gamma,\beta,\theta,\eta=0} {}^1\rho^c \times {}^1N_u^c \times {}^1N_u^c \times d^1V^c \times ({}^2\dot{\mathbf{q}} + \theta\Delta\dot{\mathbf{q}}) + \int_{1V^s} \frac{d}{d\alpha} \Big|_{\alpha,\gamma,\beta,\theta,\eta=0} {}^1\rho^s \times {}^1N_u^s \times {}^1N_u^s \times d^1V^s \times ({}^2\dot{\mathbf{q}} + \theta\Delta\dot{\mathbf{q}}) \right] + \\ & \left[\int_{1V^c} \frac{d}{d\alpha} \Big|_{\alpha,\gamma,\beta,\theta,\eta=0} {}^1\rho^c \times {}^1N_u^c \times {}^1N_u^c \times d^1V^c \times ({}^2\ddot{\mathbf{q}} + \eta\Delta\ddot{\mathbf{q}}) + \int_{1V^s} \frac{d}{d\alpha} \Big|_{\alpha,\gamma,\beta,\theta,\eta=0} {}^1\rho^s \times {}^1N_u^s \times {}^1N_u^s \times d^1V^s \times ({}^2\ddot{\mathbf{q}} + \eta\Delta\ddot{\mathbf{q}}) \right] \end{aligned} \quad [2.79]$$

$$\left[\int_0^{1L} \frac{d}{d\alpha} \Big|_{\alpha,\gamma,\beta,\theta,\eta=0} ({}^1N_{\delta\hat{d}}) \times {}^2\mathbf{D} \times d^1x \right] = {}^2\mathbf{K}_g \times \Delta\mathbf{q} \quad (\text{see Equation A.22 in Appendix A}) \quad [2.80]$$

$$\left[\int_0^{1L} {}^1N_{\delta\hat{d}}^T \times \frac{d}{d\alpha} \Big|_{\alpha,\gamma,\beta,\theta,\eta=0} ({}^2\mathbf{D}) \times d^1x \right] = \left[\int_0^{1L} {}^1N_{\delta\hat{d}}^T \times {}^2N_{D2} \times d^1x \right] \times \Delta\mathbf{q} = {}^2\mathbf{G}_2 \times \Delta\mathbf{q} \quad [2.81]$$

The third term on the right hand side of Equation 2.79 vanishes since ${}^1N_{\delta\hat{d}_{sc}}$ is not a function of ${}_1\mathbf{q}$:

$$\left[\int_0^{1L} \frac{d}{d\alpha} \Big|_{\alpha,\gamma,\beta,\theta,\eta=0} ({}^1N_{\delta\hat{d}_{sc}}^T) \times {}^1\bar{k}_{sc} \times {}^1N_{\delta\hat{d}_{sc}} \times {}_1\mathbf{q} \times d^1x \right] = 0 \quad [2.82]$$

In the fourth term on the right hand side of Equation 2.79, ${}_1\mathbf{q}$ is replaced by ${}_1\mathbf{q} + \alpha\Delta\mathbf{q}$ and differentiation with respect to α at $\alpha = 0$ is performed to obtain the slip stiffness matrix (${}^2\mathbf{K}_{sc}$) as shown in Equation 2.83.

$$\left[\int_0^{1L} {}^1\mathbf{N}_{\delta\hat{d}_{sc}}^T \times \frac{d}{d\alpha} \Big|_{\alpha,\gamma,\beta,\theta,\eta=0} \left({}^1\bar{\mathbf{k}}_{sc} \times {}^1\mathbf{N}_{\delta\hat{d}_{sc}} \times ({}_1\mathbf{q} + \alpha\Delta\mathbf{q}) \right) \times d^1\mathbf{x} \right] = \left[\int_0^{1L} {}^1\mathbf{N}_{\delta\hat{d}_{sc}}^T \times {}^1\bar{\mathbf{k}}_{sc} \times {}^1\mathbf{N}_{\delta\hat{d}_{sc}} \times d^1\mathbf{x} \right] \times \Delta\mathbf{q} = {}^1\mathbf{K}_{sc} \times \Delta\mathbf{q} \quad [2.83]$$

The fifth, sixth, and seventh terms on the right hand side of Equation 2.79 vanishes since differentiation of the terms $\mathbf{N}_{\delta\hat{d}_{sc}}$, ${}^1\mathbf{D}_{sc}$, and \mathbf{N}_{D2} with respect to α at $\alpha = 0$ are zero.

$$\left[\int_1^I \frac{d}{d\alpha} \Big|_{\alpha,\gamma,\beta,\theta,\eta=0} \left({}^1\mathbf{N}_{\delta\hat{d}_{sc}}^T \right) \times {}^1\mathbf{D}_{sc} \times d^1\mathbf{I} \right] = 0 \quad [2.84]$$

$$\left[\int_1^I {}^1\mathbf{N}_{\delta\hat{d}_{sc}}^T \times \frac{d}{d\alpha} \Big|_{\alpha,\gamma,\beta,\theta,\eta=0} \left({}^1\mathbf{D}_{sc} \right) \times d^1\mathbf{I} \right] = 0 \quad [2.85]$$

$$\left[\int_0^{1L} \frac{d}{d\alpha} \Big|_{\alpha,\gamma,\beta,\theta,\eta=0} \left({}^2\mathbf{N}_{D2}^T \right) \times ({}_1\hat{\mathbf{d}} - {}_1\mathbf{d}) \times d^1\mathbf{x} \right] = 0 \quad [2.86]$$

Expanding the eighth term on the right hand side of Equation 2.79 yields Equation 2.87 given below:

$$\left[\int_0^{1L} {}^2\mathbf{N}_{D2}^T \times \frac{d}{d\alpha} \Big|_{\alpha,\gamma,\beta,\theta,\eta=0} ({}_1\hat{\mathbf{d}} - {}_1\mathbf{d}) \times d^1\mathbf{x} \right] = \left[\int_0^{1L} {}^2\mathbf{N}_{D2}^T \times \frac{d}{d\alpha} \Big|_{\alpha,\gamma,\beta,\theta,\eta=0} ({}_1\hat{\mathbf{d}}) \times d^1\mathbf{x} - \int_0^{1L} {}^2\mathbf{N}_{D2}^T \times \frac{d}{d\alpha} \Big|_{\alpha,\gamma,\beta,\theta,\eta=0} ({}_1\mathbf{d}) \times d^1\mathbf{x} \right] \quad [2.87]$$

In Equation 2.87, ${}_1\hat{\mathbf{d}}$ is replaced by ${}^1\mathbf{N}_{\hat{d}} \times {}_1\mathbf{q}$ and ${}_1\mathbf{q} + \alpha\Delta\mathbf{q}$ is substituted for ${}_1\mathbf{q}$ as shown in Equation 2.88.

$$\left[\int_0^{1L} {}^2\mathbf{N}_{D2}^T \times \frac{d}{d\alpha} \Big|_{\alpha,\gamma,\beta,\theta,\eta=0} ({}_1\hat{\mathbf{d}} - {}_1\mathbf{d}) \times d^1\mathbf{x} \right] = \left[\int_0^{1L} {}^2\mathbf{N}_{D2}^T \times \frac{d}{d\alpha} \Big|_{\alpha,\gamma,\beta,\theta,\eta=0} {}^1\mathbf{N}_{\hat{d}} \times ({}_1\mathbf{q} + \alpha\Delta\mathbf{q}) \times d^1\mathbf{x} \right] - \left[\int_0^{1L} {}^2\mathbf{N}_{D2}^T \times \frac{d}{d\alpha} \Big|_{\alpha,\gamma,\beta,\theta,\eta=0} ({}_1\mathbf{d}) \times d^1\mathbf{x} \right] \quad [2.88]$$

Evaluating the differentiation of the first term on the right hand side of Equation 2.88 at $\alpha = 0$, Equation 2.89 is obtained as follows:

$$\left[\int_0^{1L} {}^2\mathbf{N}_{D2}^T \times \frac{d}{d\alpha} \Big|_{\alpha,\gamma,\beta,\theta,\eta=0} ({}_1\hat{\mathbf{d}} - {}_1\mathbf{d}) \times d^1\mathbf{x} \right] = \left[\int_0^{1L} {}^2\mathbf{N}_{D2}^T \times {}^1\mathbf{N}_{\hat{d}} \times d^1\mathbf{x} \right] \times \Delta\mathbf{q} - \left[\int_0^{1L} {}^2\mathbf{N}_{D2}^T \times \frac{d}{d\alpha} \Big|_{\alpha,\gamma,\beta,\theta,\eta=0} ({}_1\mathbf{d}) \times d^1\mathbf{x} \right] \quad [2.89]$$

In the second term on the right hand side of Equation 2.88, differentiation is performed using the chain rule of differentiation given below in a similar way while deriving

Equation 2.68. Then, ${}^1\mathbf{q} + \alpha\Delta\mathbf{q}$ is substituted into ${}^2\mathbf{N}_{D1}$ and the differentiation is evaluated at $\alpha = 0$. This process is followed by factoring out $\Delta\mathbf{q}$, which yields Equation 2.90 as given below:

$$\begin{aligned}
\int_0^{1L} {}^2\mathbf{N}_{D2}^T \times \frac{d}{d\alpha} \Big|_{\alpha,\gamma,\beta,\theta,\eta=0} ({}^1\mathbf{d}) \times d^1x &= \int_0^{1L} {}^2\mathbf{N}_{D2}^T \times \frac{\partial_1\mathbf{d}}{\partial_1^2\mathbf{D}_\Sigma} \times \frac{\partial_1^2\mathbf{D}_\Sigma}{\partial_1^2\mathbf{D}} \times \frac{d}{d\alpha} \Big|_{\alpha,\gamma,\beta,\theta,\eta=0} ({}^2\mathbf{D}) \times d^1x \\
&= \int_0^{1L} {}^2\mathbf{N}_{D2}^T \times \frac{\partial_1\mathbf{d}}{\partial_1^2\mathbf{D}_\Sigma} \times \frac{\partial_1^2\mathbf{D}_\Sigma}{\partial_1^2\mathbf{D}} \times \frac{d}{d\alpha} \Big|_{\alpha,\gamma,\beta,\theta,\eta=0} ({}^2\mathbf{N}_{D1} \times {}^2\mathbf{Q}) \times d^1x \\
&= \int_0^{1L} {}^2\mathbf{N}_{D2}^T \times {}^1\mathbf{k}^{-1} \times {}^2\mathbf{N}_{D2} \times d^1x
\end{aligned} \tag{2.90}$$

Substituting Equation 2.90 into Equation 2.89 and evaluating the integration along the element length yields Equation 2.91.

$$\begin{aligned}
\left[\int_0^{1L} {}^2\mathbf{N}_{D2}^T \times \frac{d}{d\alpha} \Big|_{\alpha,\gamma,\beta,\theta,\eta=0} ({}^1\hat{\mathbf{d}} - {}^1\mathbf{d}) \times d^1x \right] &= \left[\int_0^{1L} {}^2\mathbf{N}_{D2}^T \times {}^1\mathbf{N}_{\hat{\mathbf{d}}} \times d^1x \right] \times \Delta\mathbf{q} - \left[\int_0^{1L} {}^2\mathbf{N}_{D2}^T \times {}^1\mathbf{k}^{-1} \times {}^2\mathbf{N}_{D2} \times d^1x \right] \times \Delta\mathbf{q} \\
&= {}^2\mathbf{G}_2 \times \Delta\mathbf{q} - {}^2\mathbf{H}_{22} \times \Delta\mathbf{q}
\end{aligned} \tag{2.91}$$

The ninth, tenth, and eleventh terms do not have any variables that are functions of ${}^1\mathbf{q}$. Therefore, differentiation of these terms with respect to α at $\alpha = 0$ becomes zero as shown in Equation 2.92 through 2.94.

$$\left[\frac{d}{d\alpha} \Big|_{\alpha,\gamma,\beta,\theta,\eta=0} ({}^2\mathbf{Q}_{ext}) \right] = 0 \tag{2.92}$$

$$\left[\int_{1V^c} \frac{d}{d\alpha} \Big|_{\alpha,\gamma,\beta,\theta,\eta=0} {}^1\rho^c \times {}^1\mathbf{N}_u^{cT} \times {}^1\mathbf{N}_u^c \times d^1V^c \times {}^2\ddot{\mathbf{q}} + \int_{1V^s} \frac{d}{d\alpha} \Big|_{\alpha,\gamma,\beta,\theta,\eta=0} {}^1\rho^s \times {}^1\mathbf{N}_u^{sT} \times {}^1\mathbf{N}_u^s \times d^1V^s \times {}^2\ddot{\mathbf{q}} \right] = 0 \tag{2.93}$$

$$\left[\int_{1V^c} \frac{d}{d\alpha} \Big|_{\alpha,\gamma,\beta,\theta,\eta=0} {}^1\rho^c \times {}^1\mathbf{N}_u^{cT} \times {}^1\mathbf{N}_u^c \times d^1V^c \times {}^2\dot{\mathbf{q}} + \int_{1V^s} \frac{d}{d\alpha} \Big|_{\alpha,\gamma,\beta,\theta,\eta=0} {}^1\rho^s \times {}^1\mathbf{N}_u^{sT} \times {}^1\mathbf{N}_u^s \times d^1V^s \times {}^2\dot{\mathbf{q}} \right] = 0 \tag{2.94}$$

The expansion process of the second term on the right hand side of Equation 2.78 is summarized in Equation 2.95.

$$\begin{aligned}
\frac{d}{d\gamma}_{\alpha,\gamma,\beta,\theta,\eta=0} g(\mathbf{q} + \alpha\Delta\mathbf{q}, {}^2\mathbf{Q} + \gamma\Delta\mathbf{Q}, {}^2\mathbf{Q}_{ext} + \beta\Delta\mathbf{Q}_{ext}, {}^2\hat{\mathbf{q}} + \theta\Delta\hat{\mathbf{q}}, {}^2\ddot{\mathbf{q}} + \eta\Delta\ddot{\mathbf{q}}) = & \left[\int_0^{1L} \frac{d}{d\gamma}_{\alpha,\gamma,\beta,\theta,\eta=0} \left({}^1\mathbf{N}_{\delta\hat{\mathbf{d}}} \right) \times {}^2\mathbf{D} \times d^1\mathbf{x} \right] + \left[\int_0^{1L} {}^1\mathbf{N}_{\delta\hat{\mathbf{d}}}^T \times \frac{d}{d\gamma}_{\alpha,\gamma,\beta,\theta,\eta=0} \left({}^2\mathbf{D} \right) \times d^1\mathbf{x} \right] + \\
& \left[\int_0^{1L} \frac{d}{d\gamma}_{\alpha,\gamma,\beta,\theta,\eta=0} \left({}^1\mathbf{N}_{\delta\hat{\mathbf{d}}}^T \right) \times {}^1\bar{\mathbf{k}}_{sc} \times {}^1\mathbf{N}_{\delta\hat{\mathbf{d}}} \times (\mathbf{q} + \alpha\Delta\mathbf{q}) \times d^1\mathbf{x} \right] + \left[\int_0^{1L} {}^1\mathbf{N}_{\delta\hat{\mathbf{d}}}^T \times \frac{d}{d\gamma}_{\alpha,\gamma,\beta,\theta,\eta=0} \left({}^1\bar{\mathbf{k}}_{sc} \times {}^1\mathbf{N}_{\delta\hat{\mathbf{d}}} \right) \times (\mathbf{q} + \alpha\Delta\mathbf{q}) \times d^1\mathbf{x} \right] + \\
& \left[\int_0^{1L} \frac{d}{d\gamma}_{\alpha,\gamma,\beta,\theta,\eta=0} \left({}^1\mathbf{N}_{\delta\hat{\mathbf{d}}}^T \right) \times {}^1\mathbf{D}_{sc} \times d^1\mathbf{l} \right] + \left[\int_0^{1L} {}^1\mathbf{N}_{\delta\hat{\mathbf{d}}}^T \times \frac{d}{d\gamma}_{\alpha,\gamma,\beta,\theta,\eta=0} \left({}^1\mathbf{D}_{sc} \right) \times d^1\mathbf{l} \right] + \\
& \left[\int_0^{1L} \frac{d}{d\gamma}_{\alpha,\gamma,\beta,\theta,\eta=0} \left({}^2\mathbf{N}_{D2}^T \right) \times ({}^1\hat{\mathbf{d}} - \mathbf{d}) \times d^1\mathbf{x} \right] + \left[\int_0^{1L} {}^2\mathbf{N}_{D2}^T \times \frac{d}{d\gamma}_{\alpha,\gamma,\beta,\theta,\eta=0} \left({}^1\hat{\mathbf{d}} - \mathbf{d} \right) \times d^1\mathbf{x} \right] - \\
& \left[\frac{d}{d\gamma}_{\alpha,\gamma,\beta,\theta,\eta=0} \left({}^2\mathbf{Q}_{ext} + \beta\Delta\mathbf{Q}_{ext} \right) \right] + \\
& \left[\int_{V^c} \frac{d}{d\gamma}_{\alpha,\gamma,\beta,\theta,\eta=0} {}^1\rho^c \times {}^1\mathbf{N}_u^c \times {}^1\mathbf{N}_u^c \times d^1V^c \times ({}^2\hat{\mathbf{q}} + \theta\Delta\hat{\mathbf{q}}) + \int_{V^s} \frac{d}{d\gamma}_{\alpha,\gamma,\beta,\theta,\eta=0} {}^1\rho^s \times {}^1\mathbf{N}_u^s \times {}^1\mathbf{N}_u^s \times d^1V^s \times ({}^2\hat{\mathbf{q}} + \theta\Delta\hat{\mathbf{q}}) \right] + \\
& \left[\int_{V^c} \frac{d}{d\gamma}_{\alpha,\gamma,\beta,\theta,\eta=0} {}^1\rho^c \times {}^1\mathbf{N}_u^c \times {}^1\mathbf{N}_u^c \times d^1V^c \times ({}^2\ddot{\mathbf{q}} + \eta\Delta\ddot{\mathbf{q}}) + \int_{V^s} \frac{d}{d\gamma}_{\alpha,\gamma,\beta,\theta,\eta=0} {}^1\rho^s \times {}^1\mathbf{N}_u^s \times {}^1\mathbf{N}_u^s \times d^1V^s \times ({}^2\ddot{\mathbf{q}} + \eta\Delta\ddot{\mathbf{q}}) \right]
\end{aligned} \tag{2.95}$$

In the first term on the right hand side of Equation 2.95, ${}^1\mathbf{N}_{\delta\hat{\mathbf{d}}}$ is not function of the variable ${}^2\mathbf{Q}$. Therefore, the differentiation with respect to γ evaluated at $\gamma = 0$ vanishes and the integration along the element length becomes zero as given in Equation 2.96.

$$\left[\int_0^{1L} \frac{d}{d\gamma}_{\alpha,\gamma,\beta,\theta,\eta=0} \left({}^1\mathbf{N}_{\delta\hat{\mathbf{d}}} \right) \times {}^2\mathbf{D} \times d^1\mathbf{x} \right] = 0 \tag{2.96}$$

While expanding the second term on the right hand side of Equation 2.95, ${}^2\mathbf{D}$ is stated in terms of force interpolation functions as ${}^2\mathbf{D} = {}^2\mathbf{N}_{D1} \times {}^2\mathbf{Q}$ and ${}^2\mathbf{Q}$ is replaced by ${}^2\mathbf{Q} + \gamma \times \Delta\mathbf{Q}$. Following the evaluation of differentiation with respect to γ at $\gamma = 0$ and factoring out the term $\Delta\mathbf{Q}$, Equation 2.97 is derived as given below:

$$\begin{aligned}
\left[\int_0^{1L} {}^1\mathbf{N}_{\delta\hat{\mathbf{d}}}^T \times \frac{d}{d\gamma}_{\alpha,\gamma,\beta,\theta,\eta=0} \left({}^2\mathbf{D} \right) \times d^1\mathbf{x} \right] &= \left[\int_0^{1L} {}^1\mathbf{N}_{\delta\hat{\mathbf{d}}}^T \times \frac{d}{d\gamma}_{\alpha,\gamma,\beta,\theta,\eta=0} \left({}^2\mathbf{N}_{D1} \times \left({}^2\mathbf{Q} + \gamma\Delta\mathbf{Q} \right) \right) \times d^1\mathbf{x} \right] \\
&= \left[\int_0^{1L} {}^1\mathbf{N}_{\delta\hat{\mathbf{d}}}^T \times {}^2\mathbf{N}_{D1} \times d^1\mathbf{x} \right] \times \Delta\mathbf{Q}
\end{aligned} \tag{2.97}$$

Performing the integration of Equation 2.97 along the element length:

$$\left[\int_0^{1L} {}^2_1\mathbf{N}_{\hat{d}}^T \times \frac{d}{d\gamma} \Big|_{\alpha,\gamma,\beta,\theta,\eta=0} \left({}^2_1\mathbf{D} \right) \times d^1x \right] = \left[\int_0^{1L} {}^1\mathbf{N}_{\hat{d}}^T \times {}^2_1\mathbf{N}_{D1} \times d^1x \right] \times \Delta \mathbf{Q} = {}^2_1\mathbf{G}_1^T \times \Delta \mathbf{Q} \quad [2.98]$$

In the third, fourth, fifth, and sixth terms on the right hand side of Equation 2.95, the variables on which differentiation is being performed are not functions of ${}^2_1\mathbf{Q}$. Therefore, the result of the differentiation and integrations of the aforementioned terms become zero as stated in Equation 2.99 through 2.102.

$$\left[\int_0^{1L} \frac{d}{d\gamma} \Big|_{\alpha,\gamma,\beta,\theta,\eta=0} \left({}^1\mathbf{N}_{\hat{d}_{sc}}^T \right) \times {}^1\bar{k}_{sc} \times {}^1\mathbf{N}_{\hat{d}_{sc}} \times {}^1\mathbf{q} \times d^1I \right] = 0 \quad [2.99]$$

$$\left[\int_0^{1L} {}^1\mathbf{N}_{\hat{d}_{sc}}^T \times \frac{d}{d\gamma} \Big|_{\alpha,\gamma,\beta,\theta,\eta=0} \left({}^1\bar{k}_{sc} \times {}^1\mathbf{N}_{\hat{d}_{sc}} \right) \times {}^1\mathbf{q} \times d^1I \right] = 0 \quad [2.100]$$

$$\left[\int_0^{1L} \frac{d}{d\gamma} \Big|_{\alpha,\gamma,\beta,\theta,\eta=0} \left({}^1\mathbf{N}_{\hat{d}_{sc}}^T \right) \times {}^1D_{sc} \times d^1I \right] \times {}^1\mathbf{q} = 0 \quad [2.101]$$

$$\left[\int_0^{1L} {}^1\mathbf{N}_{\hat{d}_{sc}}^T \times \frac{d}{d\gamma} \Big|_{\alpha,\gamma,\beta,\theta,\eta=0} \left({}^1D_{sc} \right) \times d^1I \right] \times {}^1\mathbf{q} = 0 \quad [2.102]$$

In the seventh term on the right hand side of Equation 2.95, the nodal force values in ${}^2_1\mathbf{N}_{D2}$ (e.g., ${}^2_1\mathbf{P}^c$, ${}^2_1\mathbf{P}^s$) are replaced by ${}^2_1\mathbf{Q} + \gamma\Delta\mathbf{Q}$ (e.g., ${}^2_1\mathbf{P}^c + \gamma\Delta\mathbf{P}^c$, ${}^2_1\mathbf{P}^s + \gamma\Delta\mathbf{P}^s$).

Performing the differentiation of the terms of \mathbf{N}_{D2} with respect to γ at $\gamma = 0$, the resulting expression is multiplied by $({}^1\hat{\mathbf{d}} - {}^1\mathbf{d})$. Carrying out the integration along the element length and factoring out the term $\Delta\mathbf{Q}$, Equation 2.103 is derived as given below:

$$\left[\int_0^{1L} \frac{d}{d\gamma} \Big|_{\alpha,\gamma,\beta,\theta,\eta=0} \left({}^2_1\mathbf{N}_{D2}^T \right) \times ({}^1\hat{\mathbf{d}} - {}^1\mathbf{d}) \times d^1x \right] = \mathbf{M}_d^T \times \Delta\mathbf{Q} \quad (\text{see Equation A.19 in}$$

Appendix A)

[2.103]

The eighth term on the right hand side of Equation 2.95 can be decomposed into two parts as shown in Equation 2.104

$$\left[\int_0^{1L} {}^2_1\mathbf{N}_{D2}^T \times \frac{d}{d\gamma} \Big|_{\alpha,\gamma,\beta,\theta,\eta=0} \left(({}^1\hat{\mathbf{d}} - {}^1\mathbf{d}) \right) \times d^1x \right] = \left[\int_0^{1L} {}^2_1\mathbf{N}_{D2}^T \times \frac{d}{d\gamma} \Big|_{\alpha,\gamma,\beta,\theta,\eta=0} \left(({}^1\hat{\mathbf{d}}) \right) \times d^1x \right] - \left[\int_0^{1L} {}^2_1\mathbf{N}_{D2}^T \times \frac{d}{d\gamma} \Big|_{\alpha,\gamma,\beta,\theta,\eta=0} \left(({}^1\mathbf{d}) \right) \times d^1x \right]$$

[2.104]

In the first term on the right hand side of Equation 2.104, differentiation of ${}_1\hat{\mathbf{d}}$ with respect to γ vanishes since ${}_1\hat{\mathbf{d}}$ is not a function of ${}_1^2\mathbf{Q}$. Therefore, the integration along the element length also becomes zero as given below:

$$\left[\int_0^{1L} {}_1^2\mathbf{N}_{D2}^T \times \frac{d}{d\gamma} \Big|_{\alpha,\gamma,\beta,\theta,\eta=0} ({}_1\hat{\mathbf{d}}) \times d^1x \right] = 0 \quad [2.105]$$

The second term on the right hand side of Equation 2.104 is first expanded through substituting the cross-section constitutive equation of ${}_1\mathbf{d} = {}^1\mathbf{k}^{-1} \times {}_1\mathbf{D}$. Then, ${}_1\mathbf{D}$ is expressed in terms force interpolation functions as ${}_1\mathbf{D} = {}_1^2\mathbf{N}_{D1} \times {}_1\mathbf{Q}$. ${}_1\mathbf{Q}$ is rewritten in terms of ${}_1^2\mathbf{Q}$ as ${}_1\mathbf{Q} = {}_1^2\mathbf{Q} - {}_1\mathbf{Q}$. Differentiation with respect to γ is performed replacing ${}_1^2\mathbf{Q}$ by ${}_1^2\mathbf{Q} + \gamma \times \Delta\mathbf{Q}$ and it is evaluated at $\gamma = 0$. Carrying out integration along the element length, Equation 2.106 is derived.

$$\begin{aligned} \left[\int_0^{1L} {}_1^2\mathbf{N}_{D2}^T \times \frac{d}{d\gamma} \Big|_{\alpha,\gamma,\beta,\theta,\eta=0} ({}_1\mathbf{d}) \times d^1x \right] &= \left[\int_0^{1L} {}_1^2\mathbf{N}_{D2}^T \times {}^1\mathbf{k}^{-1} \times {}_1^2\mathbf{N}_{D1} \times {}_1\mathbf{Q} \times d^1x \right] \\ &= \left[\int_0^{1L} {}_1^2\mathbf{N}_{D2}^T \times {}^1\mathbf{k}^{-1} \times {}_1^2\mathbf{N}_{D1} \times ({}_1^2\mathbf{Q} - {}_1\mathbf{Q} + \gamma \times \Delta\mathbf{Q}) \times d^1x \right] \\ &= \left[\int_0^{1L} {}_1^2\mathbf{N}_{D2}^T \times {}^1\mathbf{k}^{-1} \times {}_1^2\mathbf{N}_{D1} \times d^1x \right] \times \Delta\mathbf{Q} \\ &= {}_1^2\mathbf{H}_{12}^T \times \Delta\mathbf{Q} \end{aligned} \quad [2.106]$$

Substituting Equation 2.106 and 2.105 into Equation 2.104:

$$\left[\int_0^{1L} {}_1^2\mathbf{N}_{D2}^T \times \frac{d}{d\gamma} \Big|_{\alpha,\gamma,\beta,\theta,\eta=0} ({}_1\hat{\mathbf{d}} - {}_1\mathbf{d}) \times d^1x \right] = -{}_1^2\mathbf{H}_{12}^T \times \Delta\mathbf{Q} \quad [2.107]$$

The rest of the terms on the right hand side of Equation 2.95, including the ninth, tenth, and eleventh terms do not have any variables that are functions of ${}_1^2\mathbf{Q}$. Therefore, the differentiation and also the integrations of these terms become zero as shown in Equations 2.108, 2.109, and 2.110.

$$\left[\frac{d}{d\gamma_{\alpha,\gamma,\beta,\theta,\eta=0}} \Big|_{\beta=0} ({}^2_1\mathcal{Q}_{ext}) \right] = 0 \quad [2.108]$$

$$\left[\int_{1V^c} \frac{d}{d\gamma_{\alpha,\gamma,\beta,\theta,\eta=0}} \Big|_{\beta=0} {}^1\rho^c \times {}^1N_u^{cT} \times {}^1N_u^c \times d^1V^c \times {}^2_1\dot{\mathbf{q}} + \int_{1V^s} \frac{d}{d\gamma_{\alpha,\gamma,\beta,\theta,\eta=0}} \Big|_{\beta=0} {}^1\rho^s \times {}^1N_u^{sT} \times {}^1N_u^s \times d^1V^s \times {}^2_1\dot{\mathbf{q}} \right] = 0 \quad [2.109]$$

$$\left[\int_{1V^c} \frac{d}{d\gamma_{\alpha,\gamma,\beta,\theta,\eta=0}} \Big|_{\beta=0} {}^1\rho^c \times {}^1N_u^{cT} \times {}^1N_u^c \times d^1V^c \times {}^2_1\ddot{\mathbf{q}} + \int_{1V^s} \frac{d}{d\gamma_{\alpha,\gamma,\beta,\theta,\eta=0}} \Big|_{\beta=0} {}^1\rho^s \times {}^1N_u^{sT} \times {}^1N_u^s \times d^1V^s \times {}^2_1\ddot{\mathbf{q}} \right] = 0 \quad [2.110]$$

The expanded form of the fourth term on the right hand side Equation 2.78 is presented below:

$$\begin{aligned} \frac{d}{d\beta_{\alpha,\gamma,\beta,\theta,\eta=0}} \Big|_{\beta=0} g(\mathbf{q} + \alpha\Delta\mathbf{q}, {}^2\mathcal{Q} + \gamma\Delta\mathcal{Q}, {}^2\mathcal{Q}_{ext} + \beta\Delta\mathcal{Q}_{ext}, {}^2\dot{\mathbf{q}} + \theta\Delta\dot{\mathbf{q}}, {}^2\ddot{\mathbf{q}} + \eta\Delta\ddot{\mathbf{q}}) = & \left[\int_0^{1L} \frac{d}{d\beta_{\alpha,\gamma,\beta,\theta,\eta=0}} \Big|_{\beta=0} ({}^1N_{\hat{d}}) \times {}^2_1\mathcal{D} \times d^1x \right] + \left[\int_0^{1L} {}^1N_{\hat{d}}^T \times \frac{d}{d\beta_{\alpha,\gamma,\beta,\theta,\eta=0}} \Big|_{\beta=0} ({}^2_1\mathcal{D}) \times d^1x \right] + \\ & \left[\int_0^{1L} \frac{d}{d\beta_{\alpha,\gamma,\beta,\theta,\eta=0}} \Big|_{\beta=0} ({}^1N_{\hat{d}_{sc}}^T) \times {}^2_1\bar{k}_{sc} \times {}^1N_{\hat{d}_{sc}} \times ({}^1\mathbf{q} + \alpha\Delta\mathbf{q}) \times d^1x \right] + \left[\int_0^{1L} {}^2_1N_{\hat{d}_{sc}}^T \times \frac{d}{d\beta_{\alpha,\gamma,\beta,\theta,\eta=0}} \Big|_{\beta=0} ({}^2_1\bar{k}_{sc} \times {}^2_1N_{\hat{d}_{sc}} \times ({}^1\mathbf{q} + \alpha\Delta\mathbf{q})) \times d^1x \right] + \\ & \left[\int_0^{1L} \frac{d}{d\beta_{\alpha,\gamma,\beta,\theta,\eta=0}} \Big|_{\beta=0} ({}^1N_{\hat{d}_{sc}}^T) \times {}^1\mathcal{D}_{sc} \times d^1l \right] + \left[\int_0^{1L} {}^1N_{\hat{d}_{sc}}^T \times \frac{d}{d\beta_{\alpha,\gamma,\beta,\theta,\eta=0}} \Big|_{\beta=0} ({}^1\mathcal{D}_{sc}) \times d^1l \right] + \\ & \left[\int_0^{1L} \frac{d}{d\beta_{\alpha,\gamma,\beta,\theta,\eta=0}} \Big|_{\beta=0} ({}^2_1N_{D2}^T) \times ({}^1\hat{\mathbf{d}} - {}^1\mathbf{d}) \times d^1x \right] + \left[\int_0^{1L} {}^2_1N_{D2}^T \times \frac{d}{d\beta_{\alpha,\gamma,\beta,\theta,\eta=0}} \Big|_{\beta=0} ({}^1\hat{\mathbf{d}} - {}^1\mathbf{d}) \times d^1x \right] - \\ & \left[\frac{d}{d\beta_{\alpha,\gamma,\beta,\theta,\eta=0}} \Big|_{\beta=0} ({}^2_1\mathcal{Q}_{ext} + \beta\Delta\mathcal{Q}_{ext}) \right] + \\ & \left[\int_{1V^c} \frac{d}{d\beta_{\alpha,\gamma,\beta,\theta,\eta=0}} \Big|_{\beta=0} {}^1\rho^c \times {}^1N_u^{cT} \times {}^1N_u^c \times d^1V^c \times ({}^2_1\dot{\mathbf{q}} + \theta\Delta\dot{\mathbf{q}}) + \int_{1V^s} \frac{d}{d\beta_{\alpha,\gamma,\beta,\theta,\eta=0}} \Big|_{\beta=0} {}^1\rho^s \times {}^1N_u^{sT} \times {}^1N_u^s \times d^1V^s \times ({}^2_1\dot{\mathbf{q}} + \theta\Delta\dot{\mathbf{q}}) \right] + \\ & \left[\int_{1V^c} \frac{d}{d\beta_{\alpha,\gamma,\beta,\theta,\eta=0}} \Big|_{\beta=0} {}^1\rho^c \times {}^1N_u^{cT} \times {}^1N_u^c \times d^1V^c \times ({}^2_1\ddot{\mathbf{q}} + \eta\Delta\ddot{\mathbf{q}}) + \int_{1V^s} \frac{d}{d\beta_{\alpha,\gamma,\beta,\theta,\eta=0}} \Big|_{\beta=0} {}^1\rho^s \times {}^1N_u^{sT} \times {}^1N_u^s \times d^1V^s \times ({}^2_1\ddot{\mathbf{q}} + \eta\Delta\ddot{\mathbf{q}}) \right] \end{aligned} \quad [2.111]$$

On the right hand side of 2.111, the only non-zero expression is the ninth term, since the rest of the terms do not have variables that are functions of ${}^2_1\mathcal{Q}_{ext}$. In the ninth term, the differentiation is performed with respect to β and it is evaluated at $\beta = 0$ resulting in Equation 2.112.

$$\left[\frac{d}{d\beta_{\alpha,\gamma,\beta,\theta,\eta=0}} \Big|_{\beta=0} (-{}^2_1\mathcal{Q}_{ext} - \beta\Delta\mathcal{Q}_{ext}) \right] = -\Delta\mathcal{Q}_{ext} \quad [2.112]$$

The expanded form of the fifth term on the right hand side Equation 2.78 is presented below:

$$\begin{aligned}
\frac{d}{d\theta} \Big|_{\alpha,\gamma,\beta,\theta,\eta=0} g(\mathbf{q} + \alpha\Delta\mathbf{q}, {}^2\mathbf{Q} + \gamma\Delta\mathbf{Q}, {}^2\mathbf{Q}_{ext} + \beta\Delta\mathbf{Q}_{ext}, {}^2\dot{\mathbf{q}} + \theta\Delta\dot{\mathbf{q}}, {}^2\ddot{\mathbf{q}} + \eta\Delta\ddot{\mathbf{q}}) = & \left[\int_0^{1L} \frac{d}{d\theta} \Big|_{\alpha,\gamma,\beta,\theta,\eta=0} ({}^1\mathbf{N}_{\delta\dot{c}}) \times {}^2\mathbf{D} \times d^1x \right] + \left[\int_0^{1L} {}^1\mathbf{N}_{\delta\dot{c}}^T \times \frac{d}{d\theta} \Big|_{\alpha,\gamma,\beta,\theta,\eta=0} ({}^2\mathbf{D}) \times d^1x \right] + \\
& \left[\int_0^{1L} \frac{d}{d\theta} \Big|_{\alpha,\gamma,\beta,\theta,\eta=0} ({}^1\mathbf{N}_{\delta\dot{c}}^T) \times {}^2\bar{k}_{sc} \times {}^1\mathbf{N}_{\delta\dot{c}} \times (\mathbf{q} + \alpha\Delta\mathbf{q}) \times d^1x \right] + \left[\int_0^{1L} {}^1\mathbf{N}_{\delta\dot{c}}^T \times \frac{d}{d\theta} \Big|_{\alpha,\gamma,\beta,\theta,\eta=0} ({}^2\bar{k}_{sc} \times {}^1\mathbf{N}_{\delta\dot{c}} \times (\mathbf{q} + \alpha\Delta\mathbf{q})) \times d^1x \right] + \\
& \left[\int_0^{1L} \frac{d}{d\theta} \Big|_{\alpha,\gamma,\beta,\theta,\eta=0} ({}^1\mathbf{N}_{\delta\dot{c}}^T) \times {}^1\mathbf{D}_{sc} \times d^1I \right] + \left[\int_0^{1L} {}^1\mathbf{N}_{\delta\dot{c}}^T \times \frac{d}{d\theta} \Big|_{\alpha,\gamma,\beta,\theta,\eta=0} ({}^1\mathbf{D}_{sc}) \times d^1I \right] + \\
& \left[\int_0^{1L} \frac{d}{d\theta} \Big|_{\alpha,\gamma,\beta,\theta,\eta=0} ({}^2\mathbf{N}_{D2}^T) \times ({}^1\hat{\mathbf{d}} - \mathbf{d}) \times d^1x \right] + \left[\int_0^{1L} {}^2\mathbf{N}_{D2}^T \times \frac{d}{d\theta} \Big|_{\alpha,\gamma,\beta,\theta,\eta=0} ({}^1\hat{\mathbf{d}} - \mathbf{d}) \times d^1x \right] - \\
& \left[\frac{d}{d\theta} \Big|_{\alpha,\gamma,\beta,\theta,\eta=0} ({}^2\mathbf{Q}_{ext} + \beta\Delta\mathbf{Q}_{ext}) \right] + \\
& \left[\int_{1V^c} \frac{d}{d\theta} \Big|_{\alpha,\gamma,\beta,\theta,\eta=0} {}^1\rho^c \times {}^1\mathbf{N}_u^c \times {}^1\mathbf{N}_u^c \times d^1V^c \times ({}^2\dot{\mathbf{q}} + \theta\Delta\dot{\mathbf{q}}) + \int_{1V^s} \frac{d}{d\theta} \Big|_{\alpha,\gamma,\beta,\theta,\eta=0} {}^1\rho^s \times {}^1\mathbf{N}_u^s \times {}^1\mathbf{N}_u^s \times d^1V^s \times ({}^2\dot{\mathbf{q}} + \theta\Delta\dot{\mathbf{q}}) \right] + \\
& \left[\int_{1V^c} \frac{d}{d\theta} \Big|_{\alpha,\gamma,\beta,\theta,\eta=0} {}^1\rho^c \times {}^1\mathbf{N}_u^c \times {}^1\mathbf{N}_u^c \times d^1V^c \times ({}^2\ddot{\mathbf{q}} + \eta\Delta\ddot{\mathbf{q}}) + \int_{1V^s} \frac{d}{d\theta} \Big|_{\alpha,\gamma,\beta,\theta,\eta=0} {}^1\rho^s \times {}^1\mathbf{N}_u^s \times {}^1\mathbf{N}_u^s \times d^1V^s \times ({}^2\ddot{\mathbf{q}} + \eta\Delta\ddot{\mathbf{q}}) \right]
\end{aligned} \tag{2.113}$$

In Equation 2.113, all the terms on the right hand side except the tenth term are not functions of the variable ${}^2\dot{\mathbf{q}}$. Differentiating the tenth term with respect to θ and evaluating it at $\theta = 0$, Equation 2.114 is obtained as given below:

$$\begin{aligned}
& \left[\int_{1V^c} \frac{d}{d\theta} \Big|_{\alpha,\gamma,\beta,\theta,\eta=0} {}^1\mu^c \times {}^1\mathbf{N}_u^c \times {}^1\mathbf{N}_u^c \times d^1V^c \times ({}^2\dot{\mathbf{q}} + \theta \times \Delta\dot{\mathbf{q}}) + \int_{1V^s} \frac{d}{d\theta} \Big|_{\alpha,\gamma,\beta,\theta,\eta=0} {}^1\mu^s \times {}^1\mathbf{N}_u^s \times {}^1\mathbf{N}_u^s \times d^1V^s \times ({}^2\dot{\mathbf{q}} + \theta \times \Delta\dot{\mathbf{q}}) \right] = \tag{2.114} \\
& \left[\int_{1V^c} {}^1\mu^c \times {}^1\mathbf{N}_u^c \times {}^1\mathbf{N}_u^c \times d^1V^c \times \Delta\dot{\mathbf{q}} + \int_{1V^s} {}^1\mu^s \times {}^1\mathbf{N}_u^s \times {}^1\mathbf{N}_u^s \times d^1V^s \times \Delta\dot{\mathbf{q}} \right]
\end{aligned}$$

The expanded form of the sixth term on the right hand side Equation 2.78 is given in Equation 2.115. In Equation 2.115, all the terms on the right hand side except the eleventh term are not functions of the variable ${}^2\ddot{\mathbf{q}}$. Differentiating the tenth term with respect to η and evaluating it at $\eta = 0$, Equation 2.116 is obtained. Substituting Equations 2.80 through 2.86, 2.91 through 2.94, 2.99 through 2.103, 2.107 through 2.110, 2.112, 2.114, and 2.116 into 2.78, the expanded form of the equilibrium equation can be restated as in Equation 2.117.

$$\begin{aligned}
\frac{d}{d\eta_{a,\gamma,\beta,\theta,\eta=0}} \mathbf{g}(\mathbf{q} + \alpha\Delta\mathbf{q}, {}^2\mathbf{Q} + \gamma\Delta\mathbf{Q}, {}^2\mathbf{Q}_{ext} + \beta\Delta\mathbf{Q}_{ext}, {}^2\dot{\mathbf{q}} + \theta\Delta\dot{\mathbf{q}}, {}^2\ddot{\mathbf{q}} + \eta\Delta\ddot{\mathbf{q}}) &= \left[\int_0^{1L} \frac{d}{d\eta_{a,\gamma,\beta,\theta,\eta=0}} \left({}^1\mathbf{N}_{\hat{\delta}\hat{c}} \right) \times {}^2\mathbf{D} \times d^1\mathbf{x} \right] + \left[\int_0^{1L} {}^1\mathbf{N}_{\hat{\delta}\hat{c}}^T \times \frac{d}{d\eta_{a,\gamma,\beta,\theta,\eta=0}} \left({}^2\mathbf{D} \right) \times d^1\mathbf{x} \right] + \\
&\left[\int_0^{1L} \frac{d}{d\eta_{a,\gamma,\beta,\theta,\eta=0}} \left({}^1\mathbf{N}_{\hat{\delta}\hat{c}}^T \right) \times {}^2\bar{\mathbf{k}}_{sc} \times {}^1\mathbf{N}_{\hat{\delta}\hat{c}} \times (\mathbf{q} + \alpha\Delta\mathbf{q}) \times d^1\mathbf{x} \right] + \left[\int_0^{1L} {}^1\mathbf{N}_{\hat{\delta}\hat{c}}^T \times \frac{d}{d\eta_{a,\gamma,\beta,\theta,\eta=0}} \left({}^2\bar{\mathbf{k}}_{sc} \right) \times {}^1\mathbf{N}_{\hat{\delta}\hat{c}} \times (\mathbf{q} + \alpha\Delta\mathbf{q}) \times d^1\mathbf{x} \right] + \\
&\left[\int_0^{1L} \frac{d}{d\eta_{a,\gamma,\beta,\theta,\eta=0}} \left({}^1\mathbf{N}_{\hat{\delta}\hat{c}}^T \right) \times {}^1\mathbf{D}_{sc} \times d^1I \right] + \left[\int_0^{1L} {}^1\mathbf{N}_{\hat{\delta}\hat{c}}^T \times \frac{d}{d\eta_{a,\gamma,\beta,\theta,\eta=0}} \left({}^1\mathbf{D}_{sc} \right) \times d^1I \right] + \\
&\left[\int_0^{1L} \frac{d}{d\eta_{a,\gamma,\beta,\theta,\eta=0}} \left({}^2\mathbf{N}_{D2}^T \right) \times ({}^1\hat{\mathbf{d}} - \mathbf{d}) \times d^1\mathbf{x} \right] + \left[\int_0^{1L} {}^2\mathbf{N}_{D2}^T \times \frac{d}{d\eta_{a,\gamma,\beta,\theta,\eta=0}} \left(({}^1\hat{\mathbf{d}} - \mathbf{d}) \right) \times d^1\mathbf{x} \right] - \\
&\left[\frac{d}{d\eta_{a,\gamma,\beta,\theta,\eta=0}} \left({}^2\mathbf{Q}_{ext} + \beta\Delta\mathbf{Q}_{ext} \right) \right] + \\
&\left[\int_{1V^c} \frac{d}{d\eta_{a,\gamma,\beta,\theta,\eta=0}} \left({}^1\rho^c \times {}^1\mathbf{N}_u^{cT} \times {}^2\mathbf{N}_u^c \times d^1V^c \right) \times ({}^2\dot{\mathbf{q}} + \theta\Delta\dot{\mathbf{q}}) + \int_{1V^s} \frac{d}{d\eta_{a,\gamma,\beta,\theta,\eta=0}} \left({}^1\rho^s \times {}^1\mathbf{N}_u^{sT} \times {}^2\mathbf{N}_u^s \times d^1V^s \right) \times ({}^2\dot{\mathbf{q}} + \theta\Delta\dot{\mathbf{q}}) \right] + \\
&\left[\int_{1V^c} \frac{d}{d\eta_{a,\gamma,\beta,\theta,\eta=0}} \left({}^1\rho^c \times {}^1\mathbf{N}_u^{cT} \times {}^2\mathbf{N}_u^c \times d^1V^c \right) \times ({}^2\ddot{\mathbf{q}} + \eta\Delta\ddot{\mathbf{q}}) + \int_{1V^s} \frac{d}{d\eta_{a,\gamma,\beta,\theta,\eta=0}} \left({}^1\rho^s \times {}^1\mathbf{N}_u^{sT} \times {}^2\mathbf{N}_u^s \times d^1V^s \right) \times ({}^2\ddot{\mathbf{q}} + \eta\Delta\ddot{\mathbf{q}}) \right]
\end{aligned} \tag{2.115}$$

$$\begin{aligned}
&\left[\int_{1V^c} \frac{d}{d\eta_{a,\gamma,\beta,\theta,\eta=0}} \left({}^1\rho^c \times {}^1\mathbf{N}_u^{cT} \times {}^1\mathbf{N}_u^c \times d^1V^c \right) \times ({}^2\ddot{\mathbf{q}} + \eta \times \Delta\ddot{\mathbf{q}}) + \int_{1V^s} \frac{d}{d\eta_{a,\gamma,\beta,\theta,\eta=0}} \left({}^1\rho^s \times {}^1\mathbf{N}_u^{sT} \times {}^1\mathbf{N}_u^s \times d^1V^s \right) \times ({}^2\ddot{\mathbf{q}} + \eta \times \Delta\ddot{\mathbf{q}}) \right] = \tag{2.116} \\
&\left[\int_{1V^c} {}^1\rho^c \times {}^1\mathbf{N}_u^{cT} \times {}^1\mathbf{N}_u^c \times d^1V^c \times \Delta\ddot{\mathbf{q}} + \int_{1V^s} {}^1\rho^s \times {}^1\mathbf{N}_u^{sT} \times {}^1\mathbf{N}_u^s \times d^1V^s \times \Delta\ddot{\mathbf{q}} \right]
\end{aligned}$$

$$\begin{aligned}
\mathbf{g}^{j+1} &= \mathbf{g}^j + \left({}^2\mathbf{K}_g^j + {}^2\mathbf{K}_{sc}^j + {}^2\mathbf{G}_2^j + \left({}^2\mathbf{G}_2^T \right)^j - {}^2\mathbf{H}_{22}^j \right) \times \Delta\mathbf{q} + \left(\left({}^2\mathbf{G}_1^T \right)^j + \left(\mathbf{M}_d^T \right)^j - \left(\mathbf{H}_{12}^T \right)^j \right) \times \Delta\mathbf{Q} \\
&- \Delta\mathbf{Q}_{ext} + {}^1\mathbf{M}^j \times \Delta\ddot{\mathbf{q}} + {}^1\mathbf{C}^j \times \Delta\dot{\mathbf{q}}
\end{aligned} \tag{2.117}$$

where: ${}^1\mathbf{M}^j = \left[\int_{1V^c} {}^1\rho^c \times {}^1\mathbf{N}_u^{cT} \times {}^1\mathbf{N}_u^c \times d^1V^c + \int_{1V^s} {}^1\rho^s \times {}^1\mathbf{N}_u^{sT} \times {}^1\mathbf{N}_u^s \times d^1V^s \right]$ is the consistent mass matrix

${}^1\mathbf{C}^j = \left[\int_{1V^c} {}^1\mu^c \times {}^1\mathbf{N}_u^{cT} \times {}^1\mathbf{N}_u^c \times d^1V^c + \int_{1V^s} {}^1\mu^s \times {}^1\mathbf{N}_u^{sT} \times {}^1\mathbf{N}_u^s \times d^1V^s \right]$ is the consistent damping

matrix

$\Delta\mathbf{Q}$ in Equation 2.74 is placed in Equation 2.117 as follows:

$$\begin{aligned}
\mathbf{g}^{j+1} = & \mathbf{g}^j + \left({}^2_1\mathbf{K}_g^j + {}^2_1\mathbf{K}_{sc}^j + {}^2_1\mathbf{G}_2^j + \left({}^2_1\mathbf{G}_2^T \right)^j - {}^2_1\mathbf{H}_{22}^j \right) \times \Delta \mathbf{q} \\
& + \left(\left({}^2_1\mathbf{G}_1^T \right)^j + \left(\mathbf{M}_d^T \right)^j - \left({}^2_1\mathbf{H}_{12}^T \right)^j \right) \times \left({}^2_1\mathbf{H}_{11}^{-1} \right)^j \times \left({}^2_1\mathbf{G}_1^j + \mathbf{M}_d^j - {}^2_1\mathbf{H}_{12}^j \right) \times \Delta \mathbf{q} \\
& + \left(\left({}^2_1\mathbf{G}_1^T \right)^j + \left(\mathbf{M}_d^T \right)^j - \left({}^2_1\mathbf{H}_{12}^T \right)^j \right) \times \left({}^2_1\mathbf{H}_{11}^{-1} \right)^j \times \mathbf{V}^j \\
& - \Delta \mathbf{Q}_{ext} + {}^1\mathbf{M}^j \times \Delta \ddot{\mathbf{q}} + {}^1\mathbf{C}^j \times \Delta \dot{\mathbf{q}} = 0
\end{aligned} \tag{2.118}$$

Equation 2.118 is rearranged to solve for $\Delta \mathbf{q}$ as given below:

$$\begin{aligned}
& \left[\left({}^2_1\mathbf{K}_g^j + {}^2_1\mathbf{K}_{sc}^j + {}^2_1\mathbf{G}_2^j + \left({}^2_1\mathbf{G}_2^T \right)^j - {}^2_1\mathbf{H}_{22}^j \right) + \left(\left({}^2_1\mathbf{G}_1^T \right)^j + \left(\mathbf{M}_d^T \right)^j - \left({}^2_1\mathbf{H}_{12}^T \right)^j \right) \times \left({}^2_1\mathbf{H}_{11}^{-1} \right)^j \times \left({}^2_1\mathbf{G}_1^j + \mathbf{M}_d^j - {}^2_1\mathbf{H}_{12}^j \right) \right] \times \Delta \mathbf{q} + \\
& {}^1\mathbf{M}^j \times \Delta \ddot{\mathbf{q}} + {}^1\mathbf{C}^j \times \Delta \dot{\mathbf{q}} = -\mathbf{g}^j - \left(\left({}^2_1\mathbf{G}_1^T \right)^j + \left(\mathbf{M}_d^T \right)^j - \left({}^2_1\mathbf{H}_{12}^T \right)^j \right) \times \left({}^2_1\mathbf{H}_{11}^{-1} \right)^j \times \mathbf{V}^j + \Delta \mathbf{Q}_{ext}
\end{aligned} \tag{2.119a}$$

$${}^2_1\mathbf{K}^j \times \Delta \mathbf{q} + {}^1\mathbf{M}^j \times \Delta \ddot{\mathbf{q}} + {}^1\mathbf{C}^j \times \Delta \dot{\mathbf{q}} = -\mathbf{g}^j - \left(\left({}^2_1\mathbf{G}_1^T \right)^j + \left(\mathbf{M}_d^T \right)^j - \left({}^2_1\mathbf{H}_{12}^T \right)^j \right) \times \left({}^2_1\mathbf{H}_{11}^{-1} \right)^j \times \mathbf{V}^j + \Delta \mathbf{Q}_{ext} \tag{2.119b}$$

where ${}^2_1\mathbf{K}^j = \left[\left({}^2_1\mathbf{K}_g^j + {}^2_1\mathbf{K}_{sc}^j + {}^2_1\mathbf{G}_2^j + \left({}^2_1\mathbf{G}_2^T \right)^j - {}^2_1\mathbf{H}_{22}^j \right) + \left(\left({}^2_1\mathbf{G}_1^T \right)^j + \left(\mathbf{M}_d^T \right)^j - \left({}^2_1\mathbf{H}_{12}^T \right)^j \right) \times \left({}^2_1\mathbf{H}_{11}^{-1} \right)^j \times \left({}^2_1\mathbf{G}_1^j + \mathbf{M}_d^j - {}^2_1\mathbf{H}_{12}^j \right) \right]$

and \mathbf{K} is the element tangent stiffness matrix.

Substituting Equation 2.50 into Equation 2.119b, the final form of the equilibrium equation is obtained as given below:

$$\begin{aligned}
{}^2_1\mathbf{K}^j \times \Delta \mathbf{q} + {}^1\mathbf{M}^j \times {}^2_1\ddot{\mathbf{q}}^{j+1} + {}^1\mathbf{C}^j \times {}^2_1\dot{\mathbf{q}}^{j+1} = & - \int_0^L \left({}^1\mathbf{N}_{\delta d}^T \right)^j \times {}^2_1\mathbf{N}_{D1}^j \times {}^2_1\mathbf{Q}^j \times d^1x - \int_{I'} \left({}^1\mathbf{N}_{\delta \hat{d}_{sc}}^T \right)^j \times {}^2_1\bar{\mathbf{k}}_{sc}^j \times {}^1\mathbf{N}_{\delta \hat{d}_{sc}}^j \times {}^1\mathbf{q} \times d^1I - \\
& \int_{I'} \left({}^2_1\mathbf{N}_{\delta \hat{d}_{sc}}^T \right)^j \times {}^1\mathbf{D}_{sc}^j \times d^1I + {}^2_1\mathbf{Q}_{ext}^j - \int_0^L \left({}^2_1\mathbf{N}_{D2}^T \right)^j \times \left({}^1\hat{\mathbf{d}}^j - {}^1\mathbf{d}^j \right) \times d^1x - \\
& \left(\left({}^2_1\mathbf{G}_1^T \right)^j + \left(\mathbf{M}_d^T \right)^j - \left({}^2_1\mathbf{H}_{12}^T \right)^j \right) \times \left({}^2_1\mathbf{H}_{11}^{-1} \right)^j \times \mathbf{V}^j + \Delta \mathbf{Q}_{ext}
\end{aligned} \tag{2.120}$$

where: ${}^2_1\mathbf{K}^j \times \Delta \mathbf{q} + {}^1\mathbf{M}^j \times {}^2_1\ddot{\mathbf{q}}^{j+1} + {}^1\mathbf{C}^j \times {}^2_1\dot{\mathbf{q}}^{j+1} = {}^2_1\mathbf{Q}_{ext}^{j+1} - {}^2_1\mathbf{Q}_{int}^j$

$$\begin{aligned}
{}^2_1\mathbf{Q}_{int}^j = & \left({}^2_1\mathbf{G}_1^T \right)^j \times {}^2_1\mathbf{Q}^j + {}^2_1\mathbf{K}_{sc}^j \times {}^1\mathbf{q} + \int_{I'} \left({}^1\mathbf{N}_{\delta \hat{d}_{sc}}^T \right)^j \times {}^1\mathbf{D}_{sc}^j \times d^1I + \int_0^L \left({}^2_1\mathbf{N}_{D2}^T \right)^j \times \left({}^1\hat{\mathbf{d}}^j - {}^1\mathbf{d}^j \right) \times d^1x + \\
& \left(\left({}^2_1\mathbf{G}_1^T \right)^j + \left(\mathbf{M}_d^T \right)^j - \left({}^2_1\mathbf{H}_{12}^T \right)^j \right) \times \left({}^2_1\mathbf{H}_{11}^{-1} \right)^j \times \mathbf{V}^j
\end{aligned}$$

is the element internal force vector, at j^{th} iteration of i^{th} time step and

${}^2_1\mathbf{Q}_{ext}^{j+1} = {}^2_1\mathbf{Q}_{ext}^j + \Delta\mathbf{Q}_{ext}$ is the external load at $j + 1^{\text{th}}$ iteration of i^{th} time step

${}^2_1\dot{\mathbf{q}}^{j+1} = {}^2_1\dot{\mathbf{q}}^j + \Delta\dot{\mathbf{q}}$ is the nodal velocity at $j + 1^{\text{th}}$ iteration of i^{th} time step

${}^2_1\ddot{\mathbf{q}}^{j+1} = {}^2_1\ddot{\mathbf{q}}^j + \Delta\ddot{\mathbf{q}}$ is the nodal acceleration at $j + 1^{\text{th}}$ iteration i^{th} time step

In the mixed finite element method presented in Sections 2.2.2 through 2.2.11, determining the nodal forces and displacements of the RCFT beam-column element requires the solution of element equilibrium (see Equation 2.50), compatibility (see Equation 2.51), and cross-section equilibrium equation (see Equation 2.52), simultaneously. However, all these aforementioned equations are in nonlinear nature in terms of their state variables (e.g., \mathbf{q} , \mathbf{Q} , $\dot{\mathbf{q}}$, $\ddot{\mathbf{q}}$ etc.). Therefore, an iterative solution scheme should be adopted which requires a linearization process to be performed for the available equations (e.g., element equilibrium, compatibility, cross-section equilibrium). The cross-section equilibrium equation was stated as the balance between the cross-sectional forces (\mathbf{D}_z) obtained from integration of material stresses over the RCFT cross-section and the cross-sectional forces (\mathbf{D}) determined through element flexibility (e.g., through multiplying element flexibility with nodal displacements) and force interpolation functions. The only state variable of the cross-section equilibrium was the cross-section strain vector (\mathbf{d}) and the linearization process resulted in an equation relating the incremental cross-section strain to the unbalance force between the cross-section forces as stated in Equation 2.61. In the case of compatibility equation, two types of linearization process were performed based on the state variables to be varied. The first linearization was conducted considering nodal displacements (\mathbf{q}) and nodal forces as the state variables (\mathbf{Q}). This condition is often valid at the beginning of an incremental load step or Newton-Raphson iteration since the current values of both \mathbf{q} and \mathbf{Q} are still unknown quantities. Linearization of the compatibility equation with respect to the state variables of \mathbf{q} and \mathbf{Q} produced Equation 2.74. Equation 2.74 is used in Equation 2.117 to calculate incremental nodal force values ($\Delta\mathbf{Q}$) while deriving the expressions for the element stiffness matrix. The use of Equation 2.74 is appropriate while deriving the element stiffness matrix since the element stiffness matrix is formed without determining

the current values of the states variables of \mathbf{q} and \mathbf{Q} at the beginning of an incremental step or Newton-Raphson iteration. The second linearization process for the compatibility equation was conducted based on the state variable \mathbf{Q} and Equation 2.77 was obtained relating $\Delta\mathbf{Q}$ to the incremental nodal displacements ($\Delta\mathbf{q}$). As it will be described in Section 2.2.13, Equation 2.77 will be used while calculating the $\Delta\mathbf{Q}$ corresponding to the pre-calculated $\Delta\mathbf{q}$ values. The linearization of the equilibrium was carried out with respect to the state variables of \mathbf{q} , \mathbf{Q} , \mathbf{Q}_{ext} , $\dot{\mathbf{q}}$, and $\ddot{\mathbf{q}}$. The final outcome of this linearization covered the expressions of element stiffness matrix, consistent mass matrix, consistent damping matrix, and internal force vector as can be seen in Equation 2.120.

2.2.12. Mapping of Element Forces, Displacements, and Stiffness between Natural and Global Coordinate Systems

Before proceeding to establish the details of the incremental nonlinear solution algorithm, it is critical to address the development of transformations between global (\tilde{x} , \tilde{y} , \tilde{z}), local (\hat{x} , \hat{y} , \hat{z}), and natural (x , y , z) coordinate systems. The global coordinate system is considered to be fixed in three-dimensional space and the geometry of the structure being analyzed is defined within this system. The equilibrium equation of the structure is also developed in the global coordinate system. A local coordinate system is assigned to each finite element. As the analysis proceeds, the local coordinate system follows the motion of the finite element but it is assumed to experience no deformation. The orientations of the natural and local coordinate systems are assumed to coincide with each other. However, in the natural coordinate system, the rigid body rotations are eliminated from the element deformations.

The RCFT beam-column in its natural frame is defined with 13 DOFs as shown in Figure 2.4. In the global (shown with the tilda) and local (shown with the caret) coordinates, separate translational DOFs are defined for the steel tube and the concrete core. As given in Figure 2.7, this results in 9 DOFs for each RCFT joint, including 6 translations and 3 rotations.

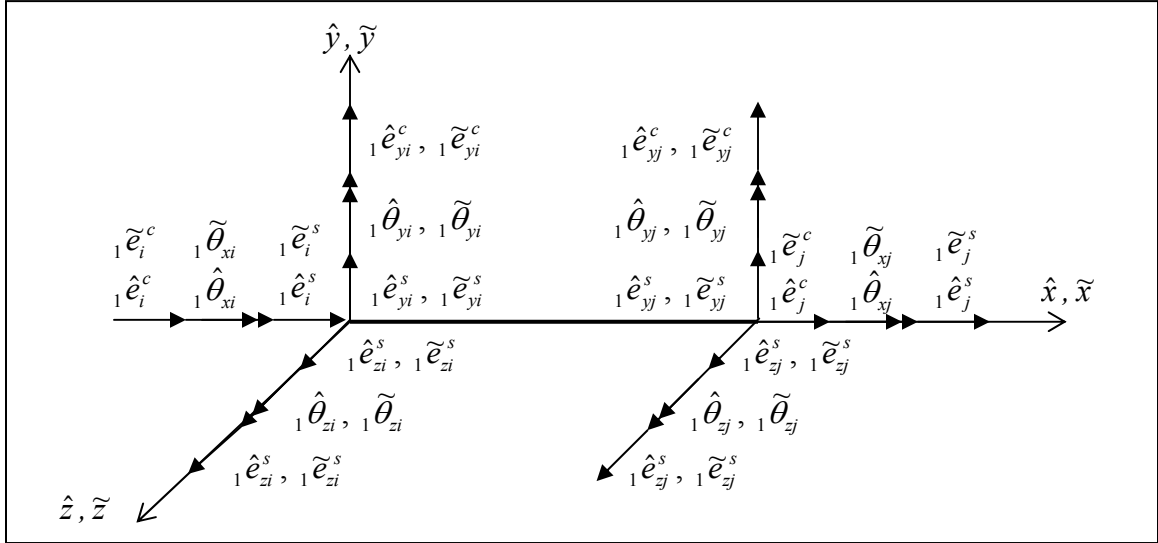


Figure 2.7 Incremental Element Displacements in Local and Global Coordinates

The numbering of the DOFs was selected in a manner that allows automatic assembly of the global stiffness matrix. RCFT beam-columns are assumed to be connected to the other members (e.g., steel girders) of a frame through the steel tube DOFs. Therefore, the first 3 DOFs were assigned to the steel tube translations, the next 3 DOFs were assigned to the rotations, which are common for both the steel tube and the concrete core, and the last 3 DOFs correspond to the concrete core translations. This approach of numbering the DOFs helped using the RCFT beam-column element with other structural members without modifying the assembly process.

2.2.12.1. Transformation of Element Forces

In Figure 2.8 and Figure 2.9, the positive sign conventions and numbering scheme for the natural and local element forces are illustrated, respectively.

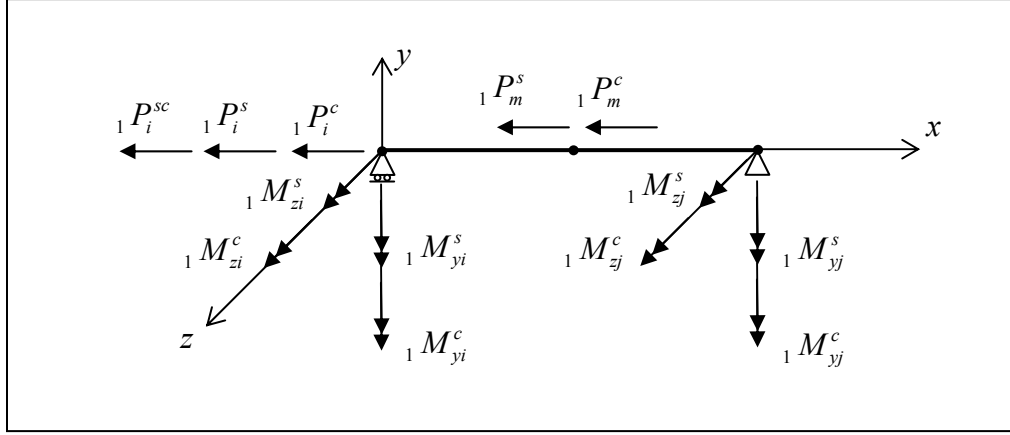


Figure 2.8 Incremental Element Forces in Natural Coordinates

Using equilibrium equations, the incremental element forces in local coordinates (${}_1\hat{\mathbf{Q}}_{int}$) can be expressed in natural coordinates (${}_1\mathbf{Q}_{int}$) as given in Equation 2.120.

$${}_1\hat{\mathbf{Q}}_{int} = \begin{bmatrix} {}_1\hat{P}_i^s & {}_1\hat{V}_{yi}^s & {}_1\hat{V}_{zi}^s & {}_1\hat{M}_{yi}^s & {}_1\hat{M}_{zi}^s & {}_1\hat{P}_i^c & {}_1\hat{V}_{yi}^c & {}_1\hat{V}_{zi}^c & {}_1\hat{P}_j^s & {}_1\hat{V}_{yj}^s & {}_1\hat{V}_{zj}^s & {}_1\hat{M}_{yj}^s & {}_1\hat{M}_{zj}^s & {}_1\hat{P}_j^c & {}_1\hat{V}_{yj}^c & {}_1\hat{V}_{zj}^c \end{bmatrix}^T \quad [2.121a]$$

$${}_1\mathbf{Q}_{int} = \begin{bmatrix} {}_1P_i^{sc} & {}_1P_i^c & {}_1M_{zi}^c & {}_1M_{yi}^c & {}_1M_{zj}^c & {}_1M_{yj}^c & {}_1P_i^s & {}_1M_{zi}^s & {}_1M_{yi}^s & {}_1M_{zj}^s & {}_1M_{yj}^s & {}_1P_m^c & {}_1P_m^s \end{bmatrix}^T \quad [2.121b]$$

$${}_1\hat{P}_i^s = -{}_1P_i^s - {}_1P_i^{sc}, \quad {}_1\hat{P}_j^s = -{}_1\hat{P}_i^s \quad [2.121c]$$

$${}_1\hat{V}_{yi}^s = ({}_1M_{zi}^s + {}_1M_{zj}^s) / L, \quad {}_1\hat{V}_{yj}^s = -{}_1\hat{V}_{yi}^s \quad [2.121d]$$

$${}_1\hat{V}_{zi}^s = ({}_1M_{yi}^s + {}_1M_{yj}^s) / L, \quad {}_1\hat{V}_{zj}^s = -{}_1\hat{V}_{zi}^s \quad [2.121e]$$

$${}_1\hat{M}_{yi}^s = -({}_1M_{yi}^s + {}_1M_{yj}^c), \quad {}_1\hat{M}_{yj}^s = -({}_1M_{yj}^s + {}_1M_{yj}^c) \quad [2.121f]$$

$${}_1\hat{M}_{zi}^s = ({}_1M_{zi}^s + {}_1M_{zi}^c), \quad {}_1\hat{M}_{zj}^s = ({}_1M_{zj}^s + {}_1M_{zj}^c) \quad [2.121g]$$

$${}_1\hat{P}_i^c = -{}_1P_i^c + {}_1P_i^{sc}, \quad {}_1\hat{P}_j^c = -{}_1\hat{P}_i^c \quad [2.121h]$$

$${}_1\hat{V}_{yi}^c = ({}_1M_{zi}^c + {}_1M_{zj}^c) / L, \quad {}_1\hat{V}_{yj}^c = -{}_1\hat{V}_{yi}^c \quad [2.121i]$$

$${}_1\hat{V}_{zi}^c = ({}_1M_{yi}^c + {}_1M_{yj}^c) / L, \quad {}_1\hat{V}_{zj}^c = -{}_1\hat{V}_{zi}^c \quad [2.121j]$$

Equations 2.121c through 2.121j can be consolidated as given in Equation 2.122.

$${}_1\hat{\mathbf{Q}}_{int} = \mathbf{T}_{NL}^T \times {}_1\mathbf{Q}_{int} \quad [2.122]$$

where:

\mathbf{T}_{NL} - transformation matrix of incremental element forces from natural to local coordinate system (see Appendix A)

In the current formulation, the torsional response of RCFT members is assumed to be linear. Therefore, the torsional moments in the local coordinates (${}_1\hat{\mathbf{T}}$) are calculated as in Equation 2.123.

$${}_1\hat{T}_i = \left(\frac{GJ}{L}\right) \times ({}_1\hat{\theta}_{jx} - {}_1\hat{\theta}_{ix}), \quad {}_1\hat{T}_j = \left(\frac{GJ}{L}\right) \times (-{}_1\hat{\theta}_{jx} + {}_1\hat{\theta}_{ix}) \quad [2.123]$$

where:

GJ - torsional stiffness of the RCFT cross-section which is often taken as the torsional stiffness of the steel tube (Gourley and Hajjar, 1994)

${}_1\hat{\theta}_{ix}$ - torsional rotation in the local coordinates at i end

${}_1\hat{\theta}_{jx}$ - torsional rotation in the local coordinates at j end

A single joint of an RCFT beam-column element is assumed to have 3 steel tube forces, 3 moment, and 3 concrete core forces. Each of these forces and moments can be decomposed into 3 orthogonal components with respect to the global coordinate system as shown in Figure 2.10 for representative force components in the local coordinates.

The components of unit vectors along the local axes with respect to the global coordinate system are designated as $(\alpha_x, \alpha_y, \alpha_z)$, $(\beta_x, \beta_y, \beta_z)$, and $(\gamma_x, \gamma_y, \gamma_z)$, respectively. These unit vectors are used in the transformation equations of ${}_1\hat{P}_i^s$, ${}_1\hat{V}_{iy}^s$, and ${}_1\hat{V}_{iz}^s$ to derive their counterparts in the global coordinate system (${}_1\tilde{P}_i^s$, ${}_1\tilde{V}_{iy}^s$, and ${}_1\tilde{V}_{iz}^s$).

$${}_1\tilde{P}_i^s = {}_1\hat{P}_i^s \times \alpha_x + {}_1\hat{V}_{iy}^s \times \beta_x + {}_1\hat{V}_{iz}^s \times \gamma_x \quad [2.124]$$

$${}_1\tilde{V}_{iy}^s = {}_1\hat{P}_i^s \times \alpha_y + {}_1\hat{V}_{iy}^s \times \beta_y + {}_1\hat{V}_{iz}^s \times \gamma_y \quad [2.125]$$

$${}_1\tilde{V}_{iz}^s = {}_1\hat{P}_i^s \times \alpha_z + {}_1\hat{V}_{iy}^s \times \beta_z + {}_1\hat{V}_{iz}^s \times \gamma_z \quad [2.126]$$

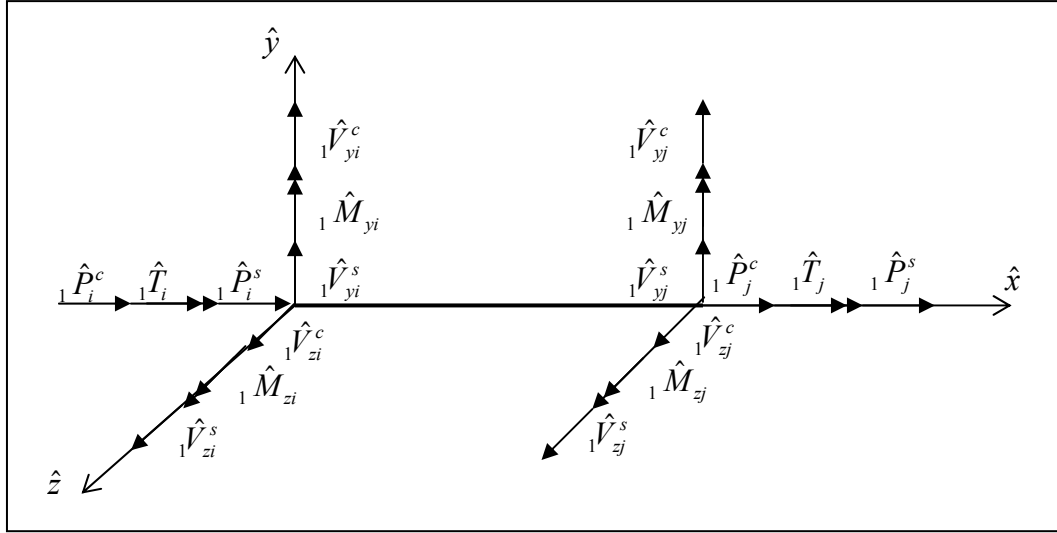


Figure 2.9 Incremental Element Forces in Local Coordinates

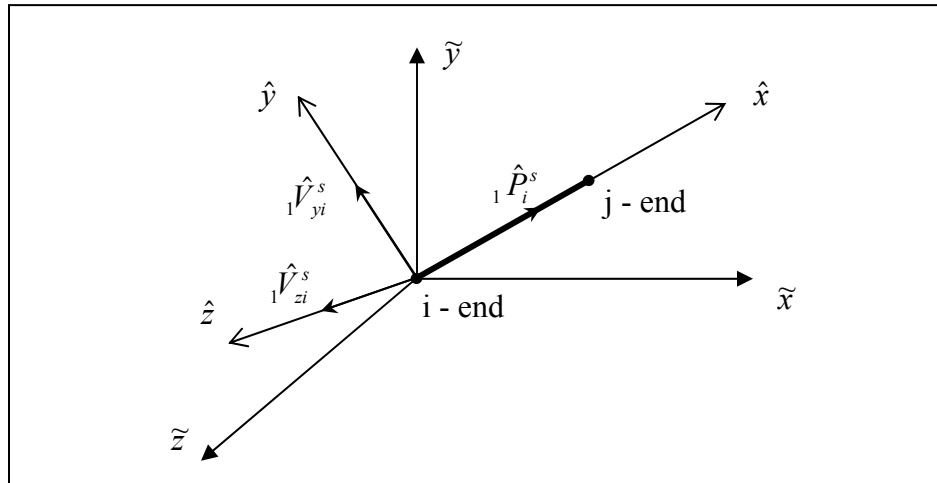


Figure 2.10 RCFT Beam-Column in Three-Dimensional Space

Similar equations can be written while transforming other components of ${}_1\hat{Q}_{int}$ and the torsional forces into the global coordinates system so that incremental element forces in the global coordinate system (${}_1\tilde{Q}$) can be derived as given below:

$${}_1\tilde{Q}_{int} = \begin{bmatrix} {}_1\tilde{P}_i^s & {}_1\tilde{V}_{yi}^s & {}_1\tilde{V}_{zi}^s & {}_1\tilde{T}_i & {}_1\tilde{M}_{yi} & {}_1\tilde{M}_{zi} & {}_1\tilde{P}_i^c & {}_1\tilde{V}_{yi}^c & {}_1\tilde{V}_{zi}^c & {}_1\tilde{P}_j^s & {}_1\tilde{V}_{yj}^s & {}_1\tilde{V}_{zj}^s & {}_1\tilde{T}_j & {}_1\tilde{M}_{yj} & {}_1\tilde{M}_{zj} & {}_1\tilde{P}_j^c & {}_1\tilde{V}_{yj}^c & {}_1\tilde{V}_{zj}^c \end{bmatrix} \quad [2.127a]$$

$${}_1\hat{Q}_{int}^r = \begin{bmatrix} {}_1\hat{P}_i^s & {}_1\hat{V}_{yi}^s & {}_1\hat{V}_{zi}^s & {}_1\hat{T}_i & {}_1\hat{M}_{yi} & {}_1\hat{M}_{zi} & {}_1\hat{P}_i^c & {}_1\hat{V}_{yi}^c & {}_1\hat{V}_{zi}^c & {}_1\hat{P}_j^s & {}_1\hat{V}_{yj}^s & {}_1\hat{V}_{zj}^s & {}_1\hat{T}_j & {}_1\hat{M}_{yj} & {}_1\hat{M}_{zj} & {}_1\hat{P}_j^c & {}_1\hat{V}_{yj}^c & {}_1\hat{V}_{zj}^c \end{bmatrix} \quad [2.127b]$$

$${}_1\tilde{\mathbf{Q}}_{int} = T_{LG}^T \times {}_1\hat{\mathbf{Q}}_{int}^{tr} \quad [2.127c]$$

where: ${}_1\hat{\mathbf{Q}}_{int}^{tr}$ is the incremental element end force vector in the local coordinates with torsion included

$$T_{LG}^T = \begin{bmatrix} \Gamma & 0 & 0 & 0 & 0 & 0 \\ 0 & \Gamma & 0 & 0 & 0 & 0 \\ 0 & 0 & \Gamma & 0 & 0 & 0 \\ 0 & 0 & 0 & \Gamma & 0 & 0 \\ 0 & 0 & 0 & 0 & \Gamma & 0 \\ 0 & 0 & 0 & 0 & 0 & \Gamma \end{bmatrix}$$

$$\Gamma = \begin{bmatrix} a_x & a_y & a_z \\ \beta_x & \beta_y & \beta_z \\ \gamma_x & \gamma_y & \gamma_z \end{bmatrix}$$

It should be noted that the transformation matrix T_{LG} is an orthogonal matrix. Therefore, Equation 2.127c can also be expressed as given below:

$$T_{LG} \times {}_1\tilde{\mathbf{Q}}_{int} = {}_1\hat{\mathbf{Q}}_{int}^{tr} \quad [2.128]$$

2.2.12.2. Transformation of Element Displacements

In an incremental nonlinear analysis, the element displacements are first calculated in the global coordinates and then transformed into the local coordinate system. A transformation similar to that of incremental element forces is performed between local (${}_1\hat{\mathbf{q}}$) and global (${}_1\tilde{\mathbf{q}}$) incremental element displacements as given in Equation 2.129.

$${}_1\tilde{\mathbf{q}} = T_{LG}^T \times {}_1\hat{\mathbf{q}} \quad [2.129]$$

or using orthogonality of T_{LG} :

$${}_1\hat{\mathbf{q}} = T_{LG} \times {}_1\tilde{\mathbf{q}} \quad [2.130]$$

Incremental element deformations in the local and natural coordinates are portrayed in Figure 2.11. These two sets of displacements are linked to each other using Equation 2.131 (Yang and Kuo, 1994).

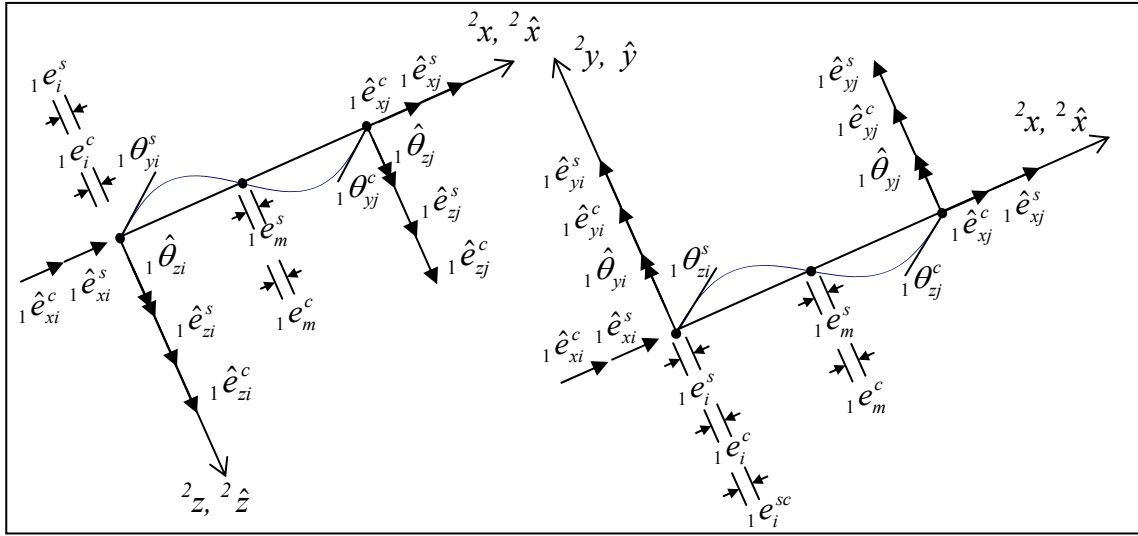


Figure 2.11 Incremental Element Displacements in Natural and Local Coordinates

$${}_1 e_i^{sc} = {}_1 \hat{e}_i^s - {}_1 \hat{e}_i^c \quad [2.131a]$$

$${}_1 e_i^s = \frac{(2 \times {}^1 L + {}_1 \hat{e}_j^s - {}_1 \hat{e}_{xi}^s) \times ({}_1 \hat{e}_{xj}^s - {}_1 \hat{e}_{xi}^s) + ({}_1 \hat{e}_{yj}^s - {}_1 \hat{e}_{yi}^s)^2 + ({}_1 \hat{e}_{zj}^s - {}_1 \hat{e}_{zi}^s)^2}{2 \times {}^1 L} \quad [2.131b]$$

$${}_1 e_i^c = \frac{(2 \times {}^1 L + {}_1 \hat{e}_j^c - {}_1 \hat{e}_{xi}^c) \times ({}_1 \hat{e}_{xj}^c - {}_1 \hat{e}_{xi}^c) + ({}_1 \hat{e}_{yj}^c - {}_1 \hat{e}_{yi}^c)^2 + ({}_1 \hat{e}_{zj}^c - {}_1 \hat{e}_{zi}^c)^2}{2 \times {}^1 L} \quad [2.131c]$$

$${}_1 \theta_{zi}^s = {}_1 \hat{\theta}_{zi} - \frac{{}_1 \hat{e}_{yj}^s - {}_1 \hat{e}_{yi}^s}{{}^1 L}, \quad {}_1 \theta_{zj}^s = -{}_1 \hat{\theta}_{zj} - \frac{{}_1 \hat{e}_{yj}^s - {}_1 \hat{e}_{yi}^s}{{}^1 L} \quad [2.131d]$$

$${}_1 \theta_{yi}^s = {}_1 \hat{\theta}_{yi} - \frac{{}_1 \hat{e}_{zj}^s - {}_1 \hat{e}_{zi}^s}{{}^1 L}, \quad {}_1 \theta_{yj}^s = -{}_1 \hat{\theta}_{yj} - \frac{{}_1 \hat{e}_{zj}^s - {}_1 \hat{e}_{zi}^s}{{}^1 L} \quad [2.131e]$$

$${}_1 \theta_{zi}^c = {}_1 \hat{\theta}_{zi} - \frac{{}_1 \hat{e}_{yj}^c - {}_1 \hat{e}_{yi}^c}{{}^1 L}, \quad {}_1 \theta_{zj}^c = -{}_1 \hat{\theta}_{zj} - \frac{{}_1 \hat{e}_{yj}^c - {}_1 \hat{e}_{yi}^c}{{}^1 L} \quad [2.131f]$$

$${}_1 \theta_{yi}^c = {}_1 \hat{\theta}_{yi} - \frac{{}_1 \hat{e}_{zj}^c - {}_1 \hat{e}_{zi}^c}{{}^1 L}, \quad {}_1 \theta_{yj}^c = -{}_1 \hat{\theta}_{yj} - \frac{{}_1 \hat{e}_{zj}^c - {}_1 \hat{e}_{zi}^c}{{}^1 L} \quad [2.131g]$$

The axial DOFs defined for the mid-node of the finite element in the natural coordinate system (${}_1 e_m^s, {}_1 e_m^c$) are eliminated through a static condensation procedure. Since the external loads are assumed to be applied only at the element ends, the mid-node DOFs are not used in the local and global coordinates. However, these DOFs are required while

calculating element internal forces and they need to be determined while transforming element displacements from local to natural coordinates. This is achieved by reversing the static condensation. The element stiffness matrix is partitioned in such a way that the equilibrium equation in natural coordinate system can be expressed in terms of retained (\mathbf{q}_r) and eliminated displacements (\mathbf{q}_c) in Equation 2.132.

$$\begin{bmatrix} \mathbf{K}_{rr} & \mathbf{K}_{rc} \\ \mathbf{K}_{cr} & \mathbf{K}_{cc} \end{bmatrix} \times \begin{bmatrix} \mathbf{q}_r \\ \mathbf{q}_c \end{bmatrix} = \begin{bmatrix} \mathbf{Q}_{ext_r} \\ \mathbf{Q}_{ext_c} \end{bmatrix} \quad [2.132]$$

From Equation 2.132, \mathbf{q}_c can be solved as given below in Equation 2.133 (McGuire et al., 2000).

$$\mathbf{q}_c = \mathbf{K}_{cc}^{-1} \times \mathbf{Q}_{ext_c} - \mathbf{K}_{cc}^{-1} \times \mathbf{K}_{cr} \times \bar{\mathbf{K}}_{rr}^{-1} \times \bar{\mathbf{Q}}_{ext_r} \quad [2.133]$$

where:

\mathbf{K} - element stiffness in natural coordinate system

\mathbf{Q}_{ext_r} - externally applied loads at retained DOFs

\mathbf{Q}_{ext_c} - externally applied loads at condensed DOFs

$${}^1\mathbf{q}_r = \begin{bmatrix} {}^1e^{sc} & {}^1e^c & {}^1\theta_{zi}^c & {}^1\theta_{yi}^c & {}^1\theta_{zj}^c & {}^1\theta_{yj}^c & {}^1e^s & {}^1\theta_{zi}^s & {}^1\theta_{yi}^s & {}^1\theta_{zj}^s & {}^1\theta_{yj}^s \end{bmatrix}^T$$

$${}^1\mathbf{q}_c = \begin{bmatrix} {}^1e_m^c & {}^1e_m^s \end{bmatrix}^T$$

$$\bar{\mathbf{Q}}_{ext_r} = \mathbf{Q}_{ext_r} - \mathbf{K}_{rc} \times \mathbf{K}_{cc}^{-1} \times \mathbf{Q}_{ext_c}$$

$$\bar{\mathbf{K}}_{rr} = \mathbf{K}_{rr} - \mathbf{K}_{rc} \times \mathbf{K}_{cc}^{-1} \times \mathbf{K}_{cr}$$

Since external loads are only applied at the element ends, \mathbf{Q}_{ext_c} can be taken equal to zero. In addition, \mathbf{q}_r can be derived as given in Equation 2.134 (McGuire et al., 2000).

$$\mathbf{q}_r = \bar{\mathbf{K}}_{rr}^{-1} \times \bar{\mathbf{Q}}_{ext_r} \quad [2.134]$$

Substituting Equation 2.134 into Equation 2.133, the simplified form of \mathbf{q}_c can be derived as follows:

$$\mathbf{q}_c = -\mathbf{K}_{cc}^{-1} \times \mathbf{K}_{cr} \times \mathbf{q}_r \quad [2.135]$$

2.2.12.3. Transformation of Element Stiffness Matrices

The element equilibrium in the global coordinates can be also expressed in Equation 2.136 as the balance between element forces and externally applied loads. Equation 2.136 is equivalent to statement of equilibrium in Equation 2.50 except that it is written at the element level in the global coordinates rather than at the cross-section level in natural coordinates.

$$\mathbf{g} = {}^2\tilde{\mathbf{Q}}_{int} - {}^2\tilde{\mathbf{Q}}_{ext} \quad [2.136]$$

where:

\mathbf{g} is the out-of-balance vector

The truncated Taylor series expansion of the out-of-balance vector at the current state (C2) about the C1 configuration can be derived as given in Equation 2.137.

$$\mathbf{g}^2 = \mathbf{g}^1 + \frac{\partial \mathbf{g}}{\partial \tilde{\mathbf{q}}} \times \Delta \tilde{\mathbf{q}} \quad [2.137]$$

where:

\mathbf{g}^2 - out of balance vector at C2 configuration

\mathbf{g}^1 - out of balance vector at C1 configuration

$\Delta \tilde{\mathbf{q}}$ - incremental element deformations in the global coordinates between C1 and C2 configurations

Substituting Equation 2.127c and Equation 2.136 into Equation 2.137 and then taking derivative with respect to $\tilde{\mathbf{q}}$ yields Equation 2.138 as given below:

$$\mathbf{g}^2 = \mathbf{g}^1 + \frac{\partial \mathbf{T}_{LG}^T}{\partial \tilde{\mathbf{q}}} \times {}^2\hat{\mathbf{Q}}_{int}^tr \times \Delta \tilde{\mathbf{q}} + \mathbf{T}_{LG}^T \times \frac{\partial^2 \hat{\mathbf{Q}}_{int}^tr}{\partial \tilde{\mathbf{q}}^2} \times \frac{\tilde{\mathbf{q}}}{\partial \tilde{\mathbf{q}}} \times \Delta \tilde{\mathbf{q}} - \frac{\partial^2 \tilde{\mathbf{Q}}_{ext}}{\partial \tilde{\mathbf{q}}^2} \times \Delta \tilde{\mathbf{q}} \quad [2.138]$$

where:

$$\hat{\mathbf{K}} = \frac{\partial^2 \hat{\mathbf{Q}}_{int}^tr}{\partial \tilde{\mathbf{q}}^2}, \mathbf{T}_{LG} = \frac{\tilde{\mathbf{q}}}{\partial \tilde{\mathbf{q}}}$$

After substituting Equation 2.136 into Equation 2.138, Equation 2.139 is obtained as follows:

$$\mathbf{g}^2 = {}^1\tilde{\mathbf{Q}}_{int} - {}^1\tilde{\mathbf{Q}}_{ext} + \frac{\partial \mathbf{T}_{LG}^T}{\partial \tilde{\mathbf{q}}} \times {}^2\hat{\mathbf{Q}}_{int}^tr \times \Delta \tilde{\mathbf{q}} + \mathbf{T}_{LG}^T \times \hat{\mathbf{K}} \times \mathbf{T}_{LG} \times \Delta \tilde{\mathbf{q}} - \frac{\partial^2 \tilde{\mathbf{Q}}_{ext}}{\partial \tilde{\mathbf{q}}^2} \times \Delta \tilde{\mathbf{q}} \quad [2.139]$$

Equating Equation 2.139 to zero for equilibrium and solving for $\Delta \tilde{\mathbf{q}}$, the linearized form of equilibrium is obtained in Equation 2.140 given below. Comparing Equation 2.140 with Equation 2.120 excluding its dynamic terms (e.g., $\mathbf{M} \times \ddot{\mathbf{q}} - \mathbf{C} \times \dot{\mathbf{q}}$), it can be seen that both equations are identical to each other. However, the former equation is written in global coordinate system while the latter equation is expressed in the natural coordinate system.

$$\left(\frac{\partial \mathbf{T}_{LG}^T}{\partial \tilde{\mathbf{q}}} \times {}^2\hat{\mathbf{Q}}_{int} + \mathbf{T}_{LG}^T \times \hat{\mathbf{K}} \times \mathbf{T}_{LG} \right) \times \Delta \tilde{\mathbf{q}} = {}^2\tilde{\mathbf{Q}}_{ext} - {}^1\tilde{\mathbf{Q}}_{int} \quad [2.140]$$

The first term on the left hand side of Equation 2.140 represents the external stiffness matrix while the second term is the 18×18 global stiffness matrix.

2.2.12.4. Derivation of External Stiffness Matrix

Equation 2.136 can be restated in local coordinates as shown in Equation 2.141, representing the force balance at C2 between externally applied loads and the element internal forces (Gattass and Abel, 1987).

$${}^1\hat{\mathbf{F}} + ({}^1\hat{\mathbf{K}}_g + {}^1\hat{\mathbf{K}}_l) \times {}_1\hat{\mathbf{q}} = {}_1\hat{\mathbf{Q}}_{ext} \quad [2.141]$$

where:

$\hat{\mathbf{K}}_l$ - linear stiffness matrix, $\hat{\mathbf{K}}_g$ - geometric stiffness matrix

Since ${}^2\hat{\mathbf{Q}}_{ext}$ represents a set of forces that are in equilibrium at C2, the left hand side of Equation 2.141 must also satisfy equilibrium at the same configuration. While conducting incremental nonlinear analysis, at the beginning of each load step, which is often referred as C1 configuration, the components of ${}^1\hat{\mathbf{F}}$ is considered to balance each other as it is illustrated in Figure 2.12. However, once the element undergoes a rigid body rotation, the nodal forces also rotates with the element (Gattass and Abel, 1987). Therefore, the components of ${}^1\hat{\mathbf{F}}$ can not satisfy equilibrium and their resultant produces unbalance force values as can be seen in Figure 2.12 and Figure 2.12. The resulting unbalance forces must be compensated by the second term on the left hand side of

Equation 2.140. Since the terms of ${}^1\hat{\mathbf{K}}_l \times {}_1\hat{\mathbf{q}}$ represent a set of forces in self equilibrium, ${}^1\hat{\mathbf{K}}_l \times {}_1\hat{\mathbf{q}}$ must include force components offsetting the unbalanced forces generated due to the rigid body motion of ${}^1\hat{\mathbf{F}}$. The geometric stiffness matrix in local coordinates can be decomposed into two parts including internal stiffness matrix (${}^1\hat{\mathbf{K}}_{gi}$) and external stiffness matrix (${}^1\hat{\mathbf{K}}_{ge}$) as follows (Gattass and Abel, 1987):

$${}^1\hat{\mathbf{K}}_g = {}^1\hat{\mathbf{K}}_{gi} + {}^1\hat{\mathbf{K}}_{ge} \quad [2.142]$$

${}^1\hat{\mathbf{K}}_{gi}$ is derived based on equilibrium considerations. Each column of ${}^1\hat{\mathbf{K}}_{gi}$ represents the reaction forces when a unit displacement is assigned to a single DOF while keeping the rest of the DOFs as zero. Therefore, the components of ${}^1\hat{\mathbf{K}}_{gi} \times {}_1\hat{\mathbf{q}}$ are considered to be in self-equilibrium. On the other hand, in order to satisfy the equilibrium of the finite element at C2 configuration, the components of ${}^1\hat{\mathbf{K}}_{ge} \times {}_1\hat{\mathbf{q}}$ must contain the nodal forces offsetting the unbalanced forces resulting from rigid body rotation of ${}^1\hat{\mathbf{F}}$. The set of unbalanced forces illustrated in Figure 2.13d and Figure 2.14d can be transformed into the ${}^1\hat{\mathbf{K}}_{ge} \times {}_1\hat{\mathbf{q}}$ format and ${}^1\hat{\mathbf{K}}_{ge}$ is derived as given in Appendix A.

While performing an iterative solution strategy to solve for element forces and displacements, the iterations to satisfy the equilibrium of the analyzed structure are conducted at the global level. This requires transforming the element stiffness (\mathbf{K}) and internal forces (\mathbf{Q}_{int}) derived in Equation 2.120 of Section 2.2.11 from natural to the local and from local to global coordinate system. In addition, to calculate element internal forces, the element displacements are transformed from global to local and from local to natural coordinate system. These processes of transformations are conducted following the rules developed in Section 2.2.12.

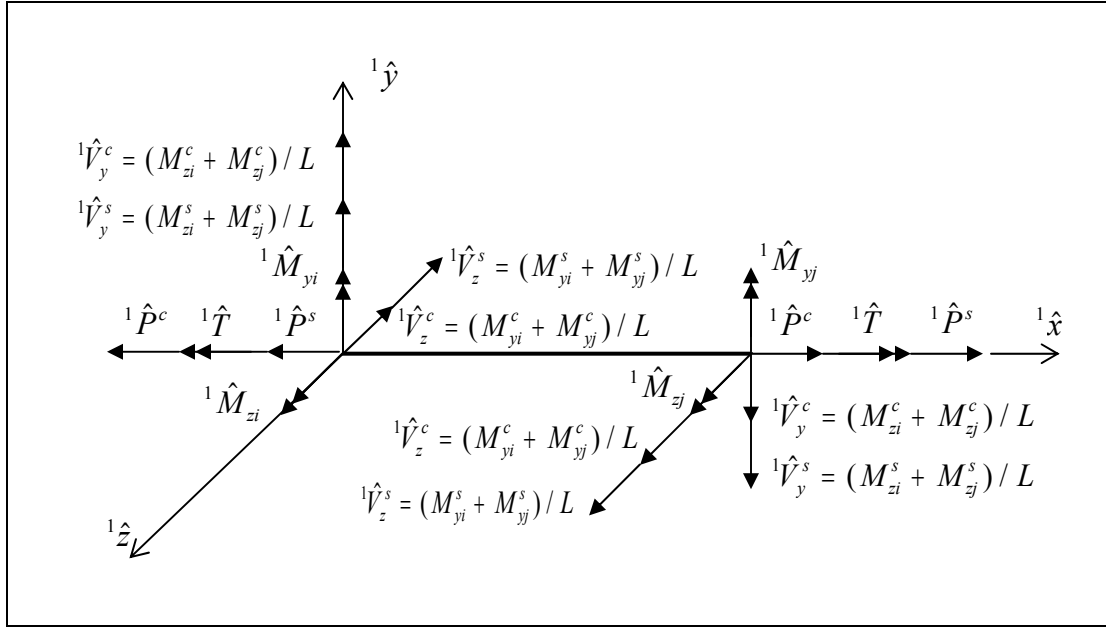


Figure 2.12 Element End Forces at C1 Configuration

2.2.13. Slip and Shear Constraints

The current RCFT formulation requires imposing relationships between the translational DOFs such that the steel tube and the concrete core adhere to compatibility of their shear deformations. In addition, it may also be necessary to provide axial deformation compatibility between the steel tube and concrete core. This condition may arise when slip is prevented using shear connectors, multiple RCFT columns frames into a joint, the size of the RCFT cross-section changes at a joint or RCFT columns are used in a moment resisting frames. The constraint equations used for RCFT columns are given in Equation 2.71 to Equation 2.73. It should be noted that the constraint equations given below are defined for a single joint. Since the steel and concrete interface is modeled through a layer of nonlinear springs, assigning a high stiffness and strength values to the springs, the constraint equation in the axial direction is ensured without introducing any special technique in the equilibrium equations (e.g., penalty function, transformation, lagrange multiplier).

$$\Delta u^s - \Delta u^c = 0 \quad [2.143]$$

$$\Delta v^s - \Delta v^c = 0 \quad [2.144]$$

$$\Delta w^s - \Delta w^c = 0 \quad [2.145]$$

In this research, Penalty Function Method is adopted to satisfy the constraint conditions between degrees of freedoms (Cook et al., 2002). Implementing the Penalty Function Method requires the knowledge of the global nodes and the unit vectors pointing the direction in which the constraints will be imposed. The directions of shear constraints can be obtained from the cross-section vectors of an RCFT joint pointing the weak and strong axes. The unit vector of axial deformation constraint is directed along the RCFT member as shown in Figure 2.15.

The constraint equations defined for RCFT columns can be restated in a vectorial form as given below:

$$\mathbf{C}_1 \times \Delta \tilde{\mathbf{q}} = 0 \quad [2.146]$$

$$\mathbf{C}_2 \times \Delta \tilde{\mathbf{q}} = 0 \quad [2.147]$$

$$\mathbf{C}_3 \times \Delta \tilde{\mathbf{q}} = 0 \quad [2.148]$$

where: $\mathbf{C}_1 = [\alpha_x \quad \alpha_y \quad \alpha_z \quad 0 \quad 0 \quad 0 \quad -\alpha_x \quad -\alpha_y \quad -\alpha_z]^T$

$$\mathbf{C}_2 = [\beta_x \quad \beta_y \quad \beta_z \quad 0 \quad 0 \quad 0 \quad -\beta_x \quad -\beta_y \quad -\beta_z]^T$$

$$\mathbf{C}_3 = [\gamma_x \quad \gamma_y \quad \gamma_z \quad 0 \quad 0 \quad 0 \quad -\gamma_x \quad -\gamma_y \quad -\gamma_z]^T$$

$n_x = (\alpha_x, \alpha_y, \alpha_z)$, $n_y = (\beta_x, \beta_y, \beta_z)$, and $n_z = (\gamma_x, \gamma_y, \gamma_z)$ are the vectors defining the global constraint directions (see Figure 2.15).

In the Penalty Function Method of satisfying constraints, a very high stiffness is provided between the DOFs imposed to be equal to each other. The Penalty Function equations are introduced to the global equilibrium equation as given below:

$$[\mathbf{K} + \alpha \times \mathbf{C}_1 \times \mathbf{C}_1^T + \alpha \times \mathbf{C}_2 \times \mathbf{C}_2^T + \alpha \times \mathbf{C}_3 \times \mathbf{C}_3^T] \times \Delta \tilde{\mathbf{q}} = \Delta \mathbf{Q}_{ext} \quad [2.149]$$

where: α - penalty function value

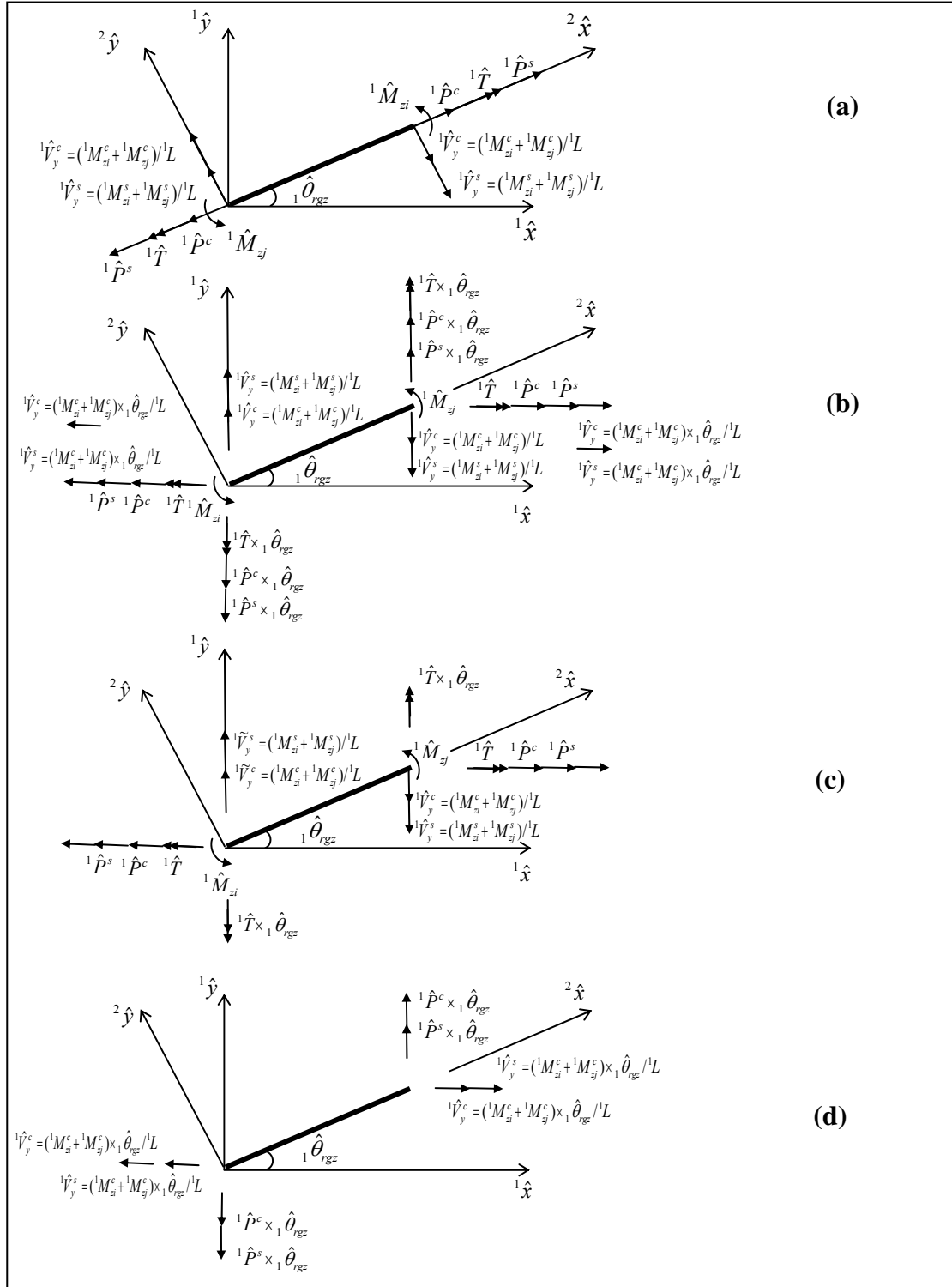


Figure 2.13 (a) Resulting forces ${}^2\mathbf{F}$ at C2 with respect to (wrt.) C2 (b) Resulting forces ${}^2\mathbf{F}$ at C2 wrt. C1 (c) Initial forces ${}^1\mathbf{F}$ at C2 wrt. C1 (d) Forces generated by \mathbf{K}_e

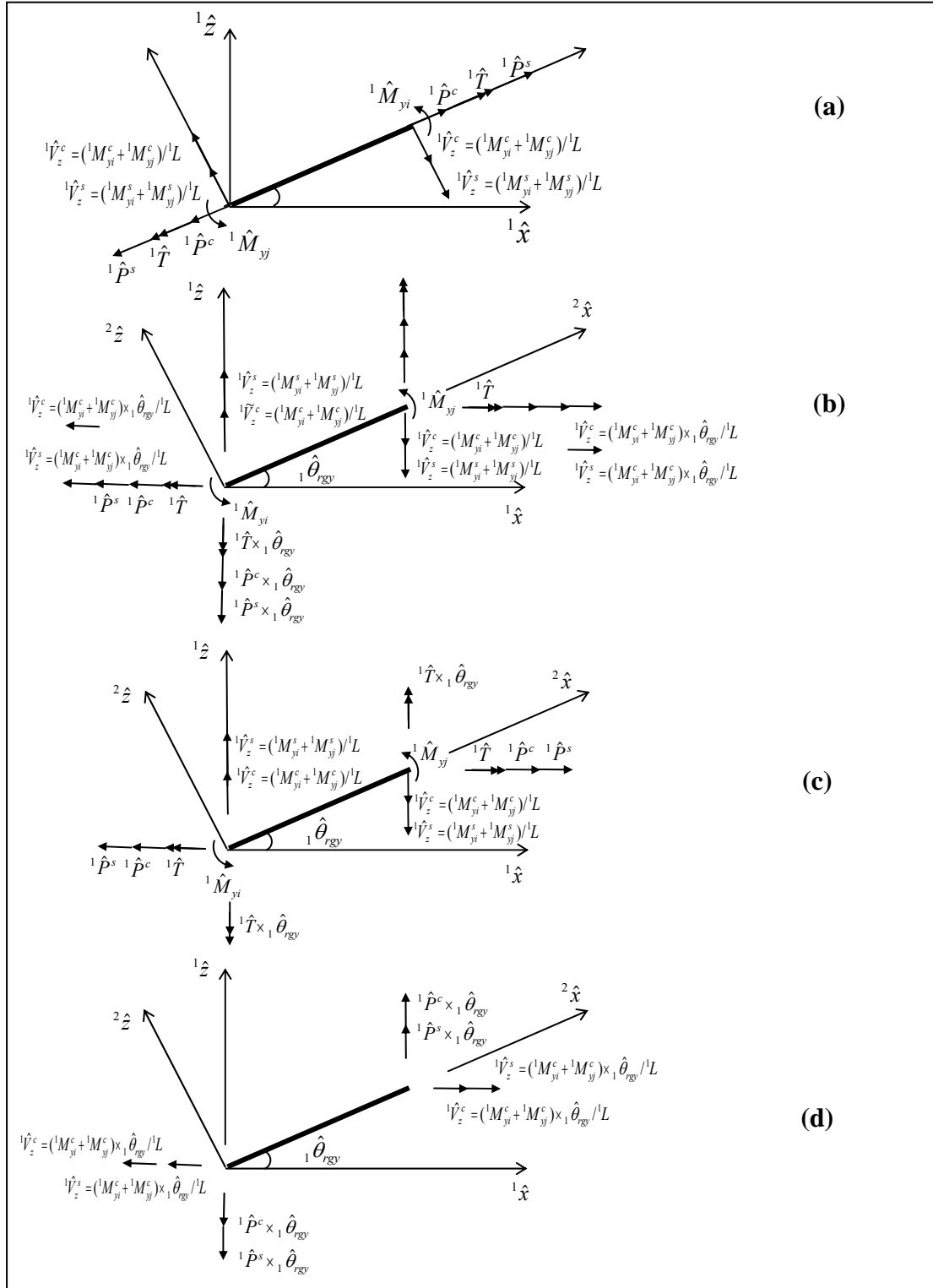


Figure 2.14 (a) Resulting forces 2F at C2 with respect to (wrt.) C2 (b) Resulting forces 2F at C2 wrt. C1 (c) Initial forces 1F at C2 wrt. C1 (d) Forces generated by K_e

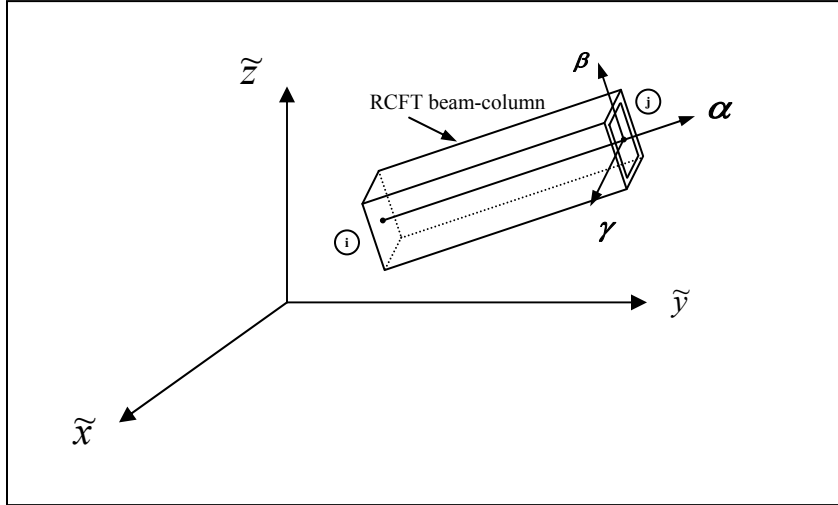


Figure 2.15 Global Constraint Directions for an RCFT joint

In the Penalty Function Method of satisfying constraints, a very high stiffness is provided between the DOFs imposed to be equal to each other. The Penalty Function equations are introduced to the global equilibrium equation as given below:

$$\left[\mathbf{K} + \alpha \times \mathbf{C}_1 \times \mathbf{C}_1^T + \alpha \times \mathbf{C}_2 \times \mathbf{C}_2^T + \alpha \times \mathbf{C}_3 \times \mathbf{C}_3^T \right] \times \Delta \tilde{\mathbf{q}} = \Delta \mathbf{Q}_{ext} \quad [2.150]$$

where: α - penalty function value

The main advantage of Penalty Function Method is that the number of equations remains unchanged. As illustrated in Equation 2.149, it is easy to incorporate in a nonlinear analysis program with minimal changes in the global equilibrium equation (Schiller and Hajjar, 1998). The penalty function method becomes more accurate as the value of α gets larger. If α is given very high values, it is possible to have numerical difficulties. Bathe (1994) recommends having an α value of 100 to 1000 times the largest diagonal term in the global stiffness matrix.

While performing geometrically nonlinear analysis, it is required to update the constraint equations to account for the changes in the geometry of the structure (Schiller and Hajjar, 1998). The transformation of the constraint directions is conducted as given below:

$${}^2\mathbf{n} = \mathbf{T}_n \times {}^1\mathbf{n} \quad [2.151]$$

where: \mathbf{T}_n is the C1 to C2 transformation matrix for constraint directions

$$T_n = \begin{bmatrix} \cos\Delta\tilde{\theta}_y \times \cos\Delta\tilde{\theta}_z & \cos\Delta\tilde{\theta}_y \times \sin\Delta\tilde{\theta}_z & \sin\Delta\tilde{\theta}_y \\ -\sin\Delta\tilde{\theta}_x \times \sin\Delta\tilde{\theta}_y \times \cos\Delta\tilde{\theta}_z & -\sin\Delta\tilde{\theta}_x \times \sin\Delta\tilde{\theta}_y \times \sin\Delta\tilde{\theta}_z & \sin\Delta\tilde{\theta}_x \times \cos\Delta\tilde{\theta}_y \\ -\cos\Delta\tilde{\theta}_x \times \sin\Delta\tilde{\theta}_z & +\cos\Delta\tilde{\theta}_x \times \cos\Delta\tilde{\theta}_z & \\ -\cos\Delta\tilde{\theta}_x \times \sin\Delta\tilde{\theta}_y \times \cos\Delta\tilde{\theta}_z & -\cos\Delta\tilde{\theta}_x \times \sin\Delta\tilde{\theta}_y \times \sin\Delta\tilde{\theta}_z & \cos\Delta\tilde{\theta}_x \times \cos\Delta\tilde{\theta}_y \\ +\sin\Delta\tilde{\theta}_x \times \sin\Delta\tilde{\theta}_z & +\sin\Delta\tilde{\theta}_x \times \cos\Delta\tilde{\theta}_z & \end{bmatrix}$$

¹ n is the unit vector in the constraint direction in configuration C1

² n is the unit vector in the constraint direction in configuration C2

$\Delta\tilde{\theta}_x, \Delta\tilde{\theta}_y, \Delta\tilde{\theta}_z$ are the incremental rotations in the global coordinates

In an iterative nonlinear solution algorithm for a structure, Equation 2.150 is utilized while assembling the global stiffness matrix of the analyzed structure. The stiffness matrix derived in Equation 2.120 of Section 2.2.11 is transformed to the local from natural and then it is transformed to the global from local coordinate system as documented in Section 2.2.12. The global stiffness matrices of the elements are assembled together with the Penalty Function equations as given in Equation 2.150 to form the structural stiffness matrix. At the beginning of each local step and Newton-Raphson iteration, the transformation matrix in Equation 2.151 is used to update the constraint directions.

2.2.14. Element Force Recovery

Incremental nonlinear analysis starts with the solution of structural displacements corresponding to the external load increment in global coordinates. This stage is also called as the predictor phase of nonlinear analysis (Yang and Leu, 1991). The structural displacements in global coordinates are then transformed to the natural coordinates to determine element deformations. The force recovery stage (also called state determination, or the corrector phase) involves the processes to calculate element forces from element deformations. The accuracy of the analysis results is often governed by the force recovery stage (Yang and Leu, 1991). Having two primary sets of unknowns (displacements and forces), the mixed-finite element formulation often has a more

elaborate force recovery procedure compared to displacement-based and force-based solutions. In this section, the steps of the force recovery stage for the RCFT beam-column element are summarized.

All force recovery calculations are performed in the corotational coordinate system. The integrations are carried out numerically based on a Gaussian-Lobatto numerical integration scheme. In this integration scheme, the location of integration points along the element length and the associated weighting parameters (W) per integration point are selected in a manner that element ends points are included in the integration. As the force and deformation values at the element ends are often the largest within the element (e.g., for cases of reverse curvature flexure), this approach enables the values at the end cross sections to be monitored directly throughout the analysis. It is assumed that the calculations are assumed to be performed while the analysis is proceeding from the j^{th} to $j + 1^{\text{th}}$ iteration of the i^{th} load step for static analysis or i^{th} time step for dynamic analysis.

The first step of force recovery is to obtain the incremental element deformations ($\Delta \mathbf{q}^{j+1}$) in natural coordinates using the transformations described in Section 2.2.12. The total element deformations with respect to the C1 configuration (beginning of step) at C2 configuration (${}^2_1 \mathbf{q}^{j+1}$) and incremental element deformation with respect to the C1 configuration (${}_1 \mathbf{q}^{j+1}$) are then updated. Interpolating the deformations along the element length using Equation 2.12a, the incremental strain and curvatures at each integration point (${}_1 \hat{\mathbf{d}}_k^{j+1}$) are evaluated based on the kinematic assumptions in Equations 2.1a, 2.3, 2.4, and 2.7 as summarized in Equation A.10 in Appendix A and as illustrated in Figure 2.16.

Following the calculation of ${}_1 \hat{\mathbf{d}}_k^{j+1}$, a clear distinction between displacement-based, force, and mixed finite element formulations can be noticed. Since a displacement-based finite element formulation is a strain driven formulation, the cross-section forces are directly calculated based on first using ${}_1 \hat{\mathbf{d}}_k^{j+1}$ in the constitutive relations to obtain stresses and cross section forces. The cross-section forces at the

integration points are then integrated through the element length to obtain nodal forces. The Newton-Raphson iterations for a load step or time step are performed based on the unbalanced load values. On the other hand, in force-based formulations, the element internal forces are calculated directly by multiplying the element stiffness by the nodal displacements. Since no displacement interpolations are employed, ${}_1\hat{\mathbf{d}}_k^{j+1}$ is not calculated. The Newton-Raphson iterations are then conducted for the residual displacements.

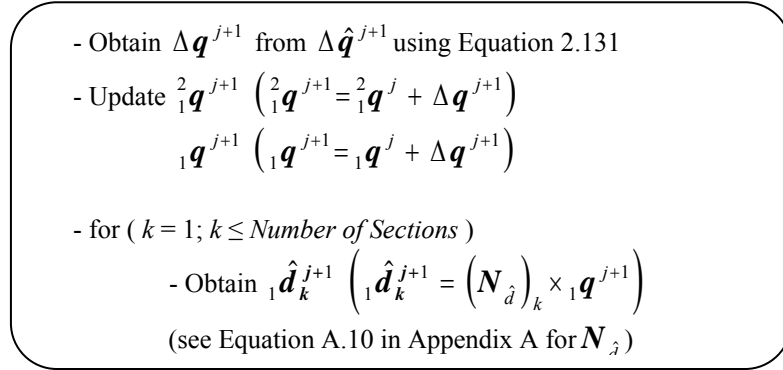


Figure 2.16 Flow Chart of Curvature and Strain Calculations at the Integration Points

In the mixed finite element method, the element nodal forces and displacements are related to each other through the linearized form of the compatibility equation (see Equation 2.77), which is derived as a function of ${}_1\hat{\mathbf{d}}_k^{j+1}$ and \mathbf{d}_k^{j+1} . The cross-sectional forces are obtained through interpolating the nodal forces along the element length (see Equation 2.14 and Equation A.6 in Appendix A) and they are compared with the cross-section forces obtained through integrating the stresses of the material fibers over the cross-section. These two sets of cross-section forces need to balance each other in order to ensure equilibrium at the cross-section level. In the mixed finite element formulation adopted in this research, iterations are only performed at the global level. The unbalances of the compatibility and cross-section equilibrium equations are converted into unbalanced nodal forces and they are eliminated together with the unbalanced nodal forces generated from element equilibrium at the global coordinate system. This approach was found to exhibit good convergence characteristics, especially, for problems with significant concrete cracking (e.g., pure bending) causing drastic changes in the

concrete terms of the cross-section stiffness matrix. However, it is also possible to eliminate the unbalances of compatibility and cross-section equilibrium iteratively without transferring them to the global level (Alemdar and White, 2005).

Figure 2.17 portrays the details of calculating incremental nodal forces. In Figure 2.17, Equation 2.51 is utilized to compute the compatibility equation (\mathbf{V}^j) producing a residual displacement vector if there exist an unbalance between cross-sectional strain vectors of ${}^1\hat{\mathbf{d}}_k^{j+1}$ and ${}^1\mathbf{d}_k^j$. It should be noted that the additional term ${}^2\mathbf{f}_k^j \times ({}^2\mathbf{D}_k^j - {}^2\mathbf{D}_{\Sigma k}^j)$ while calculating \mathbf{V}^j in Figure 2.17 accounts for the unbalance of the cross-section equilibrium in the previous iteration which is converted to strain values transferred to the unbalance of the compatibility equation. The ${}^2\mathbf{H}_{11}^j$ matrix, which can be considered as the element flexibility is obtained through Equation 2.73. Both \mathbf{V}^j and ${}^2\mathbf{H}_{11}^j$ are calculated using numerical integration along the element length as described in Figure 2.17. As it is also shown in Equation 2.77, incremental nodal forces ($\Delta \mathbf{Q}^{j+1}$), defined in Equation 2.13, are determined multiplying \mathbf{V}^j and ${}^2\mathbf{H}_{11}^j$.

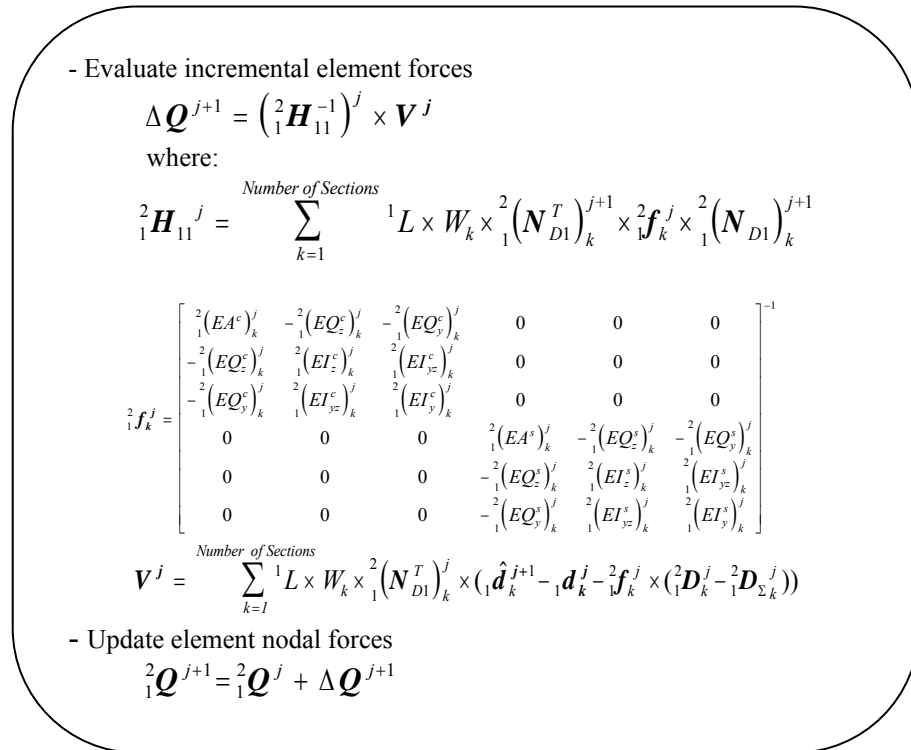


Figure 2.17 Flow Chart of Calculating Nodal Forces

As described in Figure 2.18, after the calculation of nodal forces, the force recovery of mixed finite element formulation proceeds with the interpolation of nodal forces along the element length using Equation 2.14. This process produces cross-section forces (${}^2_1\mathbf{D}_k^{j+1}$) at each integration point along the element length. The equilibrium at the integration points is checked by comparing the cross-section force vectors from force interpolation functions (${}^2_1\mathbf{D}_k^{j+1}$) with the cross-section force vectors obtained through numerical integration over the steel and concrete fibers (${}^2_1(\mathbf{D}_\Sigma)_k^j$). The resulting out-of-balance cross-section force vector is multiplied by the cross-section flexibility (${}^2_1\mathbf{f}_k^{j+1}$ or ${}^2_1(\mathbf{k}_k^{j+1})^{-1}$) to obtain the corresponding incremental cross-section deformations (${}^2_1\mathbf{d}_k^{j+1}$). However, in order to ensure the curvatures of the steel tube and concrete core to be the same, the cross-section stiffness is modified by combining the flexural terms of the steel tube and concrete core yielding ${}^2_1(\mathbf{f}^{comb})_k^{j+1}$ as shown in Figure 2.18. The similar process of combining the flexural terms is also performed for the cross-sectional forces of ${}^2_1(\mathbf{D}_\Sigma)_k^j$ and ${}^2_1\mathbf{D}_k^{j+1}$ producing, ${}^2_1(\mathbf{D}_\Sigma^{comb})_k^{j+1}$ and ${}^2_1(\mathbf{D}^{comb})_k^{j+1}$, respectively, as they are defined in Figure 2.18. The cross-section equilibrium equation is expressed as the difference between ${}^2_1(\mathbf{D}_\Sigma^{comb})_k^j$ and ${}^2_1(\mathbf{D}^{comb})_k^{j+1}$. Therefore, ${}^2_1(\mathbf{d}^{comb})_k^{j+1}$ is obtained by multiplying the unbalance of cross-section equilibrium (e.g. ${}^2_1(\mathbf{D}^{comb})_k^{j+1} - {}^2_1(\mathbf{D}_\Sigma^{comb})_k^j$) by ${}^2_1(\mathbf{f}^{comb})_k^{j+1}$. The resulting cross-section strain vector (${}^2_1(\mathbf{d}^{comb})_k^{j+1}$) contains two independent axial strain values for the steel tube (${}^2_1(\mathbf{\varepsilon}^s)_k^{j+1}$) and the concrete core (${}^2_1(\mathbf{\varepsilon}^c)_k^{j+1}$) and two curvature values (${}^2_1(\mathbf{\kappa}_y^{comb})_k^{j+1}$, ${}^2_1(\mathbf{\kappa}_z^{comb})_k^{j+1}$) with respect to the two axes of bending, both of which are defined commonly for the steel tube and concrete core. The strain values of ${}^2_1(\mathbf{d}^{comb})_k^{j+1}$ including both curvatures and axial strains are mapped on to ${}^2_1\mathbf{d}_k^{j+1}$ as it is presented in Figure 2.18.

- Evaluate the cross-section forces at each integration point
for ($k = 1; k \leq \text{Number of Sections}$)

$${}^2_1\mathbf{D}_k^{j+1} = {}^2_1(\mathbf{N}_{D1})_k^{j+1} \times {}^2_1\mathbf{Q}^{j+1}$$

where:

$${}^2_1\mathbf{Q}^{j+1} = \left(\left[{}^2_1P_i^c \quad {}^2_1P_j^c \quad {}^2_1M_{zi}^c \quad {}^2_1M_{yi}^c \quad {}^2_1M_{zj}^c \quad {}^2_1M_{yj}^c \quad {}^2_1P_i^s \quad {}^2_1P_j^s \quad {}^2_1M_{zi}^s \quad {}^2_1M_{yi}^s \quad {}^2_1M_{zj}^s \quad {}^2_1M_{yj}^s \right]^T \right)^{j+1}$$

$(\mathbf{N}_{D1})_k^{j+1}$ is the force interpolation function matrix (see Equation A.7 in

Appendix A)

$${}^2_1\mathbf{D}_k^{j+1} = \left[{}^2_1(P^c)_k^{j+1} \quad {}^2_1(M_y^c)_k^{j+1} \quad {}^2_1(M_z^c)_k^{j+1} \quad {}^2_1(P^s)_k^{j+1} \quad {}^2_1(M_y^s)_k^{j+1} \quad {}^2_1(M_z^s)_k^{j+1} \right]^T$$

- Evaluate the cross-section deformations ${}^2_1(\mathbf{d}^{comb})_k^{j+1}$ at each integration point
for ($k = 1; k \leq \text{Number of Sections}$)

$${}^2_1(\mathbf{d}^{comb})_k^{j+1} = {}^2_1(\mathbf{f}^{comb})_k^j \times \left({}^2_1(\mathbf{D}^{comb})_k^{j+1} - {}^2_1(\mathbf{D}_\Sigma^{comb})_k^j \right)$$

where:

$${}^2_1(\mathbf{f}^{comb})_k^j = \begin{bmatrix} {}^2_1(EA^c)_k^j & 0 & -{}^2_1(EQ_y^c)_k^j - {}^2_1(EQ_y^s)_k^j & -{}^2_1(EQ_z^c)_k^j - {}^2_1(EQ_z^s)_k^j \\ 0 & {}^2_1(EA^s)_k^j & -{}^2_1(EQ_y^c)_k^j - {}^2_1(EQ_y^s)_k^j & -{}^2_1(EQ_z^c)_k^j - {}^2_1(EQ_z^s)_k^j \\ -{}^2_1(EQ_y^c)_k^j - {}^2_1(EQ_y^s)_k^j & -{}^2_1(EQ_z^c)_k^j - {}^2_1(EQ_z^s)_k^j & {}^2_1(EI_{yy}^c)_k^j + {}^2_1(EI_{yy}^s)_k^j & {}^2_1(EI_{yz}^c)_k^j + {}^2_1(EI_{yz}^s)_k^j \\ -{}^2_1(EQ_z^c)_k^j - {}^2_1(EQ_z^s)_k^j & -{}^2_1(EQ_y^c)_k^j - {}^2_1(EQ_y^s)_k^j & {}^2_1(EI_{yz}^c)_k^j + {}^2_1(EI_{yz}^s)_k^j & {}^2_1(EI_{zz}^c)_k^j + {}^2_1(EI_{zz}^s)_k^j \end{bmatrix}^{-1}$$

$${}^2_1(\mathbf{d}^{comb})_k^{j+1} = \left[{}^2_1(\mathcal{E}^c)_k^{j+1} \quad {}^2_1(\mathcal{E}^s)_k^{j+1} \quad {}^2_1(\mathcal{K}_y^{comb})_k^{j+1} \quad {}^2_1(\mathcal{K}_z^{comb})_k^{j+1} \right]^T$$

$${}^2_1(\mathbf{D}^{comb})_k^{j+1} = \left[{}^2_1(P^c)_k^{j+1} \quad {}^2_1(P^s)_k^{j+1} \quad {}^2_1(M_y^c)_k^{j+1} + {}^2_1(M_y^s)_k^{j+1} \quad {}^2_1(M_z^c)_k^{j+1} + {}^2_1(M_z^s)_k^{j+1} \right]^T$$

$${}^2_1(\mathbf{D}_\Sigma^{comb})_k^j = \left[{}^2_1(P^c)_k^{j+1} \quad {}^2_1(P^s)_k^{j+1} \quad {}^2_1(M_{y\Sigma}^c)_k^{j+1} + {}^2_1(M_{y\Sigma}^s)_k^{j+1} \quad {}^2_1(M_{z\Sigma}^c)_k^{j+1} + {}^2_1(M_{z\Sigma}^s)_k^{j+1} \right]^T$$

- Evaluate cross-section deformations ${}^2_1\mathbf{d}_k^{j+1}$ at each integration point
for ($k = 1; k \leq \text{Number of Sections}$)

$${}^2_1(\mathbf{d})_k^{j+1} = \left[{}^2_1(\mathcal{E}^c)_k^{j+1} \quad {}^2_1(\mathcal{K}_y^{comb})_k^{j+1} \quad {}^2_1(\mathcal{K}_z^{comb})_k^{j+1} \quad {}^2_1(\mathcal{E}^s)_k^{j+1} \quad {}^2_1(\mathcal{K}_y^{comb})_k^{j+1} \quad {}^2_1(\mathcal{K}_z^{comb})_k^{j+1} \right]^T$$

Figure 2.18 Flow Chart of Calculating Cross-Section Deformations

At each integration point, the constitutive relations for the steel (σ_n^s) and concrete (σ_n^c) fibers are updated based on the values of ${}_1\mathbf{d}_k^{j+1}$. Performing numerical integration, an updated cross-sectional stiffness (${}_1^2\mathbf{k}_k^{j+1}$) and cross-section force values (${}_1^2(\mathbf{D}_\Sigma)_k^{j+1}$) are obtained as summarized in Figure 2.19. The kinematic equation presented in Equation 2.9 for interpolated slip deformation (${}_1\hat{\mathbf{d}}_{sc}^{j+1}$) and the slip deformation from nodal displacements in Equation 13.1a (${}_1\mathbf{e}_i^{sc}$) is utilized to calculate the incremental slip with respect to C1 configuration (${}_1\boldsymbol{\varepsilon}_k^{sc} = {}_1\hat{\mathbf{d}}_{sc}^{j+1} - {}_1\mathbf{e}_i^{sc}$) at each integration point. The stiffness of the interface between the steel tube and concrete (${}_1^2(\bar{\mathbf{k}}_{sc})_k^{j+1}$) is updated once the slip constitutive relation (σ_{sc}) is incremented based on ${}_1\boldsymbol{\varepsilon}_k^{sc}$.

The updated values of cross-sectional forces stiffnesses (e.g., ${}_1^2\mathbf{k}_k^{j+1}$, ${}_1^2(\mathbf{k}_{sc})_k^{j+1}$) and strains (e.g., ${}_1\mathbf{d}_k^{j+1}$, ${}_1\hat{\mathbf{d}}_k^{j+1}$) are used to determine the element internal forces (${}_1^2\mathbf{Q}_{int}^{j+1}$) derived in Equation 2.120 as described in Figure 2.20 and Figure 2.21. The first term in Equation 2.120 defined as ${}_1^2(\mathbf{G}_1^{j+1})^T \times {}_1^2\mathbf{Q}^{j+1}$ is obtained multiplying ${}_1^2(\mathbf{G}_1^{j+1})^T$ (see Equation 2.73) by ${}_1^2\mathbf{Q}^{j+1}$ described in Figure 2.17. The term ${}_1^2\mathbf{K}_{sc}^{j+1}$ representing the slip stiffness of the RCFT beam column element is determined through numerical integration along the element length (see Equation 2.83) and it is used to obtain the incremental force at the steel tube and concrete core interface. Similarly, the term $\int_0^L \left(\mathbf{N}_{\delta\hat{\mathbf{d}}_{sc}}^T \right)_k \times {}_1^2(\mathbf{D}_{sc})_k^{j+1} \times d^1l$ defining the force at the steel tube and concrete core interface in C1 configuration is also evaluated through numerical integration along the element length. For each integration point, ${}_1^2\left(\mathbf{N}_{\delta\hat{\mathbf{d}}_{sc}}^T \right)_k$ is calculated as defined in Equation A.13 in Appendix A and ${}_1^2(\mathbf{D}_{sc})_k^{j+1}$ representing the stress at the steel and concrete interface in C1 configuration is obtained as it is stored at the last iteration of the previous load step (or time step). The numerical integration of the term $\int_0^L {}_1^2\mathbf{N}_{D2}^T \times ({}_1\hat{\mathbf{d}} - {}_1\mathbf{d}) \times d^1x$ is carried out following the calculation of

${}^2_1(\mathbf{N}_{D2}^{j+1})_k$ and $(\hat{\mathbf{d}}_k^{j+1} - \mathbf{d}_k^{j+1})$ for each integration point. ${}^2_1(\mathbf{N}_{D2}^{j+1})_k$ is obtained using the Equation A.15 in Appendix A, $\hat{\mathbf{d}}_k^{j+1}$ and \mathbf{d}_k^{j+1} are determined from the previous steps of the force recovery given in Figure 2.16 and Figure 2.18. The term \mathbf{M}_d which is derived through linearization process of the compatibility equation is obtained using Equation A.19 in Appendix A and it accounts for the $P - \delta$ effects. The terms ${}^2_1(\mathbf{H}_{11})^{j+1}$ and ${}^2_1(\mathbf{H}_{12})^{j+1}$ described in Equation 2.73 are calculated through numerical integration along the element length. The compatibility equation (\mathbf{V}^{j+1}) with the updated values of the cross-sectional terms (e.g., $\hat{\mathbf{d}}_k^{j+1}$, \mathbf{d}_k^{j+1}) is calculated as described in Equation 2.51.

- At each integration point evaluate ${}^2_1\mathbf{k}_k^{j+1}$, ${}^2_1(\mathbf{k}_{sc})_k^{j+1}$, ${}^2_1(\mathbf{D}_\Sigma)_k^{j+1}$

for ($k = 1; k \leq \text{Number of Sections}$)

$${}^2_1(\mathbf{D}_\Sigma)_k^{j+1} = \left[\begin{array}{ccc} \sum_{n=1}^{\# \text{ conc fib.}} \sigma_n^c(\mathbf{d}^{j+1}) A_n & \sum_{n=1}^{\# \text{ conc fib.}} -\sigma_n^c(\mathbf{d}^{j+1}) A_n \bar{z} & \sum_{n=1}^{\# \text{ conc fib.}} -\sigma_n^c(\mathbf{d}^{j+1}) A_n \bar{y} \\ \sum_{n=1}^{\# \text{ stl fib.}} \sigma_n^s(\mathbf{d}^{j+1}) A_n & \sum_{n=1}^{\# \text{ stl fib.}} -\sigma_n^s(\mathbf{d}^{j+1}) A_n \bar{z} & \sum_{n=1}^{\# \text{ stl fib.}} -\sigma_n^s(\mathbf{d}^{j+1}) A_n \bar{y} \end{array} \right]$$

where: σ^c is the constitutive relation for concrete core

σ^s is the constitutive relation for steel tube

$${}^2_1\mathbf{k}_k^{j+1} = \left[\begin{array}{ccc} \sum_{n=1}^{\text{num conc fib}} (E_n(\mathbf{d}^{j+1}) A_n) & - \sum_{n=1}^{\text{num conc fib}} (E_n(\mathbf{d}^{j+1}) A_n \bar{y}) & - \sum_{n=1}^{\text{num conc fib}} (E_n(\mathbf{d}^{j+1}) A_n \bar{z}) \\ - \sum_{n=1}^{\text{num conc fib}} (E_n(\mathbf{d}^{j+1}) A_n \bar{y}) & \sum_{n=1}^{\text{num conc fib}} (E_n(\mathbf{d}^{j+1}) A_n \bar{y}^2) & \sum_{n=1}^{\text{num conc fib}} (E_n(\mathbf{d}^{j+1}) A_n \bar{y} \bar{z}) \\ - \sum_{n=1}^{\text{num conc fib}} (E_n(\mathbf{d}^{j+1}) A_n \bar{z}) & \sum_{n=1}^{\text{num conc fib}} (E_n(\mathbf{d}^{j+1}) A_n \bar{y} \bar{z}) & \sum_{n=1}^{\text{num conc fib}} (E_n(\mathbf{d}^{j+1}) A_n \bar{z}^2) \\ 0 & 0 & 0 \\ 0 & 0 & 0 \\ 0 & 0 & 0 \end{array} \right] \begin{array}{ccc} \sum_{n=1}^{\text{num stl fib}} (E_n(\mathbf{d}^{j+1}) A_n) & - \sum_{n=1}^{\text{num stl fib}} (E_n(\mathbf{d}^{j+1}) A_n \bar{y}) & - \sum_{n=1}^{\text{num stl fib}} (E_n(\mathbf{d}^{j+1}) A_n \bar{z}) \\ - \sum_{n=1}^{\text{num stl fib}} (E_n(\mathbf{d}^{j+1}) A_n \bar{y}) & \sum_{n=1}^{\text{num stl fib}} (E_n(\mathbf{d}^{j+1}) A_n \bar{y}^2) & \sum_{n=1}^{\text{num stl fib}} (E_n(\mathbf{d}^{j+1}) A_n \bar{y} \bar{z}) \\ - \sum_{n=1}^{\text{num stl fib}} (E_n(\mathbf{d}^{j+1}) A_n \bar{z}) & \sum_{n=1}^{\text{num stl fib}} (E_n(\mathbf{d}^{j+1}) A_n \bar{y} \bar{z}) & \sum_{n=1}^{\text{num stl fib}} (E_n(\mathbf{d}^{j+1}) A_n \bar{z}^2) \end{array}$$

-

$${}^2_1(\mathbf{k}_{sc})_k^{j+1} = \frac{d\sigma_{sc}}{d(\varepsilon_{sc})}({}_1\varepsilon_{sc}^{j+1})$$

where: σ_{sc} is the constitutive relation for steel tube and concrete interface

${}_1\varepsilon_{sc}^{j+1}$ is the incremental slip at the steel tube and concrete interface with respect to C1 configuration

Figure 2.19 Flow Chart of Updating Constitutive Relations and Integrating over the RCFT Cross-Section for Stiffness and Force Calculations

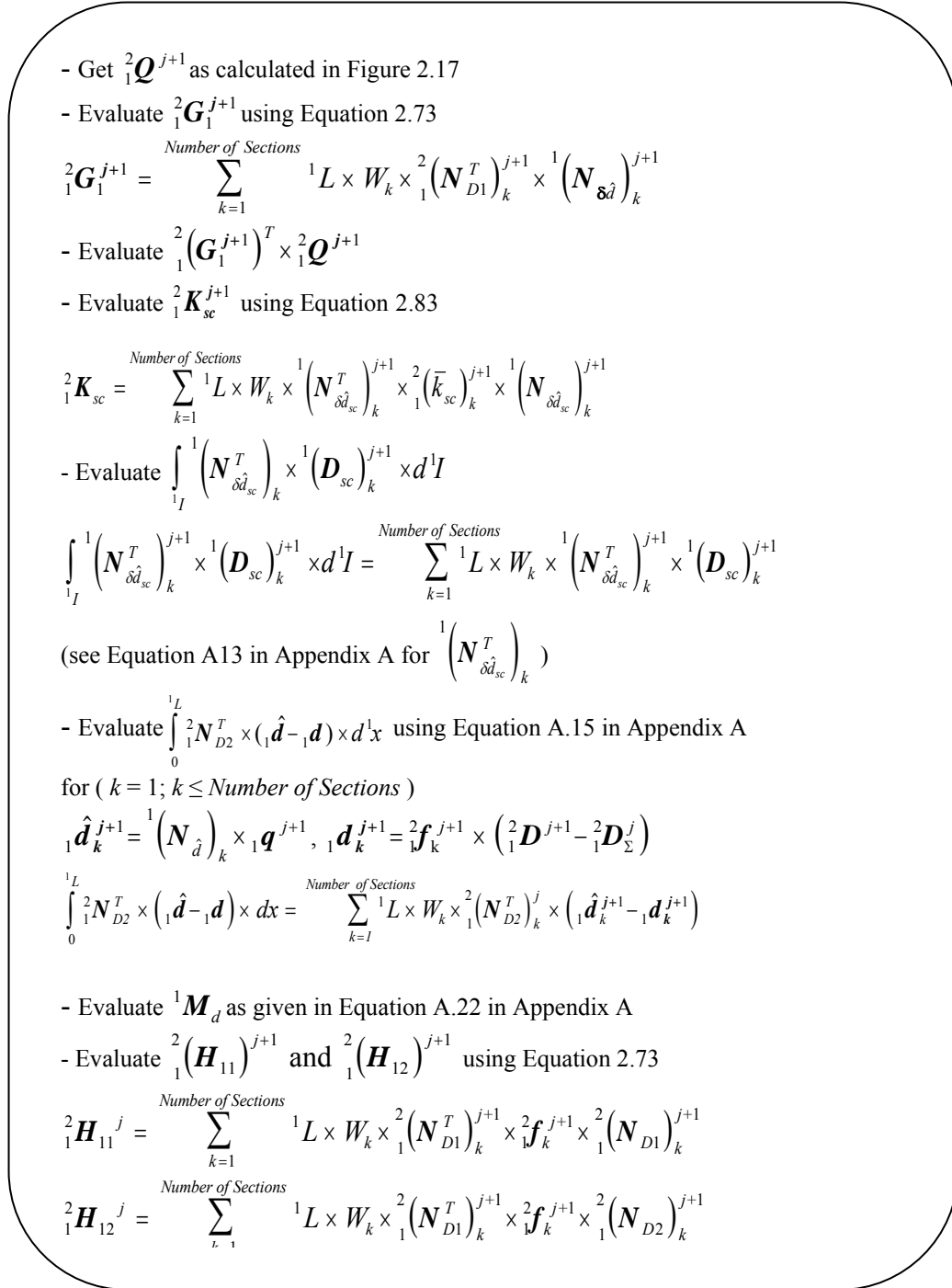


Figure 2.20 Flow Chart of Calculating Element Internal Force

- Evaluate \mathbf{V}^{j+1} using Equation 2.29

$$\mathbf{V}^{j+1} = \sum_{k=1}^{\text{Number of Sections}} {}^1L \times W_k \times {}^2(\mathbf{N}_{D1}^T)_k^j \times ({}_1\hat{\mathbf{d}}_k^{j+1} - {}_1\mathbf{d}_k^{j+1} - {}^2\mathbf{f}_k^{j+1} \times ({}^2\mathbf{D}_k^{j+1} - {}^2\mathbf{D}_{\Sigma k}^{j+1}))$$

- Evaluate ${}^2\mathbf{Q}_{int}^{j+1}$ as in Equation 2.120 using the term described above.

$${}^2\mathbf{Q}_{int}^{j+1} = {}^2(\mathbf{G}_1^T)^{j+1} \times {}^2\mathbf{Q}^{j+1} + {}^2\mathbf{K}_{sc}^{j+1} \times {}_1\mathbf{q}^{j+1} + \int_0^1 ({}^2\mathbf{N}_{\delta d_{sc}}^T) \times {}^1\mathbf{D}_{sc} \times d^1I +$$

$$\int_0^1 ({}^2\mathbf{N}_{D2}^T)^{j+1} \times ({}_1\hat{\mathbf{d}}^{j+1} - {}_1\mathbf{d}^{j+1}) \times d^1X + ({}^2(\mathbf{G}_1^T)^{j+1} + \mathbf{M}_d^T - {}^2(\mathbf{H}_{12}^T)^{j+1}) \times {}^2(\mathbf{H}_{11}^{-1})^{j+1} \times \mathbf{V}^{j+1}$$

Figure 2.21 Flow Chart of Calculating Element Internal Force (cont'd)

The additional term ${}^2\mathbf{f}_k^{j+1} \times ({}^2\mathbf{D}_k^{j+1} - {}^2\mathbf{D}_{\Sigma k}^{j+1})$ in Figure 2.21 while evaluating \mathbf{V}^{j+1} account for the unbalances of the cross-section equilibrium equation (e.g., ${}^2\mathbf{D}_k^{j+1} - {}^2\mathbf{D}_{\Sigma k}^{j+1}$), which is converted into cross-section strains and transferred to the compatibility equation. Finally, the force recovery is completed calculating the internal nodal forces using Equation 2.120. While evaluating ${}^2\mathbf{Q}_{int}^{j+1}$ in Figure 2.21, the terms $\int_0^1 ({}^2\mathbf{N}_{D2}^T)^{j+1} \times ({}_1\hat{\mathbf{d}}^{j+1} - {}_1\mathbf{d}^{j+1}) \times d^1X$ and $({}^2(\mathbf{G}_1^T)^{j+1} + (\mathbf{M}_d^T)^{j+1} - {}^2(\mathbf{H}_{12}^T)^{j+1}) \times {}^2(\mathbf{H}_{11}^{-1})^{j+1} \times \mathbf{V}^{j+1}$ represent the unbalances of compatibility and cross-section equilibrium equations converted into unbalanced nodal forces.

2.2.15. Element Stiffness Calculation

The stiffness of the RCFT beam-column element is calculated at the beginning of every iteration and time step in an incremental nonlinear analysis to determine the structural displacements. Due to the changes in the structural geometry, element forces and stiffnesses, the terms of the stiffness matrix are continually updated throughout the analysis.

A summary of the computations to obtain the stiffness matrix of the RCFT beam-column element is illustrated in Figure 2.18 as the analysis is proceeding from j^{th} iteration to the $j + 1^{\text{th}}$ iteration of the i^{th} load step (or time step).

In Figure 2.22, the geometric stiffness matrix (${}^2_1\mathbf{K}_g^j$) accounting for the $P - \Delta$ effects is evaluated through numerical integration using Equation A.22 in Appendix A. Integrating Equation 2.83 along the element length, the slip stiffness matrix (${}^2_1\mathbf{K}_{sc}^j$) of the RCFT beam-column element is calculated. The terms ${}^2_1\mathbf{G}_2^j$, ${}^2_1(\mathbf{G}_2^j)^T$, and ${}^2_1\mathbf{H}_{22}^j$ are derived to include the $P - \delta$ effects in the RCFT beam-column stiffness matrix. The aforementioned terms are evaluated by performing the numerical integrations in Equations 2.73 and 2.91. Similarly, the terms ${}^2_1\mathbf{H}_{12}^j$ and \mathbf{M}_d^j also reflects the $P - \delta$ effects in the formulation of stiffness matrix of the RCFT beam-column element. Equation 2.73 and Equation A.22 in Appendix A are utilized while evaluating the terms ${}^2_1\mathbf{H}_{12}^j$ and \mathbf{M}_d^j , respectively. The ${}^2_1(\mathbf{H}_{11})^{j+1}$ representing the element flexibility matrix is obtained as described in Equation 2.73 evaluating the numerical integration along the element length. The evaluation of the stiffness matrix (${}^2_1\mathbf{K}^j$) is accomplished through substitution of the numerical values of the terms including ${}^2_1\mathbf{K}_g^j$, ${}^2_1\mathbf{K}_{sc}^j$, ${}^2_1\mathbf{G}_2^j$, ${}^2_1(\mathbf{G}_2^j)^T$, ${}^2_1\mathbf{H}_{22}^j$, ${}^2_1\mathbf{H}_{12}^j$, \mathbf{M}_d^j , and ${}^2_1(\mathbf{H}_{11})^{j+1}$ into Equation 2.119a.

2.3. Three-Dimensional Distributed Plasticity STL Beam-Column Element

A 12 DOF steel beam-column element was also derived following the mixed finite element principles described in Section 2.2. Independent interpolation functions were utilized for the displacement and force fields along the element length. Cubic Hermitian shape functions were defined for the transverse deformations while a constant shape function was introduced for the axial deformations. The element internal forces were estimated through constant shape function for the axial load and linear shape functions for the bending moments. The kinematic equations adopted for the axial strains and curvatures were kept the same as defined for the RCFT beam-column element. The element internal forces and stiffness matrices were also obtained utilizing the same methodology derived for the RCFT beam-column element as detailed in Section 2.2.

- Evaluate ${}^2_1\mathbf{K}_g^j$ as documented Equation A.22 in Appendix A

- Evaluate ${}^2_1\mathbf{K}_{sc}^j$ using Equation 2.83

$$\left({}^2_1\mathbf{K}_{sc}\right)^j = \sum_{k=1}^{\text{Number of Sections}} {}^1L \times W_k \times {}^1\left(\mathbf{N}_{\hat{\delta d}_{sc}}^T\right)_k^j \times {}^2\left(\bar{k}_{sc}\right)_k^j \times {}^1\left(\mathbf{N}_{\hat{\delta d}_{sc}}\right)_k^j$$

- Evaluate ${}^2_1\mathbf{G}_1^j$ using Equation 2.73

$${}^2_1\mathbf{G}_1^j = \sum_{k=1}^{\text{Number of Sections}} {}^1L \times W_k \times {}^2\left(\mathbf{N}_{D1}^T\right)_k^j \times {}^1\left(\mathbf{N}_{\delta d}\right)_k^j$$

- Evaluate ${}^2_1\mathbf{G}_2^j$ using Equation 2.81

$${}^2_1\mathbf{G}_2^j = \sum_{k=1}^{\text{Number of Sections}} {}^1L \times W_k \times {}^1\left(\mathbf{N}_{\delta d}^T\right)_k^j \times \left({}^2_1\mathbf{D}\right)_k^j$$

- Evaluate ${}^2_1\left(\mathbf{H}_{11}\right)^j$, ${}^2_1\left(\mathbf{H}_{12}\right)^j$, and ${}^2_1\left(\mathbf{H}_{22}\right)^j$ using Equation 2.73, 2.73, 2.91, respectively

$${}^2_1\mathbf{H}_{11}^j = \sum_{k=1}^{\text{Number of Sections}} {}^1L \times W_k \times {}^2\left(\mathbf{N}_{D1}^T\right)_k^j \times {}^2\mathbf{f}_k^j \times {}^2\left(\mathbf{N}_{D1}\right)_k^j$$

$${}^2_1\mathbf{H}_{12}^j = \sum_{k=1}^{\text{Number of Sections}} {}^1L \times W_k \times {}^2\left(\mathbf{N}_{D1}^T\right)_k^j \times {}^2\mathbf{f}_k^j \times {}^2\left(\mathbf{N}_{D2}\right)_k^j$$

$${}^2_1\mathbf{H}_{22}^j = \sum_{k=1}^{\text{Number of Sections}} {}^1L \times W_k \times {}^2\left(\mathbf{N}_{D2}^T\right)_k^j \times {}^2\mathbf{f}_k^j \times {}^2\left(\mathbf{N}_{D2}\right)_k^j$$

- Evaluate \mathbf{M}_d^j as given in Equation A.22 in Appendix A

- Evaluate ${}^2_1\mathbf{K}^j$ using Equation 2.119a

$${}^2_1\mathbf{K}^j = \left[\begin{array}{l} \left(\left({}^2_1\mathbf{K}_g \right)^j + {}^2_1\mathbf{K}_{sc}^j + \mathbf{G}_2^j + \left(\mathbf{G}_2^T \right)^j - {}^2_1\mathbf{H}_{22}^{j+1} \right) + \\ \left(\left(\mathbf{G}_1^T \right)^j + \left(\mathbf{M}_d^T \right)^j - \left({}^2_1\mathbf{H}_{12}^T \right)^j \right) \times {}^1\left({}^2_1\mathbf{H}_{11}^{-1} \right)^j \times \left(\mathbf{G}_1^j + \mathbf{M}_d^j - {}^2_1\mathbf{H}_{12}^j \right) \end{array} \right]$$

Figure 2.22 Flow Chart of Calculating Element Stiffness

Chapter 3

3. Uniaxial Cyclic Concrete Constitutive Model for RCFT Members

3.1. Introduction

The load transfer mechanism of RCFT members allows the shedding of force between the steel tube and concrete core through the interface of the two media. This distinct feature of RCFT members allows the contribution of both the steel tube and concrete core while resisting externally applied loads. In Chapter 2, a fiber-based finite element formulation is presented, which is appropriate to simulate the load-transfer characteristics of RCFT members in a rational way. However, in order to model their nonlinear response accurately, the fiber-based finite element formulation should be implemented along with comprehensive constitutive models to trace the stress vs. strain response of the material fibers. In this chapter, the cyclic uniaxial stress vs. strain relation adopted for the concrete core is introduced. Both the advantages and limitations of the model are discussed. Several verification studies are presented to demonstrate the performance of the model.

In the literature, there exist numerous research studies focusing on the stress-strain response of concrete that are relevant to the response within RCFTs, including Chen and Chen (1975), Sheikh and Uzumeri (1982), Mander et al. (1988), Collins and Mitchell (1990), Saatcioglu and Razvi (1992), Chang and Mander (1994), Amer-Moussa and Buyukozturk (1990), Cusson and Paultre (1995), Attard and Setunge (1996), Lee and Fenves (1998), Palermo and Vecchio (2003), Grassl and Jirasek (2006). The majority of these studies cover specifically reinforced concrete structures. There are mainly two approaches to develop the stress-strain relationship of concrete. In the first method, the classical theory of plasticity is employed to simulate the multiaxial cyclic behavior of concrete (Chen and Chen, 1975). Assuming concrete as a homogeneous media and neglecting its microscopic character (e.g., interactions between aggregates and mortar),

the stress and strain tensors are related to each other incrementally. An initial yield surface (loading surface) is introduced to define the boundary between elastic and plastic deformations. The evolution of the loading surface during the loading history is described through a hardening rule. In order to obtain the incremental plastic strain, a flow rule is defined with either associative or non-associative nature. In addition, the concept of failure surface in the stress space (e.g., principle stresses) is adopted to detect the ultimate strength of concrete. The failure state (e.g., crushing, fracture) is assumed to be reached once the stress state of the material breaches the failure surface. The mathematical representation of the failure surface is critical since it is the failure criteria that determines the basis of concrete constitutive relations (Chen and Han, 1988). Despite the successful application of plasticity-based models, difficulties in capturing the salient features of concrete are not uncommon. For example, the strain softening response (e.g., strength degradation following an increase in strain), stiffness degradation, and energy dissipation during load cycles are not represented satisfactorily (Ameur-Moussa and Buyukozturk, 1990; Lee and Fenves, 1998). Therefore, the plasticity-based concrete constitutive models are often augmented with damage models. In the concrete model by Ameur-Moussa and Buyukozturk (1990), a bounding surface, usually coinciding with the failure surface, is introduced enclosing all the attainable stress states. The material damage accumulating during the loading (e.g., microcracking, tensile cracking, crushing, fracture) is represented through reducing the size of bounding surface isotropically. Lee and Fenves (1998) derived a scalar fracture-energy-based parameter to quantify the damage states of the material. The alternative way to the plasticity-based concrete models and their counterpart models with damage simulations is to develop uniaxial formulations so that the multiaxial stress conditions can be accounted for implicitly. This is often achieved through generating a family of curves defined by polynomial equations, where stress values can be obtained for a given strain history (Sheikh and Uzumeri 1982, Mander et al. 1988, Collins and Mitchell 1990, Saatcioglu and Razvi 1992, Chang and Mander 1994, Cusson and Paultre 1995, Attard and Setunge 1996, Palermo and Vecchio 2003). The advantage of this approach is its simplicity avoiding the complexities existing in the plasticity-based models. In this work, the

monotonic and cyclic stress vs. strain response of the concrete core of RCFT members is simulated via deriving a set of empirical nonlinear curves calibrated with respect to the experimental studies available in the literature.

3.2. Monotonic Compressive Response

In this section, the behavior of concrete inside short RCFT columns under uniform compression is discussed. The test results conducted on RCFT columns are examined and the reported data is utilized to derive a uniaxial constitutive equation under monotonically applied loadings.

When RCFT members are subjected to compressive strains, both the steel tube and the concrete core experience a lateral expansion. In the early stages of loading, the Poisson's ratio of the concrete core is less than that of the steel tube. However, as the loading proceeds, due to micro-cracking, the rate of the lateral expansion of the concrete core becomes larger than that of the steel tube. A radial interaction between the two media develops such that the steel tube restrains the concrete core to expand laterally. This interaction yields a confinement pressure acting on the concrete core, which puts the concrete core into a three-dimensional stress state and generates hoop stresses on the steel tube. The arching action, the trajectories of the confinement pressure, occurs between the corners of the tube and extends uniformly throughout the length of the columns under axial compression. The confinement effect improves the ductility of concrete. Nevertheless, it is usually not possible to see any significant enhancement in concrete strength since the confinement effect is restricted within the corner regions (Bridge, 1976, Inai and Sakino, 1996). Reinforced concrete sections with rectangular hoops also exhibit a similar type of confinement despite the fact that there exist some differences. In reinforced concrete sections, improvement in compressive strength of concrete due to confinement is not negligible and it is accounted for in many of the confined concrete models (Sheikh and Uzumeri, 1982, Mander et al., 1988). The steel tubes in RCFT members carry longitudinal stresses and lateral stresses at the same time while the rectangular hoops in reinforced concrete sections are subjected to longitudinal stresses alone. Therefore, the efficiency of confinement in RCFT members is relatively lower

than the reinforced concrete sections and it is not appropriate to apply reinforced concrete models directly for RCFT members (Zhang and Shahrooz, 1997).

The effect of confinement on the concrete core primarily depends on the lateral pressure (σ_r) provided by the transverse reinforcement. Several formulations have been proposed in the literature to calculate σ_r as summarized in Table 3-1 for both reinforced-concrete (RC) and RCFT cross-sections.

Table 3-1 Summary of Concrete Lateral Confinement Models (SI units)

<i>Section Type</i>	<i>Model</i>	<i>Confining Pressure (σ_r)</i>
RC	Mander et al. (1988)	$\sigma_r = k_e \times \rho_s \times f_{yr}$
RC	Saatcioglu and Razvi (1992)	$\sigma_r = k_e \times \rho_s \times f_{yr}$
RC	Cusson and Paultre (1993)	$\sigma_r = k_e \times \rho_s \times f_{yr}$
RCFT	Nakahara and Sakino (1998)	$\sigma_r = \frac{1}{2} \times \rho_s \times f_y \times \frac{t}{D}$
RCFT	Susantha et al. (2001)	$\sigma_r = 6.5 \times R \times \frac{(f_c')^{1.46}}{f_y} + 0.12 \times (f_c')^{1.03}$ $R = \frac{D}{t} \times \sqrt{\frac{12 \times (1 - \nu)}{4 \times \pi^2}} \times \sqrt{\frac{f_y}{E_s}}$

In all of the equations in Table 3.1, except the ones for RC sections, the lateral confinement stress is proportional to the volumetric ratio (ρ_s) and yield strength (f_{yr}) of the lateral reinforcement. The parameter k_e represents the effectiveness of confinement and it is developed as a function of the lay-out of the reinforcement. The formulations to calculate k_e exhibit a variation among the concrete models documented in the literature. In the case of RCFT members, the parameters of ρ_s and f_y can be considered as equivalent to the depth over thickness ratio (D/t) and yield strength of the steel tube (f_y), respectively. The parameter k_e of the RCFT members can be considered as unity

since the configuration of the steel tube at the perimeter of the concrete core remains constant. In Table 3.1, only the equation proposed by Susanta et al. (2001) takes into account the effect of compressive strength of concrete (f'_c) on the lateral confinement pressure. This approach is valid since the passive confinement observed in RCFT members is triggered by the expansion of the concrete core and the amount of expansion depends on the strength of the concrete core. In the Equations of Table 3.1 defined for RCFT sections, the confinement pressure is calculated as a function of f_y . This implies that the lateral reinforcement is assumed to yield at the maximum strength of the concrete core. Prior to reaching its maximum strength, normal strength concrete can develop strain levels allowing the steel tube to yield. On the other hand, it is possible that high strength concrete, due to its brittle nature, may not generate strain levels for the steel tube to start yielding. However, Cusson and Paultre (1995) and Claeson (1999) report that if the column section is well confined, even for high strength concrete, the transverse reinforcement reaches its yield strain at the compressive strength of the confined concrete. As RCFT members can be considered as well confined sections, the yield strength of the tube steel can be used as a parameter while quantifying the confinement pressure assuming yielding initiated before the concrete core attained its peak strength. Tort and Hajjar (2003) also found that yielding of the steel tube for RCFT members commonly takes place prior to reaching the peak load level, which often corresponds to a load level before crushing of the concrete core takes place. The confinement in RCFT members mainly influences the strain softening region of the concrete core. Therefore, in this region of the concrete constitutive model, the effects of the parameters D/t , f_y , and f'_c should be accounted for.

In many well developed confined concrete models in the literature (e.g., Park et al. 1972; Saatcioglu and Razvi, 1990), the stress-strain curve of confined concrete is made up of three sections including an ascending part up to the peak stress, a descending region and a constant stress region. It is possible to see a similar type of load-deformation response in axial load tests of RCFT columns, which can often be attributed

to the response of concrete core, especially for members with compact steel tubes experiencing no local buckling (Schneider, 1998; Nakahara et al., 1998; Varma 2000).

As described above, the proposed stress-strain curve for monotonic response has the shape and parameters given in Figure 3.1. The key parameters of the stress-strain curve given in Figure 3.1 are the compressive strength of concrete (f'_c), strain at peak strength (ϵ_{co}), slope of the descending region (K_c), and the stress level at the constant stress region (f_{rc}). In addition, the elastic modulus of concrete (E_c) is also required in order to construct the stress-strain curve.

Furlong (1967) reported that the tube steel and the concrete core resisted the applied loading independent of from each other, without any significant interaction, until the peak load. This shows that the concrete core confined in RCFTs behaves as plain concrete until its peak strength. Inai and Sakino (1996) also noted this behavior and treated the confined concrete as plain concrete until its peak strength is reached. Therefore, the ascending part of the proposed stress-strain diagram should represent the behavior of plain concrete, with microcracking leading to a gradual reduction of modulus until the peak stress is attained. A linear strength degradation response is assumed to take place following the attainment of the peak concrete strength. The effect of confinement displays itself in the form of enhancement in ductility providing a milder strength degradation slope. In the tests of concrete filled tube stub columns, it is observed that a residual strength is always preserved even after failure, and this behavior of RCFTs is simulated in the stress-strain behavior of concrete by f_{rc} (Nakahara et al., 1998).

Gourley and Hajjar (1994) adopted the model by Collins and Mitchell (1990) for RCFT beam-column members and obtained good correlations with the experiments. The concrete model by Collins and Mitchell (1990) was compared with that of Chang and Mander (1994) and no significant deviation was obtained between the results in the pre-peak response. The formulation of the concrete model recommended by Chang and Mander (1994) is presented in Equations 3.1 through 3.5.

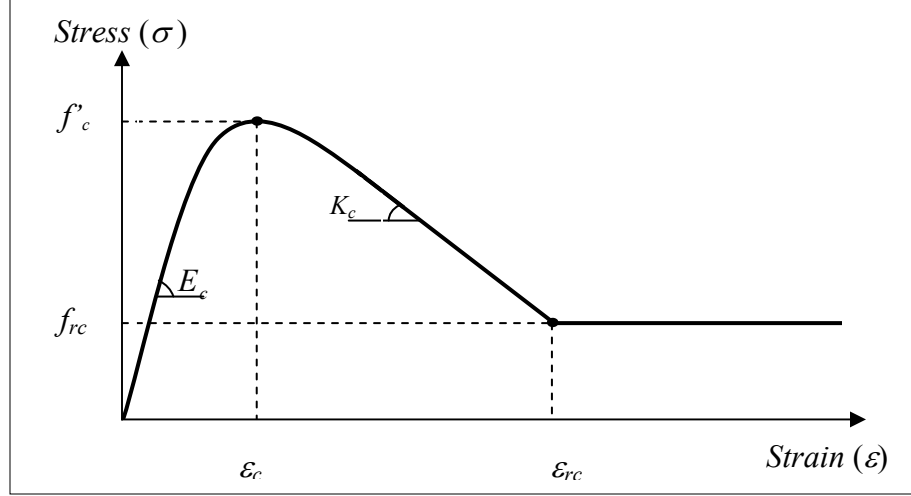


Figure 3.1 Concrete Stress-Strain Curve under Compression

$$\frac{\sigma}{f'_c} = \frac{n \times x}{D(x)}, \quad \frac{E}{E_c} = \frac{(1-x^r)}{D(x)^2} \quad [3.1a]$$

$$r = 0.19 \times f'_c - 1.9, \quad x = \left| \frac{\varepsilon}{\varepsilon_c} \right|, \quad n = \frac{r}{r-1} \quad [3.1b]$$

$$D = 1 + \left(n - \frac{r}{r-1} \right) \times x + \frac{x^r}{r-1} \quad r \neq 1 \quad [3.1c]$$

$$D = 1 + (n - 1 + \ln x) \times x \quad r = 1 \quad [3.1d]$$

$$E_c = 3320 \times \sqrt{f'_c} + 6900 \quad (\text{MPa}) \quad [3.2]$$

$$\varepsilon_c = \frac{f'_c}{E_c} \times \frac{n}{n-1} \quad (\text{MPa}) \quad [3.3]$$

The first parameter in defining the post-peak response of the concrete is the slope of the descending branch (K_c) shown in Figure 3.1. The equation defining the descending slope of concrete was derived from the computational work based on axially loaded stub column tests by Varma (2000). In addition, the results from axially loaded RCFT tests by Sakino and Yuping (1994) were utilized. Varma (2000) developed 3D finite element models of RCFT columns accounting for the interaction between steel tube

and concrete core. The finite element models estimated the experimental load-deformation response of the axially loaded column specimens with adequate accuracy. The finite element analysis results provided the data for the stress-strain response of the concrete core inside the steel tube. On the other hand, Sakino and Yuping (1994) reported experimentally obtained stress-strain data of concrete core from their experimental tests on RCFT columns. Table 3-2 summarizes the material and geometric properties of the specimens which provide the stress-strain data of concrete core.

Varma et al. (2000) investigated specimens all having 110 MPa concrete strength. Sakino and Yuping (1994) provided the test data of three groups of specimens having low, medium and high strength concrete with average f'_c values of 24 MPa, 44 MPa, and 65 MPa, respectively. Therefore, the specimens from Varma et al. (2000) and Sakino and Yuping (1994) can be examined in a total number of four different groups based on the concrete strength. Within each group, the softening slope of the concrete core (K_c) was

correlated to the parameter $R = \frac{D}{t} \times \sqrt{\frac{f_y}{E_s}} \times \frac{f'_c}{f_y}$ using linear regression as summarized in .

The parameter $R = \frac{D}{t} \times \sqrt{\frac{f_y}{E_s}} \times \frac{f'_c}{f_y}$ was adopted from Susanta et al. (2001), where

$\frac{D}{t} \times \sqrt{\frac{f_y}{E_s}}$ represents the slenderness of the steel tube and $\frac{f'_c}{f_y}$ is related to the effect of

concrete strength in the confinement pressure.

According to Figure 3.2 , for all concrete ranges, K_c increases when R gets larger. It is also evident from Figure 3.2 that the slope of the linear curves relating R to K_c gets larger as concrete strength increases. Therefore, if all the data presented in Figure 3.2 is plotted on the same graph after normalizing K_c by f'_c , a linear trend of $\frac{K_c}{f'_c}$ with respect to R can be obtained as shown in Figure 3.3. A linear curve fit is performed to the data available in Figure 3.3 and Equation 3.4 is obtained to estimate K_c with an R^2 of 0.73.

$$K_c = 332.75 \times R \times f'_c - 9.60 \times f'_c \quad [3.4]$$

As it is presented in the stress-strain curve of Figure 3.1, the concrete exhibits a constant stress region at very high strain levels due to the high level of confinement in RCFTs. The residual strength of the concrete core (f_{rc}) is also determined using the computational results by Varma (2000) and experimental results by Sakino and Yuping (1994). The available data for f_{rc} is shown in Figure 3.4. It was found that f_{rc} exhibits a decreasing trend for large values of R . A non-linear regression was performed and Equation 3.5 was derived to estimate f_{rc} with an R^2 of 0.68.

$$\frac{f_{rc}}{f'_c} = 0.32 \times R^{-0.5} \quad [3.5]$$

Table 3-2 Summary of Specimens for Concrete Stress-Strain Data¹

Reference	Type of Data	Specimen ID	D (mm)	t (mm)	D/t	f'_c (MPa)	f_y (MPa)	E_s (MPa)
Varma (2000)	Computational	SC32-80	305	8.89	34.3	110.0	560.0	197000
		SC48-80	305	6.10	50.0	110.0	660.0	194000
		SC32-46	305	8.64	35.3	110.0	257.0	197000
		SC48-46	305	5.84	52.2	110.0	473.0	204000
Sakino and Yuping (1994)	Experimental	na	175	5.65	31.0	25.2	388.5	200000
		na	175	2.92	60.0	24.9	315.9	200000
		na	175	2.30	76.1	25.5	251.1	200000
		na	175	1.64	106.7	20.9	331.6	200000
		na	175	5.65	31.0	42.9	388.5	200000
		na	175	2.92	59.9	48.3	315.9	200000
		na	175	2.30	76.1	43.6	251.1	200000
		na	175	1.64	106.7	40.7	331.6	200000
		na	175	5.65	31.0	68.1	388.5	200000
		na	175	2.92	59.9	66.7	315.9	200000
		na	175	2.30	76.1	66.7	251.1	200000
		na	175	1.64	106.7	59.8	331.6	200000

3.3. Monotonic Tensile Response

¹ E_s was not reported in the tests by Sakino and Yuping (1994), it was assumed as 200000 MPa

When subjected to tensile loads, concrete undergoes approximately a linear elastic response up to a stress level of about 80% of its peak tensile strength (Yankelevsky and Reinhardt, 1989). The initial elastic modulus often attains comparable values to that in compression. Following the attainment of the peak tensile strength, concrete experiences an abrupt strength degradation response. This is mainly attributed to the increase of microcracks between the ingredients of the concrete media. The failure state is assumed to be reached when the stress level drops to zero indicating the fully opening of a crack.

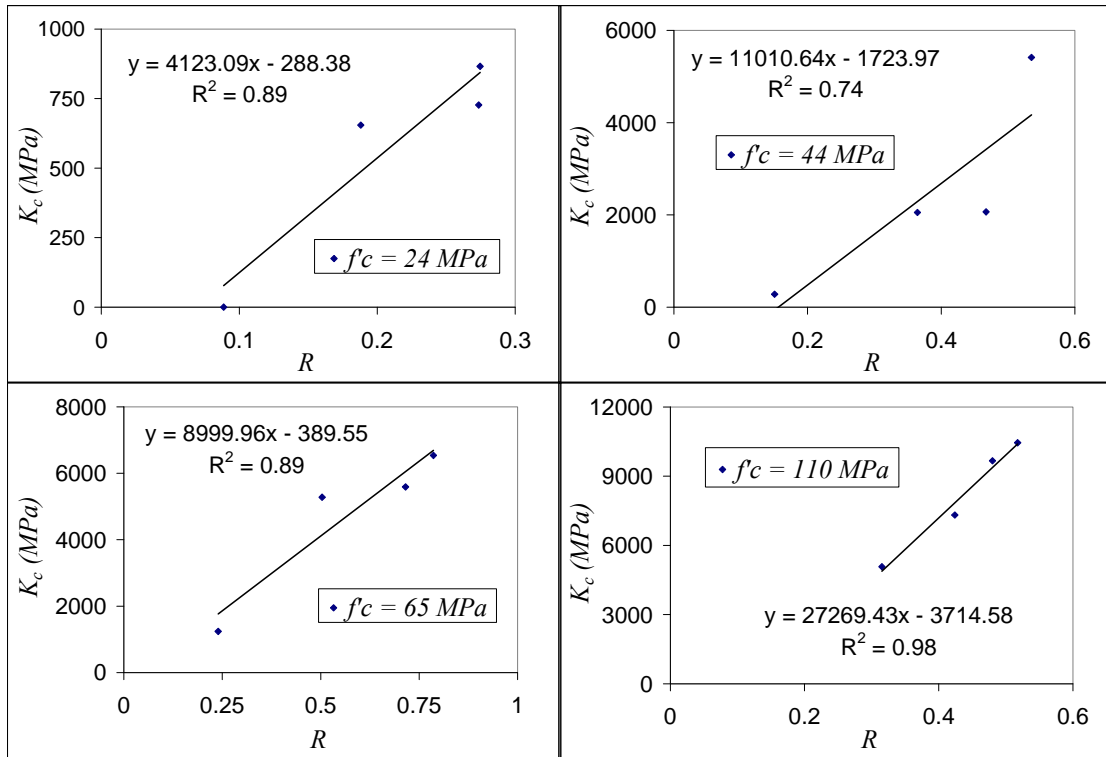


Figure 3.2 Correlation of K_c to R

In many computational models simulating the response of RCFT members, the tensile response of concrete is commonly neglected (Susantha et al., 2002, Varma et al., 2002). However, modeling the tensile response of concrete improves the accuracy of the nonlinear finite element models of RCFT members (Gourley and Hajjar, 1994). Cracking of concrete affects the distribution of stresses across the RCFT cross-section and it might influence the magnitude of deflections. The shape of the stress-strain response of concrete in tension possesses similarities to that of plain concrete in concrete. An

ascending region until the peak tensile strength is followed by a strength degradation region. However, under tensile loads the degree of nonlinearity of the ascending branch is smaller than the nonlinearity in compression. In addition, concrete experiences a more abrupt strength degradation under tensile stresses compared to the strength degradation under compressive stresses.

Due to the difficulty in testing methods to capture the unstable post-peak response in tension, tensile stress-strain models for concrete are less common than compression stress-strain models. In addition, most available models depend on parameters related to the testing methods or on parameters such as crack width that cause the concrete model to be impractical for a general purpose finite element program. Chang and Mander (1994) recommended using the equation by Tsai (1988) to simulate the tensile response of concrete as given below:

$$\sigma_t = f_t' \times \frac{n \times x}{1 + \left(n - \frac{r}{r-1} \right) \times x + \frac{x^r}{r-1}} \quad [3.6]$$

where: f_t' – tensile strength of concrete

$$x = \frac{\varepsilon}{\varepsilon_t}, \quad n = \frac{E_t \times f_c'}{f_t'}$$

E_t – elastic modulus of concrete in tension

ε_t – tensile strain value at peak stress

r – parameter to control the shape of the descending branch

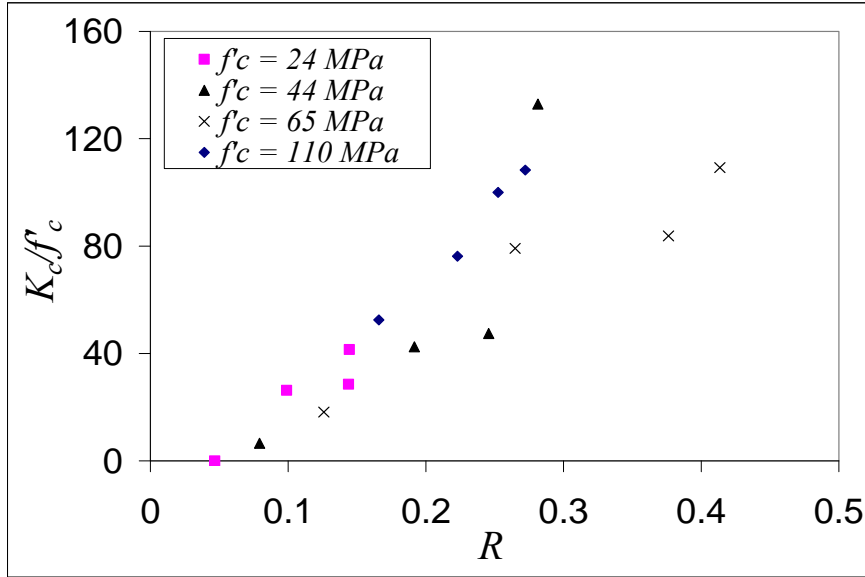


Figure 3.3 Correlation of K_c / f_c to R

Equation 3.8 was compared to the specimens tested by Gopalaram and Shah (1986). The experimental and computational stress-strain curves were found to exhibit good correlation when $r = 4.0$, as can be seen in Figure 3.5.

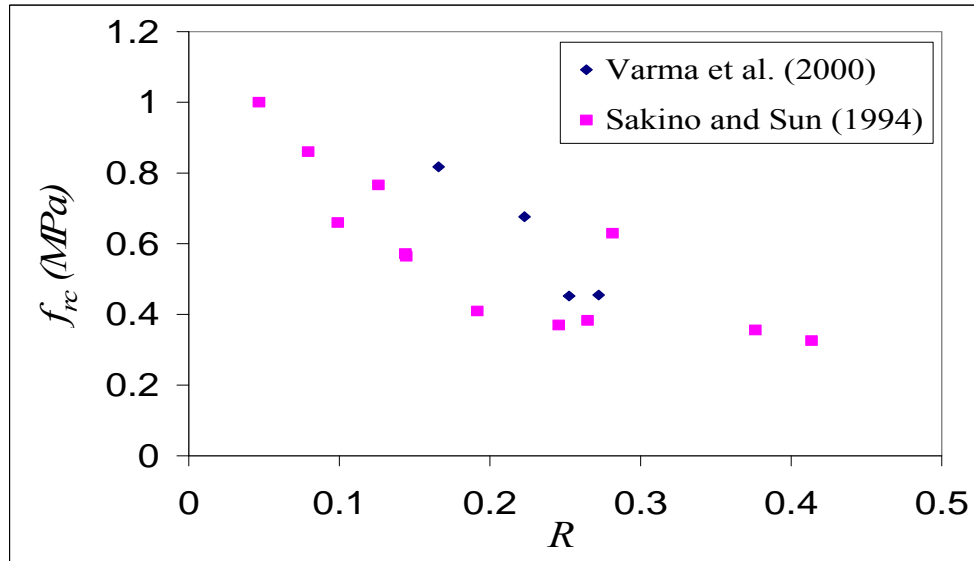


Figure 3.4 Correlation of f_{rc} to R / f_c

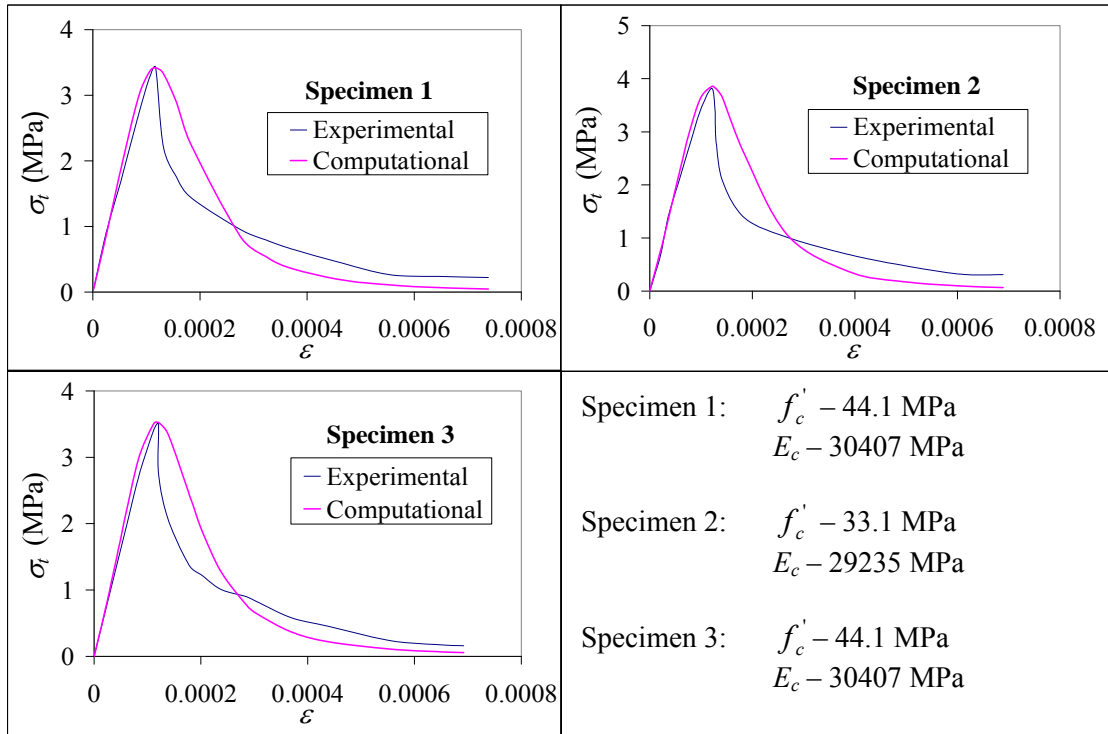


Figure 3.5 Calibration of r with Respect to the Experiments

In their direct tension tests on plain concrete specimens, Gopalatham and Shah (1986) observed that the elastic modulus of concrete in tension can be taken as equal to its monotonic counterpart. In addition, the same researchers derived Equation 3.7 to estimate tensile strength of concrete.

$$f'_t = 0.54 \times \sqrt{f'_c} \quad (\text{MPa}) \quad [3.7]$$

Examining the experimental data by Gopalatharam and Shah (1985) on the tensile strain of concrete at peak stress (ε_t), Equation 3.8 was derived to calculate ε_t as a function of f'_t and E_t .

$$\varepsilon_t = 1.23 \times \frac{f'_t}{E_t} \quad [3.8]$$

3.4. Cyclic Response of Concrete

The cyclic response concrete is investigated in numerous research studies in the literature based on theory of elasticity, theory of plasticity, plastic fracturing, and endochronic theory of plasticity (Chen and Buyukozturk, 1985; Yankelevsky and Reinhardt, 1987). Although these models are quite powerful, their high complexity leads to more simplified models having polynomial family of curves defining the cyclic behavior of concrete (Sinha et al., 1964; Karsan and Jirsa, 1969; Yankelevsky and Reinhardt, 1987; Chang and Mander, 1994; Palermo and Vecchio, 2003).

The simplified models are commonly derived from uniaxially loaded compression tests performed on short plain concrete columns or cylinders (Sinha et al., 1964; Karsan and Jirsa, 1969). The experimental results show that the cyclic stress-strain relation possesses an envelope curve bounding the unloading and reloading curves. This envelope curve can be approximately represented with the stress-strain curve obtained from monotonic tests. The unloading branch of concrete usually follows a concave nonlinear curve which has a high stiffness at the beginning and becomes flattened as the stress level decreases. The reloading branch exhibits a more complicated shape which is close to a double curvature character. However, it is commonly estimated through a family of linear curves (Sinha et al., 1964; Palermo and Vecchio, 2003). Both unloading and reloading curves become more flattened as cyclic loading progresses due to gradual stiffness degradation in the concrete from repeated cycles of concrete crushing. The intersections of the reloading and unloading curves are designated as “common points”. The common points are considered as the stability limits and stresses above these points cause additional strains. This is attributed to a drastic increase in microcracking after the common points are reached. On the other hand, the stresses at or below the common points put the stress-strain response into a closed loop.

The cyclic behavior of concrete in tension was also studied by several researchers (e.g., Gopalaratham and Shah, 1985; Yankelevsky and Reinhardt, 1989; Palermo and Vecchio, 2003). The cyclic stress-strain relation in tension also possesses an envelope curve and it approximately coincides with the stress-strain curve obtained from

monotonic tests. It is commonly observed that the loading and reloading curves in tension and in compression exhibit similar characteristics.

Behavior of concrete under random load histories is critical in nonlinear finite element analysis of RCFT structures. The chosen cyclic concrete model should be appropriate to simulate the experimental behavior of RCFT members. Gourley and Hajjar (1994) identified the following characteristics in the load-deformation response of RCFTs that can be attributed to the cyclic response of concrete.

- A decrease in the size of elastic zone (in stress-resultant-space) is evident in the tests, which is mainly caused by concrete crushing and local buckling of the steel tube.
- As cyclic loading progresses, strength degradation takes place due to concrete crushing and local buckling of the steel tube.
- RCFT members also exhibit a gradual reduction in stiffness at the later stages of cyclic loading, partly attributed to the damage accumulated in concrete.

Chang and Mander (1994) developed a concrete model that was shown to be accurate for both confined and unconfined concrete. Based on the experimental test results identified by Gourley and Hajjar (1994), this model is also considered to be appropriate to be used for RCFT members and therefore, it is implemented in this study.

The model by Chang and Mander (1994) consists of three components designated as envelope curves, connecting curves, and transition curves. Envelope curves are assumed as the backbones of the hysteretic response. Figure 3.6 illustrates the envelope curves derived in the previous section for tension and compression. Connecting curves represent the loading and unloading branches between the envelope curves. Transition curves provide the rule to shift from one connecting curve to the other going in the opposite direction. Chang and Mander (1994) proposed a single polynomial equation to represent both connecting and transition curves. If $(\varepsilon_i, \sigma_i)$ and $(\varepsilon_f, \sigma_f)$ are the strain values of the initial and final points of connecting or transition curves, the polynomial equation

defining the curve between these points is given in Equation 3.9. The derivative of Equation 3.9 produces the polynomial representation of its tangent, which can be found in Equation 3.10.

$$\sigma_{cc}(\varepsilon) = \sigma_i + (\varepsilon - \varepsilon_i) \times \left[E_i + A |\varepsilon - \varepsilon_i|^R \right] \quad [3.9]$$

$$E_{cc}(\varepsilon) = \sigma'(\varepsilon) = E_i + A(R+1) |\varepsilon - \varepsilon_i|^{R-1} \quad [3.10]$$

where: $R = \frac{E_f - E_{sec}}{E_{sec} - E_i}$

$$A = \frac{E_{sec} - E_i}{|\varepsilon_f - \varepsilon_i|^R}$$

E_i – tangent at $(\varepsilon_i, \sigma_i)$

E_f – tangent at $(\varepsilon_f, \sigma_f)$

E_{sec} – slope of secant line between $(\varepsilon_i, \sigma_i)$ and (x_f, y_f)

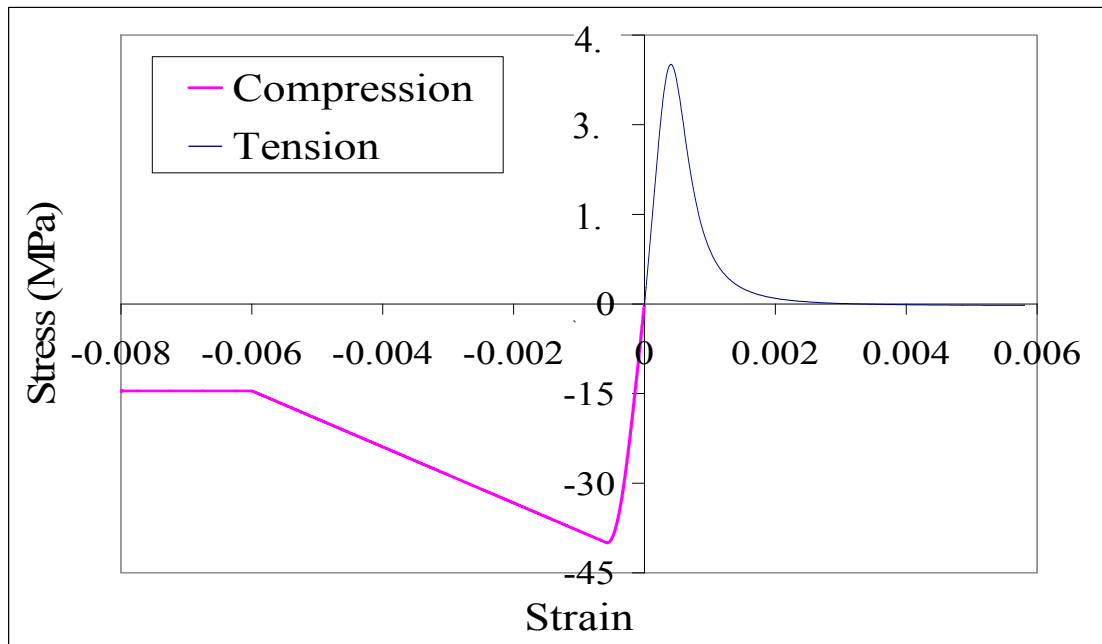


Figure 3.6 Envelope Curves of the Concrete Model

The graphical representation of the connecting and transition curves is presented in Figure 3.7. The accuracy of these curves is determined by the variables defining the coordinates and slopes at the two ends, which are often defined based on empirical equations developed by Chang and Mander (1994). The experimental tests on moderate strength concrete specimens with compressive strengths ranging from 20 MPa to 40 MPa were utilized while defining the end points of the connecting and transitions curves. However, Chang and Mander (1994) performed verification studies of the proposed equations for confined concrete specimens with compressive strengths up to 80 MPa. The empirical equations will be presented as needed while describing the cyclic rules followed by concrete. It should be noted the main assumption in developing the connecting and transition curves is that they are in single curvature. This statement forces the expression given in Equations 3.13 and 3.14 to hold as shown below:

$$\sigma_i < \sigma_{cc} < \sigma_f \quad [3.13]$$

$$(E_i > E_{sec}) \wedge (E_f < E_{sec}) \quad [3.14]$$

3.4.1. State Determination Algorithm of the Concrete Fibers

The state determination of the material fibers is often performed during force recovery phase of fiber-based nonlinear finite element solution algorithms, where the stress and stiffness of the material fibers are integrated to obtain internal forces and stiffness matrices of the elements. In Updated-Lagrangian fiber-based finite element formulations including displacement-based, force-based, and mix types, incremental strains of concrete fibers (${}_1\varepsilon$) defined with respect to the last converged configuration (C1) are added to the total strain in the last converged configuration (${}^1\varepsilon$) to obtain the total strain (${}^2\varepsilon$) in the current configuration (C2) defined with respect to C1. The equation illustrating the procedure to calculate ${}^2\varepsilon$ is given below.

$${}^2\varepsilon = {}^1\varepsilon + {}_1\varepsilon \quad [3.15]$$

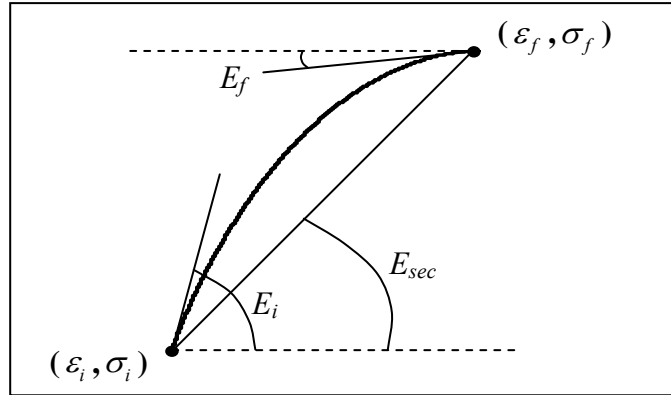


Figure 3.7 Connecting and Transition Curves of the Concrete Model

The previous strain and stress history of a material fiber is monitored through state variables, which are specific to the concrete model being used. The state variables range from stress, strain, and stiffness quantities to integer flags designating significant events experienced by the material fiber (e.g., change in direction of loading, cracking etc.). Updating the states variables is performed based on ${}^2\varepsilon$ only if it is determined that the Newton-Raphson solution step of the nonlinear solution algorithm is in a converged state.

A total of 13 rules were defined to describe the cyclic response of a concrete material fiber adopting the study by Chang and Mander (1994). Each rule states the relation between stress and strain throughout the loading history. In this study, the existing rules were fully implemented and then new rules, identified in the sections below, were developed in order to increase the breadth of the model under complicated cyclic loadings generated during nonlinear time history analysis.

In the algorithm developed to trace the cyclic stress-strain response of concrete, the state of the material fibers are decided based on the variables defined below:

1R_c – rule in C1 configuration

1R_f - cyclic rule attained before 1R_c initiated

${}^1\varepsilon$ – strain in C1 configuration

${}^2_1\varepsilon$ - strain in C2 configuration with respect to C1 configuration

- **Rule 1**

Rule 1 represents the state of the material fiber on the envelope curve defined in the compression region (see Figure 3.6, Equation 3.1 – 3.5). If no reversal exists in the strain history, the loading is compressive and the concrete fiber will retain Rule 1. Following a strain reversal, Rule 1 is recovered if the concrete fiber undergoes a compressive strain level (${}^2_1\varepsilon$) beyond the final strain level of the connecting curves that are under the reloading state. The final strain levels of the connecting curves are designated as ${}^1\varepsilon_{re}$ and ${}^1\varepsilon_{re}^*$ for full reloading and partial reloading, respectively. Full reloading and partial reloading connecting curves are described in Figure 3.8 for a sample loading history of a generic material. As it will be described in the following sections, unloading, full reloading, and partial reloading curves correspond to different cyclic rules depending on the past strain history. Figure 3.9 illustrates the possible strain histories to attain Rule 1. For example, Rule 1 can be reached following full reloading that can be defined by Rule 5, Rule 7, Rule 10, or Rule 13. It is also possible to reach Rule 1 through maintaining compressive loading after partial reloadings defined by Rule 5 and Rule 7. It should be noted whether concrete experiences full reloading by Rule 5, Rule 7, Rule 10, and Rule 13 or partial reloading by Rule 5 and 7, Rule 1 is connected to the aforementioned rules through second branch of Rule 7 introduced below.

- **Rule 2**

The envelope curve of concrete in tension, which is presented in Equation 3.6, is defined as Rule 2. Rule 2 is maintained unless there is no reversal in a tensile loading history. In the case of a load reversal, Rule 2 can be recovered only if the current strain level breaches the final strain values of the reloading curves, which are defined as ${}^1\varepsilon_{re}^+$ and ${}^1\varepsilon_{re}^{*+}$ for the full reloading and partial reloading curves, respectively. The possible strain histories for which Rule 2 can be attained are illustrated in Figure 3.10. The stress-strain rules that can be experienced prior to undergoing Rule 2 consist of

reloading curves of Rule 9, Rule 8, and Rule 6. The connection between the reloading curves and Rule 2 is always defined by the second branch of Rule 8. The details of the aforementioned reloading curves can be found in the following sections.

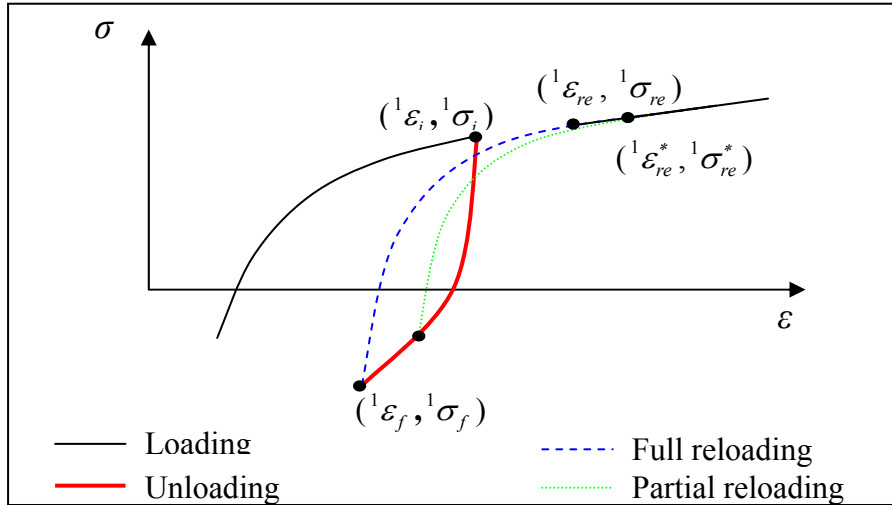


Figure 3.8 Loading, Reloading, and Unloading Curves of the Concrete Model

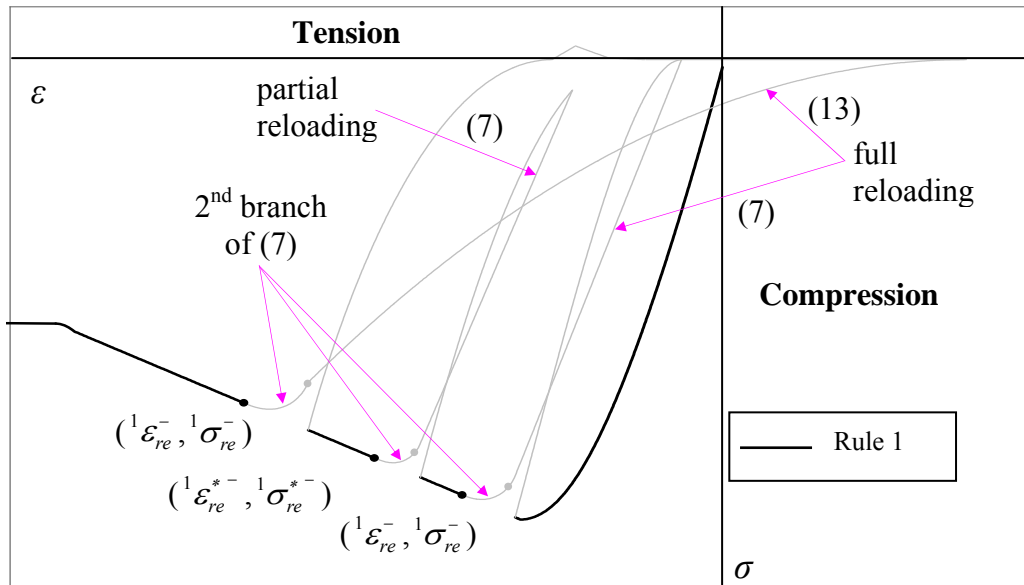


Figure 3.9 Determination of Rule 1 in the Concrete Model

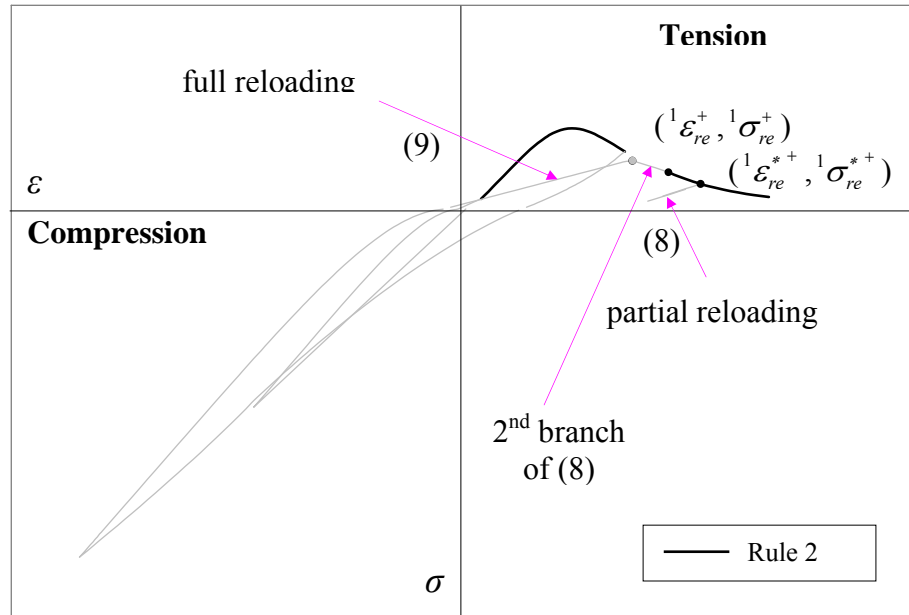


Figure 3.10 Determination of Rule 2 in the Concrete Model

- **Rule 3**

Unloading from the compression envelope curve is simulated through the connecting curve defined as Rule 3. Initiation of this branch of the concrete model is detected by tracing the sign of $\dot{\varepsilon}$, where a positive strain increment is experienced following a prior strain history of Rule 1 ($R_c=1$). In Rule 3, the strain-stress relation is determined using Equation 3.9 and 3.10 with initial and final points of $({}^1\varepsilon_{unld}^-, {}^1\sigma_{unld}^-)$ and $({}^1\varepsilon_{pl}^-, 0)$, respectively. The empirical relation to calculate ${}^1\varepsilon_{pl}^-$ can be seen in Equation 3.15. The experimental results showed that Rule 3 starts with a high tangent value, which is taken as equal to E_c (see Equation 3.2). The final point is attained with a mild slope of ${}^1E_{pl}^-$ calculated using Equation 3.16 given below. The graphical representation of Rule 3 under various strain histories can be found in Figure 3.11.

$${}^1\varepsilon_{pl}^- = {}^1\varepsilon_{unld}^- - \frac{{}^1\sigma_{unld}^-}{{}^1E_{sec}^-} \quad [3.15a]$$

(see Figure 3.2 for ${}^1E_{sec}^-$)

$${}^1E_{sec}^- = E_c \times \left(\frac{\left| \frac{{}^1\sigma_{unld}^-}{E_c \times \varepsilon_c} \right| + 0.57}{\left| \frac{{}^1\varepsilon_{unld}^-}{\varepsilon_c} \right| + 0.57} \right) \quad [3.15b]$$

(see Equation 3.2 for E_c , Equation 3.8 for ε_t)

$${}^1E_{pl}^- = 0.1 \times E_c \times \exp\left(-2 \times \left| \frac{{}^1\varepsilon_{unld}^-}{\varepsilon_c} \right|\right) \quad [3.16]$$

(see Equation 3.3 for ε_c)

- **Rule 9**

Rule 9 is the connecting curve defining the cyclic response towards the positive envelope curve following a full unloading from the negative envelope curve as described in Rule 3. The stress-strain response in Rule 9 is monitored using Equations 3.9 and 3.10, where the initial and final points are taken as $({}^1\varepsilon_{pl}^-, 0)$ and $({}^1\varepsilon_{unld}^+, {}^1\sigma_{new}^+)$, respectively. The tangent of the curve defining Rule 9 starts with a value of ${}^1E_{pl}^-$ and attains ${}^1E_{new}^+$ on the positive envelope curve. The empirical equations to calculate ${}^1\sigma_{new}^+$ and ${}^1E_{new}^+$ are given in Equations 3.17 and 3.18, respectively.

$${}^1\sigma_{new}^+ = 0.85 \times {}^1\sigma_{unld}^+ \quad [3.17]$$

$${}^1E_{new}^+ = \frac{{}^1\sigma_{new}^+}{{}^1\varepsilon_{unld}^+ - {}^1\varepsilon_{pl}^+} \quad [3.18a]$$

$${}^1\varepsilon_{pl}^+ = {}^1\varepsilon_{unld}^+ - \frac{{}^1f_{unld}^+}{{}^1E_{sec}^+} \quad [3.18b]$$

$${}^1E_{sec}^+ = E_c \times \left(\frac{\left| \frac{{}^1\sigma_{unld}^+}{E_c \times \varepsilon_t} \right| + 0.67}{\left| \frac{{}^1\varepsilon_{unld}^+ - {}^1\varepsilon_o}{\varepsilon_t} \right| + 0.67} \right) \quad [3.18c]$$

where:

${}^1\varepsilon_o$ is the offset strain (see Figure 3.12)

The values of ${}^1\varepsilon_{unld}^+$ and ${}^1\sigma_{new}^+$ in Equations 3.17 and 3.18 are obtained as shown in Figure 3.13 in the case of a full unloading from the compression envelope. The graphical representation of Rule 9 can be seen in Figure 3.14.

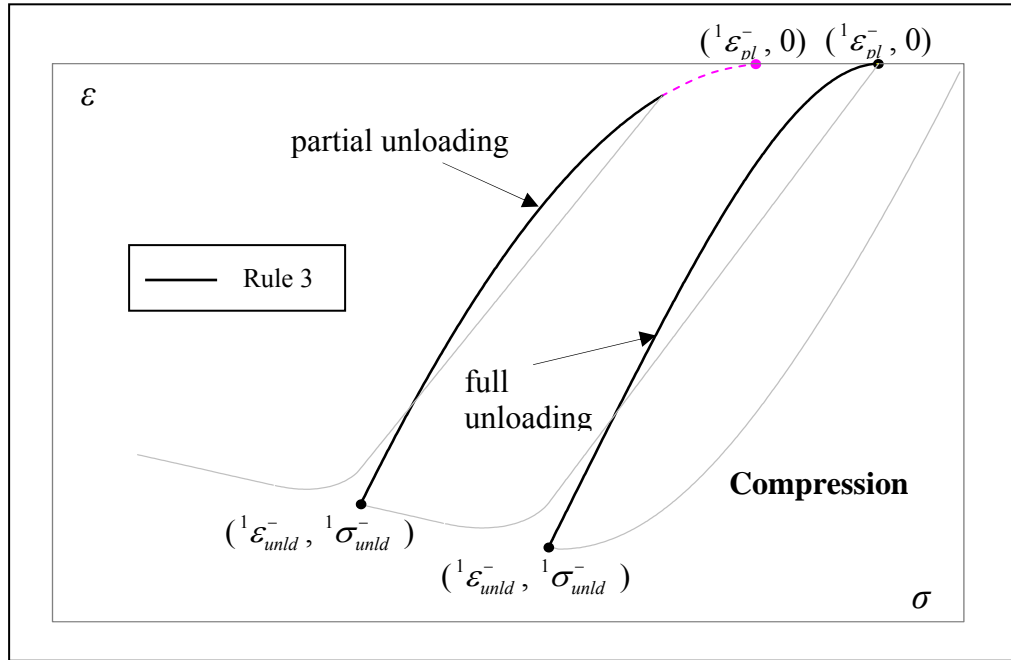


Figure 3.11 Determination of Rule 3 in the Concrete Model

- **Rule 4**

Rule 4 determines the relation between stress and strain following an unloading from the compression envelope curve. The mathematical expression of Rule 4 is stated as given in Equation 3.9 and 3.10. The cyclic response of concrete attains Rule 4 if the sign of ${}^1\varepsilon$ becomes positive when 1R_c is equal to 1. The initial and final points of the curve defining Rule 4 are $({}^1\varepsilon_{unld}^-, {}^1\sigma_{unld}^-)$ and $({}^1\varepsilon_{pl}^+, 0)$, respectively. Rule 4 starts with an initial tangent of E_c and attains E_{pl}^+ at its final point. ${}^1\varepsilon_{unld}^+$ and ${}^1\sigma_{unld}^+$ are obtained from the strain and stress points of the last converged configuration, respectively, when the cyclic response shifts to Rule 4. ${}^1\varepsilon_{pl}^+$ is calculated using Equation 3.18 while 3.19 given below is utilized to obtain E_{pl}^+ . In Figure 3.15, the graphical representation of Rule 4 is illustrated.

$$E_{pl}^+ = \frac{E_c}{\left| \frac{\mathcal{E}_{unld}^+ - \mathcal{E}_o}{\mathcal{E}_t} \right|^{1.1} + 1} \quad [3.19]$$

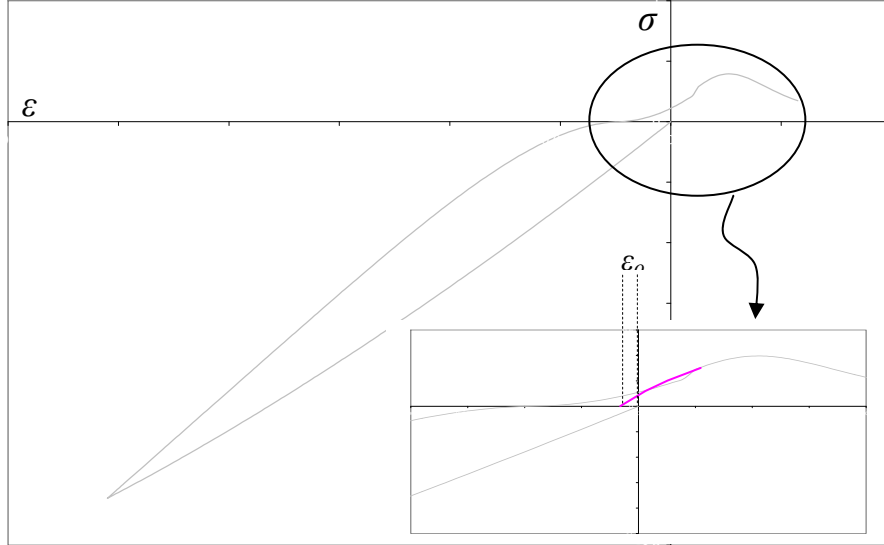


Figure 3.12 Definition of Offset Strain ${}^1\mathcal{E}_o$

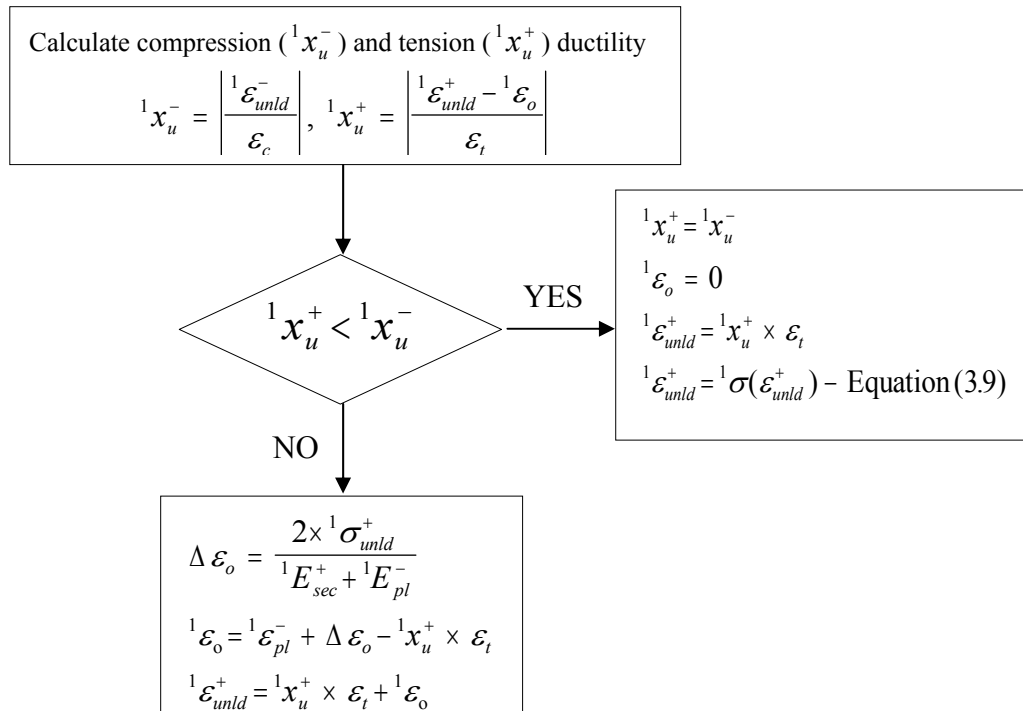


Figure 3.13 Calculation of ${}^1\mathcal{E}_{unld}^+$ and ${}^1\sigma_{new}^+$

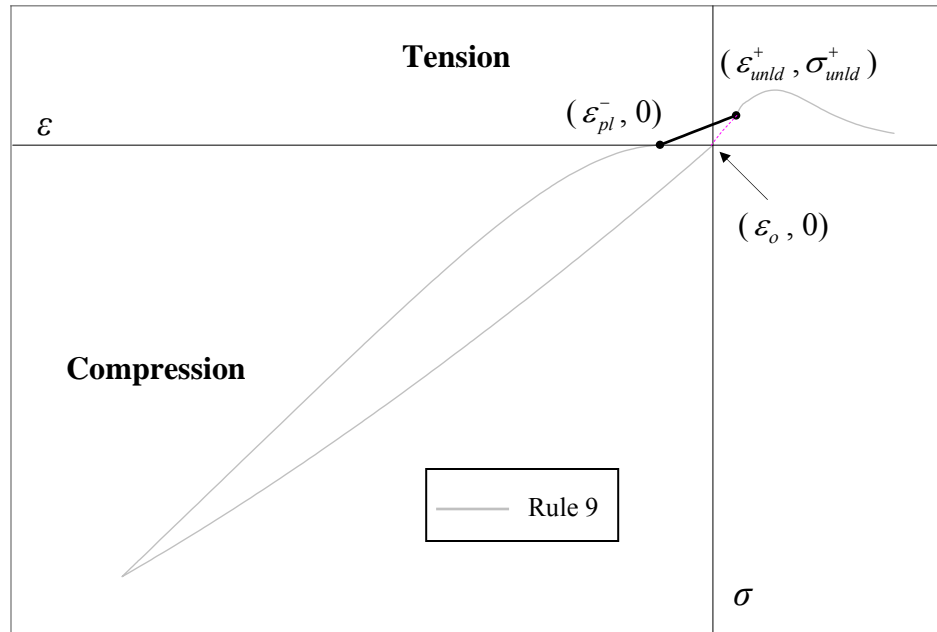


Figure 3.14 Determination of Rule 9 in the Concrete Model

- **Rule 7**

Rule 7 is developed to simulate the reloading response of concrete in compression. It is defined as a two branch curve. The first branch represents the stress-strain response with a linear nature before strain values increase significantly due to microcracking. The second branch, on the other hand, connects the reloading curve to the compression envelope beyond the stability point, where drastic increases in strain values initiate. Both branches of Rule 7 are calculated using Equations 3.9 and 3.10. The first branch ranges between $({}^1\varepsilon_r^-, {}^1\sigma_r^-)$ and $({}^1\varepsilon_{unld}^-, \sigma_{new}^{*-})$ with an initial slope of E_c and a final slope of E_{new}^{*-} . The second branch links $({}^1\varepsilon_{unld}^-, {}^1\sigma_{new}^{*-})$ and $({}^1\varepsilon_{re}^{*-}, {}^1\sigma_{new}^{*-})$, where its tangent starts with ${}^1E_{new}^{*-}$ and converges to ${}^1E_{re}^{*-}$. The first branch of Rule 7 is detected if 1R_c is equal to 3 and the sign of ${}^1\varepsilon$ becomes negative. The second branch of Rule 7 is traced when ${}^2\varepsilon$ becomes smaller than ${}^1\varepsilon_{unld}^-$ and 1R_c is equal to 3, 10, or 13 (Rule 10, 13 will be described later). The empirical

expressions to obtain ${}^1\sigma_{new}^{*-}$, ${}^1E_{new}^{*-}$, ${}^1\varepsilon_{re}^{*-}$, ${}^1\sigma_{re}^{*-}$, and ${}^1E_{re}^{*-}$ are given below. The graphical representation of Rule 7 along with the state variables can be seen in Figure 3.16.

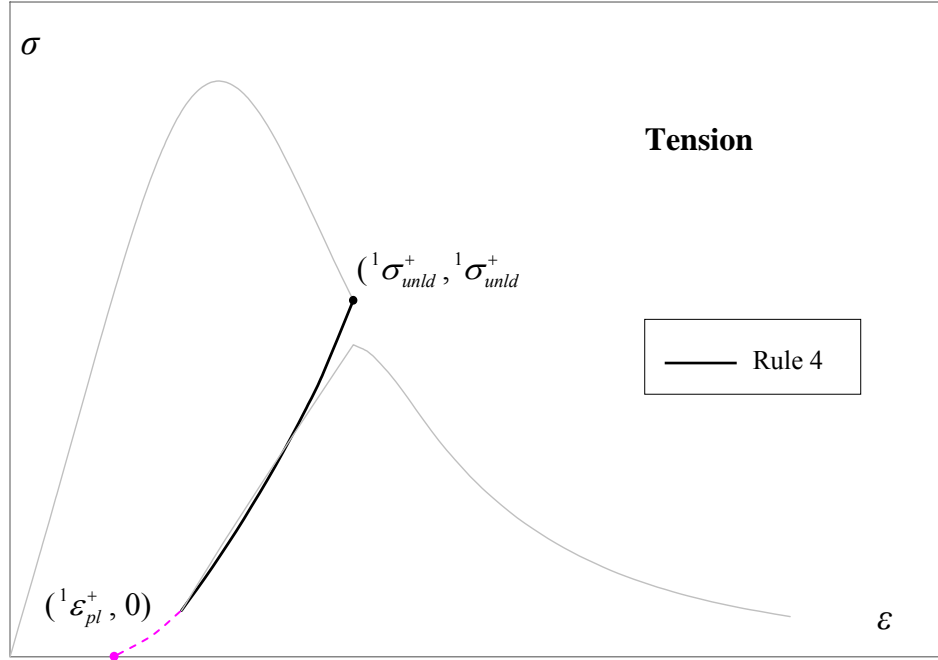


Figure 3.15 Determination of Rule 4 in the Concrete Model

$${}^1\sigma_{new}^{*-} = {}^1\sigma_{unld}^{-} - \Delta\sigma^{-} \times \frac{{}^1\varepsilon_{unld}^{-} - {}^1\varepsilon_r^{-}}{{}^1\varepsilon_{unld}^{-} - {}^1\varepsilon_{pl}^{-}} \quad [3.20a]$$

$$\Delta\sigma^{-} = 0.09 \times {}^1\sigma_{unld}^{-} \times \sqrt{\left| \frac{{}^1\varepsilon_{unld}^{-}}{\varepsilon_c} \right|} \quad [3.20b]$$

$${}^1E_{new}^{*-} = \frac{{}^1\sigma_{new}^{*-} - {}^1\sigma_r^{-}}{{}^1\varepsilon_{unld}^{-} - {}^1\varepsilon_r^{-}} \quad [3.21]$$

$${}^1\varepsilon_{re}^{*-} = {}^1\varepsilon_{unld}^{-} + \Delta\varepsilon^{-} \times \frac{{}^1\varepsilon_{unld}^{-} - {}^1\varepsilon_r^{-}}{{}^1\varepsilon_{unld}^{-} - {}^1\varepsilon_{pl}^{-}} \quad [3.22a]$$

$$\Delta \varepsilon^- = \frac{{}^1\varepsilon_{unld}^-}{1.15 + 2.75 \times \left| \frac{{}^1\varepsilon_{unld}^-}{\varepsilon_c} \right|} \quad [3.22b]$$

$${}^1\sigma_{re}^{*-} = \sigma_{cc}({}^1\varepsilon_{re}^{*-}) \quad (\text{Equation 3.1a}) \quad [3.23]$$

$${}^1E_{re}^{*-} = E_{cc}({}^1\varepsilon_{re}^{*-}) \quad (\text{Equation 3.1a}) \quad [3.24]$$

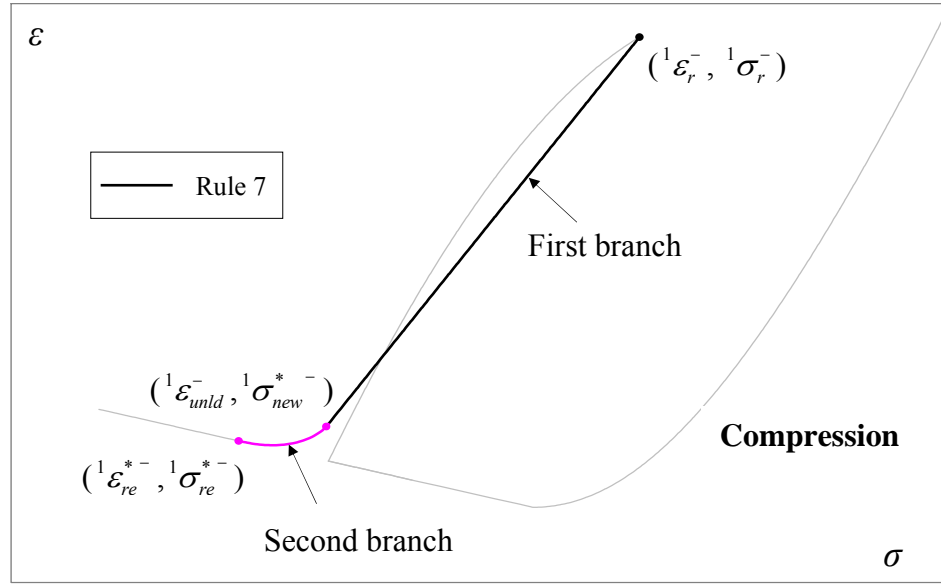


Figure 3.16 Determination of Rule 7 in the Concrete Model

- **Rule 8**

Rule 8 represents the stress-strain relation of a reloading type response following a partial unloading from the positive envelope curve. There exist two branches corresponding to the strain ranges before and after the attainment of ${}^1\varepsilon_{unld}^+$. The first branch is valid for the stress-strain points between $({}^1\varepsilon_r^+, {}^1\sigma_r^+)$ and $({}^1\varepsilon_{unld}^+, {}^1\sigma_{new}^{*+})$, where the initial and final tangents are E_c and ${}^1E_{new}^{*+}$, respectively. The second branch defines the stress-strain relation beyond $({}^1\varepsilon_{unld}^+, {}^1\sigma_{new}^{*+})$ up to $({}^1\varepsilon_{re}^{*+}, {}^1\sigma_{re}^{*+})$,

where the tangent of the curve starts with ${}^1E_{new}^{*+}$ and converges to ${}^1E_{re}^{*+}$. The empirical expressions to calculate ${}^1\sigma_{new}^{*+}$, ${}^1E_{new}^{*+}$, ${}^1\varepsilon_{re}^{*+}$, ${}^1\sigma_{re}^{*+}$, and ${}^1E_{re}^{*+}$ are given below. Rule 8 is illustrated graphically in Figure 3.17.

$${}^1\sigma_{new}^{*+} = {}^1\sigma_{unld}^+ - \Delta\sigma^+ \times \frac{{}^1\varepsilon_{unld}^+ - {}^1\varepsilon_r^+}{{}^1\varepsilon_{unld}^+ - {}^1\varepsilon_{pl}^+} \quad [3.25a]$$

$$\Delta\sigma^+ = 0.15 \times {}^1\sigma_{unld}^+ \quad [3.25b]$$

$${}^1E_{new}^{*+} = \frac{{}^1\sigma_{new}^{*+} - {}^1\sigma_r^+}{{}^1\varepsilon_{unld}^+ - {}^1\varepsilon_r^+} \quad [3.26]$$

$${}^1\varepsilon_{re}^{*+} = {}^1\varepsilon_{unld}^+ + \Delta\varepsilon^+ \times \frac{{}^1\varepsilon_{unld}^+ - {}^1\varepsilon_r^+}{{}^1\varepsilon_{unld}^+ - {}^1\varepsilon_{pl}^+} \quad [3.27a]$$

$$\Delta\varepsilon^+ = 0.25 \times {}^1\varepsilon_{unld}^+ \quad [3.27b]$$

$${}^1\sigma_{re}^{*+} = \sigma_t({}^1\varepsilon_{re}^{*+}) \quad (\text{Equation 3.6}) \quad [3.28]$$

$${}^1E_{re}^{*+} = E_t({}^1\varepsilon_{re}^{*+}) \quad (\text{Equation 3.6}) \quad [3.29]$$

- **Rule 5**

Unloading from the second branch of Rule 7 is simulated by Rule 5. This feature was not addressed in the original model by Chang and Mander (1994). Rule 5 is introduced in this study to improve the comprehensiveness of the model under complicated cyclic loadings. It was assumed that the curve defining Rule 5 can be obtained using Equations 3.9 and 3.10 where the stress-strain points at the initial and end points are $({}^1\varepsilon_{unld}^-, {}^1\sigma_{unld}^-)$ and $({}^1\varepsilon_{pl}^-, 0)$. The tangent of the curve starts with E_c and converges to E_{pl}^- . ${}^1\varepsilon_{unld}^-$ and ${}^1\sigma_{unld}^-$ are assumed to be the strain and stress values at the last converged step, respectively when 1R_c is equal to 7 and the sign of ${}_1\varepsilon$ becomes positive. ${}^1\varepsilon_{pl}^-$ and ${}^1E_{pl}^-$ can be calculated using Equations 3.15 and 3.16, respectively. The graphical representation of Rule 5 can be found in Figure 3.18.

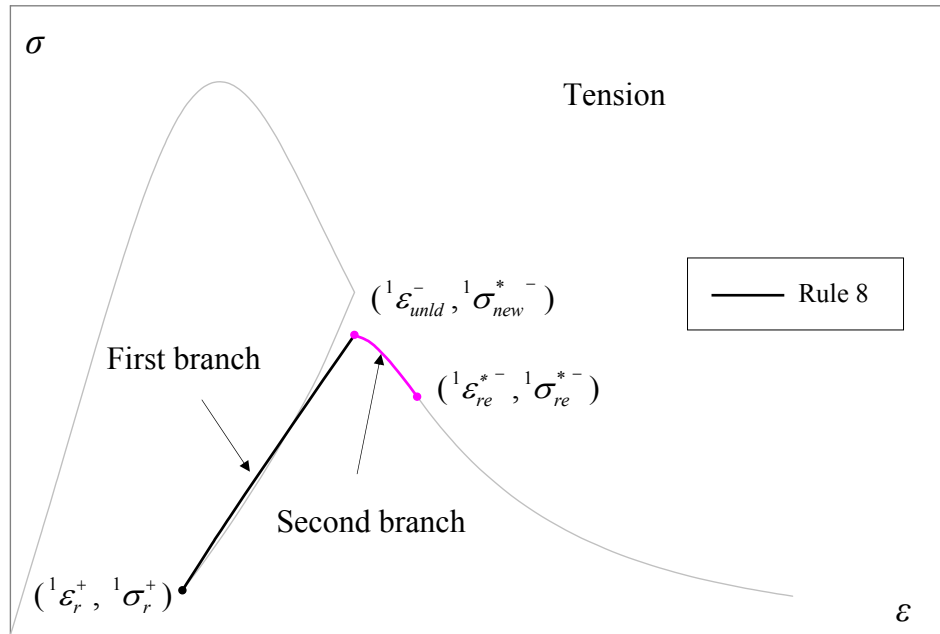


Figure 3.17 Determination of Rule 8 in the Concrete Model

- **Rule 5***

The reloading type of connecting curve linking the unloading curve of Rule 5 to the negative envelope is defined as Rule 5* as shown in Figure 3.19. It is assumed that Rule 5* simulates the cyclic response of concrete between the stress-strain points of $({}^1\varepsilon_r^-, {}^1\sigma_r^-)$ and $({}^1\varepsilon_{unld}^-, {}^1\sigma_{new}^{*-})$. The tangent of the curve representing Rule 5* starts with E_c and converges to ${}^1E_{new}^{*-}$. ${}^1\varepsilon_r^-$ and ${}^1\sigma_r^-$ are obtained as the strain and stress points at the last converged step, respectively when 1R_c is equal 5 and the sign of ${}^1\varepsilon$ becomes positive. ${}^1\sigma_{new}^{*-}$ and ${}^1E_{new}^{*-}$ are calculated using Equations 3.19 and 3.20.

- **Rule 6**

Rule 6 defines the stress-strain response of concrete in the case of an unloading from the second branch of Rule 8. It is represented using the expressions in Equations 3.9 and 3.10. The unloading type of response from Rule 8 was not described by Chang and Mander (1994). However, it is included in the current concrete model for the sake of comprehensiveness. In Rule 6, the stress-strain points lie between $({}^1\varepsilon_{unld}^+,$

${}^1\sigma_{unld}^+$) and $({}^1\varepsilon_{pl}^+, 0)$. The tangent of the curve simulating Rule 6 starts with E_c and converges to E_{pl}^+ . ${}^1\varepsilon_{unld}^+$ and ${}^1\sigma_{unld}^+$ are taken as the converged strain and stress points, respectively when 1R_c is equal to 8 and the sign of ${}^1\varepsilon$ becomes negative. ${}^1\varepsilon_{pl}^+$ and E_{pl}^+ are obtained using Equations 3.18 and 3.19, respectively. Figure 3.20 presents the graphical representation of Rule 6.

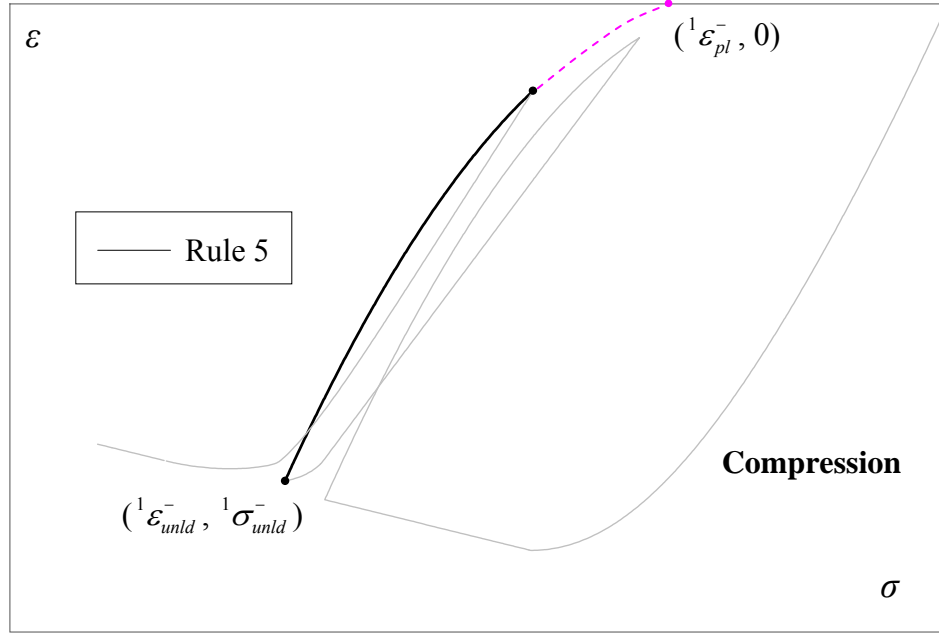


Figure 3.18 Determination of Rule 5 in the Concrete Model

- **Rule 6***

Rule 6* is devised to simulate any strain reversal that takes place when the stress-strain response is following Rule 6. The reloading type curve defined for Rule 6* is expressed using Equations 3.9 and 3.10. The initial and final points of Rule 6* are taken as $({}^1\varepsilon_r^+, {}^1\sigma_r^+)$ and $({}^1\varepsilon_{unld}^+, {}^1\sigma_{new}^{*+})$, respectively. The tangent of the curve representing Rule 6* ranges from E_c to E_{new}^{*+} . The values ${}^1\varepsilon_r^+$ and ${}^1\sigma_r^+$ are determined from strain and stress values of the last converged step when 1R_c is equal to 6 and the sign of ${}^1\varepsilon$ becomes negative. ${}^1\sigma_{new}^{*+}$ and E_{new}^{*+} are determined using Equations 3.25 and 3.26. Rule 6* is illustrated graphically in Figure 3.21 for a representative strain history.

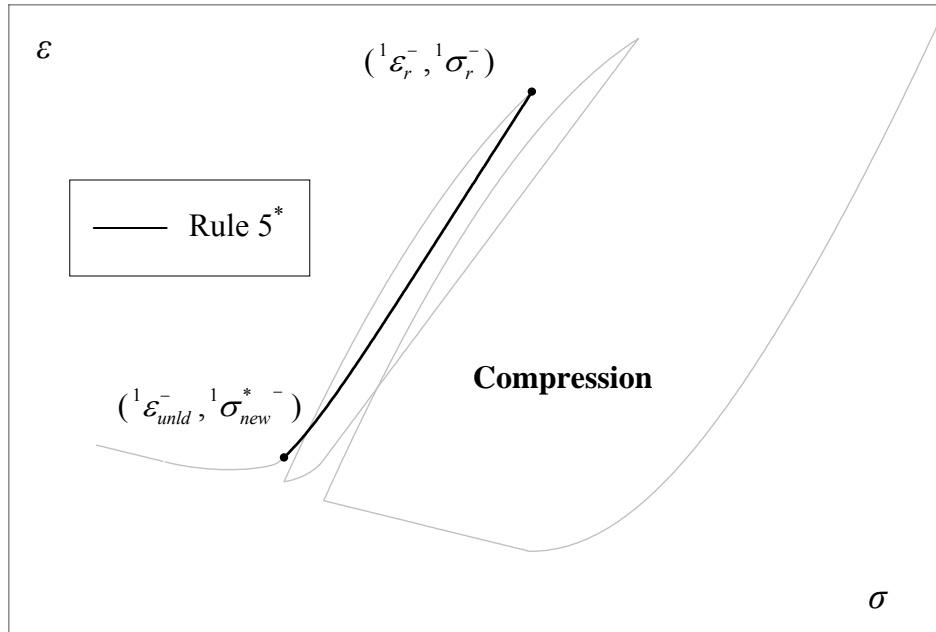


Figure 3.19 Determination of Rule 5* in the Concrete Model

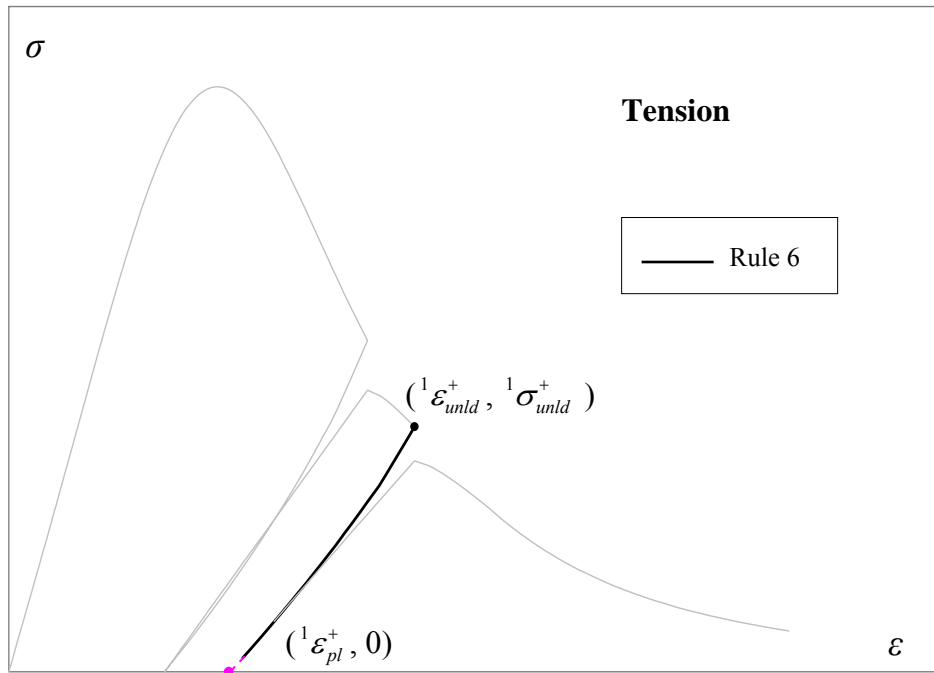


Figure 3.20 Determination of Rule 6 in the Concrete Model

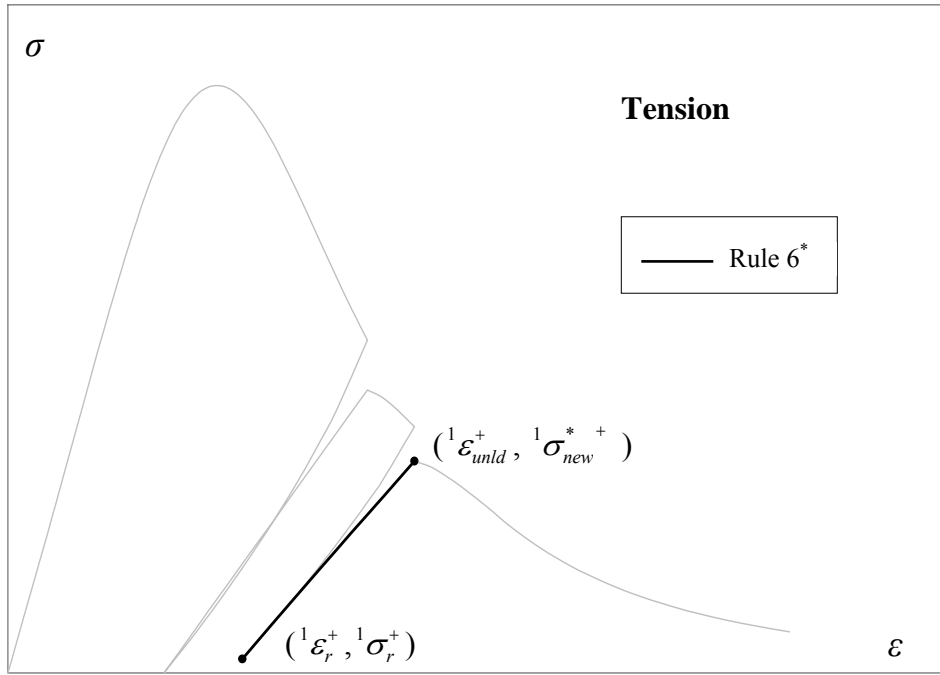


Figure 3.21 Determination of Rule 6* in the Concrete Model

- **Rule 10**

A full unloading from the positive envelope curve is connected to the negative envelope curve through Rule 10. Rule 10 is expressed using Equations 3.9 and 3.10 with initial and final points of $({}^1\varepsilon_{pl}^+, 0)$ and $({}^1\varepsilon_{unld}^-, {}^1\sigma_{new}^-)$, respectively. Having ${}^2\varepsilon$ smaller than ${}^1\varepsilon_{pl}^+$ when 1R_c is equal to 4, it is decided that the cyclic response of concrete attains Rule 10. The tangent of the curve defining Rule 10 starts with ${}^1E_{pl}^+$ and reaches E_{new}^- at its final point. ${}^1\varepsilon_{unld}^-$ is determined from the previous strain history when unloading took place from the negative envelope. ${}^1\varepsilon_{pl}^+$, and ${}^1E_{pl}^+$ are obtained from Equations 3.18 and 3.19. ${}^1\sigma_{new}^-$ and E_{new}^- are calculated using Equation 3.30, 31 given below, respectively. Figure 3.22 illustrates the stress-strain curve simulated by Rule 10 for a representative strain history.

$${}^1\sigma_{new}^- = {}^1\sigma_{unld}^- - \Delta\sigma^-, \Delta\sigma^- = 0.09 \times {}^1\sigma_{unld}^- \times \sqrt{\left| \frac{{}^1\varepsilon_{unld}^-}{\varepsilon_c} \right|} \quad [3.30]$$

$$E_{new}^- = \frac{\sigma_{new}^-}{\varepsilon_{unld}^- - \varepsilon_{pl}^-} \quad [3.31]$$

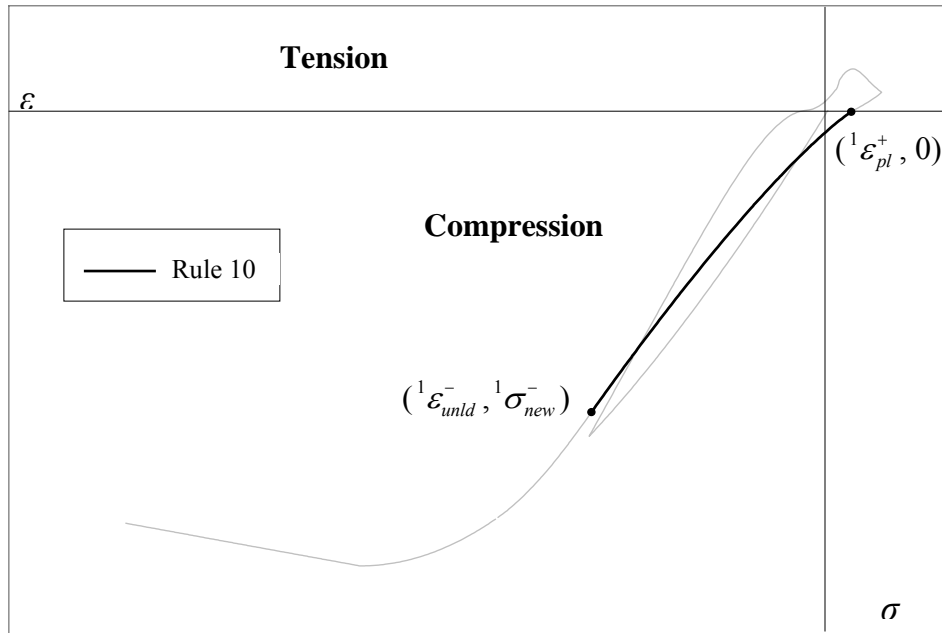


Figure 3.22 Determination of Rule 10 in the Concrete Model

- **Rule 13**

Similar to Rule 10, Rule 13 also extends the full unloading in the tension region to the negative envelope curve in the compression region. However, Rule 13 becomes active once the tensile strength of concrete vanishes. Therefore, it starts on the strain axis at point $(^1\varepsilon_r^+, 0)$ and attains $(^1\varepsilon_{unld}^-, ^1\sigma_{new}^-)$. $^1\varepsilon_r^+$ is the strain level at the last converged configuration before Rule 13 initiates with a negative value of $^1\varepsilon$ following concrete cracking with zero tensile strength. $^1\varepsilon_{unld}^-$ is obtained from the previous strain history and Equation 3.30 is used to calculate $^1\sigma_{new}^-$. The tangent of the curve defining Rule 13 starts with a zero slope and reaches to a level of E_{new}^- given in Equation 3.31. Rule 13 is illustrated graphically in Figure 3.23 for a representative strain history.

- **Rules 11 and 12**

Rule 11 and 12 are defined to simulate the unloading type of behavior from Rule 9, Rule 10, and Rule 13. Both rules were developed in this work with two linear branches where an unloading type of response is followed by a reloading type of response in the opposite direction. The unloading branch is assumed to take place with a slope of E_c at point $({}^1\varepsilon_r^+, {}^1\sigma_r^+)$ in the tension region or at point $({}^1\varepsilon_r^-, {}^1\sigma_r^-)$ in the compression region. Then, the reloading branch continues until the points of $({}^1\varepsilon_r^+, {}^1\sigma_r^+)$ and $({}^1\varepsilon_r^-, {}^1\sigma_r^-)$ in the tension and compression regions, respectively. As presented in Figures 3.24 and 3.25, the points defining Rule 11 and Rule 12 are obtained by monitoring the previous strain history. Rules 11 and 12 do not exist in the original model by Chang and Mander (1994). However, similar rules were developed based on Equations 3.9 and 3.10. In this study, linear approximations are introduced to derive Rule 11 and 12. This approach helps avoid numerical difficulties, which require implementation of special finite element techniques such as subincrementation.

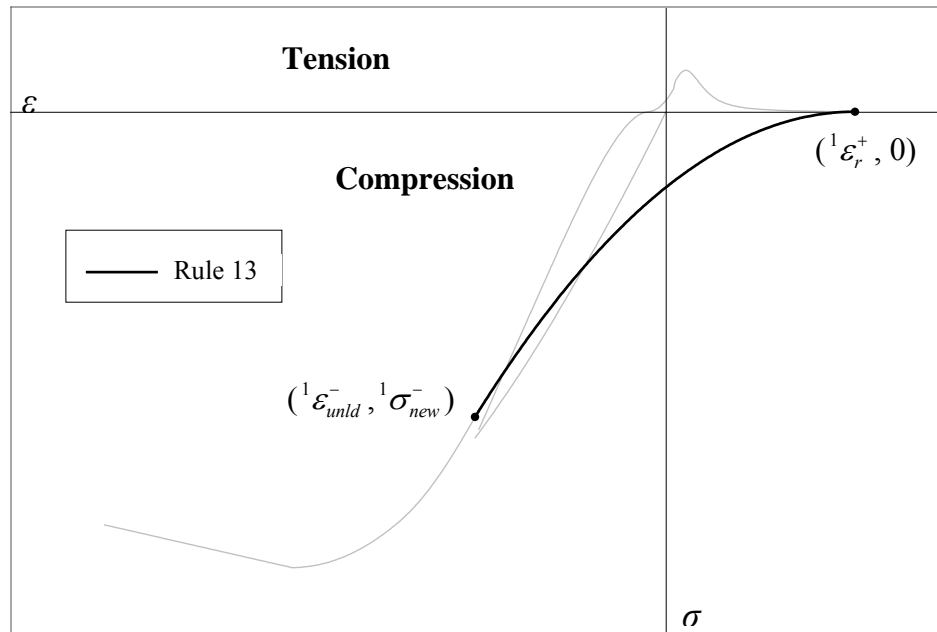


Figure 3.23 Determination of Rule 13 in the Concrete Model

3.5. Numerical Simulation Examples for Cyclic Concrete Model

The concrete model by Chang and Mander (1994) was implemented in the current work and compared to a wide range of experiments for both plain concrete and confined concrete from the literature. Experiments conducted on concrete cylinders, cubes, or short concrete columns under uniaxial pure compression were studied. The computational model was developed in OpenSees through analyzing a short truss element under a given displacement history. Good correlation was achieved between the experimental and computational results, as can be seen from the sample of results from Sinha et al. (1964), Okamoto (1976), Karsan and Jirsa (1984) and Mander et al. (1984) presented in Figures 3.26 through 3.30. Sinha et al. (1964) conducted tests on 15.2 x 30.5 cm concrete cylinders with a compressive strength of 28 MPa. The specimen by Karsan and Jirsa (1984) was a rectangular 7.62 x 12.7 cm plain concrete cube and the compressive strength of the concrete was 28 MPa. Mander et al. (1984) tested a spirally reinforced-concrete circular column. The specimen had a diameter of 19.7 in and a compressive strength of concrete of 28 MPa.

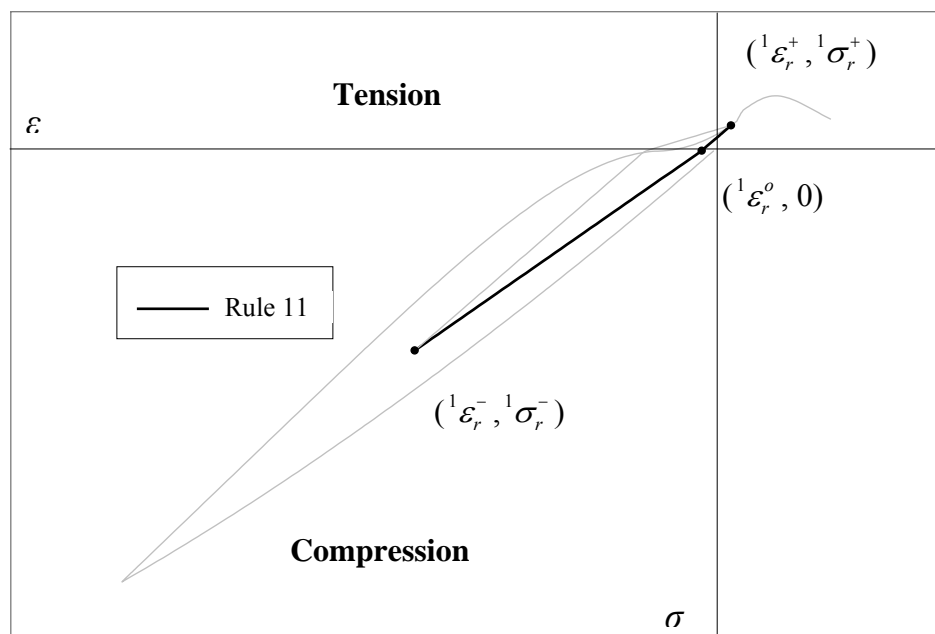


Figure 3.24 Determination of Rule 11 in the Concrete Model

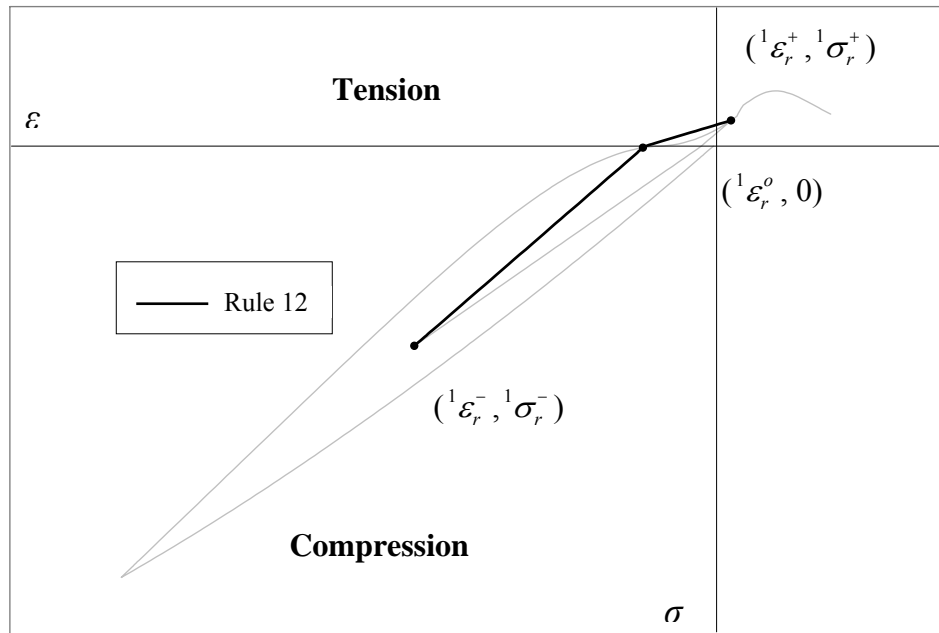


Figure 3.25 Determination of Rule 12 in the Concrete Model

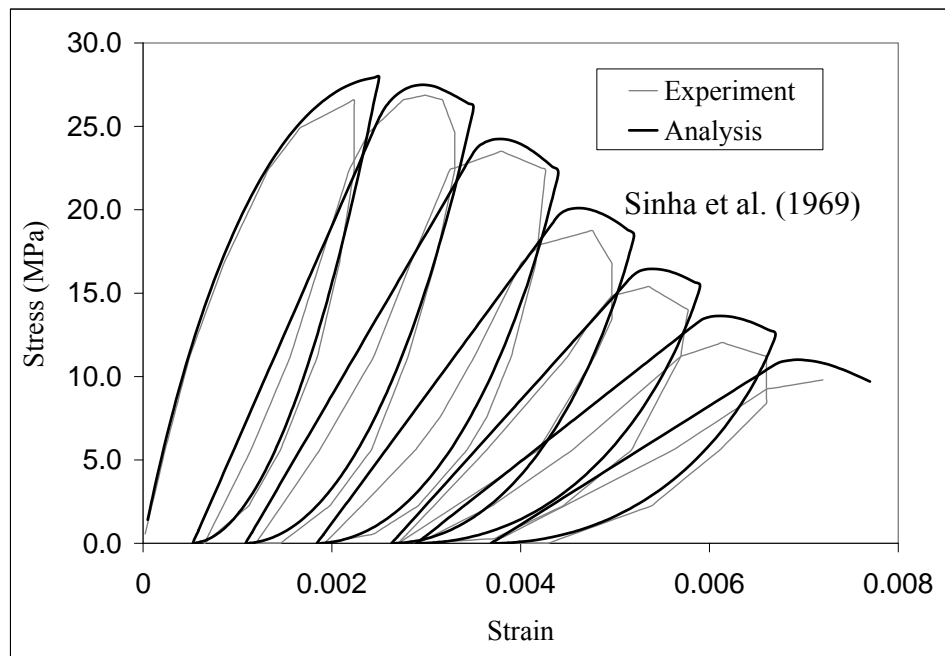


Figure 3.26 Comparison of Experimental and Analytical Results for Unconfined Concrete (Karsan and Jirsa, 1969)

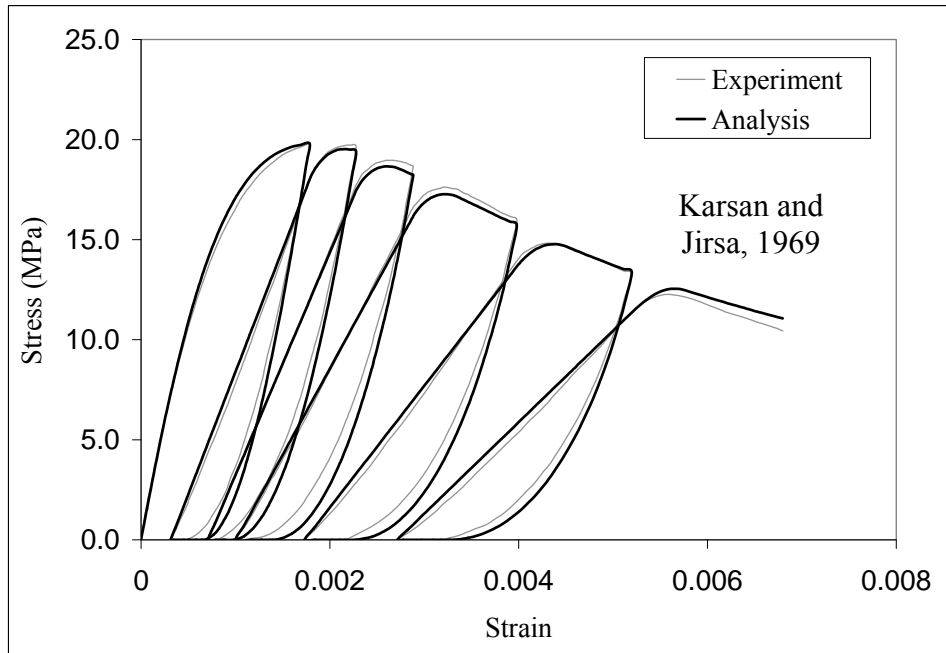


Figure 3.27 Comparison of Experimental and Analytical Results for Unconfined Concrete (Sinha et al. 1964)

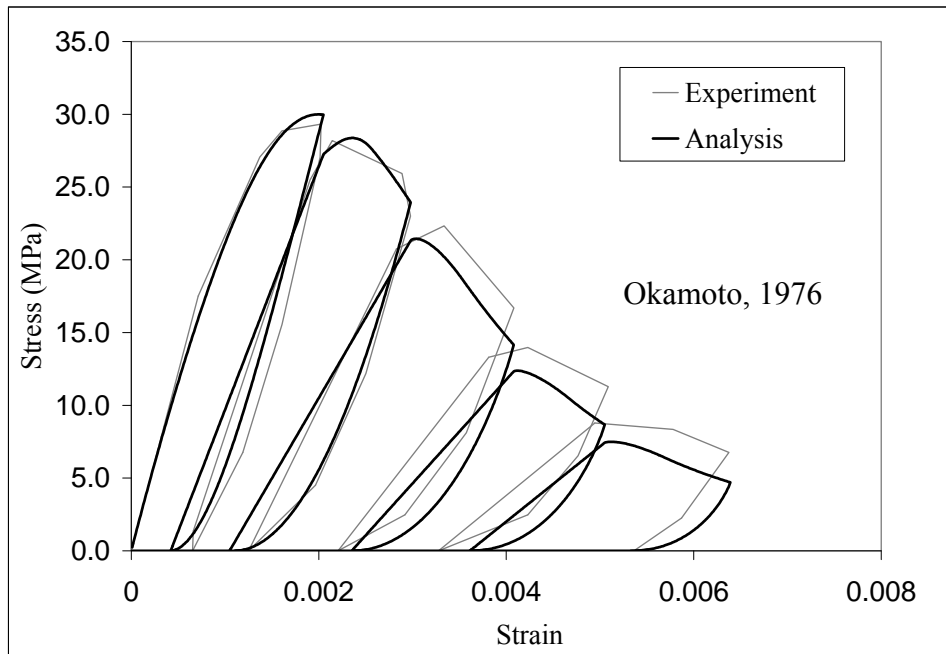


Figure 3.28 Comparison of Experimental and Analytical Results for Unconfined Concrete (Sinha et al. 1964)

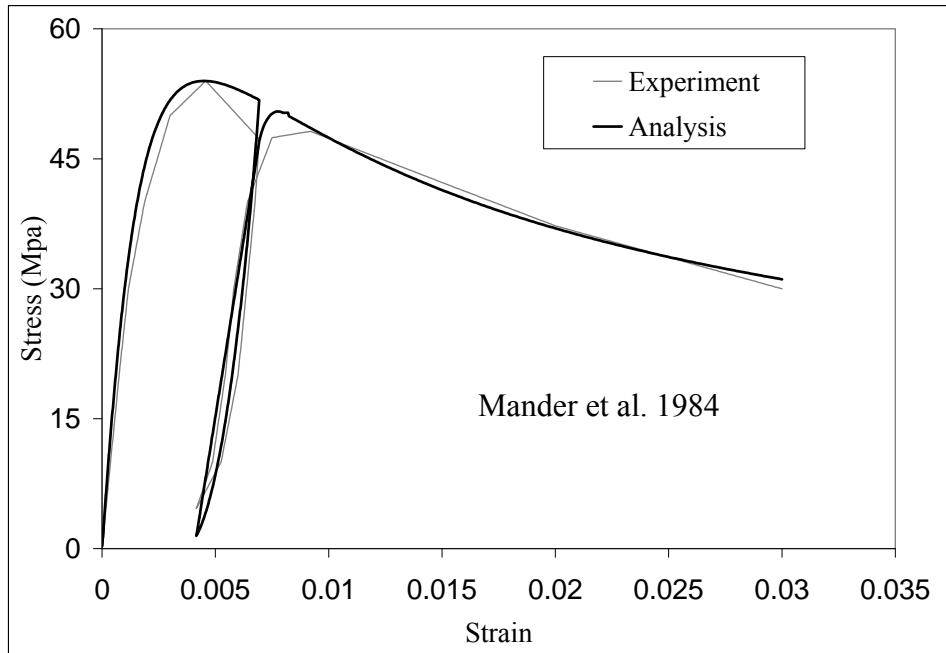


Figure 3.29 Comparison of Experimental and Analytical Results for Confined Concrete (Mander et al., 1984)

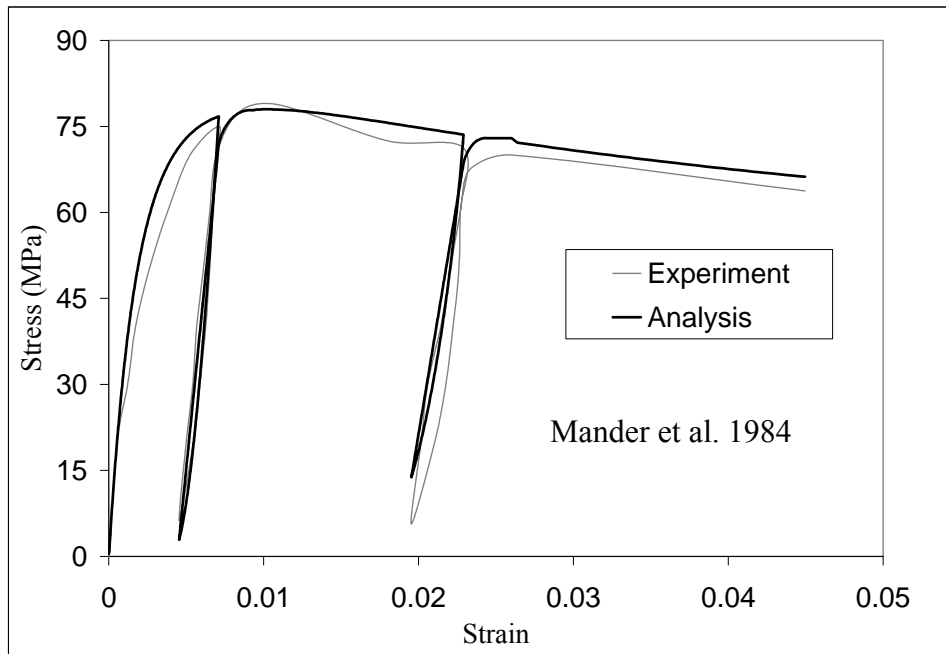


Figure 3.30 Comparison of Experimental and Analytical Results for Confined Concrete (Mander et al., 1984)

Chapter 4

4. Uniaxial Cyclic Steel Constitutive Model for RCFT Members and Steel Girders

4.1. Introduction

Cyclic excursions under earthquake loadings in RCFT beam-columns and steel girders in composite frames create complex strain histories in steel fibers. Developing a refined steel constitutive model requires capturing the loading history dependency and cyclic characteristics observed in the experimental tests. Constitutive relations derived as explicit functions of stress and strain are commonly utilized in nonlinear analysis of steel and reinforced concrete structures (Ramberg and Osgood, 1943; Menegotto and Pinto, 1973; Balan et al., 1998). Alternatively, the incremental relation between stress and strain may be established based on a set of hardening and flow rules (Dafalias and Popov, 1975; Cofie and Krawinkler, 1985; Mizuno et al., 1991; Shen et al., 1995). In these formulations, the cyclic characteristics of steel are represented by introducing internal variables and incorporating them with the constitutive relations.

Experimental research studies performed on RCFT members exhibited the following features that can be attributed to the cyclic response of the steel tube (Gourley and Hajjar, 1994; Hajjar et al., 1997). The steel constitutive model adopted to simulate the cyclic load-deformation behavior of RCFT members should be comprehensive enough to capture these characteristics including.

- Elastic unloading following a load reversal
- Decreasing elastic zone and gradual stiffness reduction as a result of cyclic loading
- Bauschinger effect causing a reduction in the yield stress when a strain history in one direction is followed with that in the opposite direction

- A bounding stiffness that is attained near the end of the tests due to the stabilizing action of the steel tube
- Local buckling of the steel tube

Steel fracture is currently neglected in this work, as RCFTs are robust members that rarely fracture until very late in cyclic loading histories. In the current research study, the emphasis will be placed on cold-formed steel tube sections. Therefore, the effects of the cold-forming process given below should also be considered in the steel model together with the aforementioned features.

- Smooth transition between elastic and plastic response, rather than formation of a significant yield plateau
- Gradient of the yield stress along the perimeter of the steel tube

Hajjar et al. (1998a, 1998b) developed a multiaxial bounding surface plasticity model for nonlinear analysis of RCFT members. An inner loading surface was introduced defining the boundary between elastic and plastic response. The stress state was assumed to be elastic if it remains inside the loading surface. The bounding surface enclosed the loading surface and the degree of plasticity attained during the loading history was expressed as function of the distance between the loading and bounding surfaces. Auxiliary surfaces were also defined to achieve a better prediction of the plastic modulus. The surfaces had the property of translation and expansion based on a set of hardening rules to capture strain hardening response and the Bauschinger effect. The effect of cold forming was incorporated into the model through assuming an initial plastic strain. Different magnitudes of initial strain were assumed for the corner and flat regions of the steel tube. The model by Molodan and Hajjar (1998) was calibrated with respect to coupon tests and verified against experimental studies ranging from individual RCFT beam-columns to 3D cruciform frames with RCFT columns and steel girders.

Varma (2000) and Domenech et al. (2002) derived a uniaxial cyclic steel constitutive models for RCFT members, where stress and strain are related to each other by defining a family of linear functions. The model had the capability of accounting for strain hardening, Bauschinger effect, biaxial stress state of the steel tube, and local buckling. The internal variables describing the compression envelope of the model were

obtained through extracting effective stress-strain curves from 3D continuum analysis of short RCFT columns under monotonic compressive loading. The model is verified with respect to RCFT beam-column tests under monotonic and cyclic loadings.

The stress-strain model employed in this research study is adopted from the uniaxial bounding surface model by Mizuno et al. (1991) and Shen et al. (1995). The envelope curves in tension and compression were modified based on experimental test results on RCFT members. In addition, new cyclic rules were introduced to account for the effect of local buckling. In the following sections, the key features of the model are documented in detail and several verification examples are presented to illustrate the performance of the model.

4.2. Monotonic Response

RCFT members exhibit a wide range of failure characteristics depending on the geometric and material properties of the specimens. For example, slender and high strength RCFT members are often susceptible to flexural buckling without exhibiting significant local damage states (except under the large deformations that are seen at incipient buckling). On the other hand, short RCFT members attain their failure state through experiencing the limit states of yielding of the steel tube, concrete crushing, and local buckling of steel tube. Therefore, the behavior of short RCFT members provides detailed insights to the constitutive models to be adopted both for the steel tube and the concrete core.

Based on the response of short RCFT columns under concentric compressive loading, the compression envelope of the steel tube is assumed to consist of four distinct regions. A linear elastic branch is maintained until the proportional limit is breached. The yielding stress is attained following a smooth nonlinear transition region. The yielding stress is preserved with a mild hardening slope until the initiation of local buckling. A linear strength degradation response is assumed once local buckling damage state is reached. At high strain levels, a constant stress response is attained.

The tension envelop curve is often assumed to be identical to its counterpart in compression (Balan et al., 1998). However, the linear strength degradation response due

to local buckling and the following constant stress region are not modeled. Figure 4.1 illustrates the compressive and tensile envelope curves adopted for the cyclic stress-strain response of the steel tube.

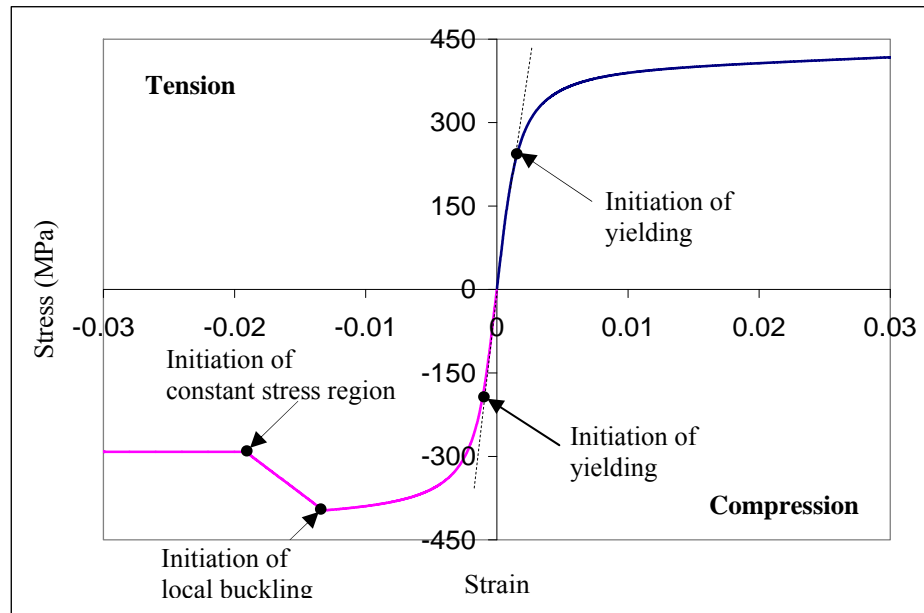


Figure 4.1 Envelope Curves of the Steel Model

The stress-strain response obtained from coupon tests of cold-formed steel sections exhibits a low proportional limit with no distinct yield plateau and transition region to hardening. Lu and Kennedy (1994) reported proportional limits at stress levels as low as 25% of the yield stress determined according to 2% offset rule. On the other hand, proportional limits more than 90% of the yield stress were reported in the tests by Karren (1967). Proportional limits on the order of 50% were also reported by Clarke and Hancock (1991) and Furlong (1968) for both corner and flat regions. This premature reduction of tangent modulus of steel is attributed to the effect of residual stresses that are generated as a result of the cold-forming process. Two types of residual stress patterns exist due to cold forming process including membrane residual stresses and through thickness residual stresses (Sherman, 1992). Membrane residual stresses exhibit a gradient around the perimeter of the steel tube and they represent the average values of through thickness residual stresses in the longitudinal direction around steel tube perimeter. The magnitude of membrane residual stresses is often small and they can be

assumed to be zero (Sully and Hancock, 1996). Through thickness residual stresses are also known as bending residual stresses and vary from tension to compression across the tube thickness. The magnitude of bending residual stresses can go up to the yield stress level. Despite their nonlinear nature, the through thickness residual stress gradient is usually assumed to be linear (Sherman 1992; Davison and Birkemoe, 1983). The welding residual stresses are observed at the regions close to the seam weld location and their magnitude can also reach to very high levels. However, due to their localized nature, it is also common to neglect welding residual stresses (Molodan and Hajjar, 1998). Therefore, in analytical modeling of cold-formed sections, only the through thickness type residual stresses needs to be accounted for. One approach to simulate the effect of cold forming is to derive a nonlinear relation to represent the response between the proportional limit and the yielding point (Davison and Birkemoe, 1983; Yan-Lin, 1992). However, since the stress-strain response until yielding is defined in two segments, it becomes difficult to adopt this method into a cyclic constitutive model that is based on a set of hardening rules. Therefore, in this study, following the prior work of Molodan and Hajjar (1998), an initial plastic strain (ϵ_{po}) of 0.0006 and 0.0004 are introduced for the corner and flat regions, respectively. As can be seen in Figure 4.2 and Figure 4.3, the steel model with the assumed plastic strain levels reproduced the stress-strain response of experimental coupon tests available in the literature with good accuracy.

The corner regions of the steel tube are often subjected to more severe residual stresses due to the higher degree of cold-forming than the flat regions. This results in variation of the material properties around the perimeter of the steel tube. Table 4.1 illustrates the material properties obtained from the coupon test results available in the literature. It can be seen that the yield strength (f_{yc}) and ultimate strength (f_{uc}) of the corner regions is consistently larger than those of the flat regions (f_{yf} , f_{uf}). In this research study, the average values of f_{yc} / f_{yf} and f_{uc} / f_{uf} from Table 4.1 are assumed as 1.09 and 1.03, respectively, while conducting analysis of RCFT members.

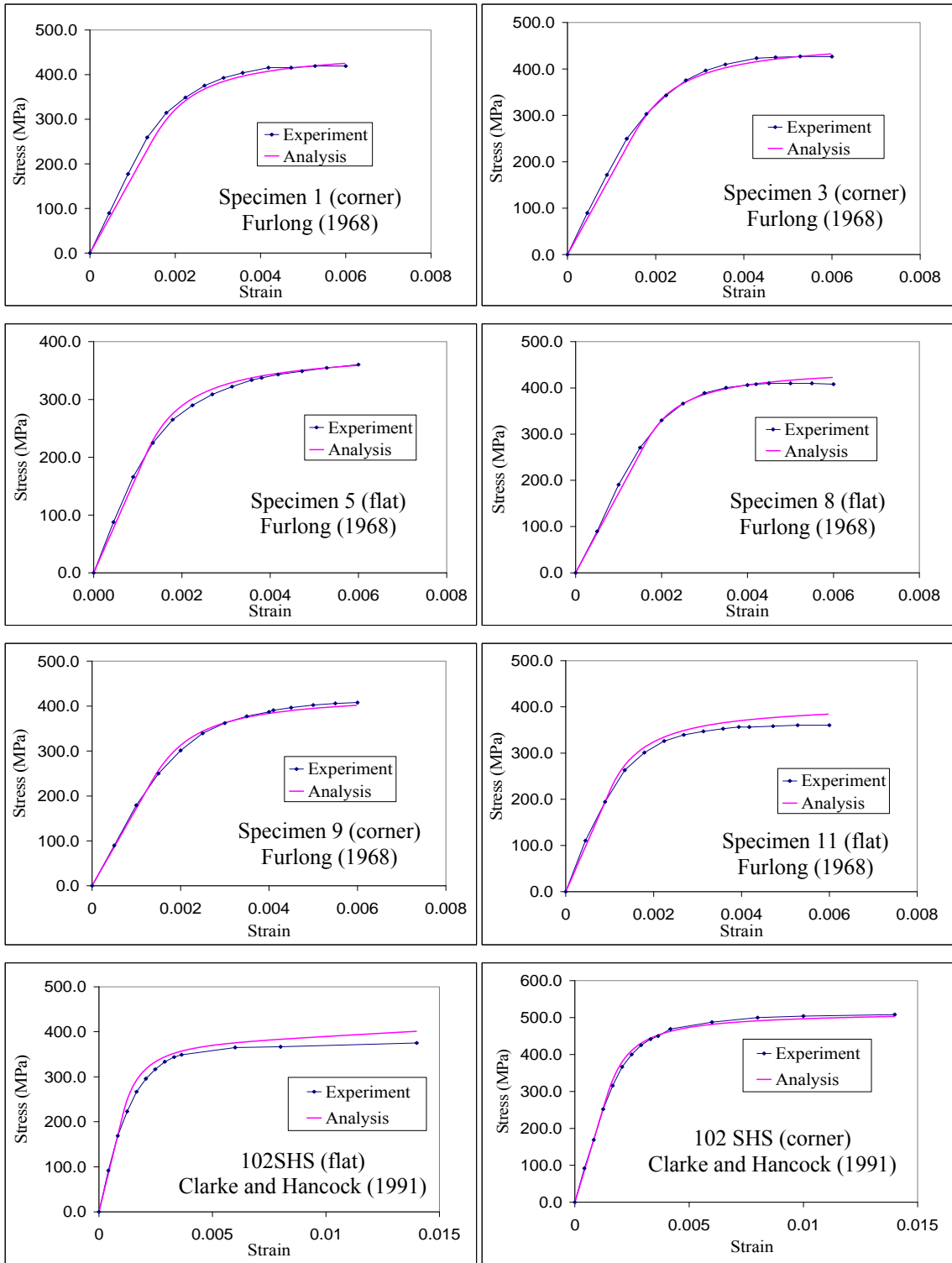


Figure 4.2 Comparison of Experimental and Computational Coupon Test Results

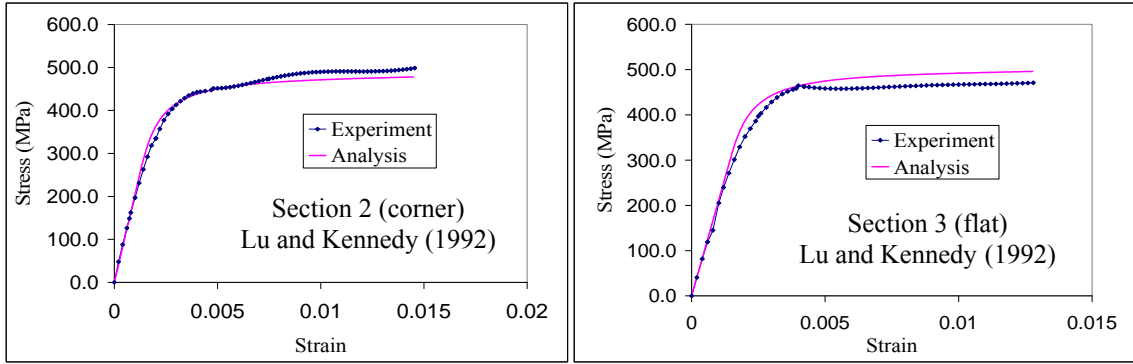


Figure 4.3 Comparison of Experimental and Computational Coupon Test Results (cont'd)

The steel tube of RCFT members are susceptible to local buckling under compressive loadings. Being in contact with a rigid medium, the local buckling takes place in the form of cosinal outward buckles due to the restraining action of the concrete core against the formation of sinusoidal inward buckles (Wright, 1993). This type of behavior is often considered as a higher mode of buckling and it provides a larger compressive capacity compared to the bare steel tubes. Examining the past research studies, a methodology will be established to determine the initiation of local buckling and to quantify its effect on the stress-strain response as shown in Figure 4.1.

Table 4-1 Variation of Steel Material Properties Due to Cold Forming Process

Reference	f_{yf} (MPa) (flat)	f_{yc} (MPa) (corner)	f_{uf} (MPa) (flat)	f_{uc} (MPa) (corner)
Clarke and Hancock (1991)	349.0	469.0	414.0	504.0
Furlong (1979)	337.4	390.1	na	na
	356.5	415.6	na	na
	408.0	423.2	na	na
Bridge (1976)	310.8	342.4	na	na
	300.8	351.5	na	na
	312.7	340.3	na	na
	297.5	331.5	na	na
Lu and Kennedy (1994)	456.0	490.0	490.0	506.0
	454.0	379.0	474.0	440.0
	433.0	405.0	444.0	416.0

The stress levels and slenderness limits of local buckling for rectangular RCFT members were investigated by several researchers. As will be described below, the

majority of the studies focused on obtaining the buckling stress either experimentally or computationally and then deriving a corresponding effective length factor of the steel tube wall. The effective length factor of plates depends on the aspect ratio and the boundary conditions (Salmon and Johnson, 1996). If the length of the plate becomes large compared to its width, the effect of aspect ratio on the effective length factor diminishes and the effective length can be obtained as 4 if the support conditions are simply supported and it becomes 6.97 in the case of fixed boundary conditions (Salmon and Johnson, 1996). Ge and Usami (1991) tested stiffened and unstiffened thin-walled short RCFT columns under cyclic axial loading. The longitudinal stiffeners placed inside the steel tubes were found to improve the local buckling strength considerably. The local buckling stress of the specimens was obtained by subtracting the axial strength of the concrete core from the experimental maximum axial load of the composite column. Then, the resulting expression was divided by the cross-sectional area of the steel tube. The buckling stress levels were compared with the empirical equation proposed by Nakai et al. (1986), where fixed boundary conditions and a buckling coefficient (k) of 10.67 was assumed. It was found that the empirical equation produced unconservative results for some of the specimens indicating that the fixity of the steel tube walls was overestimated such that a buckling coefficient less than 10.67 needs to be used. Wright (1993) obtained the limiting D/t ratios to prevent local buckling based on energy principles for the steel plates under uniform compression. Buckling shapes were assumed considering the boundary conditions of a variety of steel sections including bare steel tubes, RCFTs, steel reinforced columns, and wide flange shapes. The energy resulting from deformation of the steel plate into the buckled shape was equated to the energy applied by the external loads. Assuming the buckling stress to be equal to the yielding stress, the resulting expression was differentiated to obtain the maximum D/t corresponding to the given aspect ratio. Uy and Bradford (1996) developed a finite strip analysis method to calculate the buckling stress of steel plates in contact with a rigid medium. It was considered as a semi-analytical finite element method, where out-of-plane deformations of the plate finite element were approximated via a finite number of harmonic functions while the transverse displacements were interpolated using

polynomial functions. This approach reduced the computation time compared to the standard finite element methods. Stating the element equilibrium based on the principle of virtual displacements and developing the kinematic and constitutive relations, an eigen-value equation was derived to solve for the buckling shapes and stresses. The buckling stresses (σ_{cr}) were calculated for a range of steel plates with different boundary conditions and stress gradients. The corresponding buckling coefficients were derived using the elastic buckling equation of perfect steel plates given below (Galambos, 1998).

$$\sigma_{cr} = k \frac{\pi^2 \times E_s}{12 \times (1 - \nu^2) \times (D/t)^2} \quad [4.1]$$

where: k is the buckling coefficient

ν is the Poisson's ratio (0.3)

In the case of steel plates with clamped boundary conditions and uniform compressive stress distribution k was obtained as 10.3. Bridge et al. (1995) conducted an experimental study on short thin-walled bare steel tubes and unbonded RCFT columns under monotonic compressive loading. For the RCFT columns, the loading was applied on the steel tube alone. The experimental results indicated that concrete filling increased the local buckling resistance of the steel tubes. An elastic finite strip analysis was also performed to identify the buckling stresses and modes of deformation. Assuming clamped boundary conditions for the edges of the steel tube, a buckling coefficient of 9.99 was found to be appropriate for the steel tube in contact with the concrete core. Uy (1998) performed an experimental study to examine the local buckling characteristics of short and thin-walled RCFT columns. Two types of loading schemes were applied to the specimens such that the axial load was either introduced to the steel tube only or it was applied to the composite section. The specimens tested by the former loading scheme exhibited lower elastic local buckling strengths compared to the ones subjected to the latter loading scheme. In the case of specimens that underwent inelastic buckling, the stress level at initiation of local buckling was found to be equal to the yielding stress. Uy (1998) also developed a finite strip analysis method to calculate the buckling stresses assuming clamped boundary conditions. The computational results exhibited good comparison with the experimental results. However, based on the discrepancies observed

for the elastic local buckling, the full fixity condition of the edges of the steel tubes was found to be slightly breached. Liang and Uy (2000) carried out a computational study to investigate the post-local buckling response of steel plates with clamped boundary conditions representing the steel tube walls of short RCFT columns. The steel plate was modeled with 3D continuum elements. The analysis was conducted over a range of steel plates with different slenderness, residual stress, and initial imperfections. The steel plates were found to exhibit lower local buckling stress levels with increasing values of residual stress and initial imperfections. Upon local buckling significant reserve strengths were exhibited by the steel plates. In order to take advantage of this post-local buckling capacity in design, two effective width (b_e) formulas were introduced. The effective width accounted for the fact that following local buckling, the flexible parts of the steel tube become ineffective in resisting the load and the stresses are transferred to the stiffer regions. The effective width represents the stiff regions of the steel tube that continue to retain stress after local buckling develops. Therefore, the axial load capacity of the steel (P_{us}) can be calculated using Equation 4.1. The axial load capacities obtained based on the effective width principles for the specimens available in literature exhibited good correlation with the experimental results. Liang and Uy (2000) suggested an effective length factor 9.81 for the steel tubes of RCFT columns.

$$P_{us} = b_e \times t \times f_y \quad [4.2]$$

Bradford et al. (2002) investigated the local buckling of the steel tubes of circular CFTs (CCFT). In contrast to previous research studies adopting finite element or finite strip methods to examine local buckling, Bradford et al. (2002) employed the Rayleigh-Ritz method to determine the local buckling stresses and modes shapes. The change in the total potential of the circular steel plate is derived as the difference between strain energies and the work done by the applied loading. Minimizing the resulting expression with respect to the Ritz coefficient, the buckling stress and mode shapes of circular steel tubes in contact with a rigid media were derived. It was found that the strength of circular steel tubes when they are in contact with rigid media is 1.73 times larger than bare circular steel tubes. This factor is approximately 2.67 in the case of RCFTs, which

shows that the beneficial effect of concrete filling against local buckling is more pronounced rectangular plates. Bradford et al. (2002) adopted an effective diameter concept to evaluate the post-local buckling response of CCFTs.

As shown in Figure 4.1, in the current research study, the effect of local buckling is taken into account by introducing a strength degradation region in the stress-strain response following its occurrence. The strength degradation initiates once a threshold value of strain is breached to initiate local buckling. In the case of elastic local buckling, Equation 4.1 may be used to detect the strain level at the instant of local buckling by dividing it by the elastic modulus. However, Equation 4.1 requires the assumption of an effective length factor, which ranges from 9.81 to 10.67 and the use of these effective length factors was not justified for cold-formed steel tubes. If local buckling takes place after yielding, the critical stress level is often assumed to be equal to the yielding stress. Nevertheless, this information does not help to identify the local buckling point since cold-formed steel tubes exhibit an inelastic response maintaining approximately constant stress level following yielding. The effective width approach is useful in obtaining the reserve strength of the steel tube against local buckling. In this approach, assuming a stress redistribution along the edges, the portion of the steel tube that is active in resisting the applied loading is calculated. Local buckling is also considered not to create a change in the stress-strain response of the steel tube. However, the effective width approach is difficult to adopt in the current research study for two reasons. First, there exist limited effective width studies on cold-formed steel tubes. Second, in this study, the effect of local buckling is accounted for by modifying the stress-strain response through introducing a strength degradation region.

This research study is concerned with determining the strain level at the initiation of local buckling so that the stress-strain response can be modified to represent the post-local buckling behavior of the steel tube. It is widely accepted that the stress carried by the steel tube decreases approximately linearly once the steel tube buckles locally (Tomii and Sakino, 1979; Gourley and Hajjar, 1994; Varma 2000). There are two possible stress regions for the steel tube to experience local buckling. It can buckle elastically before

reaching the yield limit or inelastic buckling might take place after the steel tube undergoes plastic strains.

Figure 4.4 illustrates the trend of the ratio of local buckling strain (ε_{lbf}) to yield strain (ε_y) with respect to the parameter $D/t\sqrt{f_y/E_s}$. The trend in the data shows that $\varepsilon_{lbf}/\varepsilon_y$ decreases for large values of $D/t\sqrt{f_y/E_s}$ and Equation 4.3 is proposed to calculate $\varepsilon_{lbf}/\varepsilon_y$ with an R^2 of 0.61. The data presented in Figure 4.4 is obtained from the monotonically loaded column tests available in the literature (Tomii and Sakino, 1979; Schneider, 1998; Varma 2000).

$$\frac{\varepsilon_{lbf}}{\varepsilon_y} = 3.14 \times \left(\frac{D}{t} \sqrt{\frac{f_y}{E_s}} \right)^{-1.48} \quad [4.3]$$

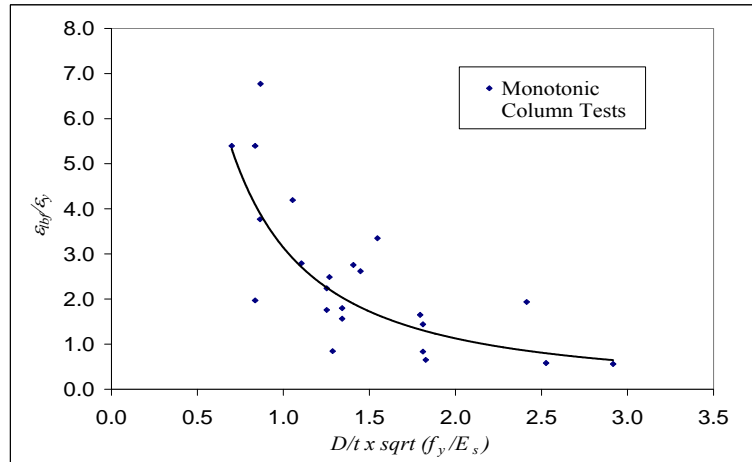


Figure 4.4 Correlation of $\varepsilon_{lbf}/\varepsilon_y$ with respect to $D/t\sqrt{f_y/E_s}$

The parameters required to define the stress-strain relation of steel tube after local buckling are determined to be the softening slope (K_s) and the residual strength (f_{rs}) (see Figure 4.1). Both of these parameters were obtained using a similar approach based the response of short RCFT columns available in the literature tested under monotonic axial load. Multiple specimens were selected based on material and geometric properties of f_y , f'_c , and D/t . It was ensured that the selected specimens will cover a wide spectrum for the aforementioned parameters. Table 4-2 gives a summary of the material and geometric properties of the specimens.

Table 4-2 Specimens Selected for Calibration of the Compressive Steel Model

Specimen	f_y	f'_c	D/t	f_y (MPa)	f'_c (MPa)	D/t
SC48-46	H ²	H	H	471.0	110.6	52.3
CR8-C-9	H	H	L ³	824.0	91.1	27.3
CR4-3-10	L	H	H	310.0	119.0	63.1
CR6-D-2	H	L	H	618.0	25.4	50.2
CR8-C-4-3	H	L	L	824.0	39.1	27.3
3	L	H	L	327.0	96.0	15.0
CR4-D-2	L	L	H	262.0	25.4	73.7
S4	L	L	L	312.0	23.8	22.3

The specimens presented in Table 4-2 all exhibited a clear region of approximately constant residual axial strength (P_{res}) toward the end of the test, after significant softening following local buckling and concrete crushing. Utilizing the concrete model, for each specimen, the residual axial stress (f_{rc}) was calculated. Then, these computationally obtained stress values were multiplied by the areas of the concrete core (A_c) to calculate the corresponding residual strengths (P_{cres}). The residual strengths of the steel tube (P_{sres}) were obtained by subtracting P_{cres} from P_{res} . Then, the residual axial stress of the steel tube (f_{rs}) can be calculated as given Equation 4.4 through dividing P_{sres} ($P_{sres} = P_{res} - P_{cres}$) by the area of the steel tube (A_s). Since no significant strain hardening is observed for cold-formed members, the residual axial stress was not allowed to exceed the yield strength of the steel tube.

$$f_{rs} = (P_{res} - P_{cres}) / A_s \leq f_y \quad [4.4]$$

According to Table 4-1, the next parameter to define the stress-strain response of the steel tube in compression was the slope of the linear strength degradation response (K_s) and it was determined by calibrating the computational load-deflection curves of the specimens to their experimental response. The computational load-deflection curve was obtained through superimposing the steel and concrete models and K_s was varied until the error

² H stands for high

³ L stand for low

between P_{exp} and P_{comp} axial load values was minimized as shown in Figure 4,5 and Figure 4.6.

$$\text{error} = \sqrt{\sum_{i=1}^{\# \text{ of data points}} (P_{comp_i} - P_{exp_i})^2} \quad [4.5]$$

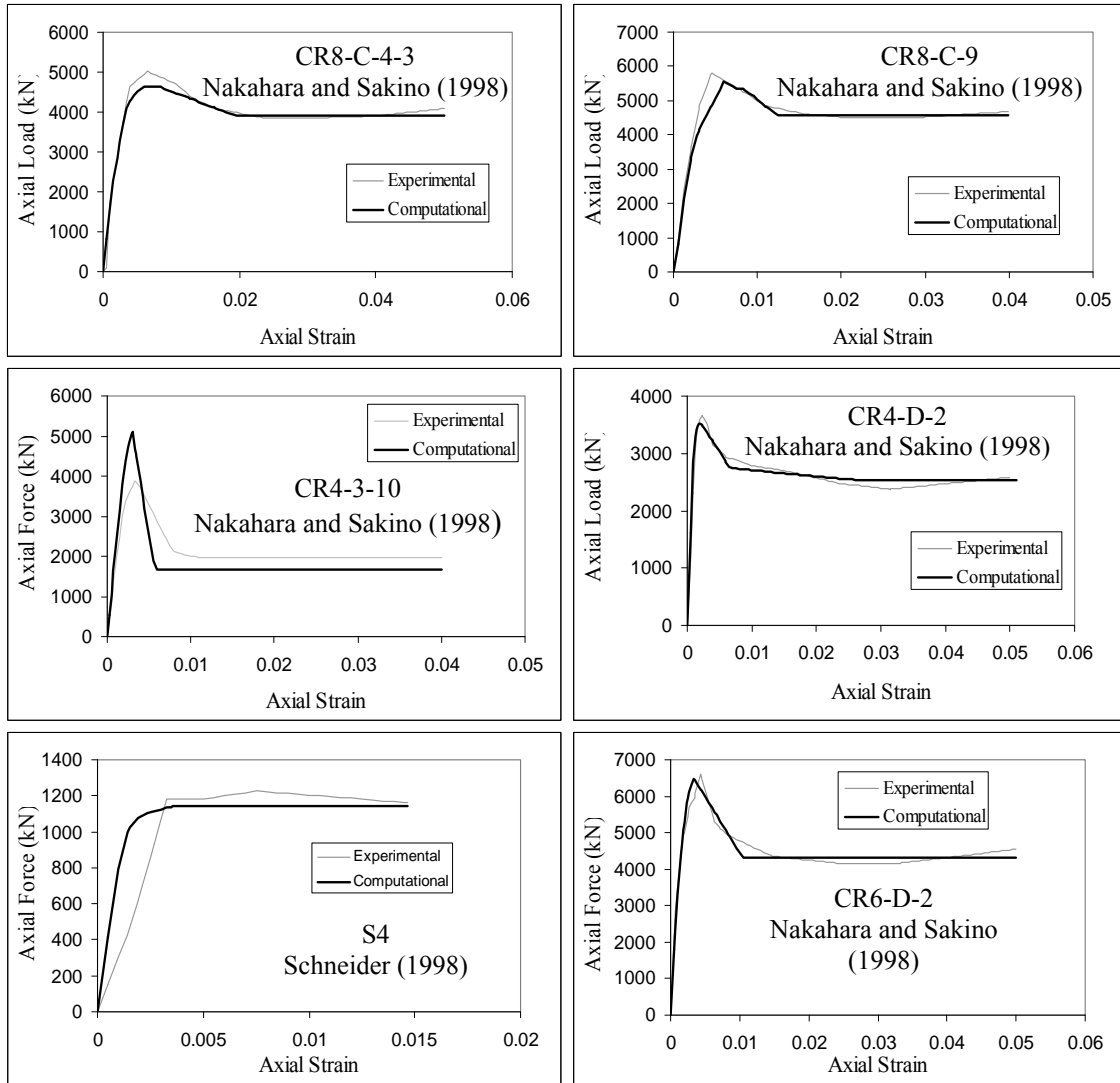


Figure 4.5 Calibration of K_s with Respect to Axially Loaded Column Tests

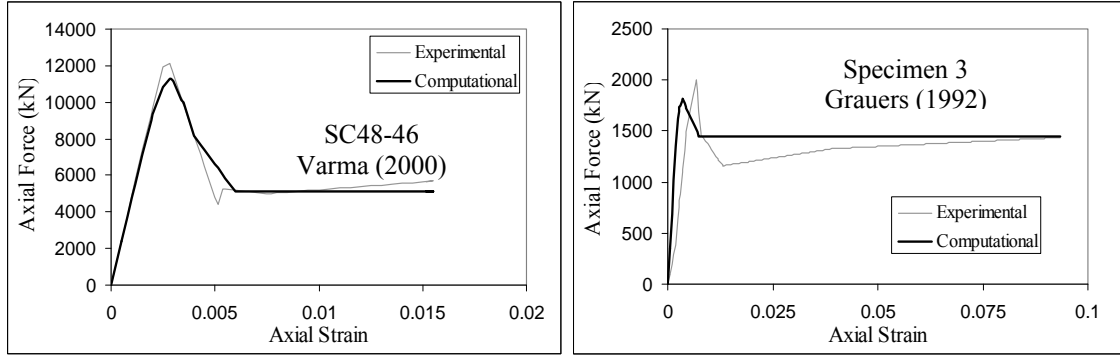


Figure 4.6 Calibration of K_s with Respect to Axially Loaded Column Tests (cont'd)

After the calibration process was completed, Equations 4.6 and 4.7 were derived to estimate K_s and f_{rs} values, respectively. Both K_s and f_{rs} were related to the parameter $D/t\sqrt{f_y/E_s}$. It was found that for large values of $D/t\sqrt{f_y/E_s}$, the specimens are affected from local buckling and concrete crushing more severely causing K_s to increase and f_{rs} to decrease. The comparisons of Equation 4.6 and Equation 4.7 with the experiments are illustrated in Figure 4.7 and Figure 4.8, respectively. For both of the equations, good correlation was attained with the experimental results.

$$K_s = 0, (D/t) \times (f_y / E_s) \leq 0.08 \quad [4.6]$$

$$K_s = 644304.39 \times (D/t) \times (f_y / E_s) - 51544.35, (D/t) \times (f_y / E_s) \geq 0.08$$

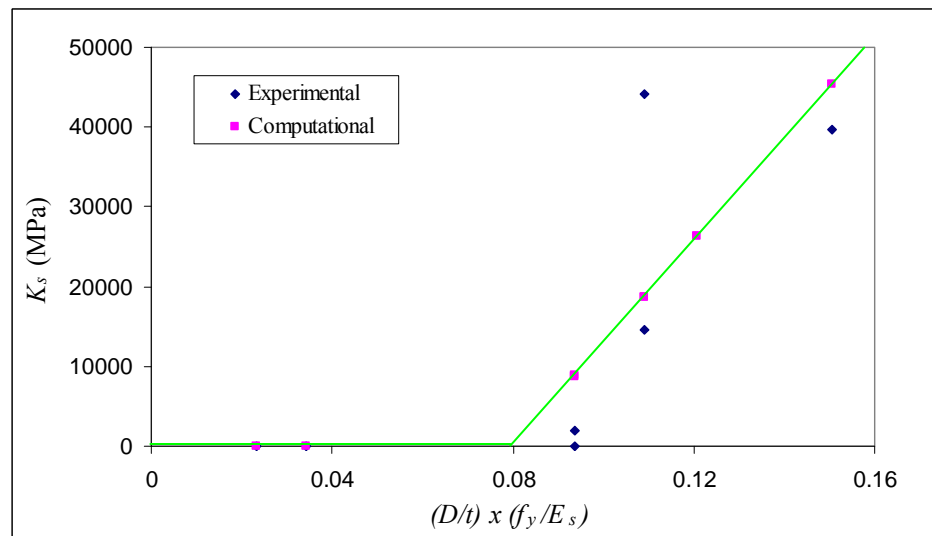


Figure 4.7 Comparison of Experimental and Computational Results for K_s

$$\frac{f_{rs}}{f_y} (\%) = 100, (D/t) \times (f_y / E_s) \leq 0.08 \quad [4.7]$$

$$\frac{f_{rs}}{f_y} (\%) = -731.13 \times (D/t) \times (f_y / E_s) + 158.55, (D/t) \times (f_y / E_s) \geq 0.08$$

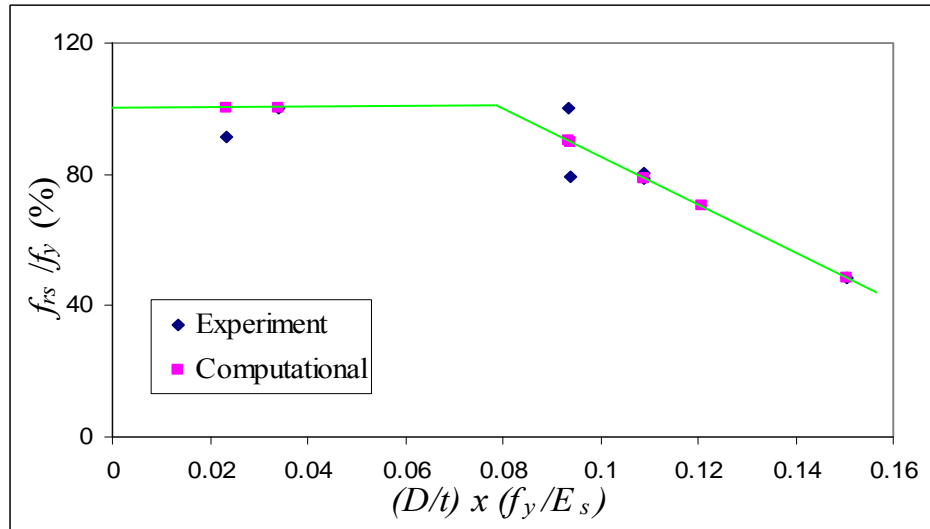


Figure 4.8 Comparison of Experimental and Computational Results for f_{rs}

The accuracy of the steel and concrete constitutive model parameters derived in Chapter 3 and Chapter 4 were tested for axially-loaded RCFT specimens from the literature. The load-deformation response of the specimens was obtained by calculating the stress values of the steel tube and the concrete core based on a given strain history. Then, these stress values were converted into axial forces by multiplying them with the corresponding cross-sectional areas. A total number 10 specimens were selected from the experimental database by Tort and Hajjar (2003). The material and geometric properties of the specimens are summarized in Table 4-3. Figure 4.9 and Figure 4.10 illustrate the comparison of computational and experimental load-deformation results of the specimens in Table 4-3. A good correlation is evident for all parts of a typical load-deformation response including initial stiffness, peak axial load, strength degradation slope, and the residual axial strength.

Table 4-3 Specimens Selected for Verification of the Compressive Steel and Concrete Model

Specimen	f_y (MPa)	f_c (MPa)	D (mm)	B (mm)	t (mm)	L (mm)
CR8-A-9	825.0	91.1	180.0	180.0	9.45	540
CR4-D-8	262.0	80.3	324.0	324.0	4.38	972
CR4-D-4	262.0	41.1	324.0	324.0	4.38	972
CR4-C-4-1	262.0	41.1	215.0	215.0	4.38	645
CR8-A-8	835.0	77.0	119.0	119.0	6.47	357
R2	383.0	26.0	152.8	76.5	4.47	635
R3	413.0	26.0	152.4	101.8	4.32	635
S3	322.0	23.8	127.0	127.0	4.55	635
IIA	339.4	21.4	100.0	100.0	2.20	300
IIIA	288.4	20.6	100.0	100.0	2.99	300

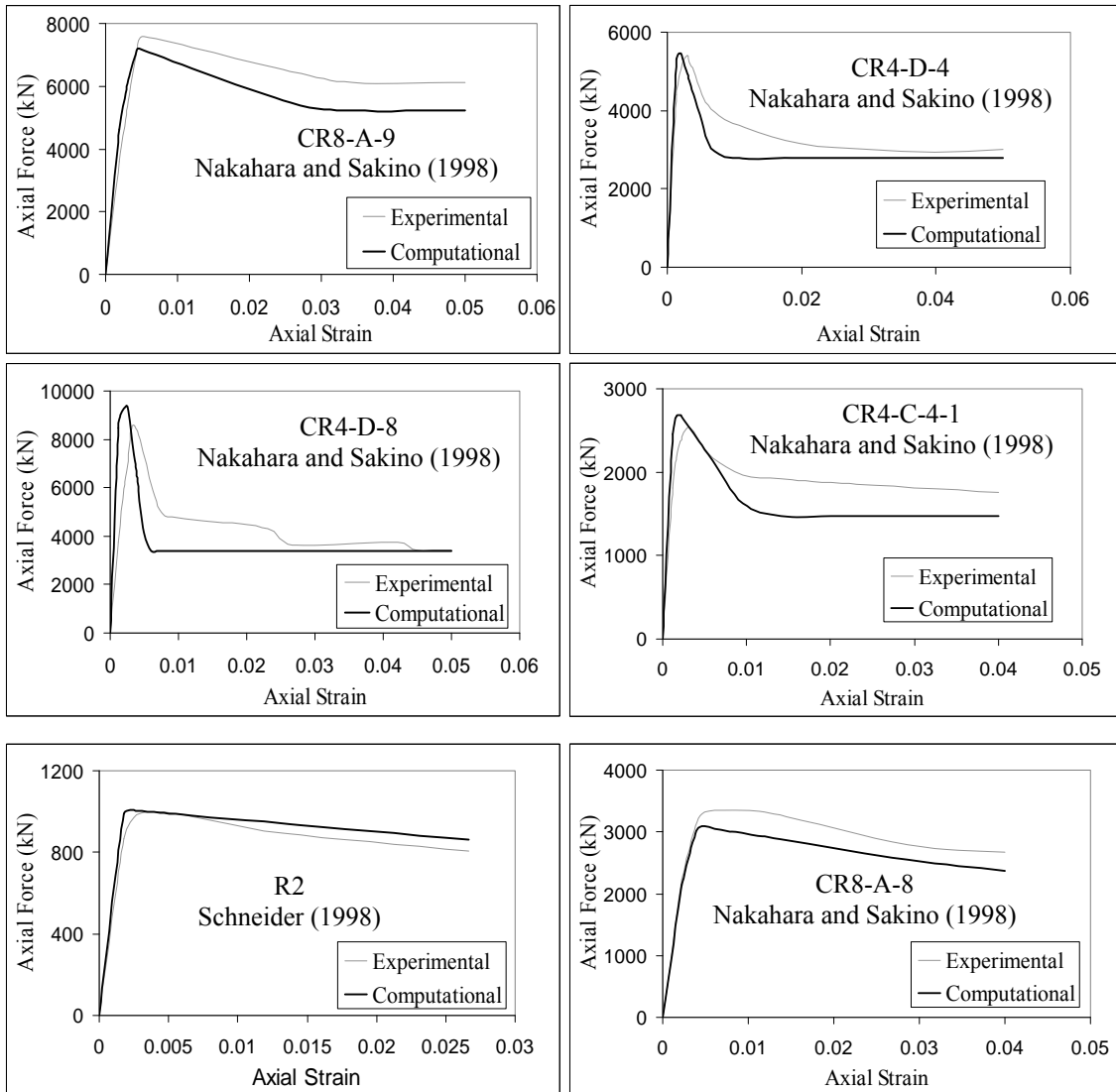


Figure 4.9 Verification of Steel and Concrete Models

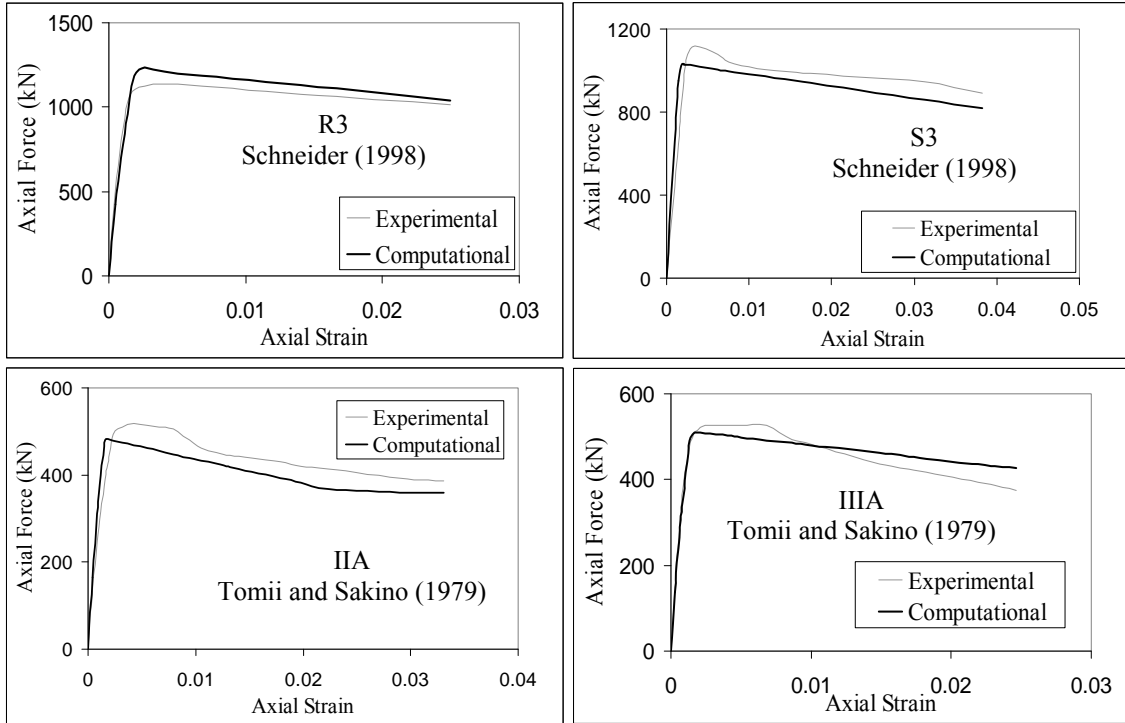


Figure 4.10 Verification of Steel and Concrete Models (cont'd)

4.3. Cyclic Response

The cyclic inelastic response of the steel tube was simulated based on the uniaxial bounding surface model proposed by Mizuno et al. (1991). The stress-strain response was formulated in an incremental form. This approach allowed accurate representation of the observed cyclic phenomena in the experiments since the past loading history dependence is accounted for comprehensively.

The total strain increment ($\Delta \varepsilon_t$) obtained during the analysis can be decomposed into its elastic ($\Delta \varepsilon_e$) and plastic ($\Delta \varepsilon_p$) parts as shown in Equation 4.8.

$$\Delta \varepsilon_t = \Delta \varepsilon_e + \Delta \varepsilon_p \quad [4.8]$$

The stress increment ($\Delta \sigma$) is related to the strain increments as given in Equation 4.9.

$$\Delta \sigma = E_t \times \Delta \varepsilon_t, \Delta \sigma = E_e \times \Delta \varepsilon_e, \Delta \sigma = E_p \times \Delta \varepsilon_p \quad [4.9]$$

Utilizing the relations of Equation 4.9 in Equation 4.8, the tangent modulus (E_t) is expressed in terms of elastic (E_e) and plastic modulus (E_p) as follows:

$$\frac{1}{E_t} = \frac{1}{E_e} + \frac{1}{E_p} \quad [4.10]$$

If the stress state is elastic, the tangent modulus is assumed to be equal to the elastic modulus. Therefore, from Equation 4.10, the plastic modulus is taken as infinity if no plastic deformation occurs. Following the initiation of plasticity, the evolution of plastic modulus takes place based on the accumulated plastic strain. A loading surface is introduced defining the boundary between elastic and plastic response. Once the loading surface is breached, inelasticity initiates. The radius of loading surface (κ) decreases as a function of the plastic strain as shown in Equation 4.11. The reduction of the elastic region can be seen schematically in Figure 4.11.

$$\frac{\kappa}{\kappa_0} = \alpha - a \times \exp(-b \times \bar{\varepsilon}^p \times 100) - (\alpha - a - 1) \times \exp(-c \times \bar{\varepsilon}^p \times 100) \quad [4.11]$$

where: κ_0 initial loading surface radius

a, b, c material constants

$\bar{\varepsilon}^p$ effective plastic strain

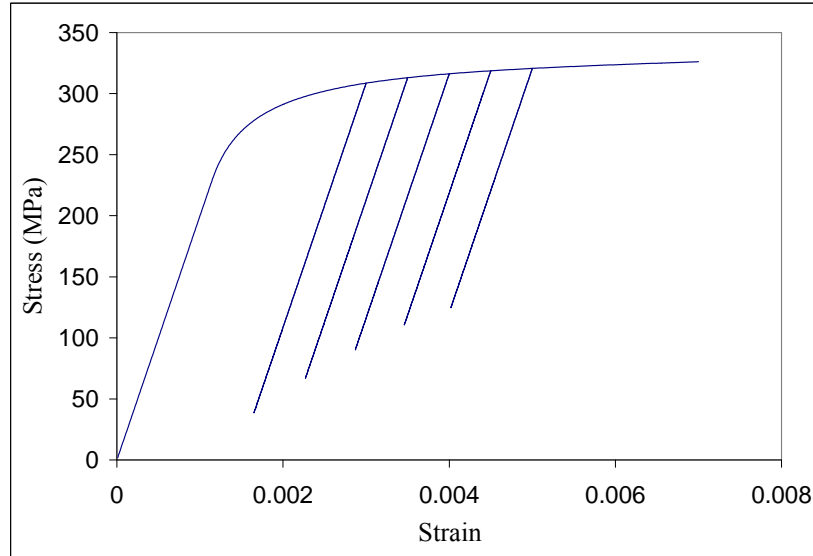


Figure 4.11 Reduction of Radius of the Loading Surface

The bounding surface encloses the attainable stress states. It is assumed to expand as a function of the plastic strain until the ultimate tensile strength of the material is reached. The cyclic rule defining the expansion of the bounding surface is given in Equation 4.12.

$$\bar{\kappa} = f_u + (\bar{\kappa}_o - f_u) \times e^{(-\zeta \rho^2)} \quad [4.12]$$

where: $\bar{\kappa}$ - bounding surface radius

$\bar{\kappa}_o$ - initial bounding surface radius

ζ - material constant

ρ - $\bar{\epsilon}^p \times 0.5$

The degree of inelasticity is determined based on the distance between loading and bounding surfaces as shown in Figure 4.12. At high levels of inelastic deformation, the rate of decrease in plastic modulus vanishes and the bounding stiffness is preserved. The plastic modulus is defined by the following relation.

$$E_p = E_{po} + h \times \frac{\delta}{\delta_{in} - \delta} \quad [4.13]$$

where: E_{po} is the slope of the bounding surface

δ is the distance between the current stress point and the bounding surface

δ_{in} is the initial distance between the current stress point and the bounding surface

$h = e \times \delta + f$ is the shape parameter (e, f are material constants)

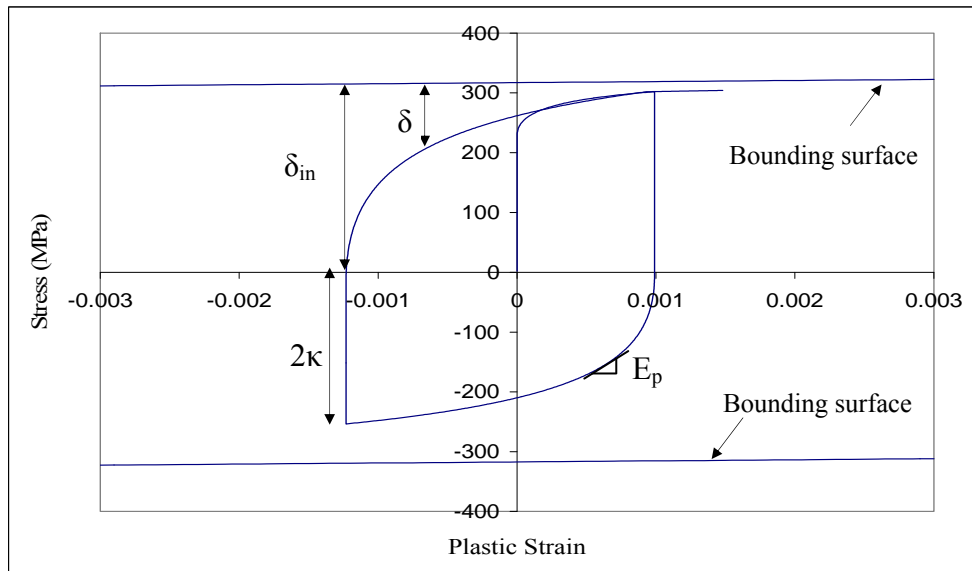


Figure 4.12 Bounding Surface Model of Steel Model

The experimental results exhibit that the slope of the bounding surface does not remain constant throughout the loading history. Mamaghani et al. (1995) assumed that as the plastic strain level increases the slope of the bounding surface experiences a reduction and approaches to zero asymptotically. In Equation 4.14, the slope of the bounding surface is expressed as a function of the plastic work (W^p).

$$E_{po} = \frac{E_{oi}^p}{1 + \omega \times W^p} \quad [4.14]$$

where: E_{oi}^p is the initial slope of the bounding surface

ω is a material constant

W^p is the plastic work

Auxiliary surfaces were introduced to prevent premature reduction of the plastic modulus due to the underestimation of the distance between loading and bounding surfaces and also the auxiliary surfaces remedies the effect of overshooting due to incorrect updating of the plasticity variables following load reversals without plastic excursions in the opposite direction. Memory surfaces are assumed to be located symmetrically in the tension and compression regions passing through the point at which the maximum stress level is reached throughout the loading history. A virtual bounding surface becomes active when a stress reversal initiates prior to breaching the memory surface. It is located by expanding the current bounding surface by an amount of δ_y , which is obtained as the distance between the point of stress reversal and the memory surface. Once inelastic response in the direction of stress reversal is attained, the plastic modulus is obtained using Equation 4.14 with respect to the virtual bounding surface as described between points A and B shown in Figure 4.13. Following the breach of the memory surface, the plastic modulus evolves with respect to the bounding surface. Adopting the concept of memory and virtual bounding surfaces also provides better predictions for cyclic ratcheting and the Bauschinger effect.

The material parameters required to develop the steel model are given in Table 4-4 as reported in Mamaghani et al. (1995).

Table 4-4 Steel Model Material Parameters

Parameter	$f_y \leq 357 \text{ MPa}$	$357 \text{ MPa} < f_y \leq 524 \text{ MPa}$	$f_y \geq 524 \text{ MPa}$
$\bar{\kappa}_o$	1.5	1.13	1.06
$\frac{f_y}{f_y}$			
a	-0.505	-0.528	-0.553
b	2.17	1.88	6.47
c	14.4	18.7	34.8
e	500	316	700
$\frac{f_y}{E_s}$	0.3	0.484	0.361
α	0.191	0.217	0.175
$w \times f_y$	3.08	4.0	2.67
$\frac{E_{oi}^p}{E_s}$	0.00896	0.0101	0.00785
$\zeta \times \varepsilon_y^2$	0.0000989	0.00152	0.00804

Despite the comprehensiveness of the cyclic characteristics accounted for by Mizuno et al. (1991), as described above, the softening type cyclic response that might occur in the steel members was not adequately addressed. RCFT members with slender steel tube sections often have the potential of experiencing local buckling effects. Local buckling manifests itself as a softening type cyclic response, where the strength attained by the RCFT member diminishes as the loading progresses. This type of behavior is typical in the RCFT beam-column tests conducted by subjecting the member into constant axial load and cyclic shear loading (Sakino and Tomii, 1981; Inai et al., 2004; Varma et al., 2002). In Section 4.1, a formulation was proposed to determine the instant of local buckling based on a strain limit. It was assumed that a strength degradation response with negative stiffness takes place following local buckling. This approach works well under monotonically applied loading conditions. However, under cyclic loading schemes, the damage due to local buckling aggregates even if the strain level attained by the material fibers is not increased. Therefore, the model by Mizuno et al. (1991) should further be modified so that the cyclic characteristics of the local buckling

phenomena can be captured.

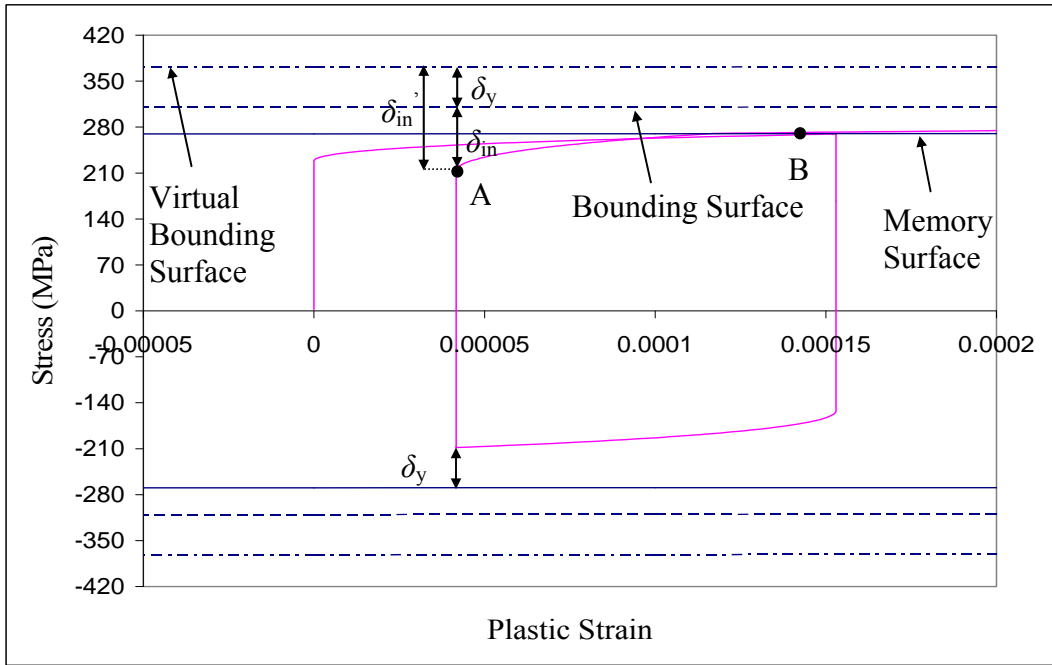


Figure 4.13 Memory and Virtual Bounding Surfaces of Steel Model

In the concentrated plasticity model by Hajjar and Gourley (1994), the effect of local buckling in the RCFT members was simulated by reducing the bounding surface size based-on the accumulated plastic work. A similar mechanism was also adopted in the stress-strain space and Equation 4.15 was derived to represent the reduction in the size of the bounding surface, where the bounding surface radius ($\bar{\kappa}$) was assumed to be a linear function of the accumulated plastic work (W^p). In Equation 4.15, the parameter γ_{cc} is introduced as the rate of the bounding surface reduction.

$$\bar{\kappa} = (-\gamma_{cc} \times W^p + 1) \times \bar{\kappa}_o \quad [4.15]$$

The numerical values of γ_{cc} were determined by studying the cyclic RCFT tests available in the literature. The selected specimens were modeled utilizing the mixed finite element formulation introduced in Chapter 2. The analysis of the specimens was conducted for multiple values of γ_{cc} until close agreement between experimental and computational results was achieved. The first specimen to be studied was CIVS3-2 by Sakino and Tomii (1981). It was modeled with 2 elements per member with 3 integration

points. The specimen was subjected to a constant axial load and cyclically-applied shear loading putting the member into double curvature. Figure 4.14 illustrates the computational results for γ_{cc} values of 0.0345, 0.0690 compared to the experimental data. For specimen CIVS3-2, γ_{cc} of 0.0345 shows the best correlation. The second specimen was selected as SR4A4C from the experimental study by Inai et al. (2004). The analysis of SR4A4C was conducted with the same mesh density of CIVS3-2 for γ_{cc} values of 0.0690 and 0.138. As presented in Figure 4.15, it was found that when γ_{cc} is 0.138, the computational results achieves better comparison with the experimental results.

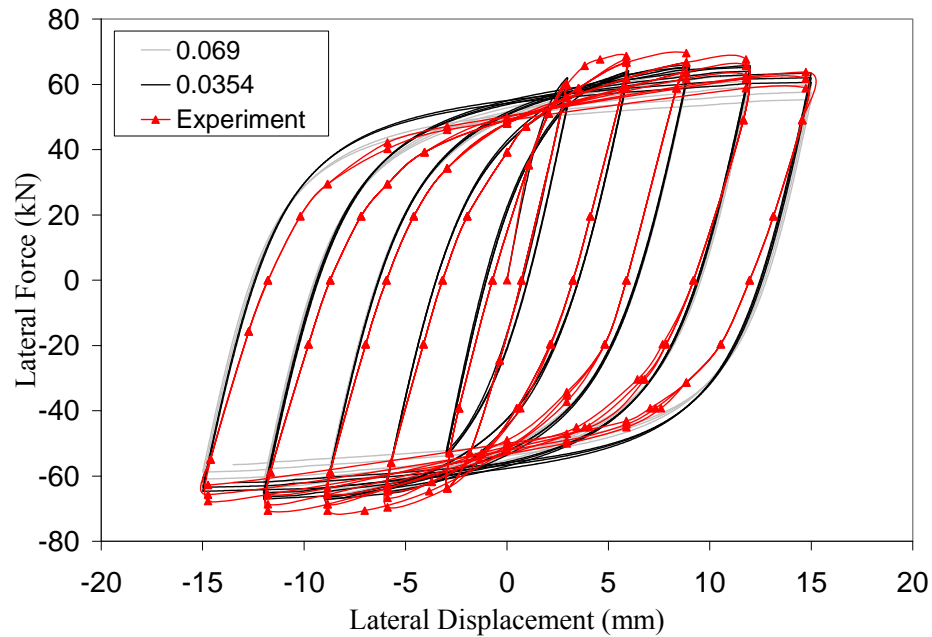


Figure 4.14 Calibration of γ_{cc} with respect to CIVS3-2 (Sakino and Tomii (1981), Tube: 100x100x4.21, $f_y = 295$ MPa, $f'_c = 24$ MPa, $L/D = 6.0$, $D/t = 24$)

The γ_{cc} values determined for CIVS3-2 and CIVS3-2 were correlated linearly to the parameter $\lambda_{cc} = (D/t) \times \sqrt{f_y / E_s}$, which represents the slenderness of the steel tube against local buckling. This process yielded Equation 4.16 to estimate γ_{cc} as a function of $\lambda_{cc} = (D/t) \times \sqrt{f_y / E_s}$.

$$\gamma_{cc} = 0.0345 \quad \lambda_{cc} < 0.92 \quad [4.16a]$$

$$\gamma_{cc} = 0.196 \times \lambda_{cc} - 0.146 \quad 0.92 \leq \lambda_{cc} \leq 1.45 \quad [4.16b]$$

$$\gamma_{cc} = 0.138 \quad \lambda_{cc} > 1.45 \quad [4.16c]$$

Substituting Equation 4.16 into Equation 4.15, the radius of the bounding surface can be determined during the cyclic loading history. Since $\bar{\kappa}$ is stated as a decreasing function of W^p , in order to keep $\bar{\kappa}$ bounded, its value was not allowed to be go below $0.5 \times \bar{\kappa}_0$.

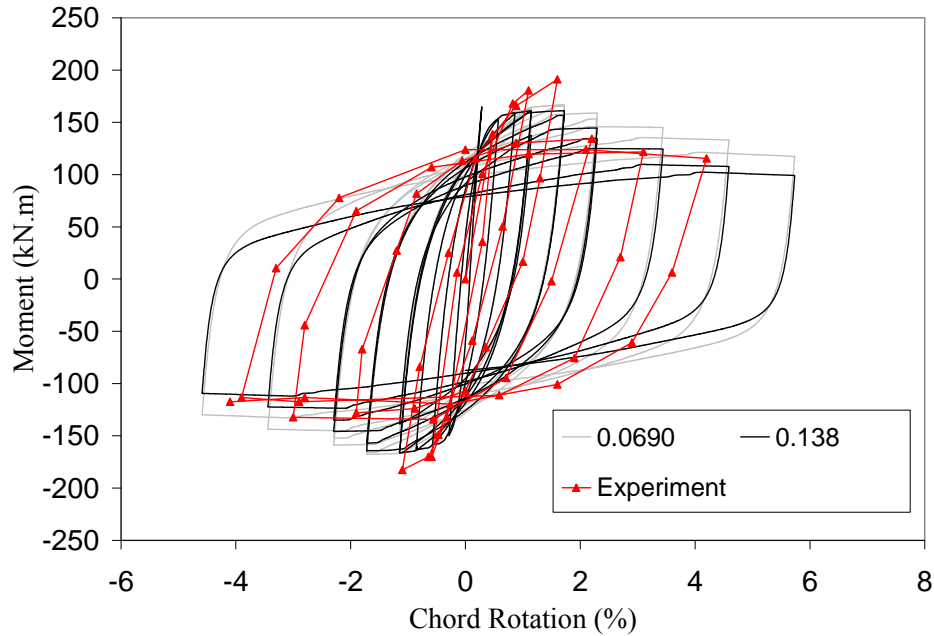


Figure 4.15 Calibration of γ_{cc} with respect to SR4A4C (Inai et al. (2004), Tube: 210x210x5.80 mm, $f_y = 323$ MPa, $f'_c = 39.2$ MPa, $L/D = 6.0$, $D/t = 36$)

4.3.1. Verification of the Cyclic Response

In this section the capability of the steel model in predicting the cyclic phenomena observed during the tests is presented. For this purpose, stress-strain response is generated under various strain histories including constant stress range, constant strain range, symmetric increasing strains, and unsymmetric increasing strains.

The stabilization of stress-strain response is evident when the steel fibers are subjected to a constant range of strain histories as shown in Figure 4.16. This type of

behavior is attributed to the fact that the bounding and loading surfaces remains constant since the effective plastic strain does not increase.

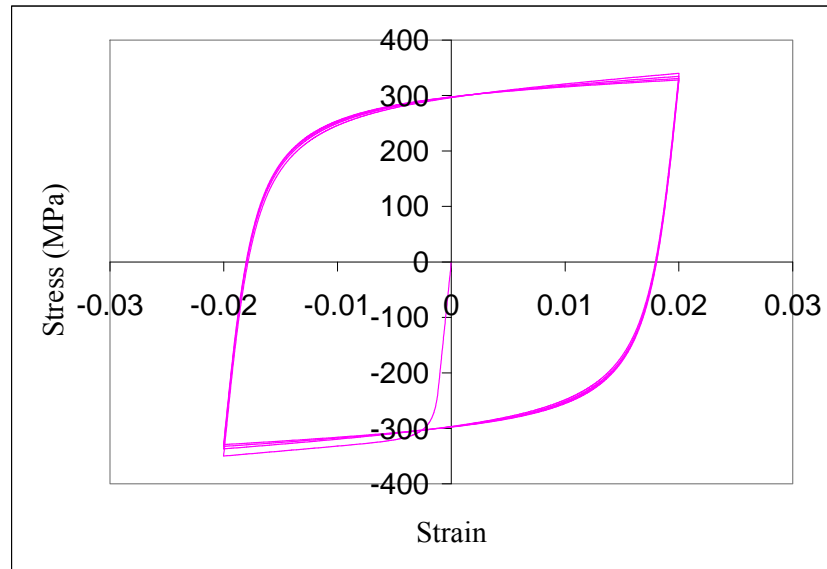


Figure 4.16 Steel Model Subjected to Symmetric Constant Strain Cycles

The next cyclic phenomenon to investigate is the cyclic hardening under increasing symmetric strain cycles as shown in Figure 4.17. The steel model successfully predicts the mild increase in the stress as the range of plastic strain increases at each subsequent cycle. The reduction in the bounding stiffness is also evident during the applied loading history.

The phenomenon of cyclic hardening under increasing unsymmetrical strain cycles is illustrated in Figure 4.18. The steel model produced a realistic simulation in predicting the mild increase in the maximum stress level and the reduction in the plastic modulus during the loading history.

Another cyclic phenomenon to emphasize is the cyclic ratcheting, which is also known as cyclic creep. A strain history producing a constant stress range with non-zero mean stress was generated for the steel model. The stress-strain response obtained from the analysis exhibited a limited amount of increase in plastic strains due to cyclic ratcheting as shown in Figure 4.19.

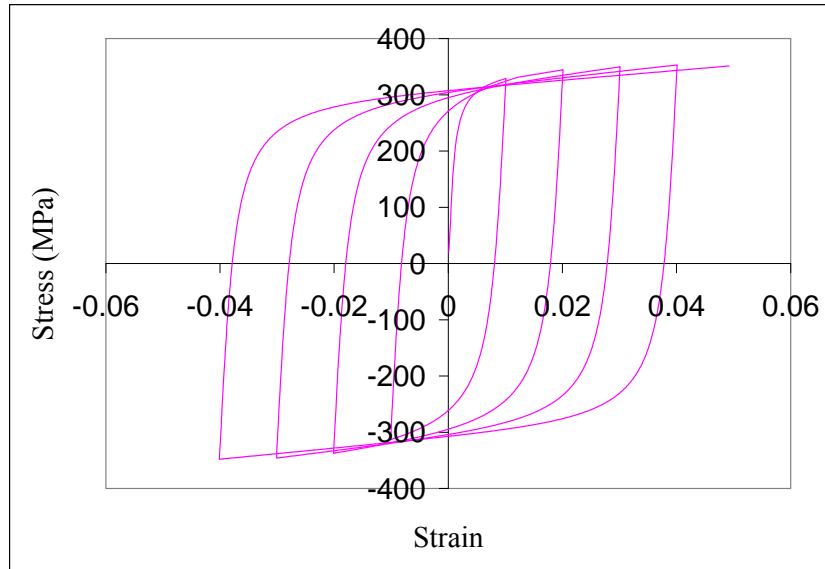


Figure 4.17 Steel Model Subjected to Symmetric Increasing Strain Cycles

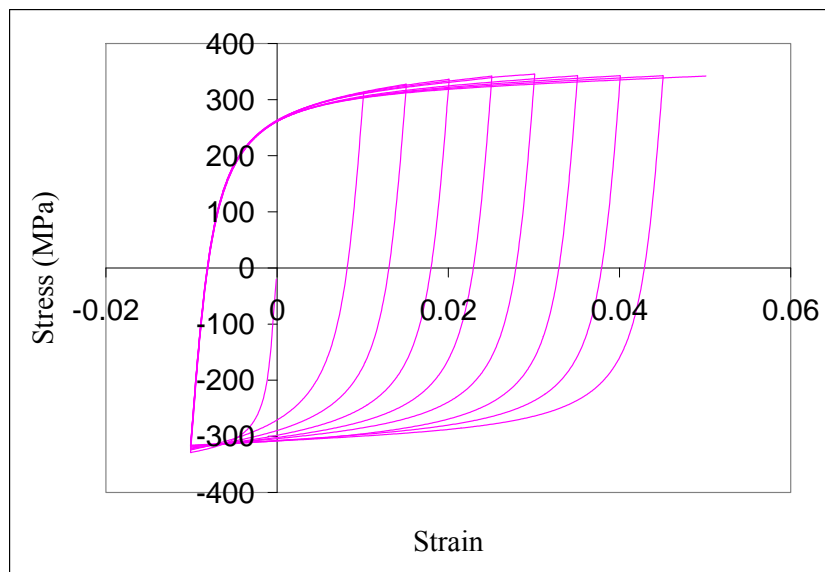


Figure 4.18 Steel Model Subjected to Symmetric Increasing Strain Cycles

Two of the coupon tests performed by Mizuno et al. (1991) were simulated with the steel model. The experimental and computational stress-strain responses were compared in Figure 4.20 and Figure 4.21. It can be seen that good correlation was achieved with the experimental results under complicated strain histories.

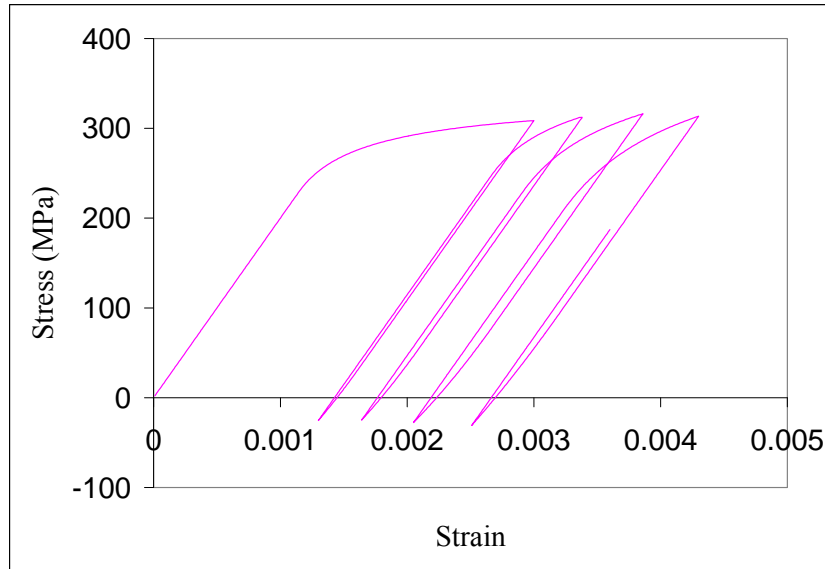


Figure 4.19 Steel Model Subjected to Cyclic Ratcheting

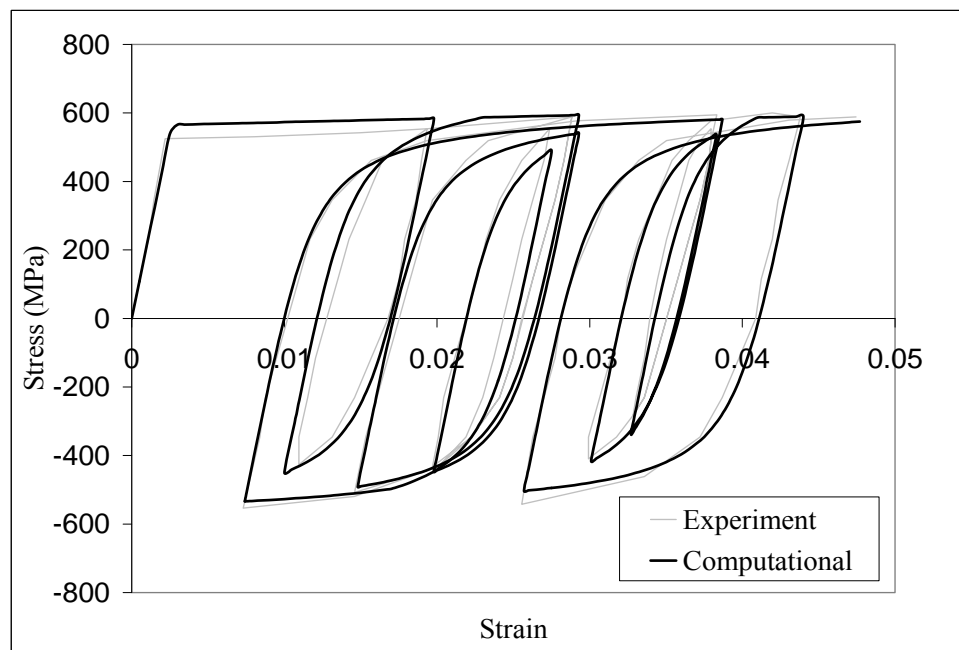


Figure 4.20 Comparison of Experimental and Computational Results of Steel Coupon Specimen SM58E (Mizuno et al. (1991), $f_y = 524$ MPa)

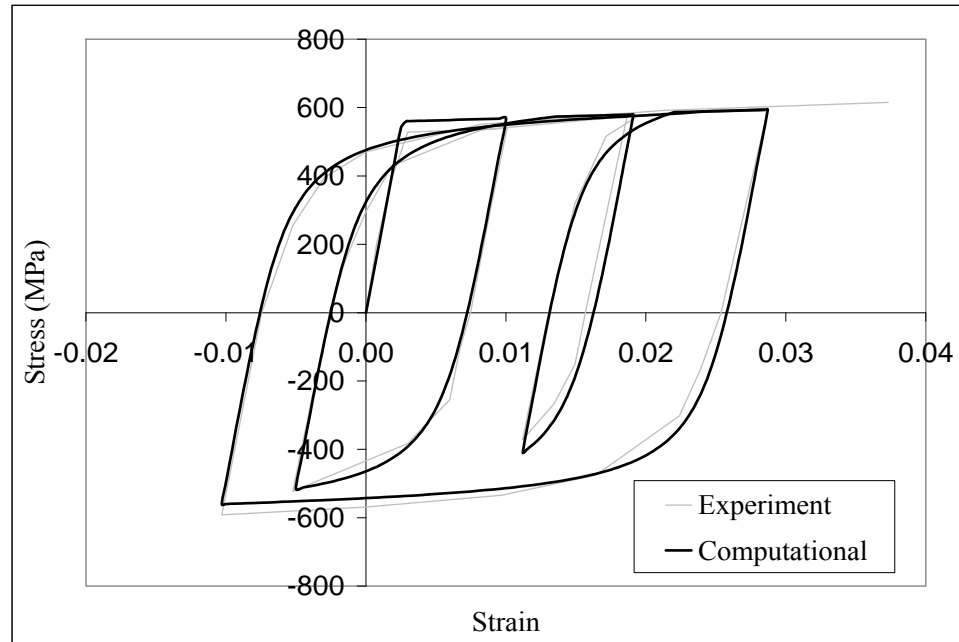


Figure 4.21 Comparison of Experimental and Computational Results of Steel Coupon Specimen SM58F (Mizuno et al. (1991), $f_y = 524$ MPa)

4.4. Steel Model for Hot-Rolled Steel Girders

The strong column weak-beam design criteria adopted in seismic design leads to a significant contribution of steel girders to the structural behavior. The cruciform RCFT frame tests by Koester (2000) and Peng (2001) with split-tee connections also exhibited plastic hinging in the steel girders as a main energy dissipation mechanism. Therefore, one of the essential tasks of simulating the response of RCFT frames is to develop an accurate material constitutive relation of the cross-section fibers of steel girders framing into RCFT columns.

The common approaches adopted in modeling the stress-strain response of hot-rolled steel include multi-linear models, bounding surface models and algebraic models (White, 1986). In the multi-linear models, the stress-strain response is represented through a set of piece-wise linear functions (Muhummud, 2003; Huang, 2005). Despite the efficiency of these models, it is often required to derive a significant number of state variables to capture the material characteristics. The bounding surface models introduce multiple regions in the stress-strain space to define to elastic and inelastic response of the

material (Dafalias and Popov, 1976; Cofie and Krawinkler, 1985; Mizuno et al., 1991). These surfaces undergo changes in size to represent the main features of the material. The bounding surface models do not suffer from extensive conditional statements and large number of state variables. The algebraic models are similar to multilinear models in the sense that stress is expressed as an explicit function of strain (Menegotto and Pinto, 1973; White, 1986). However, in the case of algebraic models, the function does not necessarily have a linear nature. This approach eliminates the need for large number of state variables in multilinear models and produces more accurate simulations since the nonlinear stress-strain relations are calibrated with respect to experimental results.

In this research study, the steel model developed by Mizuno et al. (1991) was adopted to simulate the inelasticity of the material fibers in hot-rolled steel girder cross-sections. The existing model was augmented by introducing new rules to account for the effect local buckling of steel girders.

4.4.1. Monotonic Response

Hot-rolled structural steel experiences a linear response until the attainment of yield stress. The linear elastic response is followed by a flat region, which is often referred as the yielding plateau. At high strain levels, the yielding plateau transforms into a hardening curve with a nonlinear nature. The response in tension and compression often exhibit identical characteristics. For the sake of simplicity of the constitutive relation, in this research study, the yielding plateau and the hardening curve are not modeled. Instead, it is assumed that the steel undergoes hardening once the yielding stress is attained. Therefore, the typical stress-strain response under monotonic loading can be obtained as given in Figure 4.22.

Under seismic loading conditions, steel girders experience large deformation demands, which might cause local buckling to occur in the flange and/or web of the cross-section. In order to perform realistic evaluation of the seismic performance of RCFT frames under large hazard levels, the effect of local buckling is to be modeled. The flexural tests on steel girders by Lukey and Adams (1969) and Green et al. (2002) indicated that local buckling results in a gradual strength drop in the post-peak region of

the load-deformation response. Therefore, the compression part of the stress-strain response given in Figure 4.22 was modified to account for the effect of local buckling. It was assumed that a linear strength degradation region initiates with a negative slope of K_{sg} and it is followed by a constant stress region. Figure 4.23 illustrates the stress-strain response accounting for the phenomena of local buckling. The parameters that are required to define the compressive response with local buckling include the strain level at initiation of local buckling (ϵ_{slbf}), K_{sg} , and the constant stress (f_{rsg}) that is maintained following the stress degradation region.

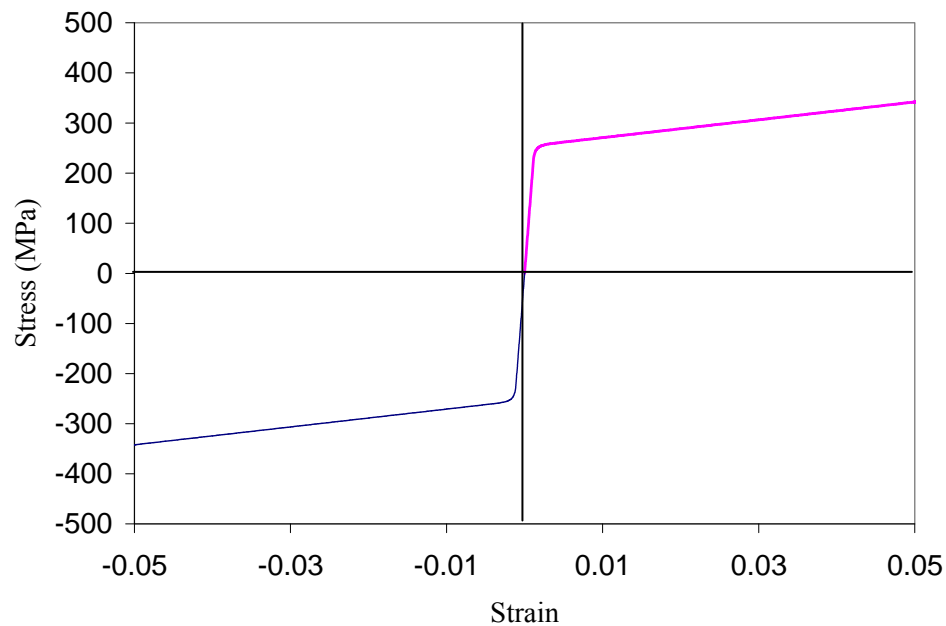


Figure 4.22 Monotonic Stress-Strain Response of Hot-Rolled Steel

Experimental tests in the literature were utilized to determine the ranges of values of local buckling strain levels and develop equations to relate those limiting strain values into geometric and material properties of the steel cross-section. Lukey and Adams (1969) tested steel girders under three-point bending. The experimental results were presented in terms of end-rotation vs. moment plots and the initiation of local buckling was clearly reported. In order to utilize the local buckling data values while developing the compressive steel constitutive relation, a computational study was conducted. Representative specimens from Lukey and Adams (1969) were analyzed using the

mixed-finite element formulation presented in Chapter 2. As given in Figure 4.24, the specimens were modeled using 4 finite elements with 3 integration points. The support conditions were assumed to be pinned and roller. The analysis was performed under displacement-controlled solution scheme by selecting the transverse displacement of the node located at the mid-length as the controlling degree-of-freedom (Yang and Kuo, 1994). Two types of analyses were performed for the selected specimens. In the first analysis, no local buckling was assumed as shown in Figure 4.22. It was found that the experimental and computational results exhibited good correlation until the initiation of local buckling. Then, from the computational results at the end-rotation value of local buckling as reported in the experiments, the strain level at the most stressed steel fiber of the cross-section at the mid-node of the steel girder was determined. The strain level was assumed to be the limiting value to initiate local buckling (ϵ_{slbf}). In Figure 4.25, the summary of the steps to obtain the local buckling strain level can be found. The second type of analysis was conducted multiple times for each selected specimen until close agreement is achieved between experimental and computational results for the post-local buckling response for a range of assumed K_{sg} values. Figure 4.26 and Figure 4.27 illustrates the calibration of the material model with respect to K_{sg} for Specimens B2 and B5 by Lukey and Adams (1969).

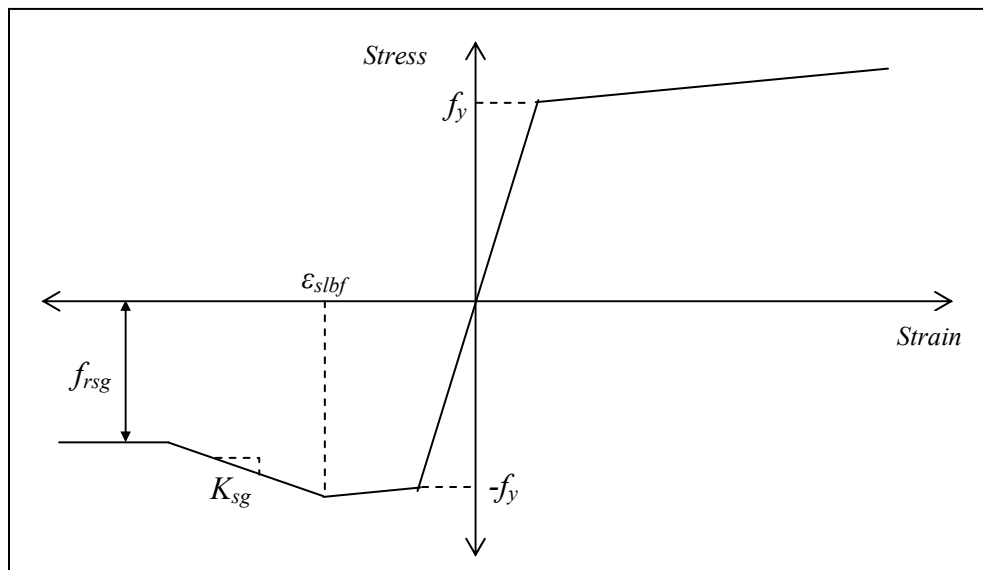


Figure 4.23 Monotonic Stress-Strain Response of Hot-Rolled Steel with Local Buckling

The specimens by Lukey and Adams (1969) were classified based on a slenderness of parameter of λ_c expressed in terms of slenderness of flanges (λ_f) and webs (λ_w) as defined below:

$$\lambda_f = \frac{b}{2t_f} \sqrt{\frac{f_y}{E_s}}, \quad \lambda_w = \frac{h}{t_w} \sqrt{\frac{f_y}{E_s}}, \quad \lambda_c = \sqrt{\lambda_f^2 + \lambda_w^2} \quad [4.17]$$

where:

b - flange width, t_f - flange thickness, h - depth of web, t_w - thickness of web

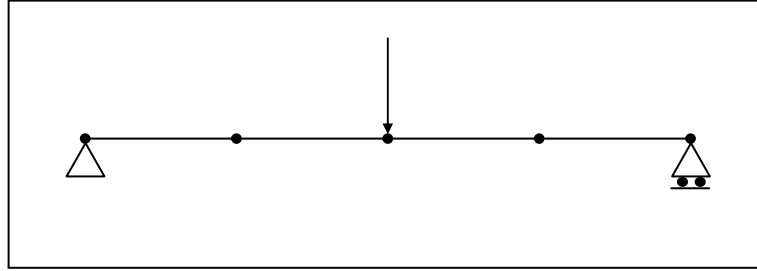


Figure 4.24 Computational Modeling of Specimens by Lukey and Adams (1969)

Specimen B2 and B5 by Lukey and Adams (1969) were selected to represent the steel cross-sections with low and high slenderness values, respectively. The geometric and material properties of the specimens are presented in Table 4.4, as well as, the calibrated values of ε_{slbf} and K_{sg} .

Utilizing the data values presented in Table 4-5, Equations 4.18 and 4.19 were derived to calculate ε_{slbf} and K_{sg} as a function of λ_c .

$$\varepsilon_{slbf} = -0.0159 \quad \lambda_c > 1.940 \quad [4.18a]$$

$$\varepsilon_{slbf} = 1.333 \times \lambda_c - 2.601 \quad 1.923 \leq \lambda_c \leq 1.940 \quad [4.18b]$$

$$\varepsilon_{slbf} = -0.0384 \quad \lambda_c < 1.923 \quad [4.18c]$$

$$K_{sg} = -1103.2 \quad \lambda_c > 1.940 \quad [4.19a]$$

$$K_{sg} = -24513 \times \lambda_c + 46450 \quad 1.923 \leq \lambda_c \leq 1.940 \quad [4.19b]$$

$$K_{sg} = -689.5 \quad \lambda_c < 1.923 \quad [4.19c]$$

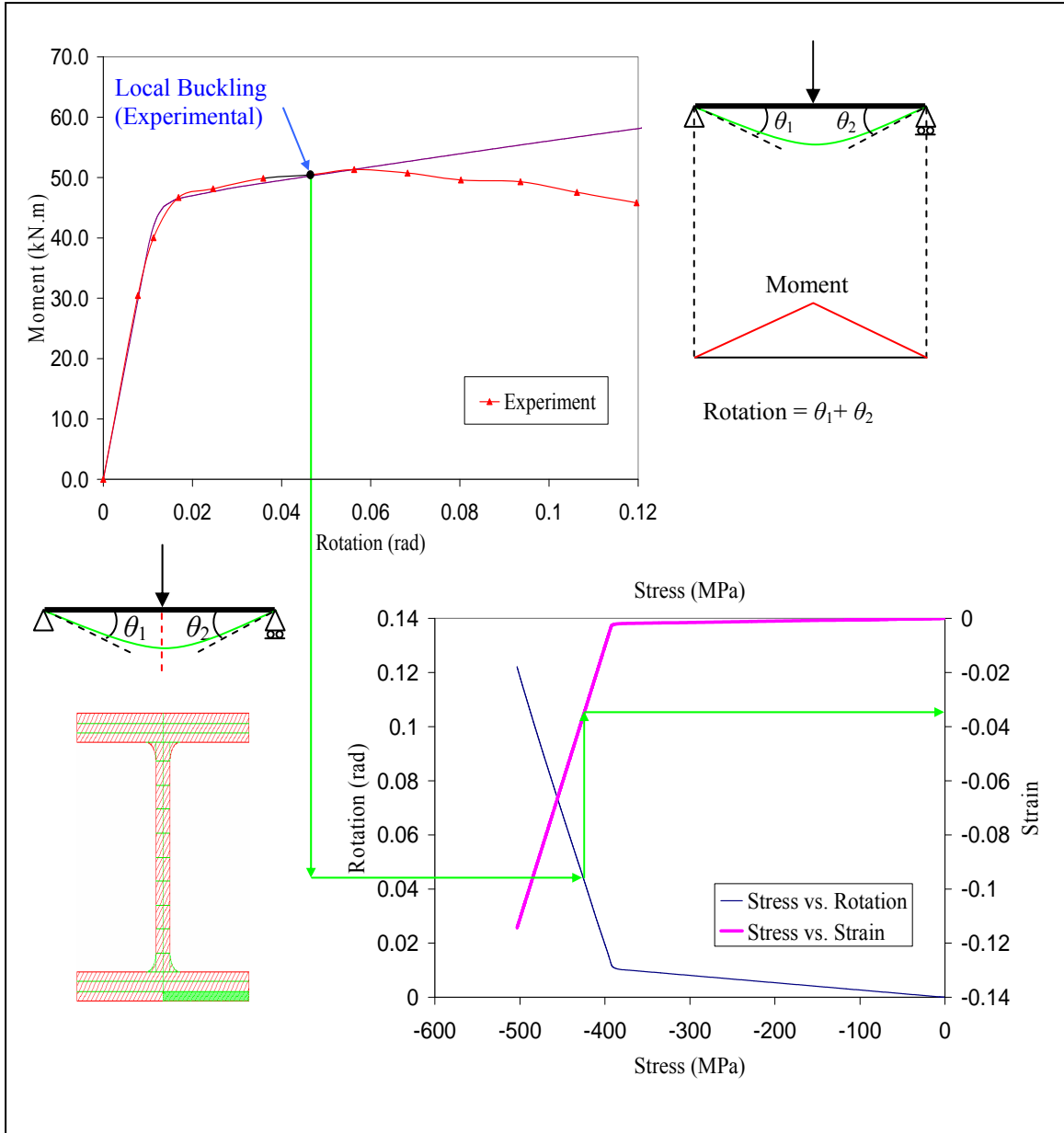


Figure 4.25 Determination of Local Buckling Strain Level for Specimens by Lukey and Adams (1969)

Table 4-5 Geometric and Material Properties of Representative Specimens of Low and High Slenderness Values

Specimen	d (mm)	b_f (mm)	t_f (mm)	t_w (mm)	f_{yf} (MPa)	f_{yw} (MPa)	λ_f	λ_w	λ_c	ϵ_{slbf}	K_{sg} (MPa)
B2	200.2	73.9	5.28	4.445	373.0	396.5	0.302	1.899	1.923	0.0384	689.5
B5	200.2	96.8	5.28	4.445	373.0	396.5	0.396	1.899	1.940	0.0159	1103.2

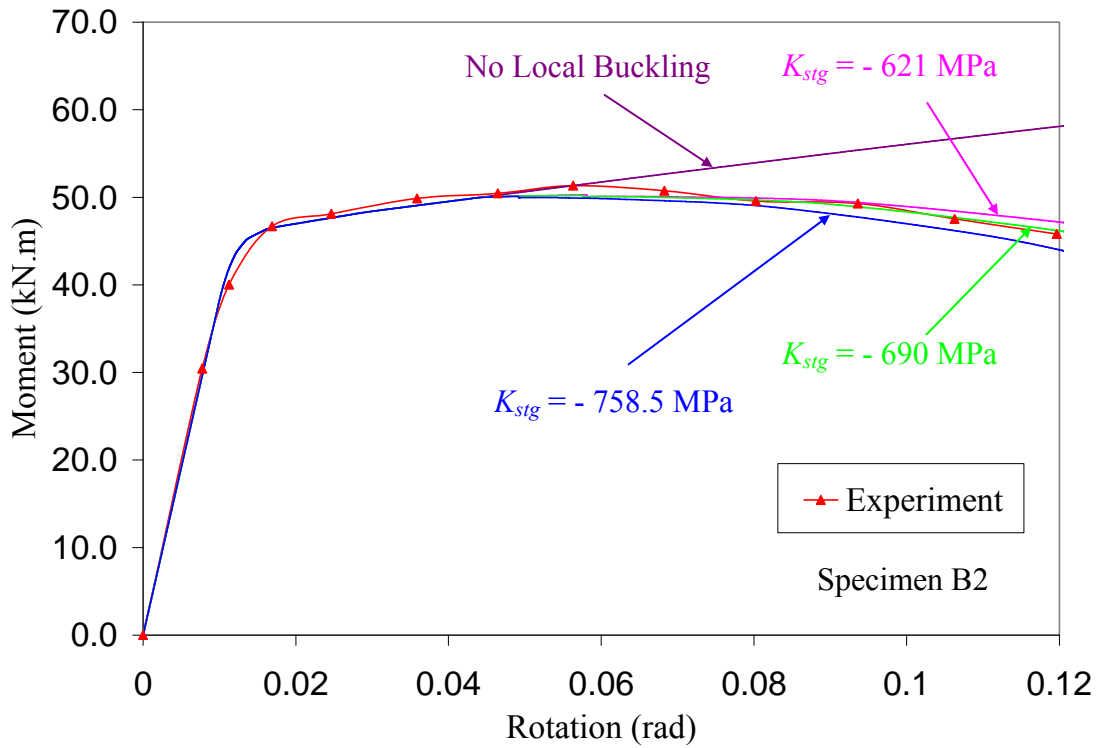


Figure 4.26 Calibration of K_{sg} for Specimen B2 (Lukey and Adams, 1969)

In the steel material model, the constant stress attained at high strain levels (f_{rsg}) was assumed to be 50% of the yield stress of the steel cross-section.

$$f_{rsg} = 0.5 \times f_y \quad [4.20]$$

The limiting value of f_{rsg} in Equation 4.20 was also found to be consistent with three-dimensional continuum analysis studies by Huang (2005) on steel girders under flexural loading. Figure 4.28 shows the comparison of Equation 4.17 with the f_{rsg} values suggested by Huang (2005) for flanges of steel girders across a range of steel cross-section sizes.

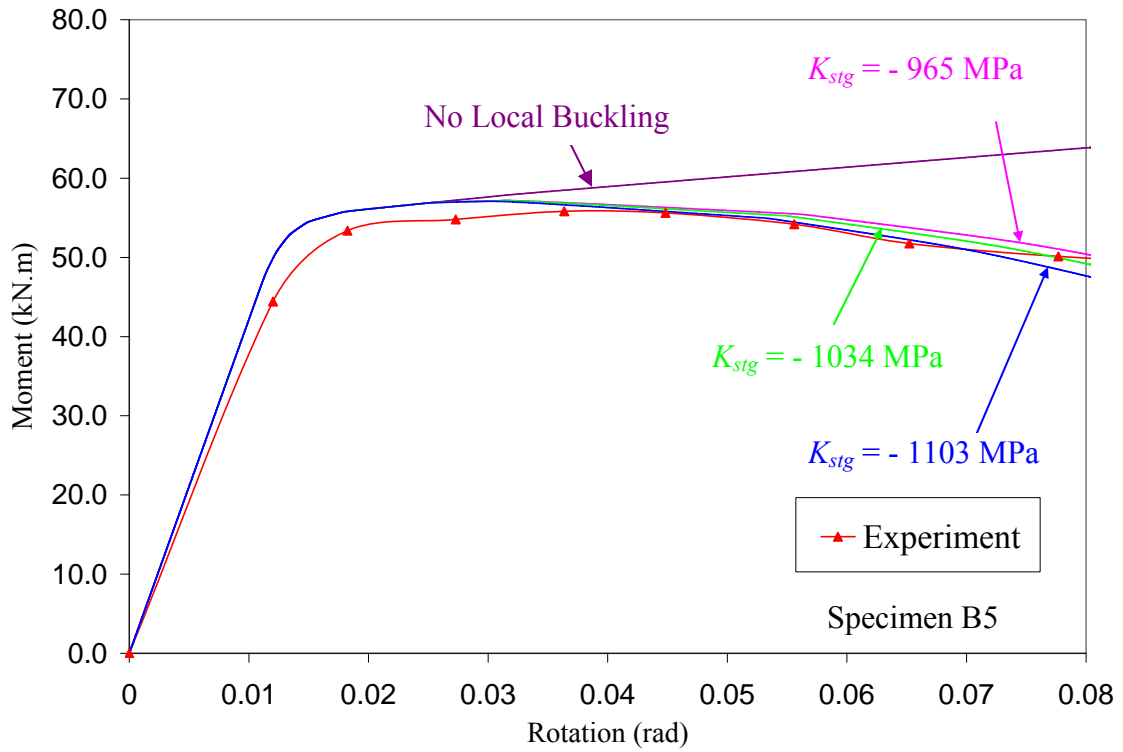


Figure 4.27 Calibration of K_{sg} for Specimen B5 (Lukey and Adams, 1969)

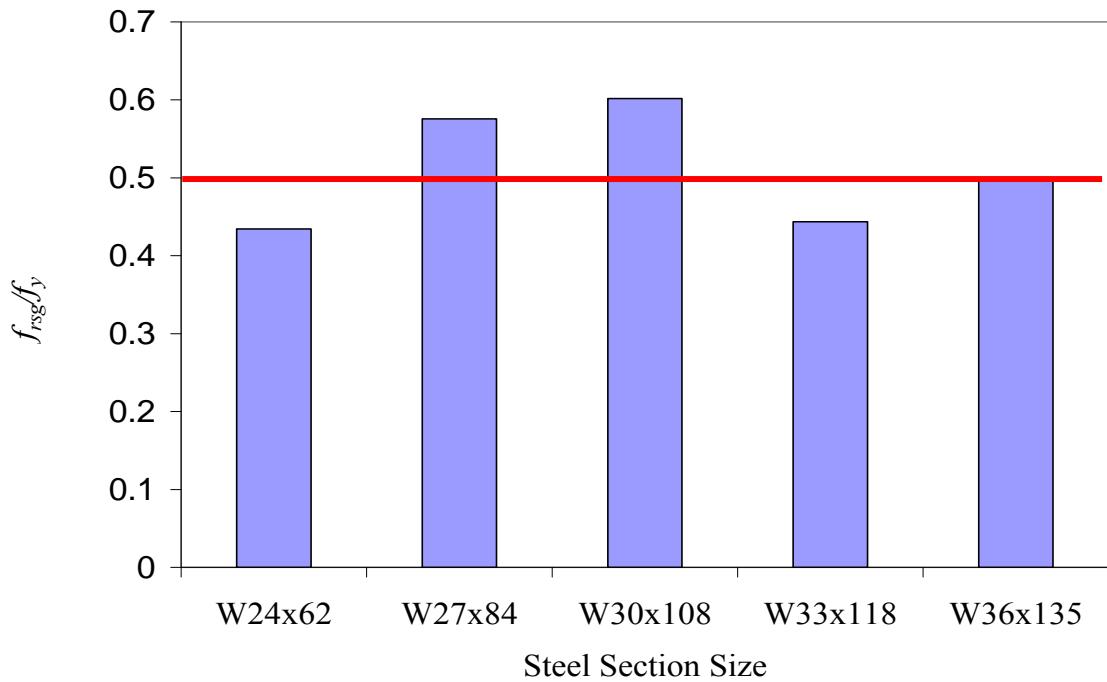


Figure 4.28 Comparison of $f_{rsg} = 0.5 \times f_y$ with the results from Huang (2005)

4.4.2. Cyclic Response

Structural steel sections are often known for their stable hysteresis response under cyclic loading as it is shown in Figure 4.29 (a). This feature makes them ideal for seismic applications since they contribute to the energy dissipation mechanism significantly. However, undesirable types of behavior associated with strength and stiffness degradation might also occur. Steel beams can be subjected to fracture due to local imperfections coupled with high stress and strain levels. This leads to a sudden deterioration of the cyclic response as can be seen in Figure 4.29 (b) (Gupta and Krawinkler, 1999). Moreover, steel members with slender cross-sections are susceptible to the local buckling phenomena, which results in stiffness and strength degradation in a gradual manner as cyclic loading is being applied (see Figure 4.29 (c)). Despite the strict compactness checks provided by the design provisions, local buckling might still take place under high seismic forces, which need to be considered for low-level performance objectives like Collapse Prevention. This requires developing an analysis tool that is capable of simulating the structural response following local buckling.

In the previous section, a computational model was developed to estimate the strain level at initiation of local buckling and the slope of the strength degradation response was also determined. However, it is not sufficient to examine the structural response under seismic forces since the effect of local buckling considering the cyclic deterioration effects was not addressed. The gradual increase in damage due to local buckling makes the accumulated plastic work a parameter that needs special attention to model local buckling. The bounding surface model by Mizuno et al. (1991) was modified assuming that the radius of the bounding surface decreases in size as function of accumulated plastic work (W^p) once local buckling takes place. The expression adopted to realize this idea is given in Equation 4.21, where the parameter γ represents the rate of reduction in the radius of bounding surface radius ($\bar{\kappa}$). In Equation 4.21, $\bar{\kappa}$ remains unbounded unless a limiting value to be maintained is specified for large values of W^p . Following the same approach in deriving f_{rsg} in Equation 4.17, $\bar{\kappa}$ was not allowed to attain values less than 50% of its initial value as described in Figure 4.30.

$$\bar{\kappa} = (\gamma \times W^p + I) \times \bar{\kappa}_o \quad [4.21]$$

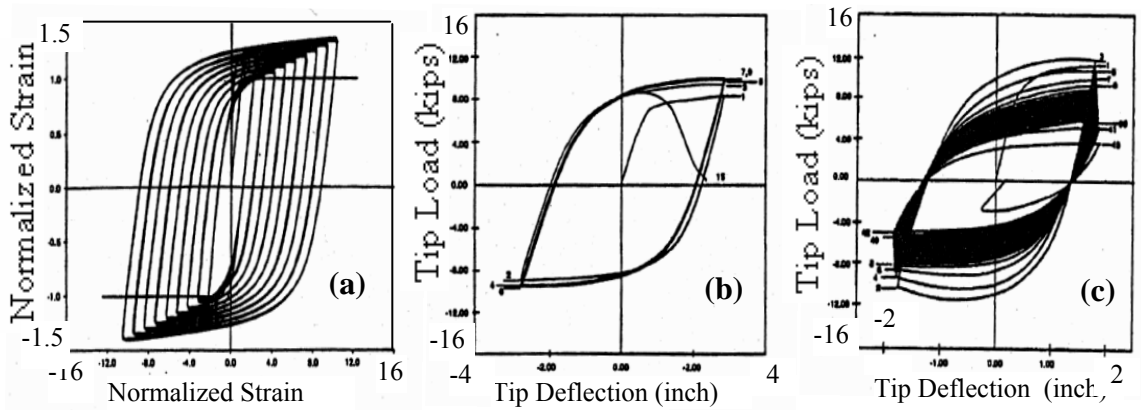


Figure 4.29 Cyclic Response of Structural Steel (Krawinkler et al., 1983)

The steel girder tests performed by Bertero et al. (1996) were utilized to calibrate numerical values for γ . The experiments consisted of W shape steel girder and steel column subassemblies, where the steel girder is tested under cyclic tip loadings as shown in Figure 4.31. A computational model of the test-setup was prepared using the mixed finite element formulation developed in Chapter 2. The column (W24x76) was defined with 4 finite elements while the girder (W30x99) was modeled with 3 elements per member. The number of integration points was selected as 3. The analysis was conducted for multiple values of γ including 0.0345, 0.0690, and 0.138 MPa. The comparison of experimental and computational results indicated that γ of 0.0690 gives the best correlation with the experimental results as can be seen in Figure 4.32.

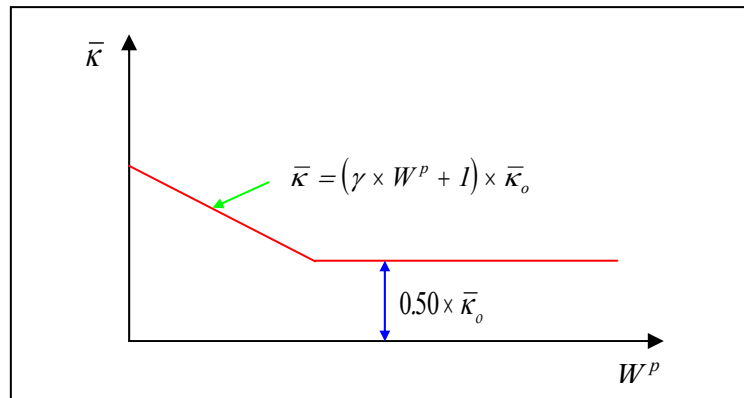


Figure 4.30 Evolution of Bounding Surface Radius as a Function of Accumulated Plastic Work

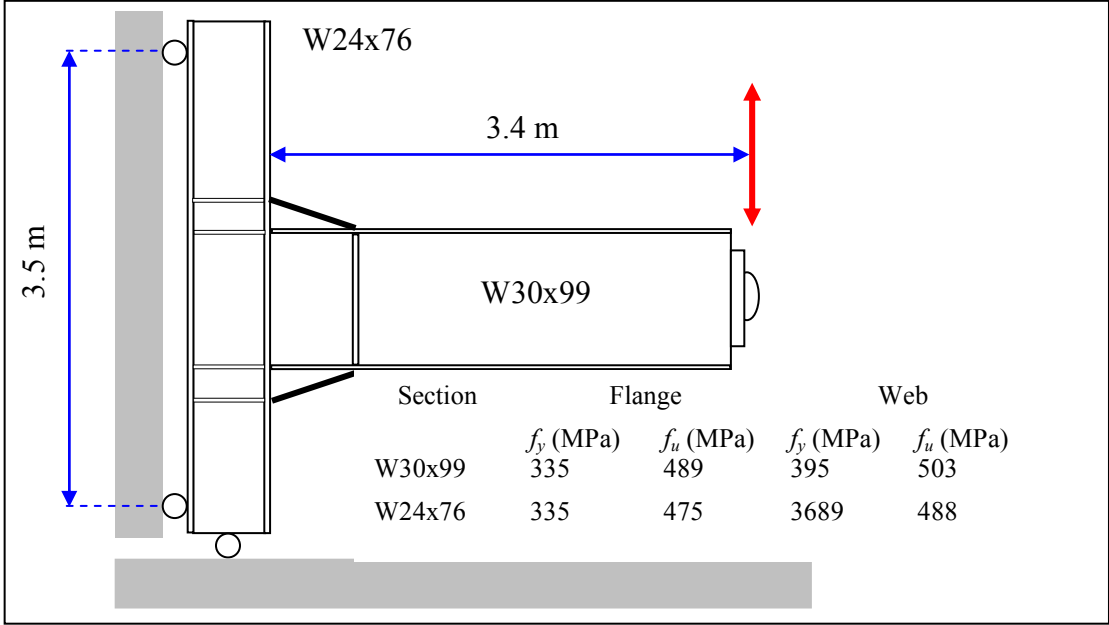


Figure 4.31 Test Setup for EERC-RN2 (Bertero et al., 1996)

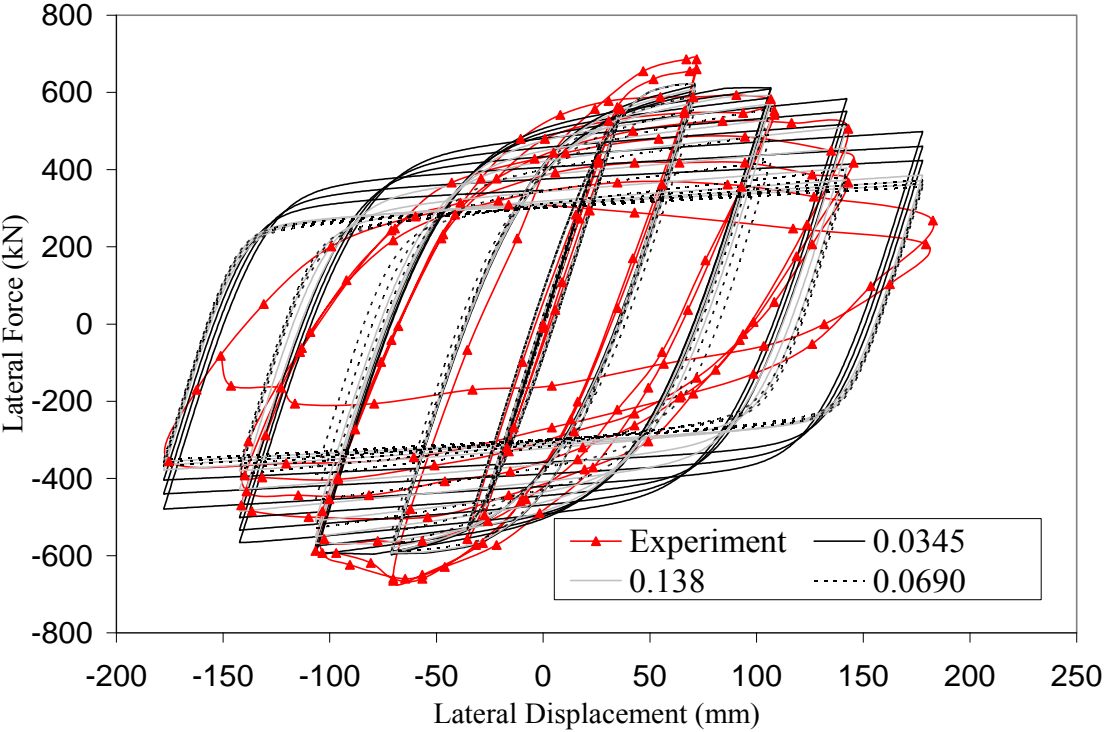


Figure 4.32 Calibration of γ with respect to EERC-RN2 (Bertero et al., 1996)

Chapter 5

5. Verification of the Mixed Finite Element Formulation

5.1. Introduction

Numerical implementation results of the mixed fiber-based beam-column element are documented in this chapter. It is aimed to provide comprehensive analysis results to investigate the accuracy of the formulation. Various types of RCFT members were analyzed with different loading types and boundary conditions. The accuracy of the analysis is decided based on the comparisons of computational results with analytical solutions and experimental results where available. The comparisons are performed not only at the load-deformation level but also at the cross-section and stress-strain level. While analyzing frame type of structures, the vertical members are modeled using the mixed RCFT beam-column element. An equivalent mixed steel beam-column element is utilized to simulate the horizontal members and additional verification studies are also provided to evaluate its accuracy.

The first verification set is prepared for geometrically nonlinear elastic problems. In these problems, the formation of slip is prevented since there exist no analytical solution available in the literature to compare to if the steel tube and the concrete core experience differential displacement. The cross-sectional stiffness values are hard-coded into the analysis program and they are shared equally between the two media. This approach is adopted for convenience. The analysis results did not exhibit any variation with respect to the proportion of cross-sectional stiffnesses assigned to the steel tube and the concrete core.

A total number of 6 verification sets are prepared for geometrically and materially nonlinear static problems of RCFTs. The RCFT specimens to be analyzed are selected from the experimental database by Tort and Hajjar (2003). The specimens to be used for

verification are grouped with respect to the loading schemes as slip critical, axially loaded, pure-bending, proportionally-loaded, non-proportionally loaded, and cyclically loaded. The verification study for steel girders consists of pure bending tests under monotonic and cyclic loading schemes.

In the case of dynamic problems, two verification sets are provided. The first set contains geometrically nonlinear elastic type damped and undamped problems. A plane frame test performed at the University of Lehigh by Herrera (2005) was analyzed to verify the fully-nonlinear dynamic analysis feature of the formulation.

5.2. Geometrically Nonlinear Elastic Problems

5.2.1. Euler Buckling of a Simply Supported RCFT Column

The ability of the mixed finite element formulation in producing the Euler buckling load is studied by analyzing a simply supported column as shown in Figure 5.1. The column is assumed to be perfectly straight without any imperfections. A linearly increasing concentric axial load is applied. The critical load of the column (P_{cr}) is calculated using the formula given in Equation 5.1 assuming an effective length factor (K) of 1.

$$P_{cr} = \frac{\pi^2 EI}{(KL)^2} \quad [5.1]$$

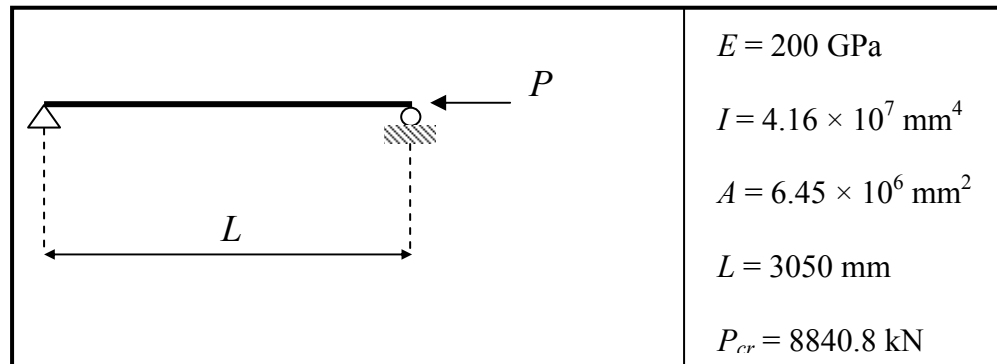


Figure 5.1 Buckling of a Simply Supported RCFT Column

Buckling of the column is decided when the minimum-eigen value of the global stiffness matrix becomes negative. The analysis is performed using 1, 3, and 5 elements per member. As it is portrayed in Figure 5.2, the discrepancy between the theoretical and computational results diminishes significantly as the number elements increases. The effect of the number of integration points on the analysis results is studied by using 3 and 5 integration points per element. However, the variation in the results is found to be insignificant. In Figure 5.2, the analysis results are reported when 5 gauss points are introduced. Schiller and Hajjar (1998) previously studied the same problem using a mixed-based finite element formulation and the current buckling load predications are found to be compatible with those obtained by Schiller and Hajjar (1998).

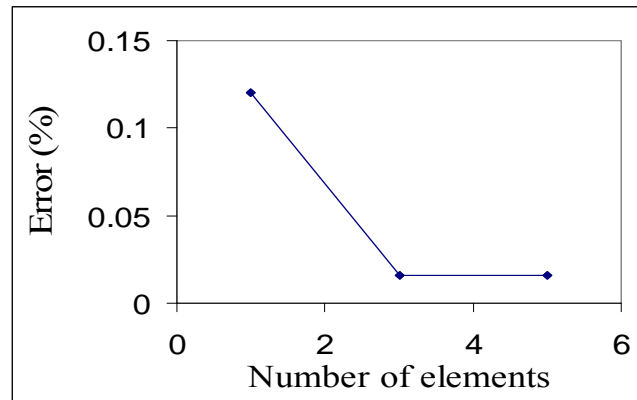


Figure 5.2 Buckling of a Simply Supported RCFT Column

5.2.2. Elastic Stability of a Cantilever Column

The cantilever column shown in Figure 5.3 is subjected to a linearly increasing concentric axial load. The theoretical buckling load (P_{cr}) is calculated as 2210 kN using Equation 5.1 with a K factor of 2. The analysis results are presented for a constant axial load increment of 2.2 kN. The cantilever column is analyzed using 1, 3, and 5 elements along its length. The number of integration points is also varied as 4 and 6. It is found that even with a single element, excellent correlation with the theoretical buckling load is attained. The change in the number of gauss points does not affect the accuracy of the results. However, increasing the number of elements produced slightly improved the correlation with the theory.

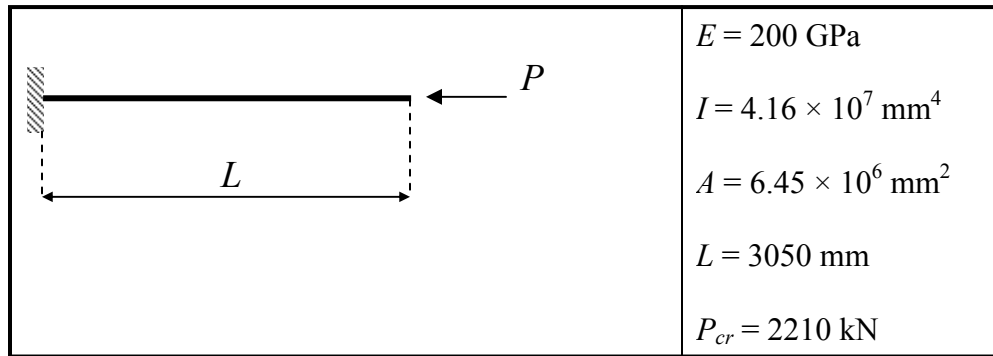


Figure 5.3 Buckling of Cantilever RCFT Column

Table 5-1 Analysis Results for Cantilever RCFT Column with Axial Load

Number of Elements	Number of Gauss Points	Load Step Size	P_{cr} (kN)	Error (%)
1	4	0.001	2212.9	0.131
1	6	0.001	2212.9	0.131
3	4	0.001	2210.6	0.027
3	6	0.001	2210.6	0.027
5	4	0.001	2210.6	0.027
5	6	0.001	2210.6	0.027

5.2.3. RCFT Cantilever Under Pure Bending

The problem presented in Figure 5.4 is a cantilever subjected to linearly increasing end moment. This problem is selected to test the performance of the mixed finite element formulation under large displacements, large rotations, and small strains.

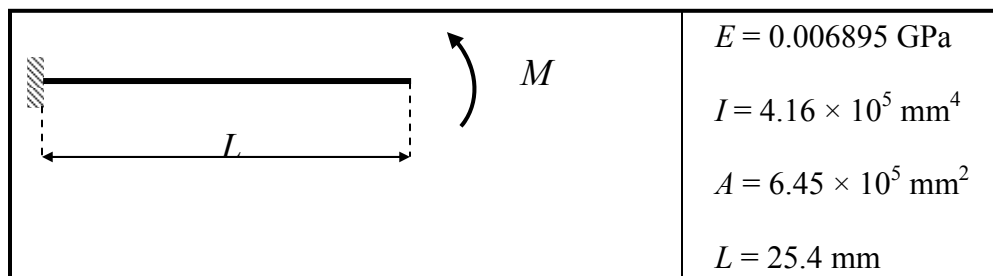


Figure 5.4 Cantilever RCFT Column under Pure Bending

A constant moment increment of 0.71 kN.m is applied until the cantilever is fully wrapped around the support as it is illustrated in Figure 5.6. The analytical solution of

the problem can be found in Morales (1994). The analysis is performed using 3, 5, and 10 finite elements per member. Figure 5.5 shows that a good correlation can be obtained between analytical and computational results if the number of finite elements is more than 3. The number of integration points was found not to have a significant effect on the accuracy of the results. Therefore, in Figure 5.5, the analysis results are presented when 4 integration points per member are used.

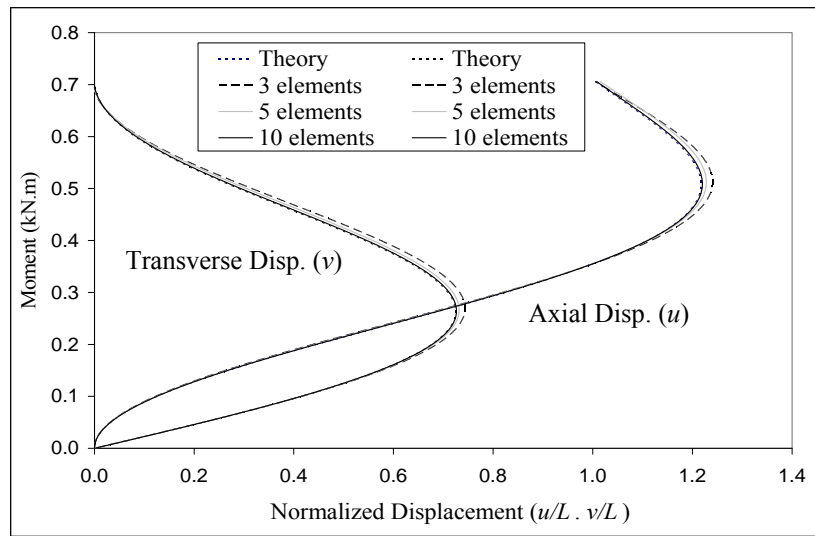


Figure 5.5 Analysis Results for RCFT Cantilever under Pure Bending

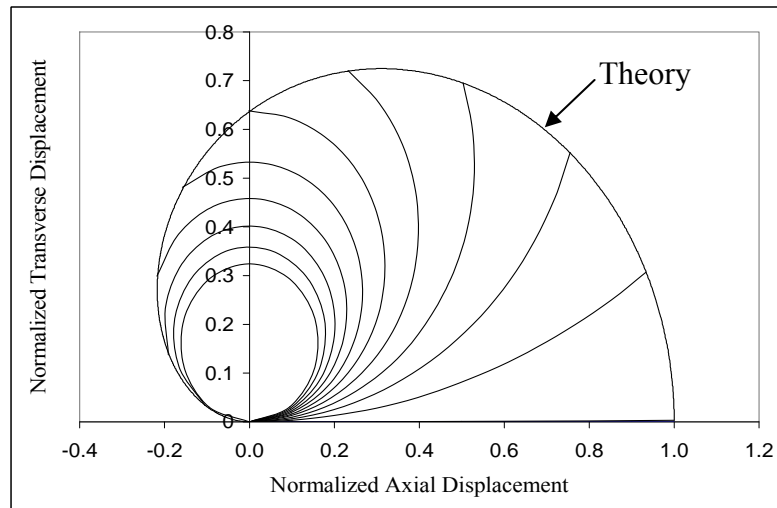


Figure 5.6 Displaced Shape of RCFT Cantilever under Pure Bending

5.2.4. RCFT Cantilever Under Transverse Tip Loading

An RCFT cantilever subjected to a transverse tip loading as shown in Figure 5.7 is analyzed. The cantilever undergoes large displacements and rotations causing significant axial elongation. This problem helps to investigate the performance of the mixed finite element formulation in simulating a tension stiffening type of geometrically nonlinear behavior.

The analysis results are compared to the analytical solution given by Mattiasson (1981). A constant shear force increment of 0.04448 kN is applied until the transverse displacement reaches 81% of the undeformed length of the RCFT cantilever.

The analysis is conducted using 3, 5, and 10 finite elements per member. The number of integration points is kept as 4 since it was observed that the analysis results did not exhibit significant variation with respect to the number of integration points. As it is portrayed in Figure 5.8, good correlation is achieved between the analytical and computational results. It is found that increasing the number of elements improved the accuracy of the transverse displacements. On the other hand, the degree correlation of the axial displacements is very good irrespective of the size of the finite element mesh. The displaced shape of the cantilever at intervals of 10% of the total applied load can be seen in Figure 5.9.

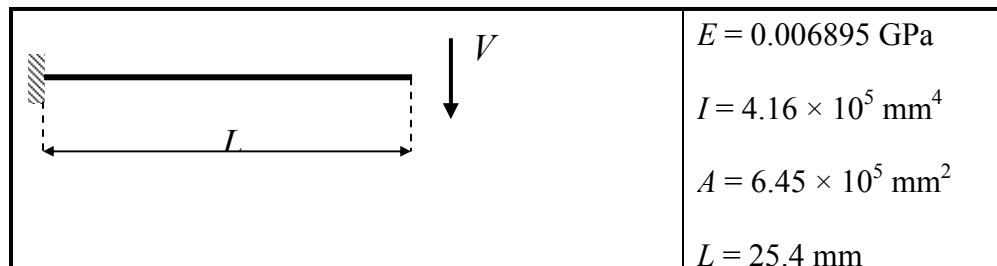


Figure 5.7 RCFT Cantilever under Transverse Tip Loading

5.2.5. Harrison's Portal Frame

A rectangular portal frame is modeled using two RCFT columns and a steel girder. As defined in Figure 5.10, the portal frame is subjected to two vertical loads and a

lateral load. The RCFT columns and the steel girder are modeled using 3 elements per member with 4 integration points. The analysis is conducted by applying the lateral force in 100 load steps and it was determined that reducing the load increments did not produce significant changes in the final response of the frame.

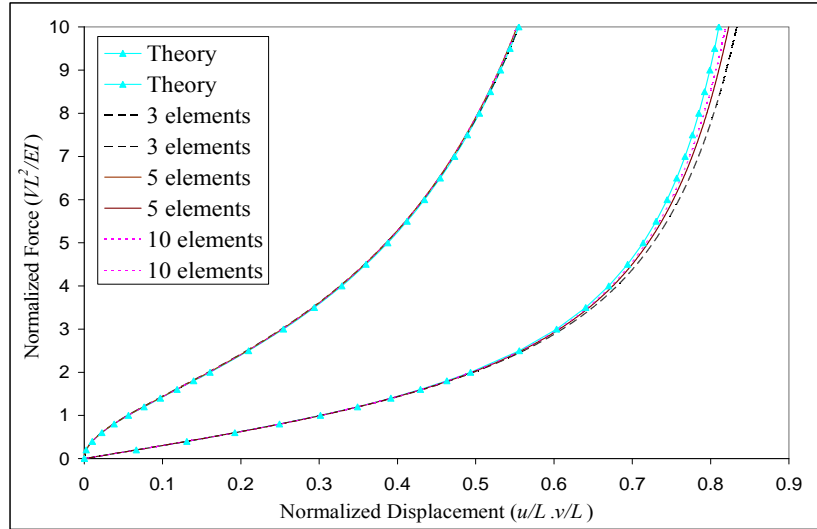


Figure 5.8 Load-Deflection Response of RCFT Cantilever under Transverse Tip Loading

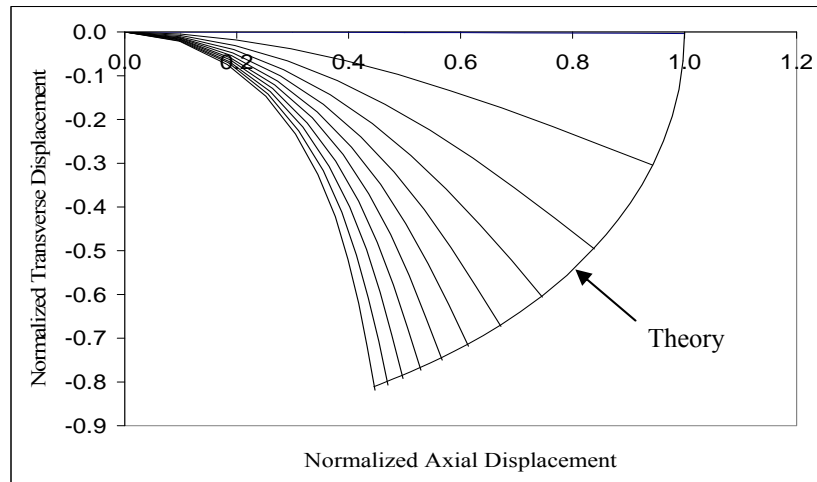


Figure 5.9 Displaced Shape of RCFT Cantilever under Transverse Tip Loading

The analysis results for the maximum moment and lateral deflection of the windward column are compared with the stability function results reported in Clarke et

al. (1993) in Table 5-2. It is found that good correlation is obtained with respect to both displacements and forces. The error increases as the lateral load attains its final value.

The discrepancy of displacements from the stability function results is larger than that of the maximum moment values. The largest error for displacements is found to be 2.30 % while a 0.25% error is obtained as the largest error for the maximum moment values. The load-deflection response of the portal frame is shown in Figure 5.11, where the good correlation between mixed finite element and stability function results is evident.

5.2.6. Right-Angled Simply Supported Frame

The next benchmark problem for geometrically nonlinear elastic analysis is selected as the right-angled simply supported frame by Lee et al. (1968). This problem is analyzed numerically by several researchers in the past including Nukala (1997), Souza (2000), and Alemdar and White (2005). The motivation in investigating the right-angled frame is to assess the performance of the mixed finite element formulation when RCFT beam-columns and steel girders are used together in a frame. The accuracy of the results shows the quality of the transformation relations between corotational and global coordinates. In addition, with this problem, it is possible to test how accurately the mixed finite element formulation handles large rotations and elongations in the corotational frame.

As it is introduced in Figure 5.12, the vertical member is defined as an 18 DOF RCFT column while the horizontal member is simulated as a 12 DOF steel girder. The support conditions are assumed to be pinned. Two types of discretization schemes are employed including 3 and 5 elements per member. The analysis is conducted using the generalized displacement control algorithm proposed by Yang and Kuo (1994). The magnitude of the reference load vector is selected as 80064 kN and the initial load factor is assumed to be 0.01.

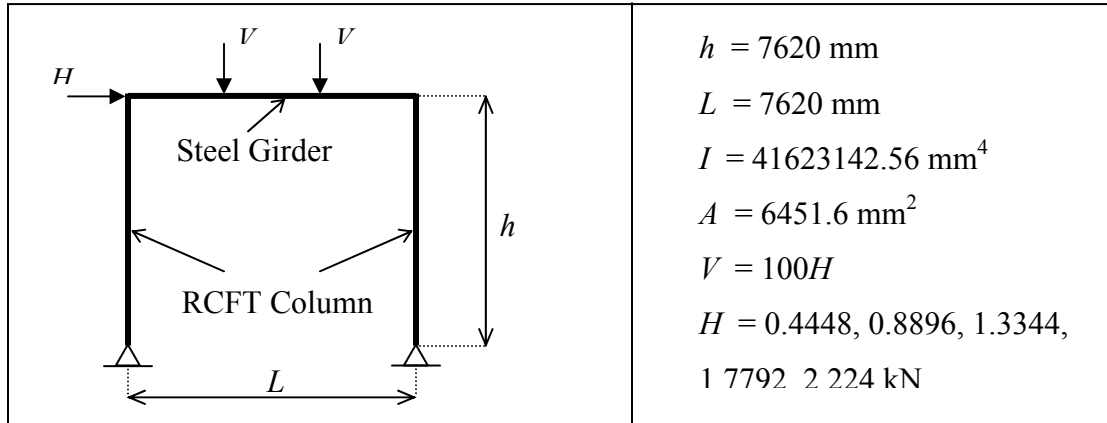


Figure 5.10 Harrison's Portal Frame

Table 5-2 Analysis Results for Harrison's Portal Frame

V (kN)	Stability Function	Finite Element	Error (%)	Stability Function	Finite Element	Error (%)
	Sway (mm)	Sway (mm)		M_{\max} (kN.m)	M_{\max} (kN.m)	
44.48	7.16	7.16	0.0	69.04	68.96	0.12
88.96	18.34	18.37	0.16	139.44	139.24	0.14
133.44	37.06	37.20	0.38	211.54	211.14	0.19
177.92	74.02	74.64	0.84	286.34	285.64	0.25
222.4	184.18	188.41	2.30	368.83	367.90	0.25

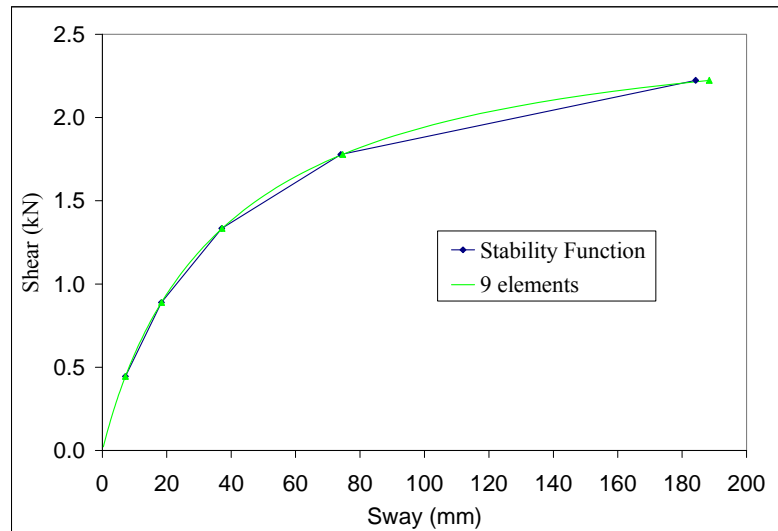


Figure 5.11 Load-Deflection Response of Harrison's Portal Frame

The analysis results are illustrated for the vertical and horizontal displacements of the node where the transverse force is being applied. As it is shown in Figure 5.13, the complete load-path is simulated and a good agreement is obtained between the computational and analytical results. The buckling load of the frame is determined to be 84293.0 kN, which is comparable to the critical load of 82699.4 kN reported by Alemdar and White (2005).

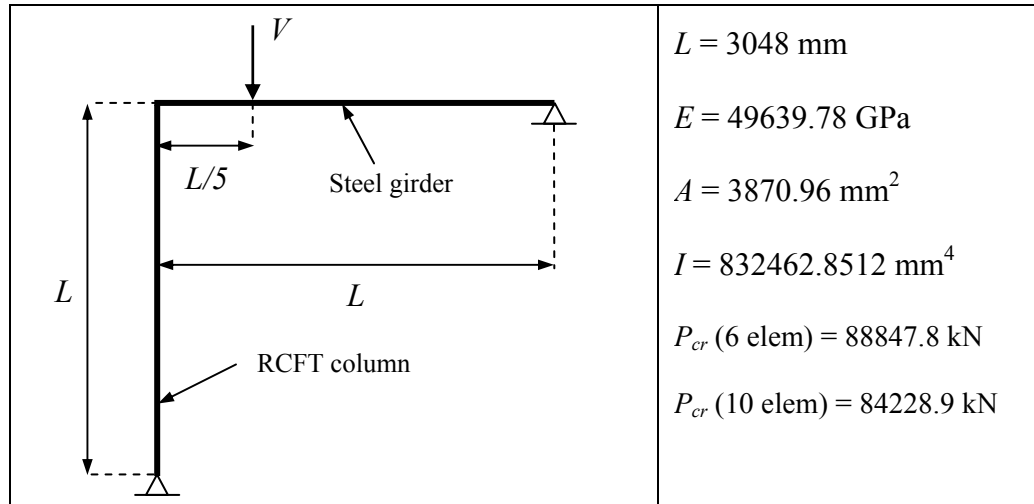


Figure 5.12 Right-Angled Simply Supported Frame

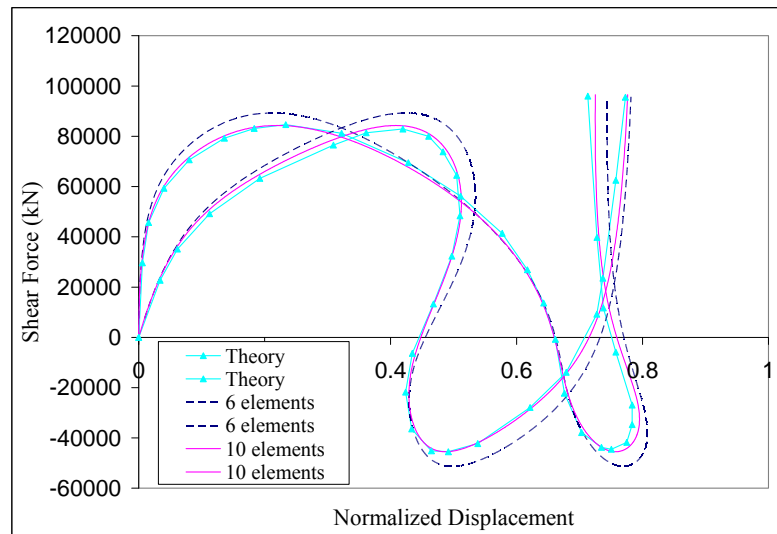


Figure 5.13 Load-Deflection Response of Hinged Right-Angle Frame

In Figure 5.14, the deformed shape of the frame is presented at equal time intervals until the end of the analysis. The buckled shapes in Figure 5.14 illustrate the severity of geometric nonlinearity involving large rotations and elongations.

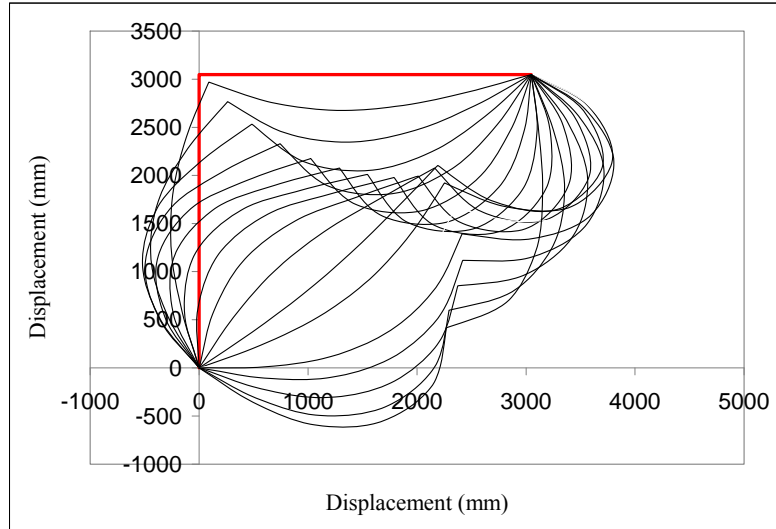


Figure 5.14 Displaced Shape of Right Angled Simply Supported Frame

5.1.7 Post-Buckling Response Axially Loaded RCFT Cantilever

The post-buckling response of an RCFT cantilever is investigated as described in Figure 5.15. A small bending moment is introduced at the free end of the cantilever creating a perturbation. The analyses are performed using 3, 5, and 10 elements per member. The number of integration points is kept as 4.

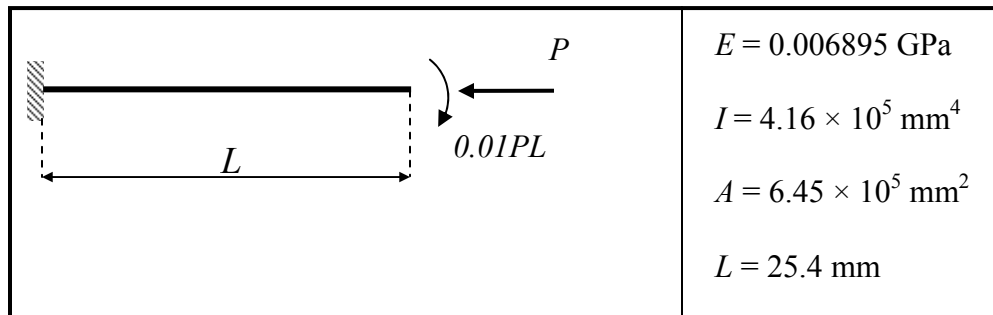


Figure 5.15 Axially Loaded RCFT Cantilever

The analysis results are compared to the analytical solution given in Southwell (1941). As it is illustrated in Figure 5.16, the mixed finite element formulation produced accurate simulations compared to the analytical results. An increase in the correlation can be noticed as the finite element discretization gets finer.

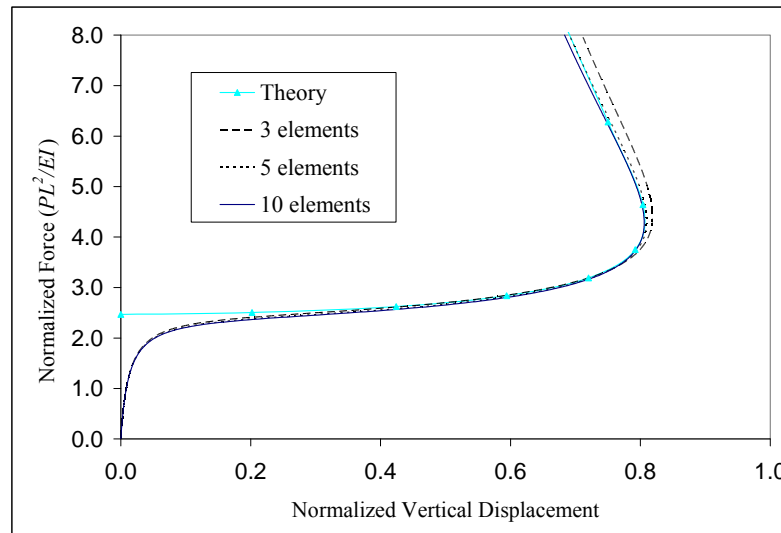


Figure 5.16 Load Deformation Response of Axially Loaded RCFT Cantilever

5.3. Geometrically and Materially Nonlinear Problems

5.3.1. Slip Critical Materially and Geometrically Nonlinear Problems

The majority of the computational studies to date on analysis of RCFT columns do not simulate the load transfer mechanism between the steel tube and the concrete core. It is usually assumed that strain compatibility is strictly satisfied, especially, if line elements are utilized in the analysis. Using this approach, the studies conducted by Gourley and Hajjar (1994) and Huang (2005) produced accurate simulations of experimental specimens and frame structures. However, both of the aforementioned studies focused on structures having steel girders attached to RCFT columns via moment connections, where initiation of slip is not expected. On the other hand, in the case of gravity or braced frames, steel girders may be attached to RCFT columns without

penetrating into the concrete core by means of connection components welded to the steel tube such as fin-plates and tee cleats (Shakir-Khalil and Mahmoud, 1995). In the RCFT frames of this sort, the gravity and live loads are first transferred to the girders, then from girders to the steel tubes, and finally to the concrete core through the interface. Since the interface is stressed to ensure the load transfer, strain compatibility may not be satisfied causing the formation of differential axial deformation, which is referred as slip throughout the text.

As described in the preceding sections, Hajjar et al. (1998a, 1998b) developed a fiber-based finite element formulation allowing the force exchange between the steel tube and the concrete core. The constitutive relationship of the interface was represented through a nonlinear constitutive rule as given in Figure 5.17. The interface possesses a very high initial stiffness (k_{sc}) until the attainment of the bond strength (f_{sc}). Following the breachment of the bond strength, the stress level is maintained with a mild stiffness without any deterioration. The tests conducted to examine the cyclic response of the steel and concrete interface indicated that repeated stress-reversals do not have a significant detrimental effect of the bond strength and stiffness (Morishita et al., 1979a, 1979b; Shakir-Khalil 1993a, 1993b). Therefore, the unloading and reloading stiffnesses of the interface are taken as equal to its initial values exhibiting a cyclic bond stress vs. slip relation as presented in Figure 5.17.

Implementing the nonlinear slip vs. bond stress relationship in a finite element formulation requires the calibration of the bond strength and stiffness values. This can be achieved through studying the RCFT experiments in the literature and analyzing the information related to the slip behavior. Hajjar et al. (1998a, 1998b) reviewed the push-out experiments in the literature and identified two types of push-out tests depending on the nature of the loading scheme as concrete-loaded and steel-loaded. The concrete-loaded tests were performed by introducing different boundary conditions as shown in Figure 5.18.

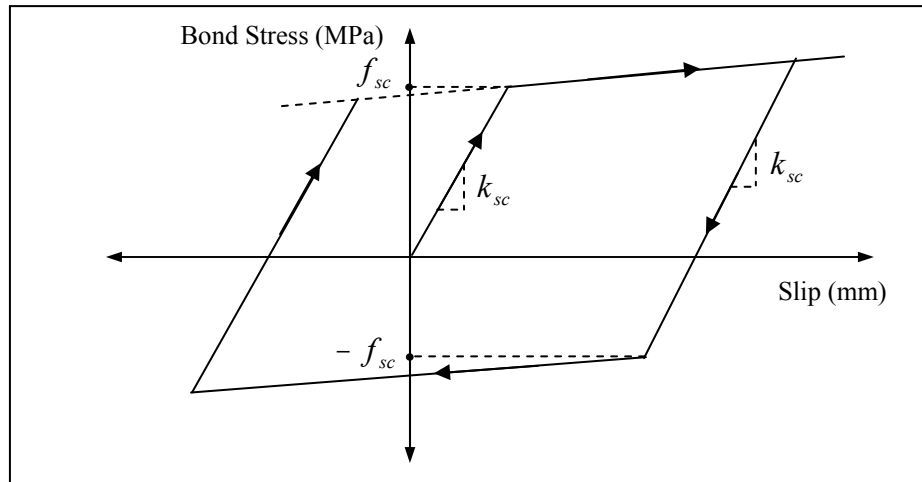


Figure 5.17 Constitutive Rule of Steel and Concrete Interface

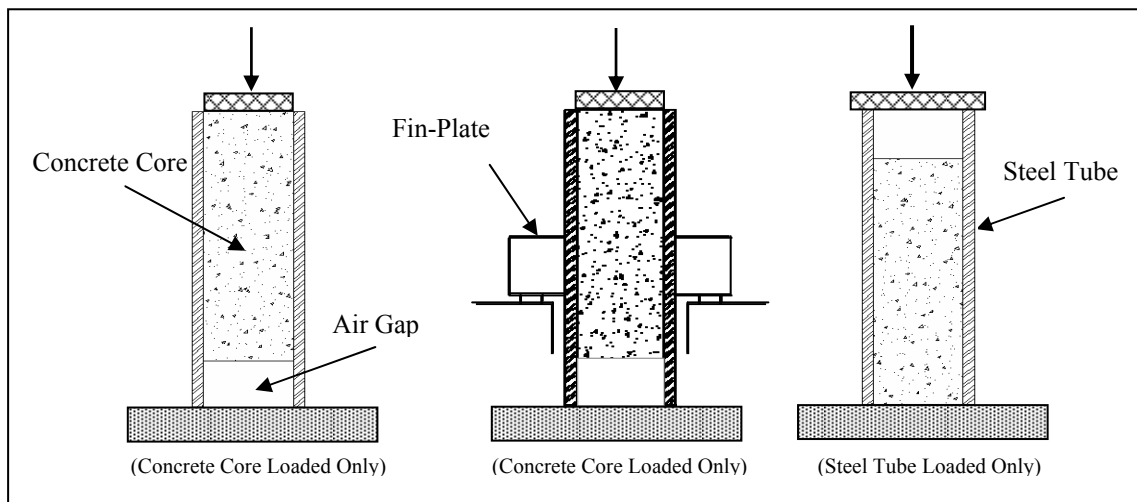


Figure 5.18 Experimental Setup of Push-out Tests

Virdi and Dowling (1980), Shakir-Khalil (1993a, 1993b), and Roeder et al. (1999) tested RCFT columns under concentric axial loading where the concrete core was loaded alone while the specimen was resting on the steel tube at the bottom. Morishita et al. (1979a, b) conducted push-out tests by loading the steel tube alone at the top while the RCFT specimen was supported on the steel tube and the concrete core simultaneously at the bottom. The main purpose of the push-out tests is to study the range of bond strength and also to identify the factors affecting its limiting values. In Figure 5.19, the bond strength values from the concrete-core loaded push-out tests by Shakir-Khalil

(1993a, 1993b) and Shakir-Khalil and Hassan (1994) are plotted with respect to the compressive strength of concrete. Only the specimens without any shear connectors inside the steel tube are considered. The bond strength values exhibit a large variation ranging from 0.15 MPa to 0.75 MPa.

The same trend can also be observed in Figure 5.20 when the axial load is applied on to the steel tube. Figure 5.20 was generated using the experimental data by Morishita et al. (1979a, 1979b), where the inside surfaces of the steel tubes were free of any shear connectors. The bond strength values are smaller compared to the results from the concrete core loaded type push-out tests. The minimum and maximum bond strength values are 0.13 MPa and 0.36 MPa, respectively.

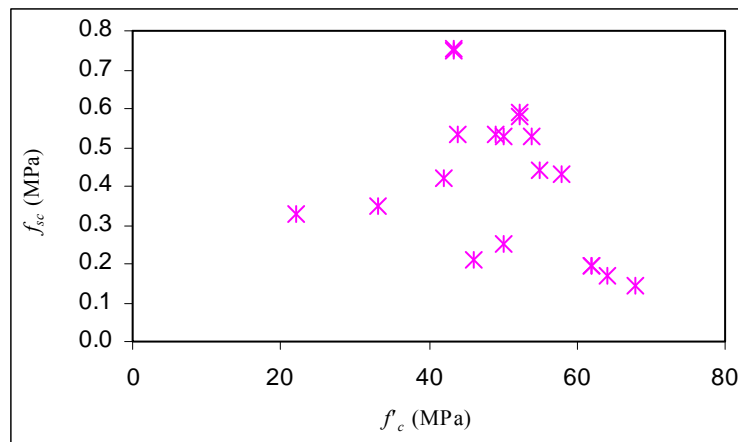


Figure 5.19 Variation of Bond Strength wrt. Compressive Strength of Concrete

To calibrate and verify bond strength and stiffness values, Hajjar et al. (1998a, 1998b) utilized connection tests in the literature, where RCFT columns are framed by steel girders using simple connection types. Transverse loading is applied to the steel girders while the axial load on the RCFT column is also increased. This loading scheme is considered to be a rational approach to investigate the load-transfer mechanism and to evaluate its characteristics. Based on parametric studies on connection tests, Hajjar et al. (1998a, 1998b) recommended a bond strength value of 0.6 MPa and an interface stiffness of 10^4 MPa. The same values were also adopted in the current study to test the ability of mixed finite element formulation in simulating the force exchange between the steel tube and the concrete core. Representative connection tests from Shakir-Khalil (1994) and

Dunberry et al. (1987) were analyzed to assess the performance of the proposed finite element formulation.

The test setup by Shakir-Khalil (1994) for specimen E6 is shown in Figure 5.21. The steel girders are attached to the RCFT column using tee-cleat type simple connections. Axial load on the column and transverse force applied to the girders are increased proportionally, where the direction of loading is upwards. The compatibility of the axial strains at the end of the RCFT column is ensured via applying the load to the composite cross-section uniformly. Shakir-Khalil (1994) provided strain data of the steel tube before material inelasticity takes place at the connection region. This allows investigating the load transfer mechanism more reliably since the strain profile of the steel tube is directly attributed to the interaction taking place at the interface. Due to the lack of any slip measurement, the experimental tests by Shakir-Khalil (1994) were considered to be appropriate for investigating the ranges of slip stiffness values. The RCFT column was modeled using a total number of 11 elements to ensure a sufficient resolution in comparing the results, and 4 integration points were introduced for each finite element. As defined in Figure 5.21, the transverse loading was assumed to be applied at three locations by introducing a load distribution of 25%-50%-25% at the bottom, middle, and top points of the connection region, respectively.

The comparison of the experimental and computational strain profile along the length of the RCFT column can be seen in Figure 5.22 at a load level 600 kN. Three sets of analysis were conducted. In each of the analyses, the stiffness of the interface was assumed to have a different value including 10^3 MPa, 10^4 MPa, and 10^6 MPa. The computational results exhibited a good correlation with the experimental strain profile. An error analysis of the results is presented in Table 5-3. The average error for each analysis case is not more than 6%. The least amount error was obtained when the interface stiffness was set to 10^6 MPa.

The analysis of Specimen E6 by Shakir-Khalil (1994) was also conducted until an axial load level of 800 kN. Three cases were studied by varying the initial stiffness of the interface (i.e., prior to breaching of the bond strength) as 10^3 MPa, 10^4 MPa, and 10^6 MPa. Figure 5.23 illustrates the comparison of computational and experimental results

for the strain distribution in the steel tube. The reported strain data is well predicted by the computational results. The comparisons below the connection region are found to be better than those above the connection region. This trend is valid for each value of the interface stiffness. In Table 5-4, the error analysis of the computational results is presented. It is found that the interface stiffness of 10^6 MPa produced the lowest value of average error and standard deviation. The length of the load transfer region is over predicted when lower values are introduced for the stiffness of the interface.

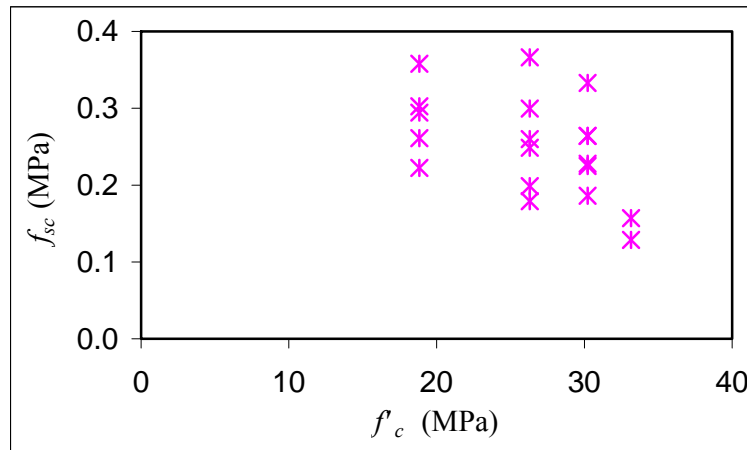


Figure 5.20 Variation of Bond Strength wrt. Compressive Strength of Concrete

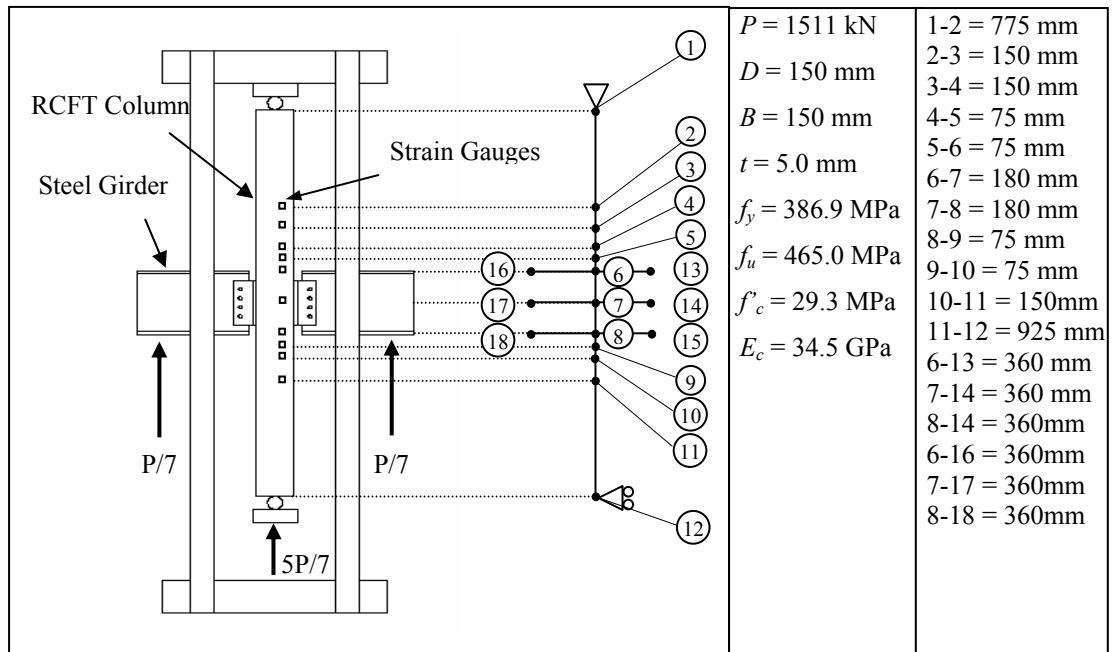


Figure 5.21 Simple Connection Tests Setup by Shakir-Khalil (1994)

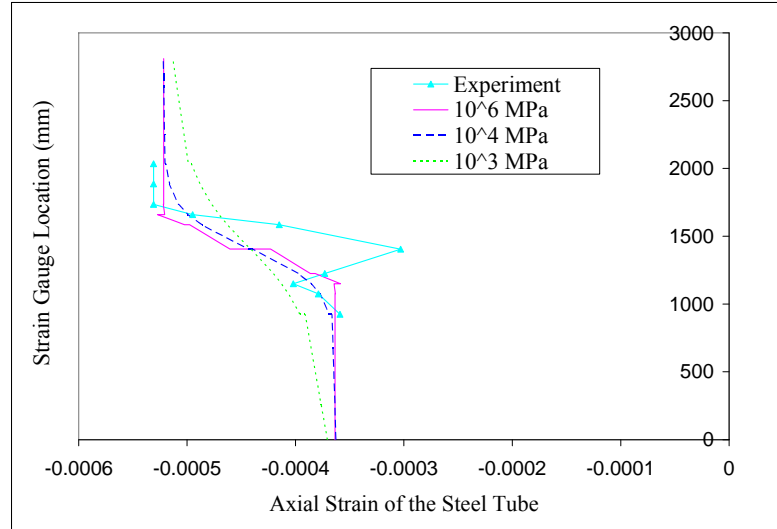


Figure 5.22 Axial Strain Distribution of the Steel Tube at 600 kN (Specimen E6, Shakir-Khalil, 1994)

Table 5-3 Error Analysis of Strain Distribution of the Steel Tube at 600 kN (Specimen E6, Shakir-Khalil, 1994)

Strain Gauge	Error (%)		
	$\bar{k}_{sc} = 10^6 \text{ MPa}$	$\bar{k}_{sc} = 10^4 \text{ MPa}$	$\bar{k}_{sc} = 10^3 \text{ MPa}$
1	1.28	2.03	8.94
2	-4.14	-0.42	7.23
3	-9.35	-4.15	2.71
4	3.57	6.43	12.65
5	39.60	45.02	45.58
6	19.95	17.30	11.57
7	6.53	0.87	-4.95
8	-1.71	-4.43	-10.13
9	-1.77	-2.75	-8.08
10	-1.77	-2.17	-6.59
Average	5.22	5.77	5.89
Std. Dev	14.40	15.23	16.33

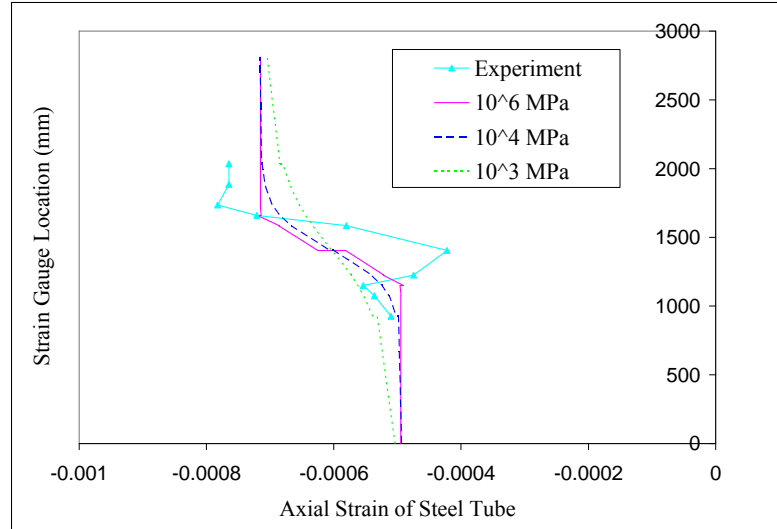


Figure 5.23 Axial Strain Distribution of the Steel Tube at 800 kN (Specimen E6, Shakir-Khalil, 1994)

Table 5-4 Error Analysis of Strain Distribution of the Steel Tube at 800 kN (Specimen E6, Shakir-Khalil, 1994)

Strain Gauge	Error (%)		
	$\bar{k}_{sc} = 10^6 \text{ MPa}$	$\bar{k}_{sc} = 10^4 \text{ MPa}$	$\bar{k}_{sc} = 10^3 \text{ MPa}$
1	1.28	2.03	8.94
2	-4.14	-0.42	7.23
3	-9.35	-4.15	2.71
4	3.57	6.43	12.65
5	39.60	45.02	45.58
6	19.95	17.30	11.57
7	6.53	0.87	-4.95
8	-1.71	-4.43	-10.13
9	-1.77	-2.75	-8.08
10	-1.77	-2.17	-6.59
Average	2.34	2.87	3.07
Std. Dev	15.45	16.37	18.05

Specimen E8 by Shakir-Khalil (1994) was tested using the experimental test setup shown in Figure 5.21. The analysis model was constructed similar to the specimen E6 by

defining 11 finite elements with 4 integration points. The load distribution at the connection region was also selected as 25%-50%-25% at the bottom, middle, and top points, respectively. The material strengths for the specimen E8 were designed to have slightly higher concrete strengths than specimen E6 with $f'_c = 32.5 \text{ MPa}$ and $E_c = 36.7 \text{ GPa}$. The other nominal material and geometric properties of the specimen E6 and E8 are identical. The strain distribution of the steel tube for specimen E8 is exhibited in Figure 5.24. Due to the limited published data, the comparisons can only be seen for three strain readings. The correlation of strain values is not satisfactory at the connection region. However, the strain value away from the connection is well predicted with a maximum error value of 13%, which is obtained with the lowest interface stiffness. In addition, the rate of load transfer matches with the experimental observations. The error analysis of the results for the specimen E8 in Table 5.5 shows that the lowest average value of error is obtained when the stiffness of the interface is 10^6 MPa .

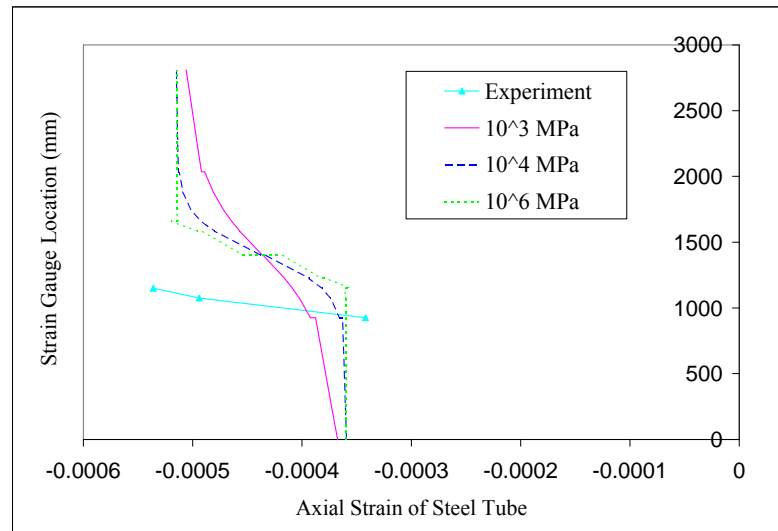


Figure 5.24 Axial Strain Distribution of the Steel Tube at 600 kN (Specimen E8, Shakir-Khalil, 1994)

Hajjar et al. (1998a, 1998b) performed verification and calibration studies on the bond strength using the connection tests conducted by Dunberry et al. (1987), where tee cleat type simple connections were utilized. The RCFT column is subjected to proportional axial loading at the top and also around the mid-height as it is demonstrated

in Figure 5.25. The element ends are capped ensuring strain compatibility of the steel tube and the concrete core. Specimen D1 tested by Dunberry et al. (1987) is analyzed using 10 finite elements and 4 integration points within each element. The force distribution over the connection region is assumed to be 20-20-60 % at the top, middle and bottom locations, respectively. The initial stiffness of the interface is assumed to be 10^4 MPa. The analysis is conducted for different values of bond strength including 0.4 MPa, 0.6 MPa, and 0.8 MPa. In Figure 5.26, the computational and experimental slip values along the length of the RCFT column are presented. The slip distribution from the analysis well matches with the measured values. A better correlation of the slip values is obtained below the connection region compared to the region above the connection. A similar trend was also noticed by Hajjar et al. (1998a, 1998b).

Table 5-5 Error Analysis of Strain Distribution of the Steel Tube at 600 kN (Specimen E8, Shakir-Khalil, 1994)

Strain Gauge	Error (%)		
	$\bar{k}_{sc} = 10^6 \text{ MPa}$	$\bar{k}_{sc} = 10^4 \text{ MPa}$	$\bar{k}_{sc} = 10^3 \text{ MPa}$
1	5.32	6.11	13.33
2	-27.09	-24.39	-18.56
3	-32.65	-28.79	-23.75
Average	12.44	15.73	24.08
Std. Dev.	28.16	26.10	27.41

The error analysis of the slip results is given in Table 5-6. In the regions away from the connection, very high error values are obtained. This is attributed to the fact that the reported slip values in the experiments are very small compared to the computational results. However, the maximum slip values produced a better correlation as can be seen in Table 5-6. Based on Figure 5.26, the maximum slip is predicted more accurately if the bond strength is assumed as 0.6 MPa.

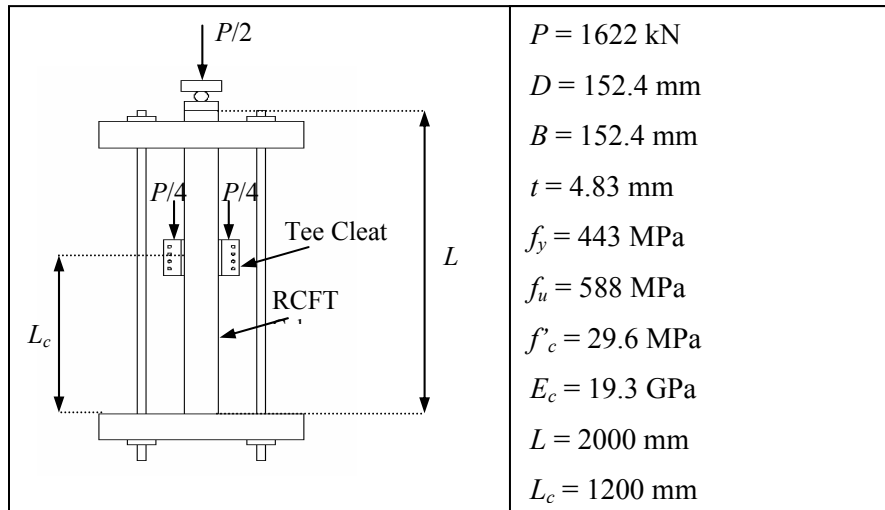


Figure 5.25 Simple Connection Tests Setup (Dunberry et al., 1987, Specimen D1)

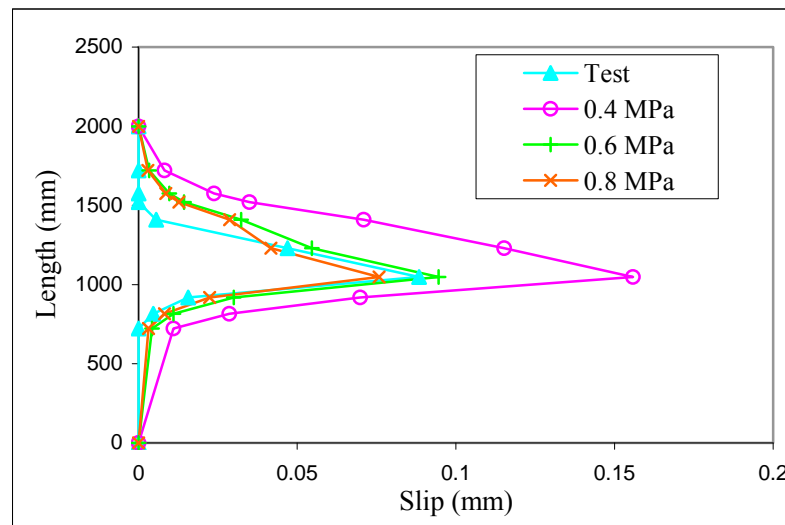


Figure 5.26 Slip Distribution (Dunberry et al., 1987, Specimen D1)

Dunberry et al. (1987) also reported axial force distribution in the steel tube and the concrete core along the element length. This data provided valuable comparisons to monitor the accuracy of load exchange estimated by the mixed finite element formulation. The comparison of the axial force distribution for specimen D1 is illustrated in Figure 5.27. Since the axial force is directly applied to the steel tube DOFs, in Figure 5.27, abrupt increase in the axial force of the steel tube is evident at the load application points. On the other hand, the concrete core experiences a gradual growth of the axial

load since it is transferred through the interface. The general trend of the force distribution reveals a good correlation with the published results for every bond strength value. The numerical values of the axial loads match with the reported values better above the connection region compared to the portion of the element length below the connection. The error analysis of the axial load distribution can be found in Table 5-7. The axial load estimations of the steel tube produced more accurate results compared to the concrete core. The best correlation is obtained when the bond strength value is set to 0.8 MPa.

Table 5-6 Error Analysis of Slip Value (Dunberry, 1987, Specimen D1)

Location (mm)	Error (%)		
	0.4 MPa	0.6 MPa	0.8 MPa
815.34	522.7	139.3	77.5
919.48	346.3	91.9	42.6
1049.02	76.2	6.9	-14.3
1229.36	145.2	16.4	-11.2
1409.7	1184.2	485.1	419.4
Average Error	454.9	147.9	102.8
Std. Dev.	443.7	196.3	181.1

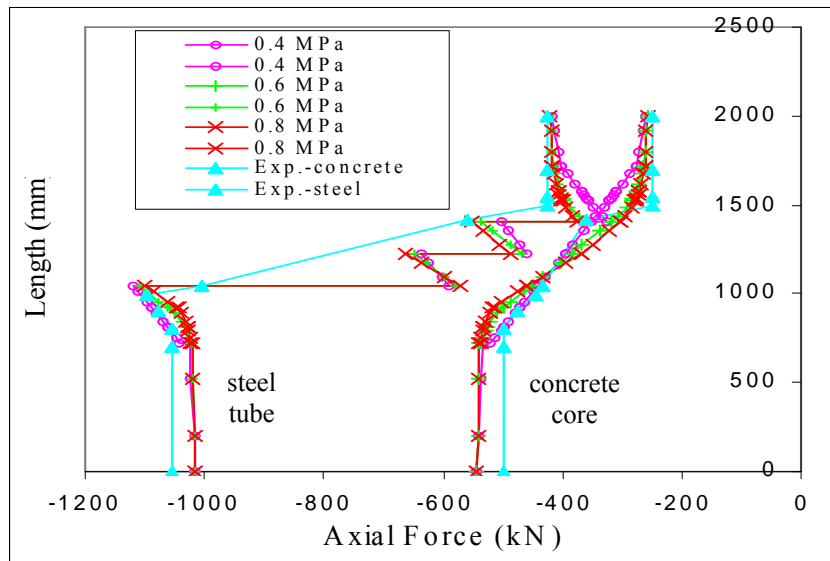


Figure 5.27 Axial Force Distribution (Dunberry et al., 1987, Specimen D1)

The analysis results of slip critical RCFT columns indicated that a slip stiffness of 10^6 MPa and a bond strength of 0.8 MPa produced the best correlation with the experimental results with lower values of average error and standard deviation for the majority of specimens. However, the degree of correlation achieved by 10^6 MPa slip stiffness and 0.6 MPa bond strength is not significantly different than it was achieved by the aforementioned values. For the sake of consistency with the prior work by Hajjar et al. (1998a, 1998b), in this research study, 10^6 MPa slip stiffness and 0.6 MPa bond strength were utilized in the analysis results.

Table 5-7 Error Analysis of Axial Load (Dunberry, 1987, Specimen D1)

Location (mm)	Concrete Core - Error (%)			Steel Tube - Error (%)		
	0.4 MPa	0.6 MPa	0.8 MPa	0.4 MPa	0.6 MPa	0.8 MPa
0	9.4	9.4	9.4	-3.7	-3.8	-3.6
707	8.7	7.6	8.9	-3.3	-2.8	-3.4
804	6.2	0.8	7.3	-2.5	0.4	-2.7
902	6.1	0.1	8.9	-3.7	0.7	-3.2
989	6.4	2.3	9.4	-3.7	0.8	-2.1
1043	4.3	1.6	6.6	5.9	11.4	9.3
1413	-12.4	-3.2	-16.6	12.7	-13.0	-4.4
1500	16.6	32.5	13.6	12.1	-17.5	-6.4
1543	13.3	28.1	11.1	23.5	-14.9	-4.9
1696	7.0	13.8	6.2	-8.0	-6.5	-2.1
2000	4.2	5.0	4.1	-5.6	-1.4	-0.9
Average	6.4	8.9	6.3	2.2	-4.2	-2.2
Std. Devi.	7.3	11.6	8.0	10.0	8.4	4.1

Specimen C1 by Dunberry et al. (1987) was selected to verify the accuracy of the selected slip stiffness and bond strength values. The test was performed using the experimental setup described in Figure 5.28. The axial load was applied through tee-clip type connections at the mid-height of the RCFT column. The top of the specimen was left uncapped allowing the steel tube to slip with respect to the concrete core. The analysis of the Specimen C1 was conducted by defining 7 elements per member with 4 integration points. The fine mesh was selected to provide consistency with the location of the strain gauges used in the experiment. The bond strength and stiffness of the interface are assumed to be 0.6 MPa and 10^4 MPa as recommended by Schiller and Hajjar

(1998) and Hajjar et al. (1998a, 1998b). Figure 5.29 illustrates the axial force distribution in the concrete core along the length of the specimen. The gradual transfer of axial load to the concrete core is evident starting at the top of the specimen. In general, a good correlation is attained between the computational and experimental axial load values of the concrete core. The axial force estimations above the connection region were found to be more satisfactory compared to region above the connection. The largest error in the estimations is obtained as 5.9%.

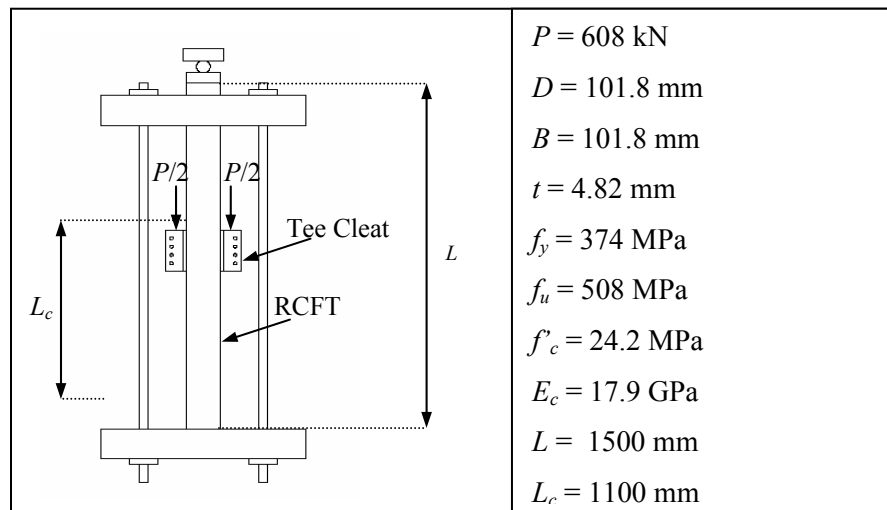


Figure 5.28 Simple Connection Tests Setup (Dunberry et al., 1987, Specimen C1)

5.4. Materially and Geometrically Nonlinear RCFT Column Tests

Understanding the response of short RCFT columns ($L / D < 10$) under uniaxial compression provide significant insights into the interaction of the steel tube and the concrete core. The load-deformation behavior is significantly affected by the confinement effects resulting from the passive lateral pressure exerted on to the concrete core from the steel tube. In addition, expansion of the concrete core due to crushing accelerates the formation of local buckling on the steel tube walls. Since the severity of confinement and local buckling effects is significant under uniaxial compression,

studying short RCFT columns helps calibrating and verifying the analysis models to account for these two phenomena. The RCFT columns that are examined in this section experience negligible geometric nonlinearity due their low slenderness ratio. However, in the analysis, the geometric nonlinear features of the finite element formulation were not suppressed for the sake of consistency in the breadth of the analysis method.

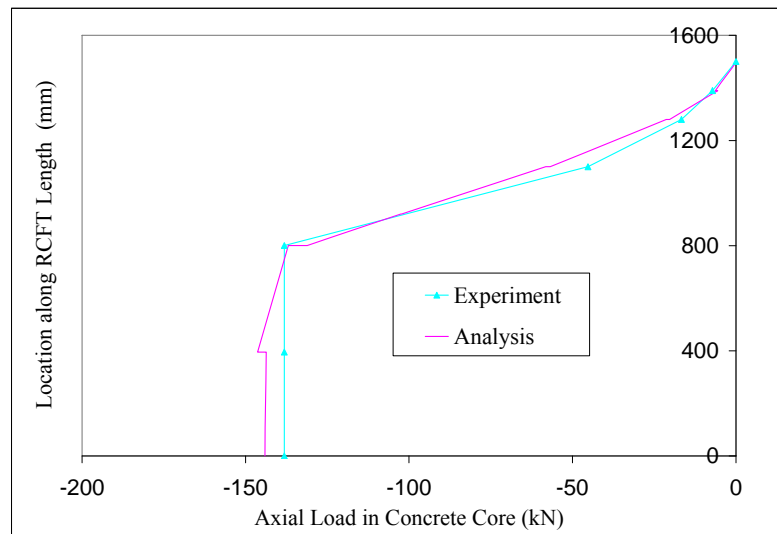


Figure 5.29 Simple Connection Tests Setup (Dunberry et al., 1987, Specimen C1)

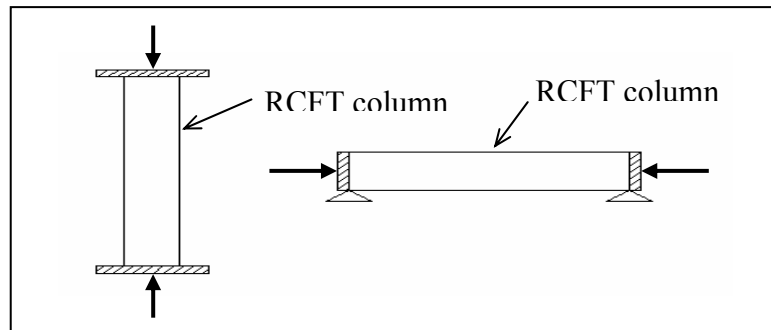


Figure 5.30 Short RCFT Columns under Concentric Axial Loading

The first specimen studied is CR4-D-2 tested by Nakahara et al. (1998). It is found to experience the typical limit states observed in RCFT stub column experiments including steel tube yielding, concrete crushing, and local buckling of the steel tube. Therefore, it is selected for investigating the mesh sensitivity of the results. A displacement-controlled load incrementation scheme is employed in the analyses (Yang

and Kuo, 1994). Six discretization schemes are studied. 1, 2, and 3 elements per member are used while the number of integration points is selected as 4 and 6. The number material fibers were kept as constant with 4 fibers along the depth and width of the concrete core and 4 fibers along the width of the flange and the depth of the web of the steel tube. A single layer of fiber along the depth of the flange and width of the web of the steel tube was introduced. Figure 5.31 illustrates the axial force vs. deformation response for each analysis. The results are presented individually for the concrete core, the steel tube, and the composite cross-section. The specimen undergoes severe local buckling at the early stages of loading due the high D/t ratio of the steel tube. Softening type of response initiates following the formation of concrete crushing. The computational results are found to exhibit almost no variation with respect to the size of the mesh. This might be attributed to the fact that the specimen does not suffer from geometric nonlinearity due its small L/D ratio. This creates a uniform strain distribution at each interpolation point along the element length. In addition, the axial displacement field is well predicted with the quadratic interpolation functions employed in the natural coordinates. The progression of damage for the specimen CR4-D-2 is initiated by yielding of the steel tube at 90% of the peak axial load acting on the composite section. Yielding of the steel tube is followed by local buckling of the steel tube at 97% of the peak axial load. The computational results detected crushing of concrete to take place simultaneously with the attainment of peak axial load.

Varma (2000) conducted an experimental study on short RCFT columns utilizing high strength materials. The specimen SC48-46 is analyzed using 2 elements per member with 4 integration points. The comparison of the experimental and computational results is presented in Figure 5.32 and good comparison is obtained with respect to initial stiffness, peak axial load, and the strength degradation stiffness. The progression of local damages started with steel tube yielding and local buckling occurring at 71.06 % and 79.18 % of the peak axial load, respectively. Concrete crushing is detected at the same time when the peak load is reached.

The next specimen studied is IVA, which was tested by Tomii and Sakino (1979) using the pinned-ended support conditions portrayed in Figure 5.30. The specimen was

constructed using low strength materials for the steel tube and the concrete core. The analysis of IVA is conducted using 2 elements per member with 4 integration points along the element length. Similar to the experimental results documented by Tomii and Sakino (1979), a stable response is obtained without any significant strength degradation. The comparison of the analysis and experimental results is given in Figure 5.33, where a good correlation is attained. The progression of damage states is found to initiate with steel tube yielding at 80% of the peak axial load. Concrete crushing takes place following steel tube yielding around 91% of the peak axial load. The analysis detected local buckling of the steel tube at the same time when the peak axial load is reached. Due to the small D/t ratio of the specimen IVA, no strength degradation is observed even after local buckling of the steel tube takes place.

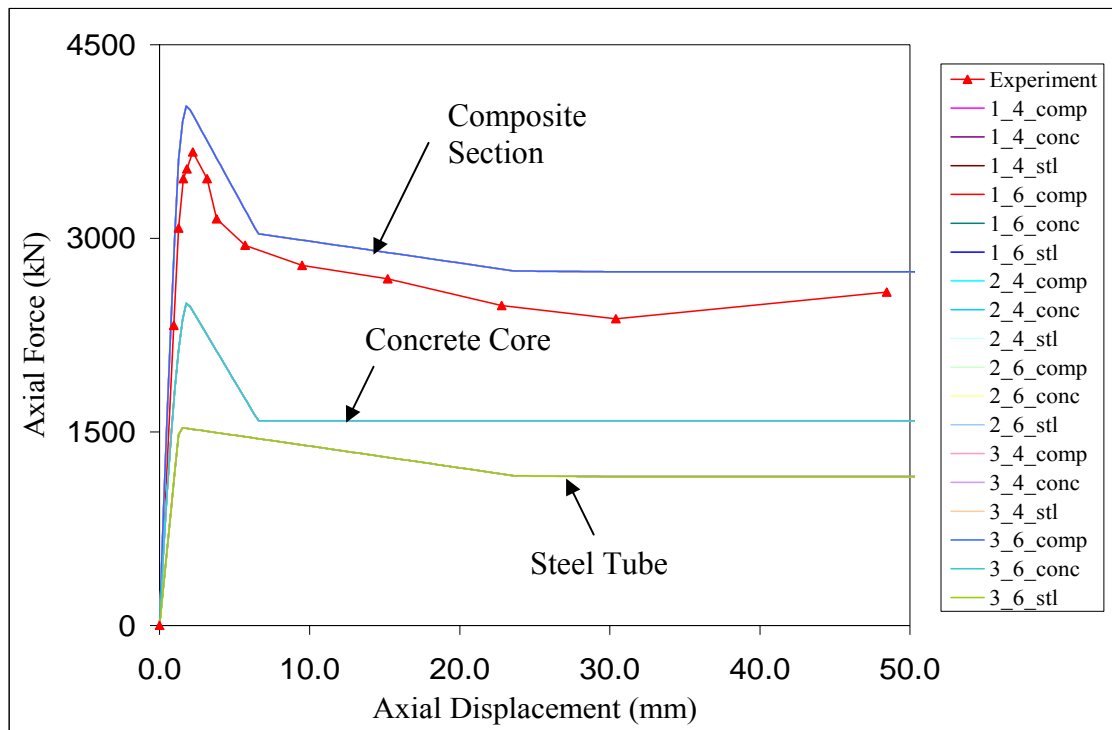


Figure 5.31 Comparison of Computational and Experimental Results for an RCFT Stub Column Test (Nahakara et al., 1998, Specimen CR4-D-2, $f_y = 262$ MPa, $f'_c = 41.1$ MPa, $D/t = 73.7$, $L/D = 3$)

The geometrically and materially nonlinear short RCFT columns analyzed until this point represent RCFT members covering extreme values with respect to the parameters of f'_c and D/t . The comparisons of experimental and computational results in Figures 5.31 through 5.33 showed that the mixed finite element formulation successfully predicts a wide range of behavioral characteristics of short RCFT columns. In order to extend the verification of the mixed finite element formulation to other RCFT columns available in the literature, multiple specimens from the experimental database by Tort and Hajjar (2003) were studied. The selected specimens were examined in three different groups with respect to the parameters of f'_c and D/t since these characteristics govern the load-deformation response significantly. Group 1 was assumed to have specimens with high f'_c values. The specimens having high D/t values were placed in Group 2. Group 3 contained the specimens with moderate values of f'_c and D/t . In Table 5-8, the material and geometric properties of specimens are summarized, where measured values are presented. The right superscripts attached to the name of the specimens denoted the corresponding group number.

The discretization scheme of the specimens is selected as 2 elements per member with 4 integration points. The constant-displacement arc length method is utilized as the global nonlinear solution scheme (Yang and Kuo, 1994). Two types of boundary conditions are introduced as fixed-fixed or pinned-roller. The slip between the steel tube and the concrete core is restricted at the supports but allowed at the mid-joint, consistent with the experiment boundary conditions. Figure 5.34– Figure 5.58 portray the comparison of computational and experimental results in terms of axial load vs. axial deformation response. In each plot, three sets of analysis data are presented, including the steel tube, the concrete core, and the composite section. This helps to examine local damage states (e.g., steel tube yielding, concrete crushing, local buckling) and their contribution to the global response.

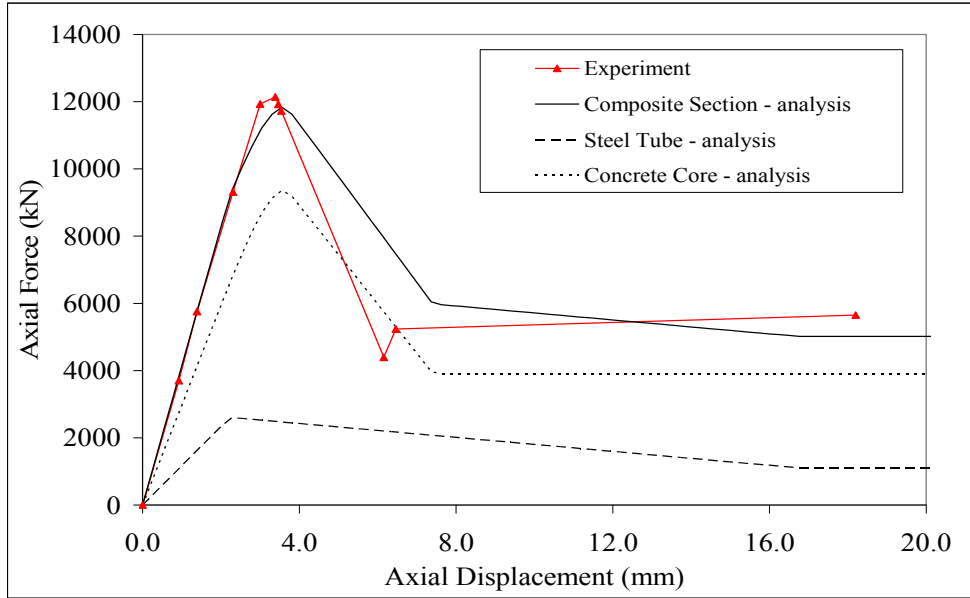


Figure 5.32 Comparison of Computational and Experimental Results for an RCFT Stub Column Test (Varma, 2000, Specimen SC48-46, $f_y = 471$ MPa, $f'_c = 110$ MPa, $D/t = 52.6$, $L/D = 4$)

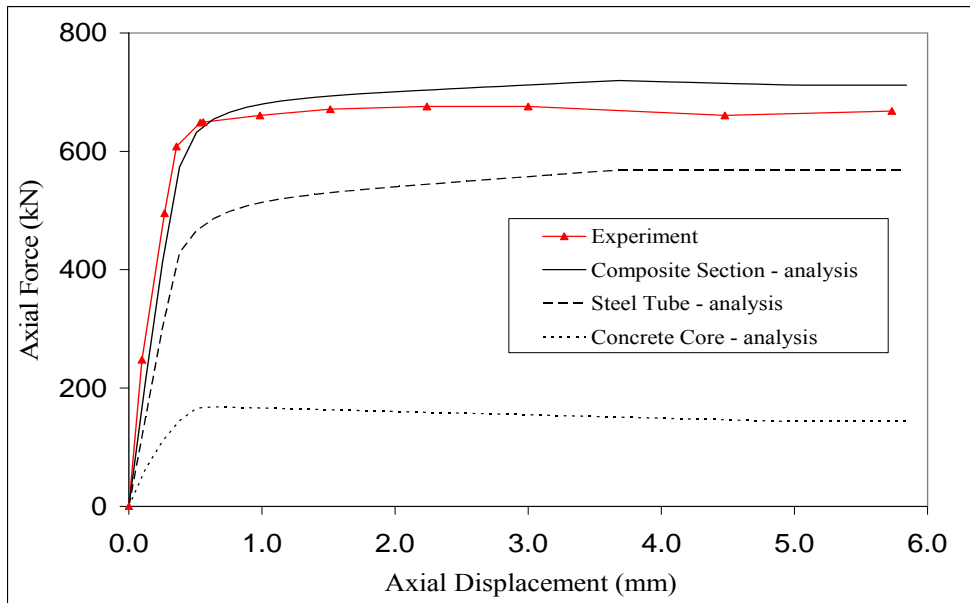


Figure 5.33 Comparison of Computational and Experimental Results for an RCFT Stub Column Test (Tomii and Sakino, 1979, Specimen IVA, $f_y = 284$ MPa, $f'_c = 19.81$ MPa, $D/t = 24$, $L/D = 3$)

Table 5-8 Concentrically Loaded RCFT Column Tests

Specimen Label	E_s (MPa)	f_y (MPa)	f'_c (MPa)	D (mm)	B (mm)	t (mm)	D/t	L (mm)	L/D
g3¹	209615	327.0	96.0	119.9	119.9	5.00	24.0	500	4
g4¹	210048	439.0	96.0	119.9	119.9	5.00	24.0	500	4
g8¹	209740	323.0	103.0	119.9	119.9	8.00	15.0	500	4
g27¹	210556	379.0	91.0	249.9	249.9	8.00	31.2	500	4
SC32-46¹	197000	269.0	110.6	303.5	303.5	8.64	35.1	1220	4
SC32-80¹	197000	600.0	110.6	305.3	305.3	8.89	34.3	1220	4
I-A²	206010	194.2	38.3	100.0	100.0	2.29	43.7	300	3
II-A²	213858	339.4	21.4	100.1	100.1	2.21	45.3	300	3
III-A²	206010	288.4	20.5	100.1	100.1	2.21	45.3	300	3
S1²	180518	356.0	30.5	127.3	127.3	3.15	40.4	635	5
R1²	190164	430.0	30.5	152.3	76.0	3.00	50.8	635	4
CR4-D-8²	206000	262.0	80.3	324.1	324.1	4.37	74.2	969	3
CR4-C-4-1²	206000	262.0	41.1	214.9	214.9	4.37	49.2	645	3
CR8-C-8²	206000	835.0	41.1	214.9	214.9	4.37	49.2	525	3
g1³	209655	304.1	47.0	119.9	119.9	5.00	24.0	500	4
g2³	209567	438.0	46.0	119.9	119.9	4.98	24.1	500	4
S2³	190164	357.0	26.0	127.0	127.0	4.32	29.4	635	5
S3³	205322	322.0	23.8	127.0	127.0	4.55	27.9	635	5
S4³	203974	312.0	23.8	126.5	126.5	5.67	22.3	635	5
S5³	204633	347.0	23.8	127.2	127.2	7.47	17.0	635	5
R2³	213593	382.7	26.0	152.9	76.5	4.47	34.2	635	4
R3³	214968	413.7	26.0	152.4	101.9	4.32	35.3	635	4
R4³	206011	365.0	23.8	152.7	102.9	4.57	33.4	635	4
R5³	204633	324.1	23.8	151.4	101.3	5.72	26.5	635	4
R6³	205322	357.9	23.8	152.4	102.1	7.37	20.7	635	4

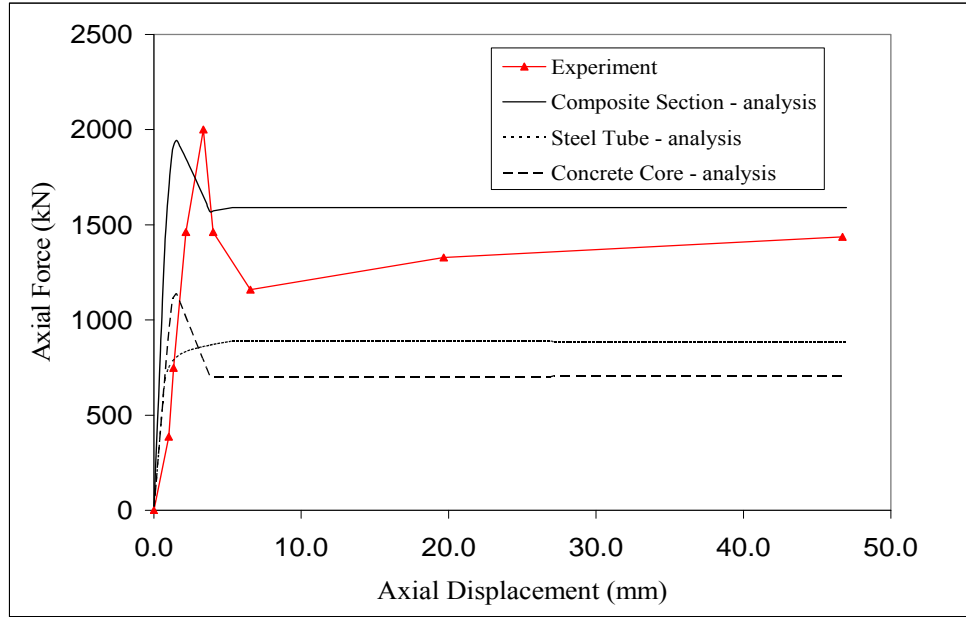


Figure 5.34 Comparison of Computational and Experimental Results for an Axially-Loaded RCFT Short Column (Grauers, 1993, Specimen 3)

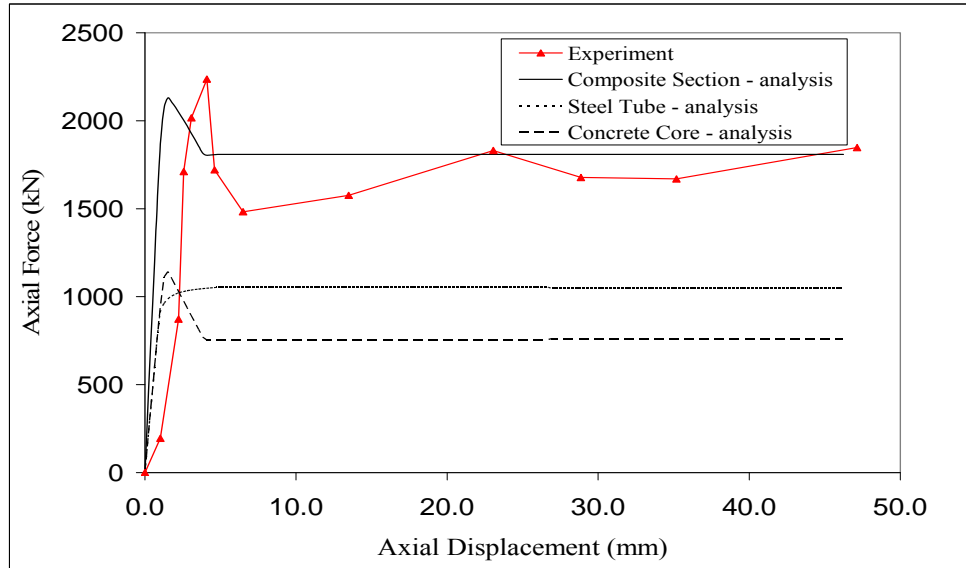


Figure 5.35 Comparison of Computational and Experimental Results for an Axially-Loaded RCFT Short Column (Grauers, 1993, Specimen 4)

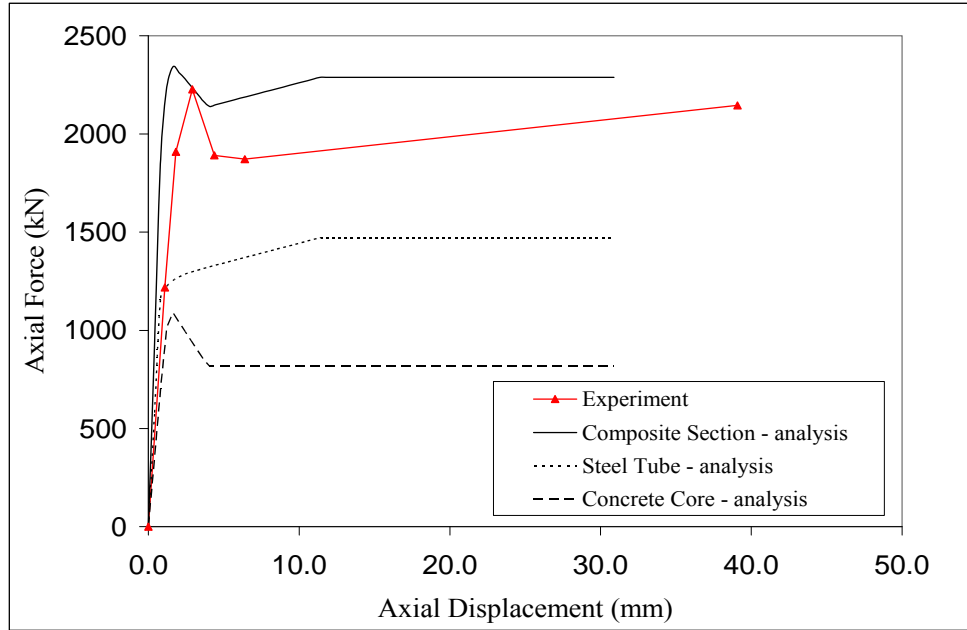


Figure 5.36 Comparison of Computational and Experimental Results for an Axially-Loaded RCFT Short Column (Grauers, 1993, Specimen 8)

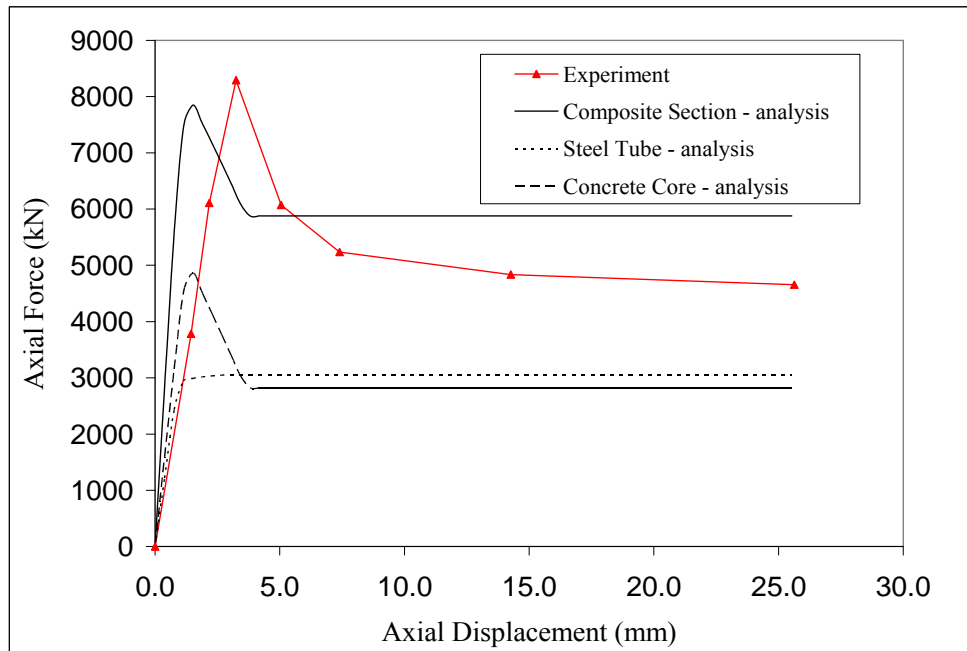


Figure 5.37 Comparison of Computational and Experimental Results for an Axially-Loaded RCFT Short Column (Grauers, 1993, Specimen 27)

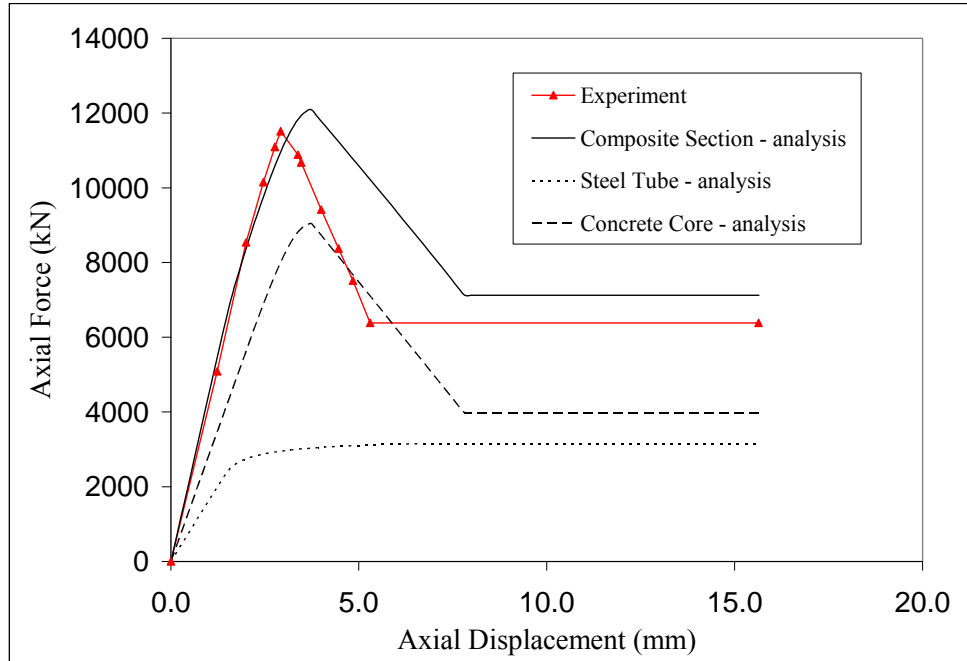


Figure 5.38 Comparison of Computational and Experimental Results for an Axially-Loaded RCFT Short Column (Varma, 2000, SC32-46)

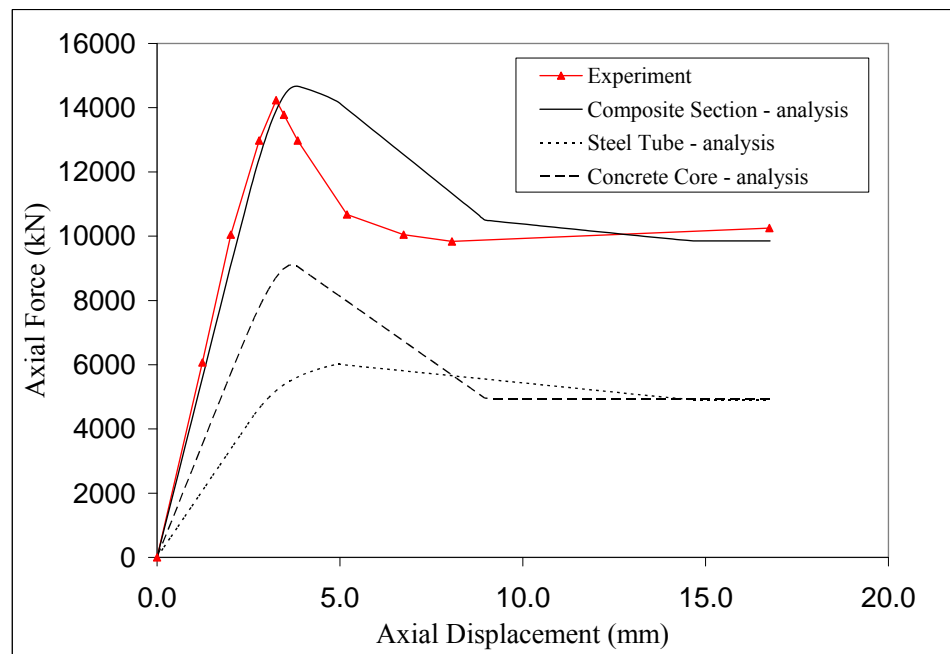


Figure 5.39 Comparison of Computational and Experimental Results for an Axially-Loaded RCFT Short Column (Varma, 2000, SC32-80)

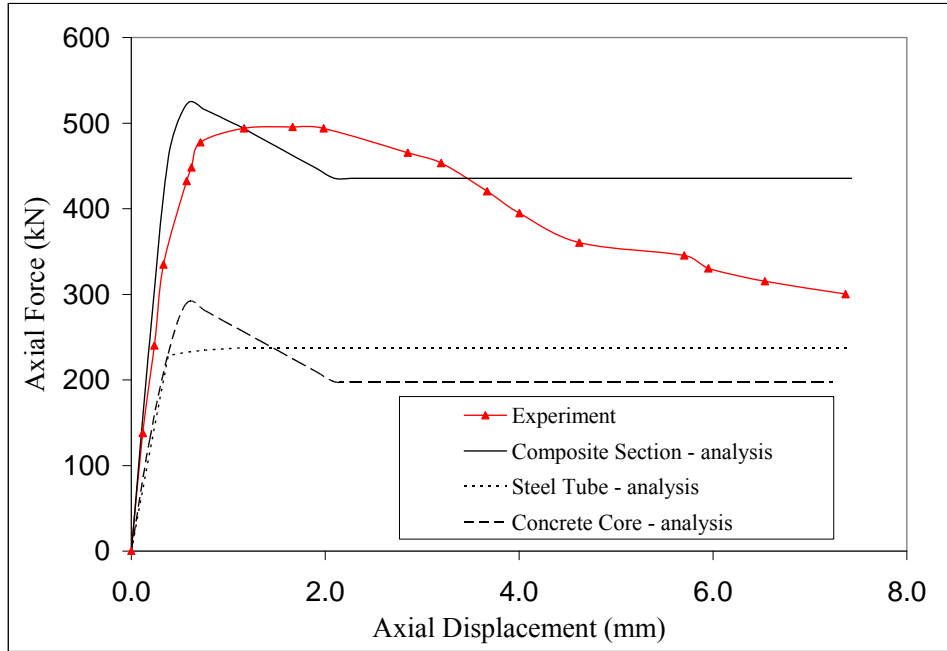


Figure 5.40 Comparison of Computational and Experimental Results for an Axially-Loaded RCFT Short Column (Tomii and Sakino, 1979, IA)

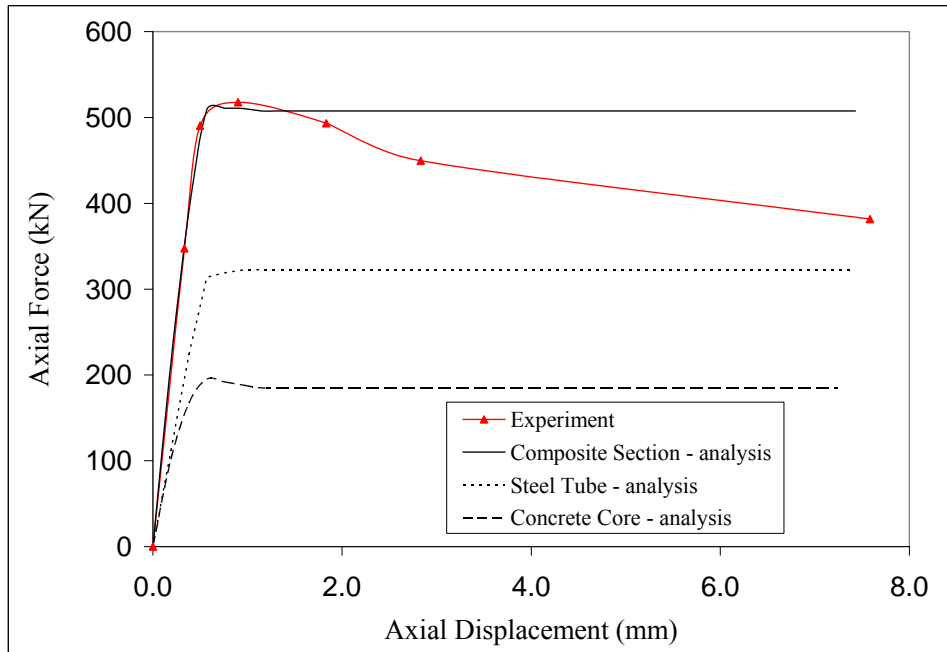


Figure 5.41 Comparison of Computational and Experimental Results for an Axially-Loaded RCFT Short Column (Tomii and Sakino, 1979, IIA)

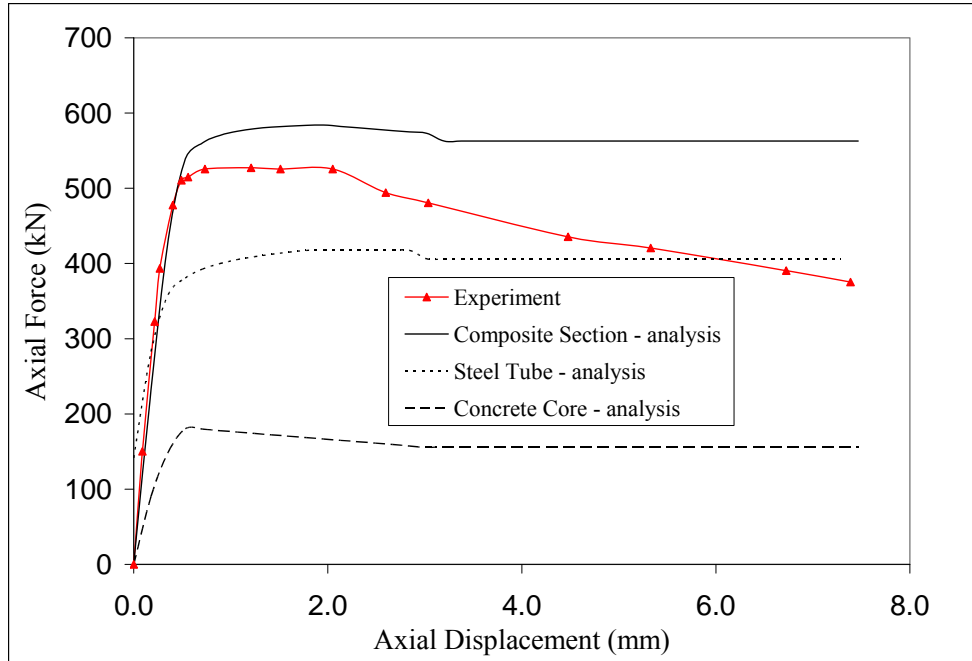


Figure 5.42 Comparison of Computational and Experimental Results for an Axially-Loaded RCFT Short Column (Tomii and Sakino, 1979, IIIA)

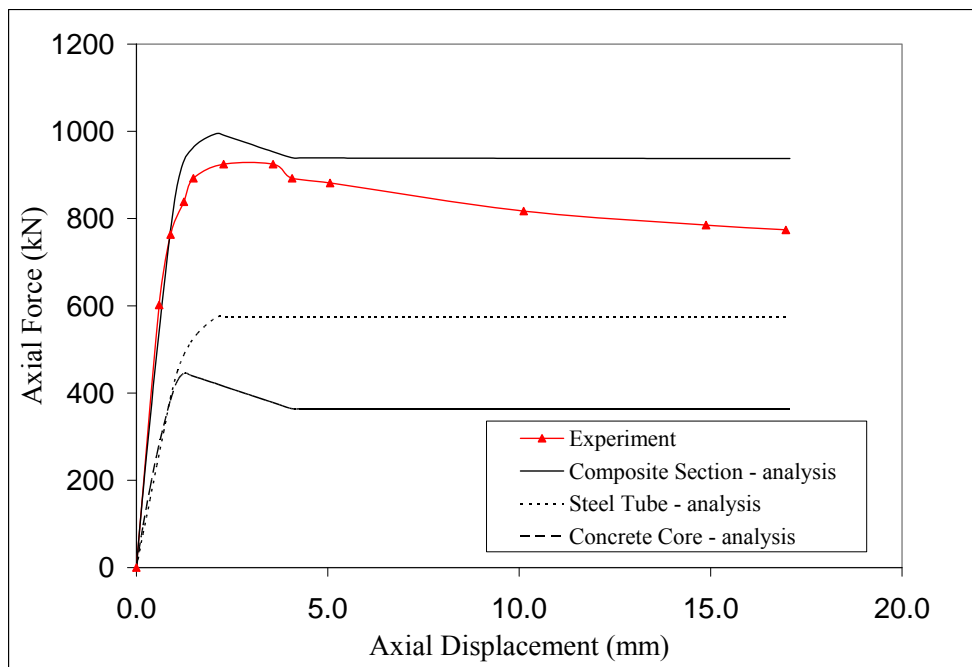


Figure 5.43 Comparison of Computational and Experimental Results for an Axially-Loaded RCFT Short Column (Schneider, 1998, S1)

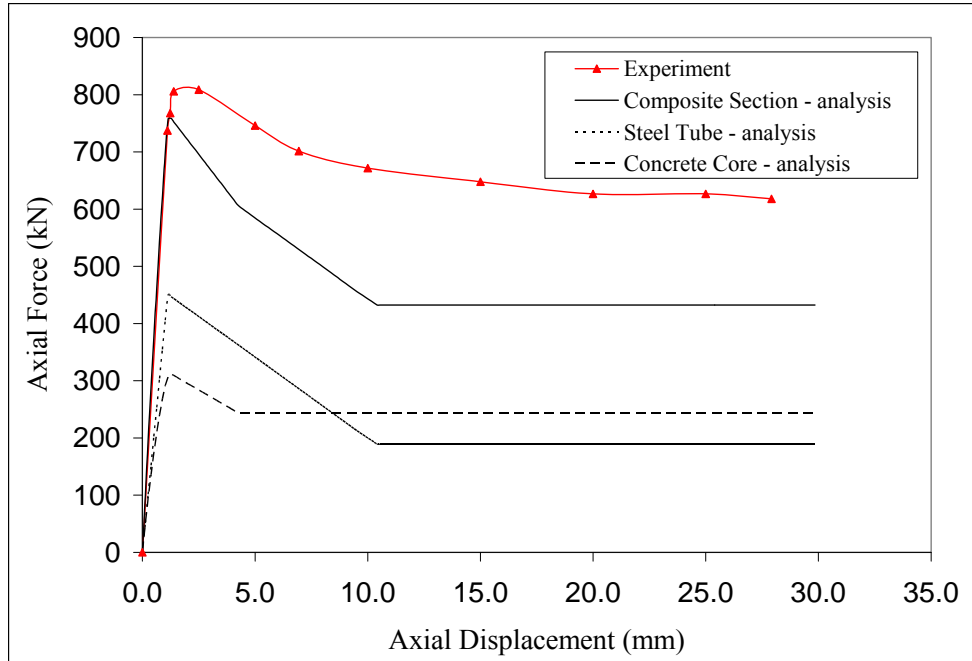


Figure 5.44 Comparison of Computational and Experimental Results for an Axially-Loaded RCFT Short Column (Schneider, 1998, R1)

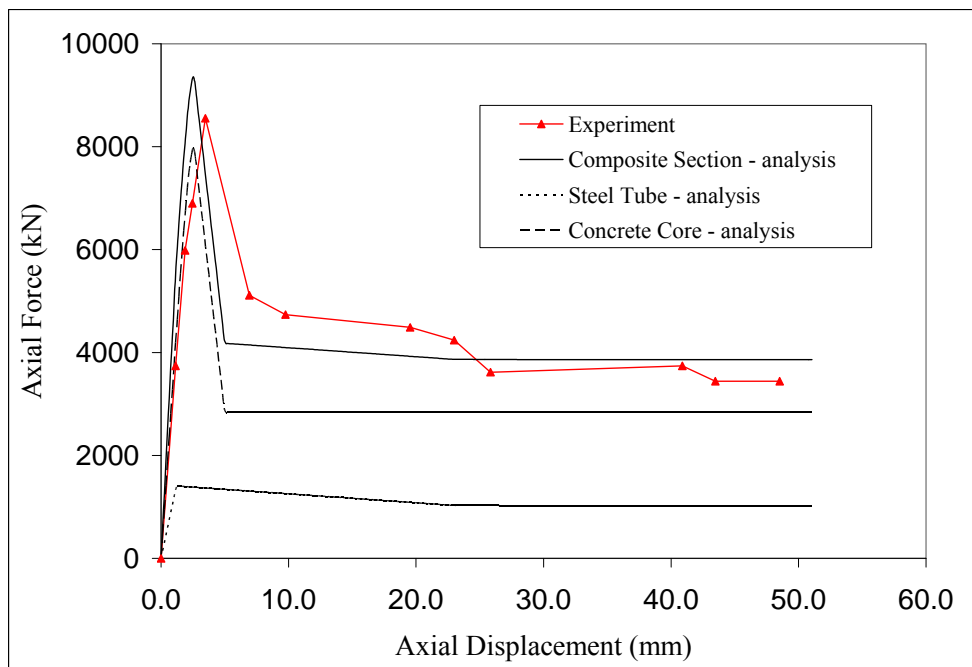


Figure 5.45 Comparison of Computational and Experimental Results for an Axially-Loaded RCFT Short Column (Nakahara et al., 1998, CR4-D-8)

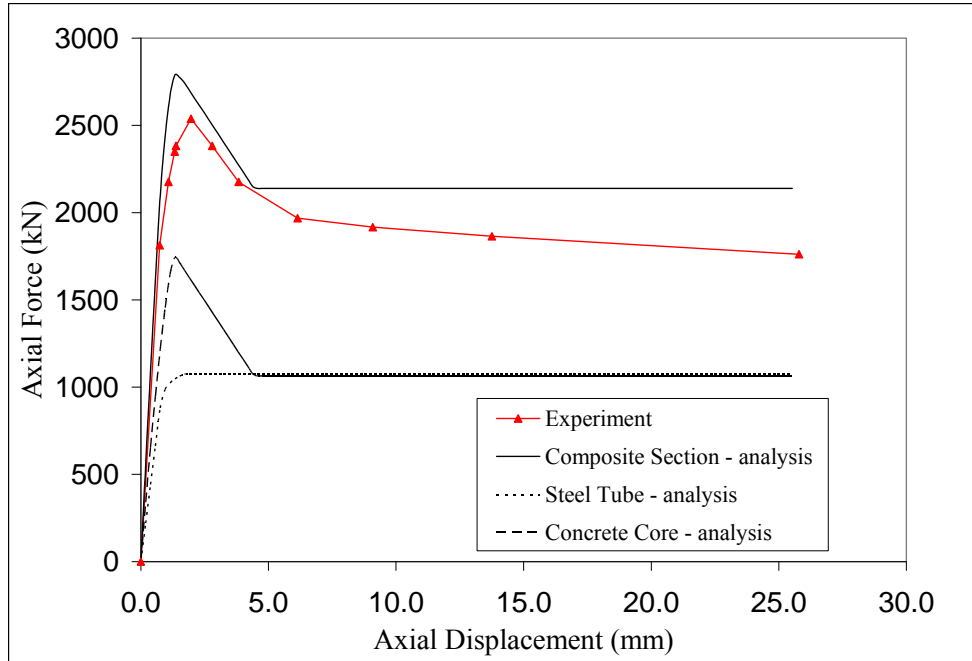


Figure 5.46 Comparison of Computational and Experimental Results for an Axially-Loaded RCFT Short Column (Nakahara et al., 1998, CR4-C-4-1)

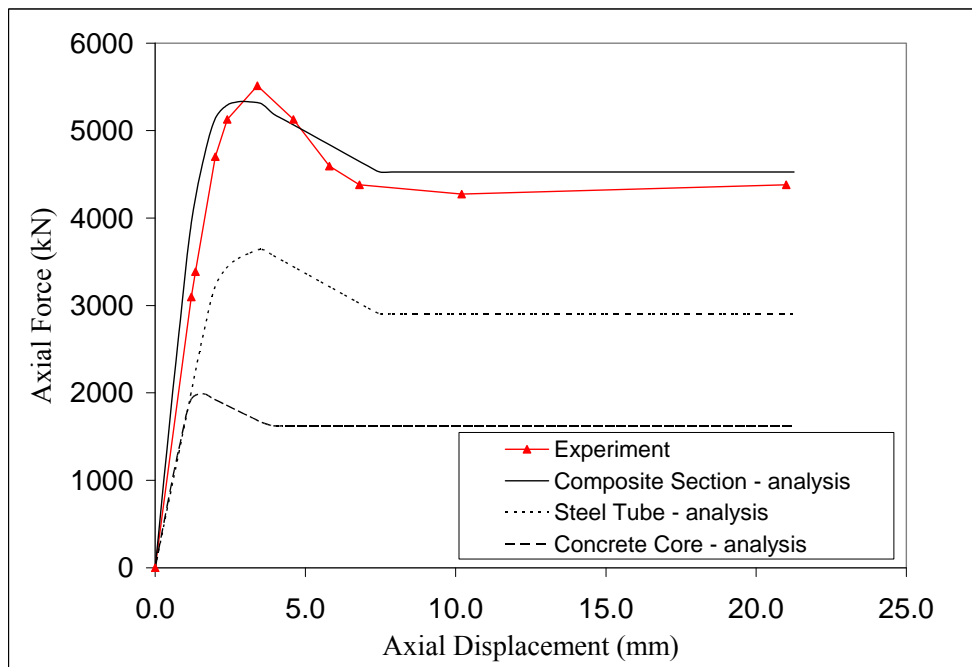


Figure 5.47 Comparison of Computational and Experimental Results for an Axially-Loaded RCFT Short Column (Nakahara et al., 1998, CR8-C-8)

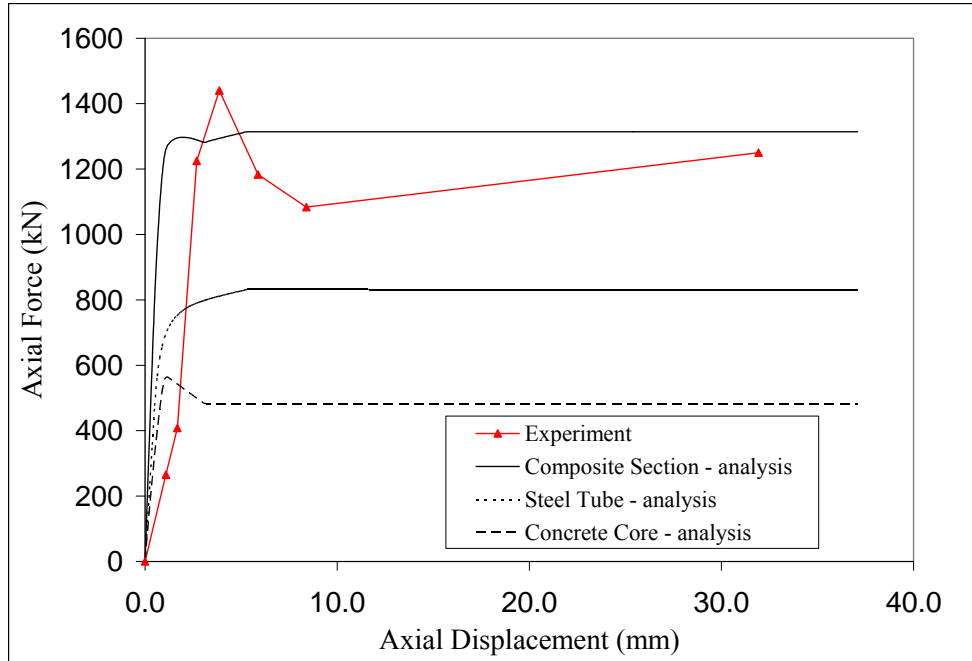


Figure 5.48 Comparison of Computational and Experimental Results for an Axially-Loaded RCFT Short Column (Grauers, 1993, Specimen 1)

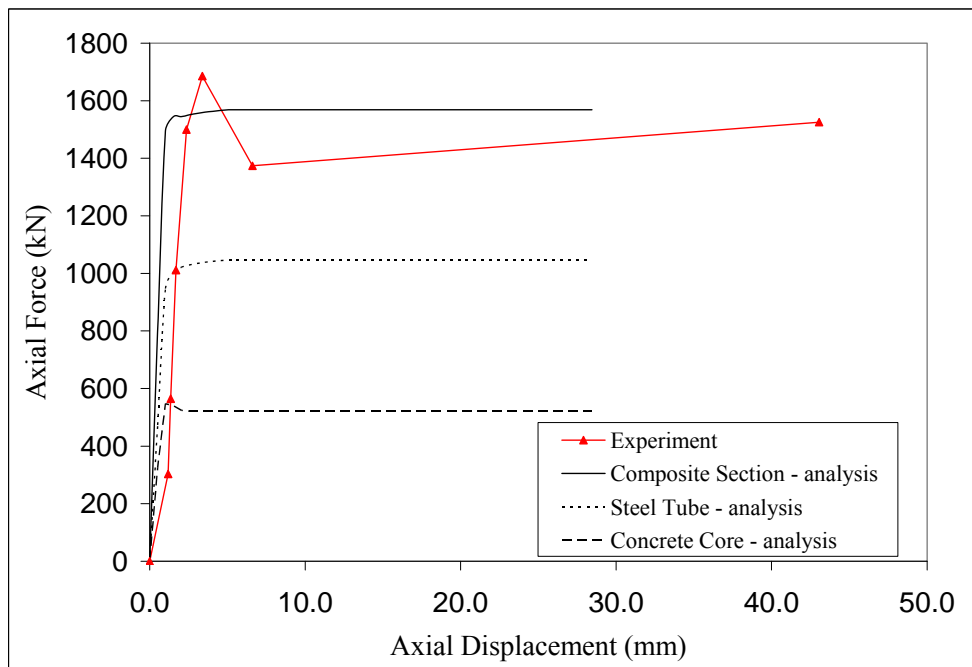


Figure 5.49 Comparison of Computational and Experimental Results for an Axially-Loaded RCFT Short Column (Grauers, 1993, Specimen 2)

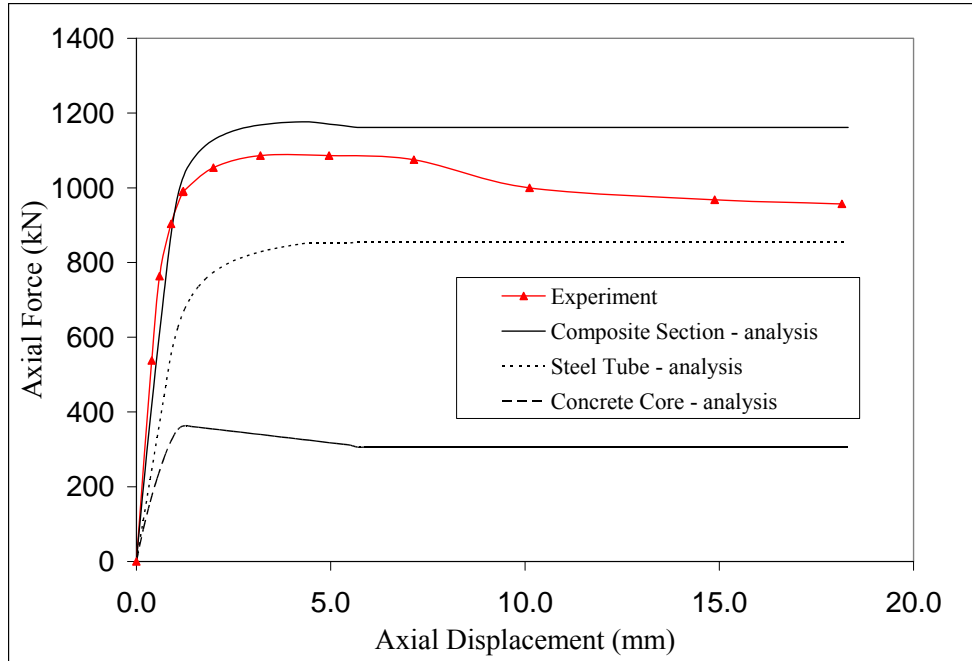


Figure 5.50 Comparison of Computational and Experimental Results for an Axially-Loaded RCFT Short Column (Schneider, 1998, S2)

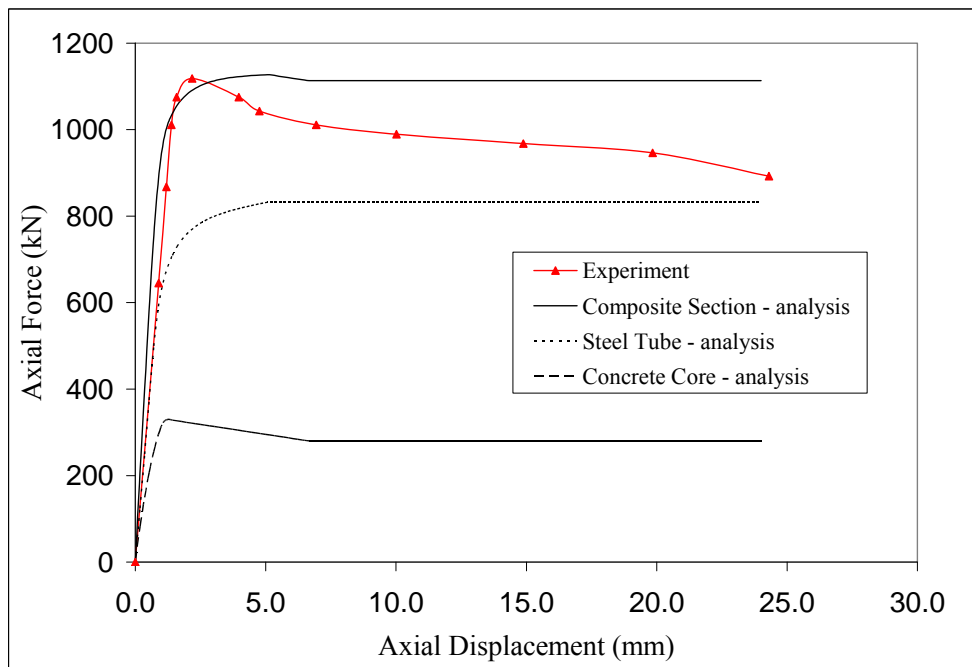


Figure 5.51 Comparison of Computational and Experimental Results for an Axially-Loaded RCFT Short Column (Schneider, 1998, S3)

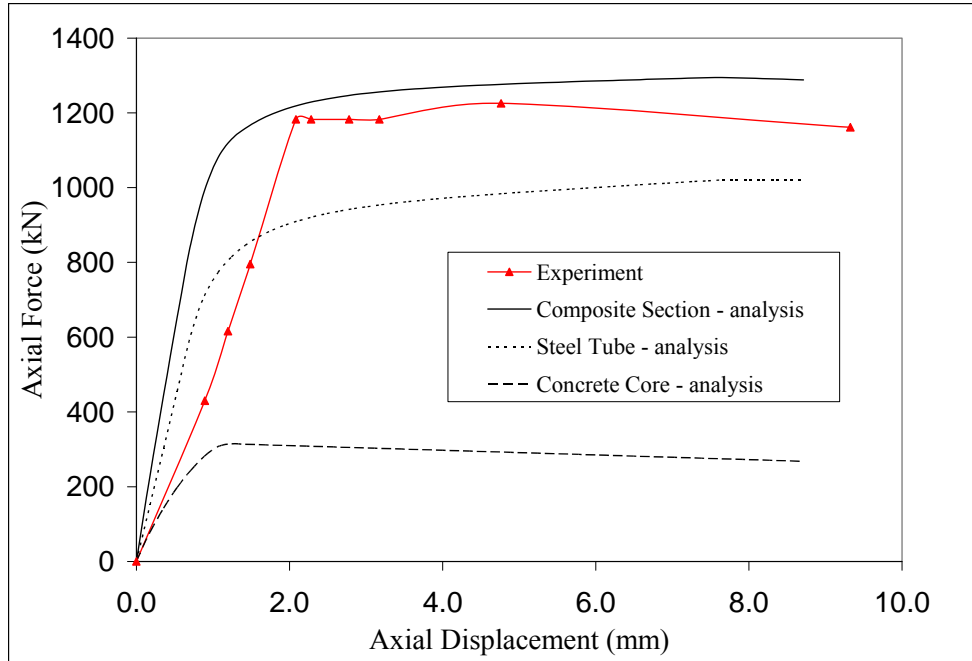


Figure 5.52 Comparison of Computational and Experimental Results for an Axially-Loaded RCFT Short Column (Schneider, 1998, S4)

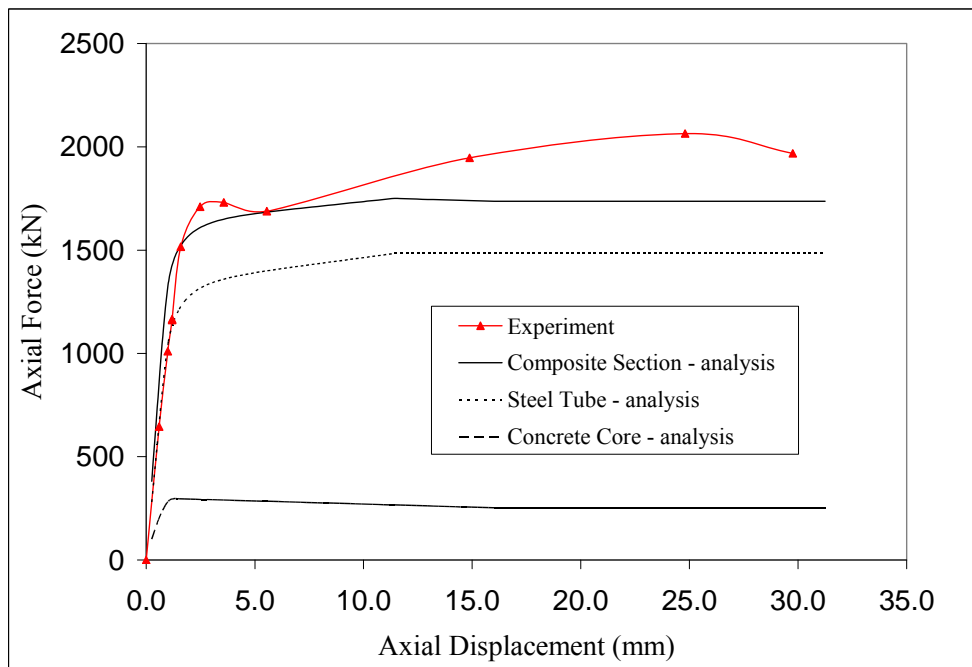


Figure 5.53 Comparison of Computational and Experimental Results for an Axially-Loaded RCFT Short Column (Schneider, 1998, S5)

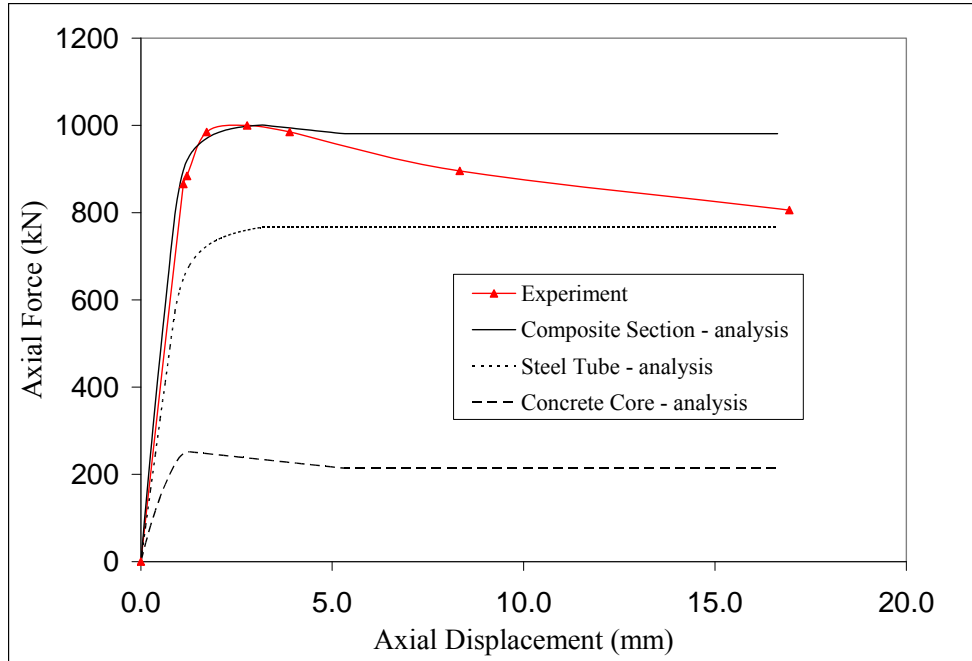


Figure 5.54 Comparison of Computational and Experimental Results for an Axially-Loaded RCFT Short Column (Schneider, 1998, R2)

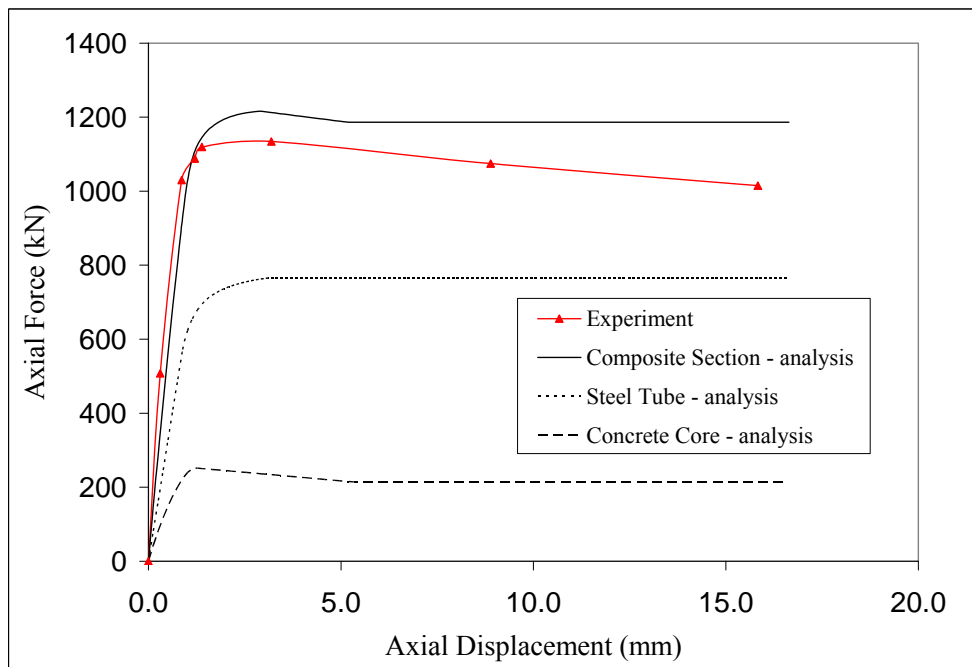


Figure 5.55 Comparison of Computational and Experimental Results for an Axially-Loaded RCFT Short Column (Schneider, 1998, R3)

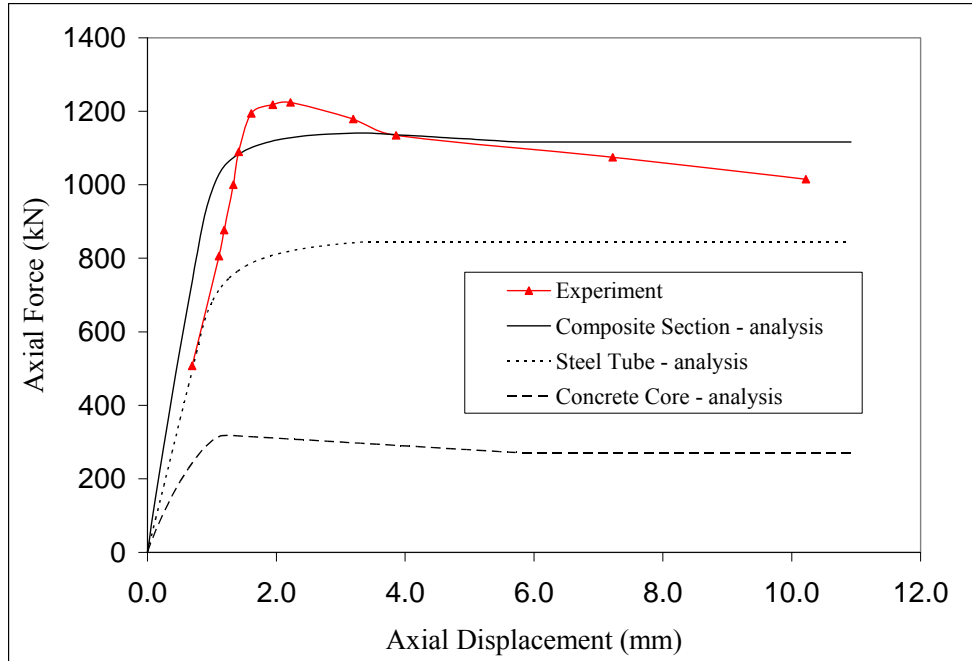


Figure 5.56 Comparison of Computational and Experimental Results for an Axially-Loaded RCFT Short Column (Schneider, 1998, R4)

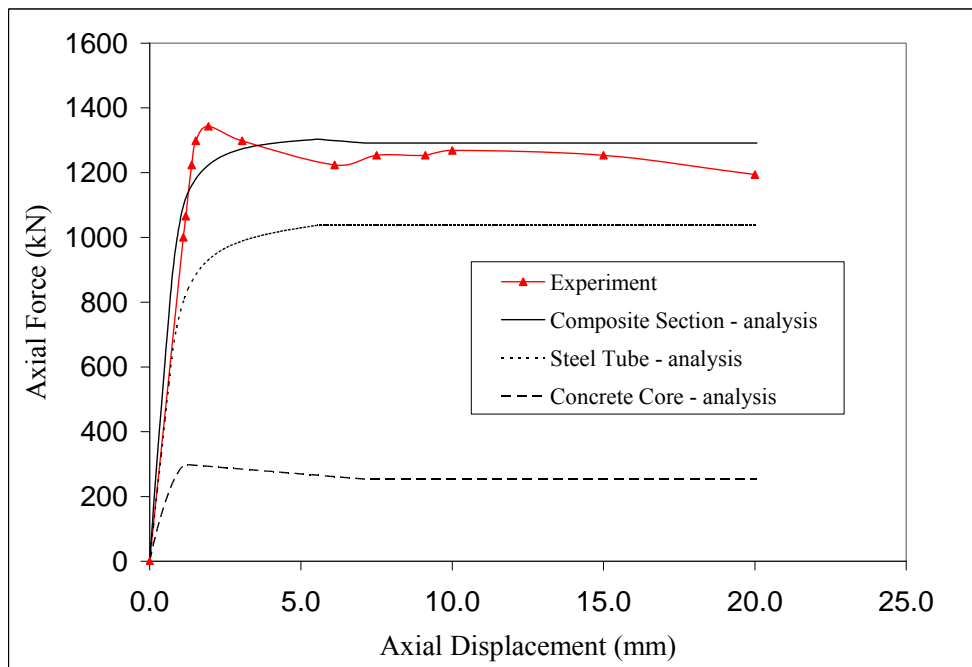


Figure 5.57 Comparison of Computational and Experimental Results for an Axially-Loaded RCFT Short Column (Schneider, 1998, R5)

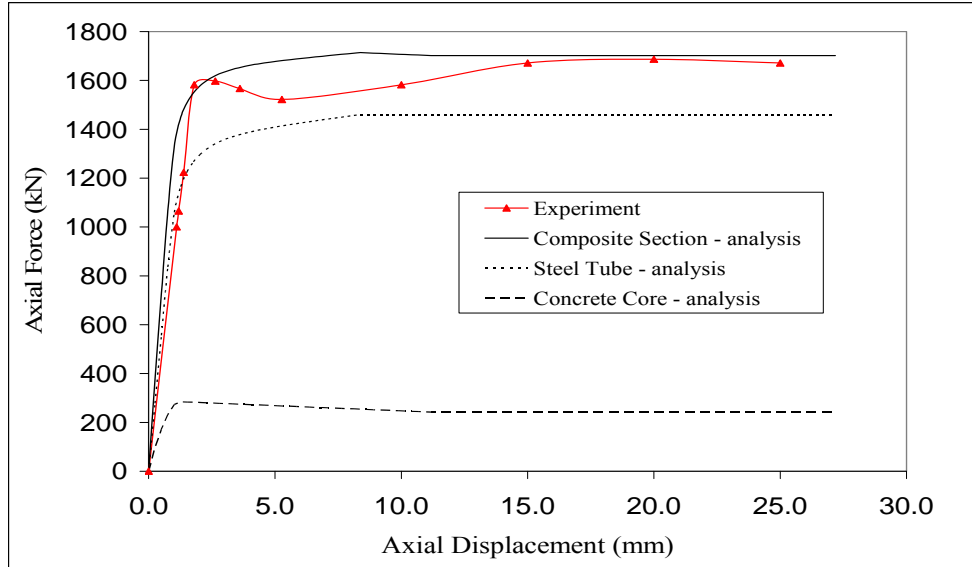


Figure 5.58 Comparison of Computational and Experimental Results for an Axially-Loaded RCFT Short Column (Schneider, 1998, R6)

As may be seen from the figures, the overall correlation between the experimental and computational results is generally excellent for the full range of geometric and material properties common within RCFTs. More detailed error analysis of the computational results presented in Figures 5.34 through 5.58 is given in Table 5.9. Four types of data values are obtained from the experimental plots including initial stiffness (E_i), peak axial load (P_o), displacement at peak axial load (d_o), and residual strength at high deformation levels (P_{res}). The experimental data values are then compared to the computational results and the associated error values are computed.

Figures 5.58 to Figure 5.61 illustrate the variation of the absolute value of the error with respect to the structural parameters of $(D/t) \times \sqrt{f_y / E_s}$ and f'_c . These two parameters characterize the response of RCFT columns. For example, $(D/t) \times \sqrt{f_y / E_s}$ signifies the slenderness of the steel tube against local buckling, which influences the peak strength and the post-peak behavior of the RCFT columns. The value of f'_c , on the other hand, has significant contribution in every segment of the load deformation response of RCFT columns, which is attributed to the nonlinear response of concrete.

Table 5-9 Comparison of Experimental and Computational Results for Concentrically-Loaded Short Column Tests

Specimen Label	Experimental Results				Computational Results				Error (%)			
	E_i (kN/mm)	P_o (kN)	d_o (mm)	P_{res} (kN)	E_i (kN/mm)	P_o (kN)	d_o (mm)	P_{res} (kN)	E_i (kN/mm)	P_o (kN)	d_o (mm)	P_{res} (kN)
I-A ²	1162.7	495.5	1.16	300.3	1288.3	522.1	0.57	435.6	-10.8	-5.4	50.9	-45.1
II-A ²	1052.8	517.8	0.90	381.5	1042.3	509.2	0.57	507.6	1.0	1.7	36.7	-33.0
III-A ²	1676.7	525.5	0.73	375.4	1305.4	584.1	0.89	562.6	22.1	-11.1	-21.9	-49.9
IV-A ³	2515.1	649.3	0.56	668.2	1697.8	719.4	0.76	711.9	32.5	-10.8	-35.7	-6.5
g1 ³	410.0	1440.0	3.87	1250.0	1633.9	1314.3	1.91	1314.3	-298.5	8.7	50.6	-5.1
g2 ³	641.5	1685.4	3.39	1525.3	1569.8	1568.7	1.52	1568.7	-144.7	6.9	55.2	-2.8
g3 ¹	631.6	2000.0	3.36	1437.0	1883.6	1944.2	1.52	1591.2	-198.2	2.8	54.8	-10.7
g4 ¹	605.0	2237.3	4.10	1847.5	1885.5	2130.3	1.52	1809.2	-211.7	4.8	62.9	2.1
g8 ¹	1111.5	2227.3	2.92	2145.5	2301.9	2342.2	1.63	2288.1	-107.1	-5.2	44.2	-6.6
g27 ¹	2626.3	8290.9	3.25	4654.6	7371.2	7851.3	1.52	5877.0	-180.7	5.3	53.2	-26.3
S1 ²	1011.6	924.7	2.28	774.2	981.5	995.3	2.13	937.6	3.0	-7.6	6.6	-21.1
S2 ³	1354.8	1086.0	3.19	956.9	1102.9	1176.8	4.45	1161.6	18.6	-8.4	-39.5	-21.4
S3 ³	722.6	1118.3	2.18	892.5	1161.4	1126.9	1.60	1113.5	-60.7	-0.8	26.6	-24.8
S4 ³	481.7	1182.8	2.08	1161.3	1289.9	1295.0	1.60	1288.0	-167.8	-9.5	23.1	-10.9
S5 ³	1024.0	2064.5	2.48	1967.7	1083.9	1750.2	1.78	1736.2	-5.8	15.2	28.2	11.8
R1 ²	663.6	806.0	1.39	617.9	787.5	758.8	1.27	432.6	-18.7	5.8	8.6	30.0
R2 ³	779.1	1000.0	1.72	806.0	988.1	1000.6	1.52	980.8	-26.8	-0.1	11.6	-21.7
R3 ³	1660.8	1119.4	1.39	1014.9	1174.4	1216.1	1.65	1186.5	29.3	-8.6	-18.7	-16.9
R4 ³	730.7	1223.9	2.20	1014.9	1167.5	1140.8	1.52	1116.3	-59.8	6.8	30.9	-10.0
R5 ³	900.0	1343.3	1.94	1194.0	1287.5	1303.1	1.65	1291.6	-43.1	3.0	14.9	-8.2
R6 ³	900.0	1686.6	1.81	1641.8	1477.5	1714.0	2.03	1701.9	-64.2	-1.6	-12.2	-3.7
CR4-D-8 ²	3298.2	8553.3	3.46	3441.2	4928.2	9359.9	2.54	3861.8	-49.4	-9.4	26.6	-12.2
CR4-C-4-1 ²	2459.6	2538.0	1.97	1761.0	2942.7	2788.8	1.33	2138.7	-19.6	-9.9	32.5	-21.4
CR8-C-8 ²	2581.9	5512.9	3.40	4380.4	3436.6	5328.2	2.76	4526.9	-33.1	3.4	18.8	-3.3
CR4-D-2 ²	2447.4	3668.4	2.22	2583.4	3393.5	4025.4	1.78	2740.4	-38.7	-9.7	19.8	-6.1
SC32-46 ¹	4135.6	11511.6	2.92	6383.7	4420.8	12087.4	3.73	7121.8	-6.9	-5.0	-27.7	-11.6
SC32-80 ¹	4893.8	14232.6	3.26	10255.8	4501.0	14673.0	3.81	9852.0	8.0	-3.1	-16.9	3.9
SC48-46 ¹	4013.4	11920.2	3.47	5651.2	4135.9	11835.0	3.56	5017.7	-3.1	0.7	-2.6	11.2
Mean of Error									-58.4	-1.5	17.2	-11.4
Standard Deviation of Error									84.7	7.1	29.7	16.6
Median of Error									-30.0	-1.2	21.5	-10.4

The predictions of the initial stiffness show a significant scatter. The mean value of the error from Table 5-9 is obtained as -58.4 % while the standard deviation is 84.7 %. From Figure 5.59, it can be seen that the error values for the specimens with low $(D/t) \times \sqrt{f_y / E_s}$ (<1.0) and medium strength concrete ($40 \text{ MPa} < f'_c < 80 \text{ MPa}$) are usually the highest. Due to less variation in the modulus of elasticity of the steel tube compared to the concrete, the error in E_i may be attributed the inaccuracy in calculating E_c .

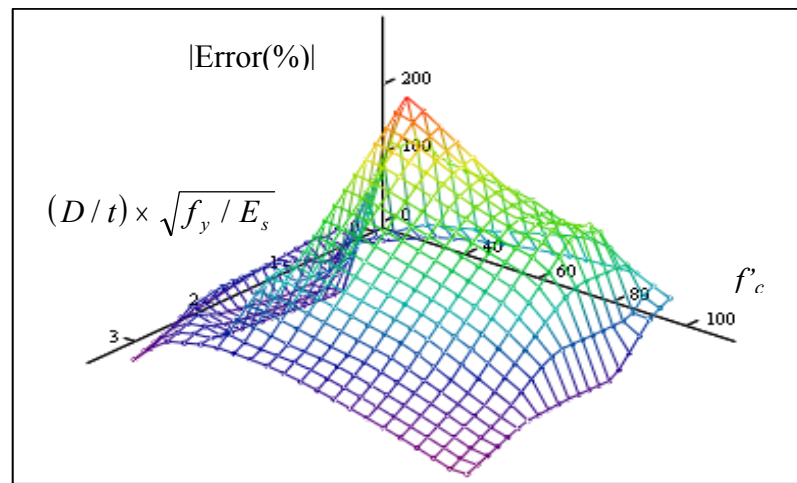


Figure 5.59 Variation of error for E_i with respect to $(D/t) \times \sqrt{f_y / E_s}$ and f'_c

The correlation of the experimental and computational results for P_o is often found to be satisfactory. The mean error and the standard deviation are calculated as -1.5 % and 7.11 %, respectively. In Figure 5.60, the largest error values are obtained for the specimens with low values of $(D/t) \times \sqrt{f_y / E_s}$ and f'_c . This might be attributed to the fact that the material model utilized for the cold formed steel tube underestimates the hardening response following yielding.

Figure 5.61 shows the comparison of experimental and computational values of d_o . The mean value of the error is 17.2 % and the standard deviation is 29.7%. In the case of specimens with low $(D/t) \times \sqrt{f_y / E_s}$ values, the error values are found to be the largest. This error may be due to the unsatisfactory predictions of E_i for the specimens having low $(D/t) \times \sqrt{f_y / E_s}$ values.

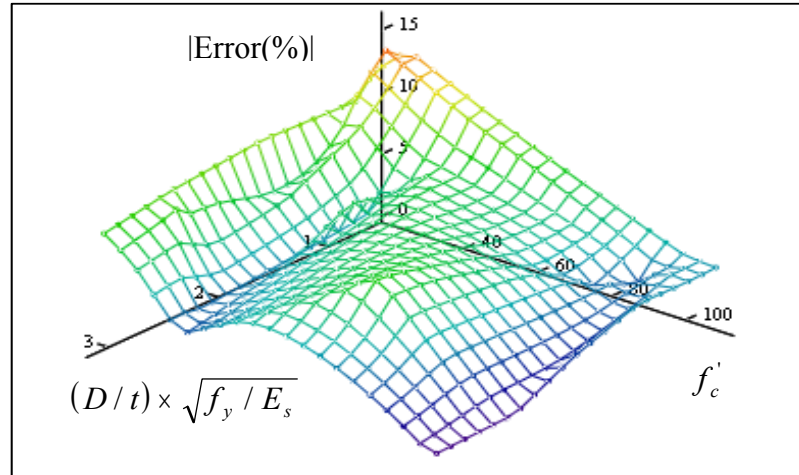


Figure 5.60 Variation of error for P_o with respect to $(D/t) \times \sqrt{f_y / E_s}$ and f'_c

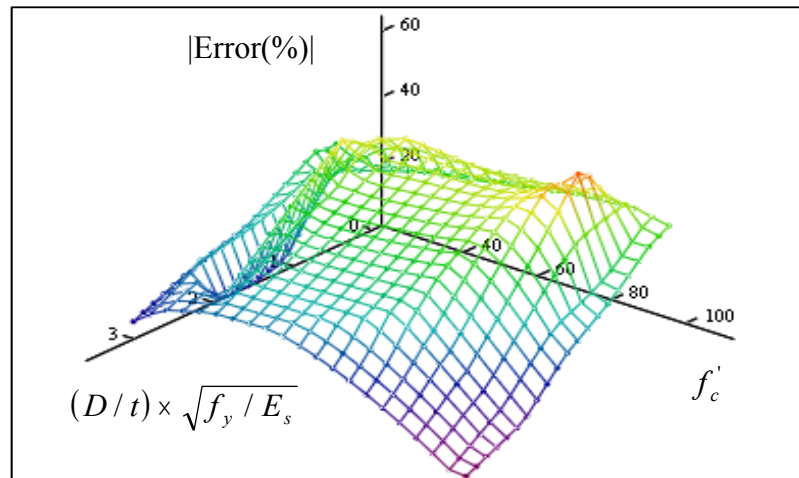


Figure 5.61 Variation of error for d_o with respect to $(D/t) \times \sqrt{f_y / E_s}$ and f'_c

The comparison of experimental and computational values for P_{res} is presented in Figure 5.62. The magnitude of the error is found to be the minimum for the specimens with f'_c values ranging from 40 to 80 MPa. No clear trend is observed for the error values due to the change in the slenderness of the steel tube. The average error values and the standard deviation are found to be -11.4% and 16.6%, respectively.

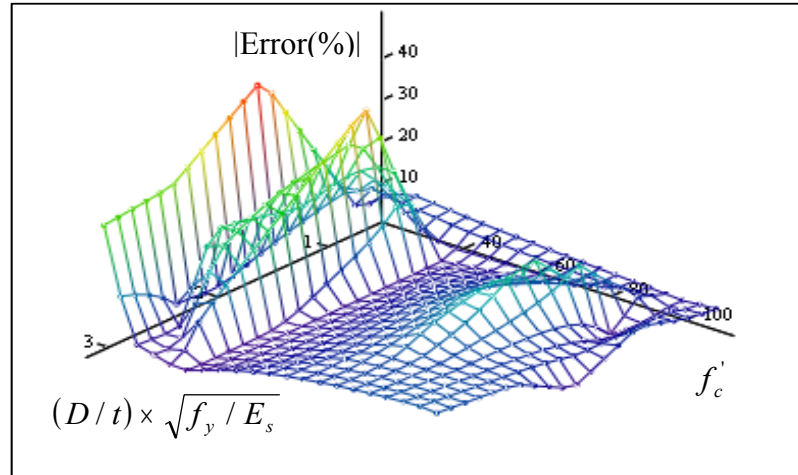


Figure 5.62 Variation of error for d_o with respect to $(D/t) \times \sqrt{f_y / E_s}$ and f'_c

5.5. Materially and Geometrically Nonlinear RCFT Beam Tests

The main motivation in conducting pure-bending tests is to understand the flexural response of the RCFT composite section and to quantify the contribution of concrete core to the moment capacity (Lu and Kennedy, 1994). From the experimental database by Tort and Hajjar (2003), two types of loading schemes were identified as depicted in Figure 5.63. Lu and Kennedy (1994) tested RCFT members under four point loading creating a center portion of the beam under constant bending moment. Tomii and Sakino (1979) applied bending moment directly at the supports and the RCFT member was subjected to a uniform moment along its whole length.

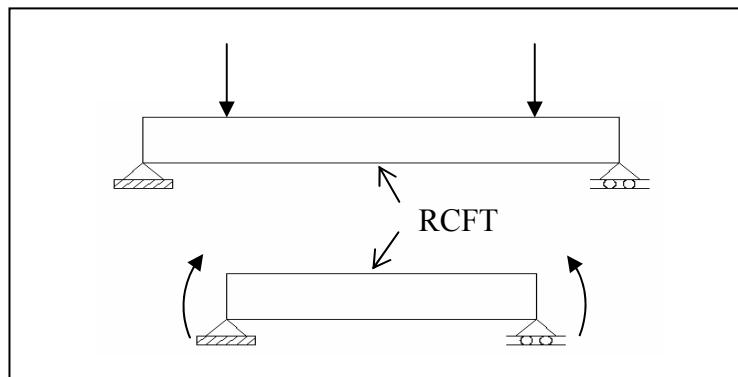


Figure 5.63 Pure Bending of RCFT Beams

The accuracy of the mixed finite element formulation in simulating pure bending tests is assessed in this section. First, a mesh convergence study was performed on the

specimen CB12 by Lu and Kennedy (1994). A total number of six analyses were conducted by varying the number of elements per member from 2 to 4 and varying the number of integration points as 4 and 6. The same fiber discretization was used for each analysis. The number of material fibers was kept as 4 along the depth and width of the concrete core and the steel tube. A single layer of fiber layers around the perimeter of the steel tube was defined. A displacement-controlled solution algorithm was utilized by selecting the steel tube transverse displacement of the node under the left shear loading as the control degree-of-freedom (Yang and Kuo, 1994). Figure 5.64 shows the comparison of load deformation response for each case of the analyses. In the legend of Figure 5.64, the first character indicates the number of elements while the second shows the number of integration points. Until the attainment of the peak load, the computational results are not exhibiting a noticeable deviation from each other. However, in the post-peak region a slight discrepancy is evident. It was found that using 3 elements per member with 4 integration points produces a maximum error in moment less than 0.5% compared to the finest mesh with 4 elements per member with 6 integration points. Therefore, using 3 elements with 4 integration points is determined to be a mesh density producing an acceptable level of accuracy. It should be noted that even with a relatively coarse mesh of 2 elements with 4 integration points, the analysis produced satisfactory results. This can be attributed to the superior representation of inelastic curvatures in mixed-finite element formulation.

Lu and Kennedy (1994) documented experimental moment-curvature plots for the specimens tested under four point bending. Figure 5.65 illustrates the comparison of the computational and experimental results for the Specimen CB12. A good correlation is achieved with respect to the initial stiffness and moment capacity. However, the computational response overestimated the strength degradation following the attainment of the peak moment. In Figure 5.65, the moment vs. curvature response is presented for the steel tube, concrete core, and composite section, individually. It can be seen that the strength degradation in the post-peak region is attributed to concrete crushing. The contribution of the concrete core to the moment capacity is found to reach up to a level of 35% throughout the loading history.

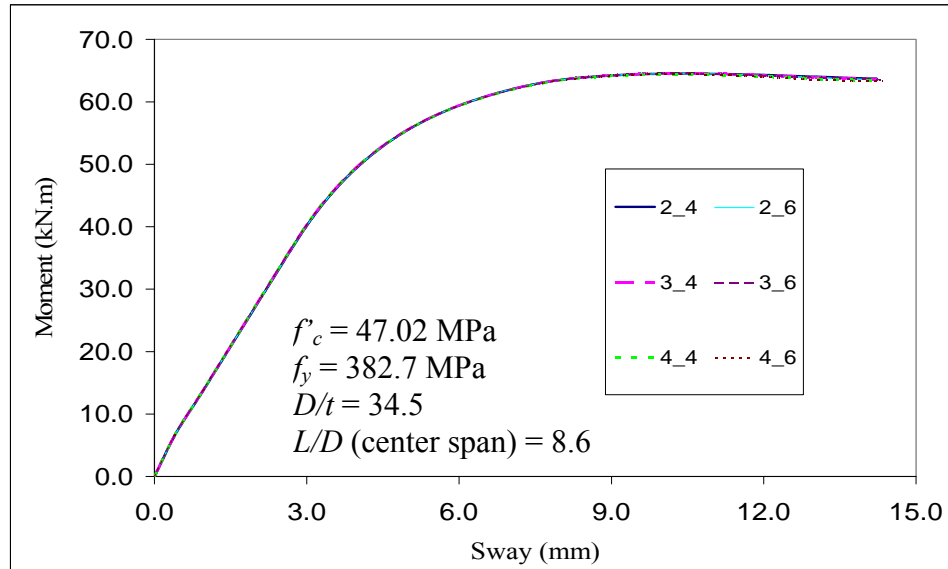


Figure 5.64 Mesh-Convergence of Pure Bending of RCFT Beams

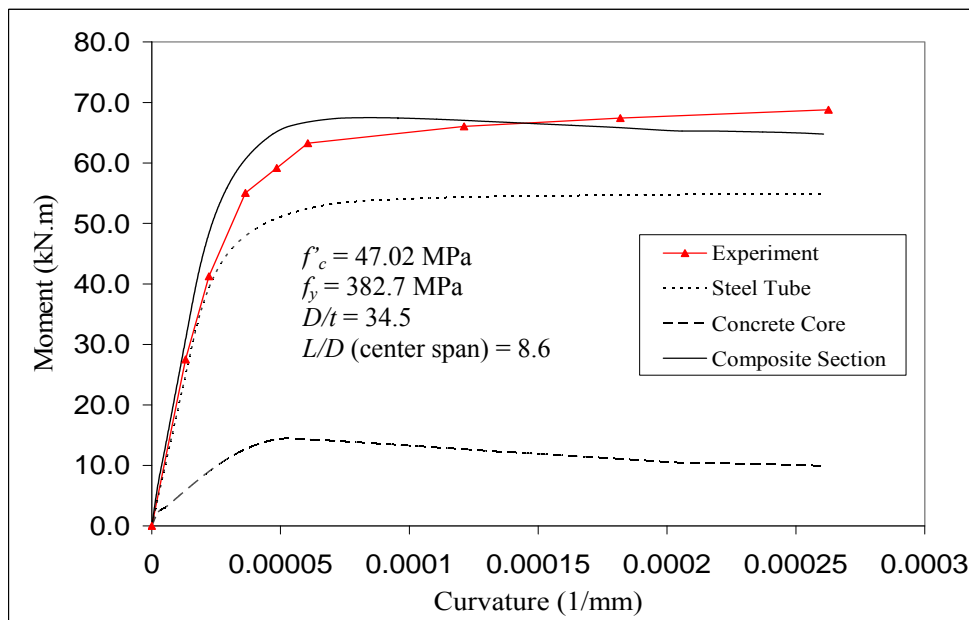


Figure 5.65 Comparison of Computational and Experimental Results for an RCFT Beam Pure Bending Test (Lu and Kennedy, 1994, Specimen CB12)

Gho and Liu (2004) also performed four point bending tests on RCFT beams. A higher strength concrete is utilized compared to the specimens by Lu and Kennedy (1994). Specimen B04 by Gho and Liu (2004) is analyzed by using 3 elements per member for the edge spans and 4 elements per member for the center span. The number of elements is increased by one for the center span due to the fact that the experimental

results are given for bending displacement of the middle of the specimen. The maximum bending displacement is obtained as the difference in total displacement of the node located at the middle of the specimens and the node on which the transverse loading is being applied. The comparison of the experimental and computational results can be found in Figure 5.66. A good correlation in initial and bounding stiffness (post-peak stiffness) is achieved. However, discrepancy in the maximum moment value can be noticed. This might be attributed to the overestimation of the initial plastic strain due to residual stress in the steel tube.

In the tests by Tomii and Sakino (1979), RCFT beams are subjected to bending moments applied directly at the elements ends as it is illustrated in Figure 5.63. The specimen IV-0 by Tomii and Sakino (1979) is analyzed with 3 finite elements per member with 4 gauss points. Displacement control algorithm is utilized by selecting the in-plane rotation at one end of the member as the controlling degree-of-freedom (Yang and Kuo, 1994). In Figure 5.67, the computational and experimental load deformation response of Specimen IV-0 can be seen. The finite element results are found to estimate the initial stiffness and the maximum value of the moment accurately. On the other hand, the effect of residual stress is overestimated causing earlier yielding of the specimen.

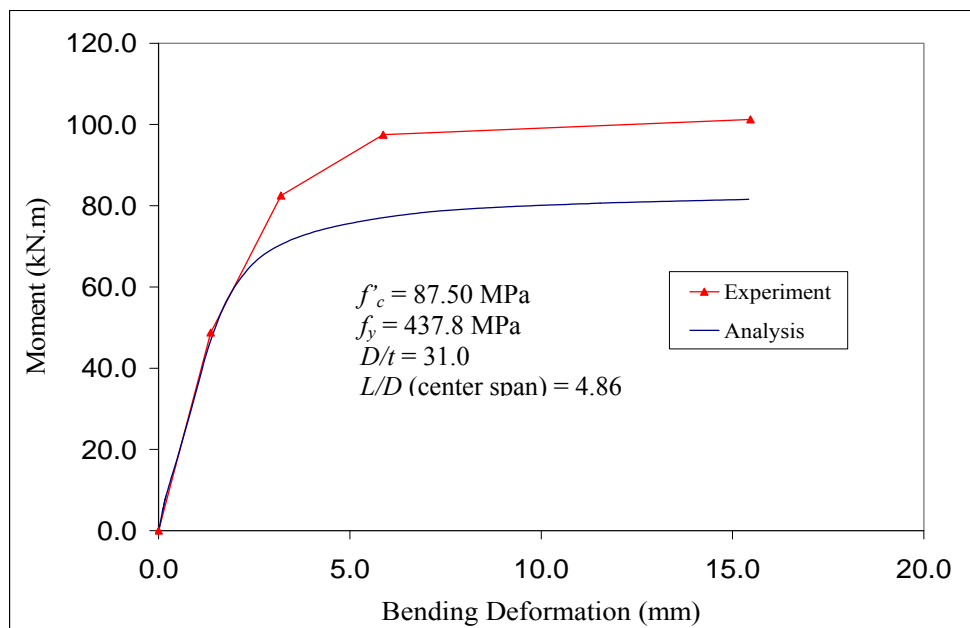


Figure 5.66 Comparison of Computational and Experimental Results for an RCFT Beam Pure Bending Test (Gho and Liu, 2004, Specimen B04)

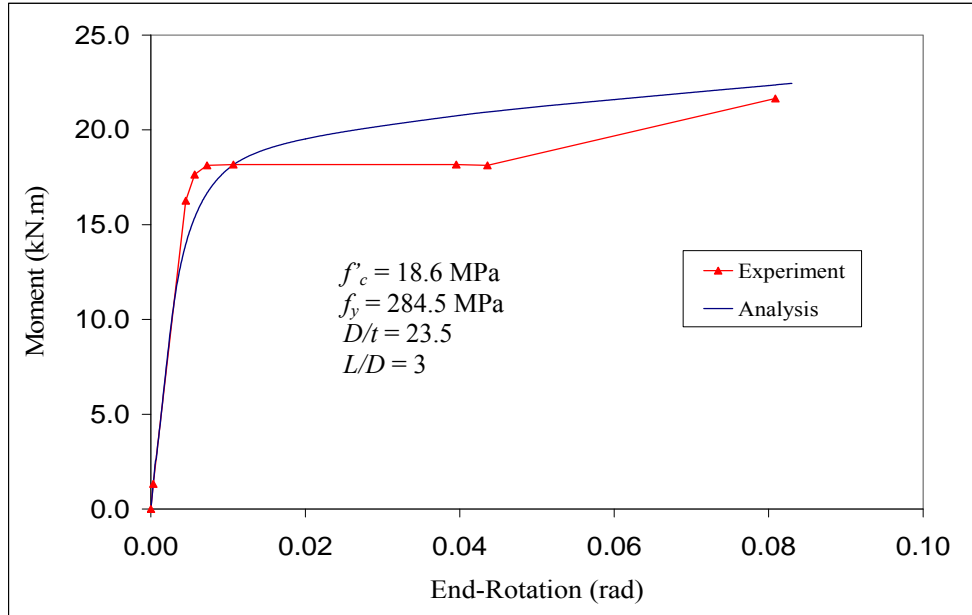


Figure 5.67 Comparison of Computational and Experimental Results for an RCFT Beam Pure Bending Test (Tomii and Sakino, 1979, Specimen IV0)

The verification studies conducted on pure bending tests until this point was aimed to illustrate the capability of the mixed-finite element formulation to model representative RCFT members characterizing the behavioral aspects in pure bending tests with respect to the material properties and boundary conditions. The response patterns exhibited by the computational results were identified and discussed.

To examine the ability to model the results from the experimental database of pure bending tests by Tort and Hajjar (2003), RCFT members with a wider range of geometric and material properties were selected. The assessment of the accuracy of the computational results was performed based on comparisons of key numerical quantities in the experimental and computational load-deformation response including initial stiffness, peak moment, and bounding stiffness.

The minimum mesh density of the specimens analyzed was 3 elements per member with 4 integration points. The constant-displacement arc length method was utilized as the global nonlinear solution scheme. The local response parameters including cross-section forces and deformations were determined through Newton-Raphson nonlinear solution algorithm due to the fact the load vector at the local level is decided based on the operations performed at the global level (see chapter 2). This restricted the

use of limit-state algorithms such as arc-length method or displacement-control. In Figure 5.68, the numerical representations of the pure bending test setups are illustrated. Pinned-roller boundary conditions were introduced for all of the specimens. The slip between the steel tube and concrete core was allowed at every joint along the element length, consistent with the experiment boundary conditions.

Figure 5.69-Figure 5.83 show the comparison of computational and experimental results in terms of moment vs. curvature, moment vs. bending displacement, or moment vs. end-rotation response. The moment-curvature response was obtained for the most stressed cross-section, which was usually located at the mid-length of the specimen. Since the steel tube and the concrete core rotational degrees of freedom are introduced independently in the natural coordinates, the moment curvature response is presented individually for the steel tube, the concrete core, and the composite section in a single plot.

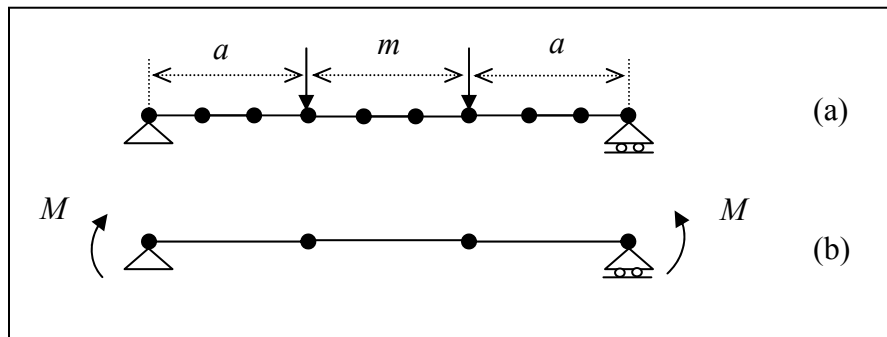


Figure 5.68 Concentrically Loaded Short RCFT Column Computational Model

A total number of 18 specimens were analyzed from the database by Tort and Hajjar (2003). The specimens exhibited a distinct gradient with respect to boundary conditions, material properties, and geometric properties. The specimens were first grouped as “ a ” and “ b ” according to the boundary conditions introduced in Figure 5.68. The second classification of the specimens was performed with respect to the concrete strength, where Group 1 was assumed to have low-strength concrete specimens and Group 2 was assumed to have high-strength concrete specimens. Table 5-10 gives a full summary of the measured material and geometric properties of the specimens, where available. The nomenclature to denote the classification of the specimens was designed as superscripts attached to their experimental label. For example, the specimen “CB12^{a1}” has type “ a ” boundary conditions and it belongs to Group 1 with respect to the concrete

strength. This type of classification of the specimens helps to analyze the sources of errors between the experimental and computational results and to recommend ways for improving the correlations with the experiments.

Table 5-10 Pure Bending Tests of RCFT Beams

Specimen Label	E_s (MPa)	f_y (MPa)	f'_c (MPa)	D (mm)	B (mm)	t (mm)	D/t	L (mm)
CB12 ^{a1}	212001	383.0	47.0	152.4	152.4	4.43	34.4	a = 235, m = 1305
CB13 ^{a1}	212001	409.8	42.8	152.4	152.4	4.43	34.4	a = 463, m = 1305
CB15 ^{a1}	212001	383.0	41.2	152.4	152.4	4.43	34.4	a = 768, m = 1305
CB22 ^{a1}	205402	490.0	46.9	152.4	152.4	8.95	17.0	a = 236, m = 1305
CB31 ^{a1}	208401	379.0	46.7	253.4	152.0	6.17	41.1	a = 26, m = 1508
CB35 ^{a1}	208401	379.0	44.3	253.4	152.0	6.17	41.1	a = 1276, m = 1508
CB41 ^{a1}	200003	405.0	46.2	253.0	152.2	9.04	28.0	a = 261, m = 1508
CB45 ^{a1}	200003	405.0	43.8	253.0	152.2	9.04	28.0	a = 1276, m = 1508
CB52 ^{a1}	208401	379.0	47.1	253.4	152.0	6.17	41.1	a = 235, m = 1305
CB53 ^{a1}	208401	379.0	42.1	253.4	152.0	6.17	41.1	a = 463, m = 1305
CB55 ^{a1}	208401	379.0	40.5	253.4	152.0	6.17	41.1	a = 768, m = 1305
B1CSN ^{a1}	199955	350.0	39.0	140.0	140.0	3.90	35.9	a = 325, m = 300
B1DRN ^{a1}	199955	360.0	39.0	200.0	100.0	4.70	42.6	a = 325, m = 300
B02 ^{a2}	205002	438.0	56.3	150.2	150.4	4.87	30.8	a = 365, m = 730
B04 ^{a2}	205002	438.0	87.5	150.0	150.2	4.84	31.0	a = 365, m = 730
II0 ^{b1}	208953	305.1	21.6	100.0	100.0	2.27	44.1	300
III0 ^{b1}	210956	289.4	20.6	100.0	100.0	2.98	33.6	300
IV0 ^{b1}	225630	284.5	18.6	100.0	100.0	4.25	23.5	300

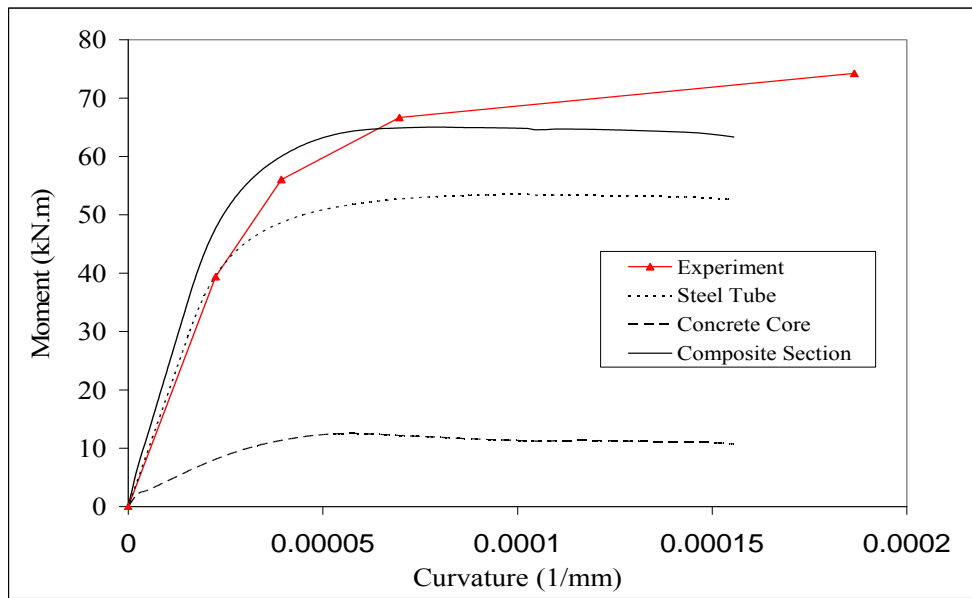


Figure 5.69 Comparison of Computational and Experimental Results for an RCFT Beam under Four Point Bending (Lu and Kennedy, 1994, Specimen CB13)

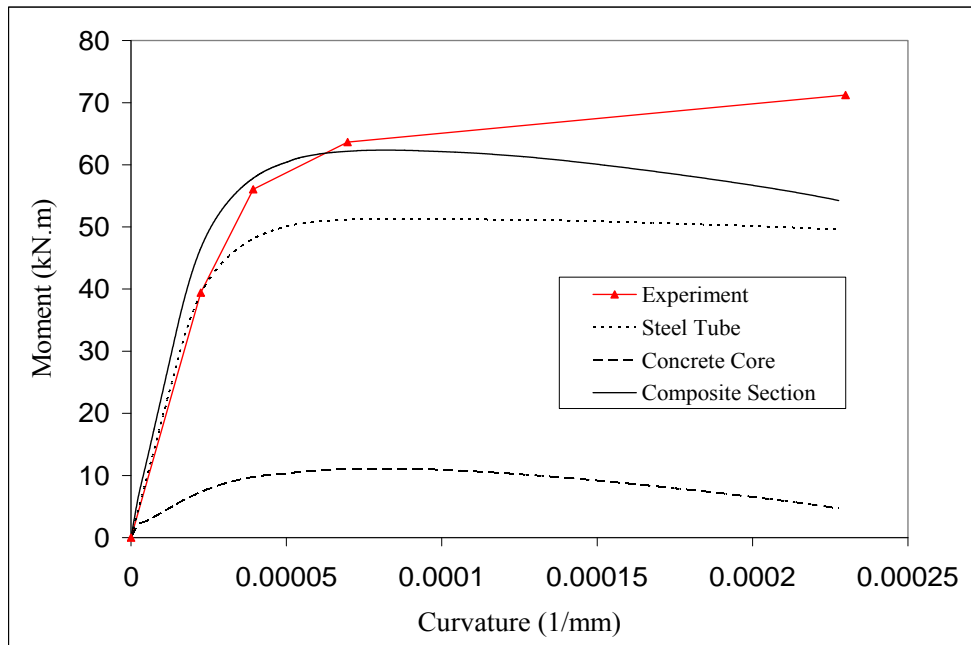


Figure 5.70 Comparison of Computational and Experimental Results for an RCFT Beam under Four Point Bending (Lu and Kennedy, 1994, Specimen CB15)

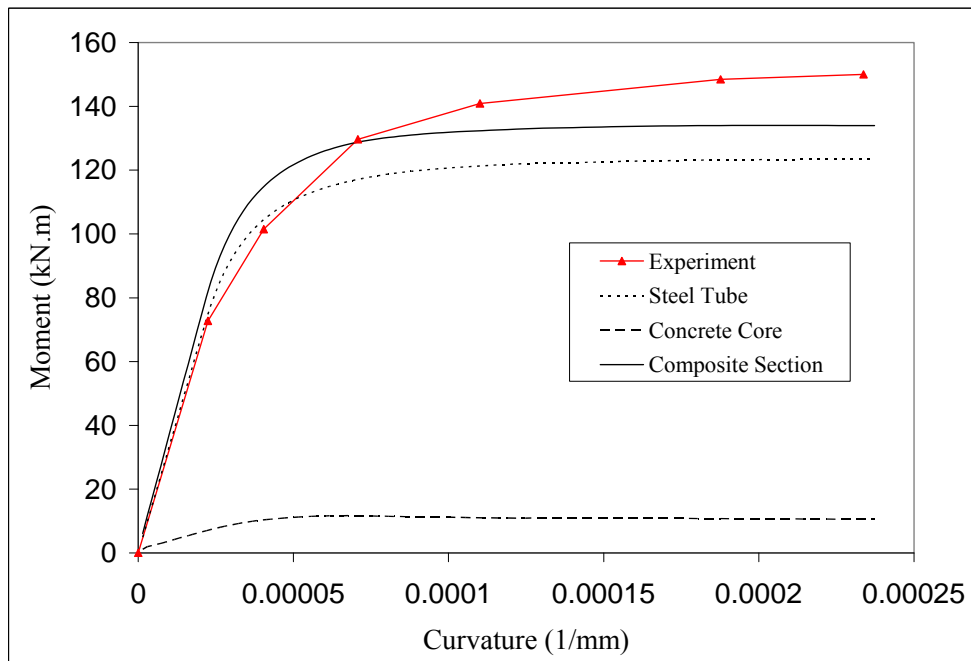


Figure 5.71 Comparison of Computational and Experimental Results for an RCFT Beam under Four Point Bending (Lu and Kennedy, 1994, Specimen CB22)

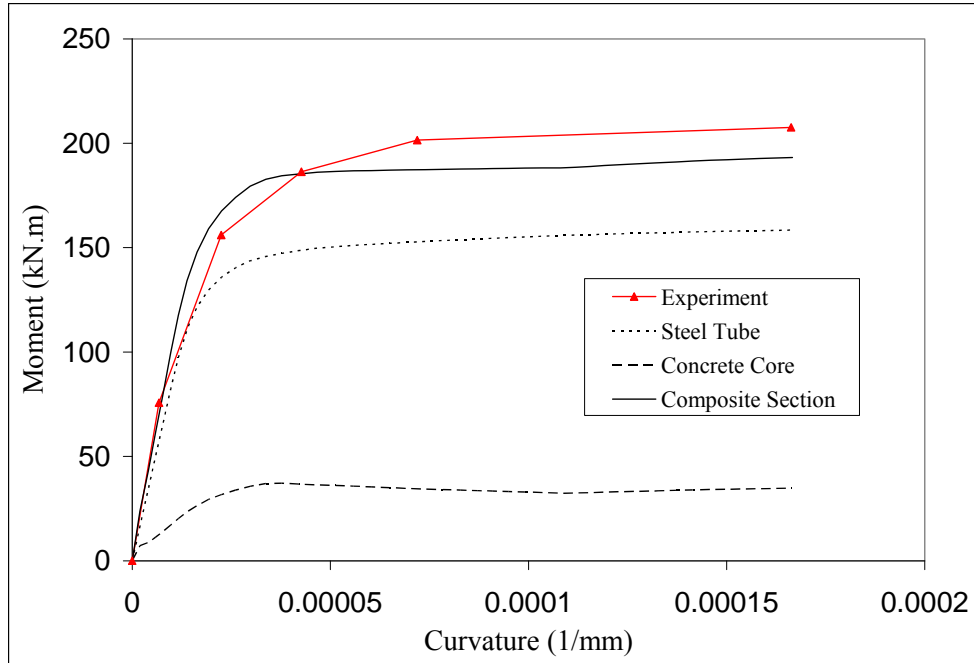


Figure 5.72 Comparison of Computational and Experimental Results for an RCFT Beam under Four Point Bending (Lu and Kennedy, 1994, Specimen CB31)

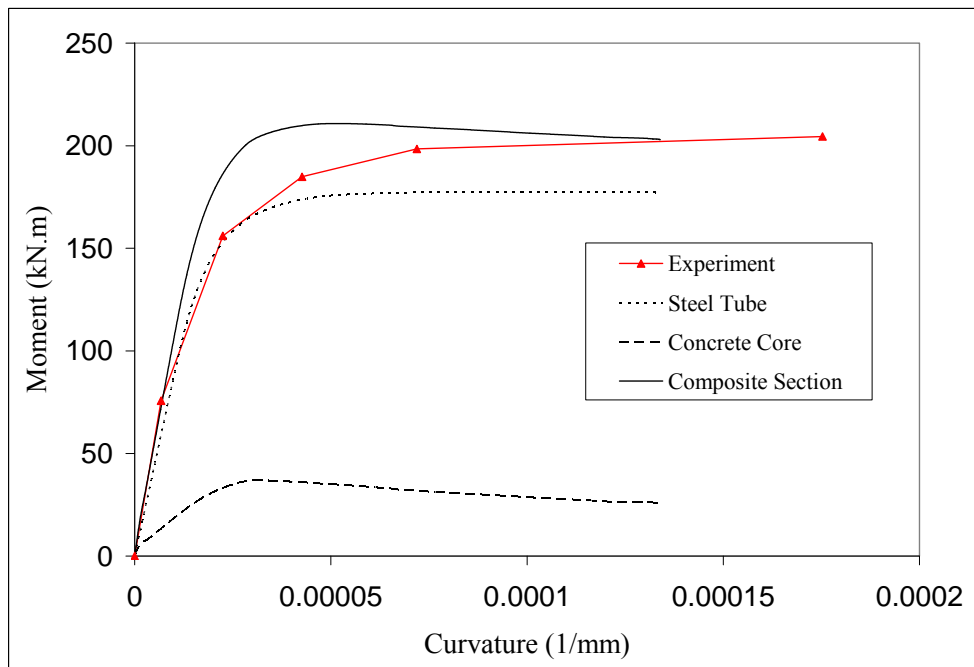


Figure 5.73 Comparison of Computational and Experimental Results for an RCFT Beam under Four Point Bending (Lu and Kennedy, 1994, Specimen CB35)

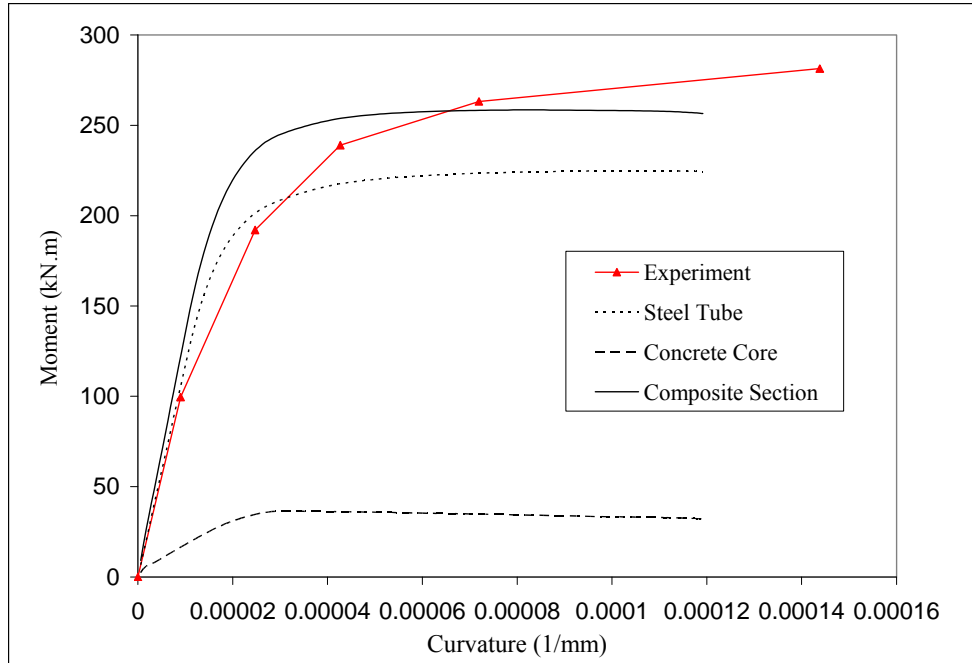


Figure 5.74 Comparison of Computational and Experimental Results for an RCFT Beam under Four Point Bending (Lu and Kennedy, 1994, Specimen CB41)

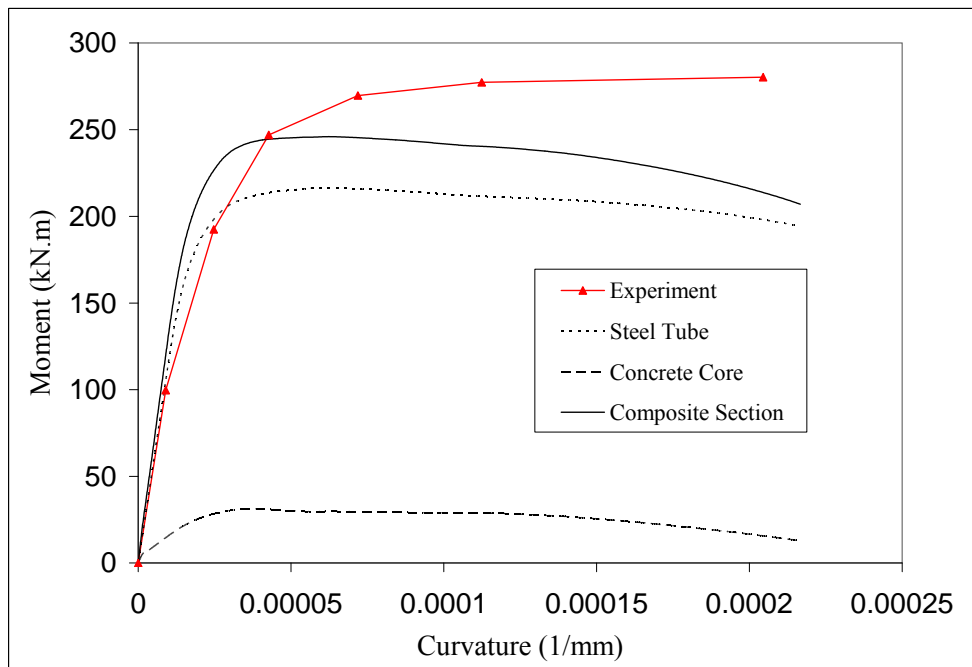


Figure 5.75 Comparison of Computational and Experimental Results for an RCFT Beam under Four Point Bending (Lu and Kennedy, 1994, Specimen CB45)

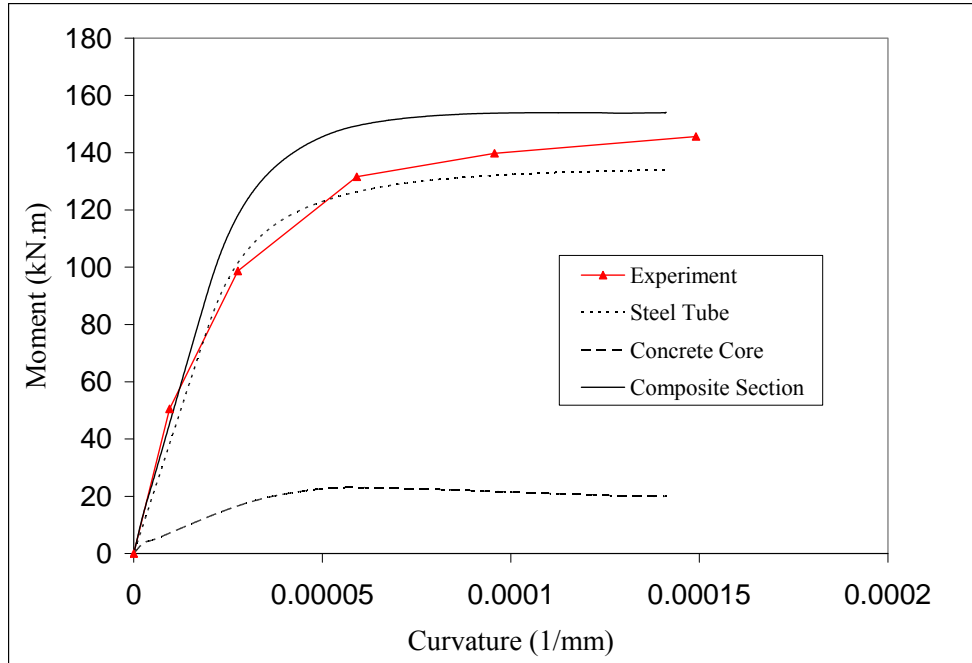


Figure 5.76 Comparison of Computational and Experimental Results for an RCFT Beam under Four Point Bending (Lu and Kennedy, 1994, Specimen CB52)

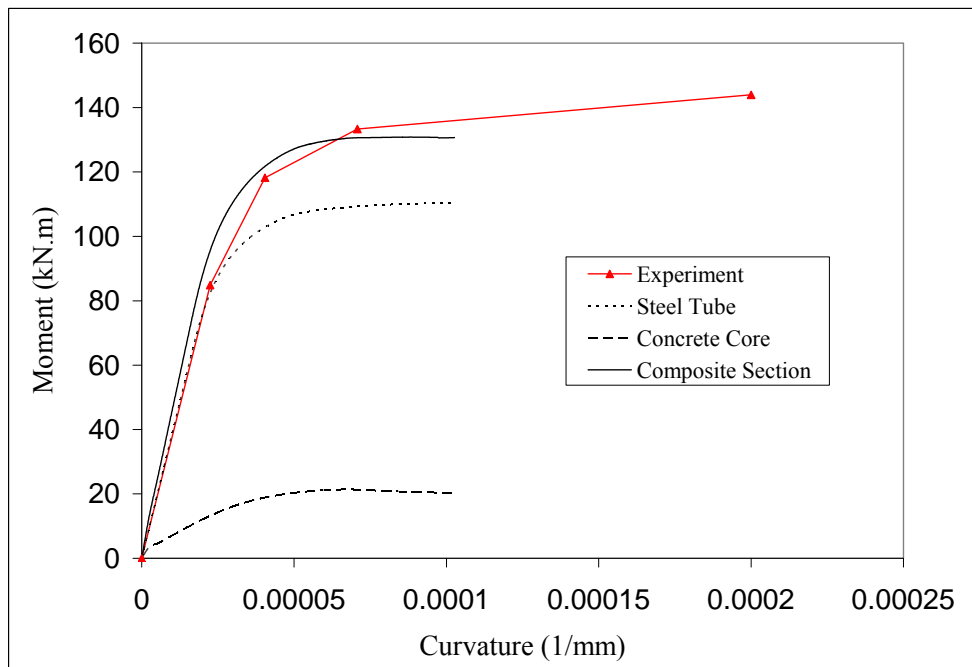


Figure 5.77 Comparison of Computational and Experimental Results for an RCFT Beam under Four Point Bending (Lu and Kennedy, 1994, Specimen CB53)

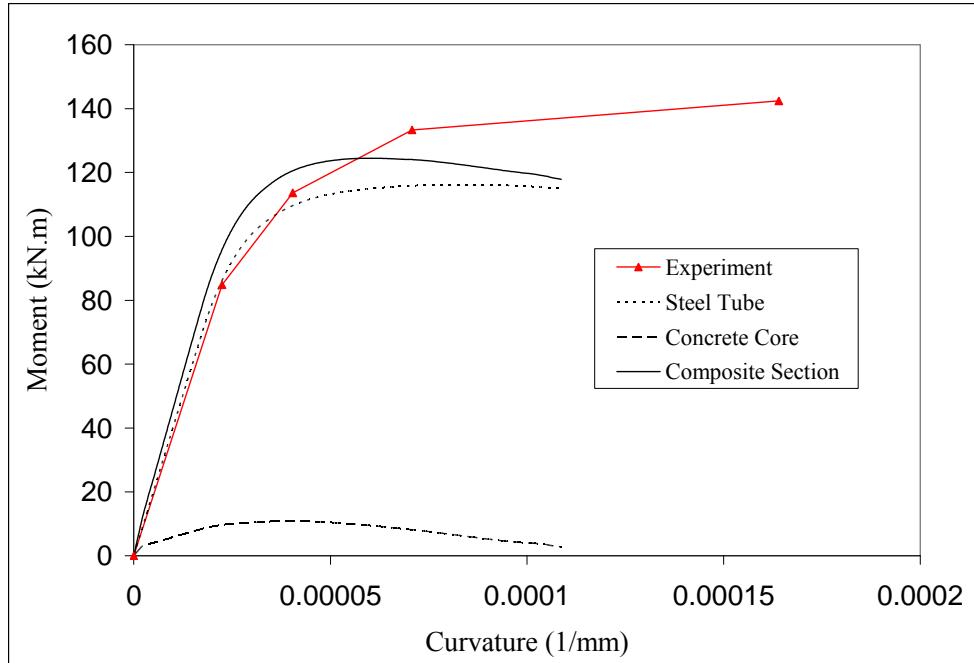


Figure 5.78 Comparison of Computational and Experimental Results for an RCFT Beam under Four Point Bending (Lu and Kennedy, 1994, Specimen CB55)

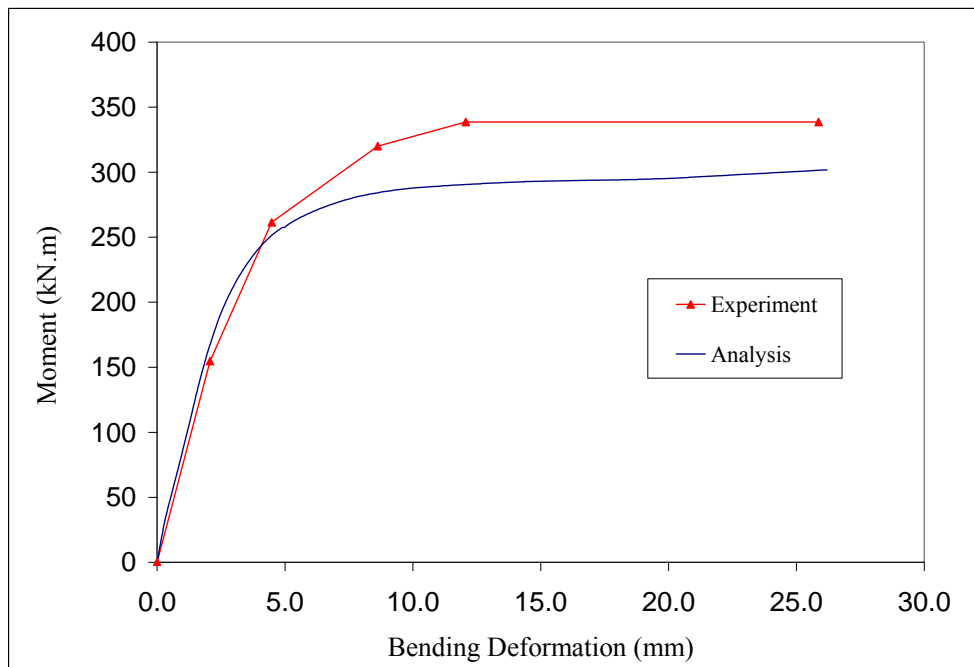


Figure 5.79 Comparison of Computational and Experimental Results for an RCFT Beam under Four Point Bending (Assi et al., 2003, Specimen B1CSN)

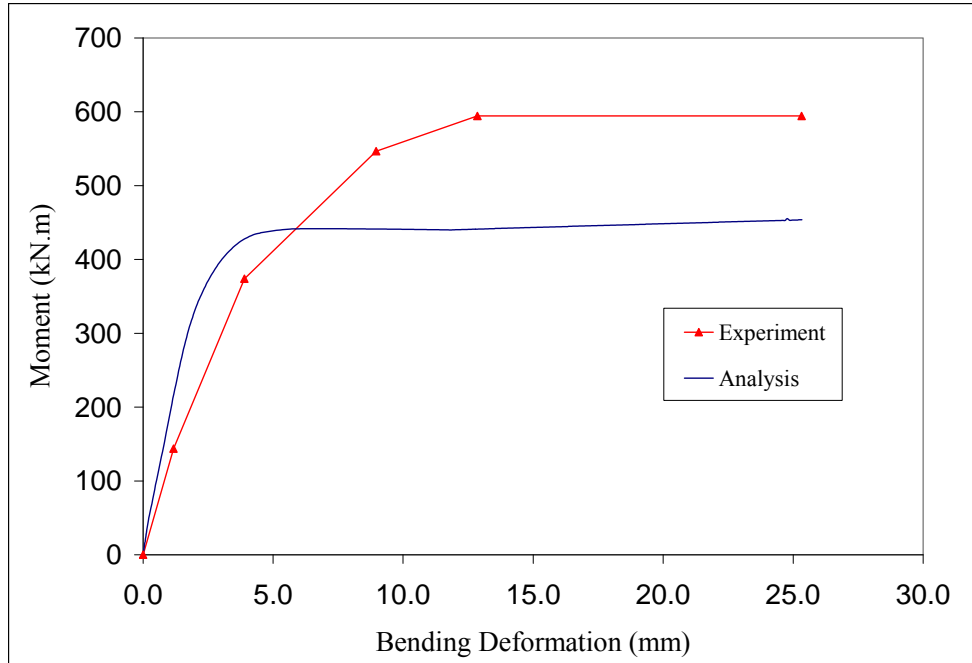


Figure 5.80 Comparison of Computational and Experimental Results for an RCFT Beam under Four Point Bending (Assi et al., 2003, Specimen B1DRN)

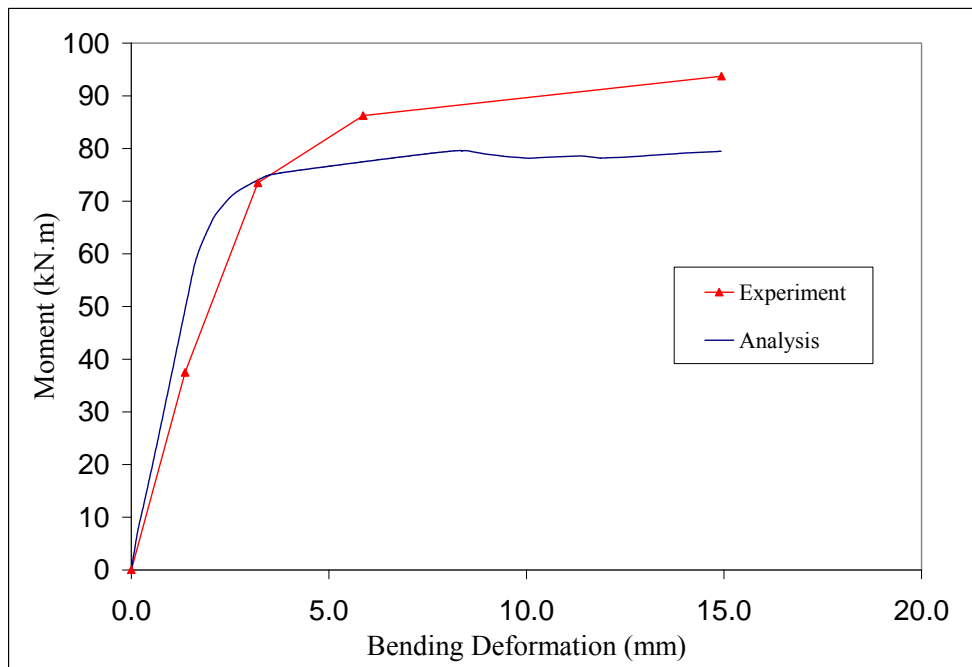


Figure 5.81 Comparison of Computational and Experimental Results for an RCFT Beam under Four Point Bending (Assi et al., 2003, Specimen B02)

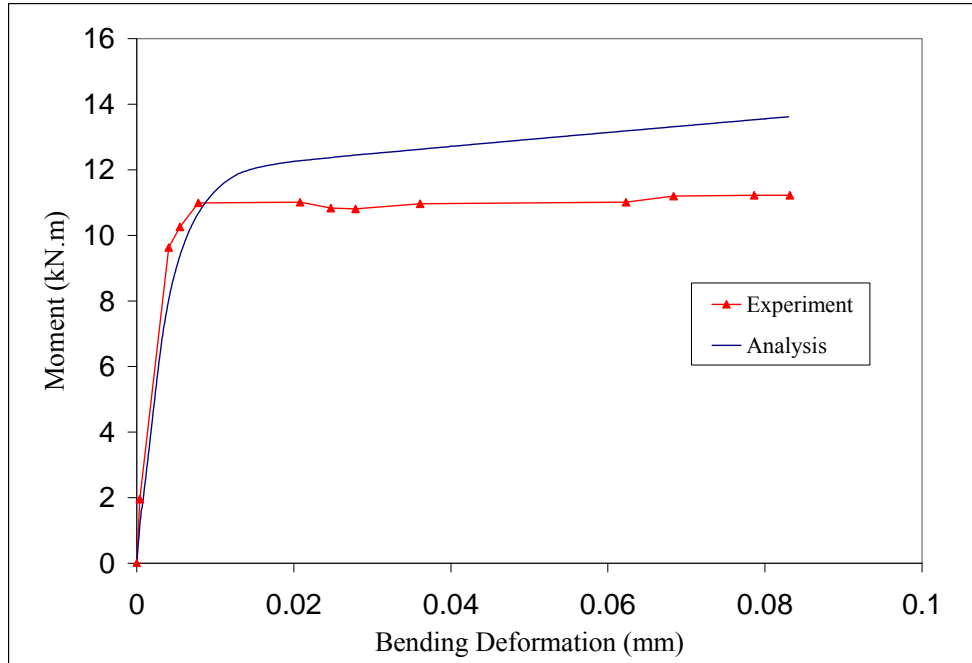


Figure 5.82 Comparison of Computational and Experimental Results for an RCFT Beam under Four Point Bending (Tomii and Sakino, 1979 Specimen II0)

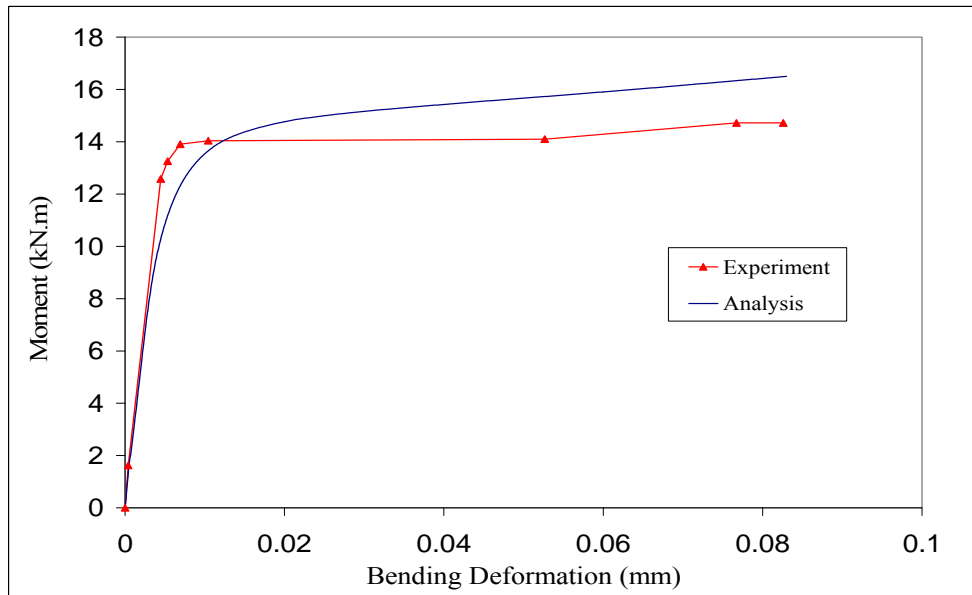


Figure 5.83 Comparison of Computational and Experimental Results for an RCFT Beam under Four Point Bending (Tomii and Sakino, 1979, Specimen III0)

As may be seen from the figures, the overall correlation between the experimental and computational results is generally excellent for the full range of geometric and material properties common within RCFTs. A detailed evaluation of the accuracy of the

computational results is presented in Table 5-11 in the form of an error analysis. Three types of data values obtained from the computational load deformation curves are compared their counterparts from the experiments including initial stiffness (E_i), peak moment (M_o), and bounding stiffness (K_b). The corresponding percentage of error is then calculated.

Figure 5.84 and Figure 5.85 illustrate the variation of the absolute value of the error with respect to the structural parameters of $(D/t) \times \sqrt{f_y / E_s}$ and f'_c . These two parameters constitute the two main properties dominating the response of RCFT beams. For the majority of the specimens, the computational initial stiffness values are determined to be larger than the experimental initial stiffnesses. The mean error and the standard deviation are calculated as 32.0% and 32.3%, respectively. From Figure 5.84, it can be seen that the largest percent error in absolute value corresponds to the specimens with slender steel tubes and low strength concrete. The discrepancy might be due to inaccurate estimation of the elastic modulus of the concrete.

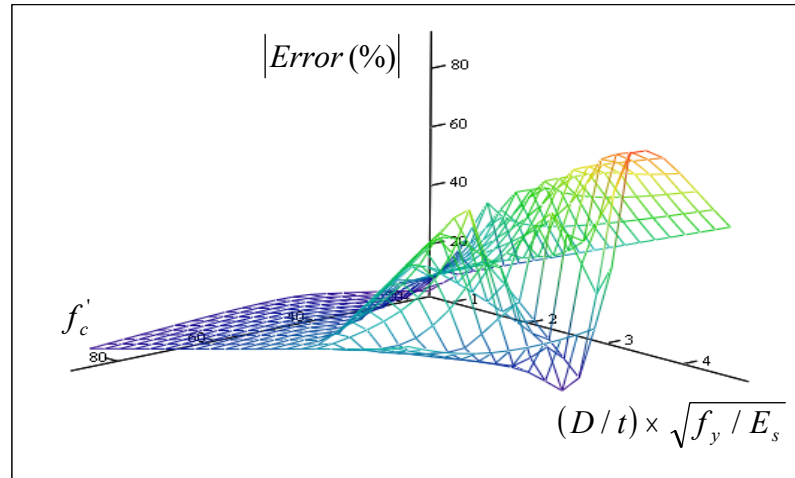


Figure 5.84 Variation of error for E_i with respect to $(D/t) \times \sqrt{f_y / E_s}$ and f'_c

As can be seen from Table 5-11 and Figure 5.85, the computational results exhibited a good correlation with M_o . The mean value of error is -6.3% and the standard deviation is 12.1%. In the case of specimens having concrete strength below 40 MPa, the error values are found to be consistently larger. No significant trend in the error values can be seen with respect to $(D/t) \times \sqrt{f_y / E_s}$.

Table 5-11 Comparison of Computational and Experimental Results for an RCFT Beam under Pure Bending

Specimen Label	Experimental Results			Computational Results			Error (%)		
	E_i (kN.m.mm)	M_o (kN.m)	K_b (kN.m.mm)	E_i (kN.m.mm)	M_o (kN)	K_b (kN.m.mm)	E_i	M_o	K_b
CB12 ^{a1}	2096108	68.8	26424.0	2901346	54.9	-19686.0	38.4	-20.2	-174.5
CB13 ^{a1}	1753030	74.2	64831.0	2870240	65.0	-18702.0	63.7	-12.4	-128.8
CB15 ^{a1}	1753030	71.2	47271.0	2851924	62.3	-99971.0	62.7	-12.5	-311.5
CB22 ^{a1}	3236364	150.0	118565.0	4118179	134.8	-58495.0	27.2	-10.1	-149.3
CB31 ^{a1}	11237374	207.6	64214.0	12119057	197.2	62489.0	7.8	-5.0	-2.7
CB35 ^{a1}	11237374	204.5	58630.0	13254193	210.9	-97624.0	17.9	3.1	-266.5
CB41 ^{a1}	11071340	281.3	252386.0	15801100	258.5	-0.1	42.7	-8.1	-100.0
CB45 ^{a1}	11091288	280.3	71898.0	15665686	246.0	-220425.0	41.2	-12.2	-406.6
CB52 ^{a1}	5326404	145.7	153164.0	5576125	154.1	-262.9	4.7	5.8	-100.2
CB53 ^{a1}	3775758	143.9	82082.0	5427300	131.0	12976.0	43.7	-9.0	-84.2
CB55 ^{a1}	3775758	142.4	97481.0	5487917	124.5	-169524.0	45.3	-12.6	-273.9
Specimen Label	E_i (kN.m/mm)	M_o (kN.m)	K_b (kN.m/mm)	E_i (kN.m/mm)	M_o (kN)	K_b (kN.m/mm)	E_i	M_o	K_b
B02 ^{a2}	27.6	93.8	0.8	46.6	79.6	0.21	69.1	-15.1	-74.5
B04 ^{a2}	35.8	101.3	0.4	46.7	87.5	0.38	30.2	-13.6	-3.9
B1CSN ^{a1}	74.8	338.7	0.0	109.2	301.8	0.77	46.1	-10.9	76800.0
B1DRN ^{a1}	123.1	594.5	0.0	234.0	455.3	0.69	90.2	-23.4	68780.0
Specimen Label	E_i (kN.m/rad)	M_o (kN.m)	K_b (kN.m/rad)	E_i (kN.m/rad)	M_o (kN)	K_b (kN.m/rad)	E_i	M_o	K_b
II0 ^{b1}	4994.2	11.2	6.1	2893.8	13.8	21.24	-42.1	23.1	246.8
III0 ^{b1}	4082.3	14.7	10.1	3355.2	16.7	26.20	-17.8	13.4	158.7
IV0 ^{b1}	4106.4	21.7	44.1	4330.6	23.2	35.08	5.5	7.1	-20.4
mean error							32.0	-6.3	7993.8
standard deviation of error							32.3	12.1	23613.7
median error							39.8	-10.5	-92.1

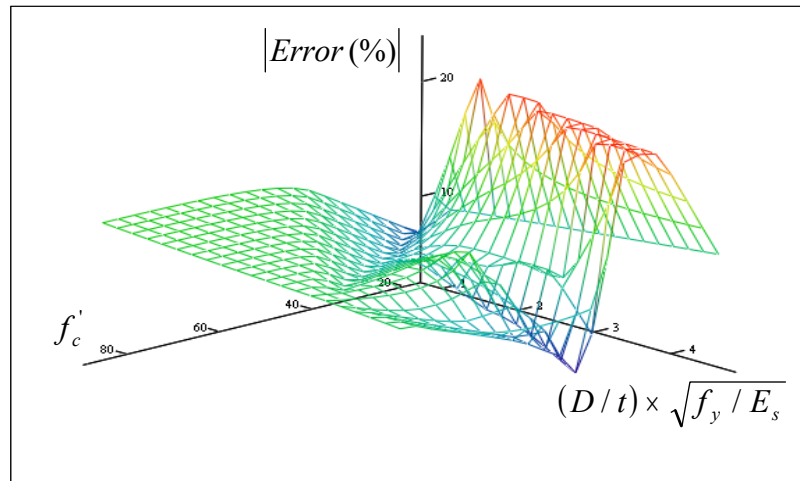


Figure 5.85 Variation of error for M_o with respect to $(D/t) \times \sqrt{f_y / E_s}$ and f'_c

The bounding stiffness values from the computational results exhibited a huge dispersion. For two of the specimens, very high values of percent error are obtained, which is due to the fact the experimental bounding stiffness is very close to zero.

5.6. Materially and Geometrically Nonlinear Proportionally-Loaded RCFT Beam-Column Tests

Proportionally-loaded column tests are often conducted to investigate the interaction of axial load and bending moment in RCFT columns (Bridge, 1976; Shakir-Khalil and Mouli, 1990; Shakir-Khalil and Zeghiche, 1989; Shakir-Khalil, 1994; Chung et al., 2001). As shown in Figure 5.86, pin-ended RCFT specimens are subjected to eccentrically-applied axial loading. The eccentricity can be introduced either uniaxially or biaxially by adjusting the inclination of the loading axis with respect to the strong axis of the RCFT cross-section.

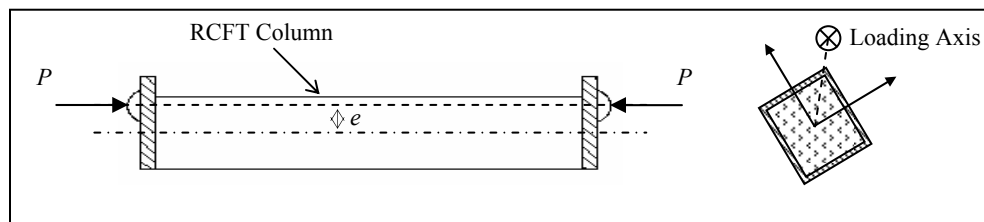


Figure 5.86 RCFT Columns under Eccentric Axial Loading

Two representative specimens were selected to analyze using the mixed-finite element formulation. However, first, a mesh convergence study was conducted for the specimen tested under uniaxial bending by varying the number of elements and integration points. Figure 5.87 shows four sets of analysis results with different number of finite elements and integration points. In the legend of Figure 5.87, the first number designates the number of finite elements and the second number refers to the number of integration points. 2 elements per member with 4 integration points and 8 elements with 6 integration points were decided to be the coarsest and the finest mesh densities, respectively. The fiber discretization scheme was kept as constant with 4 fibers along the depth and width of the concrete core and the steel tube. A single layer of fibers was introduced around the perimeter of the steel tube. It was found that 6 finite elements with 4 integration points was an acceptable mesh density to produce consistent results and this mesh density was employed for the rest of the analysis studies on eccentrically-loaded RCFT columns. The slip at the element ends was restricted but it was allowed at the nodes remaining between the supports. While incrementing the axial load, a constant displacement arc length method was utilized (Yang and Kuo, 1994). The controlling degree-of-freedom was selected to be the steel tube transverse displacement of the node located at the mid-height. However, in the case of specimens tested under biaxial-bending, generalized displacement control method is used to increment the axial loading since the selection of the controlling degree-of-freedom was not obvious (Yang and Kuo, 1994).

Grauers (1993) conducted an experimental study on eccentrically-loaded square RCFT columns. The specimens were subjected to uniaxial bending. The effect of concrete strength on the interaction of axial load and bending moment was investigated. The specimen designated as 13 was analyzed using the mixed finite element formulation. As can be seen from Figure 5.88, a good correlation is evident between the computational and experimental results. The initial stiffness and maximum axial load level is slightly underestimated, which might be attributed to inaccurate estimation of modulus of elasticity of concrete.

The second specimen studied for verification of the mixed-finite element formulation belongs to the experimental research by Shakir-Khalil and Zeghiche (1989). Specimen 6 was tested under bi-axial bending. Due to its rectangular shape, it was subjected to bending moments with respect to both weak and strong axis. The weak and strong axis eccentricities were 16 mm and 40 mm, respectively. Therefore, the inclination of the loading axes to the strong axis of the cross-section was 33.7° . The comparison of experimental and computational results of Specimen 6 with respect to both weak and strong axis is presented in Figure 5.89. It was found that the mixed finite element formulation was able to simulate the experimental test with good accuracy. Especially, good correlation was achieved for the initial stiffness. The comparison for the maximum bending moment and bounding (post-peak) stiffness was found to be better for the weak axis.

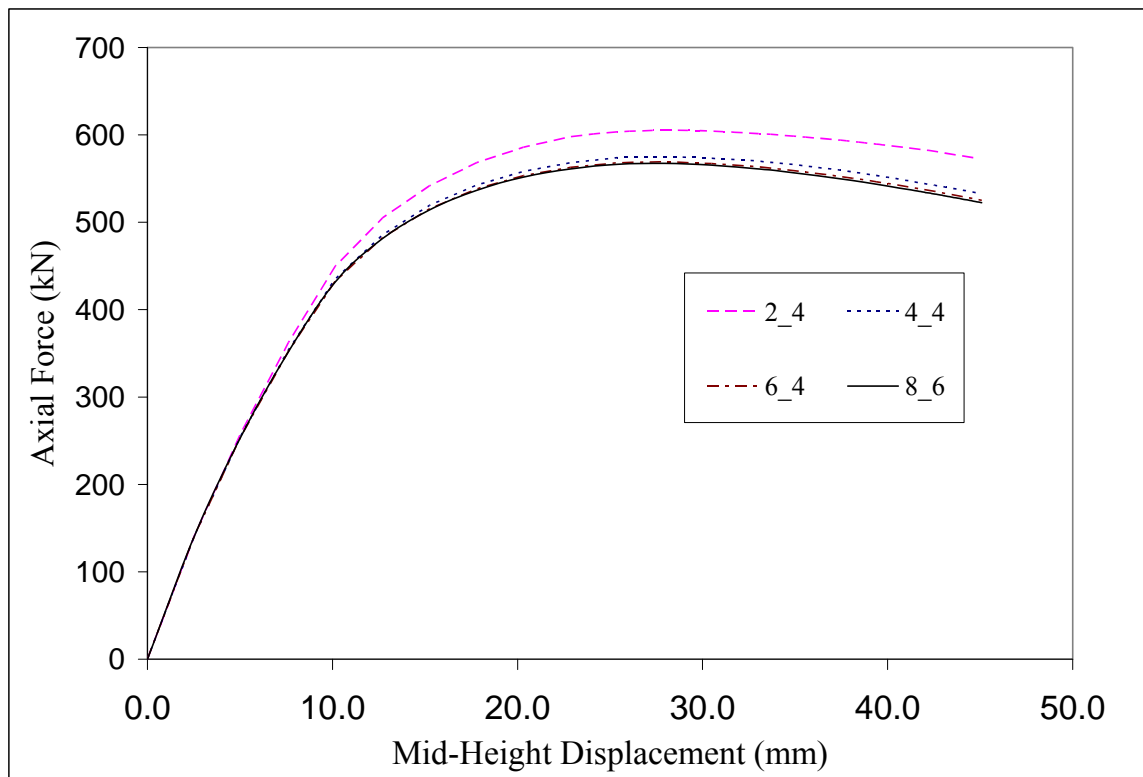


Figure 5.87 Mesh-Convergence of Eccentrically-Loaded RCFT Columns

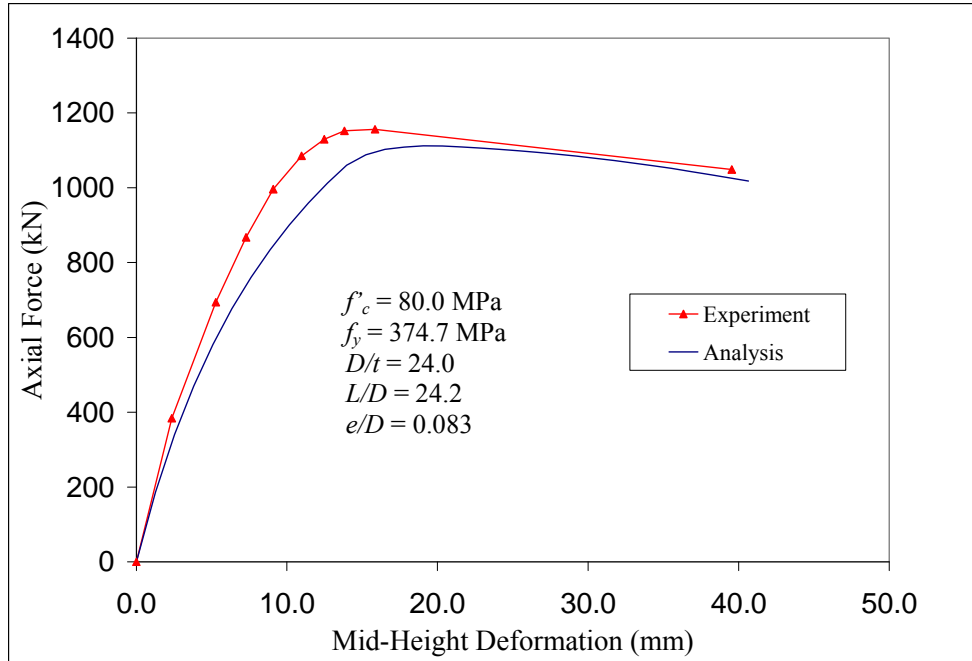


Figure 5.88 Comparison of Computational and Experimental Results for an Eccentrically Loaded RCFT Column Test (Grauers, 1993, Specimen 13)

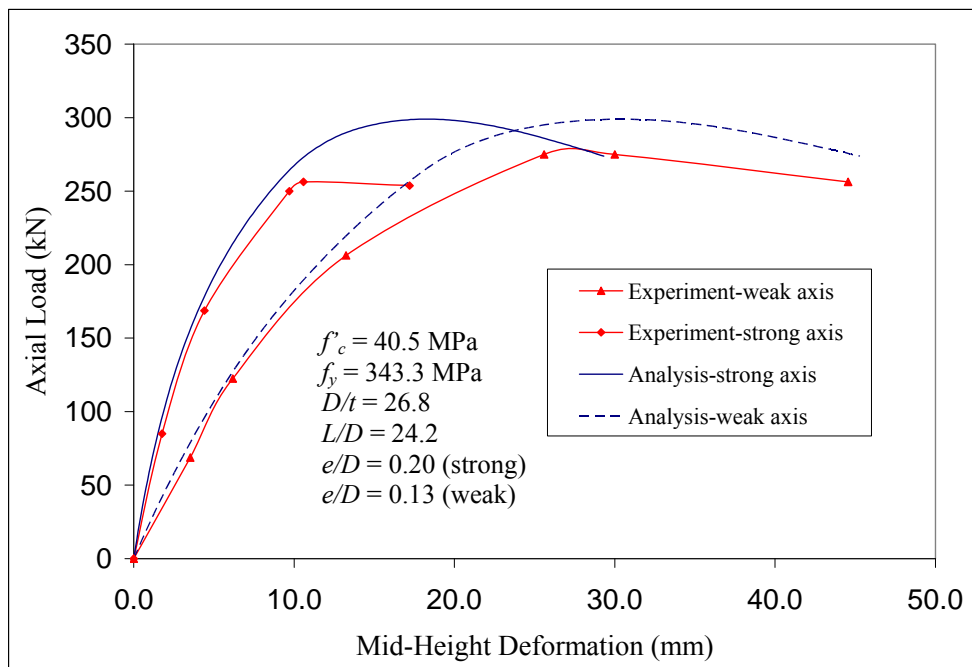


Figure 5.89 Comparison of Computational and Experimental Results for an Eccentrically Loaded RCFT Column Test (Shakir-Khalil and Zeghiche 1989, Specimen 6)

In addition to the specimens presented above, more verification studies were performed on proportionally-loaded RCFT columns. Multiple specimens covering a comprehensive range of material and geometric properties were selected from the experimental database of Tort and Hajjar (2003). The specimens were classified with respect to the boundary conditions and compressive strength of concrete. The right superscripts “ a ” and “ b ” attached to the experimental label of the specimens denotes uniaxial bending and biaxial bending, respectively. The distinction between the specimens based on concrete strength was performed via right superscripts of “1” and “2” attached to their experimental label, where “1” represents low strength concrete while “2” identified high strength concrete. The computational load-deformation data of the specimens was compared with that obtained during the experiments. Utilizing the results of the mesh-convergence study, all the specimens were analyzed using 6 finite elements per member with 4 integration points. The constant-displacement arc length method and generalized displacement control method were utilized as limit point algorithms for the specimens under uniaxial bending and biaxial bending, respectively (Yang and Kuo, 1994). The computational model employed in the analyses is described in Figure 5.90. Pin-roller boundary conditions were assumed for all of the specimens. The eccentricity was introduced through elastic steel beam elements attached to the RCFT column at the ends. The slip between the steel tube and concrete core was restricted at the element ends but no slip constraint is defined for the nodes located between the supports.

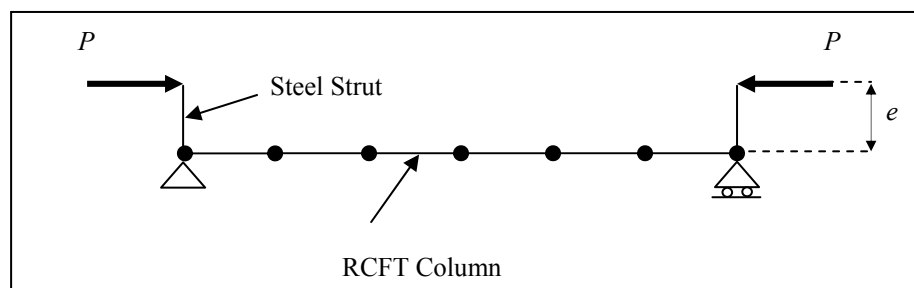


Figure 5.90 Proportionally-Loaded RCFT Column Computational Model

The computational and experimental behavior of the eccentrically-loaded specimens is presented in terms of axial load vs. mid-height deflection as can be seen from Figure 5.91 through Figure 5.107. The summary of measured material and geometric properties of the specimens can be found in Table 5-12.

Table 5-12 Proportionally-Loaded RCFT Beam-Column Tests

Specimen Label	E_s (MPa)	f_y (MPa)	f'_c (MPa)	D (mm)	B (mm)	t (mm)	e (mm)	L (mm)
1 ^{al}	210000	291.9	46.9	120.0	120.0	5.00	20.0	2895.6
2 ^{al}	210000	420.3	46.2	120.0	120.0	5.00	20.0	2895.6
6 ^{al}	210000	287.9	46.2	120.0	120.0	8.00	20.0	2895.6
7 ^{al}	210000	360.7	46.9	120.0	120.0	8.00	20.0	2895.6
9 ^{a2}	210000	364.1	102.7	120.0	120.0	8.00	20.0	2895.6
10 ^{al}	210000	364.1	39.3	120.0	120.0	8.00	20.0	2895.6
SHC1 ^{al}	205000	291.0	31.0	203.7	204.0	9.96	38.0	2130.0
SHC3 ^{bl}	205000	313.0	37.2	203.2	202.7	10.03	38.0 $\alpha = 30^\circ$	2130.0
SHC4 ^{bl}	205000	317.0	39.2	202.7	203.5	9.88	38.0 $\alpha = 45^\circ$	2117.3
SHC5 ^{bl}	205000	319.0	44.3	203.2	202.7	10.01	38.0 $\alpha = 30^\circ$	3050.0
SHC6 ^{bl}	205000	317.0	36.1	203.2	203.2	9.78	64.0 $\alpha = 45^\circ$	3050.0
SHC7 ^{al}	205000	254.0	35.0	152.4	152.4	6.48	38.0	3050.0
SHC8 ^{al}	205000	254.0	35.0	152.4	152.4	6.48	38.0	3050.0
2 ^{al}	205000	386.3	40.0	120.0	80.0	5.00	24.0	2760.0
3 ^{al}	205000	384.7	40.0	120.0	80.0	4.47	24.0	2760.0
5 ^{al}	205000	343.3	43.0	80.0	120.0	4.47	24.0	2760.0
7 ^{bl}	205000	357.5	44.0	120.0	80.0	4.44	$e_{major} = 60.0$ $e_{minor} = 40.0$	2760.0

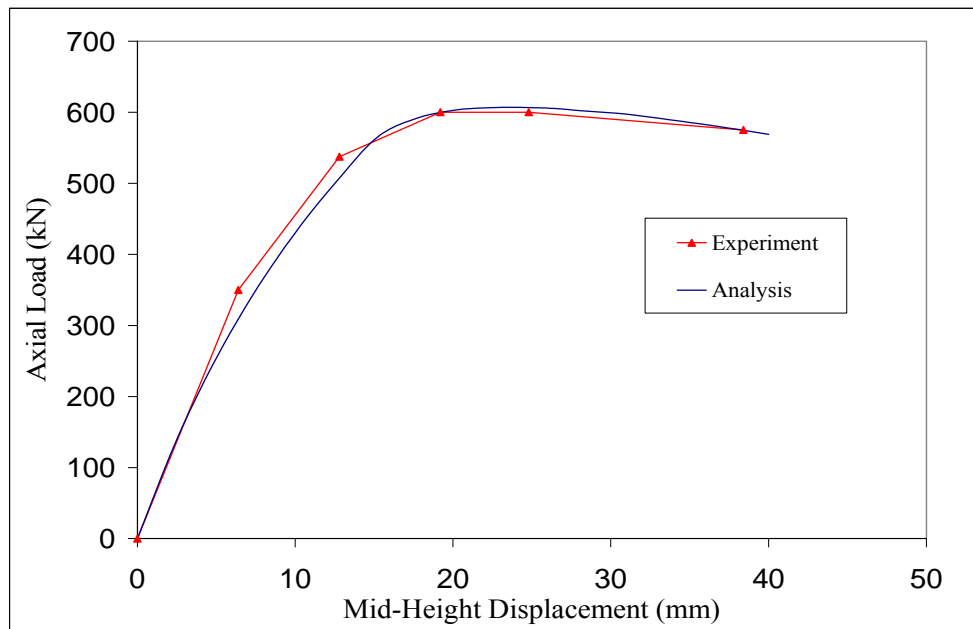


Figure 5.91 Comparison of Computational and Experimental Results for an Eccentrically-Loaded RCFT Column (Grauers 1993, Specimen 1)

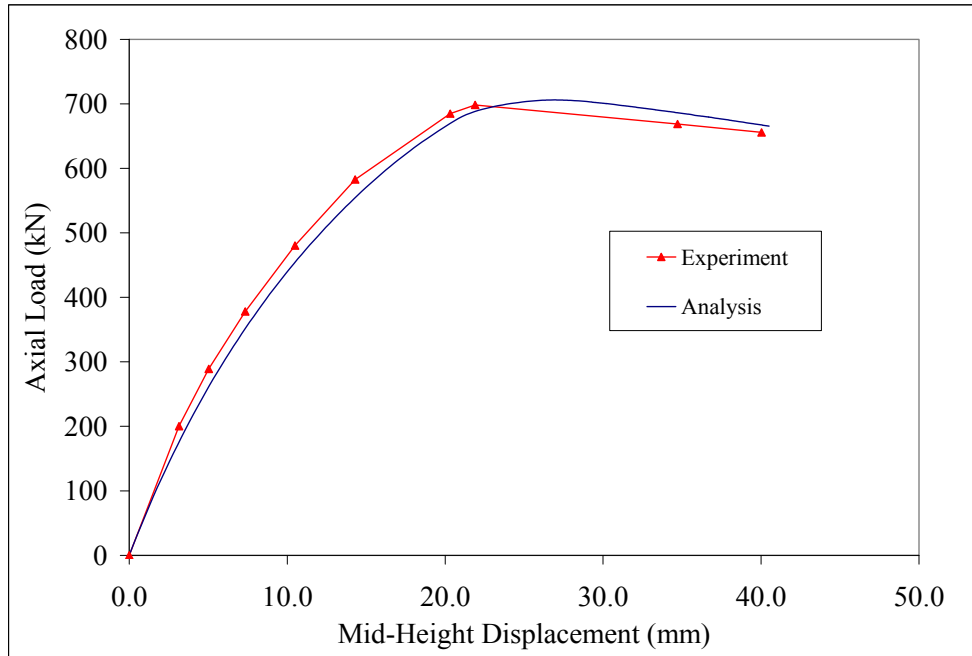


Figure 5.92 Comparison of Computational and Experimental Results for an Eccentrically-Loaded RCFT Column (Grauers 1993, Specimen 2)

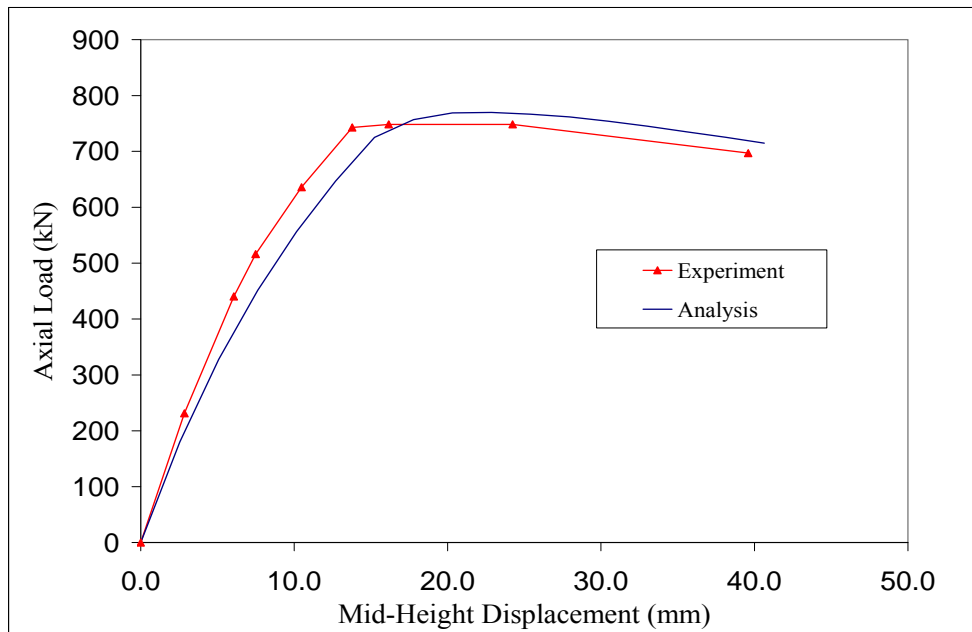


Figure 5.93 Comparison of Computational and Experimental Results for an Eccentrically-Loaded RCFT Column (Grauers 1993, Specimen 6)

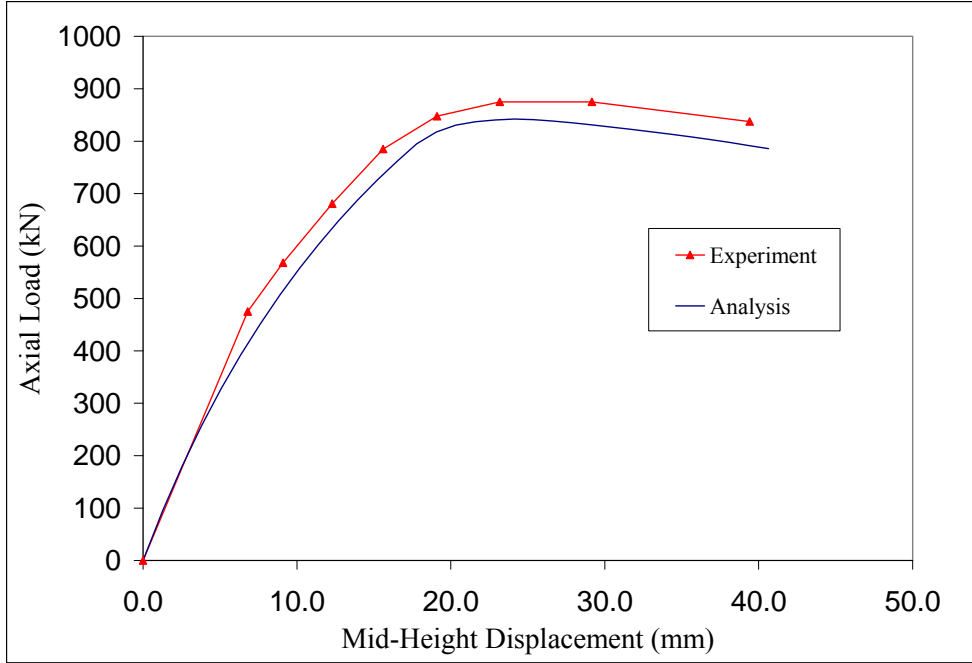


Figure 5.94 Comparison of Computational and Experimental Results for an Eccentrically-Loaded RCFT Column (Grauers 1993, Specimen 7)

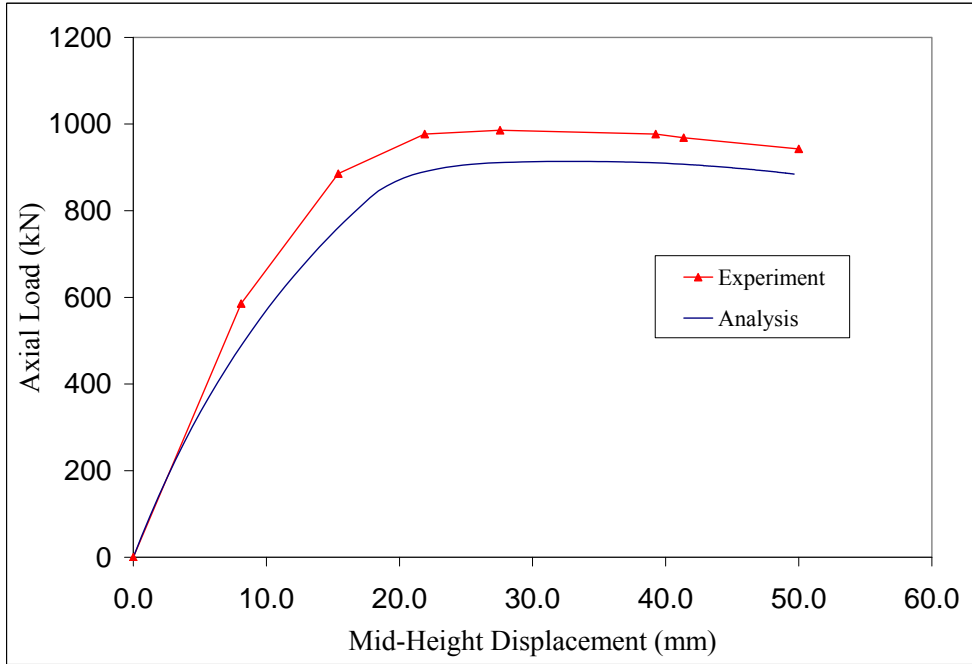


Figure 5.95 Comparison of Computational and Experimental Results for an Eccentrically-Loaded RCFT Column (Grauers 1993, Specimen 9)

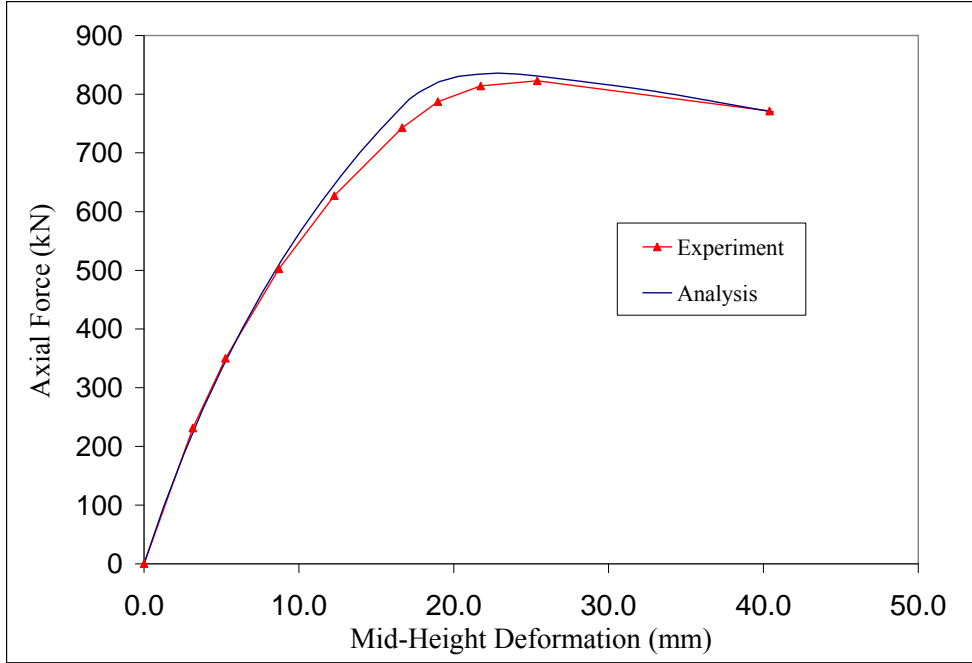


Figure 5.96 Comparison of Computational and Experimental Results for an Eccentrically-Loaded RCFT Column (Grauers 1993, Specimen 10)

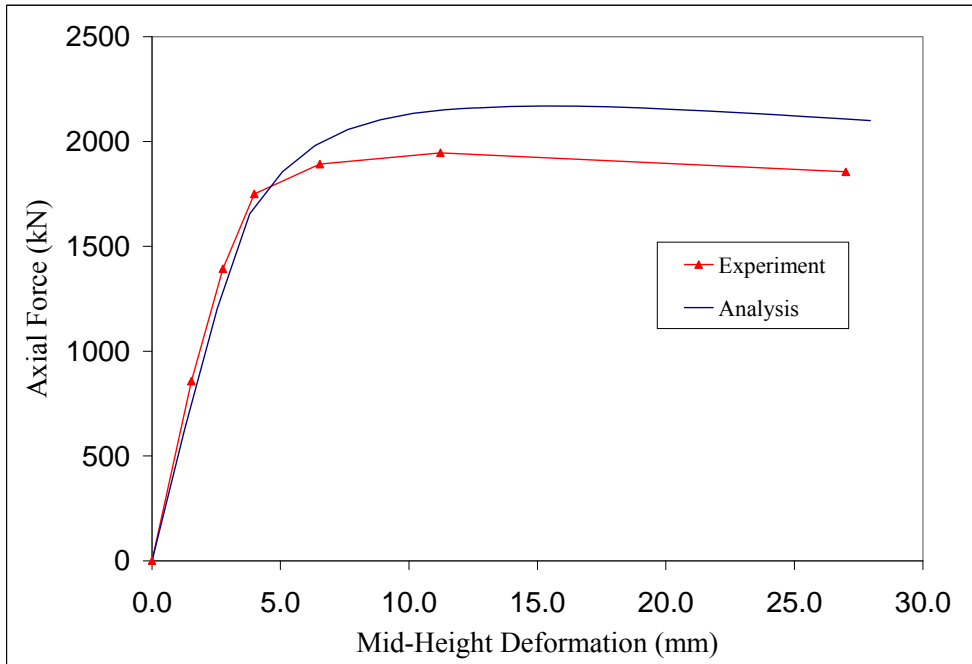


Figure 5.97 Comparison of Computational and Experimental Results for an Eccentrically-Loaded RCFT Column (Bridge 1976, SHC-1)

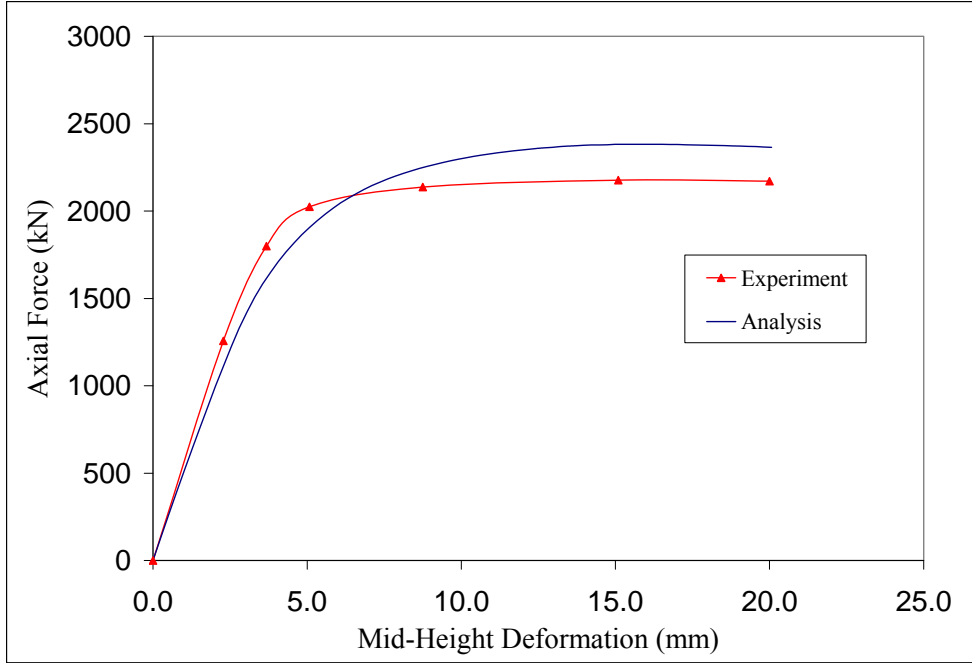


Figure 5.98 Comparison of Computational and Experimental Results for an Eccentrically-Loaded RCFT Column (Bridge 1976, SHC-3)

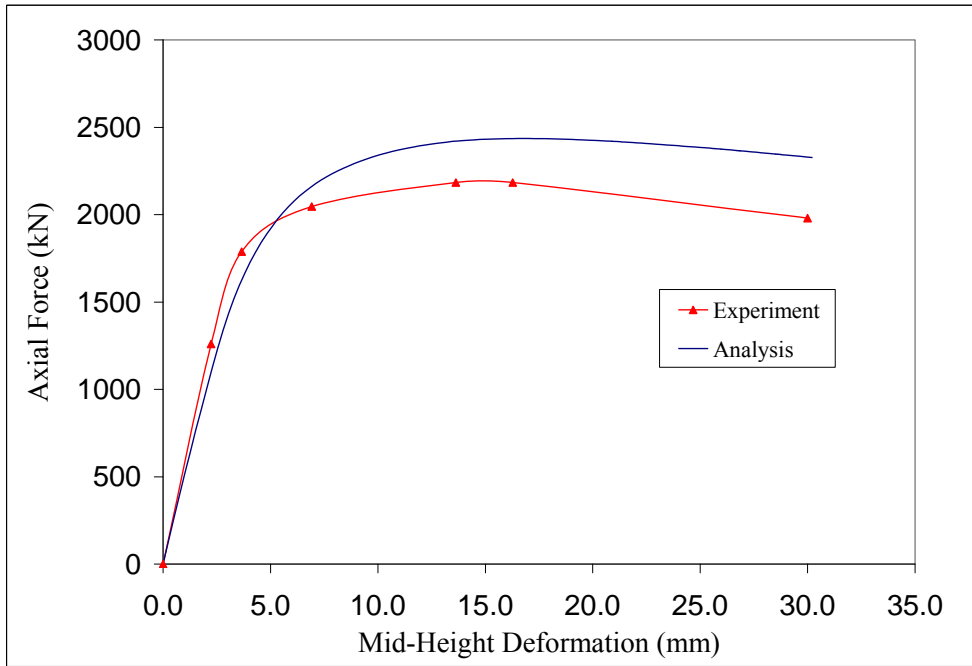


Figure 5.99 Comparison of Computational and Experimental Results for an Eccentrically-Loaded RCFT Column (Bridge 1976, SHC-4)

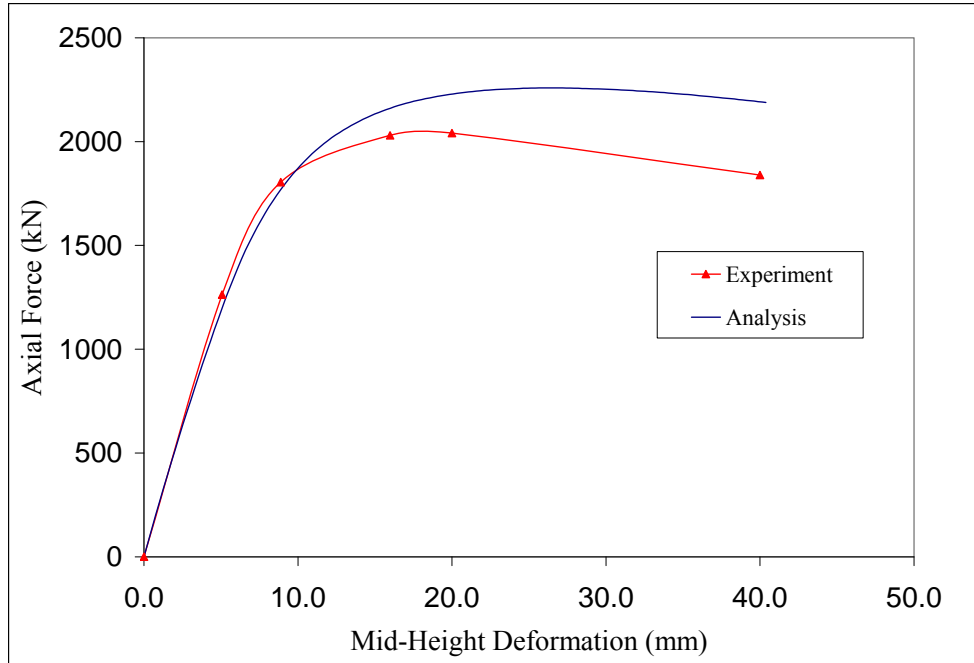


Figure 5.100 Comparison of Computational and Experimental Results for an Eccentrically-Loaded RCFT Column (Bridge 1976, SHC-5)

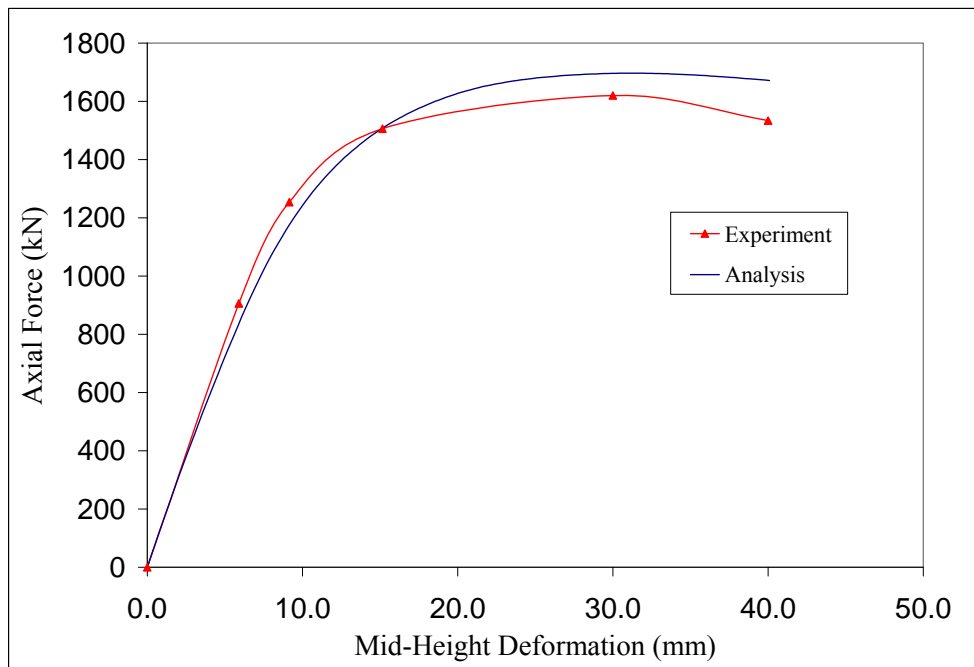


Figure 5.101 Comparison of Computational and Experimental Results for an Eccentrically-Loaded RCFT Column (Bridge 1976, SHC-6)

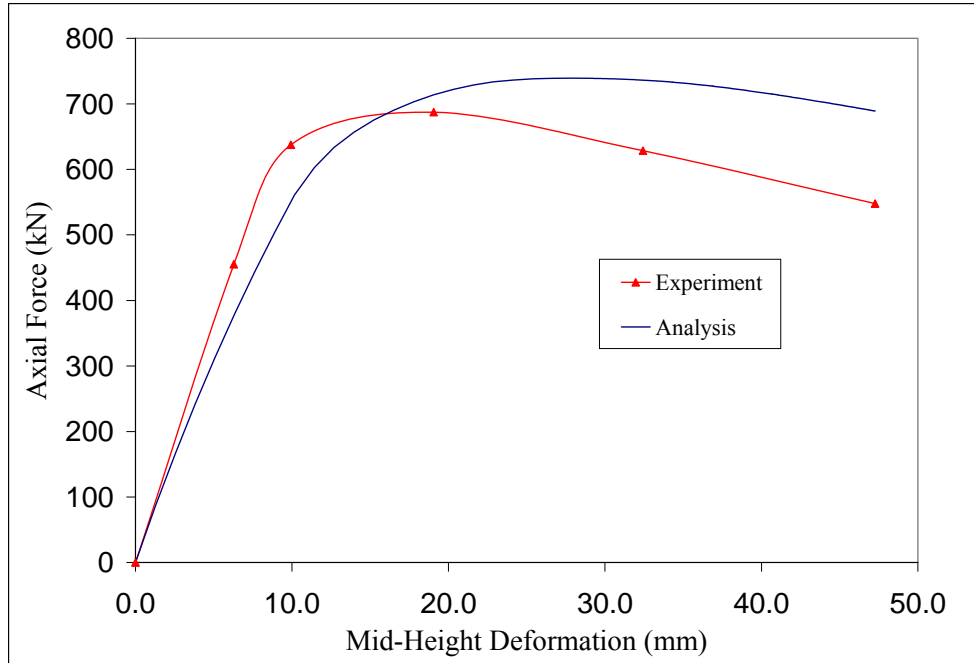


Figure 5.102 Comparison of Computational and Experimental Results for an Eccentrically-Loaded RCFT Column (Bridge 1976, SHC-7)

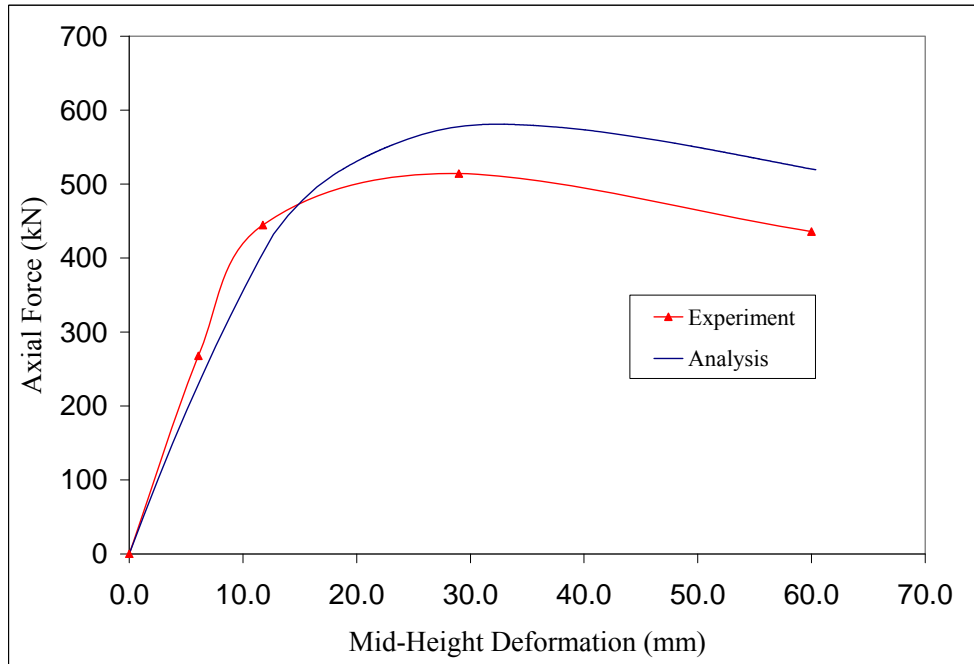


Figure 5.103 Comparison of Computational and Experimental Results for an Eccentrically-Loaded RCFT Column (Bridge 1976, SHC-8)

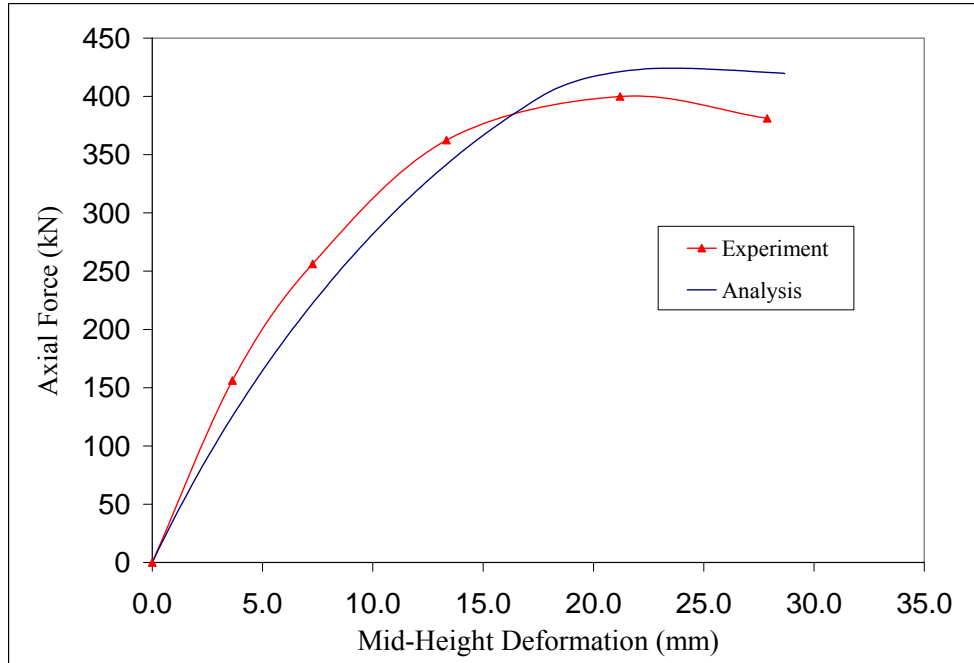


Figure 5.104 Comparison of Computational and Experimental Results for an Eccentrically-Loaded RCFT Column (Shakir-Khalil and Zeghiche 1989, Specimen 2)

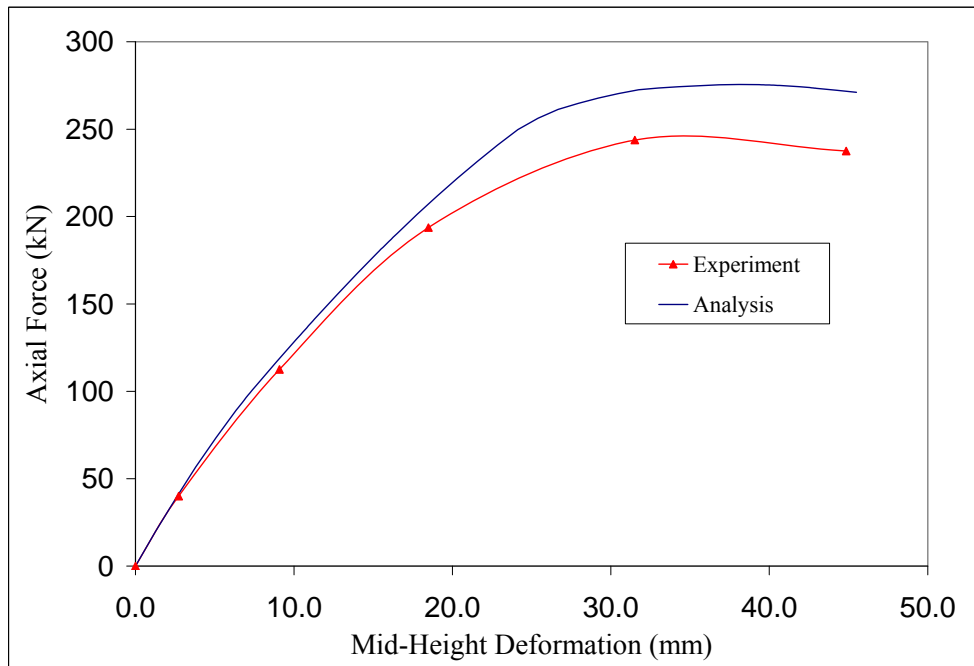


Figure 5.105 Comparison of Computational and Experimental Results for an Eccentrically-Loaded RCFT Column (Shakir-Khalil and Zeghiche 1989, Specimen 3)

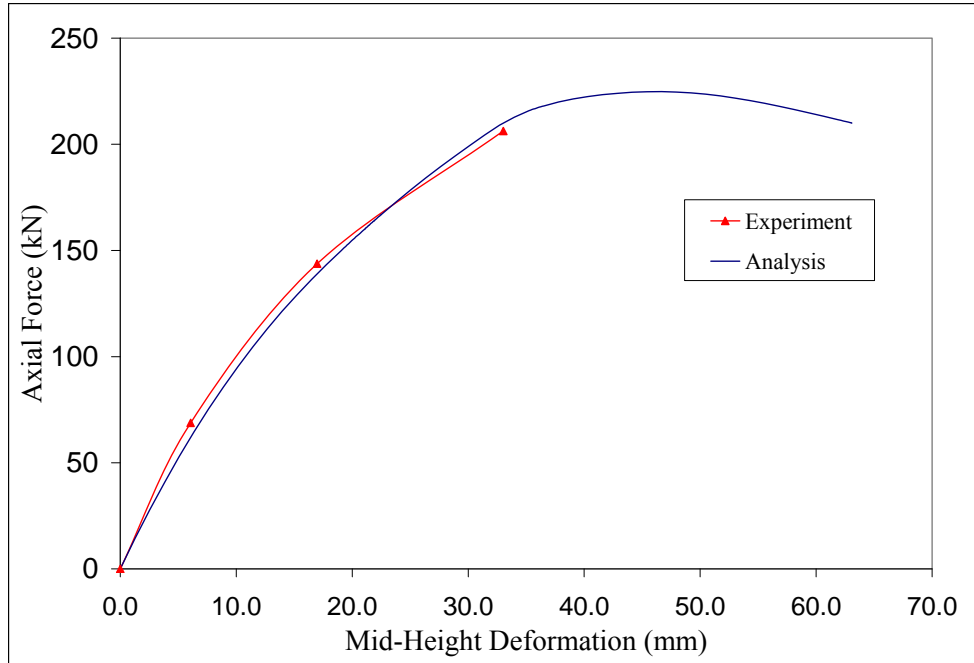


Figure 5.106 Comparison of Computational and Experimental Results for an Eccentrically-Loaded RCFT Column (Shakir-Khalil and Zeghiche 1989, Specimen 5)

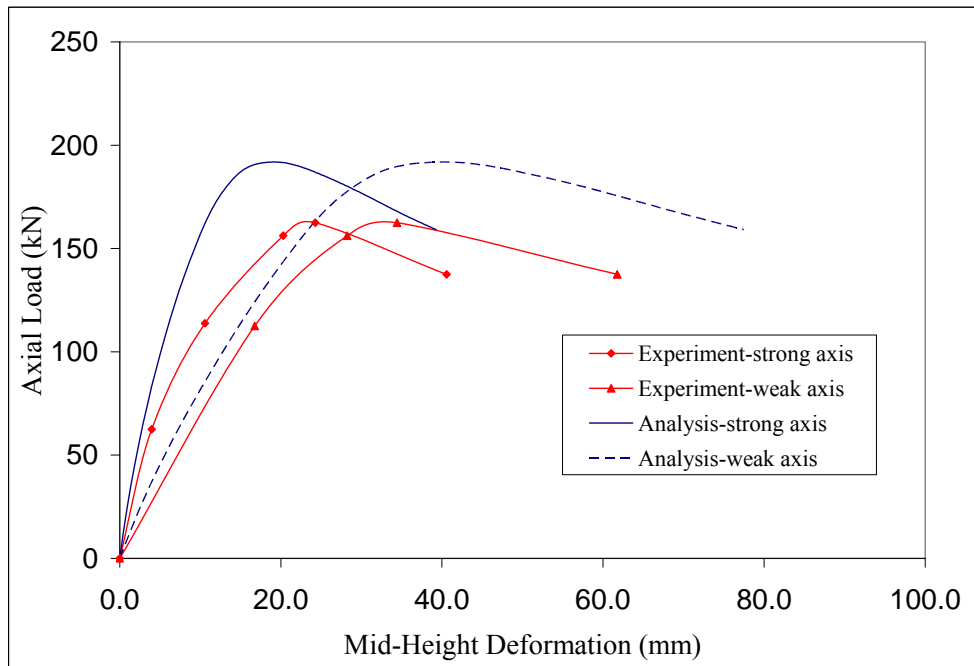


Figure 5.107 Comparison of Computational and Experimental Results for an Eccentrically-Loaded RCFT Column (Shakir-Khalil and Zeghiche 1989, Specimen 7)

In addition to the graphical presentation of the computational and experimental results, an error analysis was conducted on the key quantities sufficient to define the load-deformation curve of the specimens including peak axial load (P_o), initial stiffness (E_i), and bounding stiffness (K_b). The numerical values of the aforementioned parameters together with the associated percent errors are given in Table 5-13. The specimens in Group 2 with high strength concrete exhibited very good correlation with the experimental response parameters. The largest error was less than 25%, which was obtained while estimating E_i . The performance in predicting the response parameters for the specimens in Group *a*, which were tested under uniaxial bending, was better compared to the Group *b* specimens, which experienced biaxial bending. For the majority of the specimens in Table 5-13, the error values determined for P_o and E_i were smaller than that determined for K_b . For some of the specimens, very large error values were calculated for K_b and this was attributed to fact that for those specimens the experimental K_b values are close to zero.

5.7. Materially and Geometrically Nonlinear Non-Proportionally-Loaded RCFT Beam-Column Tests

Constant axial load and monotonically increasing bending moment represents the loading conditions of column members in moment frame structures. Since the force components are incremented in different proportions, this type of loading scheme is also known as non-proportional loading. There exist several tests on RCFT members in the literature to understand their response under non-proportional loading (Tomii and Sakino, 1979; Nakahara and Sakino, 1998; Varma 2000). These tests are often conducted on simply supported members. The constant axial load is first applied and then the bending moment is introduced at each end putting the member into single curvature as shown in Figure 5.108.

Table 5-13 Comparison of Computational and Experimental Results for an Eccentrically-Loaded RCFT Beam-Column Tests

Specimen Label	Experimental Results			Computational Results			Error (%)		
	E_i (kN/mm)	P_o (kN)	K_b (kN/mm)	E_i (kN/mm)	P_o (kN)	K_b (kN/mm)	E_i	P_o	K_b
1 ^{al}	54.7	610	-1.8	50.6	606.6	-2.6	7.5	0.6	44.4
2 ^{al}	63.6	700	-2.3	61.7	706.2	-3.1	3.0	0.9	34.8
6 ^{al}	81.3	770	-3.4	59.1	769.6	-3.5	27.3	0.1	2.9
7 ^{al}	69.8	870	-3.7	70.9	842.3	-3.5	1.6	3.2	5.4
9 ^{a2}	72.2	1000	-1.9	74.3	914.1	-2.2	2.9	8.6	15.8
10 ^{al}	73.4	820	-3.4	69.2	835.9	-3.8	5.7	1.9	11.8
13 ^{a2}	163.4	1160	-4.5	123.1	1112.1	-4.4	24.7	4.1	2.2
SHC1 ^{al}	560	1956	-5.7	436.6	2169.1	-6.9	22.0	10.9	21.1
SHC3 ^{bl}	550.9	2180	-1.1	512.3	2382.3	-7.1	7.0	9.3	545.5
SHC4 ^{bl}	563.2	2162	-14.9	515.6	2435.9	-9.3	8.5	12.7	37.6
SHC5 ^{bl}	249	2037	-10.1	263.8	2258.5	-5.1	5.9	10.9	49.5
SHC6 ^{bl}	153.6	1623	-8.6	156.7	1696.7	-3.1	2.0	4.5	64.0
SHC7 ^{al}	72.5	680	-5	63.4	739.3	-3.2	12.6	8.7	36.0
SHC8 ^{al}	44.1	513	-2.5	39.2	580.9	-2.3	11.1	13.2	8.0
2 ^{'al}	43	393	-2.8	38.6	424.2	-0.9	10.2	7.9	67.9
3 ^{'al}	14.7	232	-0.5	14.9	275.6	-0.6	1.4	18.8	20.0
5 ^{'al}	11.3	210	na	10.7	224.8	-1	5.3	7.0	NA
6 ^{'bl}	48.2, 19.5	256, 275	0.4, 1.3	65.1, 23.9	299.0	2.6, 1.9	35.2, 22.6	16.8, 8.7	585.2, 49.1
7 ^{'bl}	15.7, 6.7	162.5, 162.5	1.5, 0.9	25.7, 9.4	191.9	1.8, 1.0	63.3, 40.1	18.1, 18.1	18.8, 7.2
mean error							15.2	8.8	81.4
standard deviation of error							15.8	6.0	166.8
median error							8.5	8.7	28.0

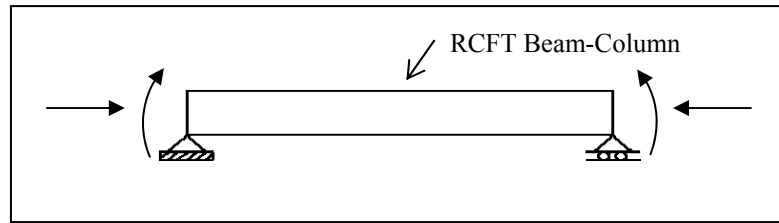


Figure 5.108 RCFT Beam-Column under Non-Proportional Loading

The analysis of non-proportionally-loaded RCFT members is considered to be critical in order to assess the ability of the mixed finite element formulation when the material fibers experience strain reversals. A mesh-convergence study was first performed to determine the finite element resolution producing consistent results. A representative specimen was analyzed by varying number of elements and integration points. A total number of 8 material fibers along the depth and width of the concrete core and the steel tube were defined. A single layer of material fibers was introduced around the perimeter of the steel tube. The results of the mesh convergence study are given in Figure 5.109 as moment vs. end rotation response. In the legend of Figure 5.109, the first number indicates the number of finite elements while the second number denotes the number of integration point. It can be seen that the computational load-deformation plots do not deviate from each other significantly as the mesh size gets smaller. This observation is due to the fact that the inelastic curvatures are accurately estimated by the mixed finite element formulation. In addition, the effect of geometric nonlinearity is reduced as the slenderness of the RCFT member (L/D) is small. Therefore, utilizing 2 elements with 4 integration points was adopted as the mesh size to be used in the analysis of non-proportionally load RCFT beam-columns. The constant displacement arc-length method with full Newton-Raphson solution algorithm was adopted in the analysis model (Yang and Kuo, 1994). The controlling degree-of-freedom was selected as the in-plane rotation defined at the end of the RCFT beam-column with roller support.

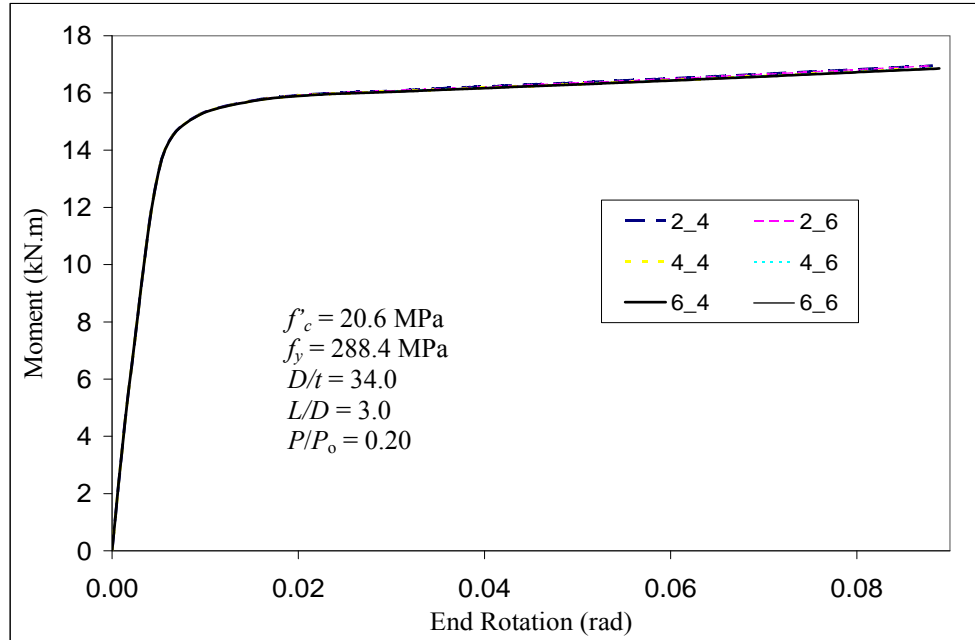


Figure 5.109 Mesh-Convergence of Non-Proportionally-Loaded RCFT Columns

Two specimens representing the typical load-deformation response of RCFT columns under non-proportional loading were analyzed using the mixed finite element formulation. The first specimen was tested by Tomii and Sakino (1979). The experimental response exhibited approximately an elastic-plastic response without any significant strength deterioration. The computational and experimental load-deformation behavior is presented in Figure 5.110. There was a very good agreement between two sets of data in initial and post-peak stiffness. The computational peak moment value was slightly larger than its experimental value. This discrepancy might be due to overestimation of the gradient in yield strength of the steel tube due to the cold-forming process.

The next specimen analyzed using the mixed finite element formulation was selected from the experimental study by Nakahara and Sakino (1998). A softening type of load-deformation response was observed during the test. As can be seen in Figure 5.111, excellent correlation was achieved in all significant response parameters such initial stiffness, post-peak stiffness, and peak moment values. In Figure 5.111, the moment-rotation response was presented for the steel tube and the concrete core, independently. This data was determined from the moment-curvature response of the cross-section located at the mid-length of the RCFT beam-column. The curvature was

multiplied with the depth of the RCFT cross-section to obtain the moment-rotation response. It was found that the deterioration in strength following the attainment of the peak moment was due to crushing of concrete. The contribution of the concrete core to the moment capacity of the RCFT beam-column was determined to be approximately 40%.

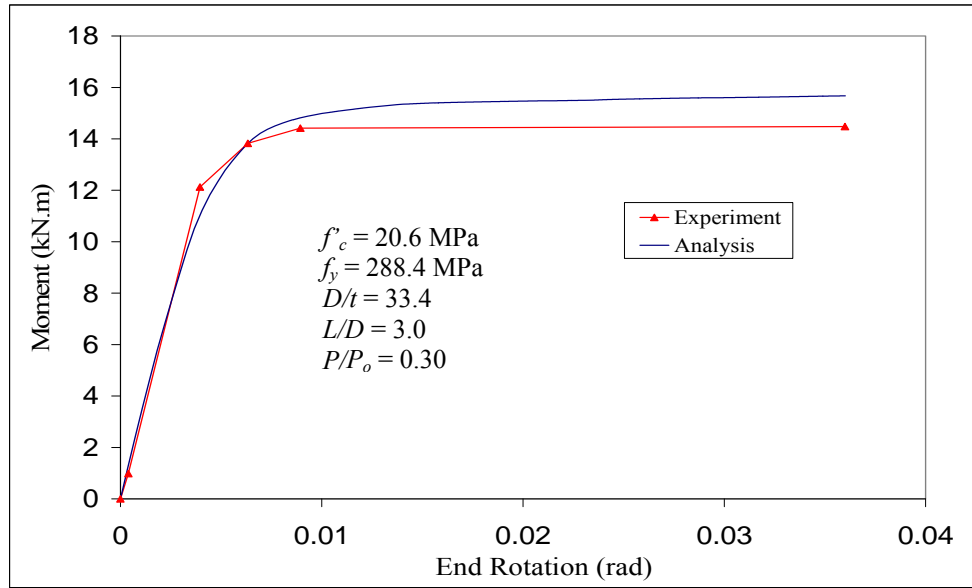


Figure 5.110 Comparison of Computational and Experimental Results for a Non-Proportionally-Loaded RCFT Beam-Column (Tomii and Sakino, 1979, Specimen III-3)

The breadth of the verification study was increased by analyzing several specimens from the experimental database by Tort and Hajjar (2003). The analyses were conducted with a mesh density of 2 elements with 4 integration points. The constant displacement arc-length algorithm with full-Newton-Raphson solution method was utilized (Yang and Kuo, 1994). It was aimed to cover a comprehensive range of material and geometric properties while selecting the RCFT specimens. In Table 5-14, the analyzed specimens are described by documenting their measured geometric and material properties. The specimens were examined in two groups with respect to the range of material strengths. Group 1 consisted of specimens having low strength materials while Group 2 cover the specimens constructed using high strength materials. The right superscripts of “1” and “2” were attached to the labeling of the specimens to identify their classification with respect to the material strength.

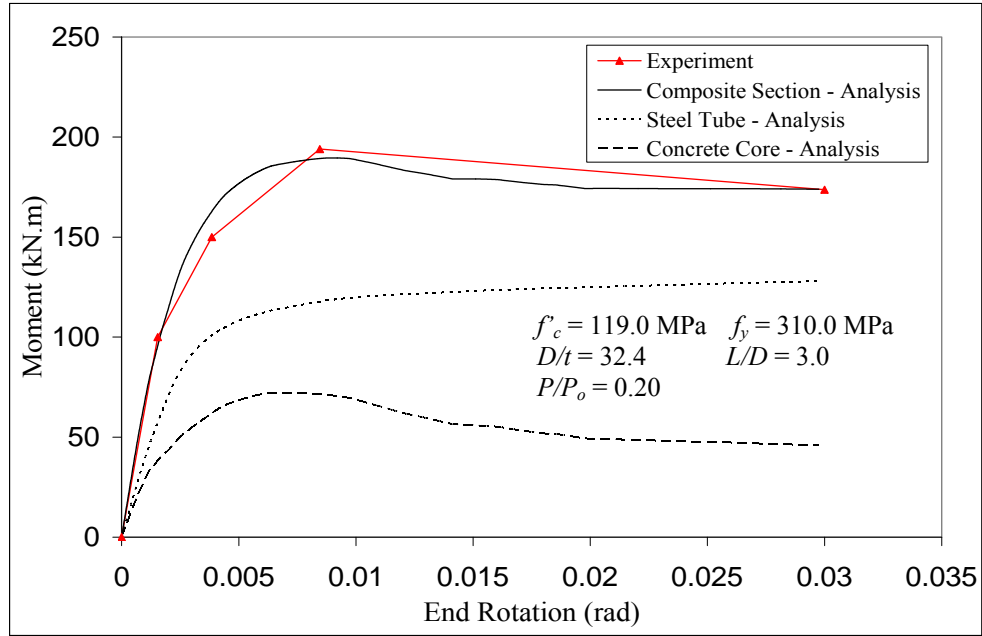


Figure 5.111 Comparison of Computational and Experimental Results for a Non-Proportionally-Loaded RCFT Beam-Column (Nakahara and Sakino, 1998, Specimen BR4-6-10-02)

Table 5-14 Proportionally-Loaded RCFT Beam-Column Tests

Specimen Label	E_s (MPa)	f_y (MPa)	f'_c (MPa)	D (mm)	B (mm)	t (mm)	P / P_o	L (mm)
III-1 ¹	210915	289.4	20.6	100.1	100.1	2.97	0.1	300
III-2 ¹	210915	288.4	20.6	100.1	100.1	2.97	0.2	300
III-4 ¹	206010	288.4	20.6	100.1	100.1	3.00	0.4	300
III-5 ¹	206010	288.4	20.6	100.1	100.1	3.00	0.5	300
III-6 ¹	206009	288.4	20.6	100.1	100.1	3.00	0.6	300
BR4-6-10-04 ²	209001	310.0	119.0	200.0	200.0	6.17	0.4	600
BR8-6-10-02 ²	212001	781.2	119.0	200.0	200.0	6.39	0.2	600
BC32-80-20 ²	197000	600.0	110.0	305.3	305.3	8.90	0.2	1500
BC32-80-40 ²	197000	600.0	110.0	305.3	305.3	8.90	0.4	1500
BC-32-46-20 ²	196997	269.0	110.0	305.3	305.3	8.60	0.2	1500
BC32-46-40 ²	196997	269.0	110.0	305.3	305.3	8.60	0.4	1500
BC48-46-20 ²	204002	471.0	110.0	305.3	305.3	5.79	0.2	1500

Figure 5.109 through 5.130 illustrate the comparison of experimental and computational load-deformation response of the specimens. The computational results were presented for the steel tube and the concrete independently, where appropriate.

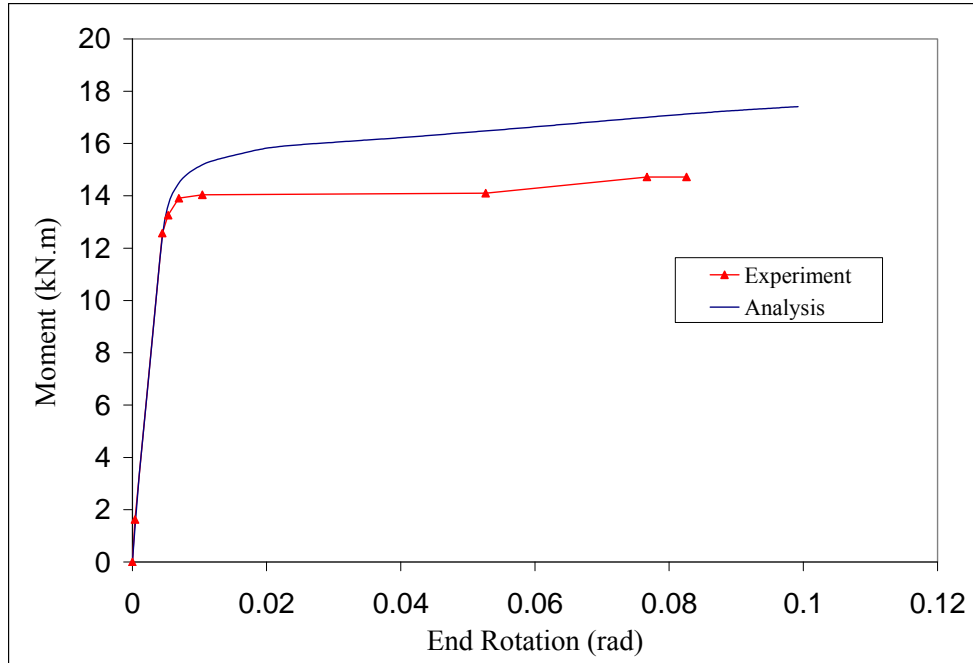


Figure 5.112 Comparison of Computational and Experimental Results for a Non-Proportionally-Loaded RCFT Beam-Column (Tomii and Sakino, 1979, Specimen III-1)

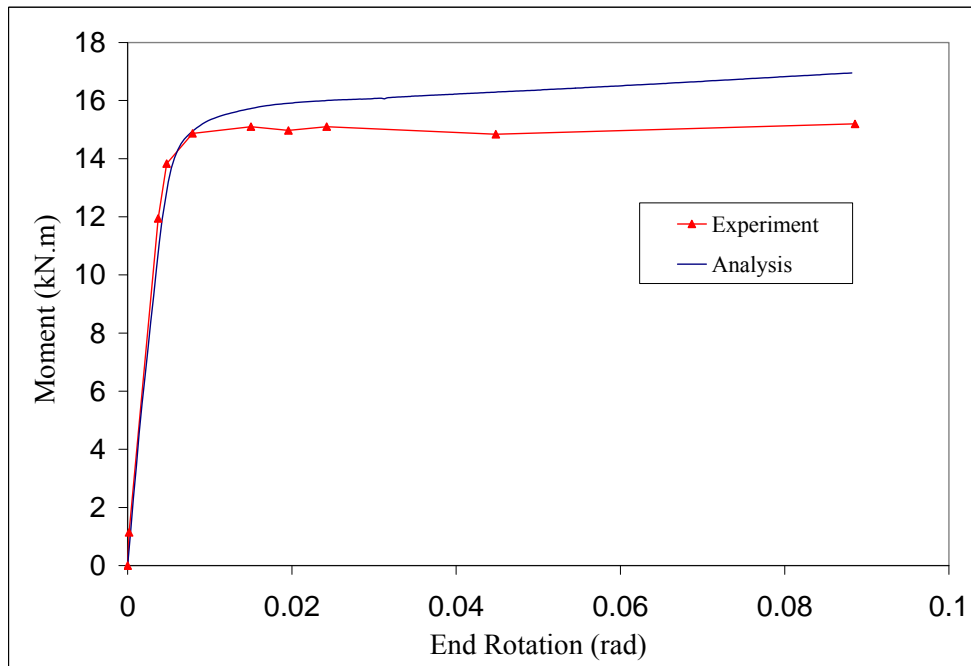


Figure 5.113 Comparison of Computational and Experimental Results for a Non-Proportionally-Loaded RCFT Beam-Column (Tomii and Sakino, 1979, Specimen III-2)

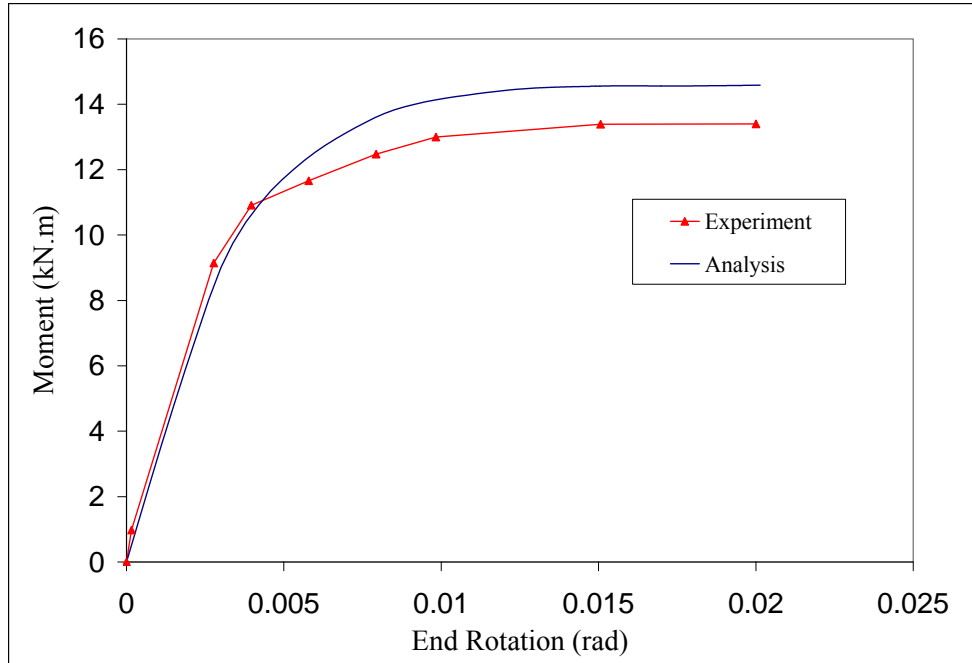


Figure 5.114 Comparison of Computational and Experimental Results for a Non-Proportionally-Loaded RCFT Beam-Column (Tomii and Sakino, 1979, Specimen III-4)

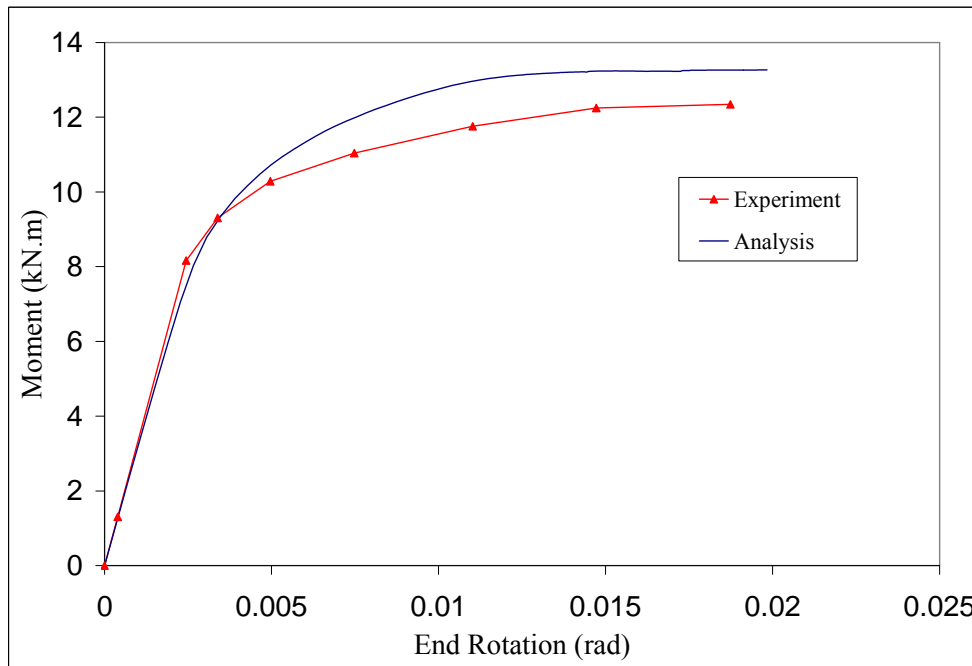


Figure 5.115 Comparison of Computational and Experimental Results for a Non-Proportionally-Loaded RCFT Beam-Column (Tomii and Sakino, 1979, Specimen III-5)

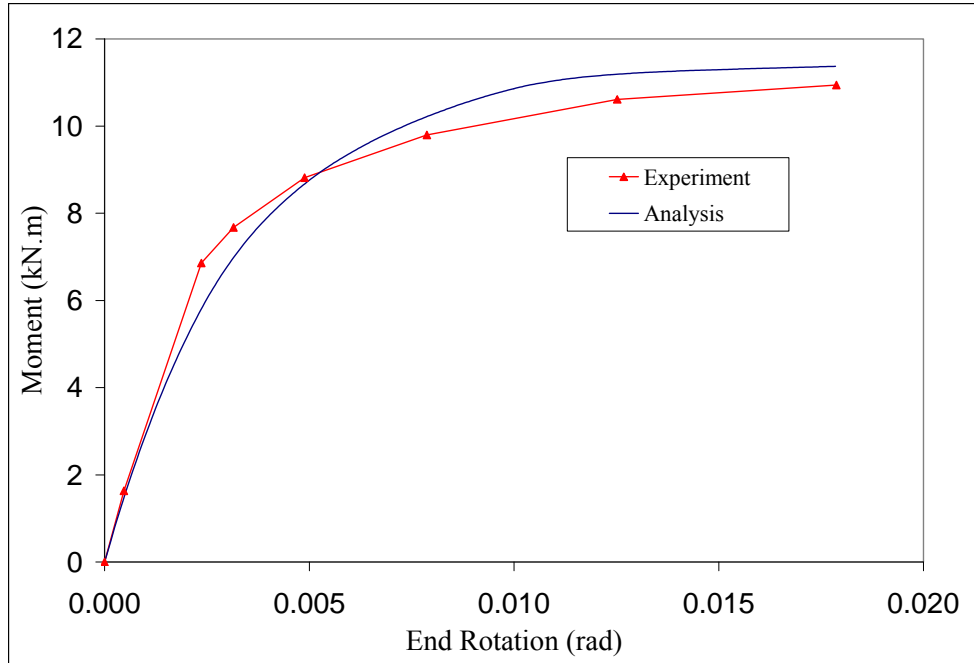


Figure 5.116 Comparison of Computational and Experimental Results for a Non-Proportionally-Loaded RCFT Beam-Column (Tomii and Sakino, 1979, Specimen III-6)

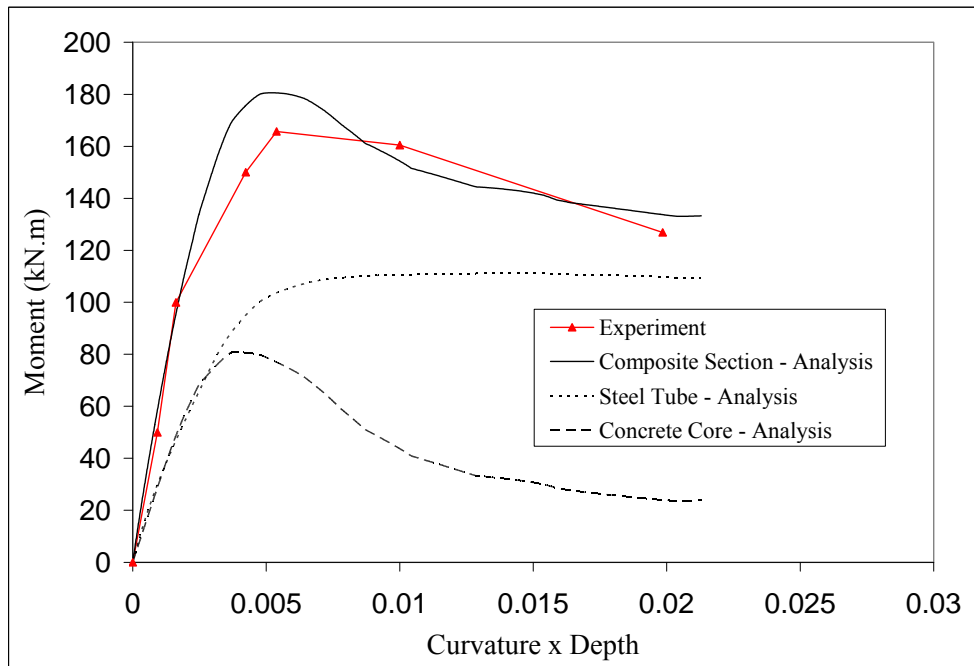


Figure 5.117 Comparison of Computational and Experimental Results for a Non-Proportionally-Loaded RCFT Beam-Column (Nakahara and Sakino, 1998, Specimen BR4-6-10-04)

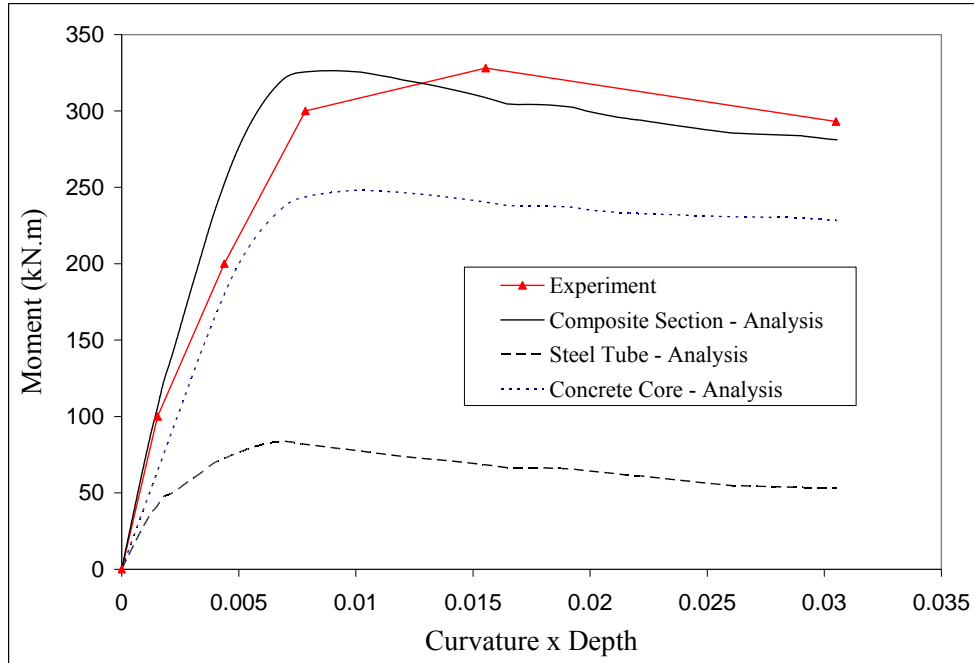


Figure 5.118 Comparison of Computational and Experimental Results for a Non-Proportionally-Loaded RCFT Beam-Column (Nakahara and Sakino, 1998, Specimen BR8-6-10-02)

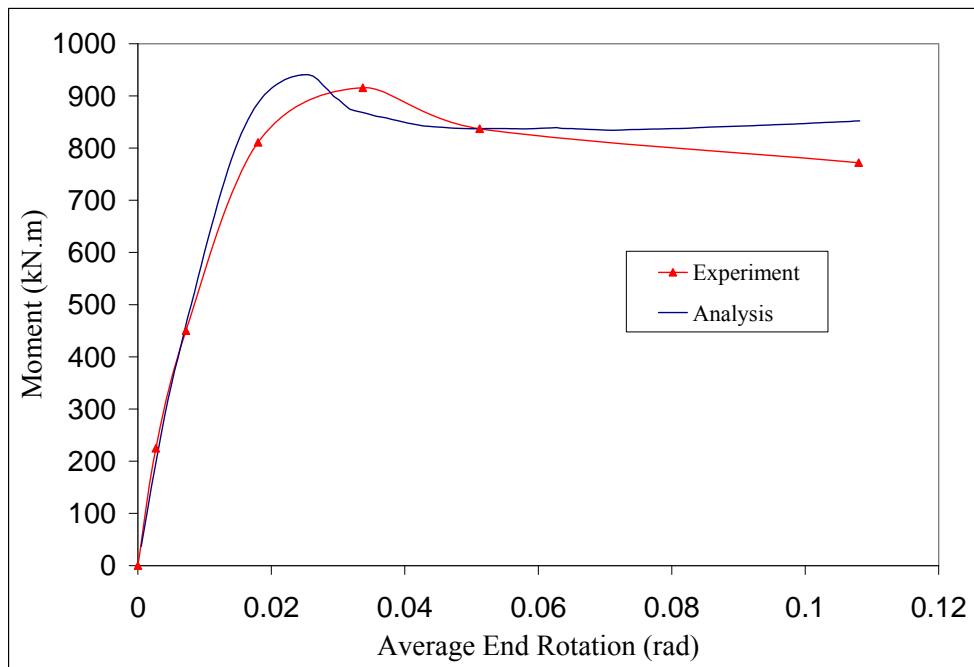


Figure 5.119 Comparison of Computational and Experimental Results for a Non-Proportionally-Loaded RCFT Beam-Column (Varma, 2000, Specimen BC32-80-20)

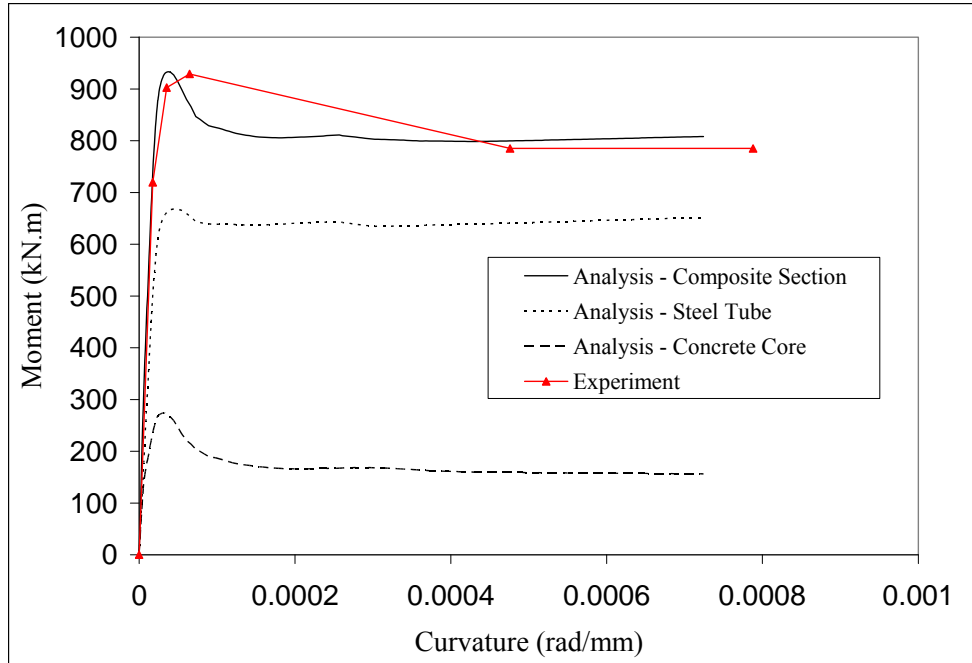


Figure 5.120 Comparison of Computational and Experimental Results for a Non-Proportionally-Loaded RCFT Beam-Column (Varma, 2000, Specimen BC32-80-20)

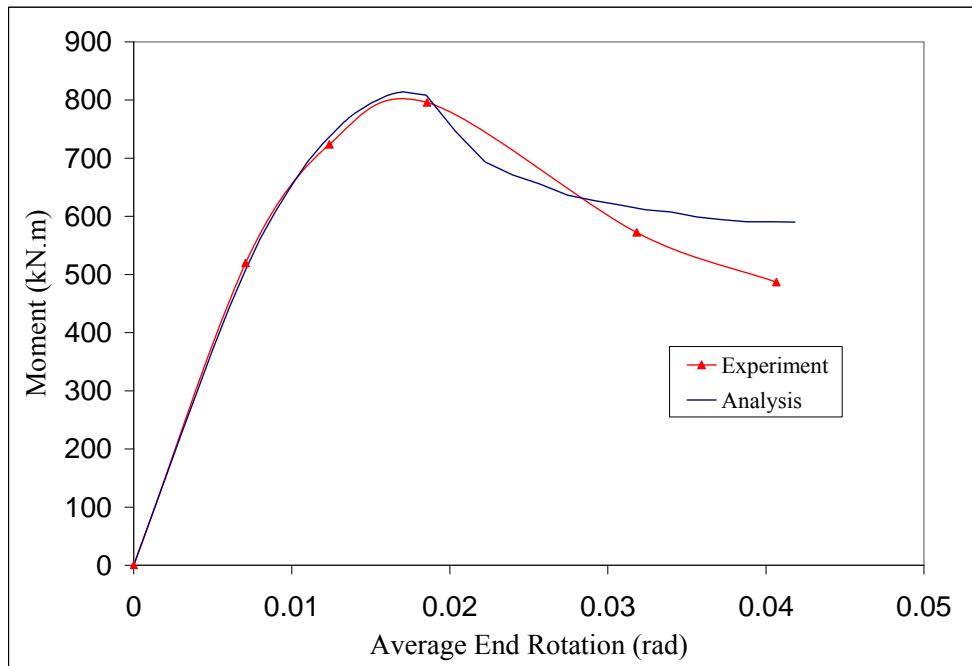


Figure 5.121 Comparison of Computational and Experimental Results for a Non-Proportionally-Loaded RCFT Beam-Column (Varma, 2000, Specimen BC32-80-40)

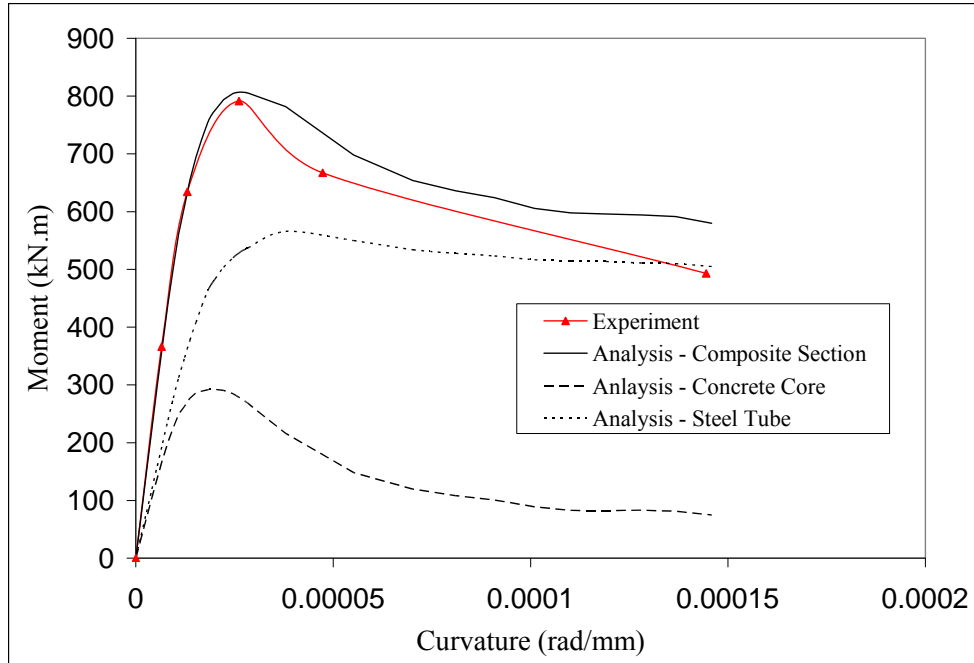


Figure 5.122 Comparison of Computational and Experimental Results for a Non-Proportionally-Loaded RCFT Beam-Column (Varma, 2000, Specimen BC32-80-40)

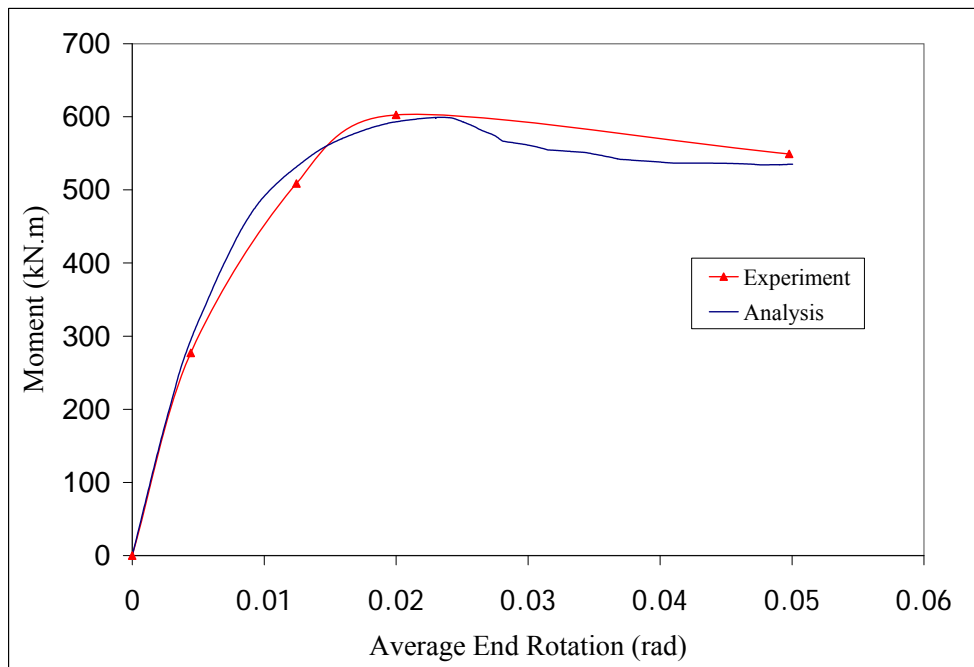


Figure 5.123 Comparison of Computational and Experimental Results for a Non-Proportionally-Loaded RCFT Beam-Column (Varma, 2000, Specimen BC32-46-20)

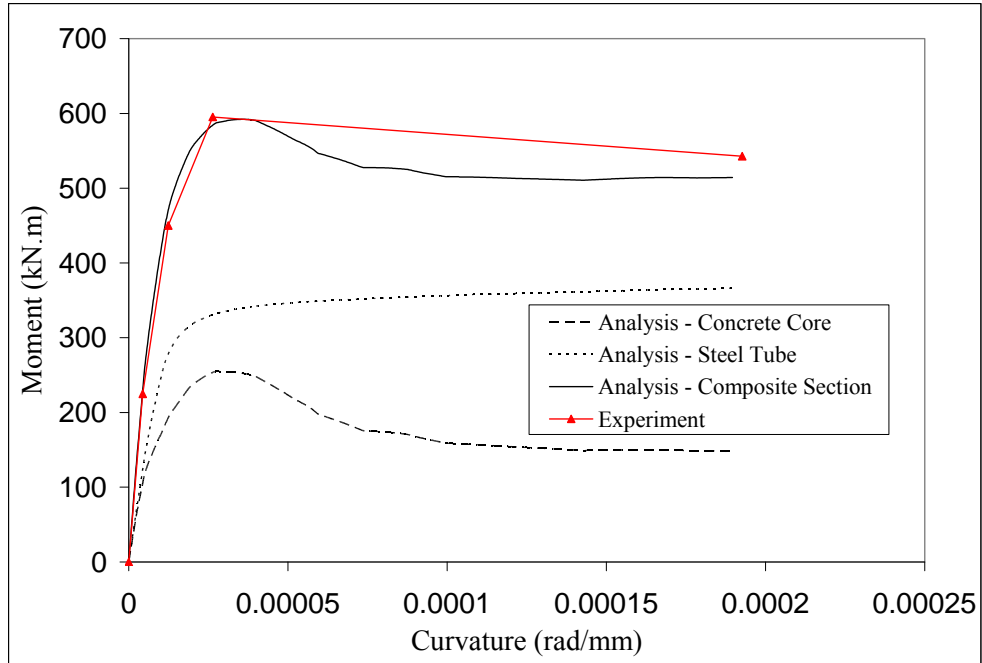


Figure 5.124 Comparison of Computational and Experimental Results for a Non-Proportionally-Loaded RCFT Beam-Column (Varma, 2000, Specimen BC32-46-20)

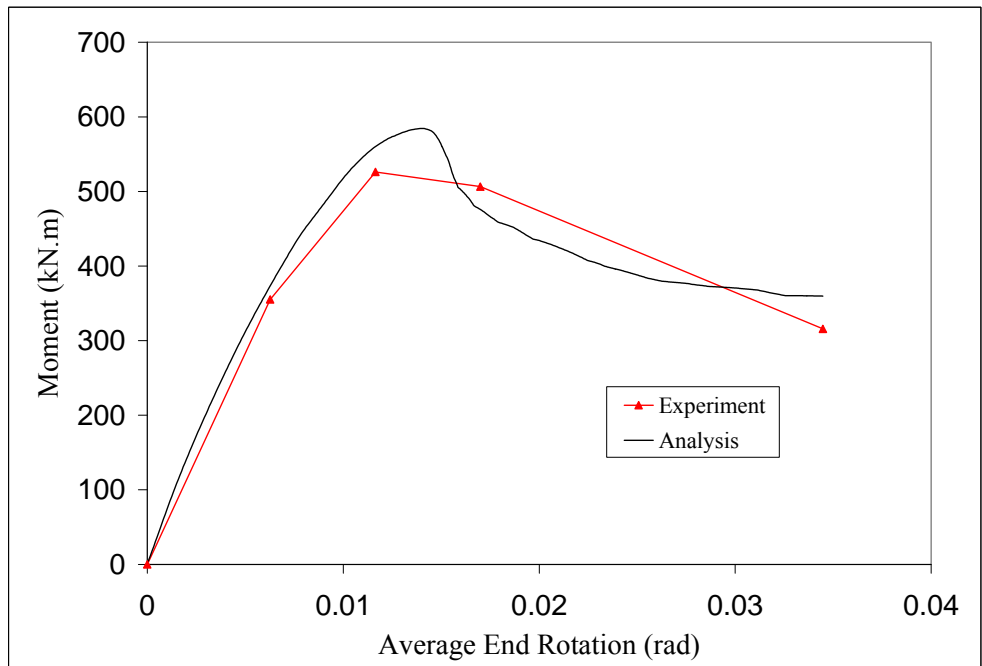


Figure 5.125 Comparison of Computational and Experimental Results for a Non-Proportionally-Loaded RCFT Beam-Column (Varma, 2000, Specimen BC32-46-40)

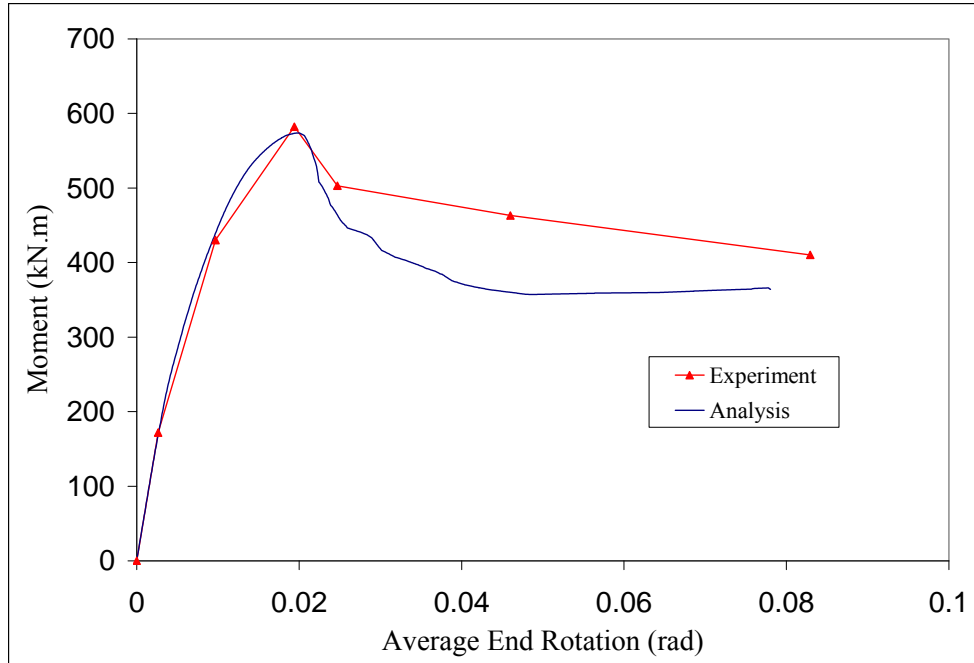


Figure 5.126 Comparison of Computational and Experimental Results for a Non-Proportionally-Loaded RCFT Beam-Column (Varma, 2000, Specimen BC48-46-20)

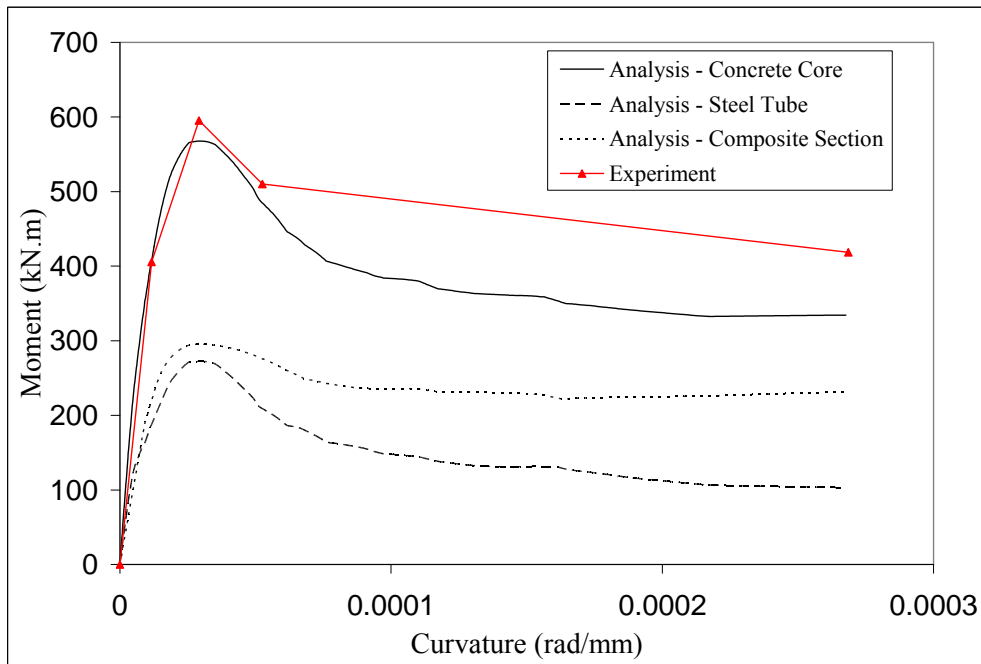


Figure 5.127 Comparison of Computational and Experimental Results for a Non-Proportionally-Loaded RCFT Beam-Column (Varma, 2000, Specimen BC48-46-20)

The experimental and computational results achieved excellent correlation for specimens with wide ranges of material and geometric properties. A detailed error analysis of the results is presented in Table 5-15, where the computational and experimental values for the response parameters of initial stiffness (E_i), peak moment (M_o), and bounding stiffness (K_b) are compared. The degree of correlation for E_i and M_o were found to be similar for both Group 1 and Group 2 specimens. However, very large error values of K_b were obtained for some of the Group 1 specimens, which is attributed to fact that those specimens exhibit approximately an elastic-perfectly plastic response with small K_b values.

5.8. Materially and Geometrically Nonlinear Cyclically-Loaded RCFT Beam-Column Tests

The accuracy of the mixed-finite element formulation in simulating RCFT members under quasi-statically applied cyclic loading is studied in this section. These tests provide useful information about the load-path dependency characteristics of these composite structural systems.

The computational model to analyze RCFT members in a configuration that is typical of many of the cyclic tests is illustrated in Figure 5.128. A displacement-controlled algorithm was utilized to trace the nonlinear cyclic load-deformation response. This is achieved by defining displacement constraints for the controlling node of the structural model in the direction of the applied loading. First, the constant axial load is applied monotonically and then the specimens are subjected to a cyclic lateral displacement history. The current mixed finite element formulation was developed such that the loads are only applied to the steel degrees of freedom. Therefore, it is those degree-of-freedoms of the controlling node, where displacement histories are imposed.

The specimen by Sakino and Tomii (1981) is presented here first. The loading scheme shown in Figure 5.128 was introduced, where the specimen experienced double curvature under constant axial load and cyclic shear force. The analysis was conducted until a drift ratio of 2.5% is reached. Two elements with 3 integration points each were utilized to model the RCFT column. A total number of 10 material fibers were

Table 5-15 Comparison of Computational and Experimental Results for Non-Proportionally-Loaded RCFT Beam-Column Tests

Specimen Label	Experimental Results			Computational Results			Error (%)		
	E_i (kN.m/rad)	M_o (kN.m)	K_b (kN.m/rad)	E_i (kN.m/rad)	M_o (kN.m)	K_b (kN.m/rad)	E_i	M_o	K_b
III-1 ¹	2769	14.7	10.1	3280	17.4	16.0	18.5	18.4	58.8
III-2 ¹	3138	15.1	1.6	3375	17.0	15.1	7.6	12.5	869.7
III-3 ¹	3092	14.5	-1.8	3279	15.7	12.8	6.1	8.3	803.6
III-4 ¹	3218	13.4	70.0	3236	14.6	7.2	0.6	9.0	89.7
III-5 ¹	3347	12.3	116.5	3193	13.3	18.9	4.6	7.5	83.8
III-6 ¹	2864	10.9	113.0	3193	11.4	51.1	11.5	3.9	54.8
BR4-6-10-02 ²	64935	194.0	-946.4	71912	189.6	-724.9	10.7	2.3	23.4
BR4-6-10-04 ²	61486	165.7	-2797.8	70198	180.6	-2961.1	14.2	9.0	5.8
BR8-6-10-02 ²	65000	328.0	-2329.8	72688	326.3	-2062.1	11.8	0.5	11.5
BC32-80-20 ²	61320	915.7	-1743.1	65919	940.9	-4311.9	7.5	2.7	147.4
BC32-80-40 ²	59288	796.1	-14219.0	74667	814.0	-934.7	25.9	2.3	93.4
BC-32-46-20 ²	62377	602.9	-1799.0	73254	599.4	-2178.4	17.4	0.6	21.1
BC32-46-40 ²	56673	526.3	-9639.5	73182	584.5	-9249.1	29.1	11.1	4.1
BC48-46-20 ²	42719	582.4	-2276.0	65526	573.7	-2362.0	53.4	1.5	3.8
mean error							15.6	6.4	162.2
standard deviation of error							13.5	5.3	289.2
median error							11.7	5.7	56.8

defined along the depth of the cross-section as shown in Figure 5.129. The comparison of computational and experimental response is illustrated in Figure 5.130. Very good correlation with respect to the maximum shear forces and the evolution of the stiffness were achieved. However, the computational results slightly underestimated strength degradation throughout the loading history, which is attributed to the discrepancy between computational experimental values of the rate of reduction of the bounding surface. Figure 5.131 shows the typical stress-strain response experienced by concrete and steel fibers located at the fixed-end of the specimen.

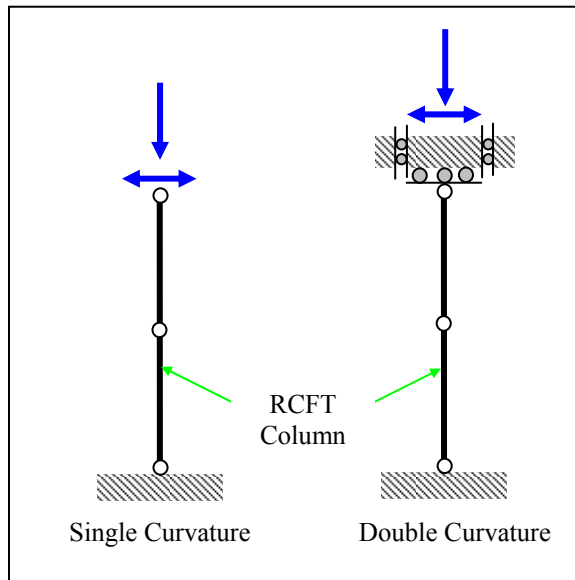


Figure 5.128 Computational Modelling of Cyclically-Loaded RCFT Beam-Column Tests

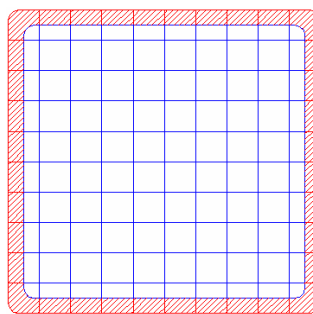


Figure 5.129 Fiber Discretization of RCFT Cross-Section

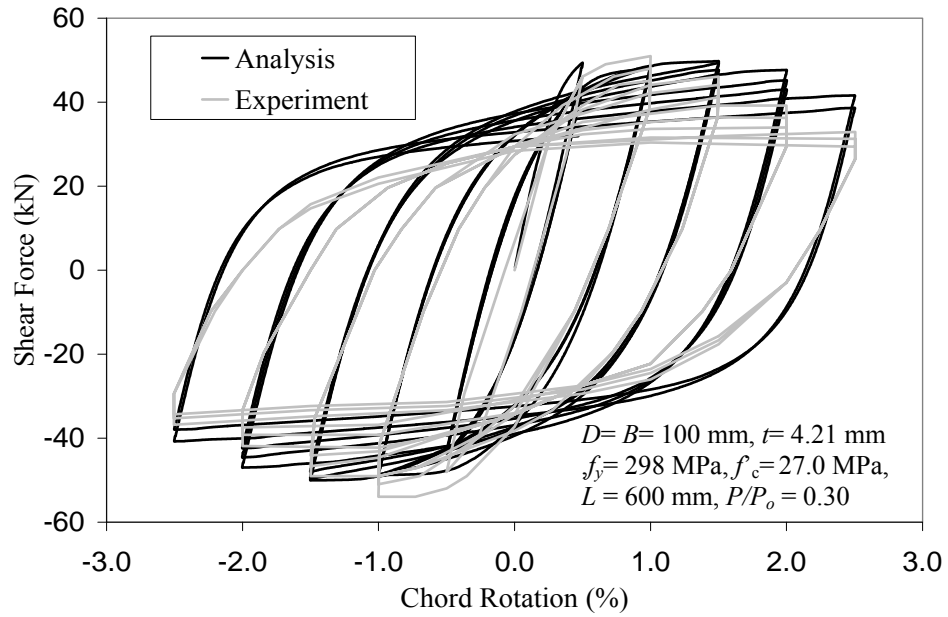


Figure 5.130 Comparison of Computational and Experimental Results for a Cyclically-Loaded RCFT Beam-Column (Sakino and Tomii, 1981, Specimen CIIS3-3)

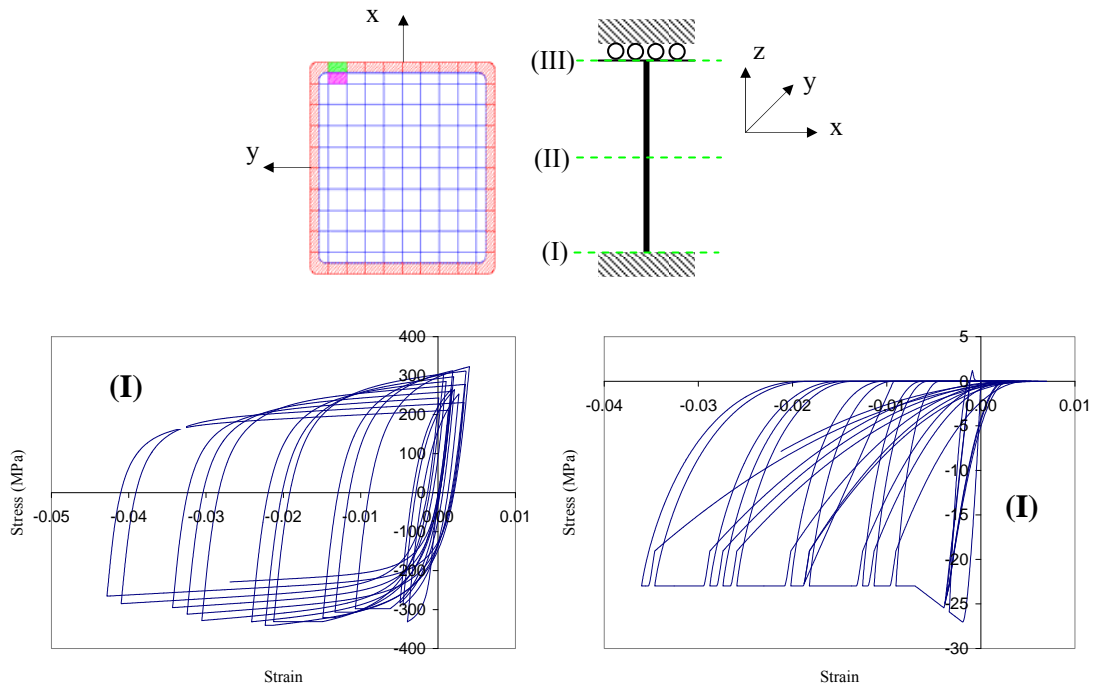


Figure 5.131 Stress-Strain Response of Steel and Concrete Fibers (Sakino and Tomii, 1981)

The RCFT beam-column specimen SR6A4C by Inai et al. (2004) was analyzed using the mixed finite element formulation. The specimen was tested under constant axial load and cyclic shear loading putting the member into double curvature as described in Figure 5.128. The same mesh size was used as Specimen CIIS3-3 presented above. The comparisons of the experimental and computational results are shown in Figure 5.132. Specimen SR6A4C exhibited very good correlation with the experimental results except that the maximum moment capacity was slightly underestimated, which might be attributed to the discrepancy in the experimental and computational values of the initial size of the bounding surface or the rate of increase in size of the bounding surface until the initiation of local buckling. Figure 5.130 shows the typical stress-strain response experienced by concrete and steel fibers located at the fixed-end of the specimen.

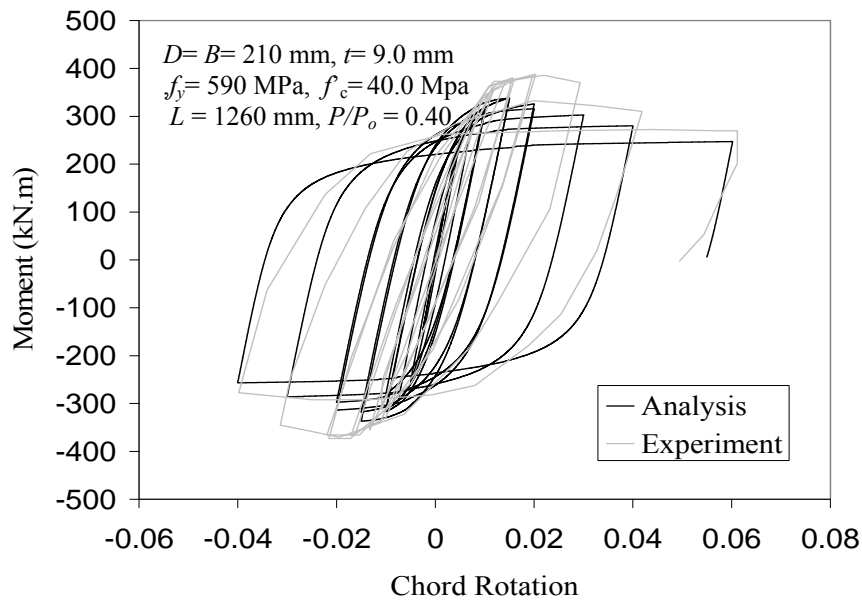


Figure 5.132 Comparison of Computational and Experimental Results for a Cyclically-Loaded RCFT Beam-Column (Inai et al., 2004, Specimen SR6A4C)

The performance of the mixed-finite element formulation under 3D loading conditions was examined by analyzing the cruciform RCFT frame tested by Kawaguchi and Morino (2001) as shown in Figure 5.134. A simply supported RCFT column is framed by in-plane and out-of-plane steel girders. The in-plane steel girders are subjected to cyclic shear loading applied at their ends. A displacement-controlled

loading scheme was created by introducing axial forces to the steel struts attached to the ends of the steel girders so that a deformation pattern identical to the experiment was obtained. The effect of gravity loading was represented by applying constant forces to the end of the out-of-plane steel girder and to the top of the RCFT column. The RCFT column and the in-plane steel girders were modeled with 3 elements and 4 integration points. The connection and girders in the specimen were designed to remain elastic. The computational model adopted to perform the analysis can be seen in Figure 5.135. The number of material fibers along the depth was decided as 10 for both the RCFT column and steel girders. The cross-section discretization scheme, illustrating the geometric location and properties of the material fibers, is shown in Figure 5.136.

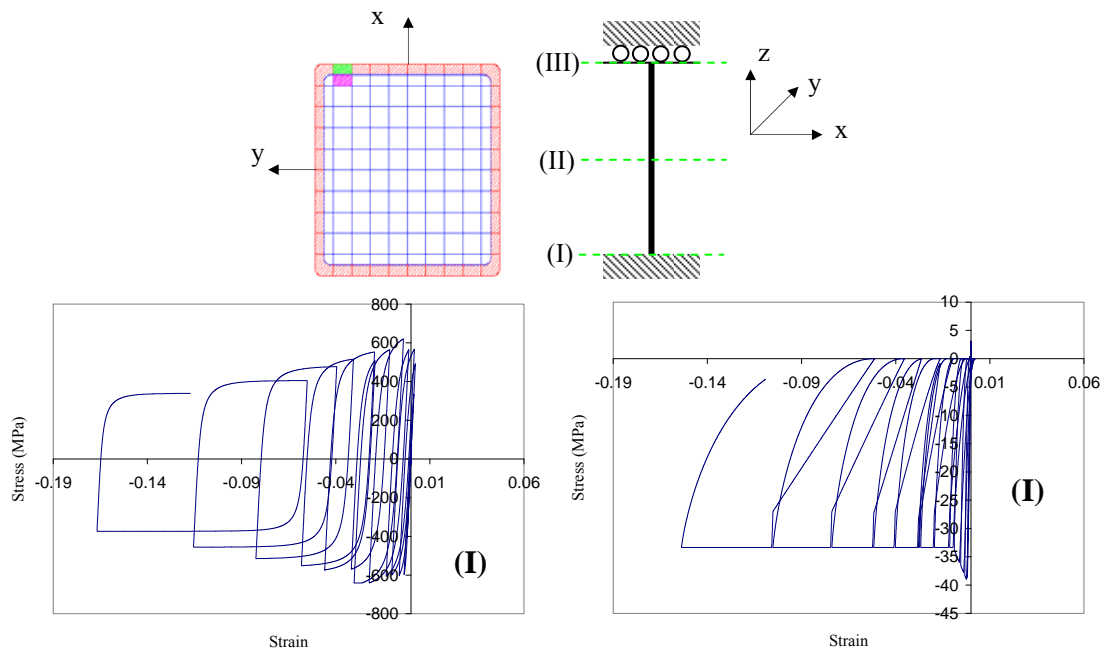


Figure 5.133 Stress-Strain Response of Steel and Concrete Fibers (Inai et al., 2004)

The comparison of the experimental and computational results is presented in Figure 5.137 in the form of shear force vs. chord rotation response. The shear force was calculated as the average of the shear forces of the in-plane steel girders. The chord rotation was obtained using the response of the 9th and 12th nodes of the frame, matching the location of the measurements in the experiments. It was calculated as the ratio of the summation of shear displacements along the z axes divided by the distance between the

nodes. Excellent correlation was achieved with respect to the lateral stiffness of the frame. However, the computational results slightly underestimated the experimental peak shear load, where the largest error was obtained as 20% at a chord rotation level of -0.03. This discrepancy is mainly attributed to the mismatch in the experimental and computational values of initial bounding surface of the steel tube.

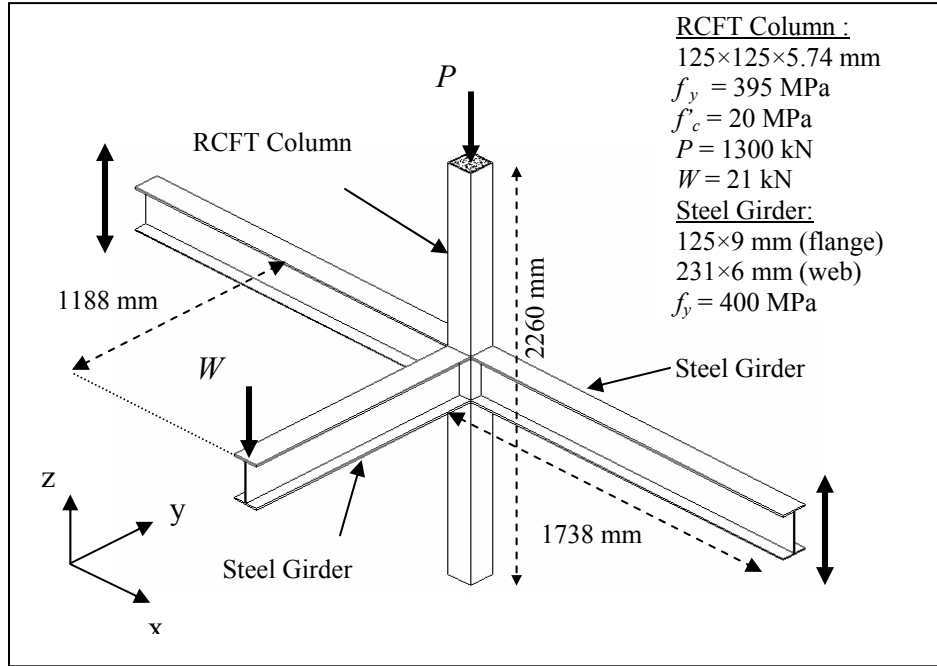


Figure 5.134 Cyclically-Loaded RCFT Cruciform Frame (Kawaguchi and Morino, 2001)

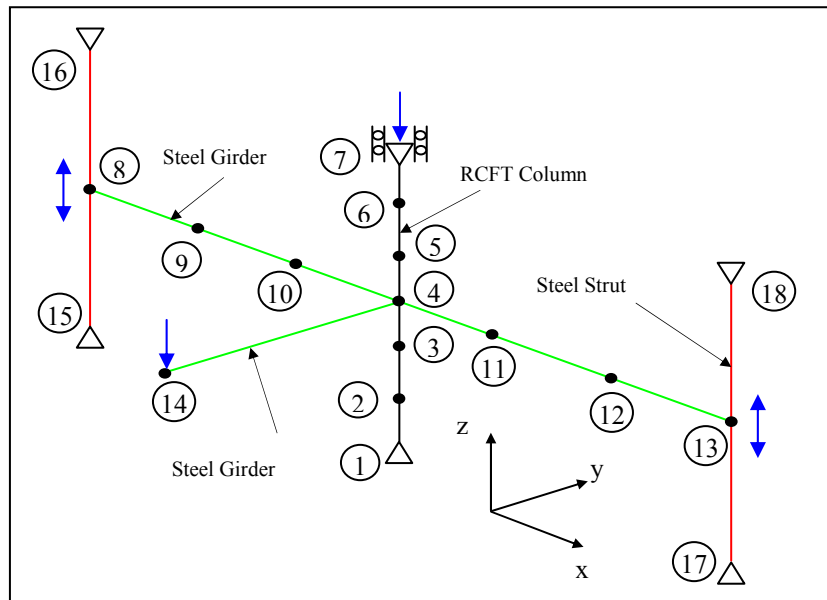


Figure 5.135 Computational Modeling of Cyclically-Loaded RCFT Cruciform Frame

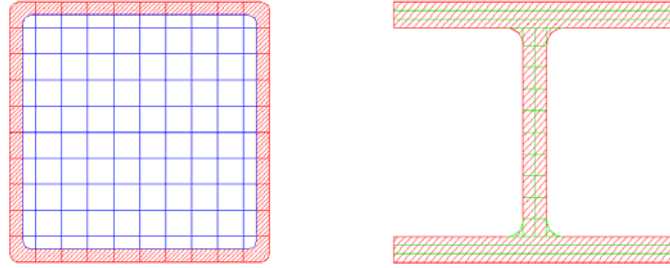


Figure 5.136 Fiber Discretization of RCFT and Steel Cross-Sections

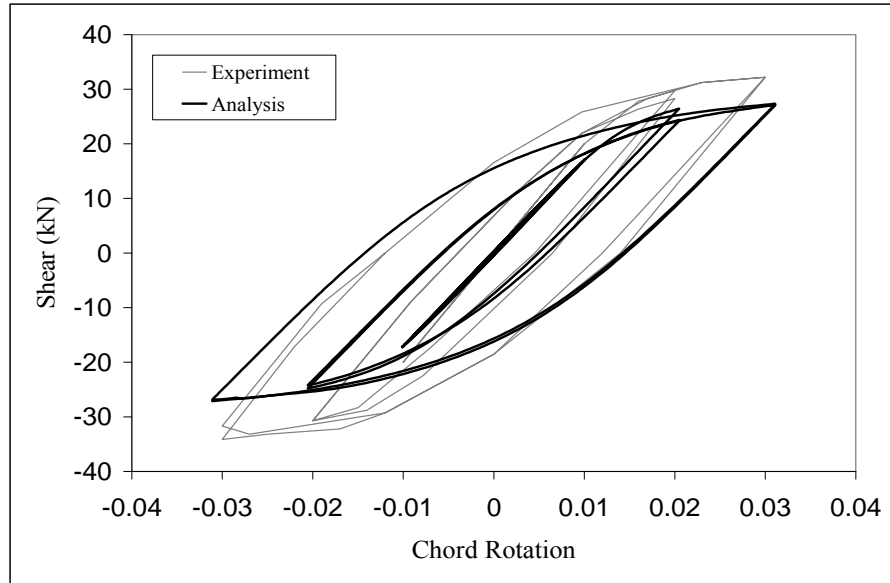


Figure 5.137 Comparison of Computational and Experimental Results for a Cyclically-Loaded RCFT Cruciform Frame (Kawaguchi and Morino, 2001)

The distribution of the damage was investigated based on the stress-strain response of material fibers over the cross-sections located at the integration points along the RCFT column and steel girders. Figure 5.138 through Figure 5.143 shows the stress-strain response monitored at key locations of the cruciform frame. At each integration point, several material fibers along the depth of the cross-section were studied. The material fibers at the mid-height of the RCFT column experienced significant cracking and crushing of the concrete fibers. The steel tube material fibers underwent yielding in both tension and compression. Local buckling was also observed. However, no strength degradation took place since the RCFT column has a small D/t ratio of 22. As can be seen in Figure 5.144 and Figure 5.145, the material fibers of the steel girders were found to exhibit a linear response.

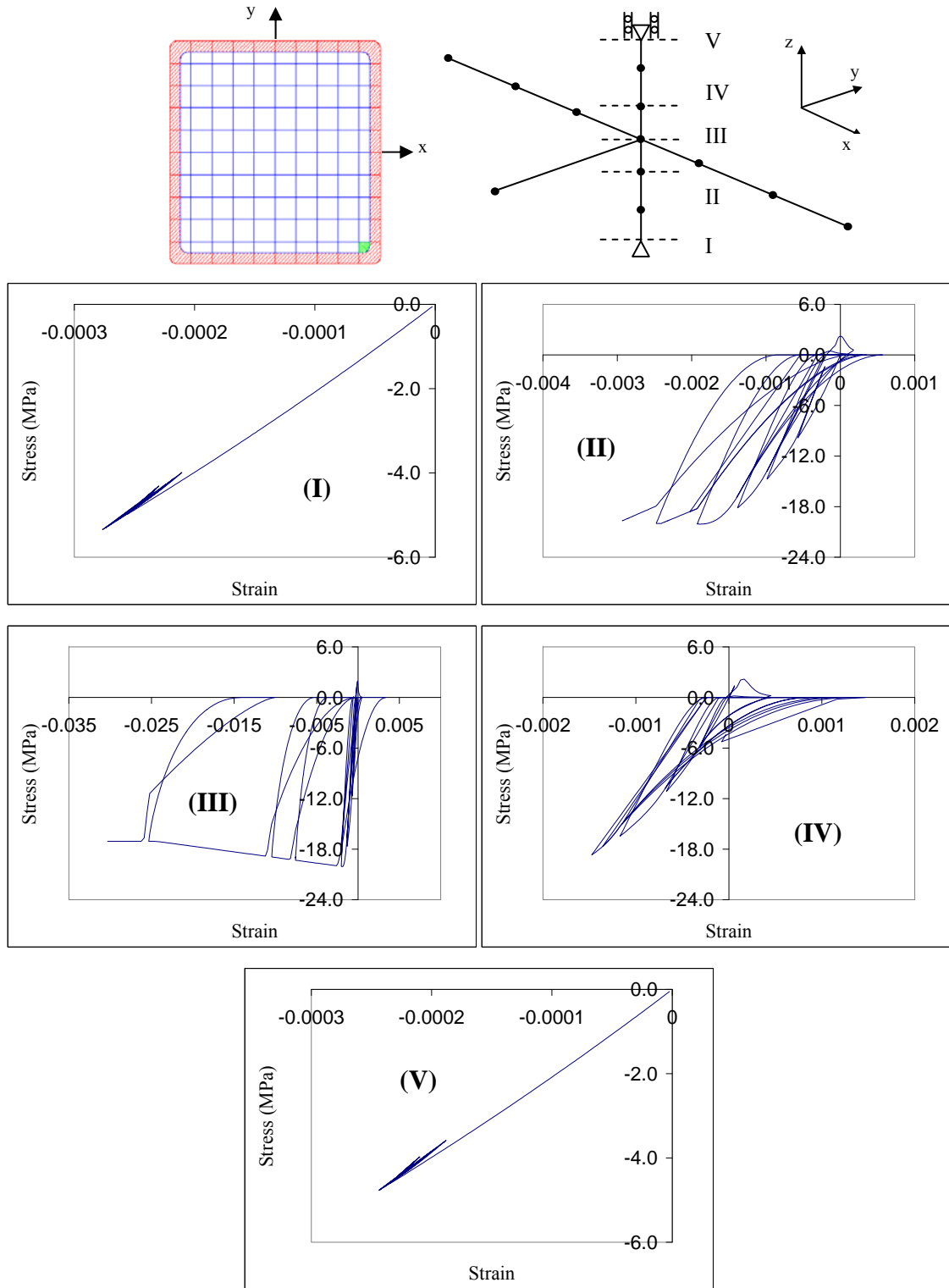


Figure 5.138 Stress-Strain Response of Concrete Fibers (Kawaguchi and Morino, 2001)

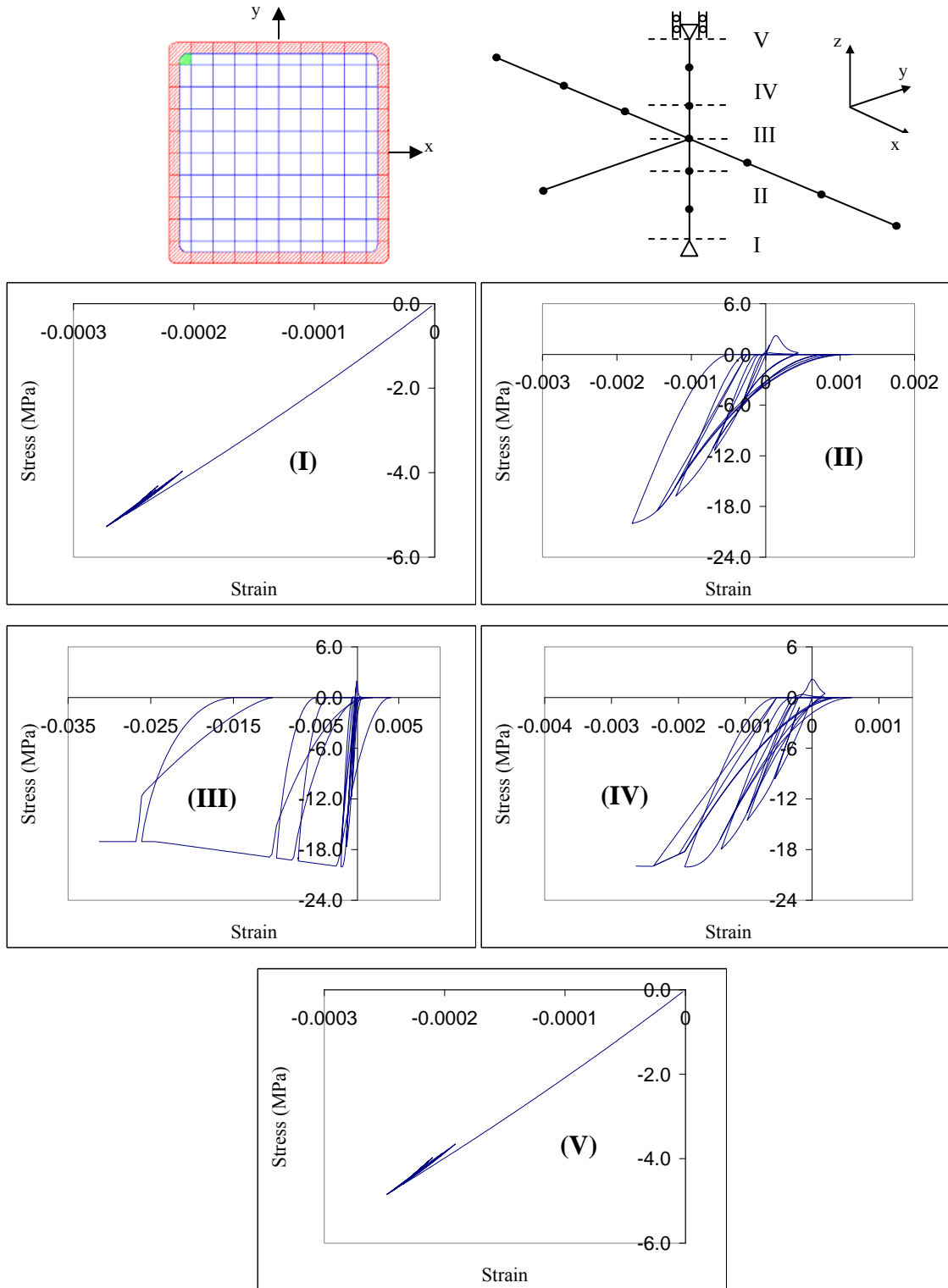


Figure 5.139 Stress-Strain Response of Concrete Fibers (Kawaguchi and Morino, 2001)

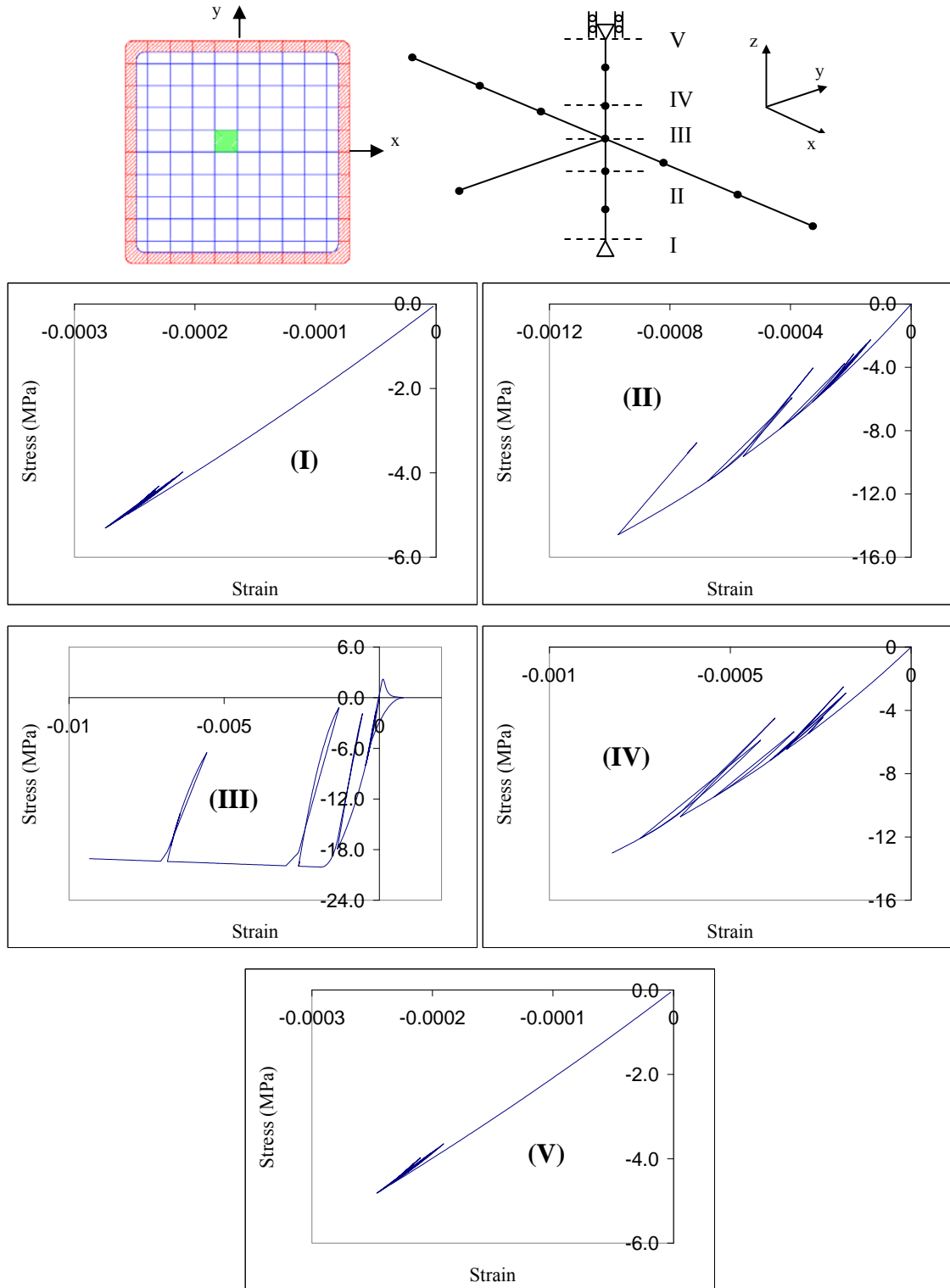


Figure 5.140 Stress-Strain Response of Concrete Fibers (Kawaguchi and Morino, 2001)

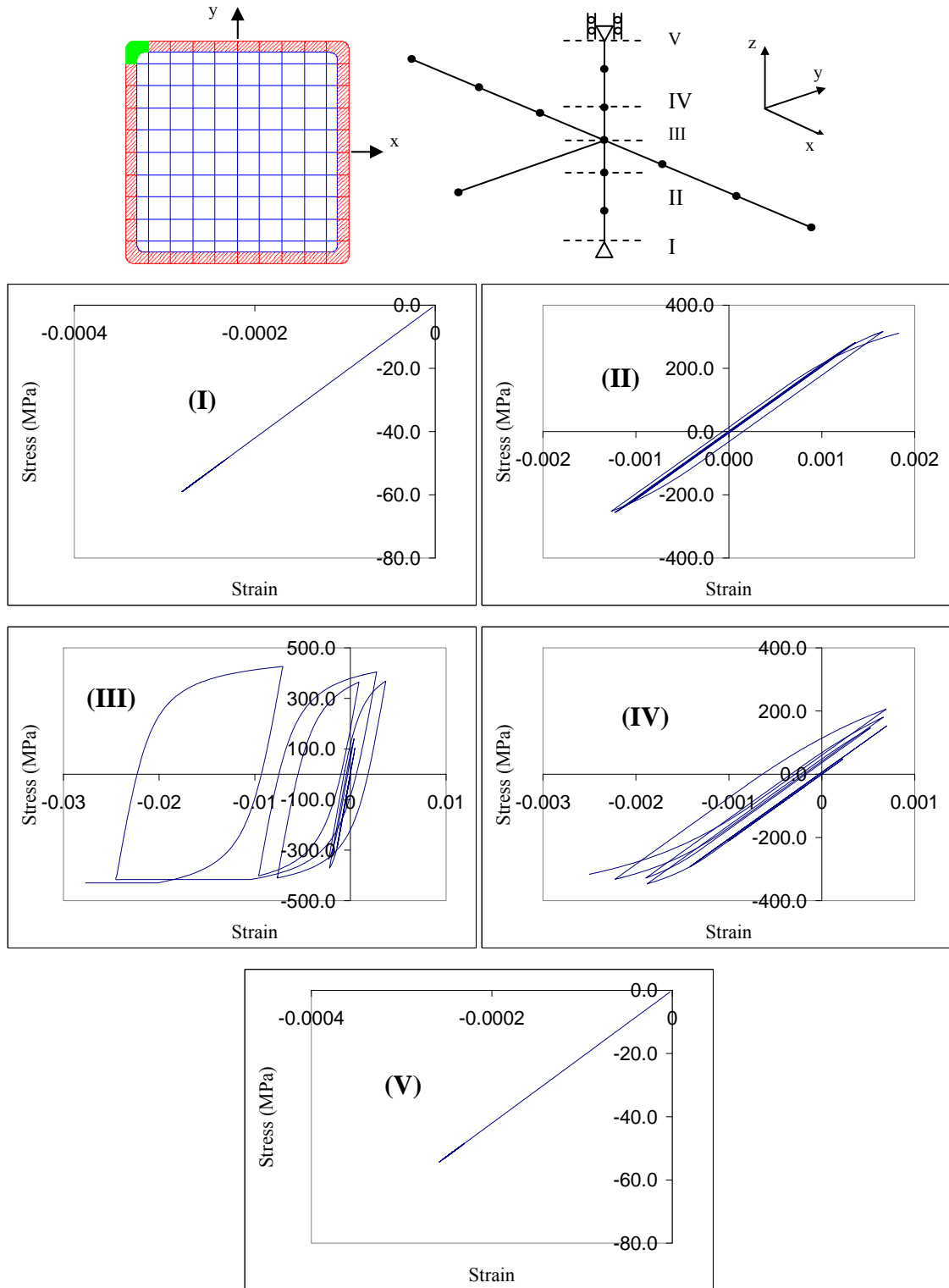


Figure 5.141 Stress-Strain Response of Steel Fibers (Kawaguchi and Morino, 2001)

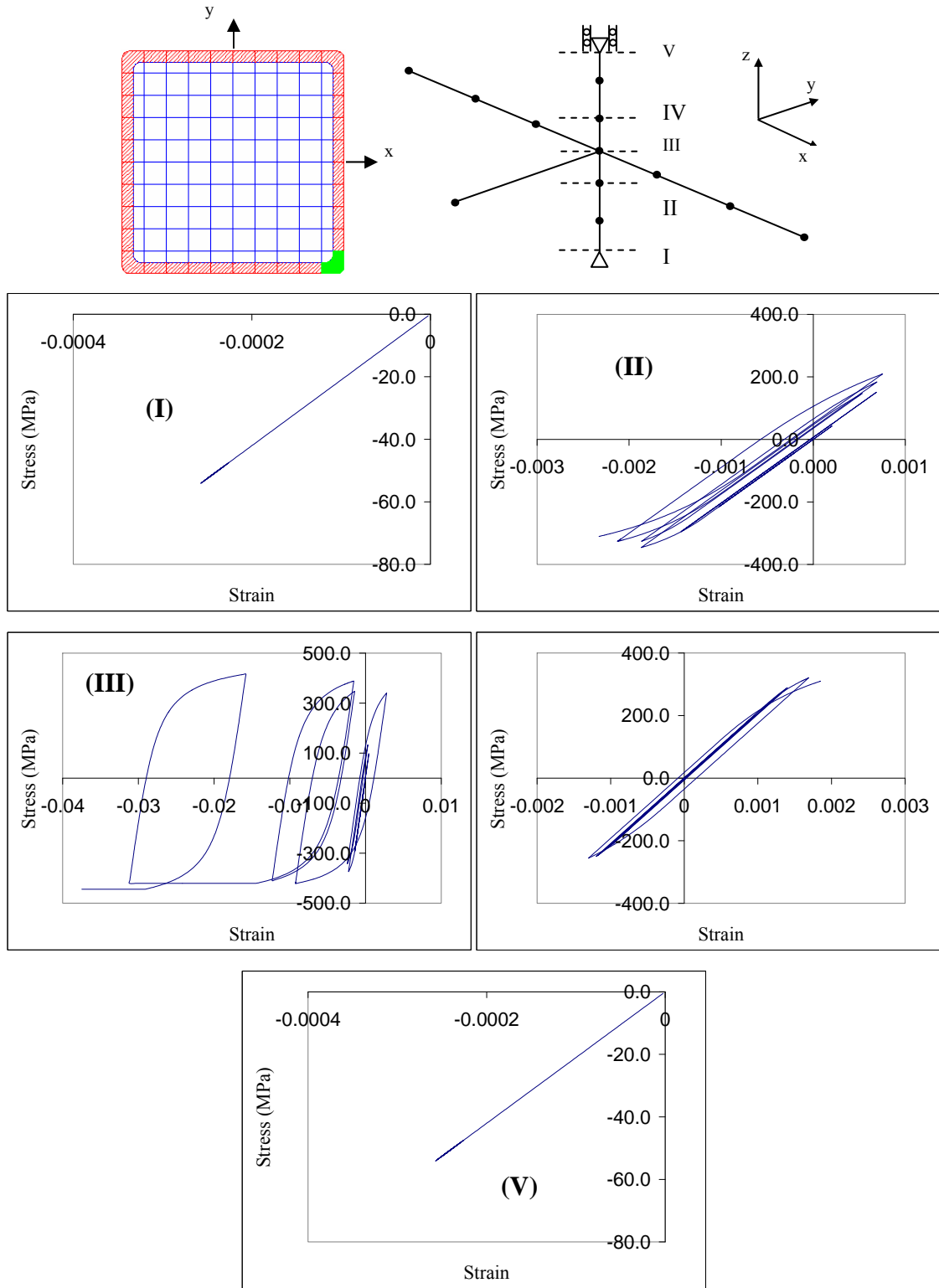


Figure 5.142 Stress-Strain Response of Steel Fibers (Kawaguchi and Morino, 2001)

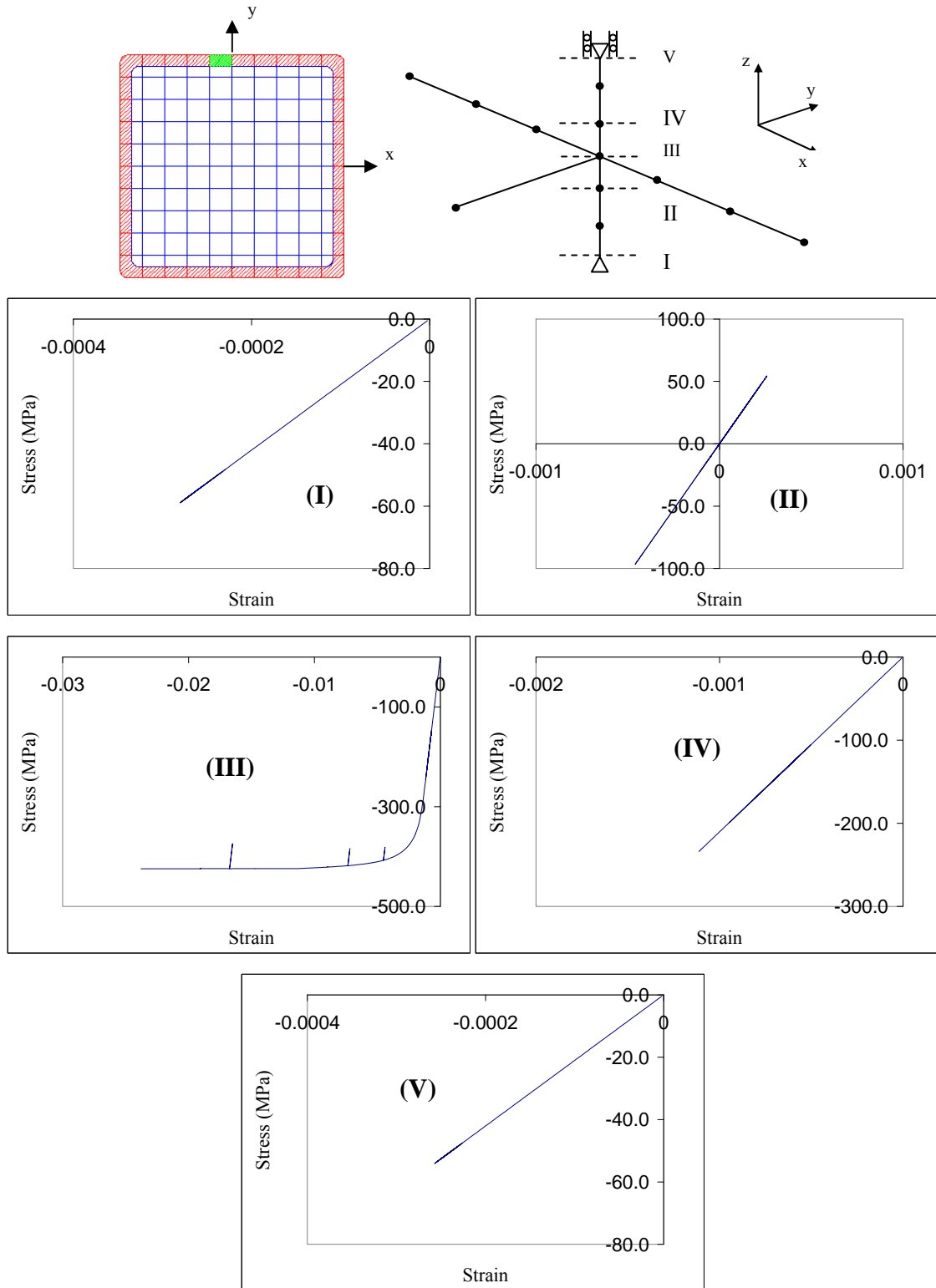


Figure 5.143 Stress-Strain Response of Steel Fibers (Kawaguchi and Morino, 2001)

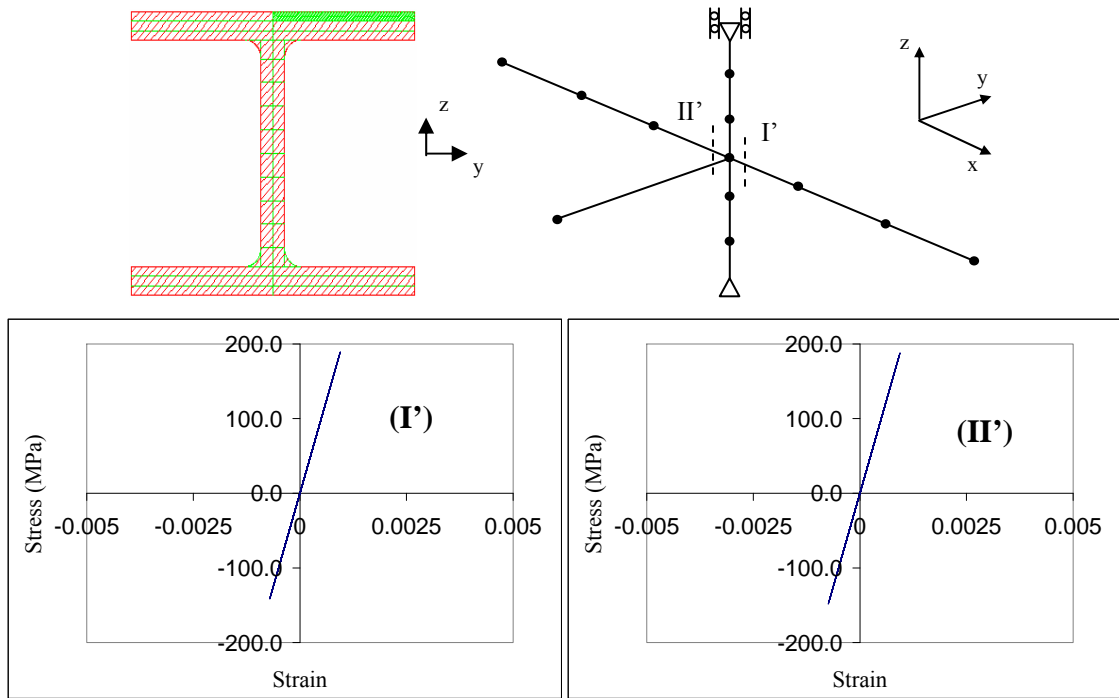


Figure 5.144 Stress-Strain Response of Steel Fibers (Kawaguchi and Morino, 2001)

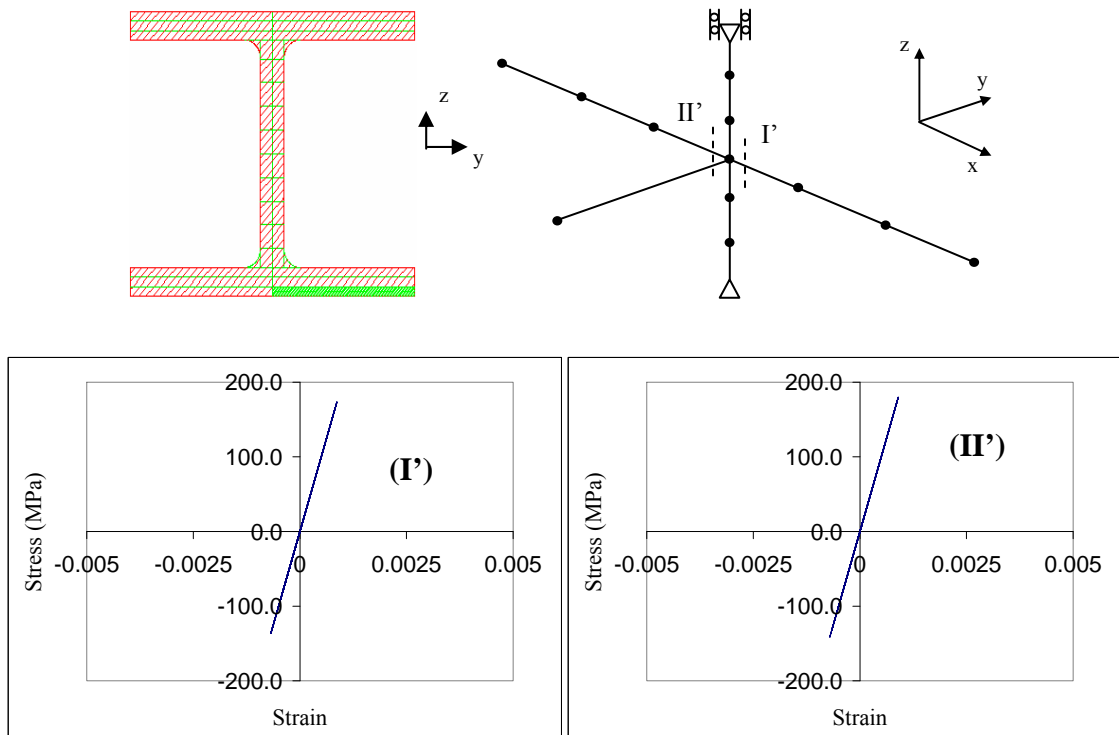


Figure 5.145 Stress-Strain Response of Steel Fibers (Kawaguchi and Morino, 2001)

The portal frame specimen, 21C30C, with RCFT columns and a steel girder by Kawaguchi (2000), shown in Figure 5.146, was also analyzed. The analysis was conducted under constant axial load and cyclic shear loading. The shear loading was applied at the supports, putting the columns into double curvature. A displacement-controlled loading scheme was utilized by introducing the shear loading into steel struts having large axial and flexural stiffness. The steel struts were attached to the supports of the RCFT columns. Three elements per member with 4 integration points were defined in the analysis model. The number of material fibers along the depth was 8 and 10 for the RCFT columns and steel girder, respectively.

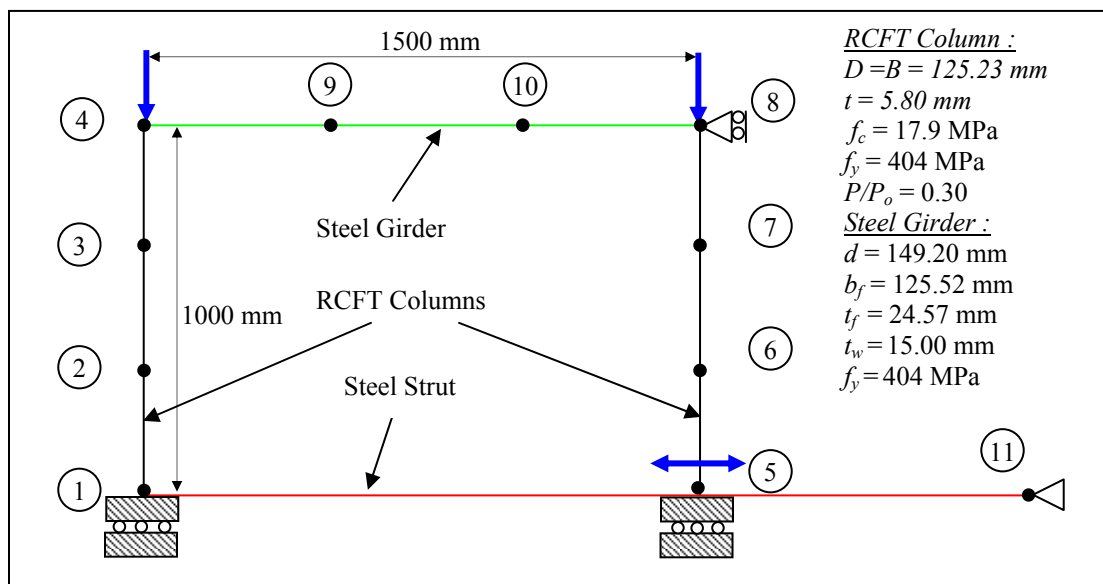


Figure 5.146 Computational Modeling of Cyclically-Loaded RCFT Portal Frame

Figure 5.147 illustrates the computational and experimental load-deformation response of the specimen. Accurate correlation is evident between the two sets of data where the stiffness of the specimen is well predicted throughout entire loading history. However, the computational results underestimate the peak lateral load value and a maximum error of 18% is obtained. The discrepancy is mainly attributed to the difference in computational and experimental values of the bounding surface radius and the rate of increase in bounding surface radius prior to local buckling, which leads to initiation of inelastic response earlier due to underestimation of the bounding surface parameters in the steel constitutive model.

The damage experienced by structural members was investigated by documenting the stress-strain response of several material fibers along the depth of the cross-sections. The cross-sections were selected at the critical points along the specimen lengths. As can be seen in Figure 5.148 through Figure 5.157, the material fibers of the RCFT cross-sections located close to the supports experience significant damage in the form of concrete crushing, concrete cracking, yielding, and local buckling. On the other hand, the material fibers of the cross-sections located at the mid-height of the RCFT columns exhibited less damage due to the fact that the columns underwent double curvature with inflection points located approximately at the mid-height. Due to the small D/t ratio of the RCFT columns, local buckling did not cause any strength degradation. Figure 5.158 and Figure 5.159 illustrate that the material fibers of the steel girders remained elastic throughout the loading history.

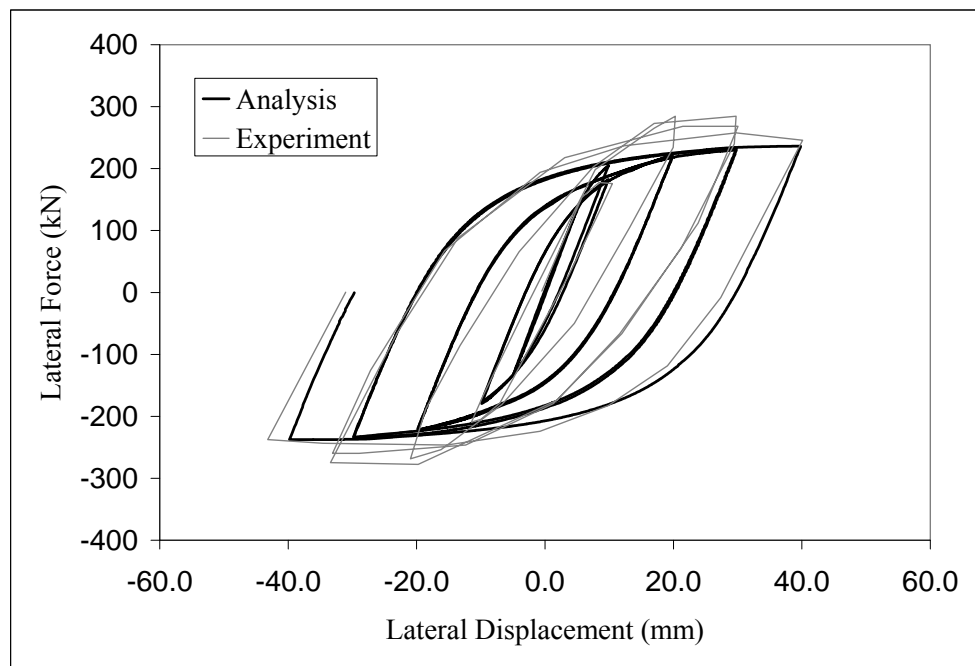


Figure 5.147 Comparison of Computational and Experimental Results for a Cyclically-Loaded RCFT Cruciform Frame (Kawaguchi and Morino, 2001)

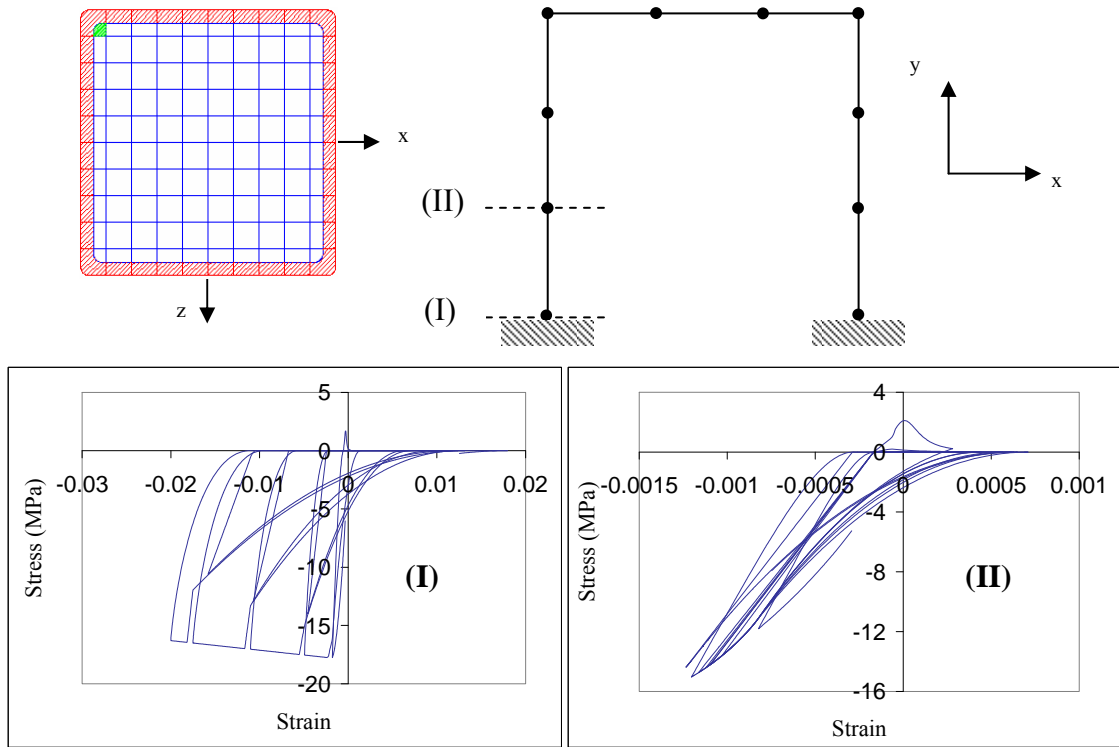


Figure 5.148 Stress-Strain Response of Concrete Fibers (Kawaguchi, 2000)

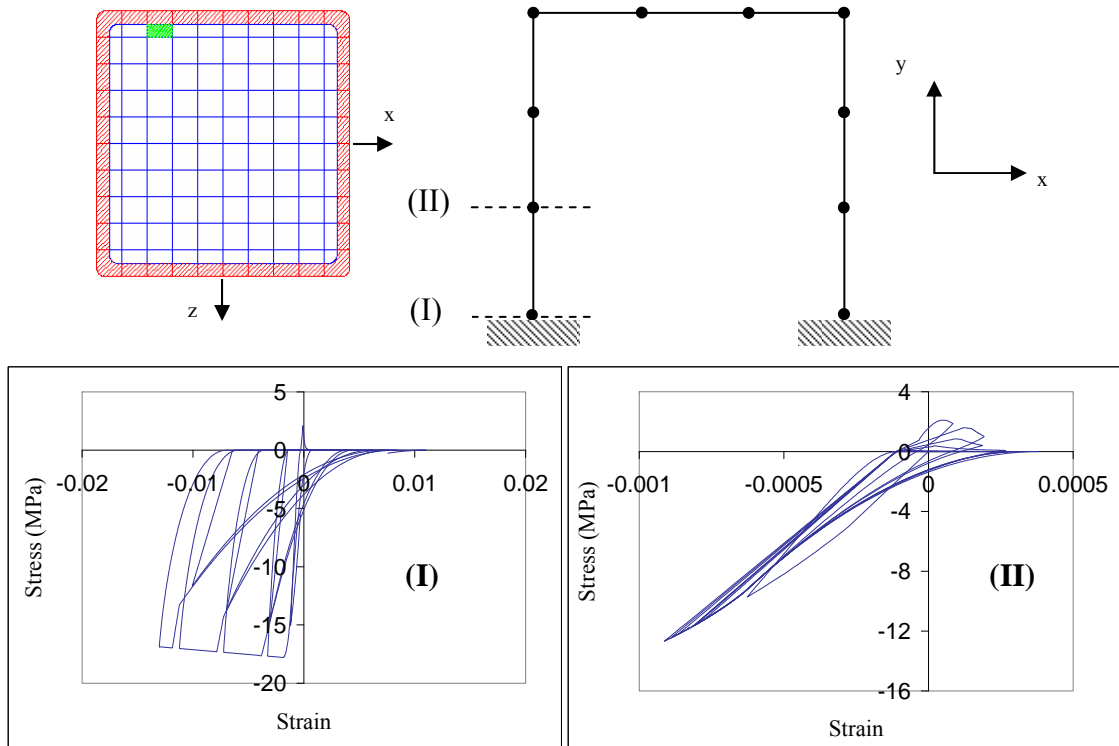


Figure 5.149 Stress-Strain Response of Concrete Fibers (Kawaguchi, 2000)

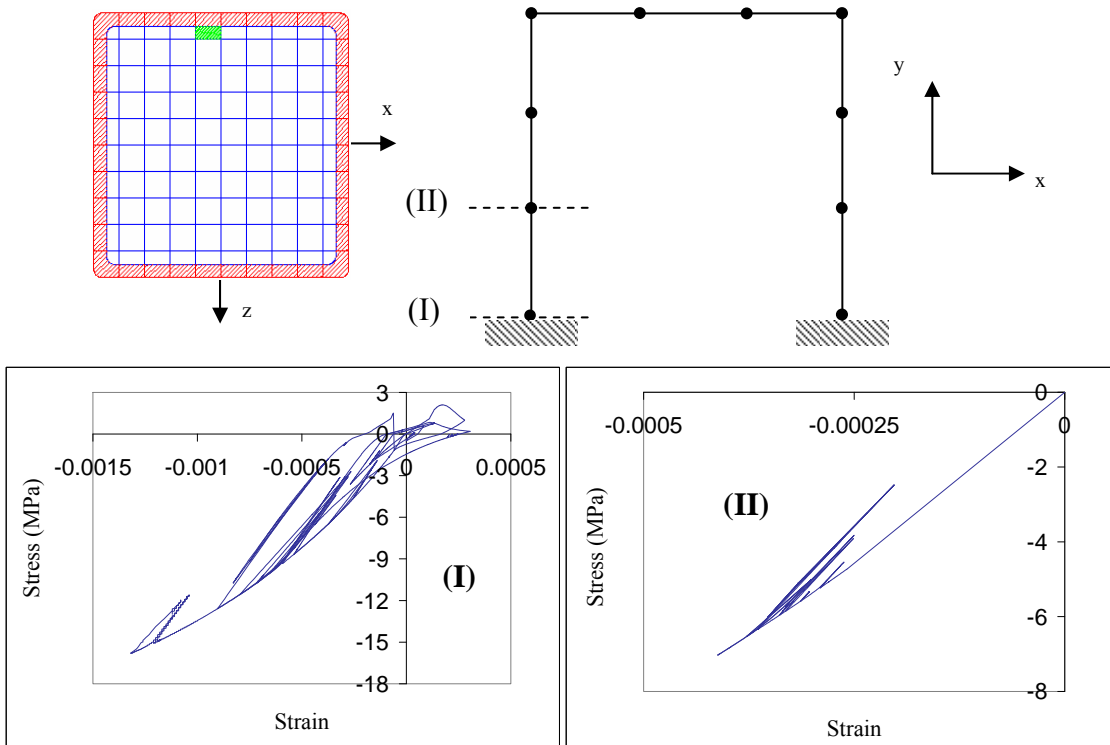


Figure 5.150 Stress-Strain Response of Concrete Fibers (Kawaguchi, 2000)

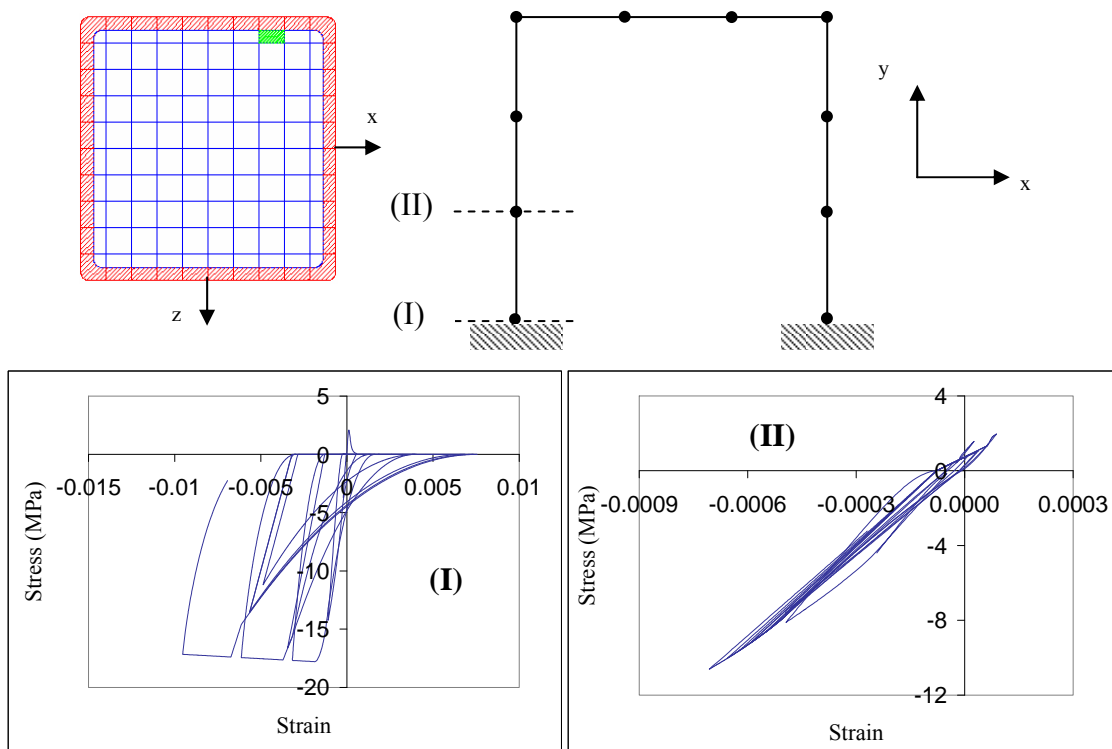


Figure 5.151 Stress-Strain Response of Concrete Fibers (Kawaguchi, 2000)

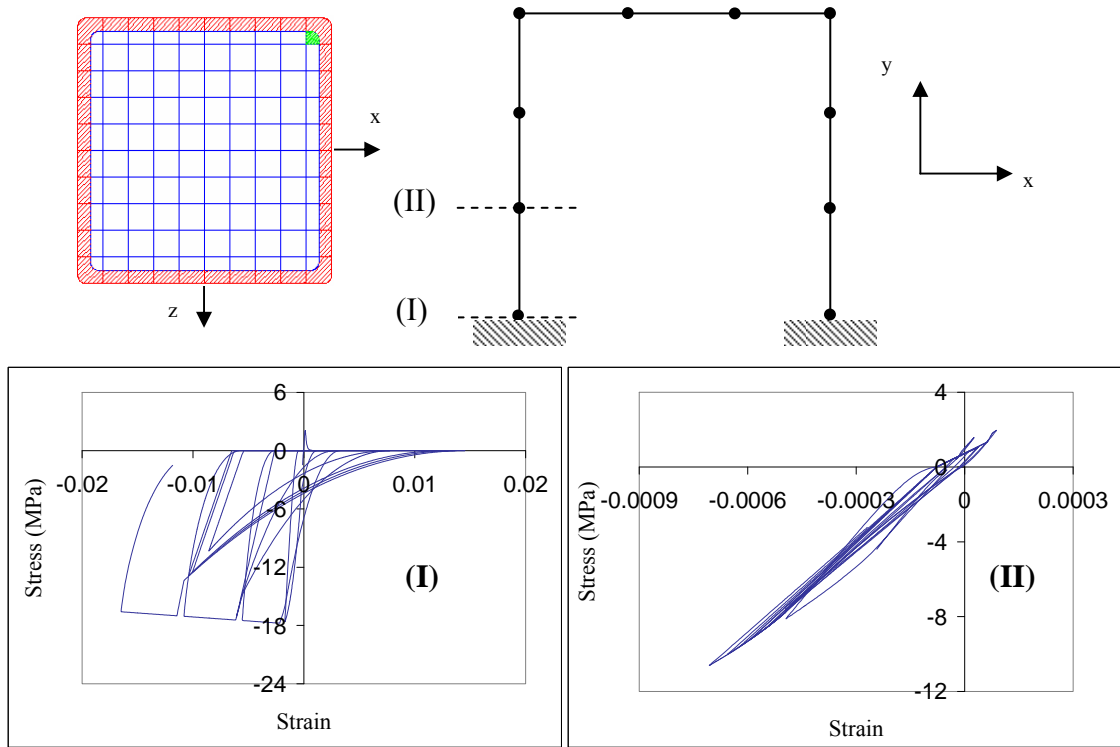


Figure 5.152 Stress-Strain Response of Concrete Fibers (Kawaguchi, 2000)

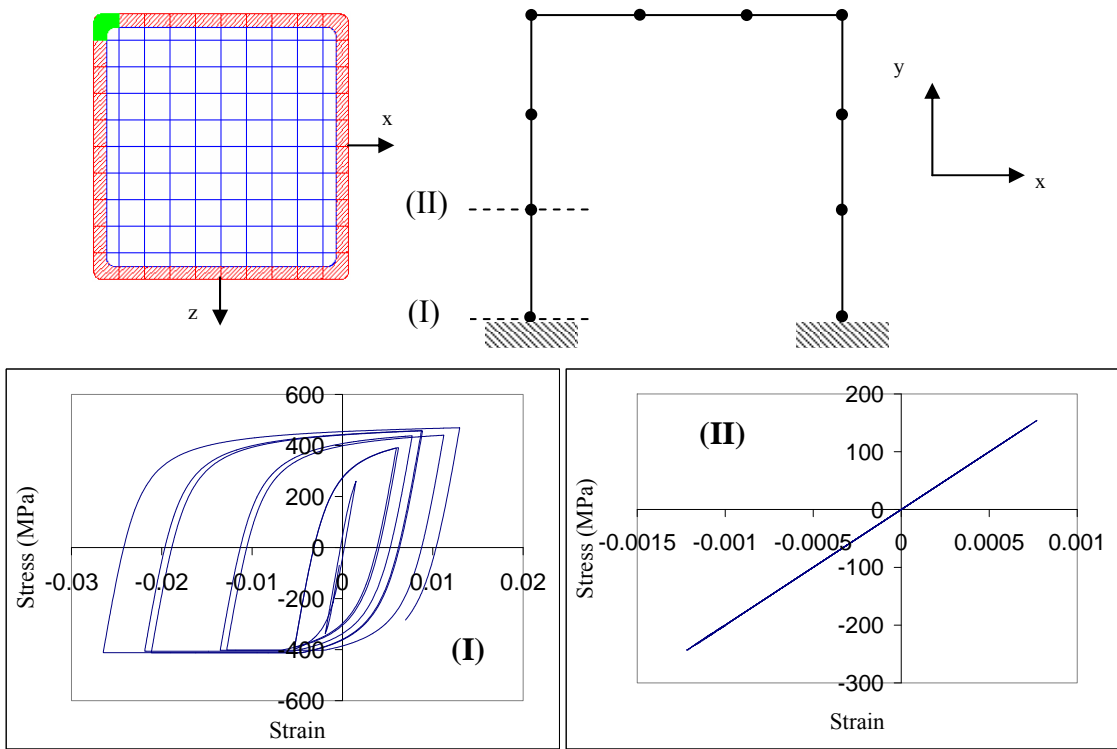


Figure 5.153 Stress-Strain Response of Steel Fibers (Kawaguchi, 2000)

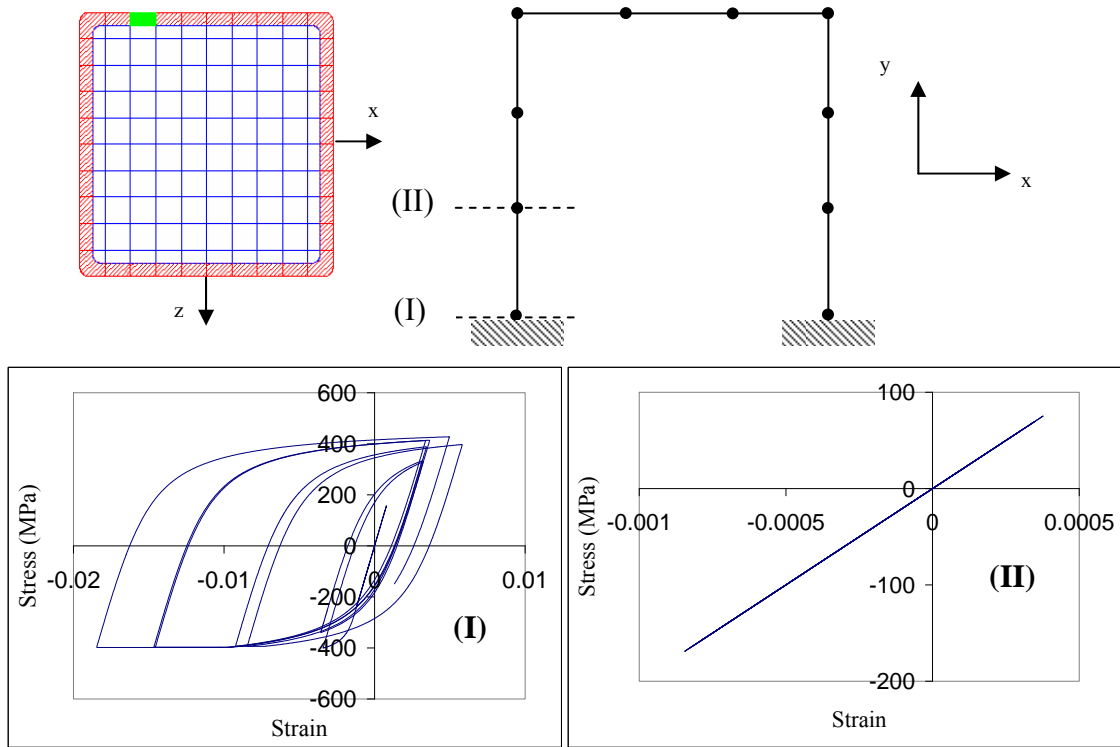


Figure 5.154 Stress-Strain Response of Steel Fibers (Kawaguchi, 2000)

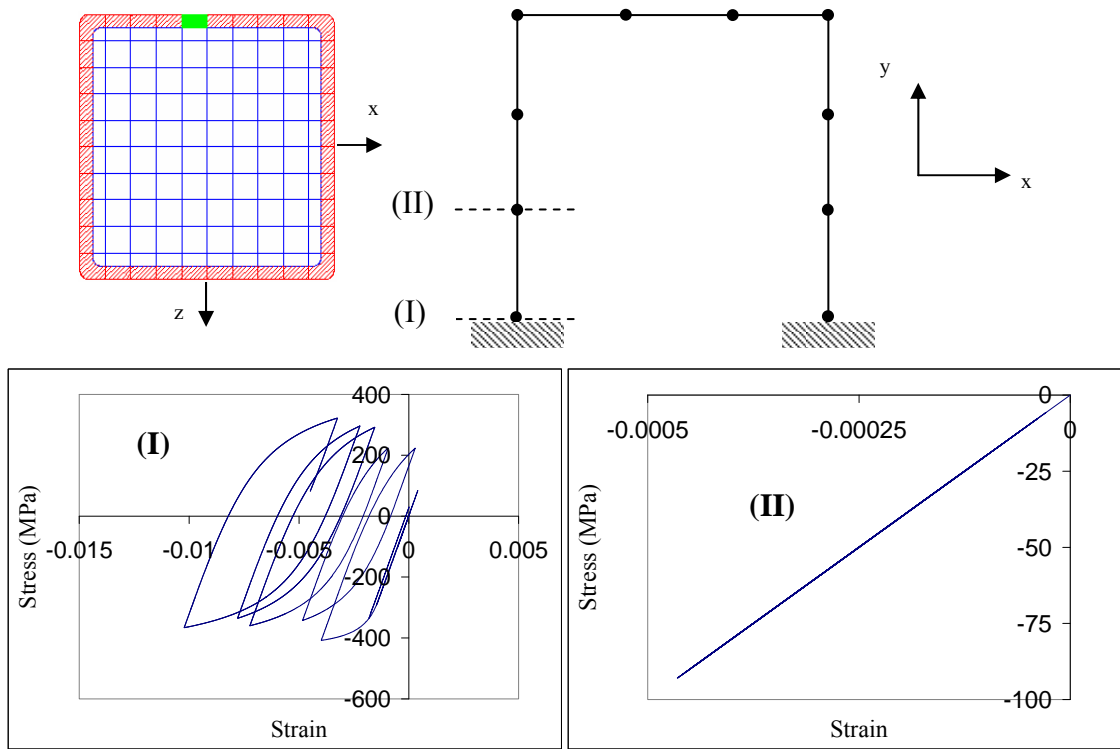


Figure 5.155 Stress-Strain Response of Steel Fibers (Kawaguchi, 2000)

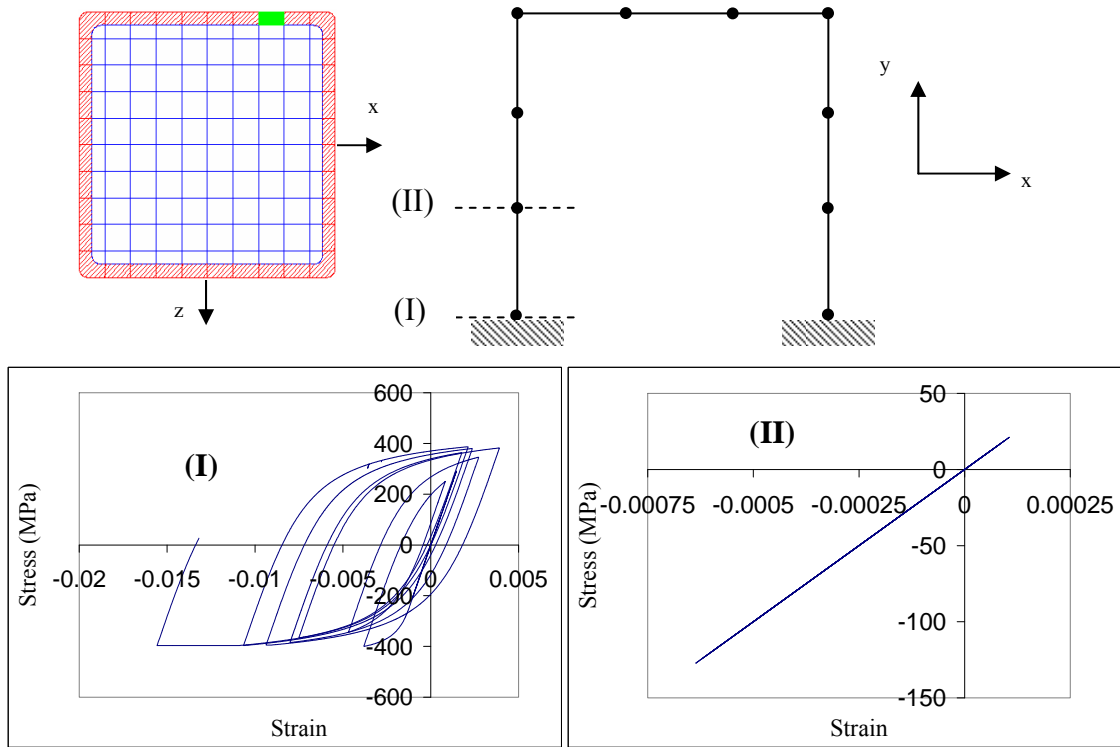


Figure 5.156 Stress-Strain Response of Steel Fibers (Kawaguchi, 2000)

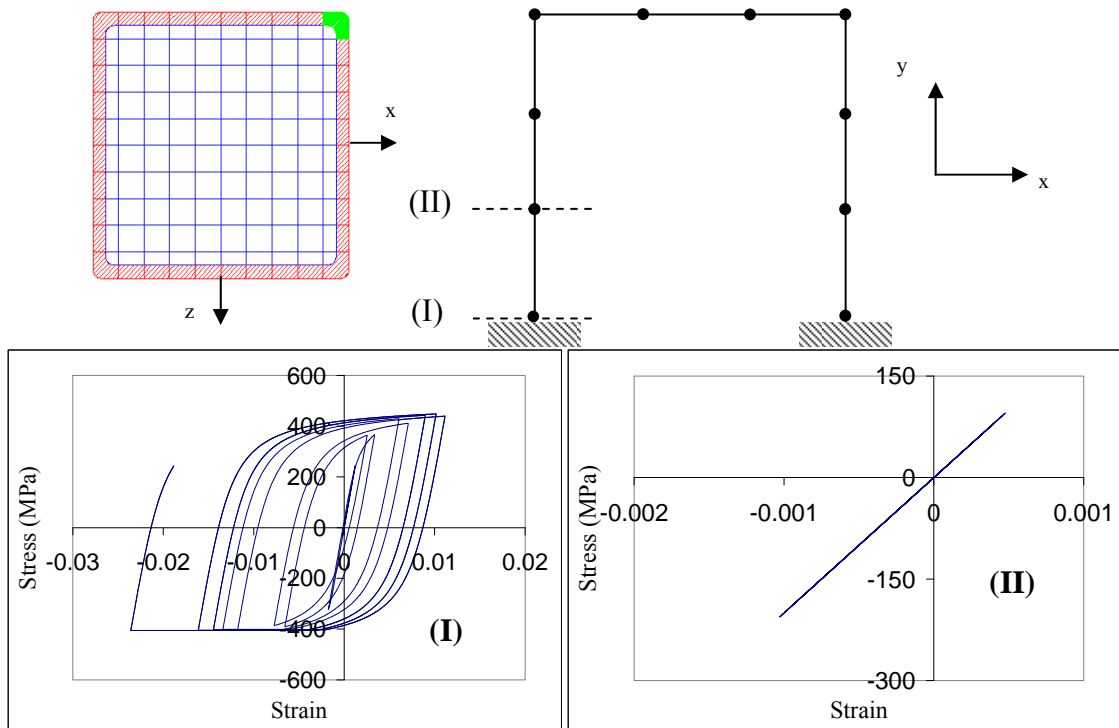


Figure 5.157 Stress-Strain Response of Steel Fibers (Kawaguchi, 2000)

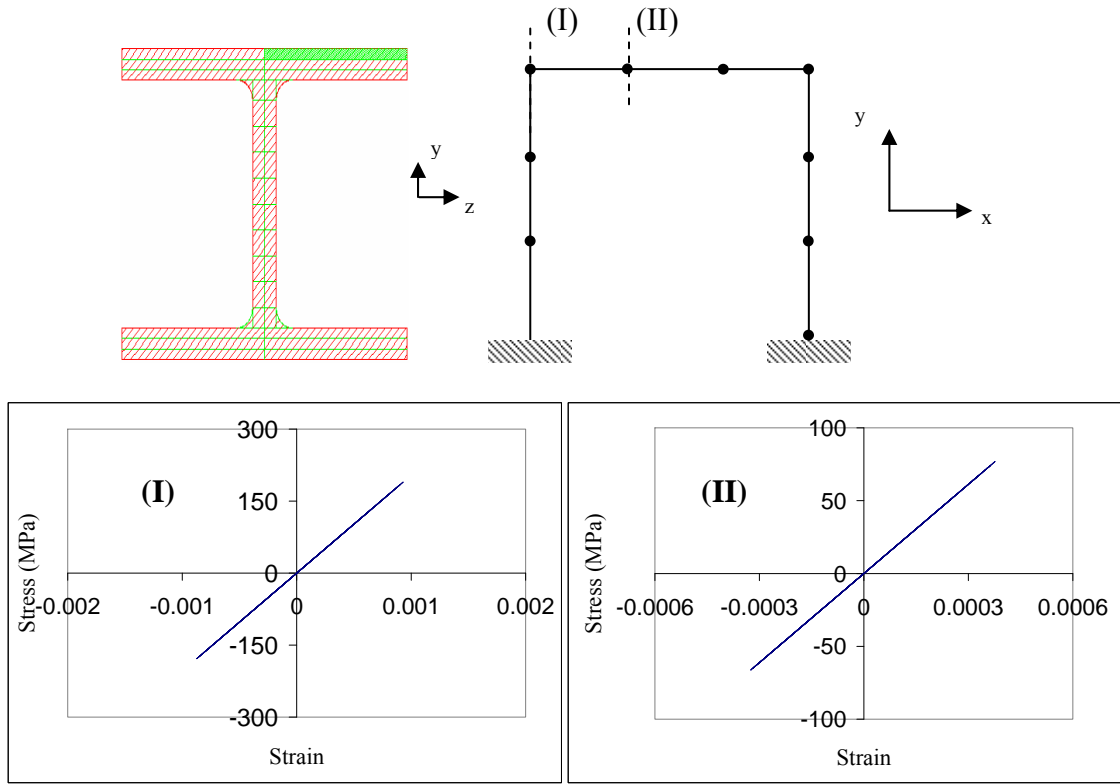


Figure 5.158 Stress-Strain Response of Steel Fibers (Kawaguchi, 2000)

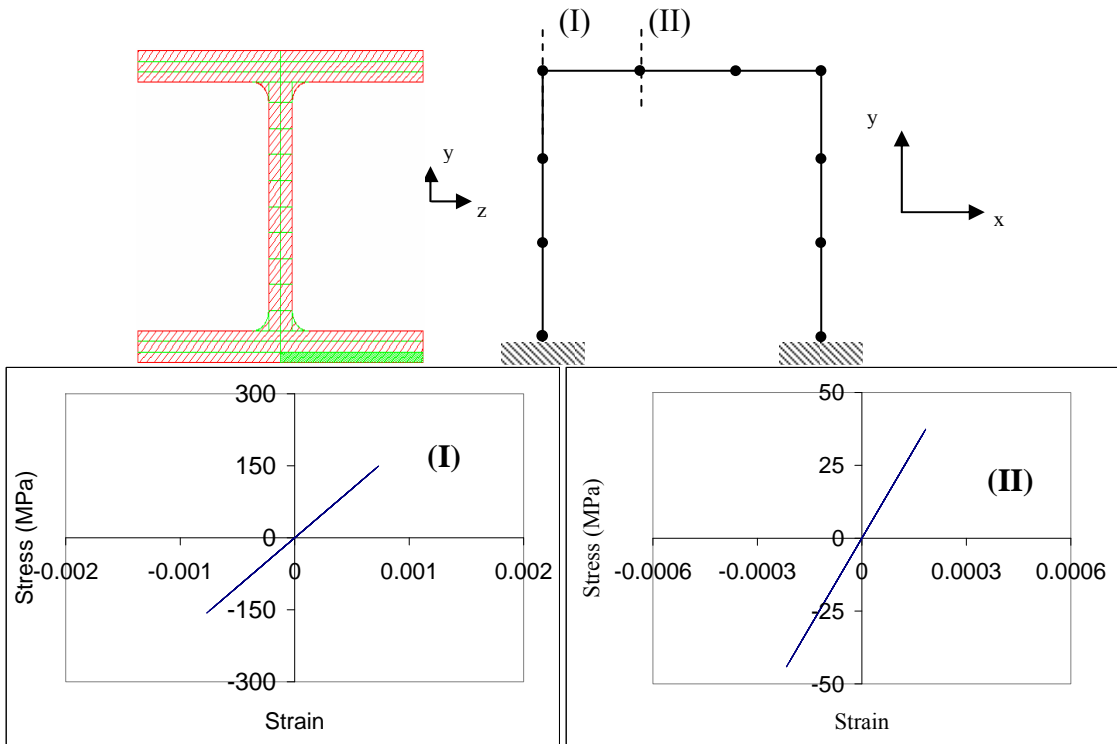


Figure 5.159 Stress-Strain Response of Steel Fibers (Kawaguchi, 2000)

5.9. Materially Linear and Geometrically Nonlinear Dynamically-Loaded RCFT Beam-Column Tests

The performance of the mixed finite element formulation under dynamic loads was investigated by analyzing materially linear and geometrically nonlinear benchmark problems from the literature. The first study consists of a clamped beam subjected to a step loading. The description of the beam is given in Figure 5.160 along with the geometric and material properties. The computational model was constructed by defining 10 elements and 4 integration points. The number of elements was kept as the same in the published results by Hsiao and Jang (1989). The time step size was chosen as $50 \mu\text{sec}$. The mass of the beam was assumed to be lumped at the nodal points and only the steel tube degrees-of-freedom were associated with masses, which was consistent with the static loading, where the applied loads are introduced to the steel tube degrees-of-freedom. The damping of the beam was taken as zero. The stiffness of the composite section was shared equally between the steel tube and the concrete core. The Newmark- β ($\gamma = 0.5, \beta = 0.25$) time integration scheme was utilized to solve for the equation of motion. The computational results from the mixed finite element formulation were compared to the results given by Hsiao and Jang (1989) in Figure 5.161 and excellent agreement was achieved.

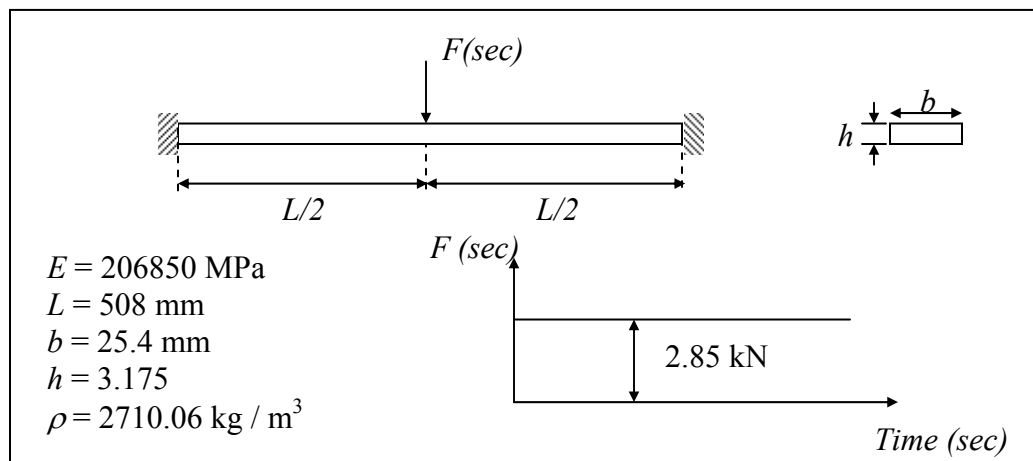


Figure 5.160 Clamped Beam Subjected to Step Loading

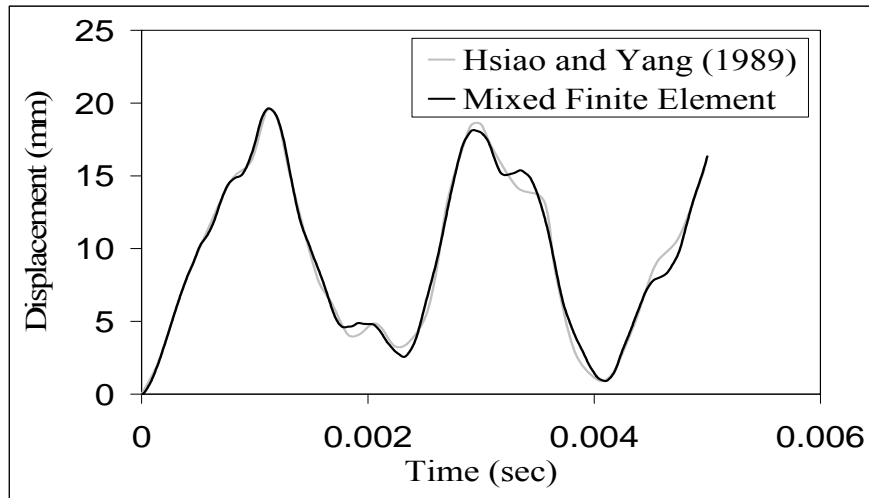


Figure 5.161 Dynamic Response of Clamped Beam Subjected to Step Loading

The second dynamic benchmark problem is a cantilever beam subjected to a concentrated end loading as shown in Figure 5.162. The beam first undergoes an end loading of finite duration, and then experiences free vibration. The mass of the beam was assumed to be lumped at the nodal points and only the steel degrees-of-freedom were associated with masses. A damping coefficient (μ) of 0.10 was introduced when the beam undergoes free vibration. The stiffness of the composite section was distributed equally to the steel tube and the concrete core. The analysis model was constructed by defining 4 elements and 4 integration points. The time step size was selected as 0.05. The Newmark ($\gamma = 0.5, \beta = 0.25$) time integration scheme was utilized to solve for the equation of motion (Chopra, 1995). Figure 5.163 shows the load-deformation results from the mixed finite element formulation and the study by Hsiao and Jang (1989). Excellent correlation is evident between the two sets of data.

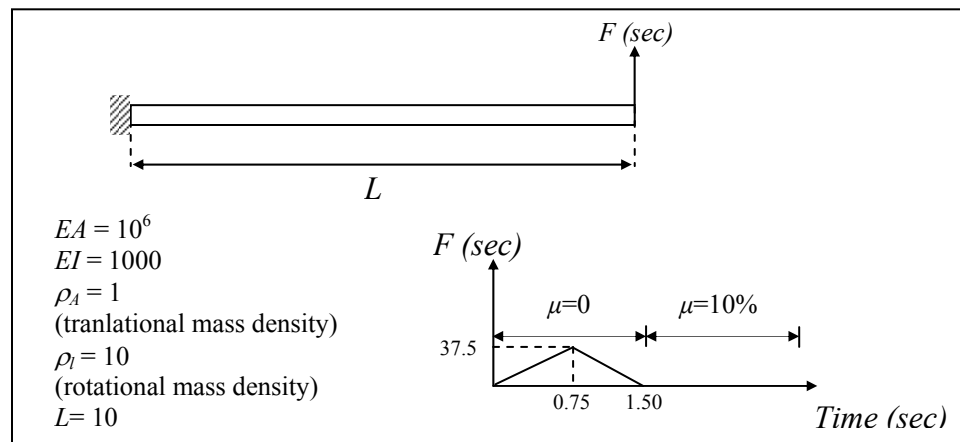


Figure 5.162 Cantilever Beam Subjected to End Loading

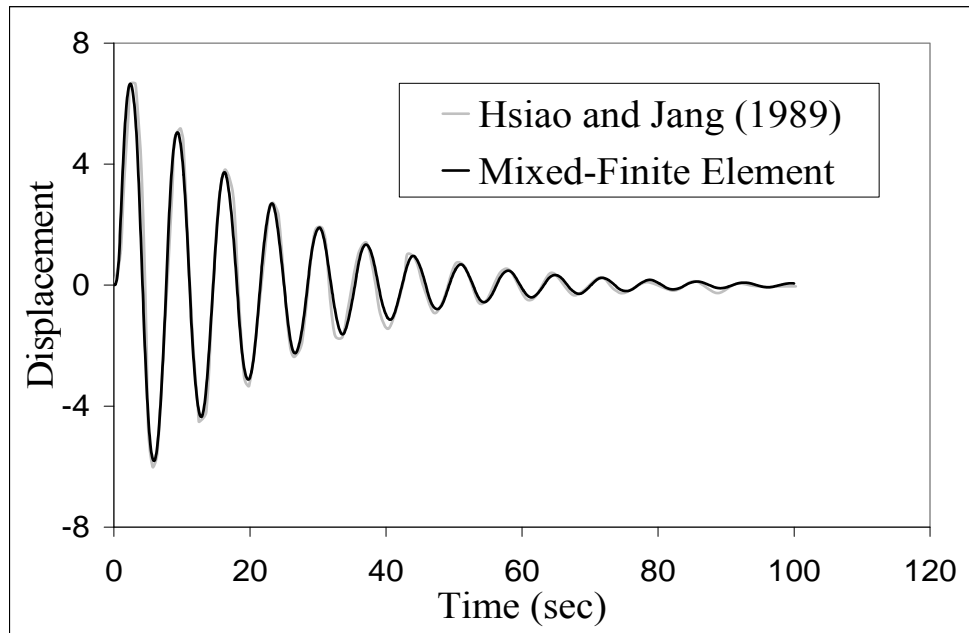


Figure 5.163 Dynamic Response of Cantilever Beam Subjected to End Loading

5.10. Materially Linear and Geometrically Nonlinear Dynamically-Loaded RCFT Beam-Column Tests

The ability of the mixed-finite element formulation in simulating the materially and geometrically nonlinear response of RCFT structures under seismic forces was studied based on the experimental study by Herrera (2005). Herrera (2005) conducted a test on an approximately half scale, two bay-four story RCFT frame. As described in Figure 5.164, in addition to the four stories above ground, the RCFT frame also had a basement-level. The test was run using pseudo-dynamic testing method, where the dynamic equation of motion is solved numerically at each time step to determine the displacement imposed on the structure. In the equation of motion, the mass and damping matrices of the structure were defined computationally while the internal element forces were determined experimentally. The $P-\Delta$ effects were represented through computationally defined leaning columns. The loading was applied to the structure through the loading beams attached to the mid-points of the steel girders. The frame was

free of slab but its effect on the structural response was accounted for by the loading beams. In the analysis model, the number of elements was determined according to the instrumentation plan of the structure, where a total number 90 RCFT elements and 100 steel beam elements were defined. The loading beams and rigid links were modeled with elastic beam elements with large stiffness values. The leaner column was modeled as a geometrically and materially nonlinear steel beam-column and its cross-sections stiffness values were determined as the summation of the cross-section stiffness values of the columns in a single story. The mass of the building was lumped on the nodes along the leaning column. A stiffness and mass proportional damping was assumed with 2% viscous damping having proportionality factors of 0.154667 and 0.001194 for the stiffness and mass matrices, respectively.

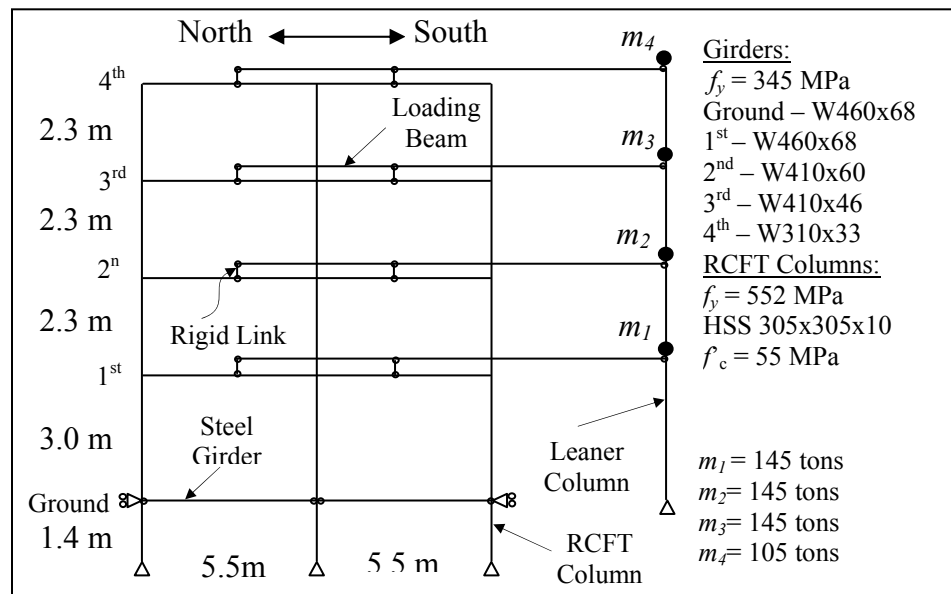


Figure 5.164 RCFT Test Structure by Herrera (2005)

The experiment was conducted under different hazard levels. First, the structure was loaded according to the Northridge Canoga Park (1994) ground motion record that is scaled to the design basis earthquake level. Then, the structure is straightened and the experiment was conducted on the same structure with the Northridge Canoga Park (1994) ground motion record that is scaled the maximum considered earthquake level. The finite element analysis of the structure was performed by first applying the design basis earthquake loading and then subjecting the structure to the maximum considered

earthquake loading. In order to simulate the effect of connections, in the analysis model, rigid links were introduced to the end of the steel girders. The sizes of these links were determined based on the connection dimension of the structure.

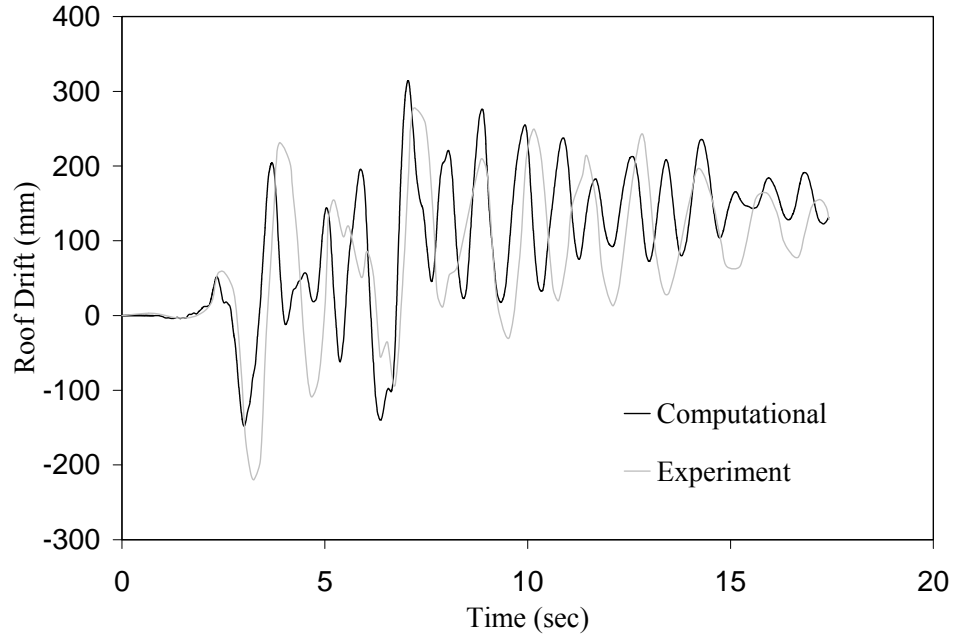


Figure 5.165 and

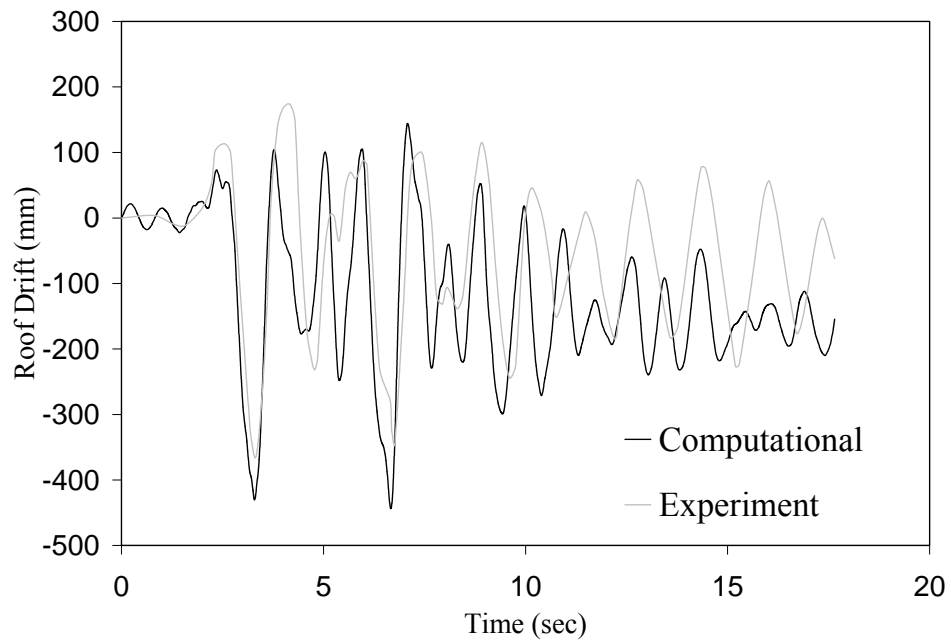


Figure 5.166 show the computational and experimental roof-drift time history results corresponding to the design level and maximum considered earthquake loadings,

respectively. The results for the maximum considered earthquake were produced by subtracting residual drift at the end of the design level earthquake loading. For both sets of results good agreement was attained with experimental data. However, under maximum considered earthquake loading, the residual drift was overestimated, which might be due the fact the analysis following the design basis earthquake loading was performed without any straightening applied to the structure that might lead to excessive residual deformations. Figure 5.167–Figure 5.170 exhibit story shear vs. drift result for the 1st and 2nd story of the test structure. It can be seen that the experimental shear force levels were successfully predicted by the analysis model. There exist some discrepancy in the deformation demand values which might be attributed to the factors that the analysis model could not capture adequately including flexibility of the connections and variation damping across different structural members.

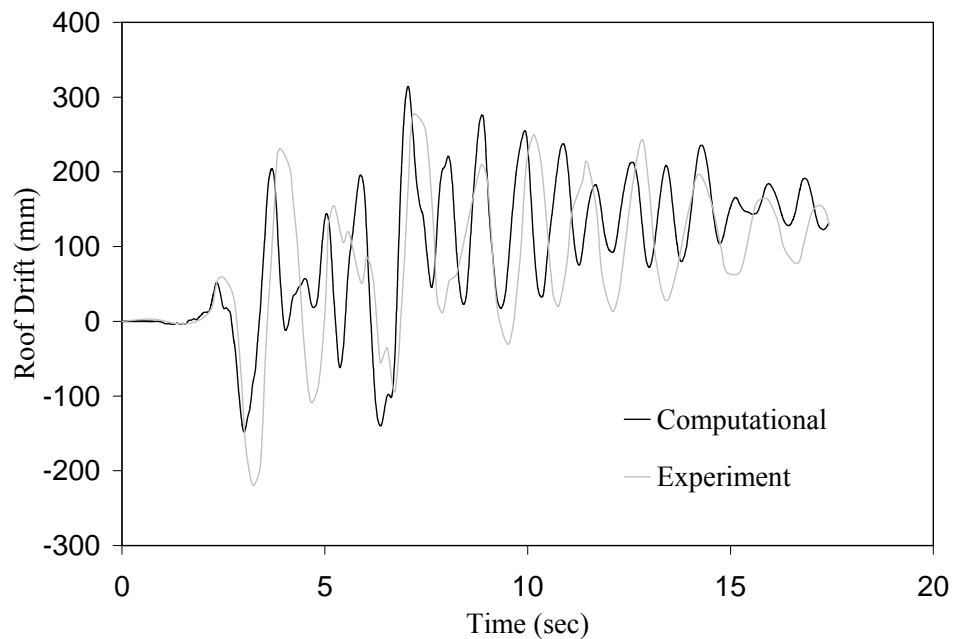


Figure 5.165 Roof Drift Time History Results for Design Basis Earthquake Loading

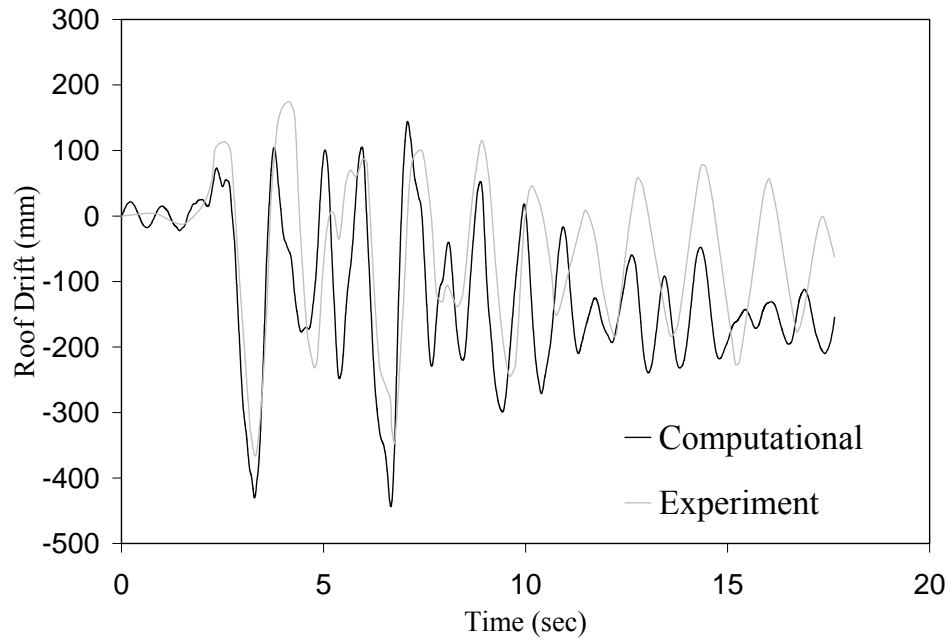


Figure 5.166 Roof Drift Time History Results for Maximum Considered Earthquake Loading

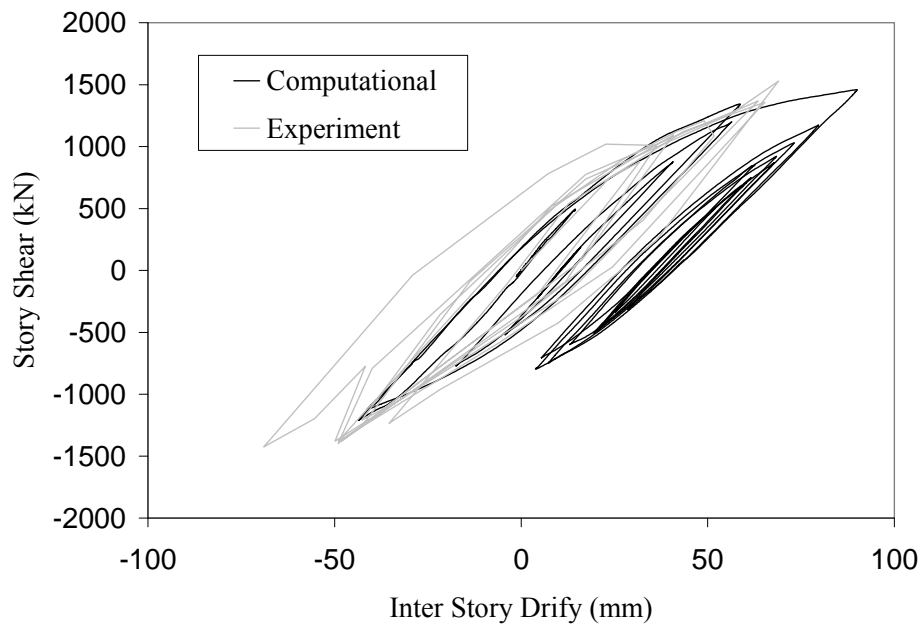


Figure 5.167 Story Shear vs, Intersory Drift Response at the 1st Story for the Design Basis Earthquake Level

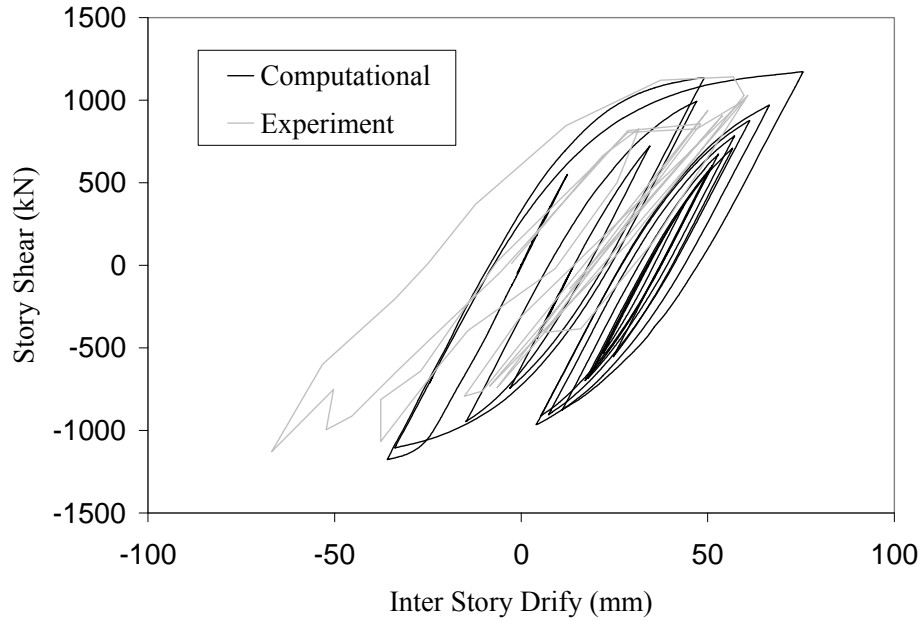


Figure 5.168 Story Shear vs, Intersory Drift Response at the 2nd Story for the Design Basis Earthquake Level

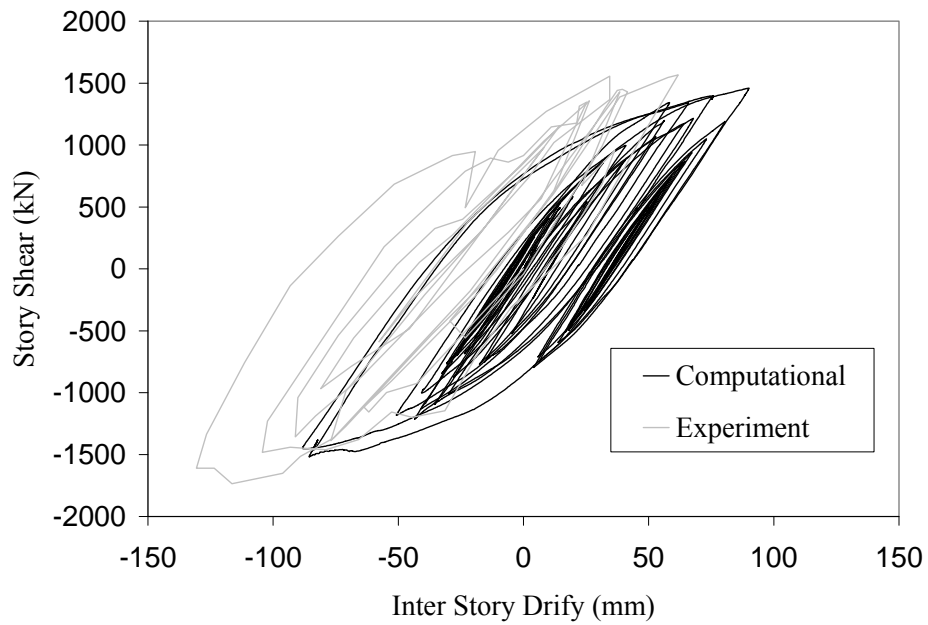


Figure 5.169 Story Shear vs, Intersory Drift Response at the 1st Story for the Maximum Considered Earthquake Level

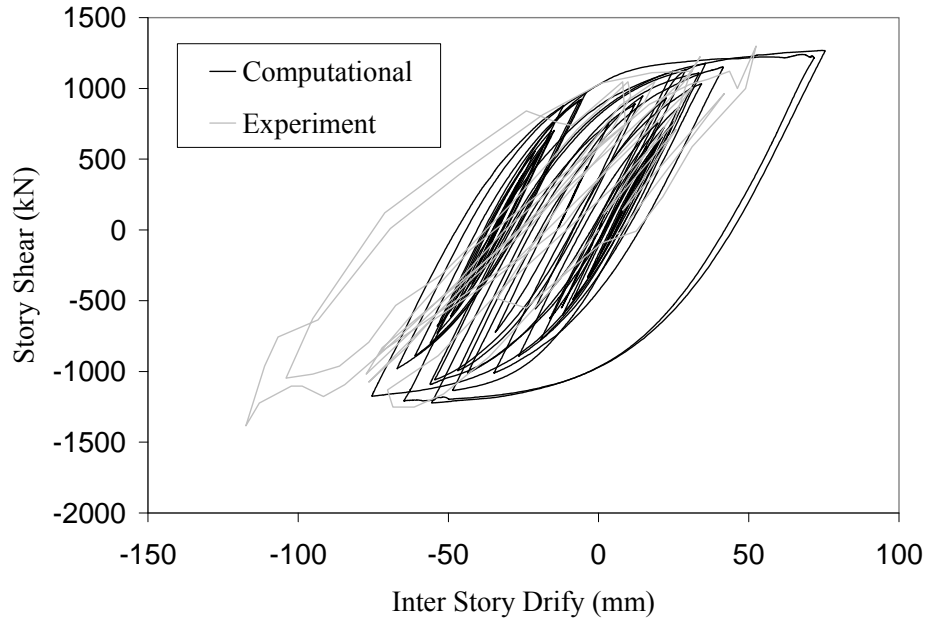


Figure 5.170 Story Shear vs, Intersory Drift Response at the 2nd Story for the Maximum Considered Earthquake Level

5.11. Materially and Geometrically Nonlinear Monotonically-Loaded Steel Girders

In order to verify the local buckling characteristic of steel girders, a total number of 5 specimens were studied by Lukey and Adams (1969). The geometric and material properties of these specimens are summarized in Table 5-16. The specimens were analyzed using the mixed finite element formulation adopting a model as described in Figure 5.171, where steel girder is loaded under three point bending. The computational and experimental results are presented in Figure 5.172 through Figure 5.176 and excellent correlation can be noticed between two sets of data.

Table 5-16 Geometric and Material Properties of Specimens to Verify the Steel Model

Specimen	d (mm)	b_f (mm)	t_f (mm)	t_w (mm)	f_{yf} (MPa)	f_{yw} (MPa)	l_f	l_w	l_c	e_{slbf}	K_{sg} (MPa)
B1	200.2	102.6	5.3	4.4	373.0	396.5	0.419	1.899	1.945	-0.0159	-1103.2
B3	200.2	86.1	5.3	4.4	373.0	396.5	0.352	1.899	1.932	-0.0263	-897.6
B4	200.2	94.0	5.3	4.4	373.0	396.5	0.384	1.899	1.938	-0.0181	-1047.7
C3	250.4	85.9	5.3	4.6	373.2	352.0	0.353	2.190	2.218	-0.0159	-1103.2
C5	250.4	89.9	5.3	4.6	373.2	352.0	0.369	2.190	2.221	-0.0159	-1103.2

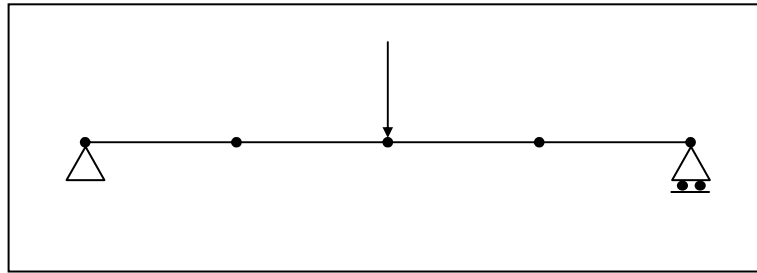


Figure 5.171 Computational Modeling of Specimens by Lukey and Adams (1969)

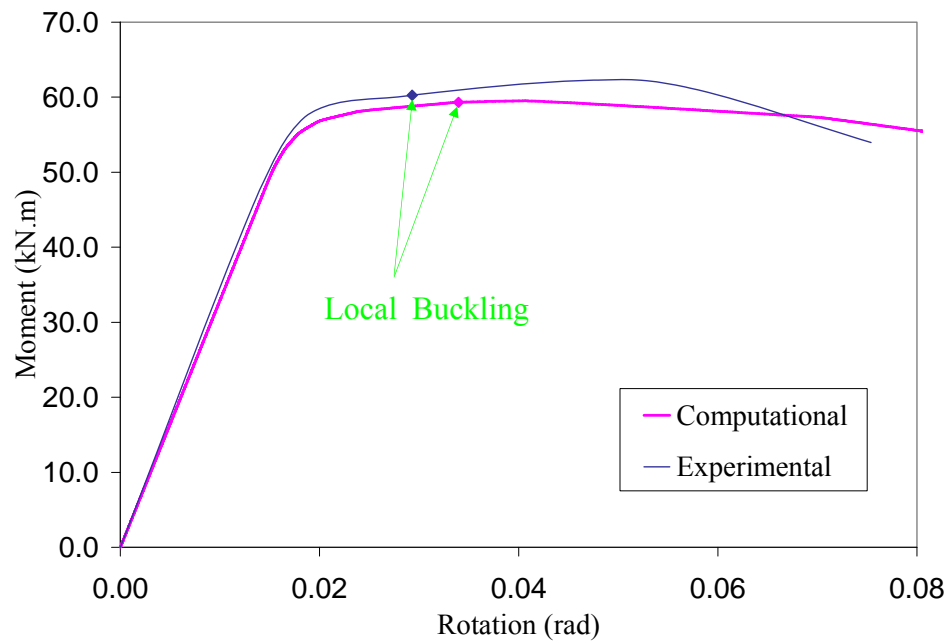


Figure 5.172 Comparison Experimental and Computational Results for Specimen B1 by Lukey and Adams (1969)

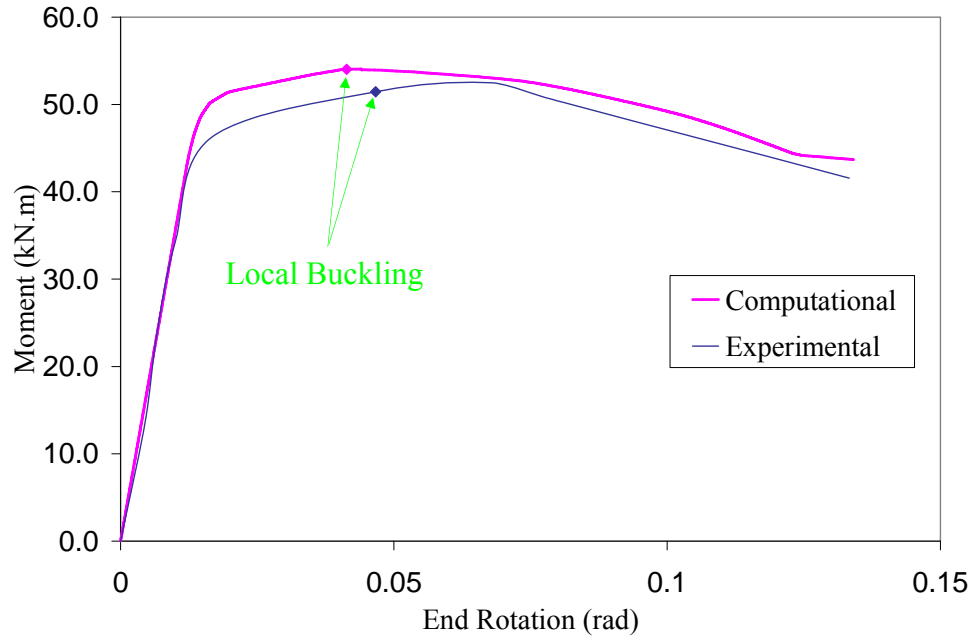


Figure 5.173 Comparison Experimental and Computational Results for Specimen B3 by Lukey and Adams (1969)

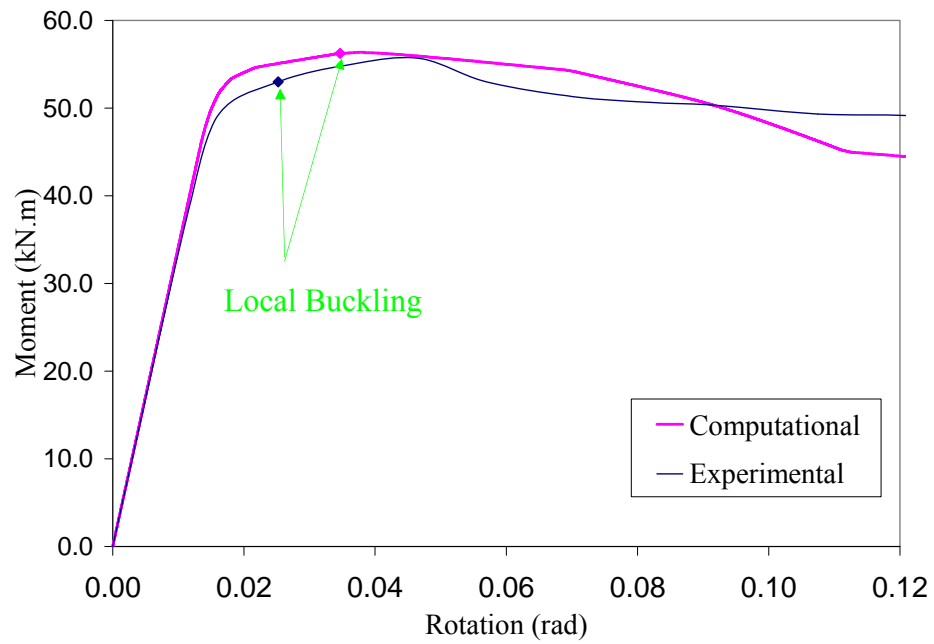


Figure 5.174 Comparison Experimental and Computational Results for Specimen B4 by Lukey and Adams (1969)

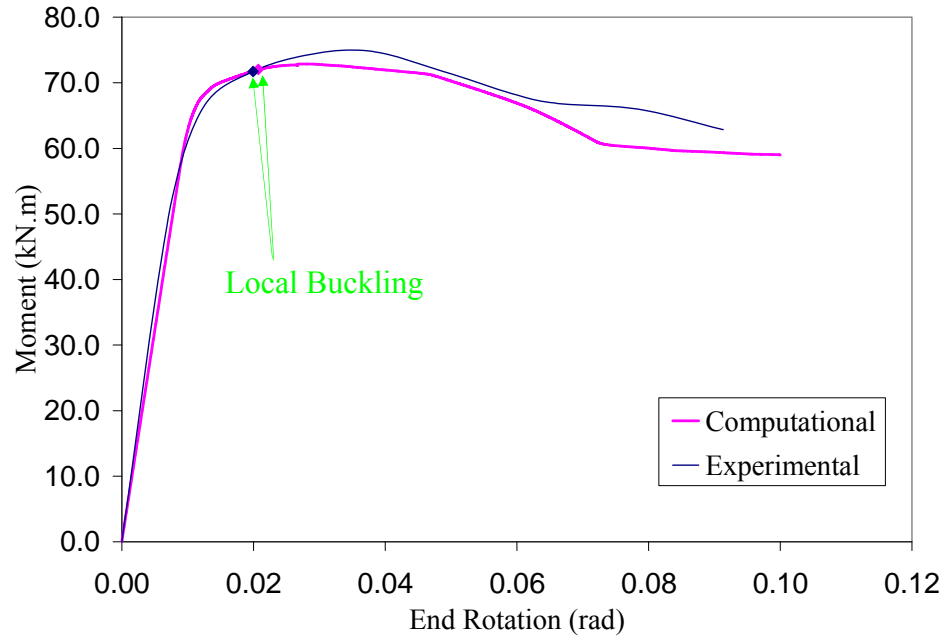


Figure 5.175 Comparison Experimental and Computational Results for Specimen C3 by Lukey and Adams (1969)

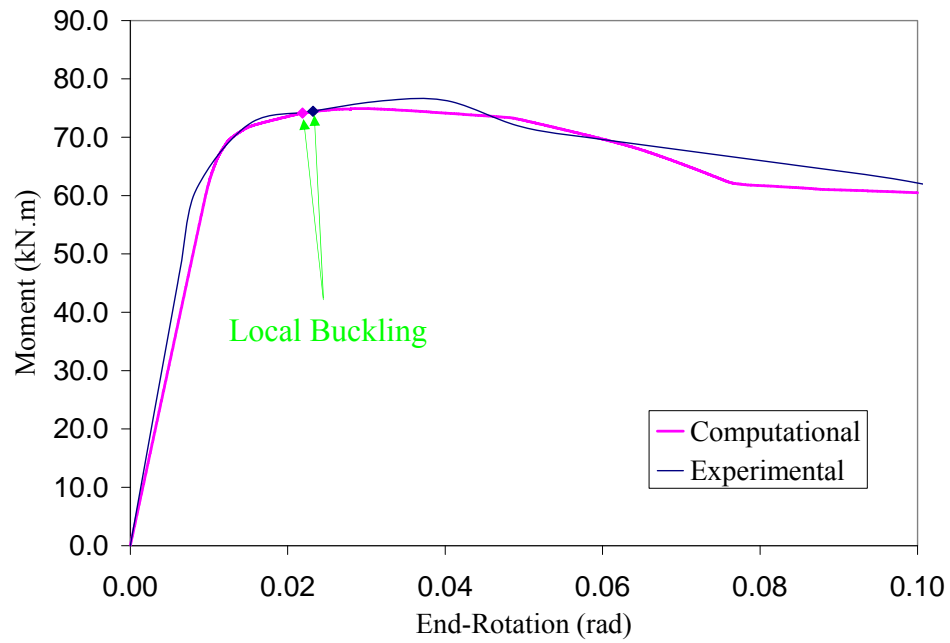


Figure 5.176 Comparison Experimental and Computational Results for Specimen C5 by Lukey and Adams (1969)

5.12. Materially and Geometrically Nonlinear Cyclically-Loaded Steel Girders

The final verification study was performed to test the performance of the mixed finite element formulation in simulating the cyclically loaded steel girders experiencing local buckling damage state. The steel girder subassembly by Kim et al. (2002) was studied as shown in Figure 5.177. A computational model of the test-setup was prepared using the mixed finite element formulation. The column (W24x76) was defined with 4 finite elements while the girder (W30x99) was modeled with 3 elements per member. The number of integration points was selected as 3 and a total number of 10 material fibers were defined for the steel cross-section as shown in Figure 5.136. A good correlation was achieved between the experimental and computational results as can be seen Figure 5.178.

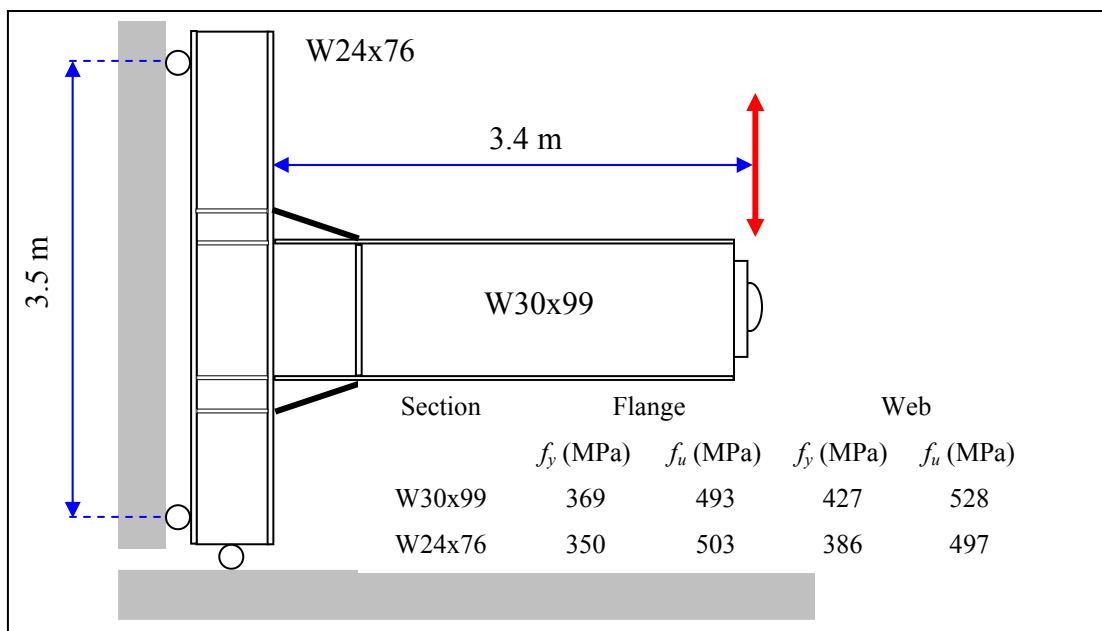


Figure 5.177 Test Setup for RC03 (Kim et al., 2002)

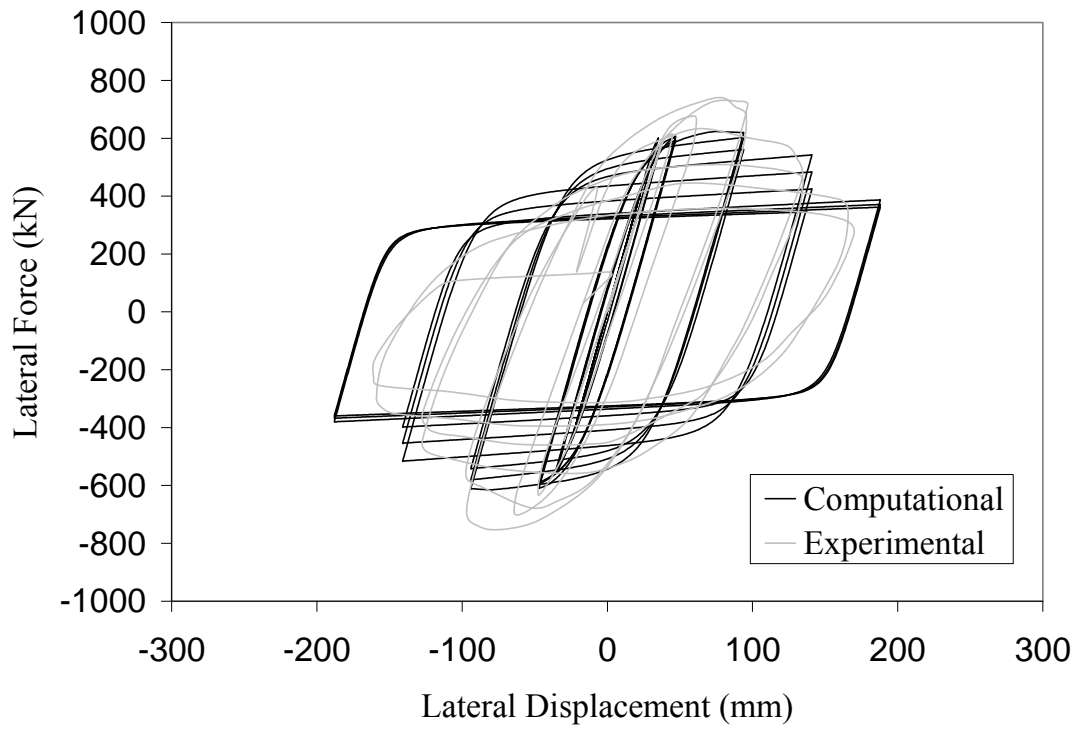


Figure 5.178 Comparison Experimental and Computational Results for Specimen RC03
by Kim et al. (2002)

Chapter 6

6. Seismic Demand Evaluation of RCFT Frames

6.1. Introduction

The effects of earthquake induced forces on structures in the forms of energy, force, and deformation, and other structural response parameters are often termed as seismic demand. Within a performance-based design framework, seismic demand evaluation is critical for understanding the typical inelastic characteristics of structures and it sheds light on the significance of the limit states, progression of damage, and coupling of the global and local response. Seismic demand evaluation is often conducted by analyzing multiple structures under a series of seismic loading having various intensities. The information obtained from these analyses can be used to establish a relation between structural response parameters and the intensity of the hazard level. Knowledge about the load and deformation levels likely to be experienced by the RCFT frames thus provides guidance to engineers in design decisions to satisfy the targeted performance objectives. In addition, the dispersion in the structural response parameters helps quantify the uncertainties and randomness in the demand evaluation process. The quantified expressions of uncertainty and randomness are often introduced as demand factors in the design provisions.

The chapter reports the results of demand analysis of RCFT frames through nonlinear time history analyses. Three-story and nine-story frame structures were analyzed under a suite earthquake records representing 2% in 50 year, 10% in 50 year, and 50% in 50 year hazard levels. The results are presented in terms of structural response parameters describing the structural response with a focus on considering the composite interaction observed in RCFT frames. The statistical measures of the structural response are discussed. Through these examples, a general methodology for characterizing demand within RCFTs at several local and global levels is presented.

6.2. Selection of Ground Motion Records

The selection of earthquake records representing the targeted hazard level is an important step in seismic demand analysis that affects the scatter in the structural response parameters from nonlinear time history analysis. Therefore, the number and type of the records should be chosen in a way that the record-to-record variability of the structural response is reduced. This can be achieved by performing the selection process based on ground motion parameters that have adequate representation of the intensity, frequency content, and duration properties since they significantly affect the inelastic behavior of structures. However, the derivation of such a comprehensive parameter is challenging since it is often dependent on the structural system and the performance level being evaluated (Krawinkler et al., 2003).

In seismic design provisions, earthquake loading is often represented in the form of an acceleration spectrum derived for a single degree-of-freedom system. The shape and amplitude of the acceleration spectra define the ground motion characteristics corresponding to the desired hazard level. In this research study, the spectral acceleration value at the fundamental period of the structure (S_a) will be used as the primary ground motion parameter while selecting the earthquake records. Despite the fact that S_a alone is not the governing parameter to affect the seismic demand, the biases in the demand evaluation that can be generated due to the ignorance of the frequency content and duration can be reduced by selecting the earthquake records from a narrow band of magnitude and distance pairs (Krawinkler et al., 2003; Bommer and Acevedo, 2004).

There exist three different sources where ground motion records are available to the engineers. Artificial ground motion records are generated through deriving a power spectral function from the acceleration spectrum and then developing sinusoidal signals with random phase angles and amplitudes. Integrating these signals and performing iterative operations produces ground motion records exhibiting a very close match with the acceleration spectrum given in the design provisions. However, the use of artificial ground motion records is often not recommended due to their common high frequency content with excessive number of cycles (Bommer and Acevedo, 2004). Alternative to

artificial ground motion records, synthetic ground motion records can be derived from advanced seismological models. Despite their comprehensiveness in accounting for a large number seismological parameters (e.g., path, site effects), the use of synthetic ground motion records requires significant expertise in seismology (Bommer and Acevedo, 2004). The last category of ground motion records are obtained from past earthquakes around the world. The current databases compiled at several earthquake research institutes offer detailed search options with respect to an array of characteristics of past earthquakes. In this research study, the demand evaluation will be performed using real earthquake records. A single database will be utilized to obtain the records so that a uniform processing of the records will be ensured.

The earthquake records can be categorized as near-field and far-field with respect to their location to the active fault. The near field earthquake records exhibit distinct directivity effects creating a high energy demand for the structures in the form a pulse-type motion. The near-fault earthquake records often have a large intensity level that breach the acceleration spectrum available in the design codes. In this research study, the near fault earthquake records will be eliminated while conducting the seismic demand analysis and only far-field earthquake records will be considered. This approach works well for western US earthquakes since the extent of damage targeted in performance-base design provisions are relevant for far-filed earthquake records (Krawinkler et al., 2003).

The ground motion is subjected to amplification or deamplification as it propagates through the soil strata. The rigidity of the soil layer underlying the structures affects the intensity of the ground motions. This necessitates including site classification as a parameter while choosing the earthquake records for demand evaluation. It was assumed that the buildings considered in this study are located on stiff soil conditions.

Medina (2002) collected a total number 40 earthquake records from the PEER strong motion database, which were all recorded on NEHRP Site Class D soil. The magnitude and distance pair of the records were identified as Large Magnitude Small Distance without any pulse-type near-field characteristics. The earthquake records used in this research study came from set provided by Medina (2002).

The scaling of the earthquake records to match the design acceleration spectrum was performed based on spectral acceleration (S_a) to minimize the difference between design and median spectra for the first mode period of the structure. The records with a scale factor greater than 4 were eliminated since large scaling reduces the advantage of using real records and also weak records scaled to a higher level may produce lower demands than unscaled records (Shome et al., 1998; Bommer and Acevedo, 2004; Iervolino, 2004). The number of earthquake records was further reduced based on the study by Shome et al. (1998), where it was concluded that “the scaling of records within a bin to the bin median spectral acceleration produces unbiased estimates of the nonlinear response median”. The earthquake records were selected in a manner that the S_a on the median spectrum (S_a^m) attains a value close to the target S_a on the design response spectrum (S_a^d) as shown in Figure 6.1.

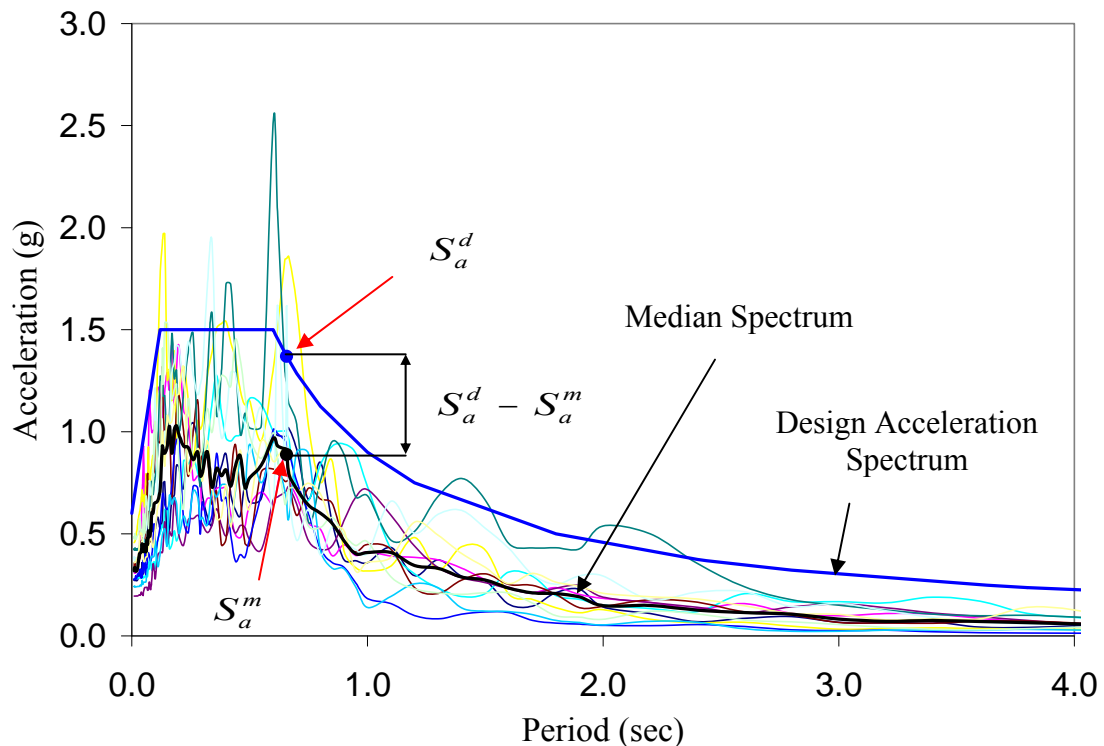


Figure 6.1 Selection of Earthquake Records

6.2. Seismic Response of RCFT Frames

Multiple three-story RCFT frame structures were subjected to earthquake records representing 2% probability of exceedence in 50 years termed as “2%/50” and to earthquake records with 10% probability of exceedence in 50 years termed as “10%/50”. The structures were designed in three-dimensions following up-to-date design provisions including ASCE 7-02 (2003), IBC (2003), AISC-LRFD (2005), and AISC *Seismic Provisions for Structural Steel Buildings 2002* (LaFore and Hajjar, 2005; Gartner and Hajjar, 2006). See LaFore and Hajjar (2005) and Gartner and Hajjar (2006) for details of the design of these three-dimensional structures and the associated two-dimensional planar frames that were extracted and analyzed in this work. The RCFT columns of the frames were designed utilizing a wide range of material and geometric properties. The variation generated in the proportions of the steel and concrete among the designed frames revealed the sensitivity of the seismic behavior against the degree and type of composite interaction. Table 6-1 illustrates the ranges of material and geometric properties of the RCFT columns used in the studied frames.

Table 6-1 Summary of Geometric and Material Properties of RCFT Columns

Frame Designation	# of Stories	f'_c (MPa)	f_y (MPa)	D/t	L/D
IIIa	3	27	317	35, 50	7, 8
III d	3	110	551	67	7

The buildings were all assumed to be located in Los Angeles. The soil conditions were assumed to be on NEHRP Site Class D. Utilizing the NEHRP Maximum Considered Earthquake Maps and adjusting with respect to the soil conditions, the maximum considered earthquake spectral response acceleration for short period (S_{MS}) and the maximum considered earthquake spectral response acceleration at 1 period (S_{MI}) were obtained as 1.5g and 0.9g, respectively. Therefore, the design spectrum representing earthquake records to have 2%/50 and 10%/50 hazard levels can be derived as shown in Figure 6.2 assuming 2% damping.

The masses of the designed frames were assumed to be lumped at the joints. The dead loads and the proportion of the live loads due to movable partitions were considered to contribute to the total mass. The computational models were constructed without

consideration of the connection regions. The ignorance of the deformation of the panel zone regions was assumed to be compensated with the reduced stiffness introduced by using centerline dimensions of the columns and girders. Despite the crudeness introduced in strength demands, this approach estimates the deformation demands with sufficient accuracy so that they can be used in performance evaluations, which are often driven by displacements (Gupta and Krawinkler, 1999).

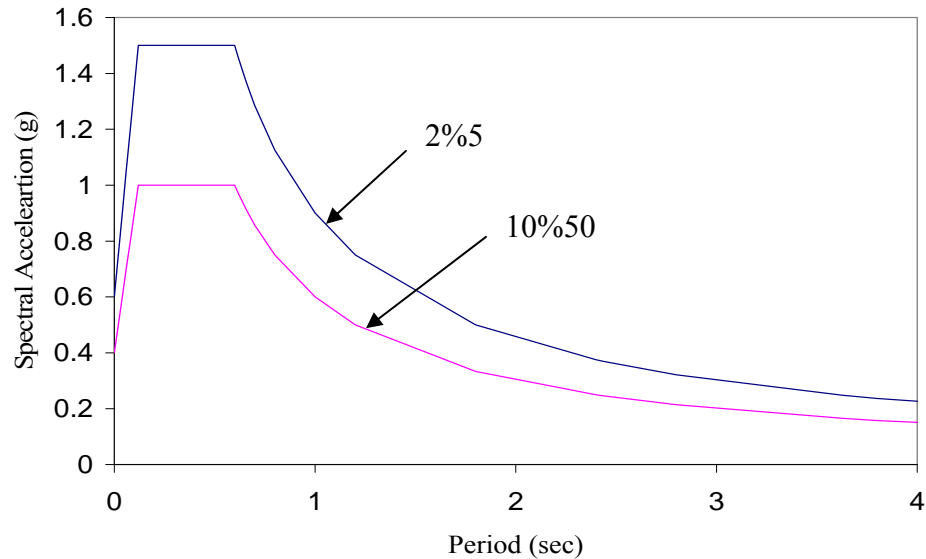


Figure 6.2 Spectrum of Acceleration at Various Hazard Levels

Both RCFT columns and steel girders were analyzed using the mixed-finite element method presented in Chapter 2. The RCFT columns were simulated with one finite element and three integration points along the element length. The steel girders were modeled with multiple elements per member as needed to account for the transverse point loads due to gravity from the out-of-plane beams framing into the span of the girders. The number of integration points for the beams were also kept as three. The number material fibers along the depth of the RCFT and steel cross-sections were chosen as eight and ten, respectively. Considering the verification studies presented in Chapter 5, the aforementioned mesh density adopted in the analysis models was found to be satisfactory. The Newmark-Beta ($\gamma = 0.5$, $\beta = 0.25$) time integration scheme was employed as the primary numerical algorithm to solve for the dynamic response of the structures. A mass and stiffness proportional damping was assumed, where the damping

matrix (C) of the structures was calculated combining their mass (M) and stiffness (K) matrices as follows:

$$C = \alpha_c M + \beta_c K \quad [6.1]$$

where: α_c is the mass proportionality factor, β_c is the stiffness proportionality factor

The calculation of α_c and β_c was conducted by assigning a viscous damping ratio (ξ) of 2% for the 1st and 3rd modes of the structures. The 2% damping ratio was selected assuming that the response of RCFT frames exhibit similar damping characteristics with steel structures (Muhumud, 2004; Herrera, 2005;). Considering Rayleigh damping α_c and β_c were calculated as follows:

$$\frac{1}{2} \begin{bmatrix} \frac{1}{w_1} & w_1 \\ \frac{1}{w_3} & w_3 \end{bmatrix} \times \begin{bmatrix} \alpha_c \\ \beta_c \end{bmatrix} = \begin{bmatrix} \xi \\ \xi \end{bmatrix} \quad [6.2]$$

$$\alpha_c = \xi \times \frac{2 \times w_1 \times w_3}{w_1 + w_3} \quad \beta_c = \xi \times \frac{2}{w_1 + w_3} \quad [6.3]$$

where: w_1 is the 1st mode frequency, w_3 is the 3rd mode frequency

The nonlinear time history analyses were conducted following the application of 100% of the gravity loads consisting of live and dead loads. The factored gravity loads were sustained on the structure during the application of the earthquake loading (FEMA 356, 2000). The time step for the analysis was selected to be smaller than the time interval defined for the ground motions records. Therefore, the time step was often selected to be less than 0.01 sec.

6.2.1. Time-History Analysis Results

Frame IIIa (as classified by LaFore and Hajjar, 2005) was chosen to represent RCFT structures having moderate values of geometric and material properties. As it is detailed in Figure 6.3, Frame IIIa consisted of three stories and four bays of RCFT columns and steel girders. The periods of vibration corresponding to the first three modes were determined by performing an eigen value analysis, which produced 0.618

sec, 0.349 sec, and 0.201 sec for the 1st, 2nd, and 3rd modes, respectively. From Equations 6.2 and 6.3, α_c of 0.307 and β_c of 0.0009656 were calculated.

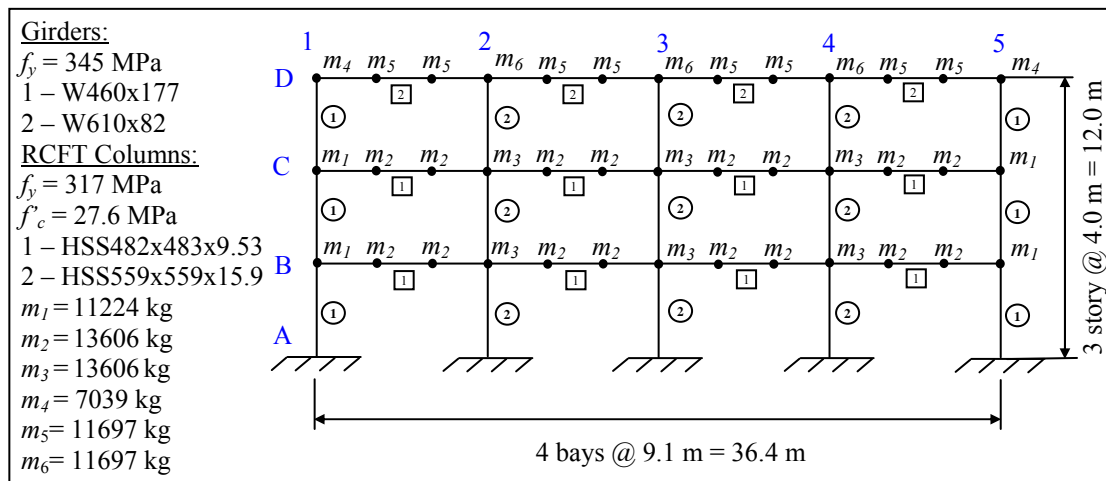


Figure 6.3 Description of Frame IIIa (LaFore and Hajjar, 2005)

A total number of 12 ground motion records were selected. Table 3-1Table 6-2 summarizes the characteristics of the chosen earthquake records including peak ground acceleration (PGA), moment magnitude (M_w), distance to the source (R_s), duration (t), and the scaling factor to 2%/50 design acceleration spectra. It can be noticed from Table 6-2, the earthquake motions were recorded between 14 to 40 km distances away from the fault. The response spectrum of the scaled ground motions with respect to S_a can be seen in Figure 6.4.

Table 6-2 Earthquake Records Selected For Frame IIIa Scaled to 2%/50

Record ID	Event	Year	M_w	R_s (km)	PGA(g)	Duration (sec)	Scale Factor
<i>IV79chi</i>	Imperial Valley	1979	6.5	28.7	0.27	40.0	1.48
<i>LP89cap</i>	Loma Prieta	1989	6.9	14.5	0.443	40.0	0.97
<i>LP89g04</i>	Loma Prieta	1989	6.9	16.1	0.212	39.9	1.80
<i>LP89hda</i>	Loma Prieta	1989	6.9	25.8	0.279	39.6	1.45
<i>NR94cen</i>	Northridge	1994	6.7	30.9	0.322	30.0	1.83
<i>NR94cnp</i>	Northridge	1994	6.7	15.8	0.42	25.0	0.70
<i>NR94far</i>	Northridge	1994	6.7	23.9	0.273	30.0	1.47
<i>NR94fle</i>	Northridge	1994	6.7	29.5	0.24	30.0	1.69
<i>NR94stc</i>	Northridge	1994	6.7	13.3	0.368	30.0	2.14
<i>NR94stin</i>	Northridge	1994	6.7	30	0.474	31.6	1.73
<i>SH87icc</i>	Superstition Hills	1987	6.7	13.9	0.358	40.0	1.71

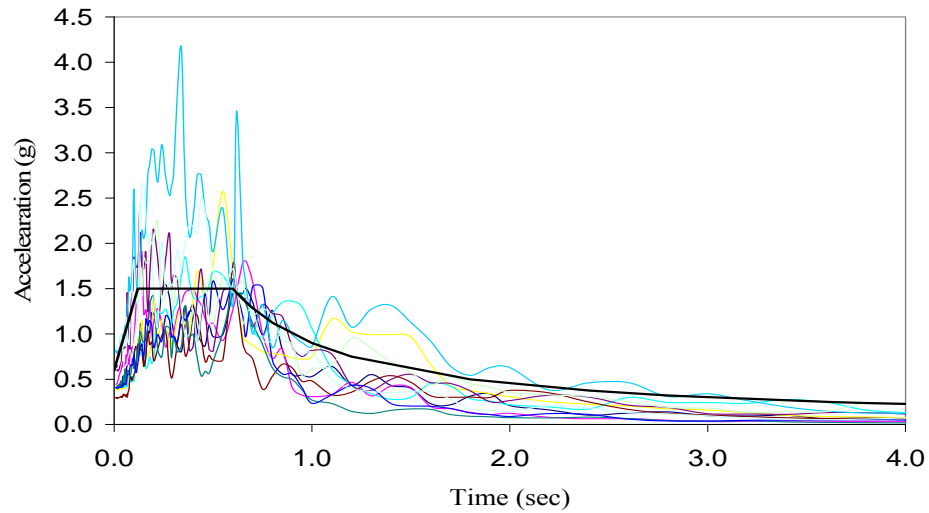


Figure 6.4 Scaled Earthquake Records of Frame IIIa to 2%50

The roof displacement (Δ_r) time history results of Frame IIIa is presented in Figure 6.5 as a percentage of the height of the frame (h_r). The maximum drift was observed between 5 sec to 15 sec of the ground motion records. The Δ_r demand values for the analyses are documented in Table 6-3 in terms of mean (μ) and 84 percentile ($\mu+\sigma$) values. The 84 percentile was assumed to be approximately equal to mean plus one standard deviation (σ) if normal distribution is assumed. Table 6-3 shows that the largest maximum and minimum roof drift demands were obtained for earthquake records of NR94stc and NR94stn.

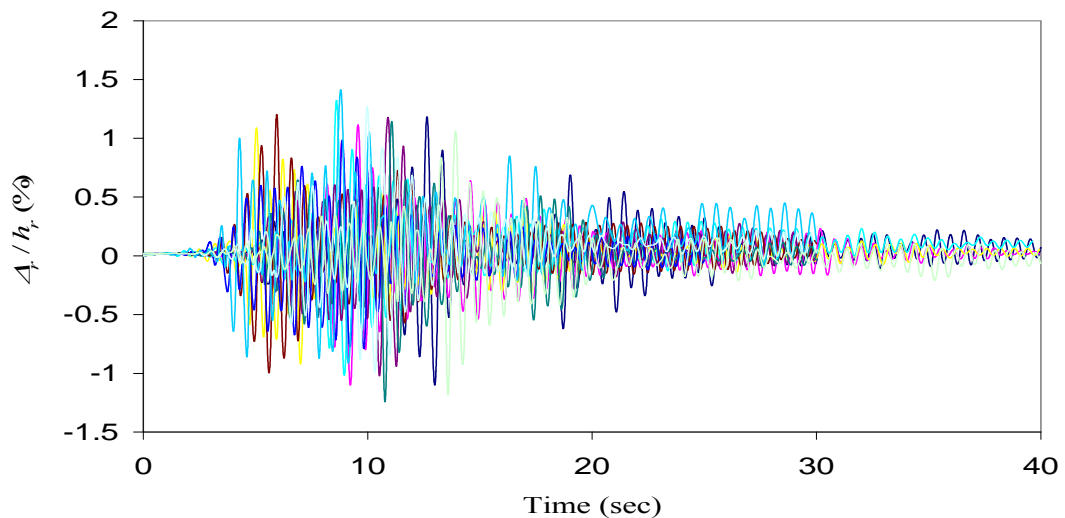


Figure 6.5 Roof Displacement Time History for Frame IIIa (2%/50)

Figure 6.6 presents the story shear (V_s) vs. interstory drift ratio (Δ_s) response of Frame IIIa for each story. Interstory drift ratio is adopted as the primary engineering demand parameter in the current performance-based design provisions (FEMA-350, 2000; FEMA-356, 2000). Both V_s and Δ_s attain their maximum values at the 1st story. The magnitude of the demands exhibited a reduction in the upper stories. The mean and 84 percentile values for the maximum and minimum interstory drift ratios and shear forces can be found in Table 6-4. The response of RCFT columns was studied based on their moment vs. axial force response as it is shown in Figure 6.7 for the exterior columns at the 1st, 2nd and 3rd stories (axial compression is shown as positive in the interaction diagram figures in this chapter). It was found that the 1st story column reaches to the highest force demands and the maximum load state breaches the cross-section strength surface given in the AISC-LRFD (2005) design specification in the bending moment and axial force space. The load state for the 2nd and 3rd story column remained well within the AISC-LRFD (2005) interaction surface.

Table 6-3 The Maximum and Minimum Roof Displacement Values (Δ_r) of IIIa for 2%/50 Earthquake Records

Record ID	Δ_r (max) (%)	Δ_r (min) (%)
IV79chi	1.184	-1.101
LP89cap	1.116	-1.101
LP89g04	1.088	-0.919
LP89hda	1.322	-1.017
NR94cen	1.178	-1.021
NR94far	1.204	-0.996
NR94stn	1.143	-1.243
NR94cnp	0.985	-0.789
NR94stc	1.414	-0.912
NR94fle	1.271	-0.990
SH87icc	1.061	-1.185
μ	1.179	-1.025
$\mu + \sigma$	1.301	-0.896

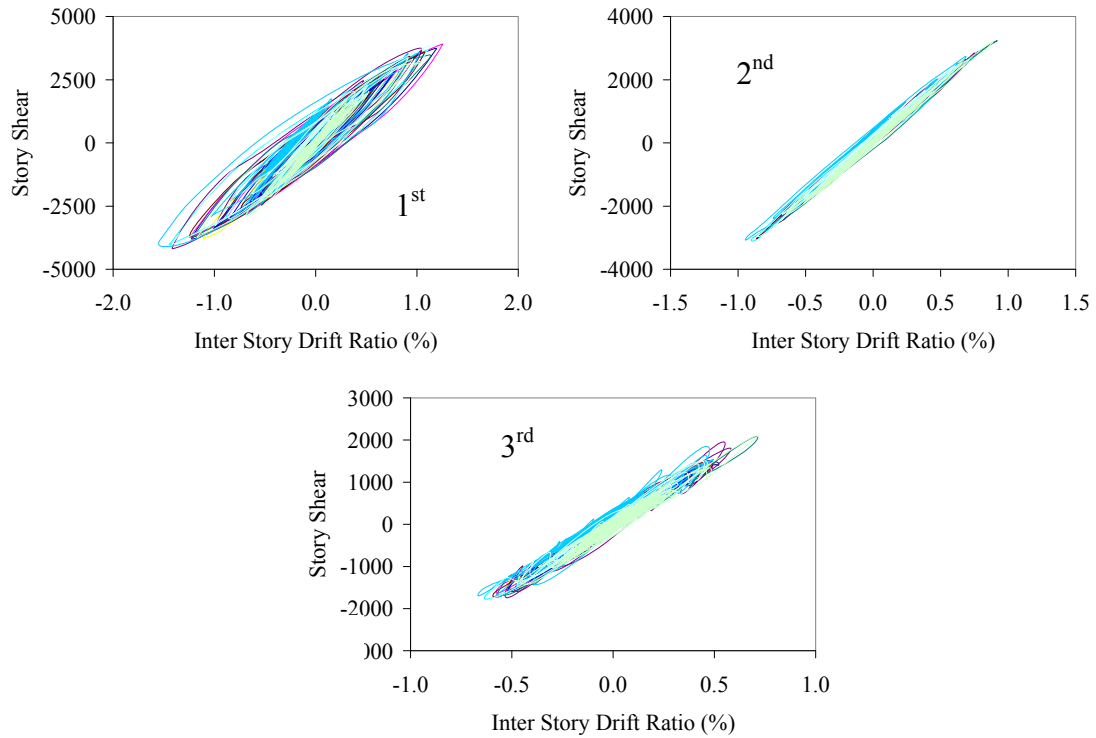


Figure 6.6 Interstory Drift Ratio and Shear Force Demand at 1st, 2nd and 3rd stories
(Frame IIIa, 2%/50)

Table 6-4 Maximum and Minimum Story Shear and Interstory Drift Ratios

Record ID	Δ_s (max) (%)	Δ_s (min) (%)	V_s (max) (kN)	V_s (min) (kN)
IV79chi	1.25	-1.25	3904	-3731
LP89cap	1.19	-1.22	3739	-3802
LP89g04	0.89	-1.11	3177	-3785
LP89hda	1.10	-1.45	3660	-4030
NR94cen	1.05	-1.42	3750	-4178
NR94far	1.07	-1.24	3593	-3716
NR94stn	1.13	-1.21	3483	-3735
NR94cnp	0.83	-1.01	3131	-3424
NR94stc	1.02	-1.55	3579	-4102
NR94fle	1.12	-1.41	3827	-4001
SH87icc	1.03	-1.17	3311	-3742
μ	1.06	-1.28	3560	-3841
$\mu + \sigma$	1.19	-1.11	3818	-3624

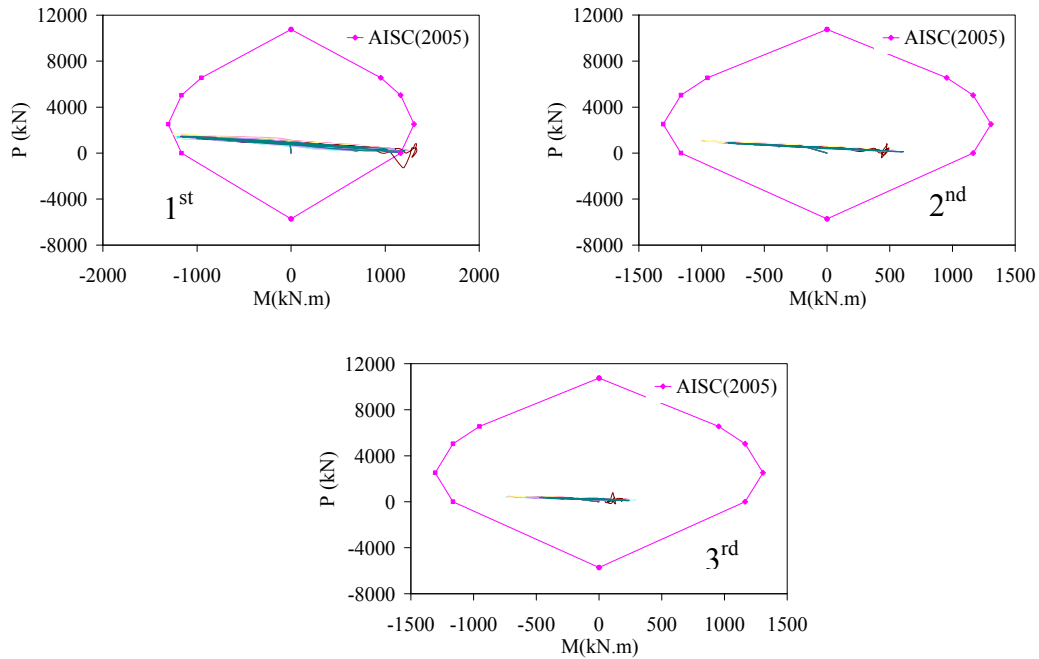


Figure 6.7 Axial Force and Bending Moment Interaction Demands for Edge Columns at 1st, 2nd and 3rd Stories (Frame IIIa, 2%50)

Tort and Hajjar (2004) proposed a deformation-based (\hat{D}) damage function equation to quantify the amount of damage experienced by the RCFT members as given in Equation 6.4.

$$\hat{D} = \frac{d_{curr}}{d_o} \quad [6.4]$$

where: d_{curr} - the deflection of the structural member at the point in the loading history at which damage is being assessed

d_o - the deflection attained when the peak load is reached

For the RCFT columns of Frame IIIa, the \hat{D} values were obtained utilizing the time-history analysis results corresponding to the ground motion records given in Table 6.2. While evaluating \hat{D} , d_o was determined from the static push-over analysis of the structure, where the chord rotation (R) vs. moment response was extracted for each RCFT column. The chord rotation of a column was calculated as the ratio of lateral displacement to the element length. d_o was assumed to be attained when the stiffness of

the RCFT column becomes 10% of its initial value. The static push-over analysis of the structure was performed using a displacement-controlled solution algorithm (Yang and Kuo, 1994), where the structure is subjected to a monotonically increasing lateral displacement history while the factored gravity loads are sustained on the structure. The distribution of the lateral loads was determined according the guidelines in FEMA-256 (2000). Figure 6.8 shows the base-shear (V_b) vs. maximum inter-story drift response of Frame IIIa from the static push-over analysis. In Figure 6.9, moment vs. R response from the static push-over analysis and time history analysis are superimposed for the windward interior column at the first story of the frame. d_{curr} was obtained from the time history analysis results as the mean maximum chord rotation experienced during the ground motions while d_o was determined from the static load deformation response when the stiffness reduces to a level less than 10% of its initial value. \hat{D} was calculated as the ratio of d_{curr} and d_o . A similar methodology was also pursued for the remaining RCFT columns to calculate \hat{D} . The distribution of the mean \hat{D} values across all of the RCFT columns is illustrated in Figure 6.10. It can be seen that mean \hat{D} values ranges from 0.41 to 1.04. The value of \hat{D} the exterior columns is larger in the first story and it diminishes in a consistent manner toward the third story. On the other hand, the interior columns experienced the largest \hat{D} value in the first and third stories. The discrepancy in the damage distribution between the exterior and interior columns is attributed to the effect of factored gravity loads, which has more impact on the top exterior columns due to the reduced stiffness at the steel girder to RCFT column junction points. Table 6-5 documents the parameters of d_o and mean d_{curr} values that were used to obtain mean \hat{D} values. In Table 6-5, d_o and d_{curr} were expressed in terms of chord rotation (R) of the RCFT columns.

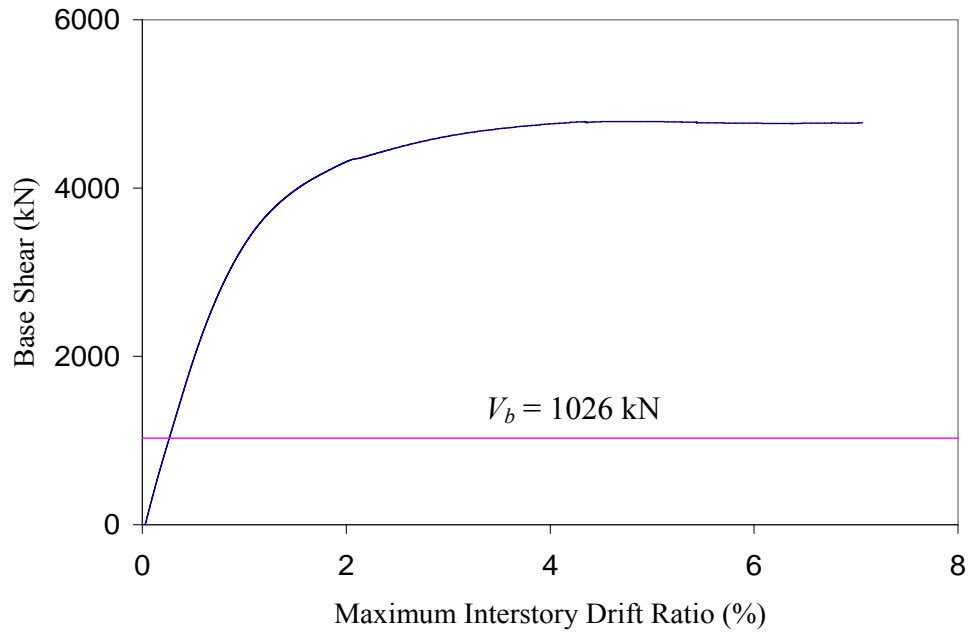


Figure 6.8 Push-Over Response of Frame IIIa

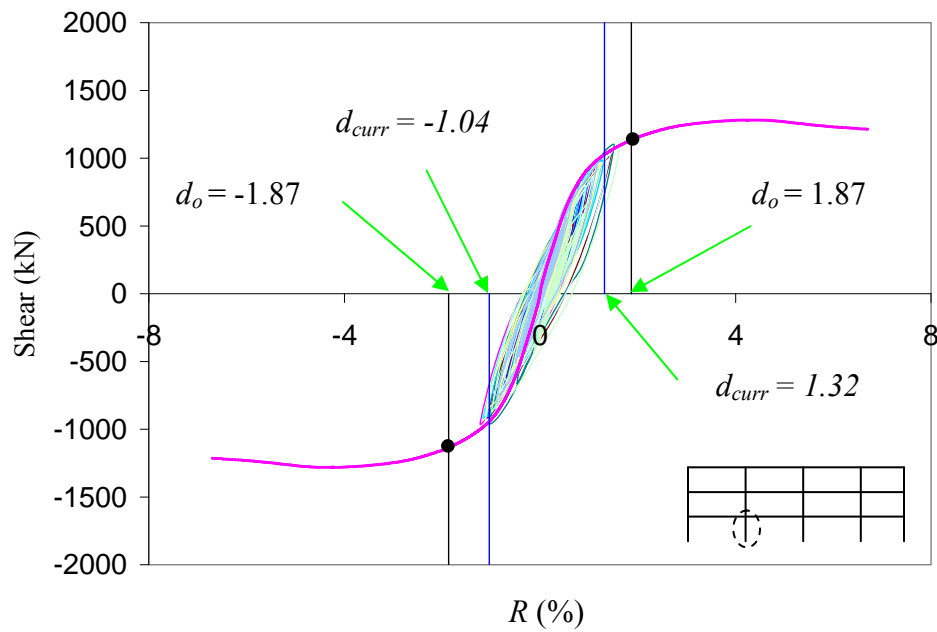


Figure 6.9 Push-Over vs. Time History Response of 1st Story Interior Column (IIIa, 2%/50)

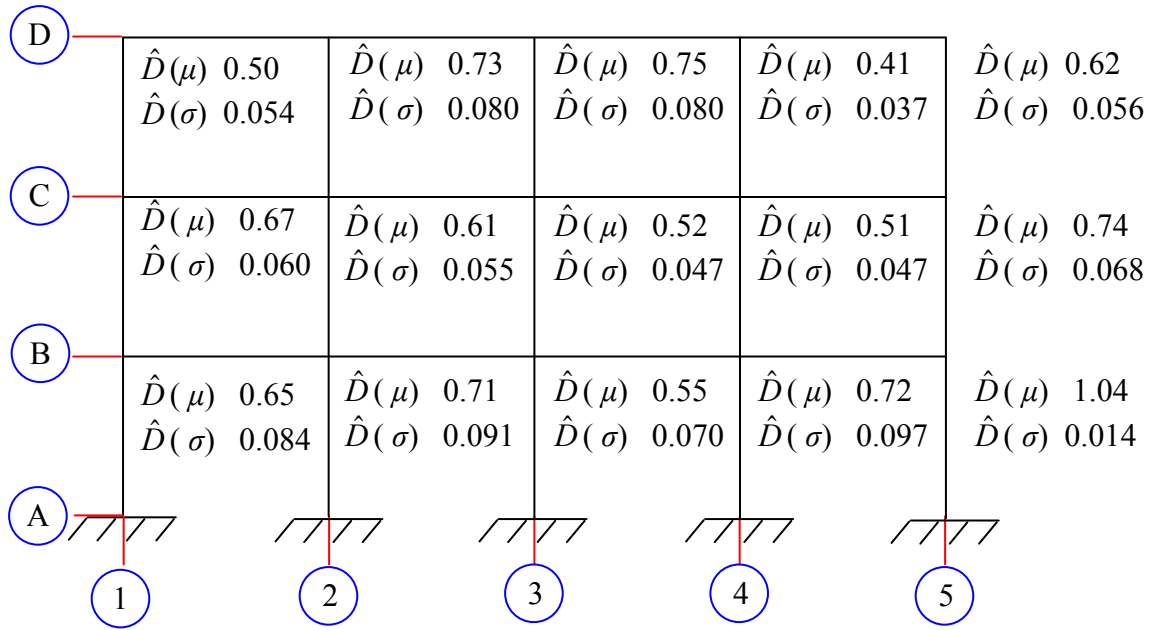


Figure 6.10 Distribution of Mean Damage Function Values for the RCFT Columns

Table 6-5 Damage Function Parameters of RCFT Columns of Frame IIIa for 2%/50 Hazard Level

RCFT Column	d_{curr}	d_o	$\hat{D} = \frac{d_{curr}}{d_o}$
	R (%)	R_o (%)	
A1-B1	1.32	2.04	0.65
B1-C1	1.37	2.01	0.68
C1-D1	1.01	1.90	0.53
A2-B2	1.32	1.87	0.71
B2-C2	1.37	2.19	0.63
C2-D2	1.02	1.28	0.80
A3-B3	1.32	2.41	0.55
B3-C3	1.37	2.59	0.53
C3-D3	1.02	1.24	0.82
A4-B4	1.25	1.68	0.74
B4-C4	1.34	2.57	0.52
C4-D4	1.01	2.40	0.42
A5-B5	1.24	1.18	1.06
B5-C5	1.34	1.77	0.76
C5-D5	1.00	1.54	0.65

The local damage states of the RCFT members were found to be concentrated at the bottom of the 1st story columns. For a representative ground motion record and for a representative RCFT column, Figure 6.11 illustrates the distribution of the limit states attained by the steel tube and concrete core material fibers as percentages of the total number of steel and concrete fibers. It was found that the tensile strain experienced by all of the concrete fibers breached the strain level to initiate cracking. 50% of the concrete fibers underwent high compressive strain levels leading to concrete crushing. The yielding limit state was found to be attained by all of the steel tube fibers. Approximately 6% of the steel tube fibers exhibited local buckling.

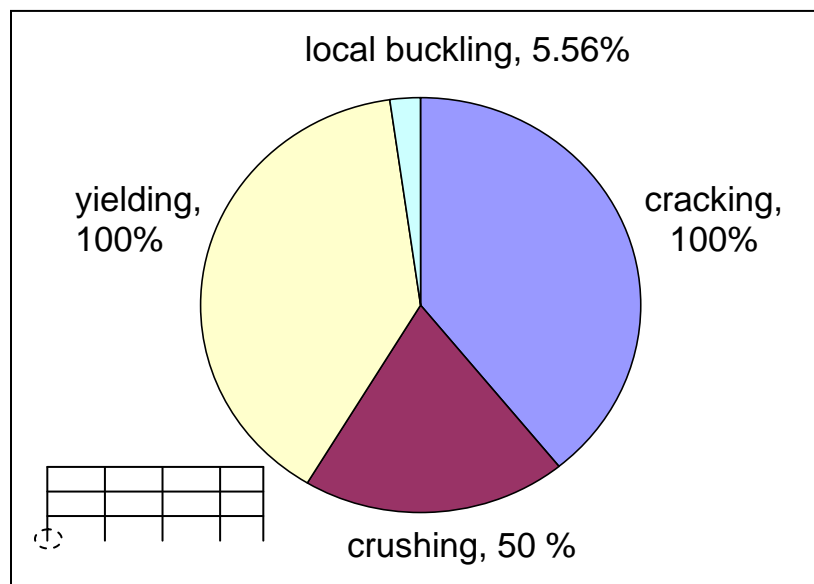


Figure 6.11 Damage Distribution of RCFT Cross-Section at the Support under IV79 Ground Motion (Frame IIIa, 2%/50)

A similar methodology to the maximum considered earthquake hazard level was followed while selecting the earthquake records representing 10%/50 hazard level, which is often referred as design level earthquake. A total number 10 ground motion records were selected as described in Table 6-6. The earthquake records were scaled with respect to the design spectrum as shown in Figure 6.12. The spectral acceleration at the first mode period (S_a) was determined as 0.971g producing scale factors ranging from 0.47 to 1.38.

Table 6-6 Earthquake Records Selected for Frame IIIa Scaled to 10%/50 Hazard Level

Record ID	Event	Year	M_w	R (km)	PGA(g)	Duration (sec)	Scale Factor
<i>IV79chi</i>	Imperial Valley	1979	6.5	28.7	0.27	40.0	0.99
<i>LP89cap</i>	Loma Prieta	1989	6.9	14.5	0.443	40.0	0.65
<i>LP89g04</i>	Loma Prieta	1989	6.9	16.1	0.212	39.9	1.20
<i>LP89hda</i>	Loma Prieta	1989	6.9	25.8	0.279	39.6	0.97
<i>NR94cen</i>	Northridge	1994	6.7	30.9	0.322	30.0	1.22
<i>NR94cnp</i>	Northridge	1994	6.7	15.8	0.42	25.0	0.47
<i>NR94far</i>	Northridge	1994	6.7	23.9	0.273	30.0	0.98
<i>NR94stc</i>	Northridge	1994	6.7	13.3	0.368	30.0	1.38
<i>NR94stn</i>	Northridge	1994	6.7	30	0.474	31.6	1.12
<i>SH87icc</i>	Superstition Hills	1987	6.7	13.9	0.358	40.0	1.10

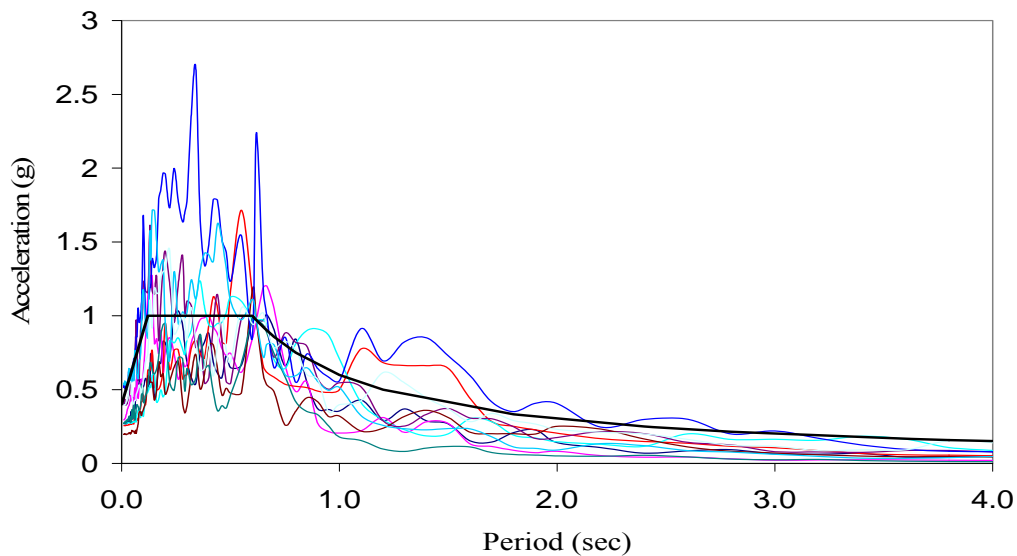


Figure 6.12 Scaled Earthquake Records of Frame IIIa to 10%/50

The demand imposed on Frame IIIa by the 10%/50 ground motion records given in Table 6-6 is presented in Figure 6.13 as the roof displacement (Δ_r) time history results as a percentage of the height of the frame (h_r). The Δ_r demand values for the analyses are documented in Table 6-7 in terms of mean (μ) and 84 percentile ($\mu+\sigma$) values. Table 6-7 shows that the largest maximum and minimum roof drift demands in absolute value were obtained for the NR94stn earthquake record. Compared to the

2%/50 ground motion records, smaller roof drift demands were obtained, where the ratio of maximum roof drift of 2%/50 hazard level to that of 10%/50 hazard level was found as 1.60.

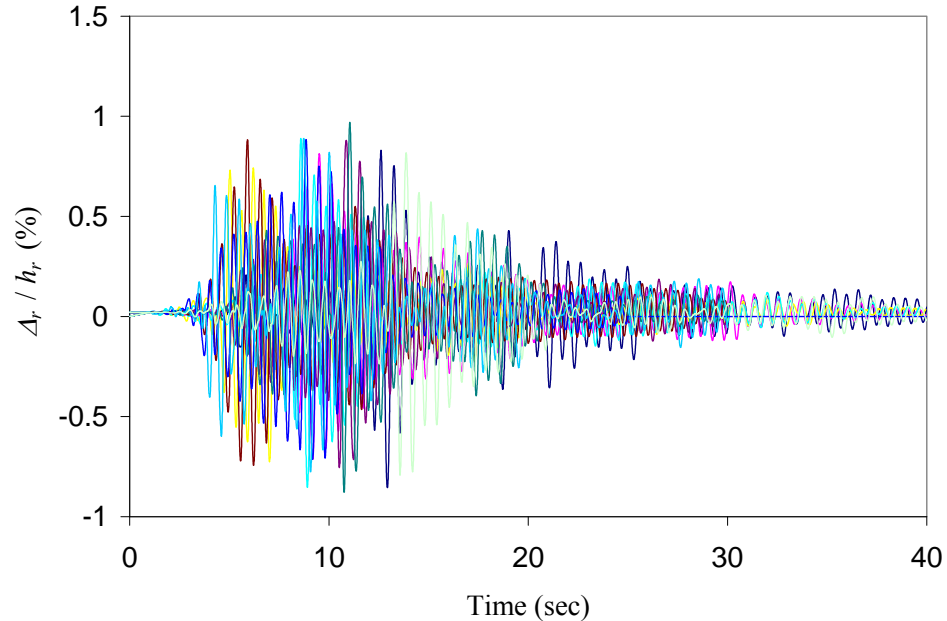


Figure 6.13 Roof Displacement Time History for Frame IIIa (10%/50)

Figure 6.14 shows the story shear (V_s) vs. interstory drift ratio (Δ_s) response of Frame IIIa for each story. Both V_s and Δ_s attain their maximum demands in absolute value at the 1st story. The mean and 84 percentile values for the maximum and minimum interstory drift ratios and shear forces can be found in Table 6-8. It was found that the displacement demands reduced more than the force demands when the hazard level was changed to 10%/50 to 2%/50. The response of RCFT columns was also studied based on their moment vs. axial force response as it is shown in Figure 6.15 for the edge columns at the 1st, 2nd and 3rd stories. It was found that 1st story column achieves to the largest force demands. However, none of the columns breached the cross-section failure surface given in the AISC-LRFD (2005) design specification indicating the level of inelasticity to be insignificant.

Table 6-7 The Maximum and Minimum Roof Displacement Values (Δ_r) of IIIa for 10%/50 Earthquake Records

Record ID	Δ_r (max) (%)	Δ_r (min) (%)
<i>IV79chi</i>	0.83	-0.86
<i>LP89cap</i>	0.81	-0.71
<i>LP89g04</i>	0.74	-0.72
<i>LP89hda</i>	0.89	-0.85
<i>NR94cen</i>	0.88	-0.76
<i>NR94cnp</i>	0.88	-0.71
<i>NR94far</i>	0.88	-0.74
<i>NR94stc</i>	0.89	-0.78
<i>NR94stn</i>	0.97	-0.88
<i>SH87icc</i>	0.82	-0.79
μ	0.86	-0.78
$\mu + \sigma$	0.92	-0.72

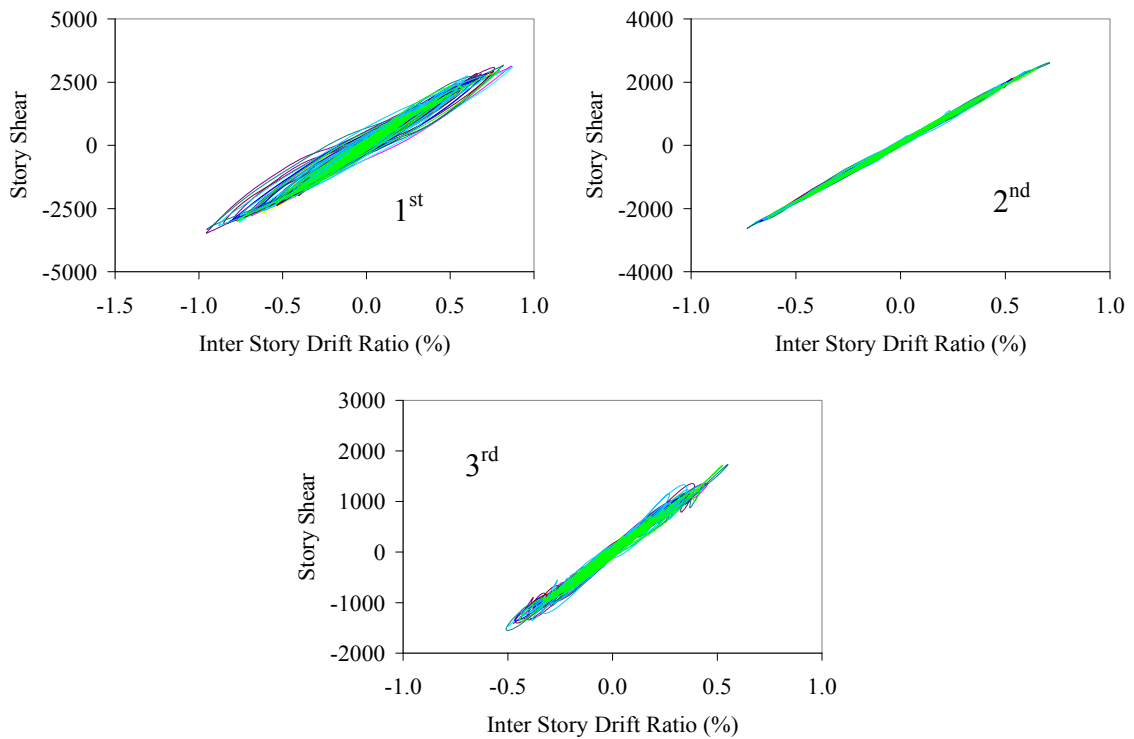


Figure 6.14 Interstory Drift Ratio and Shear Force Demand at 1st, 2nd and 3rd stories (Frame IIIa, 10%/50)

Table 6-8 Maximum and Minimum Story Shear and Interstory Drift Ratios (Frame IIIa, 10%/50)

Record ID	Δ_s (max) (%)	Δ_s (min) (%)	V_s (max) (kN)	V_s (min) (kN)
IV79chi	0.87	-0.73	3133	-2847
LP89cap	0.66	-0.79	2738	-2966
LP89g04	0.64	-0.69	2505	-2719
LP89hda	0.87	-0.76	3103	-3032
NR94cen	0.76	-0.96	3079	-3482
NR94far	0.76	-0.85	2930	-3090
NR94stn	0.82	-0.95	3171	-3333
NR94cnp	0.72	-0.83	2849	-3071
NR94stc	0.71	-0.88	2751	-3161
SH87icc	0.79	-0.77	2968	-3007
μ	0.76	-0.82	2923	-3071
$\mu + \sigma$	0.84	-0.73	3136	-2850

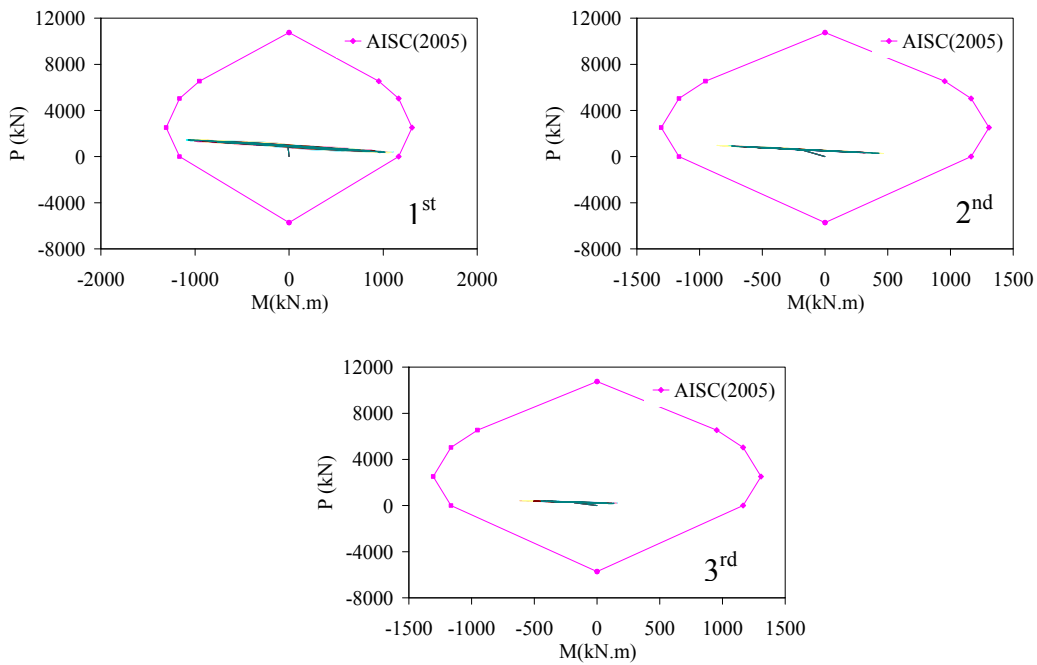


Figure 6.15 Axial Force and Bending Moment Interaction Demands for the Exterior Columns at 1st, 2nd and 3rd Stories (Frame IIIa, 10%/50)

The deformation-based damage function values attained by the RCFT columns are illustrated in Figure 6.16 and in Table 6-9. The damage function values were found to

range from 0.33 to 0.65. Despite the fact that the maximum deformation demands often occurred in the first and second story columns, the third story columns were also found to exhibit large damage function values. This is due to the fact that the columns in the third story reach their lateral load capacity sooner than the ones in the lower stories.

Compared to the results obtained for the 2%/50 hazard level, a clear reduction in \hat{D} values is evident, which impacts the limit states of the RCFT columns.

The local damage state distribution of the RCFT columns was studied by monitoring the stress strain response of the material fibers. For example, Figure 6.17 shows the limit states attained by the steel tube and concrete fibers for an RCFT cross-section located at one of the exterior supports of Frame IIIa. It was found that the damage state is not less severe than the one observed for the 2%/50 hazard level. There was a clear reduction in the number of material fibers experiencing steel yielding and concrete crushing. No local buckling was observed for the steel tube material fibers.

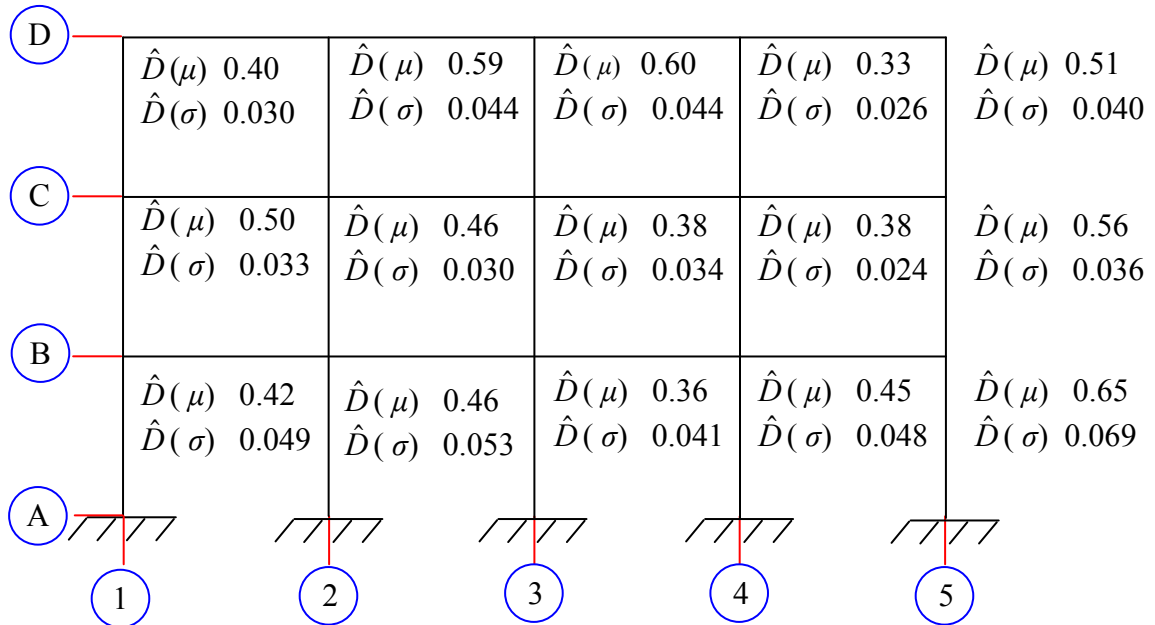


Figure 6.16 Distribution of Mean Damage Function Values for the RCFT Columns
(Frame IIIa, 10%/50)

Table 6-9 Damage Function Parameters of RCFT Columns for 10%/50 Hazard Level

RCFT Column	d_{curr}	d_o	$\hat{D} = \frac{d_{curr}}{d_o}$
	mean(R (%))	R_o (%)	
A1-B1	0.86	2.04	0.42
B1-C1	1.01	2.01	0.50
C1-D1	0.76	1.90	0.40
A2-B2	0.86	1.87	0.46
B2-C2	1.01	2.19	0.46
C2-D2	0.75	1.28	0.59
A3-B3	0.86	2.41	0.36
B3-C3	1.00	2.59	0.38
C3-D3	0.74	1.24	0.60
A4-B4	0.76	1.68	0.45
B4-C4	0.99	2.57	0.38
C4-D4	0.80	2.40	0.33
A5-B5	0.76	1.18	0.65
B5-C5	0.99	1.77	0.56
C5-D5	0.78	1.54	0.51

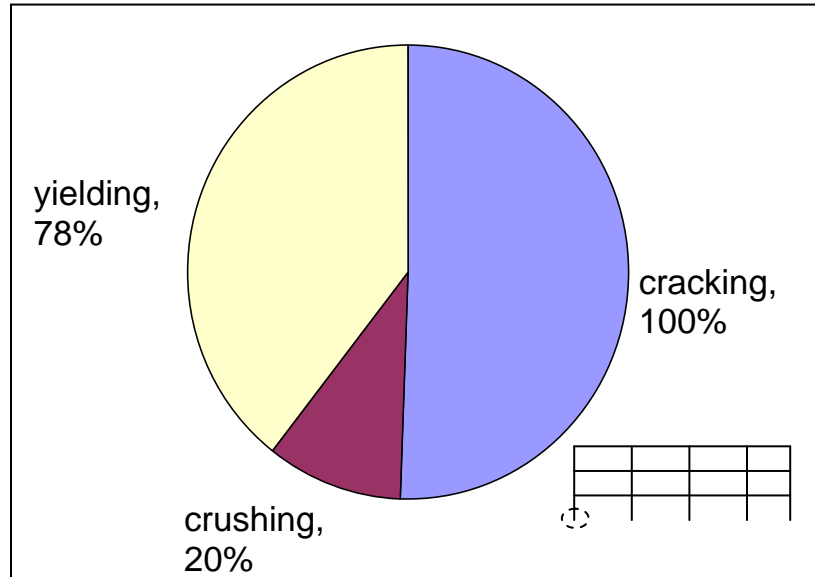


Figure 6.17 Damage Distribution of RCFT Cross-Section at the Support under IV79 Ground Motion (Frame IIIa, 10%/50)

The second RCFT frame structure selected for seismic demand evaluation is described in Figure 6.18. The frame dimensions and number of bays were kept as the same with Frame IIIa. However, material properties and therefore the resulting member

sizes exhibited a variation compared to Frame IIIa. This approach allowed investigating the effect of different limit states and the degree of interaction between the steel tube and the concrete core on the global and local seismic demand of RCFT frames. The yield strength of the steel tube and compressive strength of the concrete core were selected to be higher than the values often used in conventional designs and they were assumed to be 552 MPa and 110 MPa, respectively. The steel tube of the RCFT columns were designed as a slender cross-section with a D/t ratio of 67. Frame III d has the same seismic mass and gravity loads same with Frame IIIa. Conducting an eigen-value analysis, the periods corresponding to the first three modes were obtained as 0.66 sec, 0.53 sec, and 0.22 sec. A 2% damping ratio was assigned and the damping proportionality factors corresponding to mass and stiffness were determined to be 0.286 and 0.001061, respectively.

In order to represent the 2%/50 hazard level for Frame III d, a total number of 11 earthquake records were selected. The characteristics of the selected ground motion records are summarized in Table 6-10. The records were all scaled with respect to the S_a value at the first mode period of the structure minimizing the difference between design and median spectra. The resulting scale factors ranged between 0.74 and 2.10. Figure 6.19 shows the comparison of the acceleration response spectra of the scaled ground motions with the 2%/50 hazard level acceleration response spectra available in the design provisions. All the available acceleration spectra values coincide at 0.66 sec, which corresponds to the first mode period of the structure.

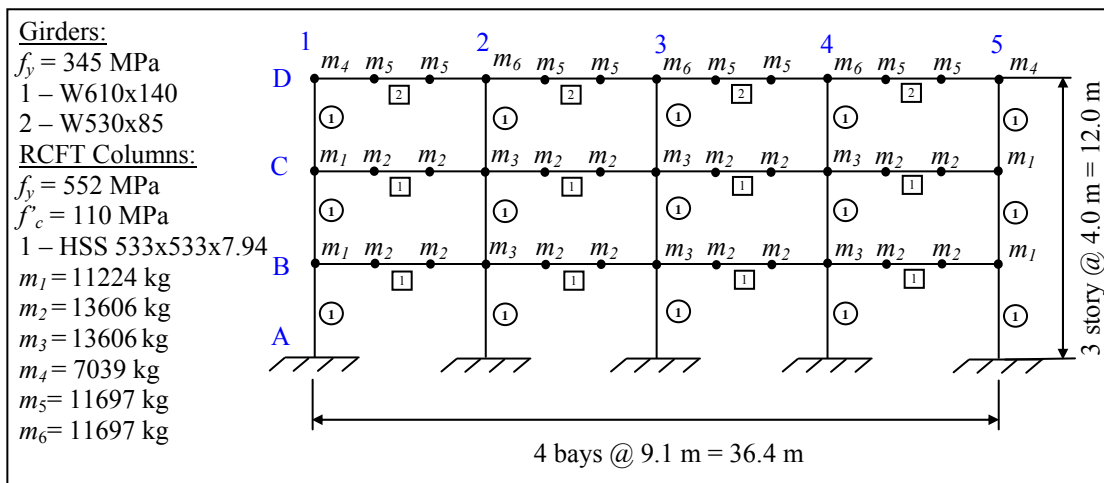


Figure 6.18 Description of Frame III d

Table 6-10 Earthquake Records Selected for Frame IIIId Scaled to 2%/50 Hazard Level

Record ID	Event	Year	M_w	R (km)	PGA(g)	Duration (sec)	Scale Factor
<i>IV79chi</i>	Imperial Valley	1979	6.5	28.7	0.27	40.0	1.38
<i>IV79qkp</i>	Imperial Valley	1979	6.5	23.6	0.31	40.0	1.61
<i>LP89cap</i>	Loma Prieta	1989	6.9	14.5	0.443	40.0	0.74
<i>LP89hda</i>	Loma Prieta	1989	6.9	25.8	0.279	39.6	1.39
<i>LP89slc</i>	Loma Prieta	1989	6.9	36.3	0.19	39.6	1.91
<i>NR94cen</i>	Northridge	1994	6.7	30.9	0.322	30.0	1.81
<i>NR94cnp</i>	Northridge	1994	6.7	15.8	0.42	25.0	1.11
<i>NR94far</i>	Northridge	1994	6.7	23.9	0.273	30.0	1.46
<i>NR94fle</i>	Northridge	1994	6.7	29.5	0.240	30.0	2.10
<i>NR94stc</i>	Northridge	1994	6.7	13.3	0.368	30.0	1.71
<i>SH87icc</i>	Superstition Hills	1987	6.7	13.9	0.358	40.0	1.55

Frame IIIId was subjected to the available ground motion records and the demand values imposed on the structure were documented. The maximum roof drift (Δ_r) is often considered as a powerful engineering demand parameter to investigate the global performance of structures. In addition, the structural design specifications often provide limiting values for the roof drift to satisfy the serviceability limit state. Therefore, in Figure 6.20, the seismic demand was studied based on the roof drift value as a percentage of the height of the structure. In Table 6-11, the roof drift response is summarized for each ground motion record and the mean and 84th percentile values are provided. Compared to Frame IIIa, the roof drift values of Frame IIIId were found to be very similar, where the 1.7% limit was not breached for both frames.

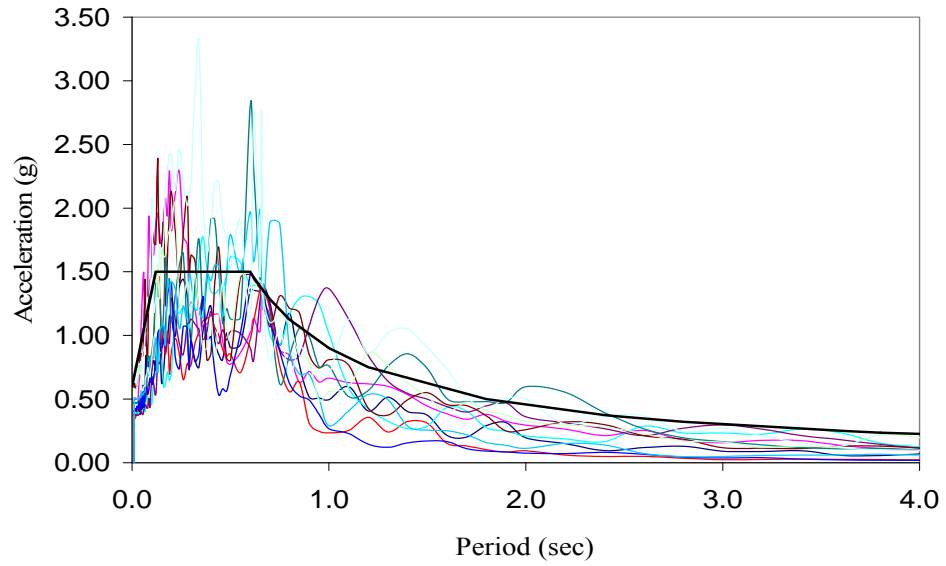


Figure 6.19 Scaled Earthquake Records of Frame IIIId to 2%/50

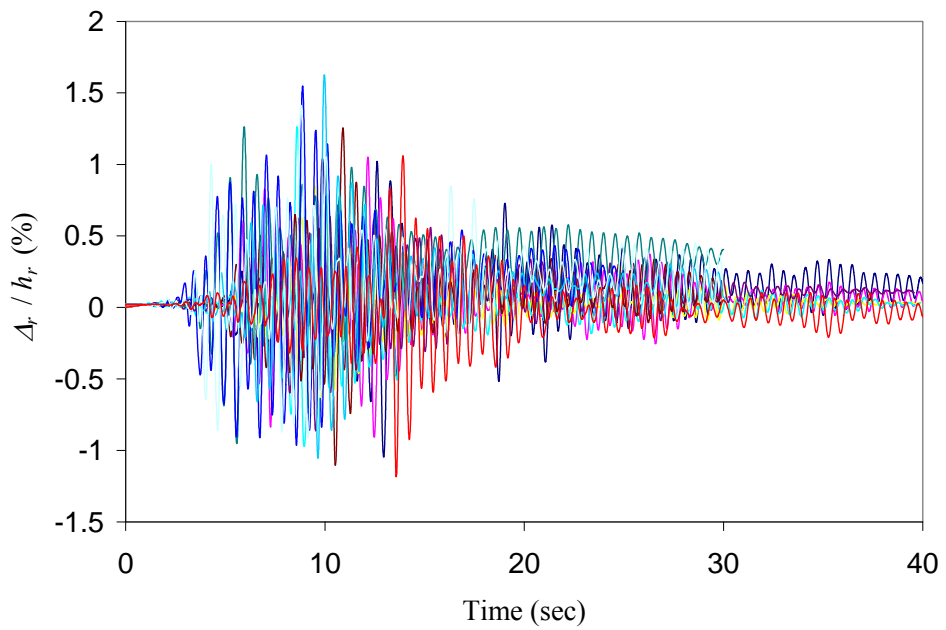


Figure 6.20 Roof Displacement Time History for Frame IIIId (2%/50)

Table 6-11 The Maximum and Minimum Roof Displacement Values (Δ_r) of IIIId for 2%/50 Earthquake Records

Record ID	Δ_r (max) (%)	Δ_r (min) (%)
IV79chi	1.02	-1.05
IV79qkp	1.05	-0.91
LP89cap	0.85	-0.71
LP89hda	1.26	-0.97
LP89slc	1.04	-0.86
NR94cen	1.26	-1.10
NR94far	1.26	-0.95
NR94cnp	1.55	-0.96
NR94fle	1.63	-1.05
NR94stc	1.41	-0.91
SH87icc	1.06	-1.19
μ	1.22	-0.97
$\mu + \sigma$	1.46	-0.84

Interstory drift ratio is adopted as the primary engineering demand parameter in the current performance-based design provisions (FEMA-350, 2000; FEMA-356, 2000). Figure 6.21 shows the interstory drift ratio vs. story shear force response of Frame IIIId for each story. It can be seen that the 1st story RCFT columns are subjected to the largest deformation demands. The 1st story and 2nd story shear force demands were found to be similar. On the other hand, the ground motion records generated the smallest deformation and shear force demands for the 3rd story RCFT columns. Table 6-12 summarizes the maximum and minimum interstory drift and shear force values across all stories for the available ground motion records.

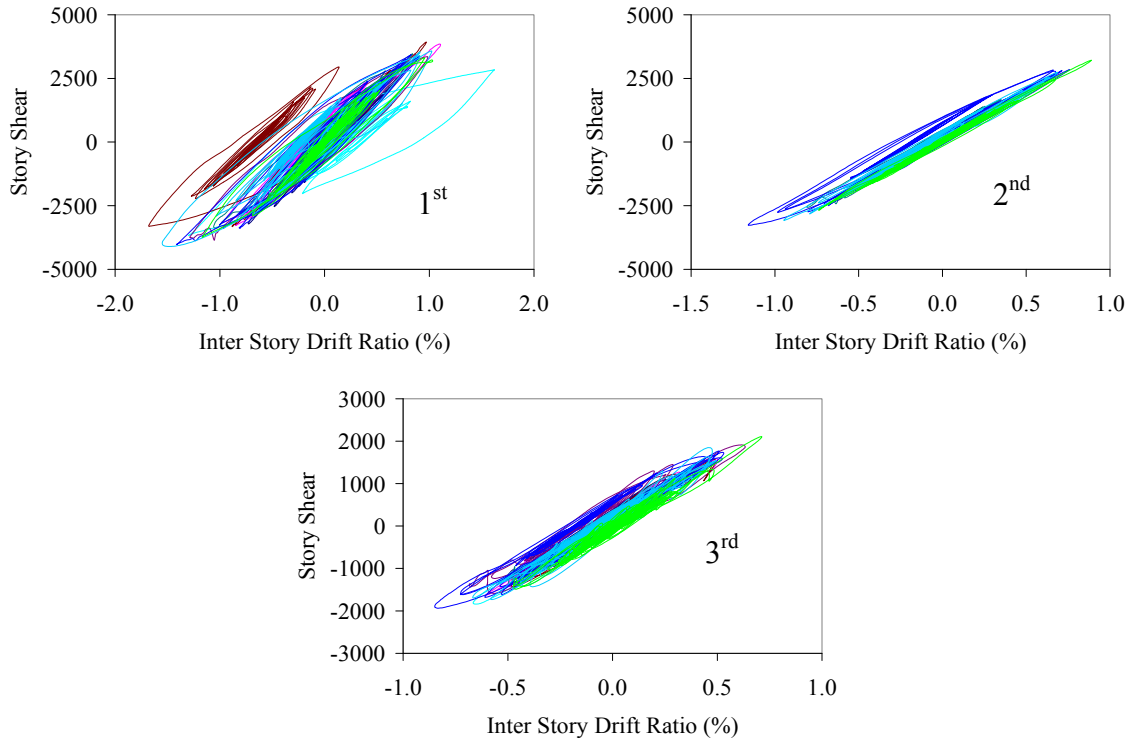


Figure 6.21 Interstory Drift Ratio and Shear Force Demand at the 1st, 2nd and 3rd stories
(Frame III_d, 2%/50)

Table 6-12 Maximum and Minimum Story Shear and Interstory Drift Ratios

Record ID	Δ_s (max) (%)	Δ_s (min) (%)	V_s (max) (kN)	V_s (min) (kN)
IV79chi	1.11	-0.98	3851	-3279
IV79qkp	1.02	-0.97	3502	-3622
LP89cap	0.77	-0.73	2901	-3220
LP89hda	1.62	-1.30	2837	-3673
LP89slc	0.84	-1.06	3467	-3387
NR94cen	0.99	-1.29	3434	-3854
NR94far	0.97	-1.68	3926	-3321
NR94cnp	0.91	-1.41	3431	-4024
NR94fle	0.97	-1.68	3926	-3321
NR94stc	1.02	-1.55	3579	-4102
SH87icc	1.03	-1.17	3311	-3742
μ	1.02	-1.26	3470	-3595
$\mu + \sigma$	1.24	-0.95	3834	-3283

The RCFT columns of Frame IIIId were checked for the cross-section strength equations given in AISC-LRFD (2005). Therefore, the moment vs. axial force response from time history analysis results were recorded. Figure 6.22 shows the interaction values attained for the exterior RCFT columns of the 1st, 2nd, and 3rd stories. It was found that the interaction values remains within the cross-section failure surface given in AISC-LRFD (2005). This is in part due to the fact the moment and axial load capacity equations of RCFT beam-columns in AISC-LRFD (2005) do not account for the detrimental effect of local buckling.

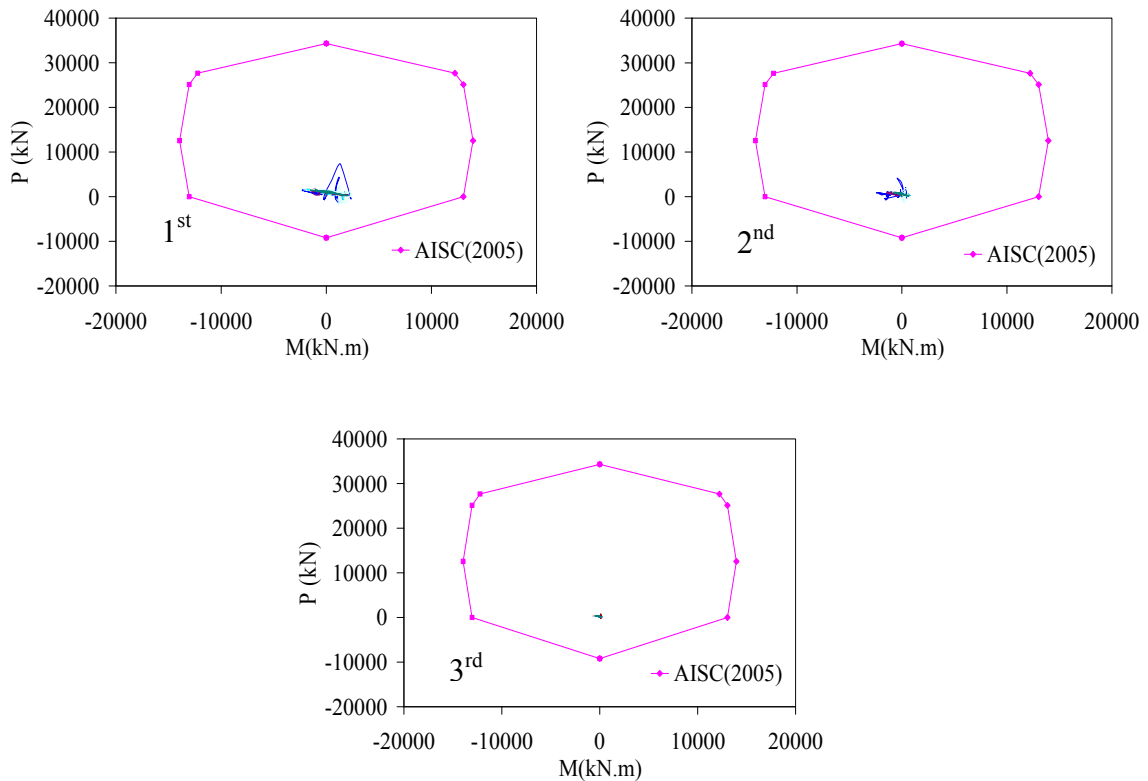


Figure 6.22 Axial Force and Bending Moment Interaction Demands for the Exterior Columns at 1st, 2nd and 3rd Stories (Frame IIIId, 2%/50)

The deformation-based damage function by Tort and Hajjar (2003) was also utilized to evaluate the demand of RCFT columns. First, static push-over analysis of Frame IIIId was conducted producing the load-deformation response given in Figure 6.23. From the static push-over analysis, the chord rotation vs. shear force response of each RCFT column was extracted. As shown in Figure 6.23, superimposing the time-history

analysis results on the static push-over curve, the parameters of d_o and d_{curr} were calculated to evaluate \hat{D} . The distribution of \hat{D} across the RCFT columns is presented in Figure 6.25. The \hat{D} values were found to range between 0.43 and 1.27. For the majority of the RCFT column, the largest damage function values were attained in the first story. Compared to Frame IIIa, \hat{D} values were found to be larger, which is attributed to the fact that severe local buckling taking place prior to yielding reduced the strength and stiffness of the RCFT columns. In Table 6-13, the parameters to obtain \hat{D} values of the RCFT columns can be found.

The degree of material inelasticity experienced by Frame IIIId was examined by studying the distribution of local damage sates at key locations. For example, Figure 6.26 illustrates the local damage levels of material fibers for the RCFT cross-section located at one of the exterior supports in the first story for a representative ground motion record. It was found out that no concrete crushing took place due to the high compressive strength. The damage mainly occurred in the steel fibers in the form of yielding and local buckling.

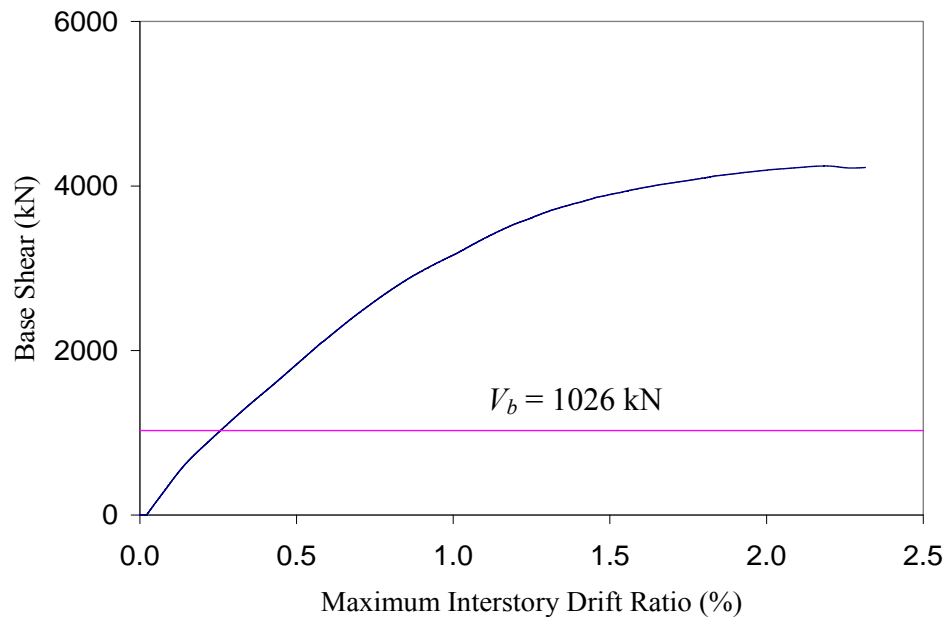


Figure 6.23 Static Push-Over Response of Frame IIIId

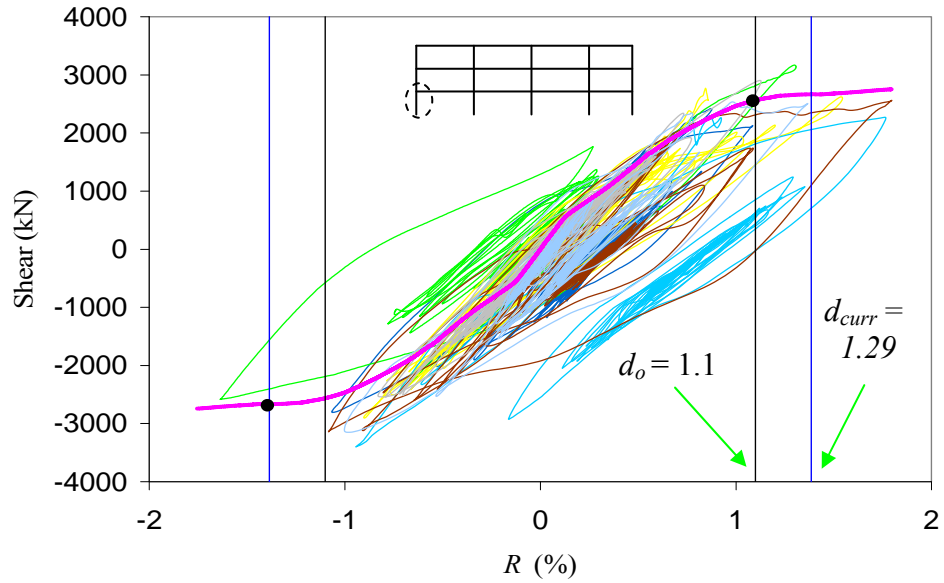


Figure 6.24 Push-Over vs. Time History Response of 1st Story Exterior Column (Frame IIIId, 2%/50)

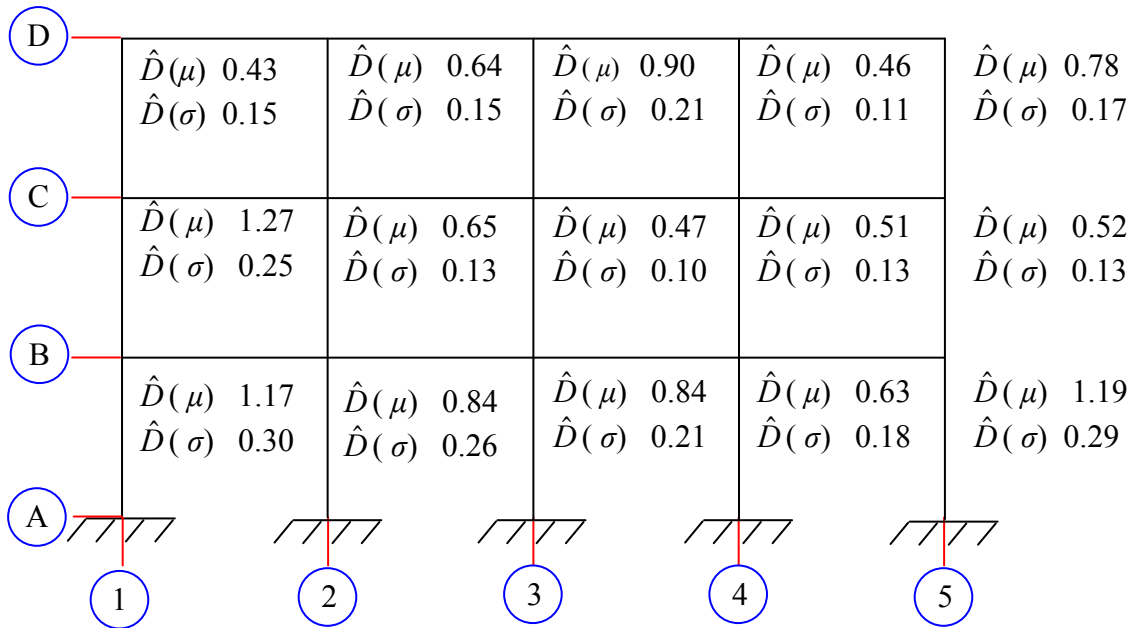


Figure 6.25 Distribution of Mean Damage Function Values for the RCFT Columns

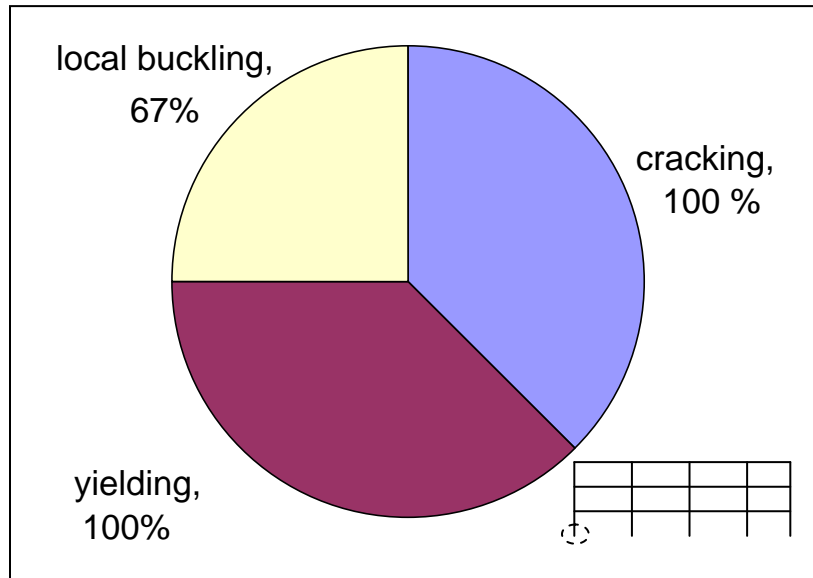


Figure 6.26 Damage Distribution of RCFT Cross-Section at the Support under IV79 Ground Motion

Table 6-13 Damage Function Parameters of RCFT Columns of Frame IIIId for 2%/50 Hazard Level

RCFT Column	d_{curr}	d_o	$\hat{D} = \frac{d_{curr}}{d_o}$
	mean(R (%))	R_o (%)	
A1-B1	1.29	1.10	1.17
B1-C1	1.31	1.03	1.27
C1-D1	1.03	1.69	0.61
A2-B2	1.29	1.23	1.05
B2-C2	1.33	2.05	0.65
C2-D2	1.01	1.59	0.64
A3-B3	1.30	1.56	0.84
B3-C3	1.30	2.74	0.47
C3-D3	0.99	1.10	0.90
A4-B4	1.09	1.72	0.63
B4-C4	1.31	2.57	0.51
C4-D4	1.06	2.32	0.46
A5-B5	1.14	0.95	1.19
B5-C5	1.32	2.55	0.52
C5-D5	1.06	1.36	0.78

The ground motion records selected to investigate the seismic demand of Frame IIIId under 10%/50 hazard level are given in Table 6-14. A total number of 8 ground motion records were selected. The scaling of the earthquake records is presented in Figure 6.27, where the spectral acceleration values coincide at 0.66 sec. The scale factors to match the response spectrum in the design provisions were found range from 0.74 to 1.45 as can be noticed in Table 6-14.

Table 6-14 Earthquake Records Selected for Frame IIIId Scaled to 10%/50 Hazard Level

Record ID	Event	Year	M_w	R (km)	PGA(g)	Duration (sec)	Scale Factor
<i>IV79chi</i>	Imperial Valley	1979	6.5	28.7	0.27	40.0	0.92
<i>LP89cap</i>	Loma Prieta	1989	6.9	14.5	0.443	40.0	0.49
<i>LP89hch</i>	Loma Prieta	1989	6.9	28.2	0.247	39.1	1.45
<i>LP89slc</i>	Loma Prieta	1989	6.9	36.3	0.19	39.6	1.28
<i>NR94cen</i>	Northridge	1994	6.7	30.9	0.322	30.0	1.21
<i>NR94cnp</i>	Northridge	1994	6.7	15.8	0.42	25.0	0.74
<i>NR94far</i>	Northridge	1994	6.7	23.9	0.273	30.0	0.98
<i>NR94stc</i>	Northridge	1994	6.7	13.3	0.368	30.0	1.14
<i>SH87icc</i>	Superstition Hills	1987	6.7	13.9	0.358	40.0	1.04

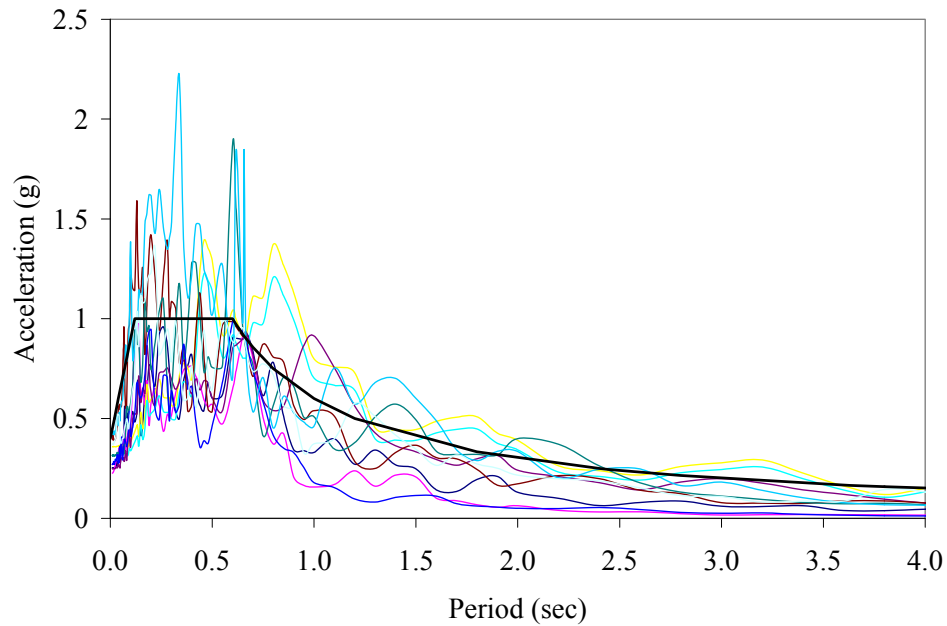


Figure 6.27 Scaled Earthquake Records of Frame IIIId to 10%/50

The time history analysis results of Frame IIIId under the ground motion records of Table 6-14 is documented in Figure 6.28 in terms of roof drift values as a percentage of the height of the structure. The maximum drift value was found to be 1.25%, which is larger than the maximum drift of 0.96% obtained for Frame IIIa under 10%/50 hazard level. A summary of the roof drift values for the selected ground motion records is provided in Table 6-15 along with the statistical properties including mean and 84th percentile values.

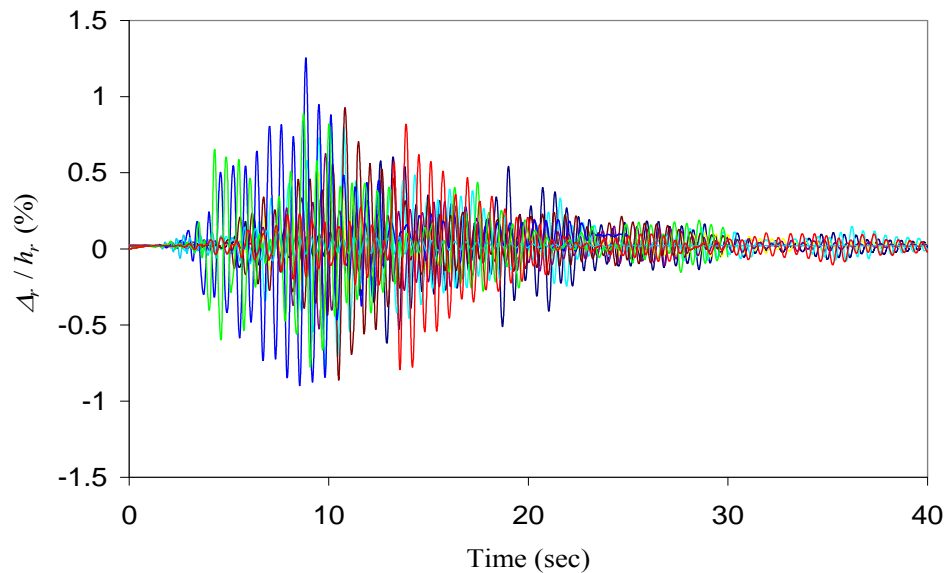


Figure 6.28 Roof Displacement Time History for Frame IIIId (10%/50)

Table 6-15 The Maximum and Minimum Roof Displacement Values (Δ_r) of IIIId for 10%/50 Earthquake Records

Record ID	Δ_r (max) (%)	Δ_r (min) (%)
IV79chi	0.603	-0.619
LP89cap	0.504	-0.425
LP89hch	0.800	-0.790
LP89slc	0.626	-0.526
NR94cen	0.926	-0.863
NR94cnp	1.255	-0.898
NR94far	0.142	-0.098
NR94stc	0.889	-0.776
SH87icc	0.819	-0.793
μ	0.729	-0.643
$\mu + \sigma$	1.041	-0.385

Studying the interstory drift vs. story shear response of Frame IIIId, in Figure 6.29, it was found that the maximum deformation and force values are concentrated in the first and second stories. Compared to the seismic response under 2%/50 earthquake records, the hysteresis response of the stories was found to be narrower, which indicates a reduction to occur in the inelastic deformations of the RCFT columns. In Table 6-16, the deformation and forced demands of Frame IIIId can be found with the corresponding mean and 84 percentile values.

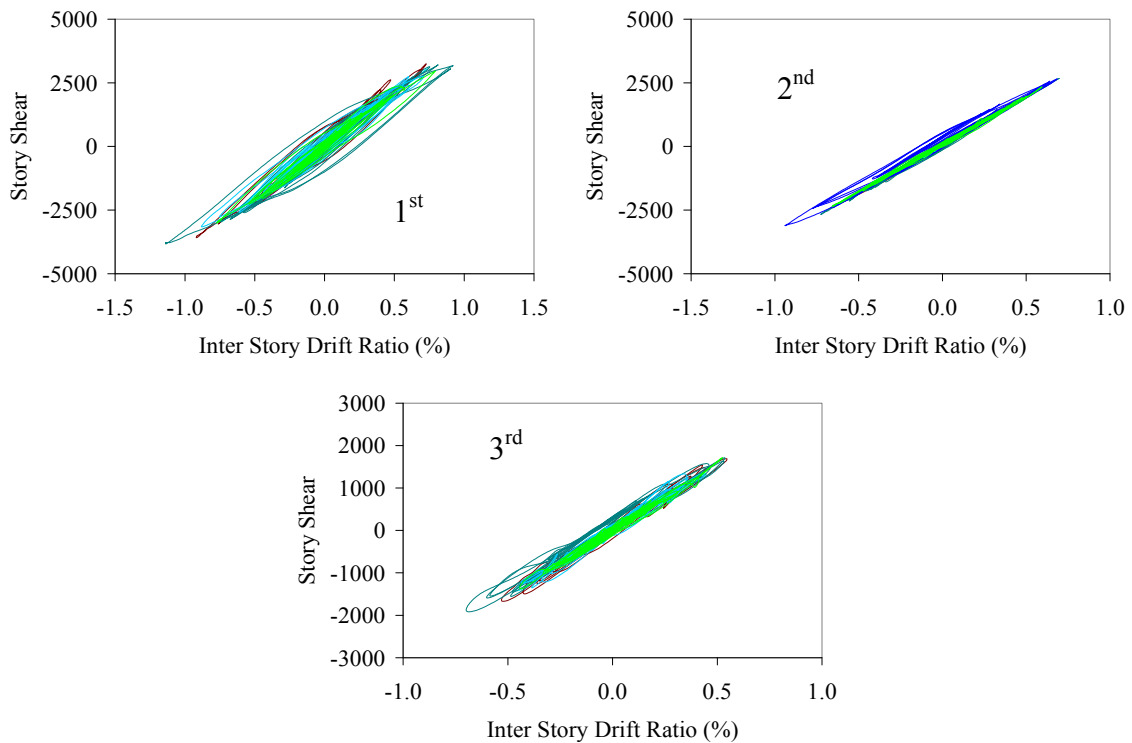


Figure 6.29 Interstory Drift Ratio and Shear Force Demand at the 1st, 2nd and 3rd stories (Frame IIIId, 10%/50)

The moment and axial force demands of the exterior RCFT columns were checked against the interaction equations available in AISC-LRFD (2005). Due to the use of high strength steel tube and concrete core, the nominal capacity of the RCFT columns were calculated to be large without any consideration given to the effect of local buckling.. Therefore, as can be seen in Figure 6.30, the interaction equation for the RCFT columns of Frame IIIId remained within the interaction surface.

Table 6-16 Maximum and Minimum Story Shear and Interstory Drift Ratios (Frame IIIId, 10%/50)

Record ID	Δ_s (max) (%)	Δ_s (min) (%)	V_s (max) (kN)	V_s (min) (kN)
IV79chi	0.54	-0.52	2364	-2340
LP89cap	0.39	-0.44	1877	-1970
LP89hch	0.74	-0.74	3047	-2964
LP89slc	0.52	-0.52	2288	-2382
NR94cen	0.73	-0.92	3244	-3583
NR94cnp	0.92	-1.14	3201	-3829
NR94stc	0.71	-0.88	2751	-3161
SH87icc	0.79	-0.77	2968	-3007
μ	0.67	-0.74	2717	-2905
$\mu + \sigma$	0.84	-0.50	3210	-2265

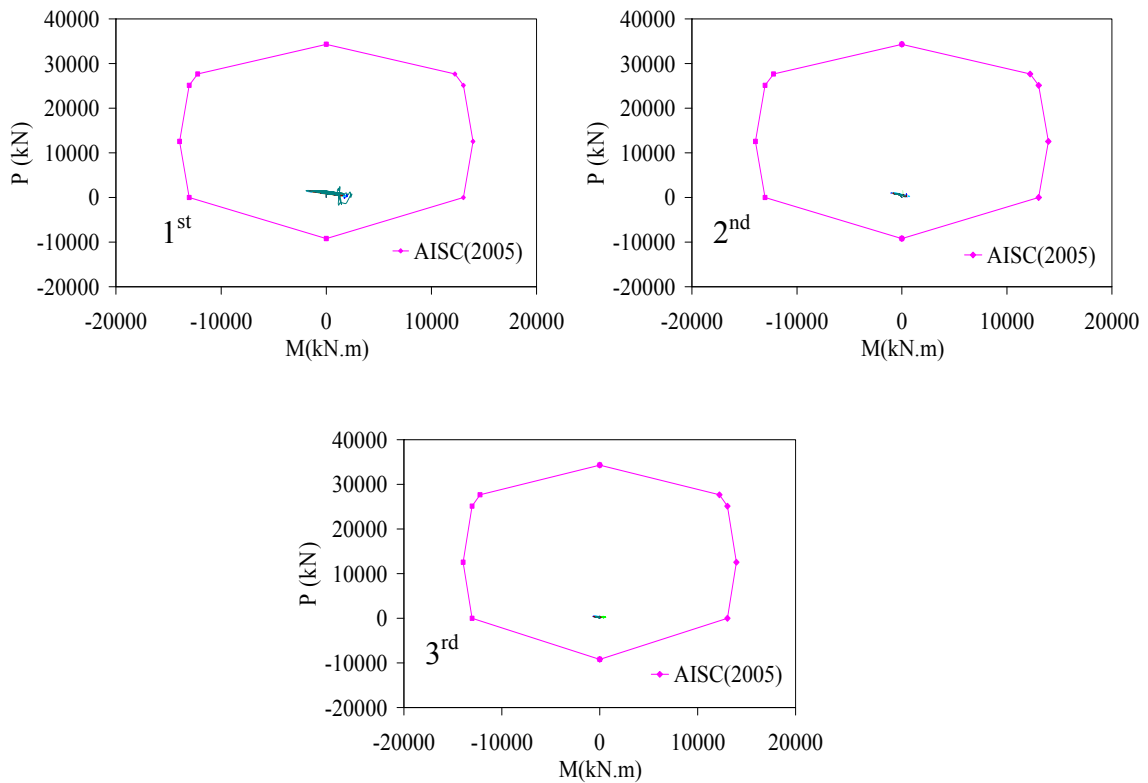


Figure 6.30 Axial Force and Bending Moment Interaction Demands for the Exterior Columns at 1st, 2nd and 3rd Stories (Frame IIIId, 10%/50)

The deformation-based damage function values attained by the RCFT columns are documented in Figure 6.31 across all of the RCFT columns in Frame IIIId. The values

of \hat{D} were found to range from 0.32 to 0.69. The damage of the RCFT columns was mainly concentrated in the 1st story. Compared to Frame IIIa, the severity of damage was found to be larger for the columns of Frame III d. The damage function parameters of d_{curr} and d_o can be found in Table 6.12.

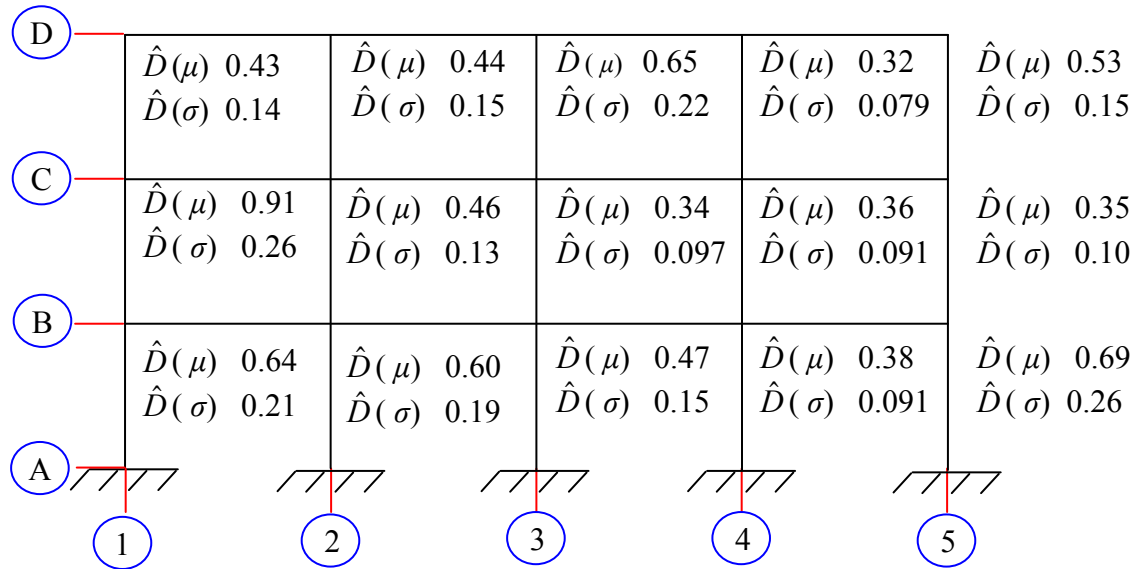


Figure 6.31 Distribution of Mean Damage Function Values for the RCFT Columns
(Frame III d, 10%/50)

Table 6.12. Damage Function Parameters of RCFT Columns of Frame IIIId for 10%/50 Hazard Level

RCFT Column	d_{curr}	d_o	$\hat{D} = \frac{d_{curr}}{d_o}$
	mean(R (%))	R_o (%)	
A1-B1	0.71	1.10	0.64
B1-C1	0.93	1.03	0.91
C1-D1	0.72	1.69	0.43
A2-B2	0.73	1.23	0.60
B2-C2	0.94	2.05	0.46
C2-D2	0.70	1.59	0.44
A3-B3	0.74	1.56	0.47
B3-C3	0.94	2.74	0.34
C3-D3	0.71	1.10	0.65
A4-B4	0.66	1.72	0.38
B4-C4	0.91	2.57	0.36
C4-D4	0.75	2.32	0.32
A5-B5	0.66	0.95	0.69
B5-C5	0.90	2.55	0.35
C5-D5	0.71	1.36	0.53

Chapter 7

7. Reliability Framework

7.1. Introduction

The primary advantage of performance-based design over prescriptive design methodologies is that the inherent uncertainty and randomness in seismic demand and capacity evaluations of structures can be accounted for. This is often realized by quantifying the confidence levels for the targeted performance objective indicating the likelihood of producing an acceptable design (FEMA-350, 2000).

Cornell et al. (2002) have proposed that the effects of uncertainty and randomness can be incorporated into a performance-based design approach similar to the conventional load and resistance factor format as given in Equation 7.1.

$$\phi\bar{C} \geq \gamma\bar{D} \quad [7.1]$$

where:

\bar{C} - median capacity value (e.g., local response parameters from the experiments, global response parameters from nonlinear time history)

\bar{D} - median demand value under a given ground motion of intensity (e.g., local and global damage parameters from structural analysis)

ϕ – capacity factor

γ – demand factor

The process to arrive at Equation 7.1 requires the identification of the probabilistic representations of the main components operating within the performance-based design. These components include ground motion hazard, seismic demand (D), and seismic capacity (C) (Cornell et al., 2002). First, ground motion hazard and seismic demand are combined to derive the annual probability of having seismic demand greater than a threshold value of d for a given hazard level with an intensity of x . The resulting annual probability expression as a function of d is often termed as drift hazard curve

(H_D) as given in Equation 7.2. In displacement-based design methods, demand is often considered as a structural deformation parameter (e.g., maximum interstory drift). On the other hand, the main parameter characterizing the ground motion is often assumed as the spectral acceleration at the first mode period of the structure (S_a). Equation 7.2 employs the total probability theorem so that all ranges of ground motion intensities are covered while assessing the probabilistic seismic demand. This approach is considered as one of the superiorities of performance-based design over prescriptive design methodologies, where the demand evaluations are performed for a single seismic hazard level (e.g., 10%/50, 2%/50) (Yun et al., 2002).

$$H_D(d) = \int P[D \geq d | S_a = x] dH(x) \quad [7.2]$$

where: P – operator to denote probability

$d(H(x))$ - the expression resulting from differentiation of seismic hazard curve (H) with respect to S_a and evaluating the differentiated seismic hazard curve at $S_a = x$ once it is multiplied by dS_a

The seismic hazard curve that is introduced in Equation 7.2 quantifies the annual probability of having a ground motion hazard with intensity greater than a threshold value of s_a . The seismic hazard curve often has the format given in Equation 7.3 and it is provided by the seismologist for the desired geographical region.

$$H(s_a) = P[S_a \geq s_a] = k_o \times s_a^{-k} \quad [7.3]$$

where: k, k_o coefficients resulting from linear regression hazard on intensity

The probabilistic representations of drift and ground motion hazard given in Equation 7.2 and 7.3 are combined together to arrive at the numerical expression of the probability of seismic capacity to be less than a threshold value of seismic demand (d). The value of this expression indicates the success of the targeted design objective as it is described in Equation 7.4.

$$P_{PL} = \int P[C \leq d] dH_D(d) \quad [7.4]$$

where: P_{PL} annual probability of having an unsatisfactory design objective

To quantify the uncertainty and randomness of the designed structure within a probabilistic design methodology, the integral expression in Equation 7.4 needs to be evaluated. This can be performed with ease through introducing simplifying relations and probability distributions among ground motion hazard, seismic demand, and capacity.

Based on time history analysis results on representative 3 story structures, Luco and Cornell (1998) correlated the median drift \bar{D} to S_a in the following format.

$$\bar{D} = a(S_a)^b \quad [7.5]$$

where: a, b - correlation coefficients ($b = 1$, Luco and Cornell, 1998)

The coefficient a in Equation 7.5 can be obtained by conducting a series of nonlinear analysis and performing a linear regression of \bar{D} on S_a .

Assuming the drift demands to be log-normally distributed around its mean value with a standard deviation of β_{D/S_a} , the first term in the integral expression of Equation 7.2 can be obtained as follows:

$$P[D \geq d | S_a = x] = 1 - \Phi\left(\frac{\ln(d) - \ln(ax^b)}{\beta_{D/S_a}}\right) \quad [7.6]$$

where: Φ is the standardized Gaussian distribution function

$$\Phi(s) = \int_{-\infty}^s \frac{1}{\sqrt{2\pi}} e^{-1/2s^2} ds$$

Substituting Equation 7.6 and 7.5 into Equation 7.2 and performing integration by parts, the drift hazard curve can be derived as follows (Jalayer, 2003).

$$H_D(d) = H(s_a^d) \times \exp\left[\frac{1}{2} \frac{k^2}{b^2} \beta_{D/S_a}^2\right] \quad [7.7]$$

where: $s_a^d = (d/a)^{1/b}$ (inverse function of Equation 7.5 (Jalayer, 2003))

Similarly, seismic capacity is also assumed to be log-normally distributed around its mean value (\bar{C}) with a standard deviation of β_c . Therefore, the first term of Equation 7.4 becomes:

$$P[C \leq d] = \Phi\left(\frac{\ln(d) - \ln(\bar{C})}{\beta_c}\right) \quad [7.8]$$

Substituting Equation 7.8 and 7.5 into Equation 7.4 and carrying out integration by parts P_{PL} becomes:

$$P_{PL} = H(s_a^{\bar{C}}) \times \exp\left[\frac{1}{2} \frac{k^2}{b^2} (\beta_{D/S_a}^2 + \beta_C^2)\right] \quad [7.9]$$

where: $s_a^{\bar{C}} = (\bar{C} / a)^{1/b}$

In reliability-based performance-based design methodologies, the performance objective is stated as satisfying a performance level (e.g., Immediate Occupancy) under a seismic hazard level expressed in terms of its probability of exceedence in a specific amount time (P_o) (e.g., 2%50, 10%50). The minimum capacity to meet the targeted performance objective (C_{P_o}) can be determined utilizing the graphics adopted from Luco and Cornell (1998). First, spectral acceleration value corresponding to P_o ($S_a^{P_o}$) is determined from the hazard curve. Then, substituting $S_a^{P_o}$ into Equation 7.5, the seismic demand (D_{P_o}) imposed on the designed structure is obtained. The capacity (C_{P_o}) should be larger than the calculated demand to satisfy the performance objective. Similarly, Figure 7.1 can also be utilized in the reverse direction such that for a given capacity (C_{PL}), the probability of the ground motion hazard level (P_{PL}) that will generate a seismic demand (D_{PL}) equal to C_{PL} can be obtained. As can be seen From Figure 7.1, these relations between hazard level, seismic demand, and seismic capacity produce the Equation 7.10 to check the adequacy of a design for the intended performance objective.

$$P_{PL} < P_o \quad [7.10]$$

Substituting Equation 7.9 and 7.3 into Equation 7.10:

$$P_{PL} = H(s_a^{\bar{C}}) \times \exp\left[\frac{1}{2} \frac{k^2}{b^2} (\beta_{D/S_a}^2 + \beta_C^2)\right] \leq P_o = k_o S_a^{P_o -k} \quad [7.11]$$

where: $s_a^{\bar{C}} = (\bar{C} / a)^{1/b}$, $s_a^{P_o} = (\bar{D}^{P_o} / a)^{1/b}$

Expanding and rearranging Equation 7.11, the performance equation that was previously introduced in Equation 7.1 can be obtained as follows:

$$e^{\left[\frac{1}{2} \frac{k}{b} \beta_C^2\right]} \times \bar{C} \geq e^{\left[\frac{1}{2} \frac{k}{b} \beta_{D/S_a}^2\right]} \times \bar{D}^{P_o} \quad [7.12]$$

where: $\phi = e^{\left[\frac{1}{2} \frac{k}{b} \beta_C^2\right]}$, $\gamma = e^{\left[\frac{1}{2} \frac{k}{b} \beta_{D/S_a}^2\right]}$

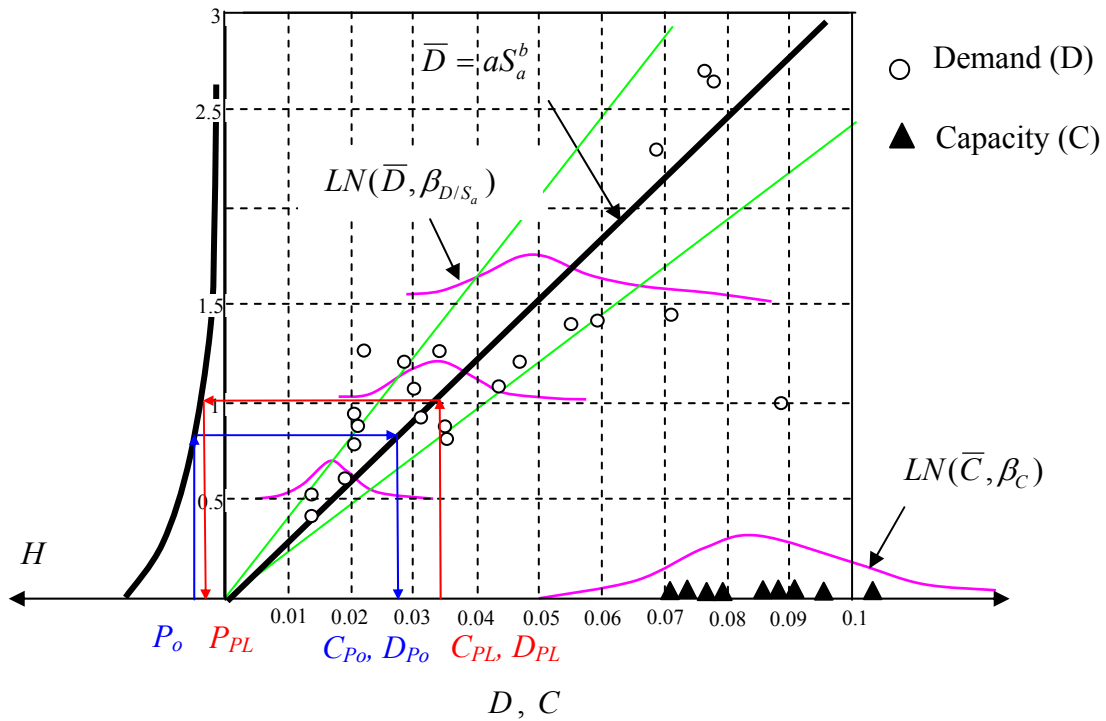


Figure 7.1 Graphical Representation of Relation Between Hazard Curve, Seismic Demand and Capacity Adopted From Luco and Cornell (1998)

7.2. Treatment of Uncertainty and Randomness

There exist two types of uncertainties to be accounted for while quantifying the components of performance-based design. In Equation 7.12, the factors of ϕ and γ captures the dispersion in seismic demand and capacity calculations due to the record to record variations, which is also known as aleatoric uncertainty. On the other hand, the second type of uncertainty to be taken into account is due to the limitations in the accuracy of scientific methods while implementing the performance-based design methodologies. This type of uncertainty is often termed as epistemic uncertainty and it is included in the performance equation as given below (Jalayer, 2003).

$$e^{\left[-\frac{1}{2b}(\beta_{RC}^2 + \beta_{UC}^2)\right]} \times \bar{C} \geq e^{\left[\frac{1}{2b}(\beta_{RD}^2 + \beta_{UD}^2)\right]} \times \bar{D}^{P_o} \quad [7.13]$$

where: $\beta_{RC} = \beta_C$ dispersion in seismic capacity due to randomness

β_{UC} dispersion in seismic capacity due to uncertainty

$\beta_{RD} = \beta_{D/S_a}$ dispersion in seismic demand due to randomness

β_{UD} dispersion in seismic demand due to uncertainty

In order to implement the aforementioned methodology in this research, the dispersion factors due to randomness and uncertainty need to be calculated for RCFT members and frames.

7.2.1. Uncertainty of Capacity at the Local Level

Tort and Hajjar (2004) proposed deformation-based damage function equations to calculate the available capacity with respect to various limit states. These equations were determined based on experimental tests available in the literature under static loading schemes. Equations 7.14, 7.15, 7.16, and 7.17 represents the capacity of RCFT beam-columns against yielding in compression (\hat{D}_{cy}), yielding in tension (\hat{D}_{ty}), local buckling of the flange (\hat{D}_{lbf}), and local buckling of the web (\hat{D}_{lbw}), respectively. The equations are valid for beam-column specimens having constant axial load and shear force putting the member into double curvature, which are common in moment frame structures.

$$\hat{D}_{cy} = \frac{d_{cy}}{d_o} = -1.60 \frac{P}{P_o} - 2.47 \frac{P_s}{P_o} + 2.64 \quad [7.14]$$

$$\hat{D}_{ty} = \frac{d_{ty}}{d_o} = 1.47 \frac{P}{P_o} - 5.28 \frac{P_s}{P_o} + 3.85 \quad [7.15]$$

$$\hat{D}_{lbf} = \frac{d_{lbf}}{d_o} = -3.68 \frac{P}{P_o} - 3.11 \frac{P_s}{P_o} + 3.97 \quad [7.16]$$

$$\hat{D}_{lbw} = \frac{d_{lbw}}{d_o} = -4.81 \frac{P}{P_o} - 10.49 \frac{P_s}{P_o} + 10.81 \quad [7.17]$$

where: d_o - deformation at the point of peak load, d_{ty} - deformation at initiation of tension flange yielding, d_{cy} - deformation at initiation of compression flange yielding, d_{lbf} - deformation at initiation of local buckling of the compression flange, d_{lbw} - deformation at initiation of local buckling of the web, P - axial load acting on the member, P_s - axial load capacity of the steel tube, P_o - axial load capacity of the RCFT cross-section

The epistemic uncertainties in the capacity equations presented above were assumed to be generated from variations in concrete strength (δ_{fc}), yield stress of the steel tube (δ_{fy}), and the dispersion due to the scatter in the experimental data points that were used to derive the capacity equations (δ_{sc}). The depth, thickness, and axial load on the specimens were all assumed to be deterministic quantities. The rest of uncertainties were assumed to be negligible such as fabrication errors, professional factor etc.

The variation in the concrete strength from its nominal values is examined based on experimental test data from the literature. Figure 7.2 shows the comparison of the measured concrete strength (f'_{cm}) and nominal concrete strength (f'_{co}) for the RCFT beam-column tests conducted by Inai et al. (2004) and Varma (2000). The coefficient of variation is defined as the normalized parameter that indicates how widely the values of the variety are spread from each other (Ang and Tang, 1975). Therefore, δ_{fc} was calculated as given in Equation 7.18 utilizing the data points of Figure 7.2 and it was evaluated as 0.036.

$$\delta_{fc} = \frac{\sum_{i=1}^N \frac{|(f'_{cm})_i - (f'_{co})_i|}{(f'_{co})_i}}{N} \quad [7.18]$$

where: N – number of data points

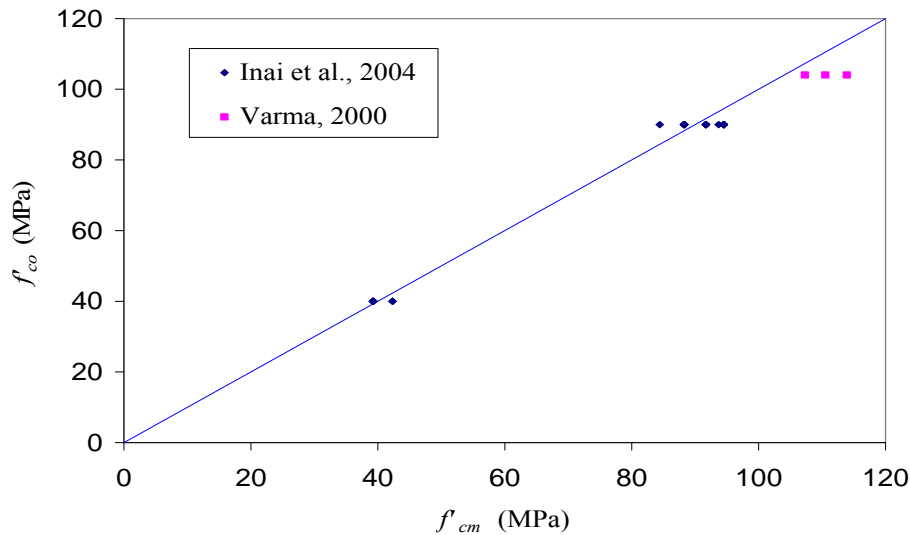


Figure 7.2 Variation of Compressive Strength of Concrete

Similarly, the variation of yield strength of the steel tube was also investigated utilizing the experimental data values reported in the literature. In Figure 7.3, the comparison of nominal (f_{yo}) and measured (f_{ym}) values of the yield strength of the steel tube is presented for the specimens tested by Tomii and Sakino (1979), Lu and Kennedy (1994), and Varma (2000). The data values were selected such that the calculated coefficient of variation will be valid for a wide of yield strengths. Evaluating Equation 7.19, δ_{fy} was determined as 0.193.

$$\delta_{fy} = \frac{\sum_{i=1}^N \frac{|(f_{ym})_i - (f_{yo})_i|}{(f_{yo})_i}}{N} \quad [7.19]$$

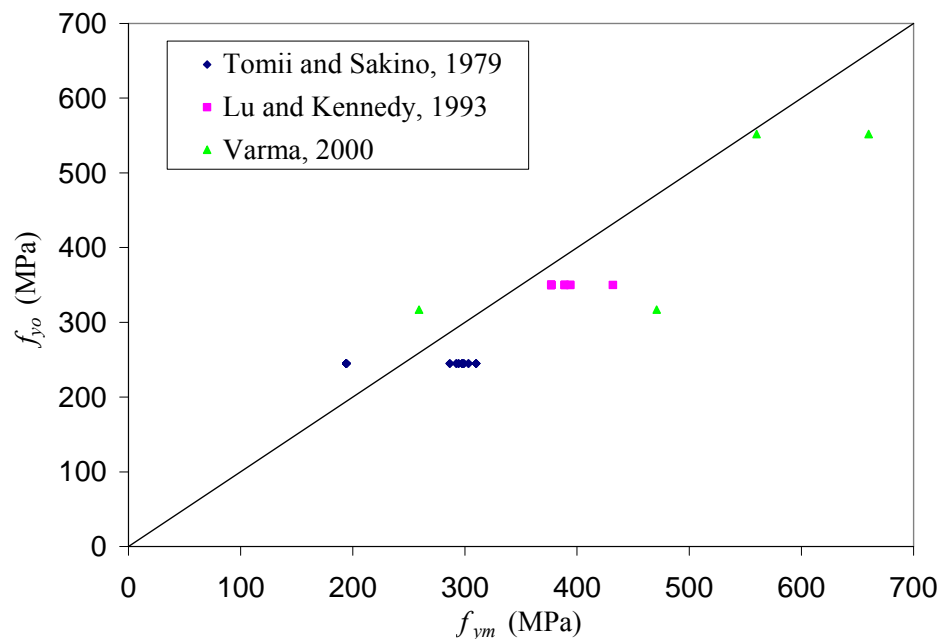


Figure 7.3 Variation of Yield Strength of the Steel Tube

The variation of the deformation-based damage function values due to scatter in the experimental data was studied separately for each limit state. The difference between nominal (\hat{D}_o) and measured (\hat{D}_m) damage function values was normalized by the nominal value to obtain the coefficient of variation. Therefore, δ_{sc} can be calculated as it is described in Equation 7.20.

$$\delta_{rc} = \frac{\sum_{i=1}^N \frac{|\left(\hat{D}_o\right)_i - \left(\hat{D}_m\right)_i|}{\left(\hat{D}_o\right)_i}}{N} \quad [7.20]$$

Figure 7.4 through Figure 7.7 shows the comparison of \hat{D}_o and \hat{D}_m for compression flange yielding, tension flange yielding, local buckling of the compression flange, and local buckling of the web, respectively. Table 7-1 summarizes the corresponding δ_{sc} values for each limit state. From the results in Table 7-1, the limit state of local buckling of the compression flange has the largest δ_{sc} due to the large scatter in the data values.

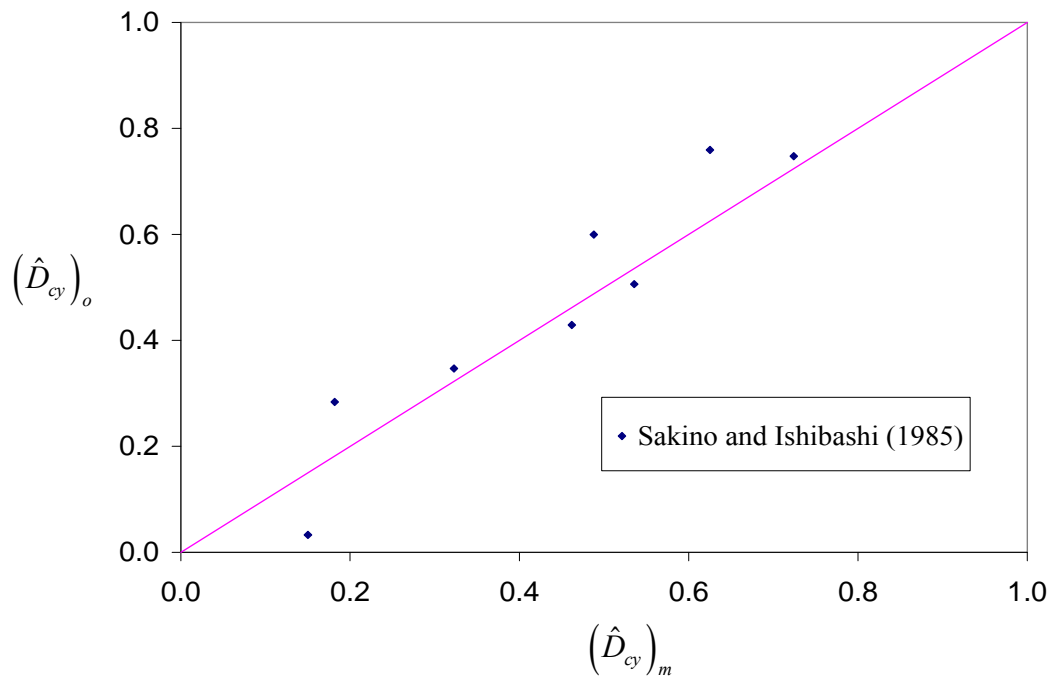


Figure 7.4 Variation of \hat{D}_{cy} due to Scatter in the Experimental Data

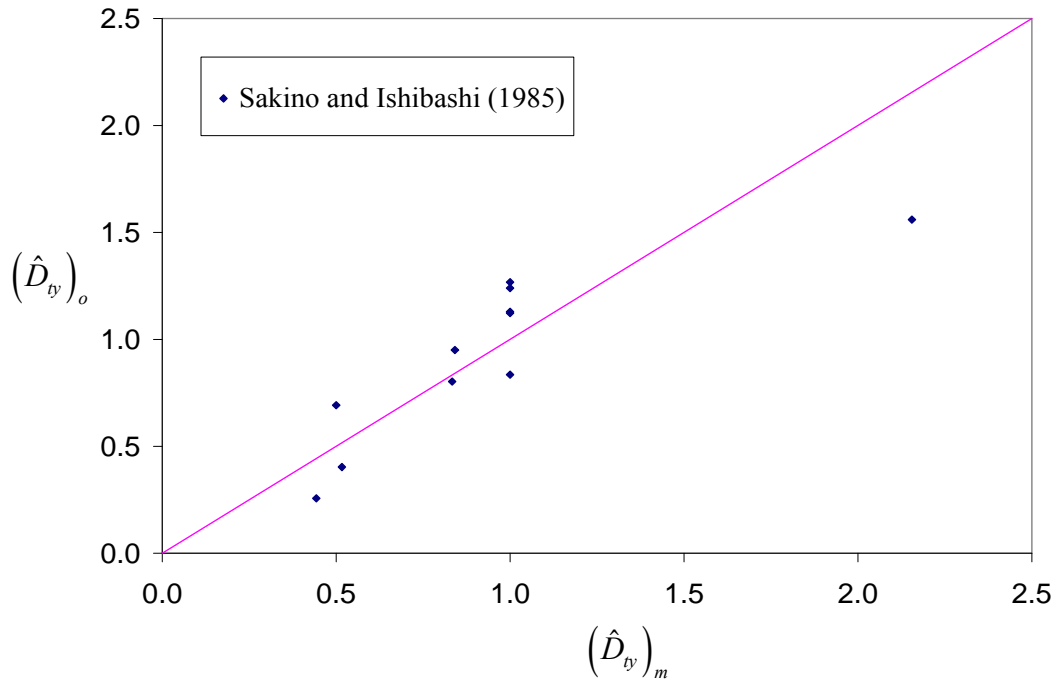


Figure 7.5 Variation of \hat{D}_{ty} due to Scatter in the Experimental Data

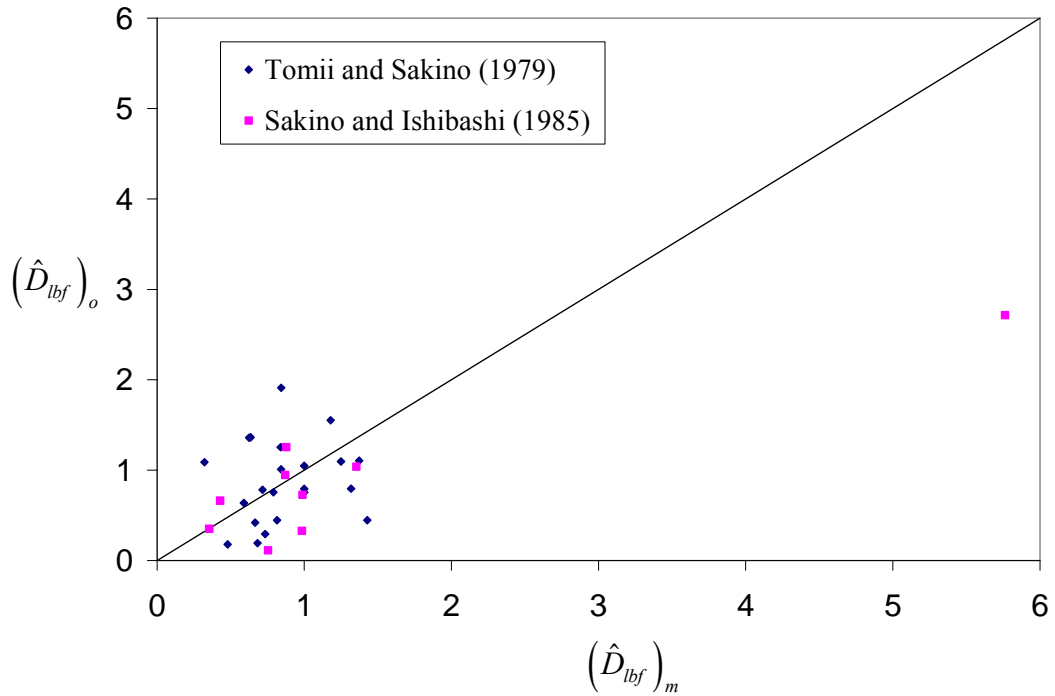


Figure 7.6 Variation of \hat{D}_{lbf} due to Scatter in the Experimental Data

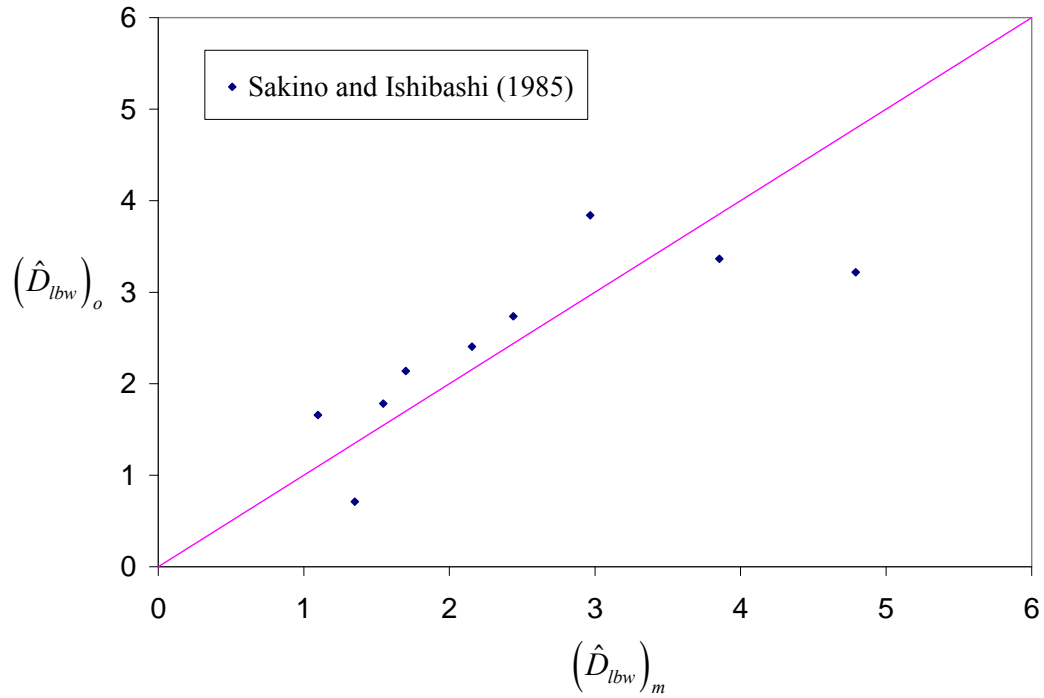


Figure 7.7 Variation of \hat{D}_{lbw} due to Scatter in the Experimental Data

Table 7-1 Summary of δ_{sc} for the Limit States of RCFT Beam-Columns

Limit States	Yielding of Compression Flange	Yielding of Tension Flange	Local Buckling of Compression Flange	Local Buckling of Web
δ_{rc}	0.53	0.24	0.76	0.29
δ_{fc}	0.036	0.036	0.036	0.036
δ_{fy}	0.193	0.193	0.193	0.193

The probabilistic representation of capacity given in Equation 7.8 was derived assuming a log-normal distribution. Therefore, the coefficients of variations in the normal space (δ) can be expressed in terms of standard deviations in the log-normal space (β) using the conversion function given below (Nowak and Collins, 2000).

$$\beta^2 = \ln(\delta^2 + 1) \quad [7.21]$$

Introducing the conversion stated Equation 7.21, the values in Table 7-1 become as follows:

Table 7-2 Summary of β_{sc} for the Limit States of RCFT Beam-Columns

Limit States	Yielding of Compression Flange	Yielding of Tension Flange	Local Buckling of Compression Flange	Local Buckling of Web
β_{rc}	0.50	0.237	0.675	0.284
β_{fc}	0.036	0.036	0.036	0.036
β_{fy}	0.191	0.191	0.191	0.191

The standard deviations of the natural logs of capacities of RCFT members can be combined as follows to obtain β_{UC} introduced in Equation 7.13. Table 7-3 summarizes the β_{UC} values for each limit states

$$\beta_{UC}^2 = \sqrt{\beta_{rc}^2 + \beta_{fc}^2 + \beta_{fy}^2} \quad [7.22]$$

Table 7-3 Summary of β_{UC} for the Limit States of RCFT Beam-Columns

Limit States	Yielding of Compression Flange	Yielding of Tension Flange	Local Buckling of Compression Flange	Local Buckling of Web
β_{UC}	0.536	0.307	0.702	0.344

7.2.2. Randomness of Capacity at the Local Level

The randomness at the local level accounts for the variation in the capacity of RCFT members due to record to record variability. To the authors' knowledge, experimental tests on individual RCFT members subjected a series ground motion records or quasi-static loading protocols are not common. Therefore, the standard deviation of the natural logs of the local capacities due to randomness (β_{RC}) will be

assumed as 0.20 as it is suggested in FEMA-350 (2000) for steel moment frame structures.

7.2.3. Uncertainty of Capacity at the Global Level

The uncertainty in evaluating the global capacity of structures is governed by the employed analysis methods. The assumptions, material models, and solution schemes utilized to obtain the seismic capacity determines the magnitude of uncertainty. In FEMA-350 (2000), the standard deviation of the natural load global capacity due to limitations in the scientific method and information (β_{UC}) is assumed as follows:

$$\beta_{UC} = \sqrt{3}\beta_{NTH} \quad [7.23]$$

where: β_{NTH} - the uncertainty in nonlinear time history analysis to represent the actual behavior ($\beta_{NTH} = 0.15$ for 3-story structures)

7.2.4. Randomness of Capacity at the Global Level

Randomness in capacity at the global level is determined based on dynamic push-over studies documented in FEMA-350 (2000), where global capacity and its dispersion due to randomness (β_{RC}) are provided for 3 story steel moment frame structures. The same capacity and dispersion values are adopted in this research study for RCFT frames, where the global capacity is assumed as an interstory drift ratio of 0.1 and β_{RC} is assumed as 0.07.

7.2.5. Uncertainty and Randomness of Demand

Two types of uncertainties that are assumed to be significant will be considered in demand evaluation. The first one is the ability of nonlinear time history analysis to simulate the actual behavior. The measure of dispersion for the accuracy of nonlinear time history analysis (β_{NTH}) will be the same at the local and global level. β_{NTH} is 0.15 for 3 story structures from Yun et al. (2002). The second type of uncertainty is called as the bias factor, which accounts for the accuracy of analysis procedure. The measure of

dispersion for the bias factor (β_{BF}) is calculated for various analysis methods such as monotonic linear elastic analysis, monotonic second-order inelastic (push-over) analysis, and linear dynamic time history analysis. The bias factors given in FEMA-350 will also be used in this research for RCFT structures. β_{BF} and β_{NTH} will be combined to calculate β_{UD} as given in Equation 7.24. β_{UD} is assumed to be the same at the local and global level.

$$\beta_{UD}^2 = \beta_{BF}^2 + \beta_{NTH}^2 \quad [7.24]$$

The randomness in demand evaluations is calculated based on nonlinear time history analysis results. The standard deviation of the natural log of the maximum interstory drift ratios from nonlinear time history analysis (β_{RD}) represents the measure of dispersion in the demand evaluations due to record-record variations. β_{RD} is assumed to be the same both at the global and local level.

The seismic demand evaluation results of Frame IIIa and Frame IIIId that were presented in Chapter 6 were utilized to obtain β_{RD} of RCFT structures. The variance of the maximum interstory drift ratios is determined for both frames at 10%50 and 2%50 hazard levels. Then, the variance is converted into standard deviation in the log-normal space to arrive at β_{RD} . Table 7-4 summarizes β_{RD} values obtained for Frame IIIa and Frame IIIId.

Table 7-4 Summary of β_{RD} for 3-story RCFT Frame Structures

Hazar Level	2%50	10%50
IIIa	0.13	0.09
IIIId	0.23	0.31

7.3. Capacity Factors

Obtaining the measure of dispersions for the local and global capacity of the structural members, the capacity factor can be calculated using the expression given below, which was previously introduced in Equations 7.12 and 7.13.

$$\phi = e^{\left[-\frac{1}{2b}(\beta_{RC}^2 + \beta_{UC}^2)\right]} \quad [7.25]$$

The factor k in Equation 7.25 represents the slope of the hazard curve and it is assumed 3 for California. The b factor is taken as equal 1 following the recommendation by Luco and Cornell (1998).

Substituting the β_{RC} and β_{UC} values of the RCFT members, the capacity factors at the local level can be quantified as given in Table 7-5.

Table 7-5 Summary of Capacity Factors for RCFT Members

Limit States	Yielding of Compression Flange	Yielding of Tension Flange	Local Buckling of Compression Flange	Local Buckling of Web
β_{UC}	0.536	0.307	0.702	0.344
β_{RC}	0.2	0.2	0.2	0.2
ϕ	0.61	0.82	0.45	0.79

The capacity factor for global response of 3 story structures can be calculated by substituting $\beta_{UC} = 0.26$ and $\beta_{RC} = 0.07$ into Equation 7.25 and ϕ factor is obtained as 0.897.

7.4. Demand Factors

The demand factor introduced in Equations 7.12 and 7.13 is assumed to consist of two parts including γ and γ_{α} as shown in Equation 7.26.

$$\gamma = e^{\left[\frac{1}{2b}(\beta_{RD}^2 + \beta_{UD}^2)\right]} = \gamma \times \gamma_{\alpha} \quad [7.26]$$

γ is termed as the demand uncertainty factor accounting for uncertainties emanating from structural response and ground motion characteristics. On the other hand, γ_{α} quantifies the bias and uncertainty introduced by using a specific analysis procedure. γ and γ_{α} can be calculated as follows from Equation 7.26.

$$\gamma = e^{\left[\frac{1}{2} \frac{k}{b} (\beta_{RD}^2) \right]} \quad [7.27]$$

The demand factor for RCFT structures is calculated by substituting β_{RD} values into Equation 7.27 as detailed in Table 7-6.

Table 7-6 Summary of γ values for 3-story RCFT Frame Structures

Hazard Level	2%50	10%50
IIIa	1.03	1.01
IIIId	1.08	1.15

The calculation γ_{α} is performed using Equation 7.28. However, its value is dependent on the analysis method to be used identified through bias factors provided in FEMA-350 (2000).

$$\gamma = e^{\left[\frac{1}{2} \frac{k}{b} (\beta_{UD}^2) \right]} = e^{\left[\frac{1}{2} \frac{k}{b} (\beta_{BF}^2 + \beta_{NTH}^2) \right]} \quad [7.28]$$

7.5. Confidence Level

The reliability framework employed in the current performance-based design provisions involves calculation of a confidence parameter that permits quantifying the confidence level to achieve a specific performance objective. The confidence parameter (λ_{con}) has the form given in Equation 7.29 as the ratio of factored demand to the factored capacity.

$$\lambda_{con} = \frac{\gamma \bar{D}^{P_o}}{\phi \bar{C}} \quad [7.29]$$

7.6. Intended Performance Based-Design Methodology

The design process starts by selecting the targeted performance level and the corresponding hazard level. Based on the selected performance level (e.g., Immediate Occupancy, Collapse Prevention), the capacity at the local level is calculated in terms of deformation-based ($\hat{D}_{capacity}$) or energy-based ($\hat{E}_{capacity}$) damage indices using the

empirical formulations proposed by Tort and Hajjar (2003a, b). Note that, in this chapter of the report, the resistance factor calculations are illustrated only for deformation-based damage functions. However, the same procedure described in Section 7.1.1 can be utilized to arrive at resistance factors for energy-based damage functions. The damage index values at the local level are compared to their limiting values reported for different performance levels by Tort and Hajjar (2003a, b). This comparison helps to identify the local damage states to be checked for the targeted performance level. The global capacity (C) corresponding to the targeted performance level is obtained from recommended value based on incremental dynamic analysis. In the second stage, load deflection curves of the RCFT members to be designed are constructed using the available finite element methods. For example Figure 7.8 shows the lateral displacement vs. shear force response of an RCFT column obtained from nonlinear static push over analysis of the whole structure that the RCFT column serves as a structural member.

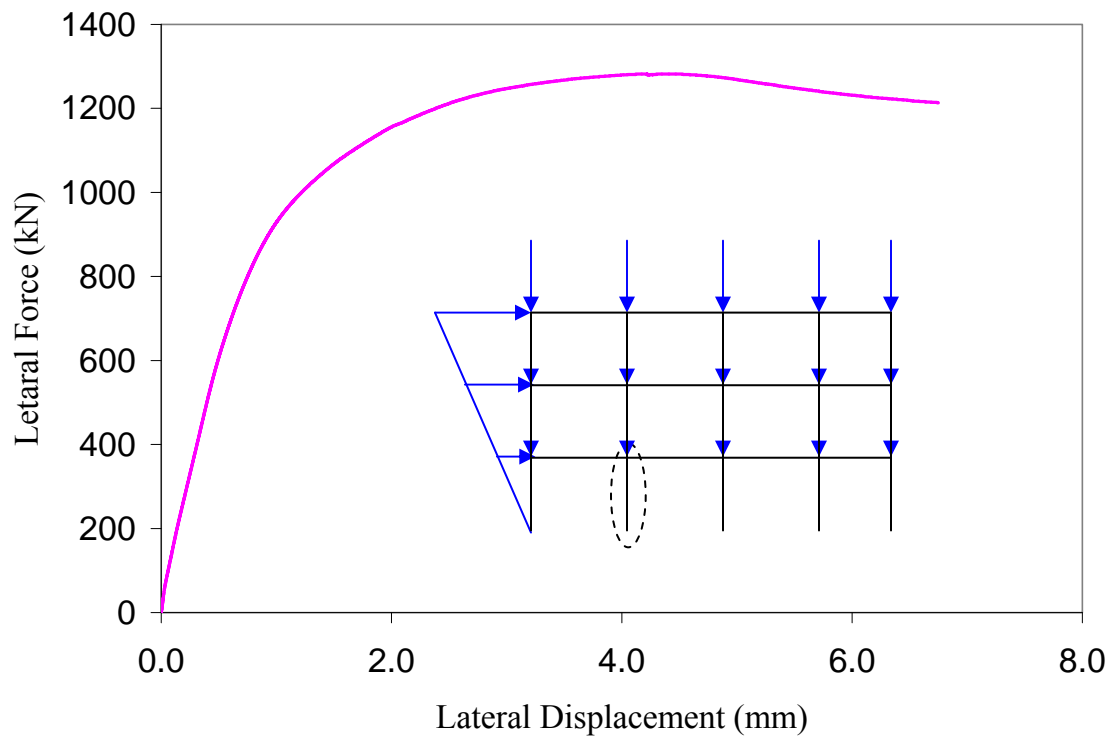


Figure 7.8 Load Deformation Response of the RCFT Column to Calculate Damage Function Values

The next stage of the design process involves the analysis of the whole structure for the selected hazard level using the available analysis methods such as equivalent static load, static push-over analysis, or nonlinear time history analysis. The maximum or mean deformation values for the RCFT members are obtained from the analysis results. Using the maximum or mean deformation values, the current states of the members are located on their load deflection curves from the previous stage. For example, Figure 7.9 shows the mean deformation level of an RCFT column obtained from nonlinear time history analysis for a set of earthquake records. The time history analysis results are superimposed on the static push-over response to evaluate the damage function values imposed on the column. Following the calculation of the energy-based (\hat{D}_{demand}) and deformation-based (\hat{E}_{demand}) damage function values, they are checked against the limiting values of the local damage states (concrete cracking, concrete crushing, steel yielding etc.) so that the achieved local performance level is decided. The global demand (D) of the structure is also determined from the analysis results. At the final stage, the quantified values of demand and capacity of the RCFT structure are adjusted for uncertainty and randomness both at the local and global level. The design is assumed to be successful if the factored values of demand are greater than the factored values of capacity and satisfies the targeted confidence level.

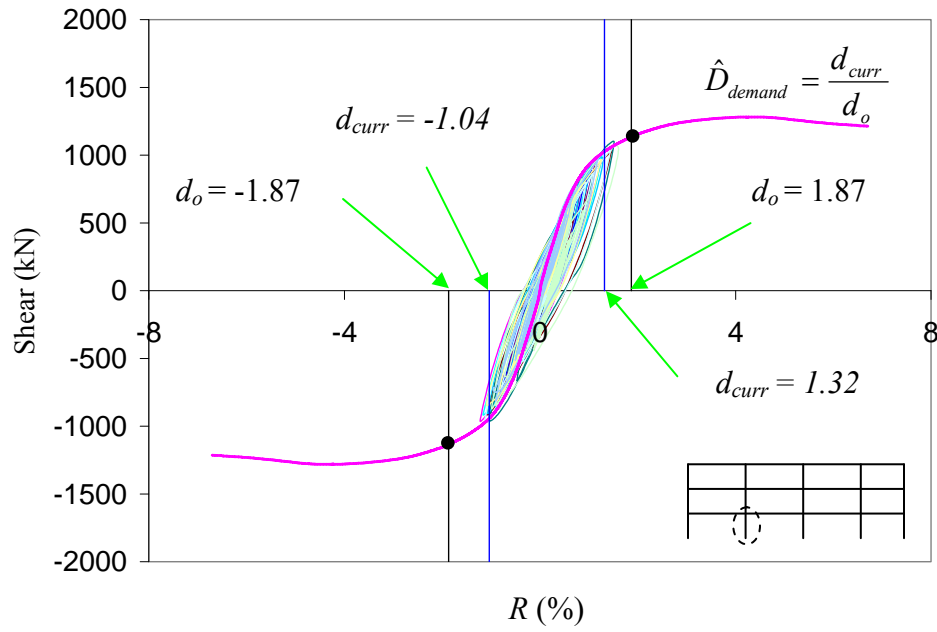


Figure 7.9 Calculation of Damage Function Values Imposed on a RCFT Column Based on Nonlinear Time History Analysis

Chapter 8

8. Conclusion

A computational study was conducted to develop an efficient and accurate analysis method that will allow investigation of the seismic response of three-dimensional steel and concrete composite structures with rectangular concrete-filled steel tube (RCFT) beam-columns and steel girders. The analysis method was tailored with comprehensive numerical algorithms and material formulations to account for the salient features of RCFT columns. Following the calibration and verification of the computational model against a large set of experimental and analytical results from the literature, the formulation was used for examining the seismic performance of representative RCFT frame structures. A reliability-based performance-based design methodology was then proposed for quantifying seismic performance of composite RCFT frames in the form of multiple structural demand and capacity parameters and also evaluating the inherent uncertainties and randomness in the seismic response assessments.

A distributed plasticity mixed finite element methodology was employed for the derivation of the three-dimensional RCFT beam-column finite element. A total number of 18 degrees-of-freedom (DOFs) were defined so that the differential axial deformations between the steel tube and the concrete core can be accounted for. For each node of the beam-column finite element, an additional 3 DOFs were introduced to define the translational deformations of the steel tube and the concrete core independently. The numbering of the DOFs was performed in such a way that automatic assembly may be done without additional computational effort when an 18-DOF RCFT beam-column is framed by 12 DOF steel girders. Among the translational DOFs, the shear translations of the steel tube and the concrete core were constrained to be equal to each other via geometrically nonlinear penalty functions. Therefore, the differential displacement between the two media can only occur in the axial (longitudinal) direction of the element,

which is governed by the bond-slip characteristics of the interface. The rotational DOFs were defined commonly due to the inherent compatibility between the steel tube and the concrete core since the concrete core placed inside the steel tube. Therefore, the first set of 3 DOFs were assumed to be steel translations, the second set of 3 DOFs were assumed to be steel and concrete rotations, and the final 3 DOFs were reserved for concrete core translations. The stiffness and element internal forces were derived in the corotational reference of frame, where rigid body modes of deformations were excluded in the derivations. The statement of equilibrium was expressed based on the principle of virtual displacements as a balance between the internal and external work done. Since the slip deformation at the interface requires an energy input, the statement of equilibrium was augmented with an extra term to account for the energy accumulation at the interface. In the addition, the rest of the energy terms in the equilibrium equation were defined separately for the steel tube and concrete core. Cubic-Hermitian and quadratic interpolation functions were introduced for the transverse and axial deformation fields, respectively. The Green-Lagrange strain measure was adopted to define the axial strains along the element length. The curvatures were assumed to be the second-order derivative of the transverse deformation fields exploiting the plane sections remain plane assumption. The kinematic expression of the slip deformation was defined as the difference between the axial deformations at the two nodes of the RCFT beam-column element. Employing a distributed plasticity mixed finite element formulation, the element internal forces were also treated as unknown variables in addition to the nodal deformations. Therefore, two new equations of element compatibility and cross-section equilibrium were introduced to be solved in addition to the element equilibrium. The compatibility equation expressed the balance between the deformations obtained from interpolated displacements and those obtained from interpolated forces. The force interpolation was achieved by introducing linear shape functions for both bending moment and axial forces. Consistent with the element deformations, the element forces were defined separately for the steel tube and the concrete core. The cross-section equilibrium defined the balance between interpolated forces and the forces obtained directly from constitutive relations. In order to trace the load-deformation response of an

RCFT beam-column element under externally applied loads, the element equilibrium, compatibility, and cross-section equilibrium are required to be solved simultaneously. However, due to their nonlinear nature, these equations are needed to be solved incrementally. Therefore, they were linearized with respect to their state variables to arrive at the expressions for element stiffness and internal forces. The calculation of the element internal forces is often considered to be the critical stage of a nonlinear finite element solution algorithm and it was outlined in detailed for the current formulation. The internal force determination starts by solving for the incremental displacements in the corrotational frame. Utilizing the displacement shape functions and kinematic relations, the axial strain and curvatures were obtained along the element length. Then, the compatibility equation was evaluated and it is multiplied by the element flexibility to obtain the nodal forces. Interpolating the nodal forces, the cross-section forces along the element length were determined. The cross-section forces were converted into cross-section deformations in the form of axial strains and curvatures and a new set of cross-section forces are calculated based on material constitutive relations. Then, the cross-section equilibrium and compatibility equation were then evaluated subsequently to determine their residuals. In the current formulation, those residual were transferred to the residual of the element equilibrium to be solved through global Newton-Raphson iterations. In order to have a finite element formulation to analyze full composite frames, a similar distributed plasticity mixed finite element formulation was also developed for an 12 DOF beam-column element to simulate steel girders or braces framing into RCFT columns.

Investigating the inelastic response of RCFT frames requires developing comprehensive material constitutive relations for the concrete core and the steel tube. The constitutive model of the concrete core was developed to simulate the uniaxial stress-strain response under both cyclic and monotonic loading schemes. Both the compressive response and the tensile response were considered in detail. Based on the uniaxial compression tests in the literature on stocky RCFT columns, it was assumed that the concrete core behaves as plain concrete until the attainment of the peak compressive stress, where it is described by an ascending type nonlinear curve. The confinement

effect provided by the steel tube becomes effective following the breachment of the peak compressive stress and it manifests itself by ensuring a mild linear strength degradation response after peak compressive stress. No strength enhancement due to confinement was considered consistent with experimental results. The concrete core was assumed to retain a constant stress level at large compressive strain ranges. The monotonic tensile response was assumed to be the same as plain concrete, where a sudden stress drop that asymptotically reaching to zero was assumed once the tensile strength is breached. The monotonic tensile response and the compressive response until the peak stress were adopted from the existing models in the literature (Chang and Mander, 1994; Tsai, 1988). In this research, empirical equations were derived to define the slope of the linear strength degradation region and also to define the magnitude of the constant stress maintained at high compressive strains. The data points to develop these equations were obtained from the experiments in the literature, where concrete core was instrumented. It was found that the slope of the strength degradation response is correlated with the strength concrete and slenderness of the steel tube as a function of its depth, thickness, and yield stress. The strength degradation becomes more severe if the strength of concrete is high. In addition, the concrete core of RCFT beam-columns with slender steel tubes experiences a larger rate of strength degradation. The same parameters were also used to derive the equations for the residual compressive stress. The specimens having high strength concrete and slender steel tubes were found to exhibit lower constant stress levels. The equations were calibrated so that they are valid for RCFT beam-columns having a wide range of material and geometric properties. The cyclic rules of the concrete model were adopted from Chang and Mander (1994) as polynomial expressions defining the unloading and reloading type response. Partial unloading and reloading type behavior, stress reversal between tension and compression were modeled. In order to increase the comprehensiveness of the formulation under random strain histories, new rules were defined and implemented. The accuracy of the model was tested against multiple cyclic loading tests conducted on confined and unconfined concrete specimens.

The constitutive relation of the steel tube was described using the uniaxial bounding surface model proposed by Mizuno et al. (1991). The model had the capability

to trace stress-strain response under both monotonic and cyclic loadings. The inelasticity was simulated based on the evolution of the bounding and loading surfaces. The bounding surface defined the limiting stress state that the material can attain. The boundary between elastic and inelastic response was described by the loading surface. Inelasticity was assumed to initiate once the stress state reaches the loading surface. It is the distance between the bounding and loading surfaces indicating the degree of plasticity that the material was subjected to. The model had the features of accounting for several key phenomena typical for steel material including hardening, Baushinger-effect, reduction of elastic response etc. The focus of this research is on RCFT beam-columns with cold-formed steel tube, which exhibit different characteristics from those with hot-rolled steel tube. The model by Mizuno et al. (1991) was modified so that the residual stress patterns generated due to cold-forming process can be captured. This was achieved by calibrating an initial plastic strain level from the coupon tests in the literature. In addition, the flat plateau response of hot-rolled steel following yielding was not implemented since cold-formed steel often exhibits a gradual yielding response. The cold-forming process results in variation of yielding stress around the perimeter of the steel tube. Therefore, different yield stress values were calibrated for the flat and corner regions based on the coupon tests available in the literature. Under large compressive strains, slender steel tubes experience local buckling type behavior leading to a strength degradation type response. In this research, the steel model by Mizuno et al. (1991) was augmented so that the local buckling phenomena can be accounted for. It was assumed that a linear strength degradation region initiates once the strain level of local buckling is reached and this softening type of response continues until a constant stress region is attained. Equations were derived to define the strength degradation response and the constant stress region based on axially-loaded stocky RCFT columns available in the literature. It was found that as the slenderness of the steel tube gets larger (e.g., small thickness, high yield stress), it becomes more susceptible to local buckling and experiences earlier local buckling with more severe strength degradation with smaller residual stress values. Examining the experiments on RCFT beam-columns under cyclic loading schemes, it was found that local buckling generates a reduction in strength even

if the amplitude of plastic strain remains approximately the same. This type of behavioral pattern was introduced into the steel model by calibrating an equation as a function of the plastic work causing a reduction in the radius of the bounding surface. Therefore, the hardening type response typically observed in the absence of local buckling turns into a softening type response once local buckling initiates. The model proposed by Mizuno et al. (1991) was also used in this research to simulate the stress-strain response of steel girders. The local buckling feature typically observed for non-compact steel girder cross-sections was added to the existing model. Examining the literature for monotonic and cyclic tests conducted on steel girders, equations were derived to define the strength degradation and constant stress regions. In addition, the reduction of the bounding surface as function of the accumulated plastic work was described through equations calibrated with respect to cyclic tests.

The bond-slip response of the interface between the steel tube and the concrete core was assumed to exhibit a bilinear type response, where a linear elastic region until the attainment of peak bond stress is followed with a linear post-peak region having an approximately zero stiffness. The push-out tests on RCFT columns available in the literature indicated that the aforementioned constitutive relation is a realistic representation of the cyclic bond-slip response.

The performance of the distributed plasticity mixed finite element formulation along with the constitutive relations was assessed by analyzing RCFT specimens tested in the literature and then conducting comparisons between computational and experimental results. This was performed for specimens under different boundary conditions and loading schemes. The verification studies were carried out under three main headings including geometrically nonlinear elastic problems, slip-critical materially and geometrically nonlinear problems, and materially and geometrically nonlinear problems. In the geometrically nonlinear elastic problems, the ability of the mixed finite element formulation was checked to predict the buckling load and the load deformation response under the existence $P-\Delta$ and $P-\delta$ type geometric nonlinearities. Several numerical algorithms were employed. The buckling load was decided based on the sign of the minimum eigen value. The problems exhibiting softening type or snap back response

were analyzed utilizing constant displacement arc length, and generalized displacement arc length methods (Yang and Kuo, 1994). The mixed finite element formulation produced excellent correlations with the analytical results for a wide range of problems with the use of at most 3 elements along the member length, with 4 integration points used per finite element.

The slip critical geometrically and materially nonlinear problems were studied to understand the load transfer mechanism existing in RCFT members. The typical test setup for these problems consisted of a simply-supported RCFT column framed by steel girders. The loading was introduced as axial load proportionally applied at the tip of the steel girders and at the top of the columns. The comparison of the results were performed based on several structural response parameters including axial strain, slip, axial force distribution along the element length. The mixed finite element formulation often produced excellent correlations with the experiments when the stiffness of the interface is set to 10^4 MPa and when the bond strength is assumed as 0.6 MPa. The geometrically and materially nonlinear problems were studied under 5 different headings given below:

1. RCFT columns under axial loading
2. RCFT beams under pure bending
3. RCFT beam-columns under proportional loading
4. RCFT beam-column under non-proportional loading
5. RCFT beam-columns under cyclic lateral loading and constant axial force

RCFT specimens with wide ranges of material and geometric properties were studied as described in Table 8-1. For the majority of the specimens, 2 to 3 finite elements per member with 4 integration points were found to produce very accurate comparisons with the experimental results.

The problems under dynamic loads were studied in two groups as geometrically nonlinear and materially linear and both geometrically and materially nonlinear types. Newmark-Beta ($\gamma = 0.5, \beta = 0.25$) time integration scheme was employed to solve for the load-deformation response of the RCFT members. Lumped mass and proportional damping idealizations were assumed. A small mesh size was selected for the geometrically and materially nonlinear type problems to alleviate the lumped mass

assumption for analytical solutions with consistent mass approach. In the case of both geometrically and materially nonlinear type problems, a four-story frame structure tested by pseudo-dynamic testing procedure was analyzed. The mesh size of the structure was decided based on the instrumentation layout. The correlation of experimental and computational results were satisfactory both at the global and local level.

The final verification study was performed for monotonically loaded steel girders under three point bending and cyclically loaded steel cantilevers, where the number of finite elements per member was selected as 4 and 3, respectively. The number of integration points retained at 4. The experimental load-deformation response of the specimens was successfully predicted. In addition, the initiation of local buckling and its effect on the load deformation response agreed with the experimental observations.

Table 8-1 Ranges of Material and Geometric Properties of RCFT Specimens Studied in Verification Study

RCFT Loading Type	f'_c (MPa)	f_y (MPa)	D/t	L/D	P/P_o
1	21-110	194-835	15-74	3.0-5.0	na
2	22-88	285-490	17-44	1.5-8.6	na
3	31-103	254-420	15-27	10.5-34.5	na
4	21-110	269-781	32-53	3.0-4.9	na
5	18-40	298-590	22-24	6.0-18.0	0.15-0.40

A seismic demand assessment study was conducted on representative RCFT frame structures. Two stiffness-controlled three-story frames with varying material and geometric properties. The first frame had RCFT columns with conventional material strengths and section sizes. On the other hand, the second frame was designed to have RCFT columns having high strength slender steel tube sections combined with high strength concrete. The records were scaled with respect to the first mode spectral acceleration to represent 2%/50 and 10%/50 seismic hazard levels. Conducting nonlinear time history analysis of the structures, the seismic demand was quantified in terms

multiple structural response parameters including roof drift, maximum inter-story drift ratio, base-shear, and deformation-based damage function values. For both structures, the damage was found to be concentrated at the 1st story columns. The material inelasticity exhibited significant differences for both frames. The first frame with conventional materials and cross-section sizes exhibited a wider range of local damage states for both the steel tube and the concrete core including steel yielding, local buckling of the flange, concrete cracking, and concrete crushing. On the other hand, for the second frame, the damage was significantly concentrated on the steel tube in the form of local buckling. However, for the studied frames, the mean values of the structural response parameters did not exhibit significant differences. This is due to fact that both frames were designed with respect to the strong column-weak beam requirement exhibiting significant overstrength with respect to the design base-shear.

The final chapter of the report was devoted to introduce the recommended reliability and performance-based design framework for RCFT frames. Following the approach adopted in FEMA-350 (2000), the demand and capacity factor format was adopted to account for the uncertainty and randomness in the components of the performance-based design such as ground motion hazard, seismic demand, and seismic capacity. The dispersion in the structural response parameters from the demand analysis study was utilized to derive the demand factor of RCFT frames. The capacity factor was calculated quantifying the dispersion in the damage function equations proposed by Tort and Hajjar (2003) to estimate the capacity of RCFT member against local damage states. Proposing the methodology to estimate the inherent randomness and uncertainty in seismic design of RCFT members, a performance-based design approach was recommended building on the prior work by Tort and Hajjar (2003) on capacity assessment of RCFT frames and members.

The studies on seismic performance of the RCFT structures indicated that the estimation of the initiation and the extent of the damage states of RCFT members is quite challenging. The composite interaction between the two media leads to significant differences in damage evolution. In their previous work, Tort and Hajjar (2003) focused on deriving empirical capacity equations to estimate the performance of the RCFT

members. Based on the available experimental data, the main criteria to identify the damage was selected as the occurrence of the limit states such as concrete cracking, concrete crushing etc. Despite the efficiency of this approach, the results in this study on inelastic seismic and inelastic non-seismic behavior of RCFT member indicated that the initiation of local damage states is sufficient to describe the performance since the effect of local damage states manifest themselves on the load-deformation response through accumulation and interaction with each other. Therefore, the performance of the RCFT member should be related to more comprehensive damage measures. The distributed mixed finite element formulation developed in this research was found to be a powerful tool to derive damage measures that will address the performance of the structure and structural members realistically.

8.1. Future Research Recommendations

Despite the intended comprehensiveness of the current study, there exist several research areas that need further exploration in future studies. The future research recommendations that will augment the current research study are summarized below:

- The experimental research studies on composite structures are increasing as new testing and instrumentation techniques become available. Therefore, verification studies can be expanded through analyzing new experimental tests in literature. The tests having complicated loading histories with variable and multiaxial loading conditions are typical examples to be investigated.
- In the material constitutive relations adopted in this research study, the phenomena like confinement, local buckling, and multiaxial stress state were implicitly accounted for through modifying the uniaxial stress-strain relations based on the observed behavior at the global load-deformation level. New multi dimensional material formulations allowing the simulation of confinement and local buckling explicitly can be developed to improve the constitutive relations.
- The analysis of RCFT frames was conducted assuming rigid connections at the beam-column joints. This assumption influences the accuracy of the assessment

of seismic and demand capacity. New connection elements compatible with the mixed finite element formulations of the RCFT columns and steel girders are recommended to be developed.

- The damage function equations provided by Tort and Hajjar (2003) provide a very comprehensive definition of local capacity of RCFT members. However, for some of the local damage states such concrete crushing and local buckling, a large dispersion is evident in the experimental results. The damage function equations by Tort and Hajjar (2002) can be improved by generating more data points from the new experimental tests or from parametric study that can be done using the current mixed finite element formulation.
- The seismic demand and capacity assessment studies can be extended to a boarder range of RCFT frames with different sizes or load resisting systems (e.g., braced frames, braced and moment frame combined).
- The mixed finite element formulation developed for the steel girders can be applied to composite girders to have a more realistic representation of RCFT frames.

APPENDIX A

A.1. RCFT Mixed Finite Element Formulation

This appendix includes the supplementary equations of the RCFT beam-column mixed finite element formulation presented in Chapter 2. It should be noted that the variables not defined in this appendix can be found in Chapter 2.

A.1.1. Finite Element Discretization

The deformation fields along the RCFT beam-column are expressed using interpolation functions of quadratic, cubic Hermitian, and linear types for axial deformations, transverse displacements, and torsional rotations, respectively.

$$\mathbf{u} = \mathbf{N}_u \times \mathbf{q} \quad [\text{A.1}]$$

$$\mathbf{u} = \left[u^c \ v^c \ w^c \ u^s \ v^s \ w^s \right] \quad [\text{A.2}]$$

$$\mathbf{q} = \left[e^{sc} \ e^c \ \theta_{zi}^c \ \theta_{yi}^c \ \theta_{zj}^c \ \theta_{yj}^c \ e^s \ \theta_{zi}^s \ \theta_{yi}^s \ \theta_{zj}^s \ \theta_{yj}^s \ e_m^c \ e_m^s \right]^T \quad [\text{A.3}]$$

$$\mathbf{N}_u = \begin{bmatrix} 1 & -i+2i^2 & 0 & 0 & 0 & 0 & 0 & 0 & 0 & 0 & 0 & 0 & -4i^2+4i & 0 \\ 0 & 0 & L(i-2i^2+i^3) & 0 & L(-i^2+i^3) & 0 & 0 & 0 & 0 & 0 & 0 & 0 & 0 & 0 \\ 0 & 0 & 0 & L(i-2i^2+i^3) & 0 & L(-i^2+i^3) & 0 & 0 & 0 & 0 & 0 & 0 & 0 & 0 \\ 0 & 0 & 0 & 0 & 0 & 0 & -i+2i^2 & 0 & 0 & 0 & 0 & 0 & 0 & -4i^2+4i \\ 0 & 0 & 0 & 0 & 0 & 0 & 0 & L(i-2i^2+i^3) & 0 & L(-i^2+i^3) & 0 & 0 & 0 & 0 \\ 0 & 0 & 0 & 0 & 0 & 0 & 0 & 0 & L(i-2i^2+i^3) & 0 & L(-i^2+i^3) & 0 & 0 & 0 \end{bmatrix} \quad [\text{A.4}]$$

where: $i = x / L$

The element end forces in the corotational coordinates are defined as axial moments and bending moments at both ends of the element defined for steel tube and concrete core, separately. Linear shape functions are employed for approximating force resultants along the element length. However, the transverse deformation fields from Equation A.1 are also included in the force interpolation functions to account for the P- δ effects while approximating moment fields. Equations A.5 and A6 illustrates the nodal

force vector at the natural coordinates and cross-section force vector at an integration point, respectively.

$$\mathbf{Q} = \left[P_i^c \ P_j^c \ M_{zi}^c \ M_{yi}^c \ M_{zj}^c \ M_{yj}^c \ P_i^s \ P_j^s \ M_{zi}^s \ M_{yi}^s \ M_{zj}^s \ M_{yj}^s \right]^T \quad [\text{A.5}]$$

$$\mathbf{D} = \mathbf{N}_{D1} \times \mathbf{Q} \quad [\text{A.6}]$$

$$\mathbf{N}_{D1} = \begin{bmatrix} i-1 & i & 0 & 0 & 0 & 0 & 0 & 0 & 0 & 0 & 0 & 0 \\ {}_1w^c & 0 & i-1 & 0 & i & 0 & 0 & 0 & 0 & 0 & 0 & 0 \\ {}_1v^c & 0 & 0 & i-1 & 0 & i & 0 & 0 & 0 & 0 & 0 & 0 \\ 0 & 0 & 0 & 0 & 0 & 0 & i-1 & i & 0 & 0 & 0 & 0 \\ 0 & 0 & 0 & 0 & 0 & 0 & {}_1w^s & 0 & i-1 & 0 & i & 0 \\ 0 & 0 & 0 & 0 & 0 & 0 & {}_1v^s & 0 & 0 & i-1 & 0 & i \end{bmatrix} \quad [\text{A.7}]$$

where: $w^c = L \times (i - 2 \times i^2 + i^3) \times \theta_{zi}^c + L \times (-i^2 + i^3) \times \theta_{zj}^c$

$v^c = L \times (i - 2 \times i^2 + i^3) \times \theta_{yi}^c + L \times (-i^2 + i^3) \times \theta_{yj}^c$

$w^s = L \times (i - 2 \times i^2 + i^3) \times \theta_{zi}^s + L \times (-i^2 + i^3) \times \theta_{zj}^s$

$v^s = L \times (i - 2 \times i^2 + i^3) \times \theta_{yi}^s + L \times (-i^2 + i^3) \times \theta_{yj}^s$

A.1.2. Hellinger-Reissner Principle

In the Hellinger-Reissner principle, the virtual work equation of equilibrium and the compatibility equation that is put in the form of a constraint using Lagrange multipliers are combined as given in Equation A.8.

$$\begin{aligned} & \int_0^1 \delta_1 \hat{\mathbf{d}}^T \times {}_1^2 \mathbf{D} \times d^1 \mathbf{x} + \int_0^1 \delta_1 \hat{\mathbf{d}}_{sc}^T \times {}_1^2 \bar{\mathbf{k}}_{sc} \times {}_1 \hat{\mathbf{d}}_{sc} \times d^1 I + \int_1^I \delta_1 \hat{\mathbf{d}}_{sc}^T \times {}_1^1 \mathbf{D}_{sc} \times d^1 I + \\ & \int_1^{V^c} {}_1^1 \rho^c \times {}_1^2 \ddot{\mathbf{u}}^c \times \delta_1 \mathbf{u}^c \times d^1 V^c + \int_1^{V^s} {}_1^1 \rho^s \times {}_1^2 \ddot{\mathbf{u}}^s \times \delta_1 \mathbf{u}^s \times d^1 V^s + \\ & \int_1^{V^c} {}_1^1 \mu^c \times {}_1^2 \ddot{\mathbf{u}}^c \times \delta_1 \mathbf{u}^c \times d^1 V^c + \int_1^{V^s} {}_1^1 \mu^s \times {}_1^2 \ddot{\mathbf{u}}^s \times \delta_1 \mathbf{u}^s \times d^1 V^s + \\ & - \delta_1 \mathbf{q}^T \times {}_1^2 \mathbf{Q}_{ext} + \int_0^1 \delta_1^2 \mathbf{D}^T \times ({}_1 \hat{\mathbf{d}} - {}_1 \mathbf{d}) \times d^1 \mathbf{x} = 0 \end{aligned} \quad [\text{A.8}]$$

The displacement (${}_1\mathbf{u}^c, {}_1\mathbf{u}^s$), velocity (${}^2\dot{\mathbf{u}}^c, {}^2\dot{\mathbf{u}}^s$), and acceleration (${}^2\ddot{\mathbf{u}}^c, {}^2\ddot{\mathbf{u}}^s$) fields defined for the steel tube and concrete core are stated in Equation A.9.

$${}_1\mathbf{u}^c = {}^1\mathbf{N}_u^c \times {}_1\mathbf{q}, \quad {}_1\mathbf{u}^s = {}^1\mathbf{N}_u^s \times {}_1\mathbf{q} \quad [\text{A.9a}]$$

$${}^2\dot{\mathbf{u}}^c = {}^1\mathbf{N}_u^c \times {}^2\dot{\mathbf{q}}, \quad {}^2\dot{\mathbf{u}}^s = {}^1\mathbf{N}_u^s \times {}^2\dot{\mathbf{q}} \quad [\text{A.9b}]$$

$${}^2\ddot{\mathbf{u}}^c = {}^1\mathbf{N}_u^c \times {}^2\ddot{\mathbf{q}}, \quad {}^2\ddot{\mathbf{u}}^s = {}^1\mathbf{N}_u^s \times {}^2\ddot{\mathbf{q}} \quad [\text{A.9c}]$$

where: ${}_1\mathbf{u}^c = [{}_1u^c \quad {}_1v^c \quad {}_1w^c]^T$, ${}_1\mathbf{u}^s = [{}_1u^s \quad {}_1v^s \quad {}_1w^s]^T$

$${}^2\dot{\mathbf{u}}^c = [{}^2\dot{u}^c \quad {}^2\dot{v}^c \quad {}^2\dot{w}^c]^T, \quad {}^2\dot{\mathbf{u}}^s = [{}^2\dot{u}^s \quad {}^2\dot{v}^s \quad {}^2\dot{w}^s]^T$$

$${}^2\ddot{\mathbf{u}}^c = [{}^2\ddot{u}^c \quad {}^2\ddot{v}^c \quad {}^2\ddot{w}^c]^T, \quad {}^2\ddot{\mathbf{u}}^s = [{}^2\ddot{u}^s \quad {}^2\ddot{v}^s \quad {}^2\ddot{w}^s]^T$$

$$i = \frac{{}^1x}{{}^1L}$$

$${}^1\mathbf{N}_u^c = \begin{bmatrix} 1 & -i + 2i^2 & 0 & 0 & 0 & 0 & 0 & 0 & 0 & 0 & 0 & -4i^2 + 4i & 0 \\ 0 & 0 & L(i - 2i^2 + i^3) & 0 & L(-i^2 + i^3) & 0 & 0 & 0 & 0 & 0 & 0 & 0 & 0 \\ 0 & 0 & 0 & L(i - 2i^2 + i^3) & 0 & L(-i^2 + i^3) & 0 & 0 & 0 & 0 & 0 & 0 & 0 \end{bmatrix}$$

$${}^1\mathbf{N}_u^s = \begin{bmatrix} 0 & 0 & 0 & 0 & 0 & 0 & -i + 2i^2 & 0 & 0 & 0 & 0 & -4i^2 + 4i \\ 0 & 0 & 0 & 0 & 0 & 0 & 0 & L(i - 2i^2 + i^3) & 0 & L(-i^2 + i^3) & 0 & 0 & 0 \\ 0 & 0 & 0 & 0 & 0 & 0 & 0 & 0 & L(i - 2i^2 + i^3) & 0 & L(-i^2 + i^3) & 0 & 0 \end{bmatrix}$$

$${}_1\mathbf{q} = [{}_1e^{sc} \quad {}_1e^c \quad {}_1\theta_{zi}^c \quad {}_1\theta_{yi}^c \quad {}_1\theta_{zj}^c \quad {}_1\theta_{yj}^c \quad {}_1e^s \quad {}_1\theta_{zi}^s \quad {}_1\theta_{yi}^s \quad {}_1\theta_{zj}^s \quad {}_1\theta_{yj}^s \quad {}_1e_m^c \quad {}_1e_m^s]^T$$

$${}^2\dot{\mathbf{q}} = [{}^2\dot{e}^{sc} \quad {}^2\dot{e}^c \quad {}^2\dot{\theta}_{zi}^c \quad {}^2\dot{\theta}_{yi}^c \quad {}^2\dot{\theta}_{zj}^c \quad {}^2\dot{\theta}_{yj}^c \quad {}^2\dot{e}^s \quad {}^2\dot{\theta}_{zi}^s \quad {}^2\dot{\theta}_{yi}^s \quad {}^2\dot{\theta}_{zj}^s \quad {}^2\dot{\theta}_{yj}^s \quad {}^2\dot{e}_m^c \quad {}^2\dot{e}_m^s]^T$$

$${}^2\ddot{\mathbf{q}} = [{}^2\ddot{e}^{sc} \quad {}^2\ddot{e}^c \quad {}^2\ddot{\theta}_{zi}^c \quad {}^2\ddot{\theta}_{yi}^c \quad {}^2\ddot{\theta}_{zj}^c \quad {}^2\ddot{\theta}_{yj}^c \quad {}^2\ddot{e}^s \quad {}^2\ddot{\theta}_{zi}^s \quad {}^2\ddot{\theta}_{yi}^s \quad {}^2\ddot{\theta}_{zj}^s \quad {}^2\ddot{\theta}_{yj}^s \quad {}^2\ddot{e}_m^c \quad {}^2\ddot{e}_m^s]^T$$

The cross-sectional strains are expressed in terms of element deformations in Equation A.10.

$${}_1\hat{\mathbf{d}} = {}^1\mathbf{N}_d \times {}_1\mathbf{q} \quad [\text{A.10}]$$

where: ${}_1\hat{\mathbf{d}} = [{}_1\varepsilon^c \quad {}_1\kappa_z^c \quad {}_1\kappa_y^c \quad {}_1\varepsilon^s \quad {}_1\kappa_z^s \quad {}_1\kappa_y^s]^T$

$$\begin{aligned}
{}^1\mathbf{N}_{\hat{d}} &= \begin{bmatrix} ({}^1\mathbf{N}_{\hat{d}})_{RR} & ({}^1\mathbf{N}_{\hat{d}})_{RS} \\ ({}^1\mathbf{N}_{\hat{d}})_{SR} & ({}^1\mathbf{N}_{\hat{d}})_{SS} \end{bmatrix} \\
({}^1\mathbf{N}_{\hat{d}})_{RR} &= \begin{bmatrix} 0 & A + \frac{A^2_1 e^c}{2} + \frac{AB_1 e^c_m}{2} & \frac{C^2 \theta_{zi}^c}{2} + \frac{CD \theta_{zj}^c}{2} & \frac{C^2 \theta_{yi}^c}{2} + \frac{CD \theta_{yj}^c}{2} & \frac{CD \theta_{zi}^c}{2} + \frac{D^2 \theta_{zj}^c}{2} & \frac{CD \theta_{yi}^c}{2} + \frac{D^2 \theta_{yj}^c}{2} \\ 0 & 0 & E & 0 & F & 0 \\ 0 & 0 & 0 & E & 0 & F \end{bmatrix} \\
({}^1\mathbf{N}_{\hat{d}})_{SS} &= \begin{bmatrix} A + \frac{A^2_1 e^s}{2} + \frac{AB e^s_m}{2} & \frac{A^2 \theta_{zi}^s}{2} + \frac{AB \theta_{zj}^s}{2} & \frac{A^2 \theta_{yi}^s}{2} + \frac{AB \theta_{yj}^s}{2} & \frac{AB \theta_{zi}^s}{2} + \frac{B^2 \theta_{zj}^s}{2} & \frac{AB \theta_{yi}^s}{2} + \frac{B^2 \theta_{yj}^s}{2} & 0 & B + \frac{AB_1 e^s}{2} + \frac{B^2 e^s_m}{2} \\ 0 & E & 0 & F & 0 & 0 & 0 \\ 0 & 0 & E & 0 & F & 0 & 0 \end{bmatrix} \\
({}^1\mathbf{N}_{\hat{d}})_{RS} &= \begin{bmatrix} 0 & 0 & 0 & 0 & 0 & B + \frac{AB_1 e^c}{2} + \frac{B^2_1 e^c_m}{2} & 0 \\ 0 & 0 & 0 & 0 & 0 & 0 & 0 \\ 0 & 0 & 0 & 0 & 0 & 0 & 0 \end{bmatrix} \\
({}^1\mathbf{N}_{\hat{d}})_{SR} &= \begin{bmatrix} 0 & 0 & 0 & 0 & 0 \\ 0 & 0 & 0 & 0 & 0 \\ 0 & 0 & 0 & 0 & 0 \end{bmatrix} \\
A &= -\frac{1}{L} + \frac{4x}{L^2}, \quad B = -\frac{8x}{L^2} + \frac{4}{L} \\
C &= 1 - \frac{4x}{L} + \frac{3x^2}{L^2}, \quad D = -\frac{2x}{L} + \frac{3x^2}{L^2} \\
E &= -\frac{4}{L} + \frac{6x}{L^2}, \quad F = -\frac{2}{L} + \frac{6x}{L^2}
\end{aligned}$$

Equation A.11 represents the first variation of cross-section strains.

$$\delta_1 \hat{\mathbf{d}} = {}^1\mathbf{N}_{\hat{d}} \times \delta_1 \mathbf{q} \quad [\text{A.11}]$$

$$\text{where: } \delta_1 \mathbf{q} = \left[\delta_1 e^{sc} \quad \delta_1 e^c \quad \delta_1 \theta_{zi}^c \quad \delta_1 \theta_{yi}^c \quad \delta_1 \theta_{zj}^c \quad \delta_1 \theta_{yj}^c \quad \delta_1 e^s \quad \delta_1 \theta_{zi}^s \quad \delta_1 \theta_{yi}^s \quad \delta_1 \theta_{zj}^s \quad \delta_1 \theta_{yj}^s \quad \delta_1 e_m^c \quad \delta_1 e_m^s \right]^T$$

$$\delta_1 \hat{\mathbf{d}} = \left[\delta_1 \varepsilon^c \quad \delta_1 \kappa_z^c \quad \delta_1 \kappa_y^c \quad \delta_1 \varepsilon^s \quad \delta_1 \kappa_z^s \quad \delta_1 \kappa_y^s \right]^T$$

$$\delta_1 \varepsilon^c = \delta_1 u_{,x}^c + {}_1 v_{,x}^c \times \delta_1 v_{,x}^c + {}_1 w_{,x}^c \times \delta_1 w_{,x}^c$$

$$\delta_1 \boldsymbol{\varepsilon}^s = \delta_1 \boldsymbol{u}_{,x}^s + {}_1 \boldsymbol{v}_{,x}^s \times \delta_1 \boldsymbol{v}_{,x}^s + {}_1 \boldsymbol{w}_{,x}^s \times \delta_1 \boldsymbol{w}_{,x}^s$$

$$\delta_1 \boldsymbol{\kappa}_z^c = \delta_1 \boldsymbol{v}_{,xx}^c$$

$$\delta_1 \boldsymbol{\kappa}_y^c = \delta_1 \boldsymbol{w}_{,xx}^c$$

$$\delta_1 \boldsymbol{\kappa}_z^s = \delta_1 \boldsymbol{v}_{,xx}^s$$

$$\delta_1 \boldsymbol{\kappa}_y^s = \delta_1 \boldsymbol{w}_{,xx}^s$$

$${}^1 \mathbf{N}_{\hat{\boldsymbol{d}}} = \begin{bmatrix} \left({}^1 \mathbf{N}_{\hat{\boldsymbol{d}}} \right)_{RR} & \left({}^1 \mathbf{N}_{\hat{\boldsymbol{d}}} \right)_{RS} \\ \left({}^1 \mathbf{N}_{\hat{\boldsymbol{d}}} \right)_{SR} & \left({}^1 \mathbf{N}_{\hat{\boldsymbol{d}}} \right)_{SS} \end{bmatrix}$$

$$\left({}^1 \mathbf{N}_{\hat{\boldsymbol{d}}} \right)_{RR} = \begin{bmatrix} 0 & A + A^2 {}_1 e^c + AB {}_1 e_m^c & C^2 \theta_{zi}^c + CD \theta_{zj}^c & C^2 \theta_{yi}^c + CD \theta_{yj}^c & CD \theta_{zi}^c + D^2 \theta_{zj}^c & CD \theta_{yi}^c + D^2 \theta_{yj}^c \\ 0 & 0 & E & 0 & F & 0 \\ 0 & 0 & 0 & E & 0 & F \end{bmatrix}$$

$$\left({}^1 \mathbf{N}_{\hat{\boldsymbol{d}}} \right)_{SS} = \begin{bmatrix} A + A^2 {}_1 e^s + AB e_m^s & C^2 \theta_{zi}^s + CD \theta_{zj}^s & C^2 \theta_{yi}^s + CD \theta_{yj}^s & CD \theta_{zi}^s + D^2 \theta_{zj}^s & CD \theta_{yi}^s + D^2 \theta_{yj}^s & 0 & B + AB {}_1 e^s + B^2 e_m^s \\ 0 & E & 0 & F & 0 & 0 & 0 \\ 0 & 0 & E & 0 & F & 0 & 0 \end{bmatrix}$$

$$\left({}^1 \mathbf{N}_{\hat{\boldsymbol{d}}} \right)_{RS} = \begin{bmatrix} 0 & 0 & 0 & 0 & 0 & B + AB {}_1 e^c + B^2 {}_1 e_m^c & 0 \\ 0 & 0 & 0 & 0 & 0 & 0 & 0 \\ 0 & 0 & 0 & 0 & 0 & 0 & 0 \end{bmatrix}$$

$$\left({}^1 \mathbf{N}_{\hat{\boldsymbol{d}}} \right)_{SR} = \begin{bmatrix} 0 & 0 & 0 & 0 & 0 \\ 0 & 0 & 0 & 0 & 0 \\ 0 & 0 & 0 & 0 & 0 \end{bmatrix}$$

The deformation of the slip layer is introduced in Equation A.12.

$${}_1 \hat{\boldsymbol{d}}_{sc} = {}^1 \mathbf{N}_{\hat{\boldsymbol{d}}_{sc}} \times {}_1 \boldsymbol{q} \quad [\text{A.12}]$$

$$\text{where: } {}^1 \mathbf{N}_{\hat{\boldsymbol{d}}_{sc}} = \begin{bmatrix} -1 & i - 2i^2 & 0 & 0 & 0 & 0 & -i + 2i^2 & 0 & 0 & 0 & 0 & -4i + 4i^2 & 4i - 4i^2 \end{bmatrix}$$

The first variation of the deformation of the slip layer is given Equation A.13.

$$\delta_1 \hat{\boldsymbol{d}}_{sc} = {}^1 \mathbf{N}_{\delta \hat{\boldsymbol{d}}_{sc}} \times \delta_1 \boldsymbol{q} \quad [\text{A.13}]$$

$$\text{where: } {}^1 \mathbf{N}_{\delta \hat{\boldsymbol{d}}_{sc}} = \begin{bmatrix} -1 & i - 2i^2 & 0 & 0 & 0 & 0 & -i + 2i^2 & 0 & 0 & 0 & 0 & -4i + 4i^2 & 4i - 4i^2 \end{bmatrix}$$

The first variation of stress-resultant field in the last term of Equation A.8 is presented in Equation A.14.

$$\delta_1^2 \mathbf{D} = \delta_1^2 \mathbf{N}_{D1} \times {}_1^2 \mathbf{Q} + {}_1^2 \mathbf{N}_{D1} \times \delta_1^2 \mathbf{Q} \quad [\text{A.14}]$$

$$\text{where: } \delta_1^2 \mathbf{N}_{D1} = \begin{bmatrix} 0 & 0 & 0 & 0 & 0 & 0 & 0 & 0 & 0 & 0 & 0 & 0 \\ \delta_1 w^c & 0 & 0 & 0 & 0 & 0 & 0 & 0 & 0 & 0 & 0 & 0 \\ \delta_1 v^c & 0 & 0 & 0 & 0 & 0 & 0 & 0 & 0 & 0 & 0 & 0 \\ 0 & 0 & 0 & 0 & 0 & 0 & 0 & 0 & 0 & 0 & 0 & 0 \\ 0 & 0 & 0 & 0 & 0 & 0 & \delta_1 w^s & 0 & 0 & 0 & 0 & 0 \\ 0 & 0 & 0 & 0 & 0 & 0 & \delta_1 v^s & 0 & 0 & 0 & 0 & 0 \end{bmatrix}$$

$$\delta_1 w^c = \delta({}_1^1 w^c + {}_1 w^c) = L \times (i - 2 \times i^2 + i^3) \times \delta_1 \theta_{zi}^c + L \times (-i^2 + i^3) \times \delta_1 \theta_{zj}^c$$

$$\delta_1 v^c = \delta({}_1^1 v^c + {}_1 v^c) = L \times (i - 2 \times i^2 + i^3) \times \delta_1 \theta_{yi}^c + L \times (-i^2 + i^3) \times \delta_1 \theta_{yj}^c$$

$$\delta_1 w^s = \delta({}_1^1 w^s + {}_1 w^s) = L \times (i - 2 \times i^2 + i^3) \times \delta_1 \theta_{zi}^s + L \times (-i^2 + i^3) \times \delta_1 \theta_{zj}^s$$

$$\delta_1 v^s = \delta({}_1^1 v^s + {}_1 v^s) = L \times (i - 2 \times i^2 + i^3) \times \delta_1 \theta_{yi}^s + L \times (-i^2 + i^3) \times \delta_1 \theta_{yj}^s$$

Multiplying the first variation of \mathbf{N}_{D1} with ${}_1^2 \mathbf{Q}$ and then factoring out the terms of $\delta_1 \mathbf{q}$ (from Equation A.7, e.g., $\delta \theta_{zi}^c$, $\delta \theta_{yi}^c$, $\delta \theta_{zj}^c$, $\delta \theta_{yj}^c$, $\delta \theta_{zi}^s$, $\delta \theta_{yi}^s$, $\delta \theta_{zj}^s$, $\delta \theta_{yj}^s$) a modified form of $\delta({}_1^2 \mathbf{D})$ can be expressed as in Equation A.15.

$$\delta_1^2 \mathbf{D} = {}_1^2 \mathbf{N}_{D2} \times \delta_1 \mathbf{q} + {}_1^2 \mathbf{N}_{D1} \times \delta_1^2 \mathbf{Q} \quad [\text{A.15}]$$

$$\text{where: } {}_1^2 \mathbf{N}_{D2} = \begin{bmatrix} 0 & 0 & 0 & 0 & 0 & 0 & 0 & 0 & 0 & 0 & 0 & 0 & 0 \\ 0 & 0 & A' \times {}_1^2 P_c & 0 & B' \times {}_1^2 P_c & 0 & 0 & 0 & 0 & 0 & 0 & 0 & 0 \\ 0 & 0 & 0 & A' \times {}_1^2 P_c & 0 & B' \times {}_1^2 P_c & 0 & 0 & 0 & 0 & 0 & 0 & 0 \\ 0 & 0 & 0 & 0 & 0 & 0 & A' \times {}_1^2 P_s & 0 & B' \times {}_1^2 P_s & 0 & 0 & 0 & 0 \\ 0 & 0 & 0 & 0 & 0 & 0 & 0 & A' \times {}_1^2 P_s & 0 & B' \times {}_1^2 P_s & 0 & 0 & 0 \\ 0 & 0 & 0 & 0 & 0 & 0 & 0 & 0 & 0 & 0 & 0 & 0 & 0 \end{bmatrix}$$

$$A' = L(i - 2i^2 + i^3)$$

$$B' = L(-i^2 + i^3)$$

${}_1^2 P^c$ is the total axial force on concrete core

${}_1^2 P^s$ is the total axial force on steel tube

Substituting Equations A.9, A.10, A.11, A.12, and A.14 into Equation A.8, the Hellinger-Reissner variational principle can restated as in Equation A.16.

$$\begin{aligned}
& \left[\int_0^{1L} {}^1\mathbf{N}_{\hat{d}}^T \times {}^2\mathbf{D} \times d^1x + \int_{1I} {}^1\mathbf{N}_{\hat{d}_{sc}}^T \times {}^1\bar{k}_{sc} \times {}^1\mathbf{N}_{\hat{d}_{sc}} \times {}_1\mathbf{q} \times d^1I + \int_{1I} {}^1\mathbf{N}_{\hat{d}_{sc}}^T \times {}^1D_{sc} \times d^1I \right. \\
& \left. - {}^2\mathbf{Q}_{ext} + \int_0^{1L} {}^2\mathbf{N}_{D2}^T \times ({}_1\hat{\mathbf{d}} - {}_1\mathbf{d}) \times d^1x + \right. \\
& \left(\int_{1V^c} {}^1\rho^c \times {}^1\mathbf{N}_u^{cT} \times {}^1\mathbf{N}_u^c \times d^1V^c + \int_{1V^s} {}^1\rho^s \times {}^1\mathbf{N}_u^{sT} \times {}^1\mathbf{N}_u^s \times d^1V^s \right) \times {}_1^2\ddot{\mathbf{q}} + \\
& \left(\int_{1V^c} {}^1\mu^c \times {}^1\mathbf{N}_u^{cT} \times {}^1\mathbf{N}_u^c \times d^1V^c + \int_{1V^s} {}^1\mu^s \times {}^1\mathbf{N}_u^{sT} \times {}^1\mathbf{N}_u^s \times d^1V^s \right) \times {}_1^2\dot{\mathbf{q}} \\
& \left. \delta_1\mathbf{q}^T \times \left[\int_0^{1L} {}^2\mathbf{N}_{D1}^T \times ({}_1\hat{\mathbf{d}} - {}_1\mathbf{d}) \times d^1x \right] = 0 \right] + \quad [A.16]
\end{aligned}$$

The terms $\delta_1\mathbf{q}^T$ and $\delta_1^2\mathbf{Q}^T$ are nonzero variables representing variations of the element displacements and forces. Therefore, Equation A.16 yields two sets of equations given below:

$$\begin{aligned}
& \left[\int_0^{1L} {}^1\mathbf{N}_{\hat{d}}^T \times {}^2\mathbf{D} \times d^1x + \int_{1I} {}^1\mathbf{N}_{\hat{d}_{sc}}^T \times {}^1\bar{k}_{sc} \times {}^1\mathbf{N}_{\hat{d}_{sc}} \times {}_1\mathbf{q} \times d^1I + \int_{1I} {}^1\mathbf{N}_{\hat{d}_{sc}}^T \times {}^1D_{sc} \times d^1I \right. \\
& \left. - {}^2\mathbf{Q}_{ext} + \int_0^{1L} {}^2\mathbf{N}_{D2}^T \times ({}_1\hat{\mathbf{d}} - {}_1\mathbf{d}) \times d^1x + \right. \\
& \left(\int_{1V^c} {}^1\rho^c \times {}^1\mathbf{N}_u^{cT} \times {}^1\mathbf{N}_u^c \times d^1V^c + \int_{1V^s} {}^1\rho^s \times {}^1\mathbf{N}_u^{sT} \times {}^1\mathbf{N}_u^s \times d^1V^s \right) \times {}_1^2\ddot{\mathbf{q}} + \\
& \left(\int_{1V^c} {}^1\mu^c \times {}^1\mathbf{N}_u^{cT} \times {}^1\mathbf{N}_u^c \times d^1V^c + \int_{1V^s} {}^1\mu^s \times {}^1\mathbf{N}_u^{sT} \times {}^1\mathbf{N}_u^s \times d^1V^s \right) \times {}_1^2\dot{\mathbf{q}} \\
& \left. \right] = 0 \quad [A.17]
\end{aligned}$$

$$V = \int_0^{1L} {}^2\mathbf{N}_{D1}^T \times ({}_1\hat{\mathbf{d}} - {}_1\mathbf{d}) \times d^1x = 0 \quad [A.18]$$

A.1.3. Consistent Linearization of Compatibility Equation

The element compatibility stated in Equation A.18 is nonlinear with respect to the state variables of ${}_1\mathbf{q}$ and ${}_1^2\mathbf{Q}$ since ${}_1\mathbf{d}$ and ${}_1\hat{\mathbf{d}}$ are functions of ${}_1^2\mathbf{Q}$ and ${}_1\mathbf{q}$, respectively. The incremental form of the compatibility equation needed to derive the consistent tangent stiffness equations can be obtained by consistent linearization. The Taylor series expansion of Equation A.18 about the current state can be stated as in Equation A.19. The second and third terms on the right hand side of Equation A.19 are expanded using

the rules of differentiation following the substitution of the terms $({}_1\mathbf{q} + \alpha\Delta\mathbf{q})$ and $({}_1^2\mathbf{Q} + \gamma\Delta\mathbf{Q})$. The third term on the right hand side of Equation A.19 is simplified into a single term since ${}_1^2\mathbf{N}_{D1}$ and ${}_1\hat{\mathbf{d}}$ are not functions of ${}_1^2\mathbf{Q}$ and therefore their derivative with respect to γ vanishes.

$$\mathbf{V}^{j+1} = \mathbf{V}^j + \frac{d}{d\alpha}_{\alpha,\gamma=0} \mid \mathbf{V}({}_1\mathbf{q} + \alpha\Delta\mathbf{q}) + \frac{d}{d\gamma}_{\alpha,\gamma=0} \mid \mathbf{V}({}_1^2\mathbf{Q} + \gamma\Delta\mathbf{Q}) \quad [\text{A.19}]$$

$$\text{where: } \Delta\mathbf{q} = \left[\Delta e^{sc} \Delta e^c \Delta \theta_{zi}^c \Delta \theta_{yi}^c \Delta \theta_{zj}^c \Delta \theta_{yj}^c \Delta e^s \Delta \theta_{zi}^s \Delta \theta_{yi}^s \Delta \theta_{zj}^s \Delta \theta_{yj}^s \Delta e_m^c \Delta e_m^s \right]^T$$

$$\begin{aligned} \frac{d}{d\alpha}_{\alpha,\gamma=0} \mid \mathbf{V}({}_1\mathbf{q} + \alpha\Delta\mathbf{q}, {}_1^2\mathbf{Q} + \gamma\Delta\mathbf{Q}) &= \int_0^{1L} \frac{d}{d\alpha}_{\alpha,\gamma=0} \mid ({}_1^2\mathbf{N}_{D1}^T) \times ({}_1\hat{\mathbf{d}} - {}_1\mathbf{d}) \times d^1x + \\ &\int_0^{1L} {}_1^2\mathbf{N}_{D1}^T \times \frac{d}{d\alpha}_{\alpha,\gamma=0} \mid ({}_1\hat{\mathbf{d}} - {}_1\mathbf{d}) \times d^1x \end{aligned}$$

$$\int_0^{1L} \frac{d}{d\alpha}_{\alpha,\gamma=0} \mid (\mathbf{N}_{D1}^T) \times ({}_1\hat{\mathbf{d}} - {}_1\mathbf{d}) \times dx = \int_0^{1L} \begin{bmatrix} 0 & 0 & 0 & 0 & 0 & 0 & 0 & 0 & 0 & 0 & 0 & 0 \\ \Delta w & 0 & 0 & 0 & 0 & 0 & 0 & 0 & 0 & 0 & 0 & 0 \\ \Delta v & 0 & 0 & 0 & 0 & 0 & 0 & 0 & 0 & 0 & 0 & 0 \\ 0 & 0 & 0 & 0 & 0 & 0 & 0 & 0 & 0 & 0 & 0 & 0 \\ 0 & 0 & 0 & 0 & 0 & 0 & \Delta w & 0 & 0 & 0 & 0 & 0 \\ 0 & 0 & 0 & 0 & 0 & 0 & \Delta v & 0 & 0 & 0 & 0 & 0 \end{bmatrix} \times ({}_1\hat{\mathbf{d}} - {}_1\mathbf{d}) \times dx$$

$$\int_0^{1L} \frac{d}{d\alpha}_{\alpha,\gamma=0} \mid (\mathbf{N}_{D1}^T) \times ({}_1\hat{\mathbf{d}} - {}_1\mathbf{d}) \times dx$$

$$= \int_0^{1L} \begin{bmatrix} 0 & 0 & A \times d_d(2) & A \times d_d(3) & B \times d_d(2) & B \times d_d(3) & 0 & 0 & 0 & 0 & 0 & 0 & 0 \\ 0 & 0 & 0 & 0 & 0 & 0 & 0 & 0 & 0 & 0 & 0 & 0 & 0 \\ 0 & 0 & 0 & 0 & 0 & 0 & 0 & 0 & 0 & 0 & 0 & 0 & 0 \\ 0 & 0 & 0 & 0 & 0 & 0 & 0 & 0 & 0 & 0 & 0 & 0 & 0 \\ 0 & 0 & 0 & 0 & 0 & 0 & 0 & 0 & 0 & 0 & 0 & 0 & 0 \\ 0 & 0 & 0 & 0 & 0 & 0 & 0 & 0 & 0 & 0 & 0 & 0 & 0 \\ 0 & 0 & 0 & 0 & 0 & 0 & A \times d_d(5) & A \times d_d(6) & B \times d_d(5) & B \times d_d(6) & 0 & 0 & 0 \\ 0 & 0 & 0 & 0 & 0 & 0 & 0 & 0 & 0 & 0 & 0 & 0 & 0 \\ 0 & 0 & 0 & 0 & 0 & 0 & 0 & 0 & 0 & 0 & 0 & 0 & 0 \\ 0 & 0 & 0 & 0 & 0 & 0 & 0 & 0 & 0 & 0 & 0 & 0 & 0 \\ 0 & 0 & 0 & 0 & 0 & 0 & 0 & 0 & 0 & 0 & 0 & 0 & 0 \end{bmatrix} \times dx \times \Delta\mathbf{q}$$

$$= \mathbf{M}_d \times \Delta\mathbf{q}$$

$$d_{-}d(2)=_{1}\hat{d}(2)-_{1}d(2) \quad d_{-}d(3)=_{1}\hat{d}(3)-_{1}d(3)$$

$$d_{-}d(5)=_{1}\hat{d}(5)-_{1}d(5) \quad d_{-}d(6)=_{1}\hat{d}(6)-_{1}d(6)$$

$$\int_0^{1L} {}^2\mathbf{N}_{D1}^T \times \frac{d}{d\alpha}_{\alpha,\gamma=0} \mid ({}_1\hat{\mathbf{d}}) \times d^1\mathbf{x} = \left(\int_0^{1L} {}^2\mathbf{N}_{D1}^T \times {}^1\mathbf{N}_{\delta\hat{d}} \times d^1\mathbf{x} \right) \times \Delta\mathbf{q} = {}^2\mathbf{G}_1 \times \Delta\mathbf{q}$$

$$\begin{aligned} \int_0^{1L} {}^2\mathbf{N}_{D1}^T \times \frac{d}{d\alpha}_{\alpha,\gamma=0} \mid ({}_1\mathbf{d}) \times d^1\mathbf{x} &= \left(\int_0^{1L} {}^2\mathbf{N}_{D1}^T \times \frac{\partial_1\mathbf{d}}{\partial_1\mathbf{D}_\Sigma} \times \frac{\partial_1^2\mathbf{D}_\Sigma}{\partial_1^2\mathbf{D}} \times \frac{\partial}{\partial\alpha}_{\alpha,\gamma=0} \mid ({}_1^2\mathbf{D}) \times d^1\mathbf{x} \right) \\ &= \left(\int_0^{1L} {}^2\mathbf{N}_{D1}^T \times {}^1\mathbf{k}^{-1} \times 1 \times \frac{\partial}{\partial\alpha}_{\alpha,\gamma=0} \mid ({}_1^2\mathbf{N}_{D1} \times {}_1^2\mathbf{Q}) \times d^1\mathbf{x} \right) \end{aligned}$$

${}^1\mathbf{k}^{-1}$ is the section flexibility matrix in C1 configuration (inverse cross-section stiffness)

$$\begin{aligned} \frac{d}{d\gamma}_{\alpha,\gamma=0} \mid V({}_1\mathbf{q} + \alpha\Delta\mathbf{q}, {}^2\mathbf{Q} + \gamma\Delta\mathbf{Q}) &= - \int_0^{1L} {}^2\mathbf{N}_{D1}^T \times \frac{d}{d\gamma}_{\alpha,\gamma=0} \mid ({}_1\mathbf{d}) \times d^1\mathbf{x} \\ &= - \int_0^{1L} {}^2\mathbf{N}_{D1}^T \times \frac{\partial_1\mathbf{d}}{\partial_1^2\mathbf{D}_\Sigma} \times \frac{\partial_1^2\mathbf{D}_\Sigma}{\partial_1^2\mathbf{D}} \times \frac{d}{d\gamma}_{\alpha,\gamma=0} \mid ({}_1^2\mathbf{D}) \times d^1\mathbf{x} \\ &= - \left(\int_0^{1L} {}^2\mathbf{N}_{D1}^T \times {}^1\mathbf{k}^{-1} \times {}^2\mathbf{N}_{D1} \times d^1\mathbf{x} \right) \times \Delta\mathbf{Q} \\ &= - {}^2\mathbf{H}_{11} \times \Delta\mathbf{Q} \end{aligned}$$

The linearized form of the compatibility equation to use in the state determination stage can be obtained by Taylor series expansion of Equation A.18 with respect to ${}^2\mathbf{Q}$ while holding ${}_1\mathbf{q}$ as constant.

$$\mathbf{V}^{j+1} = \mathbf{V}^j + \frac{d}{d\gamma}_{\alpha,\gamma=0} \mid \mathbf{V}({}_1^2\mathbf{Q} + \alpha\Delta\mathbf{Q}) \quad [\text{A.20}]$$

$$\begin{aligned} \text{where: } \frac{d}{d\gamma}_{\alpha,\gamma=0} \mid \mathbf{V}({}_1^2\mathbf{Q} + \gamma\Delta\mathbf{Q}) &= - \int_0^{1L} {}^2\mathbf{N}_{D1}^T \times \frac{d}{d\gamma}_{\alpha,\gamma=0} \mid ({}_1\mathbf{d}) \times d^1\mathbf{x} \\ &= - \int_0^{1L} {}^2\mathbf{N}_{D1}^T \times \frac{\partial_1\mathbf{d}}{\partial_1^2\mathbf{D}_\Sigma} \times \frac{\partial_1^2\mathbf{D}_\Sigma}{\partial_1^2\mathbf{D}} \times \frac{d}{d\gamma}_{\alpha,\gamma=0} \mid ({}_1^2\mathbf{D}) \times d^1\mathbf{x} \end{aligned}$$

$$\begin{aligned}
&= - \left(\int_0^{1L} {}^2\mathbf{N}_{D1}^T \times {}^1\mathbf{k}^{-1} \times {}^2\mathbf{N}_{D1} \times d^1x \right) \times \Delta \mathbf{Q} \\
&= - {}^2\mathbf{H}_{11} \times \Delta \mathbf{Q}
\end{aligned}$$

A.1.4. Consistent Linearization of Equilibrium Equation

Linearization of the equilibrium equation yields expressions to derive the element tangent stiffness. Examining Equation 2.50, it can be seen that the equilibrium equation is expressed in terms of the states variables including ${}_1\mathbf{q}$, ${}_1^2\mathbf{Q}$, ${}_1^2\mathbf{Q}_{ext}$, ${}_1^2\dot{\mathbf{q}}$, and ${}_1^2\ddot{\mathbf{q}}$. The Taylor series expansion of the equilibrium equation about the current state can be expressed as follows:

$$\begin{aligned}
\mathbf{g}^{j+1} &= \mathbf{g}^j + \frac{d}{d\alpha} \Big|_{\alpha,\lambda,\beta,\theta,\eta=0} \mathbf{g}({}_1\mathbf{q} + \alpha\Delta\mathbf{q}, {}_1^2\mathbf{Q} + \gamma\Delta\mathbf{Q}, {}_1^2\mathbf{Q}_{ext} + \beta\Delta\mathbf{Q}_{ext}, {}_1^2\dot{\mathbf{q}} + \theta\Delta\dot{\mathbf{q}}, {}_1^2\ddot{\mathbf{q}} + \eta\Delta\ddot{\mathbf{q}}) \\
&+ \frac{d}{d\gamma} \Big|_{\alpha,\lambda,\beta,\theta,\eta=0} \mathbf{g}({}_1\mathbf{q} + \alpha\Delta\mathbf{q}, {}_1^2\mathbf{Q} + \gamma\Delta\mathbf{Q}, {}_1^2\mathbf{Q}_{ext} + \beta\Delta\mathbf{Q}_{ext}, {}_1^2\dot{\mathbf{q}} + \theta\Delta\dot{\mathbf{q}}, {}_1^2\ddot{\mathbf{q}} + \eta\Delta\ddot{\mathbf{q}}) \\
&+ \frac{d}{d\beta} \Big|_{\alpha,\lambda,\beta,\theta,\eta=0} \mathbf{g}({}_1\mathbf{q} + \alpha\Delta\mathbf{q}, {}_1^2\mathbf{Q} + \gamma\Delta\mathbf{Q}, {}_1^2\mathbf{Q}_{ext} + \beta\Delta\mathbf{Q}_{ext}, {}_1^2\dot{\mathbf{q}} + \theta\Delta\dot{\mathbf{q}}, {}_1^2\ddot{\mathbf{q}} + \eta\Delta\ddot{\mathbf{q}}) \\
&+ \frac{d}{d\theta} \Big|_{\alpha,\lambda,\beta,\theta,\eta=0} \mathbf{g}({}_1\mathbf{q} + \alpha\Delta\mathbf{q}, {}_1^2\mathbf{Q} + \gamma\Delta\mathbf{Q}, {}_1^2\mathbf{Q}_{ext} + \beta\Delta\mathbf{Q}_{ext}, {}_1^2\dot{\mathbf{q}} + \theta\Delta\dot{\mathbf{q}}, {}_1^2\ddot{\mathbf{q}} + \eta\Delta\ddot{\mathbf{q}}) \\
&+ \frac{d}{d\eta} \Big|_{\alpha,\lambda,\beta,\theta,\eta=0} \mathbf{g}({}_1\mathbf{q} + \alpha\Delta\mathbf{q}, {}_1^2\mathbf{Q} + \gamma\Delta\mathbf{Q}, {}_1^2\mathbf{Q}_{ext} + \beta\Delta\mathbf{Q}_{ext}, {}_1^2\dot{\mathbf{q}} + \theta\Delta\dot{\mathbf{q}}, {}_1^2\ddot{\mathbf{q}} + \eta\Delta\ddot{\mathbf{q}})
\end{aligned} \tag{A.21}$$

The expanded forms of the terms on the right hand side of Equation A.21 are obtained following the substitution of the variables ${}_1\mathbf{q} + \alpha\Delta\mathbf{q}$, ${}_1^2\mathbf{Q} + \gamma\Delta\mathbf{Q}$, ${}_1^2\mathbf{Q}_{ext} + \beta\Delta\mathbf{Q}_{ext}$, ${}_1^2\dot{\mathbf{q}} + \theta\Delta\dot{\mathbf{q}}$, ${}_1^2\ddot{\mathbf{q}} + \eta\Delta\ddot{\mathbf{q}}$ into Equation A.17 and performing the derivatives with respect to the Taylor Series expansion parameters of α , γ , β , θ , η and evaluating the derivatives when $\alpha = 0$, $\gamma = 0$, $\beta = 0$, $\theta = 0$, and $\eta = 0$.

$$\begin{aligned}
\frac{d}{d\alpha} \Big|_{\alpha, \gamma, \beta, \theta, \eta=0} g(\mathbf{q} + \alpha \Delta \mathbf{q}, {}^1_1 \mathbf{Q} + \gamma \Delta \mathbf{Q}, {}^2_1 \mathbf{Q}_{ext} + \beta \Delta \mathbf{Q}_{ext}, {}^1_1 \hat{\mathbf{q}} + \theta \Delta \hat{\mathbf{q}}, {}^1_1 \eta \Delta \hat{\mathbf{q}}) &= \left[\int_0^{1L} \frac{d}{d\alpha} \Big|_{\alpha, \gamma, \beta, \theta, \eta=0} ({}^1 N_{\delta \hat{d}}) \times {}^2_1 \mathbf{D} \times d^1 \mathbf{x} \right] + \left[\int_0^{1L} {}^1 N_{\delta \hat{d}}^T \times \frac{d}{d\alpha} \Big|_{\alpha, \gamma, \beta, \theta, \eta=0} ({}^2_1 \mathbf{D}) \times d^1 \mathbf{x} \right] + \\
&\left[\int_0^{1L} \frac{d}{d\alpha} \Big|_{\alpha, \gamma, \beta, \theta, \eta=0} ({}^1 N_{\delta \hat{d}_{sc}}^T) \times {}^1 \bar{k}_{sc} \times {}^1 N_{\delta \hat{d}_{sc}} \times ({}^1_1 \mathbf{q} + \alpha \Delta \mathbf{q}) \times d^1 \mathbf{x} \right] + \left[\int_0^{1L} {}^1 N_{\delta \hat{d}_{sc}}^T \times \frac{d}{d\alpha} \Big|_{\alpha, \gamma, \beta, \theta, \eta=0} ({}^1 \bar{k}_{sc} \times {}^1 N_{\delta \hat{d}_{sc}} \times ({}^1_1 \mathbf{q} + \alpha \Delta \mathbf{q})) \times d^1 \mathbf{x} \right] + \\
&\left[\int_0^{1L} \frac{d}{d\alpha} \Big|_{\alpha, \gamma, \beta, \theta, \eta=0} ({}^1 N_{\delta \hat{d}_{sc}}^T) \times {}^1 \mathbf{D}_{sc} \times d^1 I \right] + \left[\int_0^{1L} {}^1 N_{\delta \hat{d}_{sc}}^T \times \frac{d}{d\alpha} \Big|_{\alpha, \gamma, \beta, \theta, \eta=0} ({}^1 \mathbf{D}_{sc}) \times d^1 I \right] + \\
&\left[\int_0^{1L} \frac{d}{d\alpha} \Big|_{\alpha, \gamma, \beta, \theta, \eta=0} ({}^2_1 N_{D2}^T) \times ({}^1_1 \hat{\mathbf{d}} - \mathbf{d}) \times d^1 \mathbf{x} \right] + \left[\int_0^{1L} {}^2_1 N_{D2}^T \times \frac{d}{d\alpha} \Big|_{\alpha, \gamma, \beta, \theta, \eta=0} ({}^1_1 \hat{\mathbf{d}} - \mathbf{d}) \times d^1 \mathbf{x} \right] - \\
&\left[\frac{d}{d\alpha} \Big|_{\alpha, \gamma, \beta, \theta, \eta=0} ({}^1_1 \mathbf{Q}_{ext} + \beta \Delta \mathbf{Q}_{ext}) \right] + \\
&\left[\int_{1V^c} \frac{d}{d\alpha} \Big|_{\alpha, \gamma, \beta, \theta, \eta=0} {}^1 \rho^c \times {}^1 N_u^{cT} \times {}^1 N_u^c \times d^1 V^c \times ({}^1_1 \hat{\mathbf{q}} + \theta \Delta \hat{\mathbf{q}}) + \int_{1V^s} \frac{d}{d\alpha} \Big|_{\alpha, \gamma, \beta, \theta, \eta=0} {}^1 \rho^s \times {}^1 N_u^{sT} \times {}^1 N_u^s \times d^1 V^s \times ({}^1_1 \hat{\mathbf{q}} + \theta \Delta \hat{\mathbf{q}}) \right] + \\
&\left[\int_{1V^c} \frac{d}{d\alpha} \Big|_{\alpha, \gamma, \beta, \theta, \eta=0} {}^1 \rho^c \times {}^1 N_u^{cT} \times {}^1 N_u^c \times d^1 V^c \times ({}^1_1 \hat{\mathbf{q}} + \eta \Delta \hat{\mathbf{q}}) + \int_{1V^s} \frac{d}{d\alpha} \Big|_{\alpha, \gamma, \beta, \theta, \eta=0} {}^1 \rho^s \times {}^1 N_u^{sT} \times {}^1 N_u^s \times d^1 V^s \times ({}^1_1 \hat{\mathbf{q}} + \eta \Delta \hat{\mathbf{q}}) \right]
\end{aligned} \tag{A.22}$$

where $\left[\int_0^{1L} \frac{d}{d\alpha} \Big|_{\alpha, \gamma, \beta, \theta, \eta=0} ({}^1 N_{\delta \hat{d}}) \times {}^2_1 \mathbf{D} \times d^1 \mathbf{x} \right] =$

$$\left(\begin{array}{cccccccccccc}
0 & 0 & 0 & 0 & 0 & 0 & 0 & 0 & 0 & 0 & 0 & 0 & 0 \\
0 & {}^2_1 P_c A^2 & 0 & 0 & 0 & 0 & 0 & 0 & 0 & 0 & 0 & {}^2_1 P_c AB & 0 \\
0 & 0 & {}^2_1 P_c C^2 & 0 & {}^2_1 P_c CD & 0 & 0 & 0 & 0 & 0 & 0 & 0 & 0 \\
0 & 0 & 0 & {}^2_1 P_c C^2 & 0 & {}^2_1 P_c CD & 0 & 0 & 0 & 0 & 0 & 0 & 0 \\
0 & 0 & {}^2_1 P_c CD & 0 & {}^2_1 P_c D^2 & 0 & 0 & 0 & 0 & 0 & 0 & 0 & 0 \\
0 & 0 & 0 & {}^2_1 P_c CD & 0 & {}^2_1 P_c D^2 & 0 & 0 & 0 & 0 & 0 & 0 & 0 \\
0 & 0 & 0 & 0 & 0 & 0 & {}^2_1 P_s A^2 & 0 & 0 & 0 & 0 & {}^2_1 P_s AB & 0 \\
0 & 0 & 0 & 0 & 0 & 0 & 0 & {}^2_1 P_s C^2 & 0 & {}^2_1 P_s CD & 0 & 0 & 0 \\
0 & 0 & 0 & 0 & 0 & 0 & 0 & 0 & {}^2_1 P_s C^2 & 0 & {}^2_1 P_s CD & 0 & 0 \\
0 & 0 & 0 & 0 & 0 & 0 & 0 & 0 & {}^2_1 P_s CD & 0 & {}^2_1 P_s D^2 & 0 & 0 \\
0 & 0 & 0 & 0 & 0 & 0 & 0 & 0 & {}^2_1 P_s CD & 0 & {}^2_1 P_s D^2 & 0 & 0 \\
0 & {}^2_1 P_c AB & 0 & 0 & 0 & 0 & 0 & 0 & 0 & 0 & 0 & {}^2_1 P_c B^2 & 0 \\
0 & 0 & 0 & 0 & 0 & 0 & {}^2_1 P_s AB & 0 & 0 & 0 & 0 & 0 & {}^2_1 P_s B^2
\end{array} \right) \times d^1 \mathbf{x} \times \Delta \mathbf{q} =$$

$$= {}^2_1 \mathbf{K}_g \times \Delta \mathbf{q}$$

$$\left[\int_0^{1L} {}^1 N_{\delta \hat{d}}^T \times \frac{d}{d\alpha} \Big|_{\alpha, \gamma, \beta, \theta, \eta=0} ({}^2_1 \mathbf{D}) \times d^1 \mathbf{x} \right] = \left[\int_0^{1L} {}^1 N_{\delta \hat{d}}^T \times {}^2_1 N_{D2} \times d^1 \mathbf{x} \right] \times \Delta \mathbf{q} = {}^2_1 \mathbf{G}_2 \times \Delta \mathbf{q}$$

$$\left[\int_0^{1L} \frac{d}{d\alpha} \Big|_{\alpha,\gamma,\beta,\theta,\eta=0} \left({}^1\mathbf{N}_{\delta\hat{d}_{sc}}^T \right) \times {}^1\bar{\mathbf{k}}_{sc} \times {}^1\mathbf{N}_{\delta\hat{d}_{sc}} \times {}^1\mathbf{q} \times d^1\mathbf{x} \right] = 0$$

$$\left[\int_0^{1L} {}^1\mathbf{N}_{\delta\hat{d}_{sc}}^T \times \frac{d}{d\alpha} \Big|_{\alpha,\gamma,\beta,\theta,\eta=0} \left({}^1\bar{\mathbf{k}}_{sc} \times {}^1\mathbf{N}_{\delta\hat{d}_{sc}} \times ({}^1\mathbf{q} + \alpha \times \Delta\mathbf{q}) \right) \times d^1\mathbf{x} \right] = \left[\int_0^{1L} {}^1\mathbf{N}_{\delta\hat{d}_{sc}}^T \times {}^1\bar{\mathbf{k}}_{sc} \times {}^1\mathbf{N}_{\delta\hat{d}_{sc}} \times d^1\mathbf{x} \right] \times \Delta\mathbf{q} = {}^1\mathbf{K}_{sc} \times \Delta\mathbf{q}$$

$$\left[\int_{1I} \frac{d}{d\alpha} \Big|_{\alpha,\gamma,\beta,\theta,\eta=0} \left({}^1\mathbf{N}_{\delta\hat{d}_{sc}}^T \right) \times {}^1D_{sc} \times d^1I \right] = 0$$

$$\left[\int_{1I} {}^1\mathbf{N}_{\delta\hat{d}_{sc}}^T \times \frac{d}{d\alpha} \Big|_{\alpha,\gamma,\beta,\theta,\eta=0} \left({}^1D_{sc} \right) \times d^1I \right] = 0$$

$$\left[\int_0^{1L} \frac{d}{d\alpha} \Big|_{\alpha,\gamma,\beta,\theta,\eta=0} \left({}^2\mathbf{N}_{D2}^T \right) \times \left({}^1\hat{\mathbf{d}} - {}^1\mathbf{d} \right) \times d^1\mathbf{x} \right] = 0$$

$$\left[\int_0^{1L} {}^2\mathbf{N}_{D2}^T \times \frac{d}{d\alpha} \Big|_{\alpha,\gamma,\beta,\theta,\eta=0} \left({}^1\hat{\mathbf{d}} - {}^1\mathbf{d} \right) \times d^1\mathbf{x} \right] = \left[\int_0^{1L} {}^2\mathbf{N}_{D2}^T \times \frac{d}{d\alpha} \Big|_{\alpha,\gamma,\beta,\theta,\eta=0} \left({}^1\hat{\mathbf{d}} \right) \times d^1\mathbf{x} - \int_0^{1L} {}^2\mathbf{N}_{D2}^T \times \frac{d}{d\alpha} \Big|_{\alpha,\gamma,\beta,\theta,\eta=0} \left({}^1\mathbf{d} \right) \times d^1\mathbf{x} \right]$$

$$= \left[\int_0^{1L} {}^2\mathbf{N}_{D2}^T \times {}^1\mathbf{N}_{\delta\hat{\mathbf{d}}} \times d^1\mathbf{x} - \int_0^{1L} {}^2\mathbf{N}_{D2}^T \times {}^1\mathbf{k}^{-1} \times {}^2\mathbf{N}_{D2} \times d^1\mathbf{x} \right]$$

$$= [{}^2\mathbf{G}_2^T \times \Delta\mathbf{q} + {}^2\mathbf{H}_{22} \times \Delta\mathbf{q}]$$

$$\left[\frac{d}{d\alpha} \Big|_{\alpha,\gamma,\beta,\theta,\eta=0} \left({}^2\mathbf{Q}_{ext} \right) \right] = 0$$

$$\left[\int_{1V^c} \frac{d}{d\alpha} \Big|_{\alpha,\gamma,\beta,\theta,\eta=0} {}^1\rho^c \times \mathbf{N}_u^{cT} \times \mathbf{N}_u^c \times d^1V^c \times {}^2\ddot{\mathbf{q}} + \int_{1V^s} \frac{d}{d\alpha} \Big|_{\alpha,\gamma,\beta,\theta,\eta=0} {}^1\rho^s \times \mathbf{N}_u^{sT} \times \mathbf{N}_u^s \times d^1V^s \times {}^2\ddot{\mathbf{q}} \right] = 0$$

$$\left[\int_{1V^c} \frac{d}{d\alpha} \Big|_{\alpha,\gamma,\beta,\theta,\eta=0} {}^1\rho^c \times \mathbf{N}_u^{cT} \times \mathbf{N}_u^c \times d^1V^c \times {}^2\dot{\mathbf{q}} + \int_{1V^s} \frac{d}{d\alpha} \Big|_{\alpha,\gamma,\beta,\theta,\eta=0} {}^1\rho^s \times \mathbf{N}_u^{sT} \times \mathbf{N}_u^s \times d^1V^s \times {}^2\dot{\mathbf{q}} \right] = 0$$

$$\begin{aligned}
\frac{d}{d\gamma}_{\alpha,\gamma,\beta,\theta,\eta=0} \Big|_{\gamma=0} g(\mathbf{q} + \alpha\Delta\mathbf{q}, {}^2\mathbf{Q} + \gamma\Delta\mathbf{Q}, {}^2\mathbf{Q}_{ext} + \beta\Delta\mathbf{Q}_{ext}, {}^2\dot{\mathbf{q}} + \theta\Delta\dot{\mathbf{q}}, {}^2\ddot{\mathbf{q}} + \eta\Delta\ddot{\mathbf{q}}) = & \left[\int_0^{1L} \frac{d}{d\gamma}_{\alpha,\gamma,\beta,\theta,\eta=0} \Big|_{\gamma=0} ({}^1\mathbf{N}_{\delta\hat{\mathbf{d}}}) \times {}^2\mathbf{D} \times d^1\mathbf{x} \right] + \left[\int_0^{1L} {}^1\mathbf{N}_{\delta\hat{\mathbf{d}}}^T \times \frac{d}{d\gamma}_{\alpha,\gamma,\beta,\theta,\eta=0} \Big|_{\gamma=0} ({}^2\mathbf{D}) \times d^1\mathbf{x} \right] + \\
& \left[\int_0^{1L} \frac{d}{d\gamma}_{\alpha,\gamma,\beta,\theta,\eta=0} \Big|_{\gamma=0} ({}^1\mathbf{N}_{\delta\hat{\mathbf{d}}_{sc}}^T) \times {}^1\bar{\mathbf{k}}_{sc} \times {}^1\mathbf{N}_{\delta\hat{\mathbf{d}}_{sc}} \times ({}_1\mathbf{q} + \alpha\Delta\mathbf{q}) \times d^1\mathbf{x} \right] + \left[\int_0^{1L} {}^1\mathbf{N}_{\delta\hat{\mathbf{d}}_{sc}}^T \times \frac{d}{d\gamma}_{\alpha,\gamma,\beta,\theta,\eta=0} \Big|_{\gamma=0} ({}^1\bar{\mathbf{k}}_{sc} \times {}^1\mathbf{N}_{\delta\hat{\mathbf{d}}_{sc}} \times ({}_1\mathbf{q} + \alpha\Delta\mathbf{q})) \times d^1\mathbf{x} \right] + \\
& \left[\int_0^{1L} \frac{d}{d\gamma}_{\alpha,\gamma,\beta,\theta,\eta=0} \Big|_{\gamma=0} ({}^1\mathbf{N}_{\delta\hat{\mathbf{d}}_{sc}}^T) \times {}^1\mathbf{D}_{sc} \times d^1I \right] + \left[\int_0^{1L} {}^1\mathbf{N}_{\delta\hat{\mathbf{d}}_{sc}}^T \times \frac{d}{d\gamma}_{\alpha,\gamma,\beta,\theta,\eta=0} \Big|_{\gamma=0} ({}^1\mathbf{D}_{sc}) \times d^1I \right] + \\
& \left[\int_0^{1L} \frac{d}{d\gamma}_{\alpha,\gamma,\beta,\theta,\eta=0} \Big|_{\gamma=0} ({}^2\mathbf{N}_{D2}^T) \times ({}_1\hat{\mathbf{d}} - {}_1\mathbf{d}) \times d^1\mathbf{x} \right] + \left[\int_0^{1L} {}^2\mathbf{N}_{D2}^T \times \frac{d}{d\gamma}_{\alpha,\gamma,\beta,\theta,\eta=0} \Big|_{\gamma=0} ({}_1\hat{\mathbf{d}} - {}_1\mathbf{d}) \times d^1\mathbf{x} \right] - \\
& \left[\frac{d}{d\gamma}_{\alpha,\gamma,\beta,\theta,\eta=0} \Big|_{\gamma=0} ({}^2\mathbf{Q}_{ext} + \beta\Delta\mathbf{Q}_{ext}) \right] + \\
& \left[\int_{1V^c} \frac{d}{d\gamma}_{\alpha,\gamma,\beta,\theta,\eta=0} \Big|_{\gamma=0} {}^1\rho^c \times {}^1\mathbf{N}_u^c \times {}^1\mathbf{N}_u^c \times d^1V^c \times ({}_1^2\dot{\mathbf{q}} + \theta\Delta\dot{\mathbf{q}}) + \int_{1V^s} \frac{d}{d\gamma}_{\alpha,\gamma,\beta,\theta,\eta=0} \Big|_{\gamma=0} {}^1\rho^s \times {}^1\mathbf{N}_u^s \times {}^1\mathbf{N}_u^s \times d^1V^s \times ({}_1^2\dot{\mathbf{q}} + \theta\Delta\dot{\mathbf{q}}) \right] + \\
& \left[\int_{1V^c} \frac{d}{d\gamma}_{\alpha,\gamma,\beta,\theta,\eta=0} \Big|_{\gamma=0} {}^1\rho^c \times {}^1\mathbf{N}_u^c \times {}^1\mathbf{N}_u^c \times d^1V^c \times ({}_1^2\ddot{\mathbf{q}} + \eta\Delta\ddot{\mathbf{q}}) + \int_{1V^s} \frac{d}{d\gamma}_{\alpha,\gamma,\beta,\theta,\eta=0} \Big|_{\gamma=0} {}^1\rho^s \times {}^1\mathbf{N}_u^s \times {}^1\mathbf{N}_u^s \times d^1V^s \times ({}_1^2\ddot{\mathbf{q}} + \eta\Delta\ddot{\mathbf{q}}) \right]
\end{aligned} \tag{A.22}$$

$$\text{where: } \left[\int_0^{1L} \frac{d}{d\gamma}_{\alpha,\gamma,\beta,\theta,\eta=0} \Big|_{\gamma=0} ({}^1\mathbf{N}_{\delta\hat{\mathbf{d}}}) \times {}^2\mathbf{D} \times d^1\mathbf{x} \right] = \mathbf{0}$$

$$\begin{aligned}
\left[\int_0^{1L} {}^1\mathbf{N}_{\delta\hat{\mathbf{d}}}^T \times \frac{d}{d\gamma}_{\alpha,\gamma,\beta,\theta,\eta=0} \Big|_{\gamma=0} ({}^2\mathbf{D}) \times d^1\mathbf{x} \right] &= \left[\int_0^{1L} {}^1\mathbf{N}_{\delta\hat{\mathbf{d}}}^T \times \frac{d}{d\gamma}_{\alpha,\gamma,\beta,\theta,\eta=0} \Big|_{\gamma=0} ({}^2\mathbf{N}_{D1} \times ({}_1^2\mathbf{Q} + \gamma\Delta\mathbf{Q})) \times d^1\mathbf{x} \right] \\
&= \left[\int_0^{1L} {}^1\mathbf{N}_{\delta\hat{\mathbf{d}}}^T \times {}^2\mathbf{N}_{D1} \times d^1\mathbf{x} \right] \times \Delta\mathbf{Q} \\
&= {}^2\mathbf{G}_1^T \times \Delta\mathbf{Q}
\end{aligned}$$

$$\left[\int_0^{1L} \frac{d}{d\gamma}_{\alpha,\gamma,\beta,\theta,\eta=0} \Big|_{\gamma=0} ({}^1\mathbf{N}_{\delta\hat{\mathbf{d}}_{sc}}^T) \times {}^1\bar{\mathbf{k}}_{sc} \times {}^1\mathbf{N}_{\delta\hat{\mathbf{d}}_{sc}} \times {}_1\mathbf{q} \times d^1I \right] = \mathbf{0}$$

$$\left[\int_0^{1L} {}^1\mathbf{N}_{\delta\hat{\mathbf{d}}_{sc}}^T \times \frac{d}{d\gamma}_{\alpha,\gamma,\beta,\theta,\eta=0} \Big|_{\gamma=0} ({}^1\bar{\mathbf{k}}_{sc} \times {}^1\mathbf{N}_{\delta\hat{\mathbf{d}}_{sc}}) \times {}_1\mathbf{q} \times d^1I \right] = \mathbf{0}$$

$$\left[\int_{1I} \frac{d}{d\gamma}_{\alpha,\gamma,\beta,\theta,\eta=0} \Big|_{\gamma=0} ({}^1\mathbf{N}_{\delta\hat{\mathbf{d}}_{sc}}^T) \times {}^1\mathbf{D}_{sc} \times d^1I \right] \times {}_1\mathbf{q} = \mathbf{0}$$

$$\left[\int_{1I} {}^1\mathbf{N}_{\delta\hat{\mathbf{d}}_{sc}}^T \times \frac{d}{d\gamma}_{\alpha,\gamma,\beta,\theta,\eta=0} \Big|_{\gamma=0} ({}^1\mathbf{D}_{sc}) \times d^1I \right] \times {}_1\mathbf{q} = \mathbf{0}$$

$$\begin{aligned}
\left[\int_0^{1L} \frac{d}{d\gamma} \Big|_{\alpha,\gamma,\beta,\theta,\eta=0} \left({}^2_1\mathbf{N}_{D2}^T \right) \times \left({}_1\hat{\mathbf{d}} - {}_1\mathbf{d} \right) \times d^1\mathbf{x} \right] &= \left[\int_0^{1L} (\Delta \mathbf{N}_{D2}^T) \times \left({}_1\hat{\mathbf{d}} - {}_1\mathbf{d} \right) \times d^1\mathbf{x} \right] \\
\int_0^{1L} (\Delta \mathbf{N}_{D2}^T) \times \left({}_1\hat{\mathbf{d}} - {}_1\mathbf{d} \right) \times d^1\mathbf{x} &= \int_0^{1L} \begin{bmatrix} 0 & 0 & 0 & 0 & 0 & 0 & 0 & 0 & 0 & 0 & 0 & 0 & 0 \\ 0 & 0 & A \times \Delta P_c & 0 & B \times \Delta P_c & 0 & 0 & 0 & 0 & 0 & 0 & 0 & 0 \\ 0 & 0 & 0 & A \times \Delta P_c & 0 & B \times \Delta P_c & 0 & 0 & 0 & 0 & 0 & 0 & 0 \\ 0 & 0 & 0 & 0 & 0 & 0 & A \times \Delta P_s & 0 & B \times \Delta P_s & 0 & 0 & 0 & 0 \\ 0 & 0 & 0 & 0 & 0 & 0 & 0 & A \times \Delta P_s & 0 & B \times \Delta P_s & 0 & 0 & 0 \\ 0 & 0 & 0 & 0 & 0 & 0 & 0 & 0 & 0 & 0 & 0 & 0 & 0 \end{bmatrix} \times \left({}_1\hat{\mathbf{d}} - {}_1\mathbf{d} \right) \times d^1\mathbf{x} \\
&= \mathbf{M}_d^T \times \Delta \mathbf{Q}
\end{aligned}$$

$$\left[\int_0^{1L} {}^2_1\mathbf{N}_{D2}^T \times \frac{d}{d\gamma} \Big|_{\alpha,\gamma,\beta,\theta,\eta=0} \left({}_1\hat{\mathbf{d}} \right) \times d^1\mathbf{x} \right] = 0$$

$$\begin{aligned}
\left[\int_0^{1L} {}^2_1\mathbf{N}_{D2}^T \times \frac{d}{d\gamma} \Big|_{\alpha,\gamma,\beta,\theta,\eta=0} \left({}_1\mathbf{d} \right) \times d^1\mathbf{x} \right] &= \left[\int_0^{1L} {}^2_1\mathbf{N}_{D2}^T \times {}^1\mathbf{k}^{-1} \times {}^2_1\mathbf{N}_{Dl} \times {}_1\mathbf{Q} \times d^1\mathbf{x} \right] \\
&= \left[\int_0^{1L} {}^2_1\mathbf{N}_{D2}^T \times {}^1\mathbf{k}^{-1} \times {}^2_1\mathbf{N}_{Dl} \times \left({}_1\mathbf{Q} - {}_1\mathbf{Q} + \gamma \times \Delta \mathbf{Q} \right) \times d^1\mathbf{x} \right] \\
&= \left[\int_0^{1L} {}^2_1\mathbf{N}_{D2}^T \times {}^1\mathbf{k}^{-1} \times {}^2_1\mathbf{N}_{Dl} \times d^1\mathbf{x} \right] \times \Delta \mathbf{Q} \\
&= {}^2_1\mathbf{H}_{12}^T \times \Delta \mathbf{Q}
\end{aligned}$$

$$\left[\frac{d}{d\gamma} \Big|_{\alpha,\gamma,\beta,\theta,\eta=0} \left({}_1^2\mathbf{Q}_{ext} \right) \right] = 0$$

$$\left[\int_{1V^c} \frac{d}{d\gamma} \Big|_{\alpha,\gamma,\beta,\theta,\eta=0} {}^1\rho^c \times {}^1\mathbf{N}_u^{cT} \times {}^1\mathbf{N}_u^c \times d^1V^c \times {}^2_1\dot{\mathbf{q}} + \int_{1V^s} \frac{d}{d\gamma} \Big|_{\alpha,\gamma,\beta,\theta,\eta=0} {}^1\rho^s \times {}^1\mathbf{N}_u^{sT} \times {}^1\mathbf{N}_u^s \times d^1V^s \times {}^2_1\dot{\mathbf{q}} \right] = 0$$

$$\left[\int_{1V^c} \frac{d}{d\gamma} \Big|_{\alpha,\gamma,\beta,\theta,\eta=0} {}^1\rho^c \times {}^1\mathbf{N}_u^{cT} \times {}^1\mathbf{N}_u^c \times d^1V^c \times {}^2_1\ddot{\mathbf{q}} + \int_{1V^s} \frac{d}{d\gamma} \Big|_{\alpha,\gamma,\beta,\theta,\eta=0} {}^1\rho^s \times {}^1\mathbf{N}_u^{sT} \times {}^1\mathbf{N}_u^s \times d^1V^s \times {}^2_1\ddot{\mathbf{q}} \right] = 0$$

$$\begin{aligned}
\frac{d}{d\beta_{\alpha,\gamma,\beta,\theta,\eta=0}} \Big|_{\beta=0} g(\mathbf{q} + \alpha\Delta\mathbf{q}, {}^2\mathbf{Q} + \gamma\Delta\mathbf{Q}, {}^2\mathbf{Q}_{ext} + \beta\Delta\mathbf{Q}_{ext}, {}^2\dot{\mathbf{q}} + \theta\Delta\dot{\mathbf{q}}, {}^2\ddot{\mathbf{q}} + \eta\Delta\ddot{\mathbf{q}}) &= \left[\int_0^{1L} \frac{d}{d\beta_{\alpha,\gamma,\beta,\theta,\eta=0}} \Big|_{\beta=0} ({}^1N_{\hat{\delta}i}) \times {}^2\mathbf{D} \times d^1x \right] + \left[\int_0^{1L} {}^1N_{\hat{\delta}i}^T \times \frac{d}{d\beta_{\alpha,\gamma,\beta,\theta,\eta=0}} \Big|_{\beta=0} ({}^2\mathbf{D}) \times d^1x \right] + \\
&\left[\int_0^{1L} \frac{d}{d\beta_{\alpha,\gamma,\beta,\theta,\eta=0}} \Big|_{\beta=0} ({}^1N_{\hat{\delta}ic}^T) \times {}^2\bar{k}_{sc} \times {}^1N_{\hat{\delta}ic} \times (\mathbf{q} + \alpha\Delta\mathbf{q}) \times d^1x \right] + \left[\int_0^{1L} {}^2N_{\hat{\delta}ic}^T \times \frac{d}{d\beta_{\alpha,\gamma,\beta,\theta,\eta=0}} \Big|_{\beta=0} ({}^2\bar{k}_{sc} \times {}^1N_{\hat{\delta}ic}) \times (\mathbf{q} + \alpha\Delta\mathbf{q}) \times d^1x \right] + \\
&\left[\int_0^{1L} \frac{d}{d\beta_{\alpha,\gamma,\beta,\theta,\eta=0}} \Big|_{\beta=0} ({}^1N_{\hat{\delta}ic}^T) \times {}^1\mathbf{D}_{sc} \times d^1I \right] + \left[\int_0^{1L} {}^1N_{\hat{\delta}ic}^T \times \frac{d}{d\beta_{\alpha,\gamma,\beta,\theta,\eta=0}} \Big|_{\beta=0} ({}^1\mathbf{D}_{sc}) \times d^1I \right] + \\
&\left[\int_0^{1L} \frac{d}{d\beta_{\alpha,\gamma,\beta,\theta,\eta=0}} \Big|_{\beta=0} ({}^2N_{D2}^T) \times (\hat{\mathbf{d}} - \mathbf{d}) \times d^1x \right] + \left[\int_0^{1L} {}^2N_{D2}^T \times \frac{d}{d\beta_{\alpha,\gamma,\beta,\theta,\eta=0}} \Big|_{\beta=0} (\hat{\mathbf{d}} - \mathbf{d}) \times d^1x \right] - \\
&\left[\frac{d}{d\beta_{\alpha,\gamma,\beta,\theta,\eta=0}} \Big|_{\beta=0} ({}^2\mathbf{Q}_{ext} + \beta\Delta\mathbf{Q}_{ext}) \right] + \\
&\left[\int_{1V^c} \frac{d}{d\beta_{\alpha,\gamma,\beta,\theta,\eta=0}} \Big|_{\beta=0} {}^1\rho^c \times {}^1N_u^c \times {}^1N_u^c \times d^1V^c \times ({}^2\dot{\mathbf{q}} + \theta\Delta\dot{\mathbf{q}}) + \int_{1V^s} \frac{d}{d\beta_{\alpha,\gamma,\beta,\theta,\eta=0}} \Big|_{\beta=0} {}^1\rho^s \times {}^1N_u^s \times {}^1N_u^s \times d^1V^s \times ({}^2\dot{\mathbf{q}} + \theta\Delta\dot{\mathbf{q}}) \right] + \\
&\left[\int_{1V^c} \frac{d}{d\beta_{\alpha,\gamma,\beta,\theta,\eta=0}} \Big|_{\beta=0} {}^1\rho^c \times {}^1N_u^c \times {}^1N_u^c \times d^1V^c \times ({}^2\ddot{\mathbf{q}} + \eta\Delta\ddot{\mathbf{q}}) + \int_{1V^s} \frac{d}{d\beta_{\alpha,\gamma,\beta,\theta,\eta=0}} \Big|_{\beta=0} {}^1\rho^s \times {}^1N_u^s \times {}^1N_u^s \times d^1V^s \times ({}^2\ddot{\mathbf{q}} + \eta\Delta\ddot{\mathbf{q}}) \right]
\end{aligned} \tag{A.23}$$

On the right hand side of Equation A.23, the only non-zero expression is the ninth term since the rest of the variables are not functions of ${}^2\mathbf{Q}_{ext}$.

$$\text{where: } \left[\frac{d}{d\beta_{\alpha,\gamma,\beta,\theta,\eta=0}} \Big|_{\beta=0} (-{}^2\mathbf{Q}_{ext} - \beta\Delta\mathbf{Q}_{ext}) \right] = -\Delta\mathbf{Q}_{ext}$$

$$\begin{aligned}
\frac{d}{d\theta_{\alpha,\gamma,\beta,\theta,\eta=0}} \Big|_{\theta=0} g(\mathbf{q} + \alpha\Delta\mathbf{q}, {}^2\mathbf{Q} + \gamma\Delta\mathbf{Q}, {}^2\mathbf{Q}_{ext} + \beta\Delta\mathbf{Q}_{ext}, {}^2\dot{\mathbf{q}} + \theta\Delta\dot{\mathbf{q}}, {}^2\ddot{\mathbf{q}} + \eta\Delta\ddot{\mathbf{q}}) &= \left[\int_0^{1L} \frac{d}{d\theta_{\alpha,\gamma,\beta,\theta,\eta=0}} \Big|_{\theta=0} ({}^1N_{\hat{\delta}i}) \times {}^2\mathbf{D} \times d^1x \right] + \left[\int_0^{1L} {}^1N_{\hat{\delta}i}^T \times \frac{d}{d\theta_{\alpha,\gamma,\beta,\theta,\eta=0}} \Big|_{\theta=0} ({}^2\mathbf{D}) \times d^1x \right] + \\
&\left[\int_0^{1L} \frac{d}{d\theta_{\alpha,\gamma,\beta,\theta,\eta=0}} \Big|_{\theta=0} ({}^1N_{\hat{\delta}ic}^T) \times {}^2\bar{k}_{sc} \times {}^1N_{\hat{\delta}ic} \times (\mathbf{q} + \alpha\Delta\mathbf{q}) \times d^1x \right] + \left[\int_0^{1L} {}^1N_{\hat{\delta}ic}^T \times \frac{d}{d\theta_{\alpha,\gamma,\beta,\theta,\eta=0}} \Big|_{\theta=0} ({}^2\bar{k}_{sc} \times {}^1N_{\hat{\delta}ic}) \times (\mathbf{q} + \alpha\Delta\mathbf{q}) \times d^1x \right] + \\
&\left[\int_0^{1L} \frac{d}{d\theta_{\alpha,\gamma,\beta,\theta,\eta=0}} \Big|_{\theta=0} ({}^1N_{\hat{\delta}ic}^T) \times {}^1\mathbf{D}_{sc} \times d^1I \right] + \left[\int_0^{1L} {}^1N_{\hat{\delta}ic}^T \times \frac{d}{d\theta_{\alpha,\gamma,\beta,\theta,\eta=0}} \Big|_{\theta=0} ({}^1\mathbf{D}_{sc}) \times d^1I \right] + \\
&\left[\int_0^{1L} \frac{d}{d\theta_{\alpha,\gamma,\beta,\theta,\eta=0}} \Big|_{\theta=0} ({}^2N_{D2}^T) \times (\hat{\mathbf{d}} - \mathbf{d}) \times d^1x \right] + \left[\int_0^{1L} {}^2N_{D2}^T \times \frac{d}{d\theta_{\alpha,\gamma,\beta,\theta,\eta=0}} \Big|_{\theta=0} (\hat{\mathbf{d}} - \mathbf{d}) \times d^1x \right] - \\
&\left[\frac{d}{d\theta_{\alpha,\gamma,\beta,\theta,\eta=0}} \Big|_{\theta=0} ({}^2\mathbf{Q}_{ext} + \beta\Delta\mathbf{Q}_{ext}) \right] + \\
&\left[\int_{1V^c} \frac{d}{d\theta_{\alpha,\gamma,\beta,\theta,\eta=0}} \Big|_{\theta=0} {}^1\rho^c \times {}^1N_u^c \times {}^1N_u^c \times d^1V^c \times ({}^2\dot{\mathbf{q}} + \theta\Delta\dot{\mathbf{q}}) + \int_{1V^s} \frac{d}{d\theta_{\alpha,\gamma,\beta,\theta,\eta=0}} \Big|_{\theta=0} {}^1\rho^s \times {}^1N_u^s \times {}^1N_u^s \times d^1V^s \times ({}^2\dot{\mathbf{q}} + \theta\Delta\dot{\mathbf{q}}) \right] + \\
&\left[\int_{1V^c} \frac{d}{d\theta_{\alpha,\gamma,\beta,\theta,\eta=0}} \Big|_{\theta=0} {}^1\rho^c \times {}^1N_u^c \times {}^1N_u^c \times d^1V^c \times ({}^2\ddot{\mathbf{q}} + \eta\Delta\ddot{\mathbf{q}}) + \int_{1V^s} \frac{d}{d\theta_{\alpha,\gamma,\beta,\theta,\eta=0}} \Big|_{\theta=0} {}^1\rho^s \times {}^1N_u^s \times {}^1N_u^s \times d^1V^s \times ({}^2\ddot{\mathbf{q}} + \eta\Delta\ddot{\mathbf{q}}) \right]
\end{aligned} \tag{A.24}$$

In Equation A.24, all the expressions on the right hand side except the tenth term are not functions of the state variable ${}^2\dot{q}$. Therefore, the only nonzero term on the right hand side of Equation A.24 is the tenth term as given below:

$$\begin{aligned}
\text{where: } & \left[\int_{1V^c} \frac{d}{d\theta_{\alpha,\gamma,\beta,\theta,\eta=0}} \Big| {}^1\mu^c \times {}^1N_u^{cT} \times {}^1N_u^c \times d^1V^c \times ({}^2\dot{q} + \theta \times \Delta\dot{q}) + \int_{1V^s} \frac{d}{d\theta_{\alpha,\gamma,\beta,\theta,\eta=0}} \Big| {}^1\mu^s \times {}^1N_u^{sT} \times {}^1N_u^s \times d^1V^s \times ({}^2\dot{q} + \theta \times \Delta\dot{q}) \right] = \\
& \left[\int_{1V^c} {}^1\mu^c \times {}^1N_u^{cT} \times {}^1N_u^c \times d^1V^c \times \Delta\dot{q} + \int_{1V^s} {}^1\mu^s \times {}^1N_u^{sT} \times {}^1N_u^s \times d^1V^s \times \Delta\dot{q} \right] \\
\frac{d}{d\eta_{\alpha,\gamma,\beta,\theta,\eta=0}} \Big| & g({}^1q + \alpha\Delta q, {}^2Q + \gamma\Delta Q, {}^2Q_{ext} + \beta\Delta Q_{ext}, {}^2\dot{q} + \theta\Delta\dot{q}, {}^2\ddot{q} + \eta\Delta\ddot{q}) = \left[\int_0^{1L} \frac{d}{d\eta_{\alpha,\gamma,\beta,\theta,\eta=0}} \Big| ({}^1N_{\delta\dot{q}}) \times {}^2D \times d^1x \right] + \left[\int_0^{1L} {}^1N_{\delta\dot{q}}^T \times \frac{d}{d\eta_{\alpha,\gamma,\beta,\theta,\eta=0}} \Big| ({}^2D) \times d^1x \right] + \\
& \left[\int_0^{1L} \frac{d}{d\eta_{\alpha,\gamma,\beta,\theta,\eta=0}} \Big| ({}^1N_{\delta\dot{q}}^T) \times {}^2\bar{k}_{sc} \times {}^1N_{\delta\dot{q}} \times ({}^1q + \alpha\Delta q) \times d^1x \right] + \left[\int_0^{1L} {}^1N_{\delta\dot{q}}^T \times \frac{d}{d\eta_{\alpha,\gamma,\beta,\theta,\eta=0}} \Big| ({}^2\bar{k}_{sc} \times {}^1N_{\delta\dot{q}} \times ({}^1q + \alpha\Delta q)) \times d^1x \right] + \\
& \left[\int_0^{1L} \frac{d}{d\eta_{\alpha,\gamma,\beta,\theta,\eta=0}} \Big| ({}^1N_{\delta\dot{q}}^T) \times {}^1D_{sc} \times d^1I \right] + \left[\int_0^{1L} {}^1N_{\delta\dot{q}}^T \times \frac{d}{d\eta_{\alpha,\gamma,\beta,\theta,\eta=0}} \Big| ({}^1D_{sc}) \times d^1I \right] + \\
& \left[\int_0^{1L} \frac{d}{d\eta_{\alpha,\gamma,\beta,\theta,\eta=0}} \Big| ({}^2N_{D2}^T) \times ({}^1\hat{d} - {}^1d) \times d^1x \right] + \left[\int_0^{1L} {}^2N_{D2}^T \times \frac{d}{d\eta_{\alpha,\gamma,\beta,\theta,\eta=0}} \Big| ({}^1\hat{d} - {}^1d) \times d^1x \right] - \\
& \left[\frac{d}{d\eta_{\alpha,\gamma,\beta,\theta,\eta=0}} \Big| ({}^2Q_{ext} + \beta\Delta Q_{ext}) \right] + \\
& \left[\int_{1V^c} \frac{d}{d\eta_{\alpha,\gamma,\beta,\theta,\eta=0}} \Big| {}^1\rho^c \times {}^2N_u^{cT} \times {}^2N_u^c \times d^1V^c \times ({}^2\dot{q} + \theta\Delta\dot{q}) + \int_{1V^s} \frac{d}{d\eta_{\alpha,\gamma,\beta,\theta,\eta=0}} \Big| {}^1\rho^s \times {}^2N_u^{sT} \times {}^2N_u^s \times d^1V^s \times ({}^2\dot{q} + \theta\Delta\dot{q}) \right] + \\
& \left[\int_{1V^c} \frac{d}{d\eta_{\alpha,\gamma,\beta,\theta,\eta=0}} \Big| {}^1\rho^c \times {}^2N_u^{cT} \times {}^2N_u^c \times d^1V^c \times ({}^2\ddot{q} + \eta\Delta\ddot{q}) + \int_{1V^s} \frac{d}{d\eta_{\alpha,\gamma,\beta,\theta,\eta=0}} \Big| {}^1\rho^s \times {}^2N_u^{sT} \times {}^2N_u^s \times d^1V^s \times ({}^2\ddot{q} + \eta\Delta\ddot{q}) \right] \\
& \tag{A.25}
\end{aligned}$$

In Equation A.25, all the expressions on the right hand side except the eleventh term are not functions of the state variable ${}^2\ddot{q}$. Therefore, the only nonzero term on the right hand side of Equation A.25 is the eleventh term as given below:

$$\begin{aligned}
\text{where: } & \left[\int_{1V^c} \frac{d}{d\eta_{\alpha,\gamma,\beta,\theta,\eta=0}} \Big| {}^1\rho^c \times {}^1N_u^{cT} \times {}^1N_u^c \times d^1V^c \times ({}^2\ddot{q} + \eta \times \Delta\ddot{q}) + \int_{1V^s} \frac{d}{d\eta_{\alpha,\gamma,\beta,\theta,\eta=0}} \Big| {}^1\rho^s \times {}^1N_u^{sT} \times {}^1N_u^s \times d^1V^s \times ({}^2\ddot{q} + \eta \times \Delta\ddot{q}) \right] = \\
& \left[\int_{1V^c} {}^1\rho^c \times {}^1N_u^{cT} \times {}^1N_u^c \times d^1V^c \times \Delta\ddot{q} + \int_{1V^s} {}^1\rho^s \times {}^1N_u^{sT} \times {}^1N_u^s \times d^1V^s \times \Delta\ddot{q} \right]
\end{aligned}$$

A.1.5. Derivation of Cross-Section Stiffness

In the current research, a fiber-based distributed plasticity approach is employed. RCFT cross-sections at each integration point along the element length are divided into

individual concrete and steel fibers as shown in Figure A.1. These material fibers are associated with a constitutive model. During nonlinear analysis, the state of each fiber is updated based on the current strain calculated at the centroid of the fibers. Exploiting the assumption that plane sections remain plane and normal to the longitudinal axis, the centroidal strain of a material fiber is calculated from the cross-sectional strain and curvatures. The cross-sectional force and stiffness terms are then calculated through numerical integration over the steel and concrete fibers.

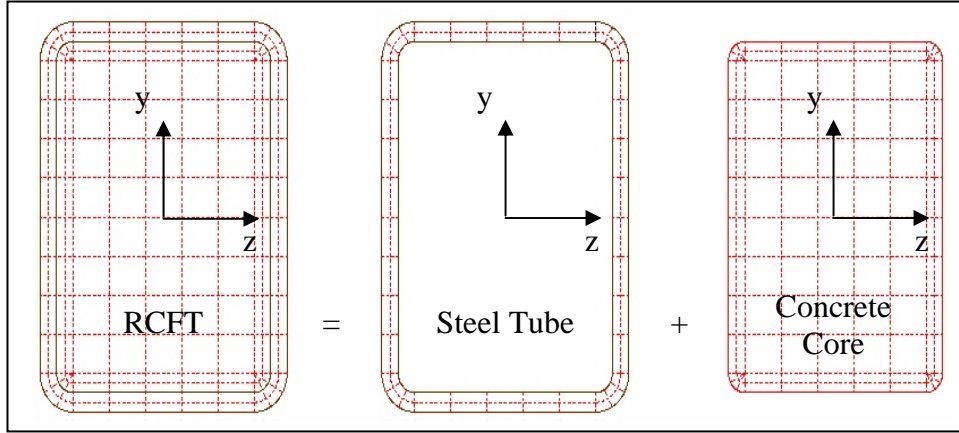


Figure A 1 Discretization Scheme for RCFT Cross-Section

Incremental cross-sectional strains can be related to the fiber strains as given in Equation A.26.

$$\Delta \boldsymbol{\varepsilon} = \begin{bmatrix} \Delta \varepsilon^c \\ \Delta \varepsilon^s \end{bmatrix} = \mathbf{Y} \times \Delta \hat{\mathbf{d}} \quad [\text{A.26}]$$

where: $\Delta \varepsilon^c$ is incremental axial strain of concrete fibers

$\Delta \varepsilon^s$ is incremental axial strain of steel fibers

\mathbf{Y} is the compatibility matrix

$$\mathbf{Y} = \begin{bmatrix} 1 & -y_c & -z_c & 0 & 0 & 0 \\ 0 & 0 & 0 & 1 & -y_s & -z_s \end{bmatrix}^T$$

y_c, z_c coordinates of concrete fibers with respect to y-z axes

y_s, z_s coordinates of steel fibers with respect to y-z axes

Using the Hooke's Law, the relationship between incremental fiber strains and stresses can be developed as follows:

$$\Delta \boldsymbol{\sigma} = \begin{bmatrix} \Delta \boldsymbol{\sigma}^c \\ \Delta \boldsymbol{\sigma}^s \end{bmatrix} = \mathbf{E}_t \times \Delta \boldsymbol{\varepsilon} = \begin{bmatrix} {}^1E^c & 0 \\ 0 & {}^1E^s \end{bmatrix} \times \begin{bmatrix} \Delta \boldsymbol{\varepsilon}^c \\ \Delta \boldsymbol{\varepsilon}^s \end{bmatrix} \quad [\text{A.27}]$$

$\Delta \boldsymbol{\sigma}^c$ is incremental axial stress of concrete fibers

$\Delta \boldsymbol{\sigma}^s$ is incremental axial stress of steel fibers

${}^1E^c$ is tangent modulus of concrete fibers

${}^1E^s$ is tangent modulus of steel fibers

Incremental cross-sectional forces can be expressed as given in Equation A.28:

$$\Delta \mathbf{D} = \int_0^{1L} \mathbf{Y}^T \times \Delta \boldsymbol{\sigma} \times dA = \left(\int_0^{1L} \mathbf{Y}^T \times \mathbf{E}_t \times \mathbf{Y} \times dA \right) \times \Delta \hat{\mathbf{d}} = \mathbf{k} \times \Delta \hat{\mathbf{d}} \quad [\text{A.28}]$$

where: \mathbf{k} is the cross-sectional stiffness matrix

$$\mathbf{k} = \left(\int_0^{1L} \mathbf{Y}^T \times \mathbf{E}_t \times \mathbf{Y} \times dA \right) = \begin{bmatrix} EA^c & -EQ_z^c & -EQ_y^c & 0 & 0 & 0 \\ -EQ_z^c & EI_z^c & EI_{yz}^c & 0 & 0 & 0 \\ -EQ_y^c & EI_{yz}^c & EI_y^c & 0 & 0 & 0 \\ 0 & 0 & 0 & EA^s & -EQ_z^s & -EQ_y^s \\ 0 & 0 & 0 & -EQ_z^s & EI_z^s & EI_{yz}^s \\ 0 & 0 & 0 & -EQ_y^s & EI_{yz}^s & EI_y^s \end{bmatrix}$$

The cross-section flexibility matrix is obtained by taking the inverse of cross-section stiffness matrix.

$$\mathbf{f} = \mathbf{k}^{-1} \quad [\text{A.29}]$$

where: \mathbf{f} is the cross-section flexibility

Within the formulation, the locations of the fibers are assumed to stay constant with respect to the reference axes located at the centroid of the cross-section.

A.2. Mapping of Element Forces, Displacements, and Stiffness between Natural and Global Coordinate Systems

A.2.1. Transformation of Element Forces

The incremental element forces in natural coordinates can be transformed into incremental element forces in local coordinates as given in Equation A.25.

$$\Delta \hat{\mathbf{Q}}_{int} = \mathbf{T}_{NL}^T \times \Delta \bar{\mathbf{Q}}_{int} \quad [\text{A.25}]$$

where: $\Delta \hat{\mathbf{Q}}_{int} = [\Delta \hat{P}_i^s \quad \Delta \hat{V}_{yi}^s \quad \Delta \hat{V}_{zi}^s \quad \Delta \hat{M}_{yi} \quad \Delta \hat{M}_{zi} \quad \Delta \hat{P}_i^c \quad \Delta \hat{V}_{yi}^c \quad \Delta \hat{V}_{zi}^c \quad \Delta \hat{P}_j^s \quad \Delta \hat{V}_{yj}^s \quad \Delta \hat{V}_{zj}^s \quad \Delta \hat{M}_{yj} \quad \Delta \hat{M}_{zj} \quad \Delta \hat{P}_j^c \quad \Delta \hat{V}_{yj}^c \quad \Delta \hat{V}_{zj}^c]$

$$\Delta \bar{\mathbf{Q}}_{int} = [\Delta \bar{P}_i^{sc} \quad \Delta \bar{P}_i^c \quad \bar{M}_{zi}^c \quad \bar{M}_{yi}^c \quad \bar{M}_{zj}^c \quad \bar{M}_{yj}^c \quad \Delta \bar{P}_i^s \quad \bar{M}_{zi}^s \quad \bar{M}_{yi}^s \quad \bar{M}_{zj}^s \quad \bar{M}_{yj}^s \quad \bar{P}_m^c \quad \bar{P}_m^s]$$

$$\mathbf{T}_{NL}^T = \begin{bmatrix} -1 & 0 & 0 & 0 & 0 & 0 & -1 & 0 & 0 & 0 & 0 & 0 & 0 & 0 \\ 0 & 0 & 0 & 0 & 0 & 0 & 0 & 1/L & 0 & 1/L & 0 & 0 & 0 & 0 \\ 0 & 0 & 0 & 0 & 0 & 0 & 0 & 0 & 1/L & 0 & 1/L & 0 & 0 & 0 \\ 0 & 0 & 0 & -1 & 0 & 0 & 0 & 0 & -1 & 0 & 0 & 0 & 0 & 0 \\ 0 & 0 & 1 & 0 & 0 & 0 & 0 & 1 & 0 & 0 & 0 & 0 & 0 & 0 \\ 1 & -1 & 0 & 0 & 0 & 0 & 0 & 0 & 0 & 0 & 0 & 0 & 0 & 0 \\ 0 & 0 & 1/L & 0 & 1/L & 0 & 0 & 0 & 0 & 0 & 0 & 0 & 0 & 0 \\ 0 & 0 & 0 & 1/L & 0 & 1/L & 0 & 0 & 0 & 0 & 0 & 0 & 0 & 0 \\ 1 & 0 & 0 & 0 & 0 & 0 & 1 & 0 & 0 & 0 & 0 & 0 & 0 & 0 \\ 0 & 0 & 0 & 0 & 0 & 0 & 0 & -1/L & 0 & -1/L & 0 & 0 & 0 & 0 \\ 0 & 0 & 0 & 0 & 0 & 0 & 0 & 0 & -1/L & 0 & -1/L & 0 & 0 & 0 \\ 0 & 0 & 0 & 0 & 0 & -1 & 0 & 0 & 0 & 0 & -1 & 0 & 0 & 0 \\ 0 & 0 & 0 & 0 & 1 & 0 & 0 & 0 & 0 & 1 & 0 & 0 & 0 & 0 \\ -1 & 1 & 0 & 0 & 0 & 0 & 0 & 0 & 0 & 0 & 0 & 0 & 0 & 0 \\ 0 & 0 & -1/L & 0 & -1/L & 0 & 0 & 0 & 0 & 0 & 0 & 0 & 0 & 0 \\ 0 & 0 & 0 & -1/L & 0 & -1/L & 0 & 0 & 0 & 0 & 0 & 0 & 0 & 0 \end{bmatrix}$$

A.2.2. Derivation of External Stiffness Matrix

The unbalanced forces (${}^1\hat{\mathbf{F}}_U$) generated due to rigid body motion (Figures 2.13d, 2.14d) are presented in vector format as given in Equation A.26.

$${}^1\hat{\mathbf{F}}_U = [{}^1\hat{\mathbf{F}}_{Psi} \quad {}^1\hat{\mathbf{F}}_{Mi} \quad {}^1\hat{\mathbf{F}}_{Pci} \quad {}^1\hat{\mathbf{F}}_{Psj} \quad {}^1\hat{\mathbf{F}}_{Mj} \quad {}^1\hat{\mathbf{F}}_{Pcj}]^T \quad [\text{A.26}]$$

where:

$${}^1\hat{\mathbf{F}}_{Psi} = \left[\left(-\frac{({}^1M_{yi}^s + {}^1M_{yj}^s)}{1L} \times {}_1\hat{\theta}_{rgy} - \frac{({}^1M_{zi}^s + {}^1M_{zj}^s)}{1L} \times {}_1\hat{\theta}_{rgz} \right) \quad -{}^1\hat{P}^s \times {}_1\hat{\theta}_{rgz} \quad -{}^1\hat{P}^s \times {}_1\hat{\theta}_{rgy} \right]^T$$

$${}^1\hat{\mathbf{F}}_{Mi} = [0 \quad 0 \quad 0]^T$$

$$\begin{aligned}
{}^1\hat{\mathbf{F}}_{Pci} &= \left[\left(-\frac{({}^1M_{yi}^c + {}^1M_{yj}^c)}{{}^1L} \times_1 \hat{\theta}_{rgy} - \frac{({}^1M_{zi}^c + {}^1M_{zj}^c)}{{}^1L} \times_1 \hat{\theta}_{rgz} \right) \quad -{}^1P^c \times_1 \tilde{\theta}_{rgz} \quad -{}^1P^c \times_1 \tilde{\theta}_{rgy} \right]^T \\
{}^1\hat{\mathbf{F}}_{Psj} &= \left[\left(\frac{({}^1M_{yi}^s + {}^1M_{yj}^s)}{{}^1L} \times_1 \hat{\theta}_{rgy} + \frac{({}^1M_{zi}^s + {}^1M_{zj}^s)}{{}^1L} \times_1 \hat{\theta}_{rgz} \right) \quad {}^1\hat{P}^s \times_1 \hat{\theta}_{rgz} \quad {}^1\hat{P}^s \times_1 \hat{\theta}_{rgy} \right]^T \\
{}^1\hat{\mathbf{F}}_{Mj} &= [0 \quad 0 \quad 0]^T \\
{}^1\hat{\mathbf{F}}_{Pcj} &= \left[\left(\frac{({}^1M_{yi}^c + {}^1M_{yj}^c)}{{}^1L} \times_1 \hat{\theta}_{rgy} + \frac{({}^1M_{zi}^c + {}^1M_{zj}^c)}{{}^1L} \times_1 \hat{\theta}_{rgz} \right) \quad {}^1\hat{P}^c \times_1 \hat{\theta}_{rgz} \quad {}^1\hat{P}^c \times_1 \hat{\theta}_{rgy} \right]^T
\end{aligned}$$

Rigid body rotation of the RCFT beam-column element with respect to local \hat{y} and \hat{z} axes produces the deformations of $\hat{\theta}_{rgy}$, $\hat{\theta}_{rgz}$ given below in Figure A.2, respectively.

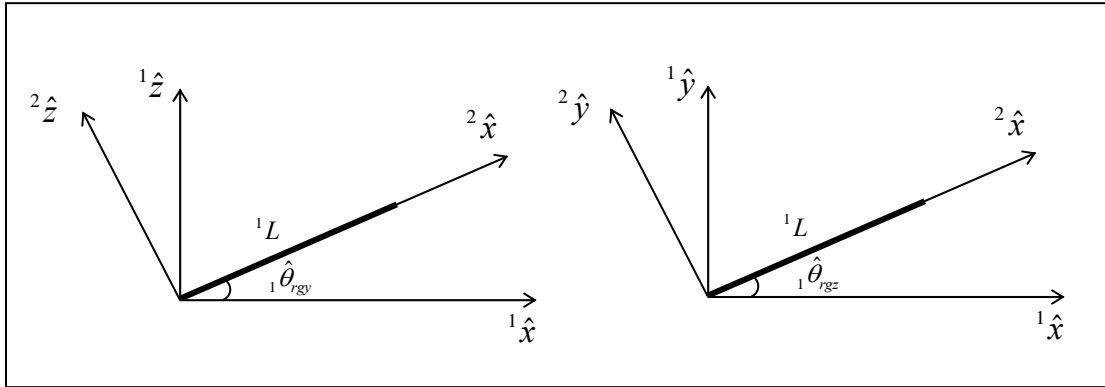


Figure A 2 Rigid Body Rotation of the RCFT Beam-Column in Local Coordinates

$\hat{\theta}_{rgy}$ and $\hat{\theta}_{rgz}$ can be expressed in terms of lateral translations as given in Equations A.27 and A.28, respectively.

$${}^1\hat{\theta}_{rgy} = \frac{{}^1e_{zj}^s - {}^1e_{zi}^s}{{}^1L} = \frac{{}^1e_{zj}^c - {}^1e_{zi}^c}{{}^1L} \quad [A.27]$$

$${}^1\hat{\theta}_{rgz} = \frac{{}^1e_{yj}^s - {}^1e_{yi}^s}{{}^1L} = \frac{{}^1e_{yj}^c - {}^1e_{yi}^c}{{}^1L} \quad [A.28]$$

Substituting Equation A.27 and A.28 into Equation A.26 and factoring out the terms of ${}^1\hat{\mathbf{q}}$, ${}^1\mathbf{K}_{ge}$ can be derived as in Equation A.29.

$${}^1\hat{\mathbf{F}}_U = {}^1\hat{\mathbf{K}}_{ge} \times {}^1\hat{\mathbf{q}} \quad [\text{A.29}]$$

where:

$${}^1\hat{\mathbf{q}} = \left[{}^1\hat{e}_{xi}^s \quad {}^1\hat{e}_{yi}^s \quad {}^1\hat{e}_{zi}^s \quad {}^1\hat{\theta}_{xi} \quad {}^1\hat{\theta}_{yi} \quad {}^1\hat{\theta}_{zi} \quad {}^1\hat{e}_{xi}^c \quad {}^1\hat{e}_{yi}^c \quad {}^1\hat{e}_{zi}^c \quad {}^1\hat{e}_{xj}^s \quad {}^1\hat{e}_{yj}^s \quad {}^1\hat{e}_{zj}^s \quad {}^1\hat{\theta}_{xj} \quad {}^1\hat{\theta}_{yj} \quad {}^1\hat{\theta}_{zj} \quad {}^1\hat{e}_{xj}^c \quad {}^1\hat{e}_{yj}^c \quad {}^1\hat{e}_{zj}^c \right]^T$$

While deriving ${}^1\mathbf{K}_{ge}$ additional terms that are canceling each other was added to ensure the symmetry. This was performed based on the assumption that the axial deformations at two ends of the members are equal to each other under rigid body deformation (e.g., ${}^1e_{xi}^s = {}^1e_{xj}^s$, ${}^1e_{xi}^c = {}^1e_{xj}^c$) (Yang, 1994).

Bibliography

- Ahmad, S. H. and Shah, S. P. (1985). "Behavior of Hoop Confined Concrete Under High Strain Rates," *ACI Journal Proceedings*, Vol. 82, No. 5, pp. 634-647.
- Alemдар, B. N. and White, D. W. (2005). "Displacement, Flexibility, and Mixed Beam--Column Finite Element Formulations for Distributed Plasticity Analysis," *Journal of Structural Engineering*, ASCE, Vol. 131, No. 12, pp. 1811-1819.
- Alemдар, B.N. (2001). "Distributed Plasticity Analysis of Steel Building Structural Systems," Ph.D. dissertation, School of Civil and Environmental Engineering, Georgia Institute of Technology, Atlanta, GA, July.
- Assi, I. M., Qudeima, E. M., and Hunaiti, Y. M. (2003). "Ultimate Moment Capacity of Foamed and Lightweight Aggregate Concrete-Filled Steel Tubes," *Steel and Composite Structures*, Vol. 3, No. 3, pp. 199-212.
- Ayoub, A. and Filippou, F. C. (2000). "Mixed Formulation of Nonlinear Steel-Concrete Composite Beam Element," *Journal of Structural Engineering*, ASCE, Vol. 126, No. 3, pp. 371-381.
- American Institute of Steel Construction (AISC) (2005). *Load and Resistance Factor Design (LRFD) Specification for Structural Steel Buildings*, AISC, Chicago, Illinois, 2005.
- Ameur-Moussa, R. and Buyukozturk, O. (1990). "A bounding surface model for concrete," *Nuclear Engineering and Design*, Vol. 121, No. 1, pp. 113-125.
- Ang, A. H. and Wilson, W. H. (1975). *Probability Concepts in Engineering Planning and Design*, John Wiley & Sons, New York, NY.
- Applied Technology Council (ATC) (1996). "Seismic Evaluation and Retrofit of Concrete Buildings," Report No. SSC 96-01, Applied Technology Council, Redwood City, CA.
- ATC (2007). "Guidelines for Seismic Performance Assessment of Buildings," ATC-58 35% Draft, Applied Technology Council, Redwood City, CA.
- Attard M. and Setunge S. (1996). "Stress-Strain Relationship of Confined and Unconfined Concrete," *ACI Materials Journal*, Vol. 93, No. 5, pp. 432-442.
- Backlund, J. (1976). "Large Deflection Analysis of Elasto-Plastic Beams and Frames," *International Journal of Mechanical Sciences*, Vol. 18, No. 6, pp. 269-277.

- Balan, T. A., Filippou, F. C., and Popov, E. P. (1998). "Hysteretic Model of Ordinary and High-Strength Reinforcing Steel." *Journal of Structural Engineering*, ASCE, Vol. 124, No. 3, pp. 288-297.
- Bathe, K. (1982). *Finite Element Procedures in Engineering Analysis*, Prentice-Hall, Inc., Englewood Cliffs, NJ.
- Bathe, K. J. and Bolourchi, S. (1979). "Large Displacement Analysis of Three-Dimensional Beam Structures," *International Journal for Numerical Methods in Engineering*, Vol. 14, No. 7, pp 961 – 986.
- Bertero V. V., Whittaker, A. S., and Gilani, A. S. (1996). "Experimental Investigations of Beam-Column Subassemblages," Report No. SAC 96-01, FEMA / SAC Joint Venture, Phase I, March.
- Bommer, J. J., Acevedo, A. N. A. B. (2004). "The Use of Real Earthquake Accelerograms as Input to Dynamic Analysis," *Journal of Earthquake Engineering*, Vol. 8, No.1, pp. 43-91.
- Bradford M. A., Loh, H. Y., and Uy B. (2002). "Slenderness limits for filled circular steel tubes," *Journal of Constructional Steel Research*, Vol. 58, No. 2, pp. 243-252.
- Bridge, R. Q., O'Shea M. D., Gardner P., Grigson R., and Tyrell J. (1995). "Local buckling of square thinwalled steel tubes with concrete in-fill," *International Conference on Structural Stability and Design*, Sydney, pp. 207-314.
- Bridge, R. Q. (1976). "Concrete Filled Steel Tubular Columns," Report No. R283, School of Civil Engineering, University of Sydney, Sydney, Australia.
- Carol, I. and Murcia, J. (1989). "Nonlinear time-dependent analysis of planar frames using an exact formulation. I: Theory," *Computers & Structures*, Vol. 33, No. 1, pp. 79-87.
- Chang, G. A. and Mander, J. B. (1994). "Seismic Energy Based Fatigue Damage Analysis of Bridge Columns: Part I – Evaluation of Seismic Capacity." Report No. NCEER-94-0006, National Center for Earthquake Engineering Research, State University of New York, Buffalo, NY.
- Chen W. F. and Han, D. J. (1988). *Plasticity for Structural Engineering*, Springer-Verlag, New York, NY.
- Chen, A. and Chen, W. (1975). "Constitutive Relations for Concrete," *Journal of the Engineering Mechanics Division*, Vol. 101, No. 4, pp. 465-481.

- Choi, Y. H., Foutch, D. A., and Lafave, J. M. (2006). "New Approach to AISC P-M Interaction Curve for Square Concrete-Filled Tube (CFT) Beam-Columns," *Engineering Structures*, Vol. 28, No.11, pp. 1586-1598.
- Chung, J., Matsui, C., and Tsuda, K. (2001). "Simplified Design Formula of Slender Concrete Filled Steel Tubular Beam-Columns," *Structural Engineering and Materials*, Vol. 12, No. 1, July, pp. 71-84.
- Clarke, M. J., Bridge R. Q., Hancock, G. J., and Trahir, N. S. (1993). "Benchmarking and Verification of Second-Order Elastic and Inelastic Frame Analysis Programs, " Plastic Hinge Based Methods for Advanced Inelastic Analysis and Design of Steel Frames, White, D. W. and Chen, W. F. (eds.), SSRC, Bethlehem, PA.
- Clarke, M. J. and Hancock, G. J. (1991). "Finite-Element Nonlinear Analysis of Stressed-Arch Frames," *Journal of Structural Engineering*, ASCE, Vol. 117, No. 10, pp. 2819-2837.
- Cleason, C. (1999). "Finite Element Analysis OF Confined Concrete Columns," Nordic Concrete Research, Publication no. 22.
- Cofie, N. G. and Krawinkler, H. (1985). "Uniaxial Cyclic Stress-Strain Behavior of Structural Steel," *Journal of Engineering Mechanics*, Vol. 111, No. 9, pp. 1105-1120.
- Collins, M. P. and Mitchell, D. (1991). *Prestressed Concrete Structures*, Prentice-Hall, New Jersey, 1991.
- Cook, R. D., Malkus, D. S., Plesha M. E., and Witt, R. J. (2002). *Concepts and Applications of Finite Element Analysis*, John Wiley & Sons, New York, NY.
- Cornell, C. A., Jalayer, F., Hamburger, R. O., and Douglas, A. F. (2002). "Probabilistic Basis for 2000 SAC Federal Emergency Management Agency Steel Moment Frame Guidelines," *Journal of Structural Engineering*, ASCE, Vol. 128, No. 4, pp. 526-533.
- Crifield, M. A. (1991). *Nonlinear Finite Element Analysis of Solids and Structures*, John Wiley & Sons, New York, NY.
- Cusson, D., and Paultre, P. (1995). "Stress-Strain Model for Confined High-Strength Concrete," *Journal of Structural Engineering*, ASCE, Vol. 121, No. 3, pp. 468-477.
- Dafalias, Y. F. and Popov, E. P. (1976). "A model of Nonlinearly Hardening Materials for Complex Loading," *Acta Mechanica*, Vol. 21, No. 3, pp. 173-192.

- Davison, T. A. and Birkemoe, P. C. (1983). "Column Behaviour of Cold-Formed Hollow Structural Steel Shapes," *Canadian Journal of Civil Engineering*, Vol. 10, No. 1, pp. 125-151.
- Domenech, A. C., Varma, A., and Harichandran, R. S. (2002). "Development of a Modified Fiber-Based Beam-Column Element for DRAIN2DX," MSU-CIL Research Report No. 2002-02, Department of Civil and Environmental Engineering, Michigan State University, East Lansing, MI.
- Dunberry, E., LeBlanc, D., and Redwood, R. G. (1987). "Cross-Section Strength of Concrete-Filled HSS Columns at Simple Beam Connections," *Canadian Journal of Civil Engineering*, Vol. 14, pp. 408-417.
- El-Tawil, S. and Deierlein, G. G. (2001a). "Nonlinear Analysis of Mixed Steel-Concrete Frames. I: Element Formulation," *Journal of Structural Engineering*, ASCE, Vol. 127, No. 6, June 2001, pp. 647-655.
- El-Tawil, S. and Deierlein, G. G. (2001b). "Nonlinear Analysis of Mixed Steel-Concrete Frames. II: Implementation and Verification," *Journal of Structural Engineering*, ASCE, Vol. 127, No. 6, June 2001, pp. 656-665.
- Federal Emergency Management Agency (FEMA) (1997a). NEHRP Guidelines for the Seismic Rehabilitation of Buildings, FEMA 273, Federal Emergency Management Agency, Washington, D.C.
- FEMA (1997b). NEHRP Recommended Provisions for Seismic Regulations for New Buildings and Other Structures – Commentary, FEMA 303, Federal Emergency Management Agency, Washington, D. C.
- FEMA (2000a). Recommended Seismic Design Criteria for New Steel Moment-Frame Buildings, FEMA 350, Federal Emergency Management Agency, Washington, D.C.
- FEMA (2000b). Prestandard and Commentary for the Seismic Rehabilitation of Buildings, FEMA 356, Federal Emergency Management Agency, Washington, D.C.
- Furlong, R. W. (1967). "Strength of Steel-Encased Concrete Beam Columns," *Journal of the Structural Division*, ASCE, Vol. 93, No. ST5, pp. 113-124.
- Furlong, R. W. (1968). "Design of Steel-Encased Concrete Beam-Columns," *Journal of the Structural Division*, ASCE, Vol. 94, No. 1, pp. 267-291.
- Galambos, T. V. (1998). Guide to Stability Design Criteria for Metal Structures, John Wiley & Sons, New York, NY.

- Gartner, S. and Hajjar, J. F. (2006). "The Design and Evaluation of Rectangular Concrete Filled Tube (RCFT) Column Frames for a Performance-Based Design Demand Assessment," Report No. ST-06-1, Department of Civil Engineering, University of Minnesota, Minneapolis, Minnesota, December.
- Gattass, M. and Abel, J. F. (1987). "Equilibrium considerations of the updated Lagrangian formulation of beam-columns with natural concepts," *International Journal for Numerical Methods in Engineering*, Vol. 24, No. 11, pp. 2119-2141.
- Ge, H. B. and Usami, T. (1994). "Strength Analysis of Concrete-Filled Thin-Walled Steel Box Columns," *Journal of Constructional Steel Research*, Vol. 30, No. 3, pp. 259-281.
- Gho, W. and Liu, D. (2004). "Flexural Behaviour of High-Strength Rectangular Concrete-Filled Steel Hollow Sections," *Journal of Constructional Steel Research*, Vol. 60, No. 11, pp 1681-1696.
- Gopalaratnam, V. S. and Shah, S. P. (1985). "Softening Response of Plain Concrete in Direct Tension," *ACI Structural Journal*, Vol. 82, No. 3, pp. 310-323.
- Gourley, B. C. and Hajjar, J. F. (1994). "Cyclic nonlinear analysis of three-dimensional concrete-filled steel tube beam-columns and composite frames," Report No. ST-94-3, Department of Civil Engineering, University of Minnesota, Minneapolis, MN, February.
- Grassl, P. and Jirasek, M. (2006). "Damage-Plastic Model for Concrete Failure," *International Journal of Solids and Structures*, Vol. 43, Nos. 22-23, pp 7166-7196.
- Grauers, M. (1993). "Composite Columns of Hollow Steel Sections Filled With High Strength Concrete," Ph.D. dissertation, Chalmers University, Goteborg, Sweden, June.
- Green, P. S., Sause, R., and Ricles, J. M. (2002). "Strength and ductility of HPS flexural members," *Journal of Constructional Steel Research*, Volume 58, Nos. 5-8, pp. 907-941.
- Gupta, A. and Krawinkler, H.(1999). "Seismic Demands for Performance Evaluation of Steel Moment Frame Structures," Report No. 132, John A. Blume Earthquake Engineering Center, Stanford University, Stanford, California.
- Hajjar, J. F., Schiller, P. H., and Molodan, A. (1998a). "A Distributed Plasticity Model for Concrete-Filled Steel Tube Beam-Columns with Interlayer Slip," *Engineering Structures*, Vol. 20, No. 8, pp. 663-676.

- Hajjar, J. F., Molodan, A., and Schiller, P. H. (1998b). "A Distributed Plasticity Model for Cyclic Analysis of Concrete-Filled Steel Tube Beam-Columns and Composite Frames," *Engineering Structures*, Vol. 20, Nos. 4-6, pp. 398-412.
- Hajjar, J. F. and Gourley, B. C. (1997). "A Cyclic Nonlinear Model for Concrete-Filled Tubes. I. Formulation," *Journal of Structural Engineering*, ASCE, Vol. 123, No. 6, June, pp. 736-744.
- Hajjar, J. F., Gourley, B. C., and Olson, M. C. (1997). "A Cyclic Nonlinear Model for Concrete-Filled Tubes. II. Verification," *Journal of Structural Engineering*, ASCE, Vol. 123, No. 6, June, pp. 745-754.
- Herrera, R. (2005). "Seismic Behavior of Concrete-Filled Tube Column-Wide Flange Beam Frames," Ph.D. dissertation, Department of Civil and Environmental Engineering, Lehigh University, Bethlehem, PA, September.
- Hooper, J. D. P., Roeder, C. W., and Klemencic, R. P. (1999). "Best of Both Worlds," *Civil Engineering Magazine*, Vol. 69, No. 1, pp. 40-42.
- Hsiao, K. and Jang, J. (1989). "Nonlinear Dynamic Analysis of Elastic Frames," *Computers & Structures*, Vol. 33, No. 4, pp. 1057- 1063.
- Huang, Z. (2005). "Seismic Behavior of Moment Resisting Frames With High-Strength Square CFT Columns," Ph.D. dissertation, Department of Civil and Environmental Engineering, Michigan State University, East Lansing, MI.
- Iervolino, I. (2004). "Record Selection for Nonlinear Seismic Analysis of Structures," Ph.D. dissertation, European School of Advanced Studies on Seismic Risk, Rose School, Italy.
- Inai, E., Mukai, A., Kai, M., Tokinoya, H., Fukumoto, T., and Mori, K. (2004). "Behavior of Concrete-Filled Tube Beam-Columns," *Journal of Structural Engineering*, Vol. 130, No. 2, pp. 189-202.
- Inai, E. and Sakino, K. (1996). "Simulation of Flexural Behavior of Square Concrete Filled Steel Tubular Columns," Proceedings of the Third Joint Technical Coordinating Committee Meeting, U.S.-Japan Cooperative Research Program, Phase 5: Composite and Hybrid Structures, Hong Kong, December 12-14, 1996, National Science Foundation, Arlington, Virginia.
- Izzuddin, B. A. and Elnashai, A. S. (1993). "Eulerian Formulation for Large-Displacement Analysis of Space Frames," *Journal of Engineering Mechanics*, Vol. 119, No. 3, pp. 549-569.

- Jalayer, F. (2003). "Direct Probabilistic Seismic Analysis: Implementing Non-Linear Dynamic Assessments," Ph.D. dissertation, Department of Civil and Environmental Engineering, Stanford University, Stanford, CA.
- Johansson, M. and Gylltoft, K. (2002). "Mechanical Behavior of Circular Steel--Concrete Composite Stub Columns," *Journal of Structural Engineering*, Vol. 128, No. 8, pp. 1073-1081.
- Karren, K. W. (1967). "Corner Properties of Cold-Formed Steel Shapes," *Journal of the Structural Division*, ASCE, Vol. 93, No. 1, pp. 401-432.
- Karsan, I. D. and Jirsa, J. O. (1969). "Behavior of Concrete Under Compressive Loadings," *Journal of the Structural Division*, ASCE, Vol. 95, No. ST12, pp. 2543-2563.
- Kawaguchi, J. and Morino, S. (2001). "Experimental Study on Elasto-Plastic Behavior of Three-Dimensional Frame Consisting of CFT Column," *J. Struct. Constr. Eng.*, AIJ, No. 541, pp. 187-195.
- Kawaguchi, J. (2000). "Experimental Study on The Elastic-Plastic Behavior of Concrete-Filled Steel Tube Structures," Internal Report, Mie University, Tsu-shi, Japan, December.
- Kim T., Whittaker, S., Gilani A. S. J., Bertero, V. V., and Takhirov, S. M. (2002). "Experimental Evaluation of Plate-Reinforced Steel Moment-Resisting Connections," *Journal of Structural Engineering*, Vol. 128, No. 4, pp. 483-491.
- Koester, D. B. (2000). "Panel Zone Behavior of Moment Connections Between Rectangular Concrete Filled Steel Tubes and Wide Flange Beams," Ph.D. Dissertation, The University of Texas at Austin, Austin, TX, 2000.
- Krawinkler, H., Medina, R., and Alavi, B. (2003). "Seismic Drift and Ductility Demands and Their Dependence on Ground Motions," *Engineering Structures*, Vol. 25, pp. 637-653.
- Krawinkler, H. (1998). "Issues and Challenges in Performance Based Seismic Design," Proceedings of the First Structural Engineers World Congress, San Francisco, California, July 18-23, 1998, Elsevier Science Ltd., Oxford, United Kingdom.
- Krawinkler et al. (1983). "Recommendations for Experimental Studies on the Seismic Behavior of Steel Components and Materials," Report No. 61, John A. Blume Earthquake Engineering Center, Stanford University, Stanford, California.

- LaFore, S. and Hajjar, J. F. (2005). "Design of Concrete-Filled Steel Tube Frames for Assessment Under Seismic Loading," Report No. ST-05-1, Department of Civil Engineering, University of Minnesota, Minneapolis, Minnesota, May.
- Lee, J. and Fenves, G. L. (1998). "Plastic-Damage Model for Cyclic Loading of Concrete Structures," *Journal of Engineering Mechanics*, ASCE, Vol. 124, No. 8, pp. 892-900.
- Lee, S., Manuel, F. S., and Rossow, E. C. (1968). "Large Deflections and Stability of Elastic Frames," *Journal of Engineering Mechanics Division*, 94 EM2, pp. 521-547.
- Liang, Q. Q. and Uy, B. (1998). "Parametric Study on the Structural Behavior of Steel Plates in Concrete-Filled Fabricated Thin-Walled Box Columns," *Advances in Structural Engineering*, Vol. 2, No. 1, pp. 57-71.
- Limkatanyu, S. and Spacone, E. (2001). "Reinforced Concrete Frame Element with Bond Interfaces. II: State Determinations and Numerical Validation," *Journal of Structural Engineering*, Vol. 128, No. 3, pp. 356-364.
- Lin, M., Weng, Y., Tsai, K., Hsiao, P., Chen, C., and Lai, J. (2004). "Pseudo -Dynamic Test OF a Full-Scale CFT/BRB Frame: Part 3 - Analysis and Performance Evaluation," 13th World Conference on Earthquake Engineering, Vancouver, B.C., Canada, August 1-6, 2004.
- Lu, Y. and Kennedy, D. (1994). "Flexural Behavior of Concrete-Filled Hollow Structural Sections," *Canadian Journal of Civil Engineering*, Vol. 21, No. 1, February, pp. 11-130.
- Luco, N. and Cornell, C. A. (2000). "Effects of Connection Fractures on SMRF Seismic Drift Demands," Proceedings of the 6th U.S. National Conference on Earthquake Engineering, Earthquake Engineering Research Institute, Oakland, California.
- Lukey, A. F. and Adams, P. F. (1969). "Rotation Capacity of Beams under Moment Gradient," *Journal of the Structural Division*, Vol. 95, No. 6, pp. 1173-88.
- Mamaghani, I. H. P., Mizuno, E., and Usami T. (1995). "Cyclic Behavior of Structural Steels. I: Experiments," *Journal of Engineering Mechanics*, ASCE, Vol. 121, No. 11, pp. 1158-1164.
- Mander, J. B., Priestly, M. J. N., and Park, R. (1988). "Observed Stress-Strain Behavior of Confined Concrete," *Journal of Structural Engineering*, Vol. 114, No. 8, pp. 1827-1849.

- Mander, J. B., Priestly, M. J. N., and Park, R. (1984). "Seismic Design of Bridge Piers," Department of Civil Engineering, University of Canterbury, Report 84-2, Canterbury, New Zealand, Feb.
- Mattiasson, K. (1981). "Numerical Results from Large Deflection Beam and Frame Problems Analyzed by Means of Elliptic Integrals," *International Journal of Numerical Methods in Engineering*, Vol. 17, No. 1, pp. 145-153.
- McGuire, W., Gallagher, R. H., and Zeimian, R. D. (2000). *Matrix Structural Analysis*, John Wiley & Sons, New York, NY.
- Medina R. A. (2002). "Seismic Demands for Non Deteriorating Frame Structures and Their Dependence on Ground Motions," Ph.D. dissertation, Department of Civil and Environmental Engineering, Stanford University, Stanford, CA.
- Mehanny, S. S. F. and Deierlein, G. G. (2000). "Modeling of Assessment of Seismic Performance of Composite Frames with Reinforced Concrete Columns and Steel Beams," Report No. 135, John A. Blume Earthquake Engineering Center, Stanford University, CA, August.
- Menegotto, M. and Pinto, P. E. (1973). "Method of Analysis for Cyclically Loaded Reinforced Concrete Plane Frames Including Changes in Geometry and Nonelastic Behavior of Elements under Combined Normal Force and Bending," In: IABSE Symp. Resistance and Ultimate Deformability of Structures Acted on by Well-Defined Repeated Loads (4th Edn. ed.), Final Report (1973), Lisbon, Portugal.
- Mizuno, E., Shen, C., Tanaka, Y., and Usami, T. (1991). "A Uniaxial Stress-Strain Model for Structural Steels under Cyclic Loading," *Stability and Ductility of Steel Structures Steels under Cyclic Loading*, Fukumoto, Y. and Lee, G. C. (eds.), CRC Press, Boca Raton, Florida, pp. 37-48.
- Morales, L. E. (1994). "Object-Oriented Software and Advanced Analysis of Steel Frames," M.S. thesis, School of Civil Engineering, Purdue University, West Lafayette, IN, August.
- Morino, S., Kawaguchi, J., Yasuzaki, C., and Kanazawa, S. (1993). "Behavior of Concrete-Filled Steel Tubular Three-Dimensional Subassemblages," *Composite Construction in Steel and Concrete II*, Proceedings of the Engineering Foundation Conference, Easterling, W. S. and Roddis, W. M. (eds.), Potosi, Missouri, June 14-19, 1992, ASCE, New York, New York, pp. 726-741.
- Morishita, Y., Tomii, M., and Yoshimura, K. (1979a). "Experimental Studies on Bond Strength in Concrete Filled Circular Steel Tubular Columns Subjected to Axial Loads," *Transactions of the Japan Concrete Institute*, Vol. 1, pp. 351-358.

- Morishita, Y., Tomii, M., and Yoshimura, K. (1979b). "Experimental Studies on Bond Strength in Concrete Filled Square and Octagonal Steel Tubular Columns Subjected to Axial Loads," *Transactions of the Japan Concrete Institute*, Vol. 1, pp. 359-366.
- Muhummud, T. (2003). "Seismic Behavior and Design of Composite SMRFs with Concrete Filled Steel Tubular Columns and Steel Wide Flange Beams," Ph.D. dissertation, Department of Civil and Environmental Engineering, Lehigh University, Bethlehem, PA, November.
- Nakahara, H. and Sakino, K. (1998). "Axial Compressive and Uniform Bending Tests of High Strength Concrete Filled Square Steel Tubular Columns," *Proceedings of the Fifth Pacific Structural Steel Conference*, Seoul, Korea, October 13-16, 1998, pp. 943-948.
- Nakahara, H., Sakino, K. and Inai, E. (1998). "Investigation of Concrete-Filled Steel Tubes Under Cyclic Bending and Buckling," *Transactions of the Japan Concrete Institute*, Vol. 20, pp. 171-178.
- Nakai, H., Kawai, T., Yoshikawa, O., Kitada, T., and Miki, T. (1982). "A survey on steel piers," *Bridge and Found. Engrg.*, Vol.16, No. 6, pp. 35-40, pp. 43-49 (in Japanese).
- Neuenhofer, A. and Filippou, F. C. (1998). "Geometrically Nonlinear Flexibility-Based Frame Finite Element," *Journal of Structural Engineering*, ASCE, Vol. 124, No. 6, pp. 704-711.
- Nishiyama, Morino, S., Sakino, K., Nakahara, H., Fujimoto, T., Mukai, A., Inai, E., Kai, M., Tokinoya, H., Fukumoto, T., Mori, K., Yoshioka, K., Mori, O., Yonezawa, K., Uchikoshi, M., and Hayashi, Y. (2002). "Summary of Research on Concrete-filled Structural Steel Tube Column System Carried Out Under The US-JAPAN Cooperative Research Program on Composite and Hybrid Structures," BRI Research Paper No. 147, Building Research Institute, Tsukuba, Japan, January.
- Nowak A. S. and Collins, K. R. (2000). *Reliability of Structures*, Mc Graw-Hill, New York, NY.
- Nukala, P. K. V. V. and White, D. W. (2004). "Variationally Consistent State Determination Algorithms for Nonlinear Mixed Beam Finite Elements," *Computer Methods in Applied Mechanics and Engineering*, Vol. 193, Nos. 33-35, pp. 3647-3666.

- Nukala, P. (1997). "Three Dimensional Second-Order Inelastic Analysis of Steel Frames," Ph.D. dissertation, Department of Civil and Environmental Engineering, Purdue University, West LaFayette, IN.
- OpenSEES 2001. Open System For Earthquake Engineering Simulation. Berkeley, CA: Pacific Earthquake Engineering Research Center, University of California at Berkeley.
- Palermo, D. and Vecchio, F. J. (2003). "Compression Field Modeling of Reinforced Concrete Subjected to Reversed Loading: Formulation," *ACI Structural Journal*, ACI, Vol. 100, No. 5, September-October, pp. 616-625.
- Park, R., Priestly, M. J. N, and Gill, W. D. (1982). "Ductility of Square-Confined Concrete Columns," *Journal of the Structural Division*, ASCE, Vol. 108, No. 4, pp. 929-950.
- Peng, S. W. (2001). "Seismic Resistant Connections for Concrete Filled Tube Column-to-WF Beam Moment Resisting Frames," Ph.D. dissertation, Department of Civil and Environmental Engineering, Lehigh University, Bethlehem, Pennsylvania, March.
- Ramberg, W. and Osgood, W. R. (1943). "Description of Stress-Strain Curves by Three Parameters"
- Reddy, J. N. (1993). *An Introduction to the Finite Element Method*, McGraw-Hill, Inc., New York, NY.
- Roeder, C. W., Cameron, B., and Brown, C. B. (1999). "Composite Action in Concrete Filled Tubes," *Journal of Structural Engineering*, ASCE, Vol. 125, No. 5, pp. 477-484.
- Saatcioglu, M. and Razvi, S. R. (1992). "Strength and Ductility of Confined Concrete," *Journal of Structural Engineering*, ASCE, Vol. 118, No. 6, pp. 1590-1607.
- Sakino, K. and Yuping, S. (1994). "Stress-strain Curve of Concrete Confined by Rectilinear Hoop," *Journal of Structural Construction Engineering*, AIJ, No. 461, July, pp. 95-104.
- Sakino, K. and Ishibashi, H. (1985). "Experimental Studies on Concrete Filled Square Steel Tubular Short Columns Subjected to Cyclic Shearing Force and Constant Axial Force," *Transactions of the Architectural Institute of Japan*, No. 353, pp. 81-89.

- Sakino, K. and Tomii, M. (1981). "Hysteretic Behavior of Concrete Filled Square Steel Tubular Beam-Columns Failed in Flexure," *Transactions of the Japan Concrete Institute*, Vol. 3, pp. 439-446.
- Salari, M. R. and Spacone, E., Shing, P. B., and Frangopol, D. M. (1998). "Nonlinear Analysis of Composite Beams with Deformable Shear Connectors," *Journal of Structural Engineering*, Vol. 124, No. 10, pp. 1148-1158.
- Salmon, C. G. and Johnson, J. E. (1996). *Steel Structures Design and Behavior*, Prentice-Hall, New Jersey, 1996.
- Schiller, P. H. and Hajjar, J. F. (1998). "A Distributed Plasticity Formulation for Three-Dimensional Rectangular Concrete-Filled Steel Tube Beam-Columns and Composite Frames," Report No. ST-96-5, Department of Civil Engineering, University of Minnesota, Minneapolis, Minnesota, November.
- Schneider, S. P. (1998). "Axially Loaded Concrete-Filled Steel Tubes," *Journal of Structural Engineering*, ASCE, Vol. 124, No. 10, October, pp. 1125-1138.
- Schneider, S. P. and Alostaz, Y. M. (1998). "Experimental Behavior of Connections to Concrete-filled Steel Tubes," *Journal of Constructional Steel Research*, Vol. 45, No. 3, pp. 321-352.
- Shakir-Khalil, H. and Al-Rawdan, A. (1995). "Behaviour of Concrete-Filled Tubular Edge Columns," Proceedings, Istanbul, Turkey, June.
- Shakir-Khalil, H. and Mahmoud, M. A. (1995). "Steel Beam Connections to Concrete-Filled Tubular Columns," Nordic Steel Construction Conference '95, Sweden, June.
- Shakir-Khalil, H. (1994). "Experimental Study of Concrete-Filled Rectangular Hollow Section Columns," *Structural Engineering Review*, Vol. 6, No. 2, pp. 85-96.
- Shakir-Khalil, H. and Hassan, N. K. A. (1994). "Push-Out Resistance of Concrete-Filled Tubes," Tubular Structures VI, Proceedings of the Sixth International Symposium on Tubular Structures, Grundy, P., Holgate, A., and Wong, W. (eds.), Melbourne, Australia, 14-16 December 1994, A. A. Balkema, Rotterdam, The Netherlands, pp. 285-291.
- Shakir-Khalil, H. (1993a). "Pushout Strengths of Concrete-Filled Steel Hollow Sections," *The Structural Engineer*, Vol. 71, No. 13, July 6, pp. 230-233.
- Shakir-Khalil, H. (1993b). "Resistance of Concrete-Filled Steel Tubes to Pushout Forces," *The Structural Engineer*, Vol. 71, No. 13, July 6, pp. 234-243.

- Shakir-Khalil, H. and Mouli, M. (1990). "Further Tests on Concrete-Filled Rectangular Hollow-Section Columns," *The Structural Engineer*, Vol. 68, No. 20, pp. 405-413.
- Shakir-Khalil, H. and Zeghiche, Z. (1989). "Experimental Behavior of Concrete-Filled Rolled Rectangular Hollow-Section Columns," *The Structural Engineer*, Vol. 67, No. 19, pp. 345-353.
- Sheikh, S. A. and Uzumeri, S. M. (1982). "Analytical Model for Concrete Confinement in Tied Columns," *Journal of the Structural Division*, Vol. 108, No. 12, pp. 2703-2722.
- Shen, C., Mamaghani, I. H. P., Mizuno, E., and Usami, T. (1995). "Cyclic Behavior of Structural Steels. II: Theory," *Journal of Engineering Mechanics*, Vol. 121, No. 11, pp. 1165-1172.
- Sherman, D. R. (1992). "Tubular Members" *Constructional Steel Design: An International Guide*, Dowling, P. J., Harding, J. E., and Bjorhovde, R. (eds.), Elsevier Science Publishers Ltd., New York, NY, pp. 91-104.
- Shome N., Cornell C.A., Bazzurro, P., Carballo J.E., (1998). "Earthquakes, Records, and Nonlinear Responses," *Earthquake Spectra*, Vol. 14, No. 3, pp. 469-500.
- Sinha, B. P., Gerstle, K. H. and Tulin, L. G. (1964). "Stress-Strain Relations for Concrete Under Cyclic Loading," *Journal of the American Concrete Institute*, Vol. 61, No. 2, February, pp. 195-211.
- Souza, R. M. (2000). "Force-based Finite Element for Large Displacement Inelastic Analysis of Frames," Ph.D. dissertation, Department of Civil and Environmental Engineering, University of California at Berkeley, Berkeley, CA, December.
- Southwell, R. V. (1941). *Introduction to The Theory of Elasticity for Engineers and Physicists*, Oxford University Press.
- Sully, R. M. and Hancock, G. J. (1996). "Behavior of Cold-Formed SHS Beam-Columns," *Journal of Structural Engineering*, ASCE, Vol. 122, No. 3, pp. 326-336.
- Susantha. K.A.S., Ge H., and Usami T. (2001). "Uniaxial stress-strain relationship of concrete confined by various shaped steel tubes," *Engineering Structures*, Vol. 23, No. 10, pp. 1331-1347.
- Taucer, F. Spacone, E., and Filippou, F. (1991). "A Fiber Beam-Column Element for Seismic Response Analysis of Reinforced Concrete Structures," Report No. UCB/EERC-91/17, College of Engineering, University of California at Berkeley, Berkeley, CA.

- Teh, L. H. and Clarke, M. J. (1998). "Co-rotational and Lagrangian formulations for elastic three-dimensional beam finite elements," *Journal of Constructional Steel Research*, Vol. 48, Nos. 2-3, pp. 123-144.
- Tomii, M. and Sakino, K. (1979). "Experimental Studies on the Ultimate Moment of Concrete Filled Square Steel Tubular Beam-Columns," Transactions of the Architectural Institute of Japan, No. 275, January, pp. 55-63.
- Tort, C. and Hajjar, J. F. (2004). "Damage Assessment of Rectangular Concrete-Filled Steel Tubes for Performance-Based Design," *Earthquake Spectra*, Vol. 20, No. 4, pp. 1317-1348.
- Tort, C. and Hajjar, J. F. (2003). "Damage Assessment of Concrete-Filled Steel Tube Members and Frames," Report No. ST-03-1, Department of Civil Engineering, University of Minnesota, Minneapolis, MN, April.
- Tsai, W. T. (1988). "Uniaxial Compressional Stress-Strain Relation of Concrete," *Journal of Structural Engineering*, Vol. 114, No. 9, pp. 2133-2136.
- Uy, B. (1998). "Local and Post-Local Buckling of Concrete Filled Steel Welded Box Columns," *Journal of Constructional Steel Research*, Vol. 47, Nos. 1-2, July-August, pp. 47-72.
- Uy, B. and Bradford, M.A. (1996). "Elastic local buckling of steel plates in composite steel-concrete members," *Engineering Structures*, Vol. 18, No. 3, pp. 193-200.
- Varma A. H. , Ricles, J. M., Sause, R., and Lu, L. (2002). "Seismic behavior and modeling of high-strength composite concrete-filled steel tube (CFT) beam-columns," *Journal of Constructional Steel Research*, Vol. 58, Nos. 5-8, pp 725-758.
- Varma, A. H. (2000). "Seismic Behavior, Analysis, and Design of High Strength Square Concrete Filled Steel Tube (CFT) Columns," Ph.D. dissertation, Department of Civil and Environmental Engineering, Lehigh University, Bethlehem, Pennsylvania, November.
- Viridi, P. J. and Dowling, K. S. (1980). "Bond Strength In Concrete Filled Steel Tubes," *IABSE Periodica*, August, pp. 125-139.
- VISION 2000 (1995). A Framework for Performance-Based Earthquake Engineering, Structural Engineers Association of California, Sacramento, CA.
- White, D. (1986). "Material and Geometric Nonlinear Analysis of Local Planar Behavior in Steel Frames Using Interactive Computer Graphics," M.S. thesis, Department of Structural Engineering, Cornell University, Ithaca, NY.

- Wright, H. D. (1993). "Buckling of Plates in Contact with a Rigid Medium," *Structural Engineer*, Vol. 71, No. 12/15, pp. 209-215.
- Yang, Y. B. and Kuo, S. R. (1994). *Theory and Analysis of Nonlinear Framed Structures*, Prentice-Hall, Inc., Englewood Cliffs, New Jersey.
- Yang, Y. and Leu, L. (1991). "Force Recovery Procedures in Nonlinear Analysis," 4. *International Conference on Civil and Structural Engineering Computing*, Vol. 1, Sept. 19-21, 1989, London, UK, pp. 275-280.
- Yankelevsky, D. Z. and Reinhardt, H. W. (1987). "Model for Cyclic Compressive Behavior of Concrete," *Journal of Structural Engineering*, ASCE, Vol. 113, No.2, pp. 228-239.
- Yankelevsky, D. Z. and Reinhardt, H. W. (1989). "Uniaxial Behavior of Concrete in Cyclic Tension," *Journal of Structural Engineering*, ASCE, Vol. 115, No. 1, pp. 166-182.
- Yan-Lin, G. (1992). "Local and Overall Interactive Instability of Thin-Walled Box-Section Columns," *Journal of Constructional Steel Research*, Vol. 22, No. 1, pp.1-19.
- Yun, S., Hamburger, R. O., Cornell, C. A., and Foutch, D. A. (2002). "Seismic Performance Evaluation for Steel Moment Frames," *Journal of Structural Engineering*, ASCE, Vol. 128, No. 4, pp. 534-545.
- Zeris, C. A. and Mahin, S. A. (1988). "Analysis of Reinforced Concrete Beam-Columns under Uniaxial Excitation," *Journal of Structural Engineering*, ASCE, Vol. 114, No. 4, pp. 804-820.
- Zhang, W. and Shahrooz, B. M. (1997). "Analytical and Experimental Studies into Behavior of Concrete-Filled Tubular Columns," Report No. UC-CII 97/01, Cincinnati Infrastructure Institute, Department of Civil and Environmental Engineering, University of Cincinnati, College of Engineering, Cincinnati, OH, May.
- Zienkiewicz, O. C., Taylor R. L., and Zhu, J. Z. (2005). *The finite element method for solid and structural mechanics*, McGraw-Hill, Inc., New York, NY.